المجلة العراقية الوطنية لعلوم الارض

INJES

P-ISSN 1682-3222
E-ISSN 2664-2816



https://earth.uomosul.edu.iq Scopus E-mail injes@uomosul.edu.iq

العدد [4] 2026 تشرين الأول المجلد [26]

Iraqi National Journal of Earth Science No. [4] October. 2026 Vol. [26]

Iraqi National Journal of Earth Science

INJES

P-ISSN 1682-3222
E-ISSN 2664-2816



https://earth.uomosul.edu.iq Scopus E-mail injes@uomosul.edu.iq

Vol. [26] October . 2026 No. [4]

المجلة العراقية الوطنية لعلوم الأرض

المجلد السادس والعشرون تشرين الأول 2026 العدد الرابع

رئيس التحرير

الأستاذ الدكتور ريان غازي ذنون

مدير التحرير

الاستاذ المساعد الدكتور عزالدين صالح الجوادي

أعضاء هيئة التحرير

الأستاذ الدكتور ماجد مجدي عبد المجيد

الأستاذ الدكتور حاجي رحاب (الجزائر)

الأستاذ الدكتور عزالدين نجم الدين بابان

الأستاذ الدكتور ألين بريت (بلجيكا)

الأستاذ الدكتوره سوسن حميد فيصل الهزاع

الأستاذ الدكتور رافع إبراهيم عبدالله الحميدي

الأستاذ المساعد الدكتور محمد فوزي عمر

الأستاذ المساعد الدكتور عمر عبدالله إسماعيل

الاستاذ المشارك الدكتور هيثم إسماعيل حامد

الأستاذ المساعد الدكتور مهدي رهناما (ايران)

الأستاذ المساعد الدكتور بشار عزيز محمود

الأستاذ الدكتور معز بن فاضل (تونس)

الأستاذ الدكتور شريف فاروق محمد (مصر)

الأستاذ الدكتور باسم سيد نبوي (مصر)

الأستاذ الدكتور مصدوق محمد إبراهيم التاج (الأردن)

الأستاذ الدكتور ستار جبار رشيد الخفاجي

الأستاذ المساعد الدكتور عاهد يونس عبدالله الملاح

الأستاذ المساعد الدكتوره نمام محمد صالح

الأستاذ المساعد الدكتور فلاح عبد محمد المعماري

الأستاذ المساعد الدكتور صدام عيسى مصطفى الخاتوني

الأستاذ المساعد الدكتور راشد بورميزراني (ايران)

إدارة المنظومة الالكترونية للمجلة

الأستاذ المساعد الدكتور صدام عيسى مصطفى الخاتوني

الشؤون الفنية والتنسيق والنشر

المدرس المساعد مُيسر سمير محمود السراج

معاون باحث ازهار نزار ادريس الكلو

الشؤون الإدارية: المدرس المساعد هبة عصام ذنون

إصدار: كلية العلوم/ جامعة الموصل

p-ISSN: 1682-3222

e-ISSN: 2664-2816

البريد الالكتروني: injes@uomosul.edu.iq

الموقع الالكتروني: http://www.iasj.net

https://earth.uomosul.edu.iq

الموبايل: 009647701610916

رقم الإيداع في دار الكتب و الوثائق ببغداد (**1310** لسنة **2009**)

المحتويات

تقدير الجريان السطحي في حوض كبيل باستخدام نموذج SCS-CN وتحليل العلاقات الارتباطية مع خصائص حوض التصريف

ناديه صديق رمضان ، جهاد ابراهيم سليم 1

تقييم صلاحية صخور الحجر الجيري في منطقة الشرقاط كمواد بناء وكركام لرصف السكك الحديدية/ شمالي العراق

لؤي موسى راوي ، نهاد سعود الجبوري ، احمد ابراهيم محمد 19

دراسة بعض الخواص تقييم استقرارية المنحدرات الصخرية على الجناح الشمالي الشرقي لطية مكحول المحدبة، شمالي العراق

رفل أمجد خضير، محمد راشد عبود ، عبد السلام مهدي ترف 26

المجلة العراقية الوطنية لعلوم الأرض

www.earth.uomosul.edu.iq

تقدير الجريان السطحي في حوض كبيل باستخدام نموذج SCS-CN وتحليل العلاقات الارتباطية مع خصائص حوض التصريف

نادية صديق رمضان[1*]، nadiaramadha9@gmail.com

جهاد ابراهيم سليم[2] jihad.salim@uod.ac

[1] قسم الجغرافيا الطبيعية، كلية العلوم الإنسانية، جامعة دهوك، دهوك، العراق.

[2] قسم الغابات، كلية علوم الهندسة الزراعية، جامعة دهوك، دهوك، العراق.

* الباحث المراسل.

تاريخ الاستلام: 25 أيار 2025 تاريخ المراجعة: 01 تموز 2025 تاريخ القبول: 18 آب 2025

تاريخ النشر الالكتروني: 01 تشرين الأول 2026

الملخص

يُعَدّ تقدير الجريان السطحي عاملًا رئيسيًا في إدارة الموارد المائية، خصوصًا في البيئات الجافة وشبه الجافة. يهدف هذا البحث إلى تحليل الخصائص الهيدرولوجية لحوض كبيل، الذي تبلغ مساحته (404.65 كم^2) باستخدام نموذج (SCS-CN)، وجدت ثلاث مجموعات من الترب الهيدرولوجية (B, C, D) استنادًا إلى عينات التربة المأخوذة من منطقة الدراسة، وتم تصنيف الغطاء الأرضي إلى ثمانية أصناف، كما تم تحليل بيانات الأمطار اليومية للسنة المائية (2023–2024) لثلاث محطات تقع داخل منطقة الدراسة (ئاكرى، دينارته، بجيل). تم الاعتماد على طريقة مضلعات ثيسين في توزيع الأمطار مكانيًا. بلغت كمية الأمطار المتساقطة في دينارته (1761.8 ملم)، وفي ئاكرى (994.9 ملم)، وفي بجيل (1502 ملم)، في حين بلغ عمق الجريان السطحي (549.46 ملم) في دينارته و(145.11ملم) في ئاكرى، و (442.89 ملم) في بجيل، بينما سُجّل حجم الجريان السطحي في حوض كبيل (132851245.8 م^3) وشكّل 24.8% من حجم السواقط على الحوض. سُجل اعلى مقدار من الجريان السطحي في محطة بجيل بمقدار (57270105.9 م^3)، تليها محطة دينارتة (48415096.8 م^3)، واقل مقدار كان في محطة ئاكرى (27166043.1 م^3)، وبنسب جريان (31.18%) و(29.48%) و(14.60%) على التوالي، وبينت الدراسة ان للسيح علاقة ارتباط موجبة مع كل من الامطار(P) ومعامل الاستخلاص الأولي (Ia) والمنسوب (E) والانحدار(LS) ونوع التربة (S). وسجلت اقوى علاقة ارتباط مع الامطار، اذ بلغت قيمة (r) 0.93، بينما علاقة الارتباط السلبية كانت مع كل من رقم المنحنى (CN) واستخدامات الارض (LCLU) حيث بلغت قيمة (r) – 0.56 و –0.46 على التوالي. وأكدت نتائج الدراسة أن نموذج (SCS-CN) يُعَدّ أداة فعالة لتقدير الجريان السطحي مما يعزز استخدامه في إدارة الموارد المائية خصوصًا في المناطق التي تعاني من تباين كبير في التساقط المطري.

الكلمات المفتاحية:

السيح السطحي، الأمطار، SCS-CN

DOI: 10.33899/injes.v26i4.56210, ©Authors, 2026, College of Science, University of Mosul.
This is an open-access article under the CC BY 4.0 license (http://creativecommons.org/licenses/by/4.0/).

==========

1. المقدمة

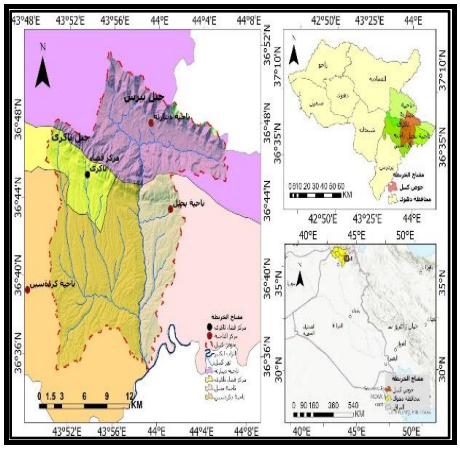
يُعد الجريان السطحي (Runoff) من أهم الموارد المائية، خاصة في البيئات الجافة وشبه الجافة. لهذا السبب لجأت العديد من الدول إلى الاستفادة من هذا المورد، وذلك من خلال إقامة السدود لخزن مياه الأمطار والتي تتحول الى جريان مائي سطحي. ولا تقتصر الغاية من دراسة الجريان السطحي على تأمين مياه الشرب والري وتغذية المخزون الجوفي، بل ايضا تقدير حجم الجريان السطحي الذي يُعد أمراً بالغ الأهمية في المشاريع المرتبطة بالرواسب والتآكل، إذ يساهم في وضع استراتيجيات للحد من التعرية وحماية الموارد المائية، والتنبؤ بمخاطر الفيضانات، وتقييم الخسائر المحتملة. هناك العديد من الطرائق المتبعة للوصول إلى تقدير حجم الجريان المائي، من ابرزها طريقة (SCS-CN) التي طورتها أدارة حفظ التربة التابعة لإدارة الزراعة (Soil Conservation Service Method, SCS) بالولايات المتحدة الأمريكية (USDA, 1986) ويهدف البحث إلى تخمين كميات الجريان السطحي في حوض كبيل وذلك عبر تحليل البيانات المناخية والهيدرولوجية، وبالاستفادة من نموذج (SCS-CN) في تقدير حجم

المياه السطحية المتاحة. وتم العمل وفقاً لهذه الطريقة ضمن برنامج (Arc GIS Pro.3.0)، ومدعما بالبيانات المستخلصة من المرئيات الفضائية. وتم تصنيف التربة بحسب أصناف الترب الهيدرولوجية التي حددتها طريقة (SCN-CN) لتحديد المناطق ذوات الجريان السطحي العالي استنادا الى معطيات الحوض ووضع حلول علمية لتوظيفها في إدارة الموارد المائية وبنيت الدراسة على فرضية مفادها ان حوض كبيل يشهد معدلات جريان سطحي مرتفعة , خصوصا خلال فترات هطول الامطار الغزيرة , مما يعزز إمكانية استثمار هذه المياه بطرق مستدامة

2. موقع الدراسة

تقع منطقة الدراسة جغرافياً في إقليم كوردستان (شمالي العراق)، وتحديداً شرقي محافظة دهوك ضمن الحدود الإدارية لقضاء ئاكرى، ويحدد موقعه الإحداثيات الجغرافية بين خطي طول (43°51'20") و (43°55'34") شرقاً ودائرتي العرض (36°45'45") و (36°53'45") شمالاً. تبلغ مساحة منطقة الدراسة (404.65) كم^2 تتوزع على ثلاثة نواحي ادارية هي دينارتة وبجيل وكردسين بنسب (3.59% و 23.15% و 28.06%) على التوالي، اما الجزء الباقي (33.99%) فيقع ضمن مركز قضاء ئاكرى كما هو مبين في الشكل (1). ويمتلك حوض كبيل طوبوغرافية متنوعة، حيث تسود في الجزء الشمالي للحوض جبال عالية ومن اهمها جبل بيرس وجبل عقرة وجبل سري صادا، وينبع من بين هذه الجبال نهر كبيل والذي يعتبر الشريان الحيوي للمنطقة، اما الجزء الوسطي والجزء الجنوبي من الحوض فهما عبارة عن تلال وهضاب وسهول تشكل مناطق زراعية خصبة ومراعي. اما الحدود الزمانية فتتحدد بالبيانات المناخية للمحطات المناخية (ئاكرى ودينارته وبجيل) لسنة (2023-2024).

أوضحت دراسة (Al-Kanani and Al-Asadi, 2020) أن نموذج (SCS-CN) يُعد من النماذج الفعالة في تقدير عمق الجريان السطحي لحوض وادي أبو غار باستخدام قيم (CN) وبيانات مطرية للفترة (2019–2009)، حيث بلغ عمق الجريان السطحي الناتج عن اعلى عاصفة مطرية (77.07) ملم. وأظهرت النتائج فعالية النموذج في احتساب الجريان السطحي بدقة. وهدفت دراسة (Al-Darrat, 2020) إلى تحليل الخصائص الهيدرولوجية لوادي الكراث الواقع ضمن بلدية طبرق شمال شرقي ليبيا، باستخدام تقنيات التحسس النائي ونموذج (SCS-CN) الأمريكي لتقدير الجريان السطحي، وأظهرت النتائج أن48% من مساحة الحوض ذات نفاذية منخفضة ما يساعد على توليد الجريان السطحي في زمن قصير من عاصفة مطرية واحدة.



الشكل1: موقع منطقة الدراسة (حوض كبيل)

3. المواد وطرائق العمل

أجرى (Al-Zarfi, 2021) دراسة هيدرولوجية في بادية المثنى باستخدام نموذج (SCS-CN) لتقدير حجم الجريان السطحي من اجل بناء نموذج الملاءمة المكانية لتحديد أفضل موقع للحصاد المائي، بعد حساب قيم معامل الجريان السطحي CN أظهرت النتائج تبايناً ملحوظاً في القيم بين الأحواض. وقام (Omar, 2022) بدراسة هيدرومورفومترية للأحواض الجنوبية لجبل بيخير، حيث ركز على دراسة الخصائص الطبيعية للمنطقة، وتم تحليل الجريان السطحي باستخدام انموذج (SCS-CN)، لتحديد معدلات الجريان في أحواض منطقة الدراسة. وكذلك دراسة (Khadir and Al-Jabouri, 2024) في وادي القصر اعتمدت على نموذج (SCS-CN)، وتم حساب حجم الجريان السطحي للحوض معتمدا على مدخلات كل من الغطاء الارضي وأنماط استخدامها وهيدرولوجية التربة وكميات الأمطار الساقطة، وتم استخراج القيم الخاصة بـ (CN) فضلاً عن تحديد المعاملات التي تعكس سعة احتفاظ التربة بالمياه، وكمية الفاقد من الأمطار قبل الجريان وإمكانية حصاد المياه في حوض وادي السكران.

4. البيانات المستخدمة

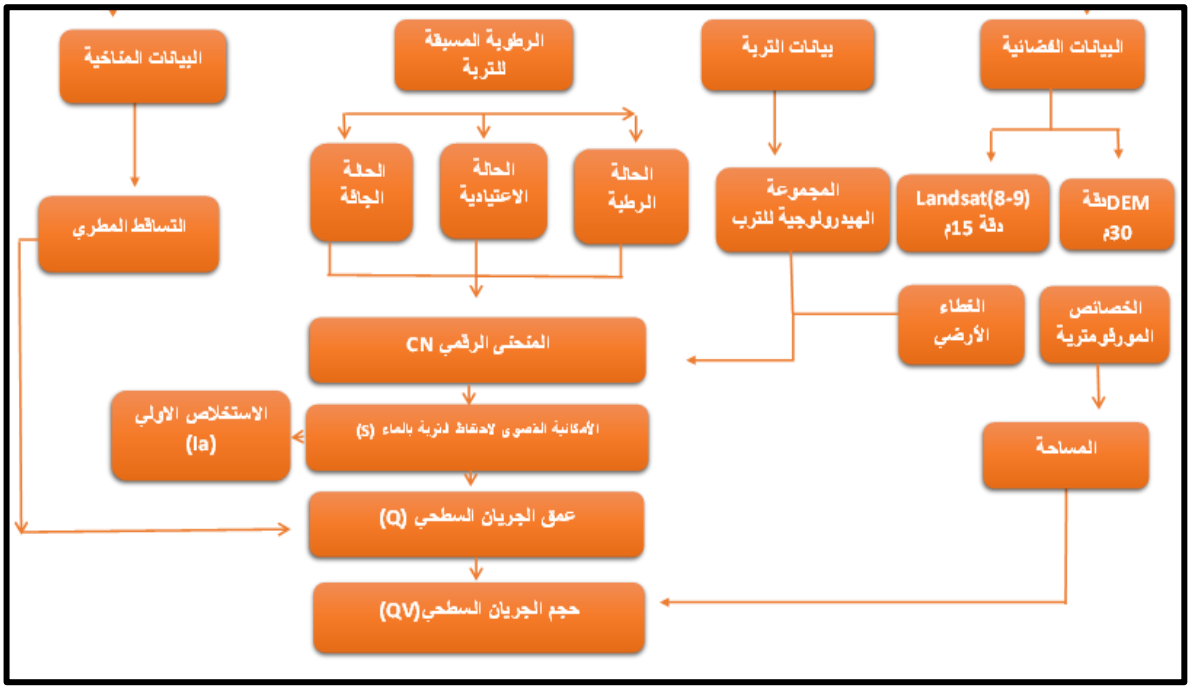
في الدراسة الحالية، تم استخدام مجموعة مختلفة من البيانات من مصادر متنوعة والمبينة ادناه:

1. البيانات الفضائية للقمر الصناعي (Landsat 8,9) الملتقطة بتاريخ (2024/5/25) بدقة (30) متر (https://earthexplorer.usgs.gov).
2. نموذج الارتفاع الرقمي (DEM) بدقة (12.5) متر (https://search.asf.alaska.edu).
3. الخريطة الجيولوجية للعراق تمثلت بخريطة التكوينات الجيولوجية اعتماداً على :-GEOLOGLCAL MAP OF AL MOSUL: QUADRANGLE, SHEET NJ-38-9, Bagdad, Iraq, 2007.
4. بيانات مناخية بالاعتماد على حكومة إقليم كوردستان العراق ووزارة النقل والاتصالات، مديرية الأنواء الجوية والرصد الزلزالي،

والإحصاء والتقارير في دهوك والمتعلقة بكميات الأمطار اليومية لسنة 2023-2024.

5. خريطة التربة بالاعتماد على عينات مختبرية.
6. خريطة الترب الامريكية USDA بعمق 30 سم، بمقياس 1:5000000

5. مراحل استخلاص خصائص الجريان



الشكل2: مخطط يوضح طريقة استخلاص رقم المنحنى والجريان السطحي.

يمكن التعبير عن طريقة (SCS-CN) رياضياً بالشكل التالي (Hassan and Abdulsalam, 2023):

المعادلة الرياضية المعتمدة لقياس منحنى الجريان (Wang and Qin, 2015) هي:

$$Q = \frac{(P-Ia)^2}{(P-Ia+S)} \quad \ldots\ldots (1)$$

حيث إن: Q = عمق الجريان السطحي(ملم)، P = الامطار الساقطة (ملم)، Ia = الفواقد الأولية، S = الامكانية القصوى للاحتفاظ بالماء بعد بدء الجريان السطحي .

ولأن Ia تساوي خُمس قيمة S، فإنها تحسب رياضياً كالاتي:

$$Ia = 0.2*S \ldots\ldots (2)$$

بناء على ذلك، يمكن صياغة المعادلة (1) على النحو التالي:

$$Q = \frac{(P-0.2S)^2}{(P+0.8S)} \quad \ldots\ldots (3)$$

يتم حساب قيمة S وفق المعادلة التالية (USDA, 1986) :

$$S = \frac{CN}{1000} - 10 \ldots\ldots (4)$$

ولتحويل وحدات (S) إلى ملم لتتوافق مع المقاييس المترية، تصبح الصيغة كما يلي:

$$S = \frac{25400}{CN} - 25 \ldots\ldots (5)$$

يشمل أسلوب النموذج الرياضي (SCS-CN) عدداً من المعادلات التي تعتمد على مجموعة من المتغيرات الأساسية لحساب الجريان السطحي. وتتضمن هذه المتغيرات هيدرولوجية التربة وأصناف الغطاء الأرضي وكمية الأمطار الساقطة كما هو موضح في الشكل (2).

ويتم استخراج حجم الجريان السطحي وفق المعادلة التالية (Al-Darrat, 2020):

$$QV = \frac{Q*A}{1000} \quad \ldots\ldots (6)$$

حيث أن QV = حجم الجريان السطحي (م3)، Q = عمق الجريان (ملم)، A = مساحة الحوض (كم2)، 1000= معامل التحويل للحصول على النتائج بـ (م3).

6. خصائص الحوض الطبيعية

A. الخصائص الجيولوجية

تعد الخصائص الصخارية للتكوينات الجيولوجية من العوامل الأساسية التي تؤثر على الخصائص الهيدرولوجية في الأحواض النهرية. وتمت دراسة الخصائص الجيولوجية لحوض كبيل من خلال الكشف عن تكوين ونوع وتوزيع الصخور التي تعكس نوعية الرواسب المعدنية التي كونت تربة الحوض السطحية أو منكشفات التكوينات، إذ تساهم الخصائص الجيولوجية في تشكيل الأحواض النهرية وتحديد أنماط شبكة التصريف النهري واتجاهاتها حيث تنشأ هذه الأنماط نتيجة للتفاعل المعقد بين التضاريس والمناخ ونوعية الصخور وبنيتها (Al-Birmani, 2019). يُعد التركيب الجيولوجي أحد العوامل الهامة التي

تحدد خصائص الحوض، فالمناطق التي تحتوي على صخور عالية المسامية ونسبة كبيرة من الفواصل والشقوق غالباً ما تزداد فيها كمية الفواقد المائية بالتسرب إلى الطبقات تحت السطحية، وبالتالي تقل كمية المياة السطحية في هذه المناطق. بالمقابل، يزداد تدفق المياه السطحية في المناطق التي تحتوي على صخور منخفضة المسامية وفواصل وشقوق قليلة .(Karbal, 1986) بالإضافة إلى ذلك، تلعب الجيولوجيا دورًا حاسماً في تحديد أنسب المواقع لحصاد المياه وفقاً للتكوينات الصخرية المختلفة الموجودة في منطقة الدراسة، وتتكشف في حوض كبيل مجموعة من التكوينات الجيولوجية التي تؤثر بشكل مباشر على خصائصها الهيدرولوجية، اذ تمتد هذه التكوينات عبر عصور جيولوجية مختلفة من الجوراسي إلى الترياسي، مما يساهم في تنوع الخصائص الهيدرولوجية للمنطقة، وينكشف اثنا عشر تكويناً في منطقة الدراسة وهي :

تكوين قمجوقة

يتكون هذا التكوين من طبقات من الصخور الجيرية والدولوماتية، وحجر الطفل الأسود، والغرين، والصلصال، والمارل، ويظهر هذا التكوين على شكل نتوءات بارزة واضحة. مكوناته الصخرية ذات مقاومة ضعيفة للتجوية الكيميائية والتعرية مما أدى إلى تكوين تجاويف في الأجزاء التي تشغلها، لذا، فإن لها أهمية كبيرة في تحقيق الجريان المائي بسبب احتوائها على هذه التجاويف .(Al-Zubaidi, 2018)

تكوين عقرة – بخمة

يتكون من طبقات من الصخور الجيرية وصخور الجير الدولوماتية التي تتميز بألوانها القهوائية المصفرة والرمادية الفاتحة وبتركيبتها البلورية الصلبة جداً. ان ما يميز تكوين عقرة هو الصخور القاسية ذات النفاذية العالية.(Al-Hayali, 2021)

تكوين كولوش

يتكون هذا التكوين من حجر الطفل والحجر الرملي والحجر الغريني والحجر الطيني الأسود. ورغم أن التكوين يتمتع بدرجات عالية من المسامية والنفاذية، إلا أن بيئته الترسيبية المتمثلة في تعاقب الحجر الرملي مع الطين الصفائحي (Hassan and Al-Koran, 2012) أسهمت في الحد من قدرة المياه على التغلغل إلى الأعماق مما أدى إلى تجمع المياه على السطح، وبالتالي ساعد ذلك في نشوء جريان سطحي فعّال وتطور شبكة تصريفية بدلالات مختلفة.

تكوين جركس

يتكون من صخور الطفل الأحمر المائل الى البنفسجي بالإضافة إلى حجر الطين وحجر الرمل والصلصال، كما يتميز هذا التكوين باحتوائه على كميات كبيرة من الجبس في طبقاته العليا إلى جانب صخور المارل .(Ali and Hamad, 2023) ونظراً لكونه يمتاز بالصلابة والمقاومة العالية، فهو يسهم في تعزيز الجريانات المائية على سطحه.

تكوين بلاسبي

يتألف هذا التكوين من قسمين علوي وسفلي، الجزء العلوي يتكون من حجر جيري وصخور طباشيرية ومحتوىً قيري. وقد توجد أيضاً صخور صلصالية بيضاء. أما الجزء السفلي فيحتوي على صخور طباقية صلبة تشمل حجر الكلس الأبيض مع الهيدروكاربونات؛ بالتالي يهيمن حجر الكلس الأبيض على التكوين. ومن حيث النفاذية والمسامية فهو ضعيف النفاذية قليل المسام (Al-Sayyab et al., 1982).

تكوين مقدادية

وهو عبارة عن حجر رملي حصوي وحجر غريني وحجر طيني. يتميز بارتفاع مساميته إلى جانب نفاذية مرتفعة ناتجة عن كبر حجم الفراغات وانتشار الشقوق والفواصل داخلها، لذلك فإن خصائص التكوين تسهم في التقليل من احتمالات الجريانات السطحية والكثافة التصريفية العالية على سطحه .(Ahmed, 2022)

تكوين باي حسن

يتكون من مدملكات ناعمة وخشنة تحتوي على مواد فتاتية بحجم السلت والرمل بلون رمادي غامق تتحول تدريجياً إلى اللون الأحمر في الطبقات العليا المكشوفة نتيجة للخصائص الصخارية المميزة (Salim, 2016). يُسهم التكوين في تعزيز معدلات الترشيح، الأمر الذي ينعكس بانخفاض واضح في حجم الجريانات السطحية.

تكوين انجانة

يتكون من الصلصال الأحمر أو الأصفر مع متداخلات من الحجر الرملي ناعمة الى خشنة وتماسكها ضعيف. يتضمن التكوين فواصلاً وشقوقاً في بعض الأحيان .(Salim, 2016) إن وجود هذه الفواصل والشقوق وبدرجة كبيرة يعزز من أهميته الهيدرولوجية، حيث يسهم في تحسين نفاذية المياه وحركتها داخل التكوين فتُقلل من فرص تشكيل المسيلات المائية .

تكوينات سرمورد، بالامبو، كراكو

يتكون تكوين سرمورد من صلصال مزرق إلى بني، مع تداخلات من صخر جيري صلصالي. أما تكوين بلامبو فتتكون طبقاته من الحجر الجيري البني الرمادي الداكن والمارل الأخضر الزيتوني والدولومايت. يتكون تكوين كراكو من الحجر الجيري الرملي الخشن الحبيبي-Al) .Koran, 2011) اما هيدرولوجيا، فتساهم هذه التكوينات الثلاثة في تقليل حجم الجريان السطحي نتيجة لخواصها المسامية التي تسهم في الترشيح إلى الطبقات العميقة.

ترسبات السهل الفيضي

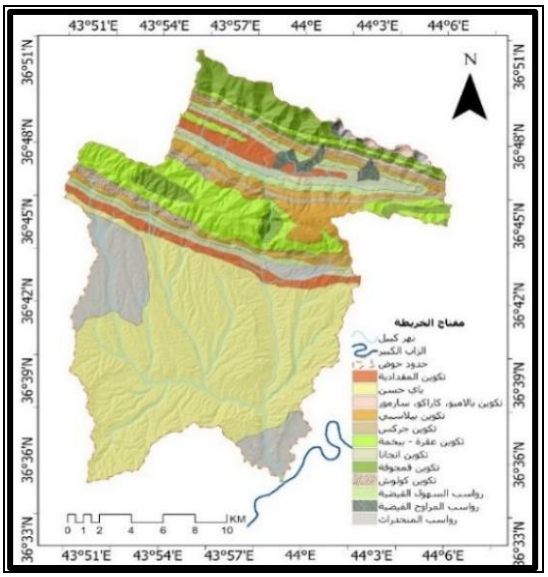
تتكون هذه الترسبات من الحصى والمواد الطينية والغرينية الناعمة والرمل(Al-Bahadli, 2021) ، وتتميز هذه الترسبات بزاوية انحدار منخفضة ومستويات واطئة يجعلها تتعرض للغمر بالمياه خلال مواسم الفيضان .

ترسبات المراوح الغرينية

تتكون من ترسبات رسوبية في المناطق المنخفضة وسفوح التلال ناتجة عن تعرية الصخور والرسوبيات من المناطق الجبلية العالية بفعل الأمطار الغزيرة .(Al-Fahdawi., 2018)

ترسبات المنحدرات

تشكلت نتيجة الجريان السطحي خلال فترات الأمطار الغزيرة، وتتألف من خليط من فتات الحصى والرمل. تظهر هذه التكوينات مع مساحاتها في الشكل (3) والجدول (1) أدناه.



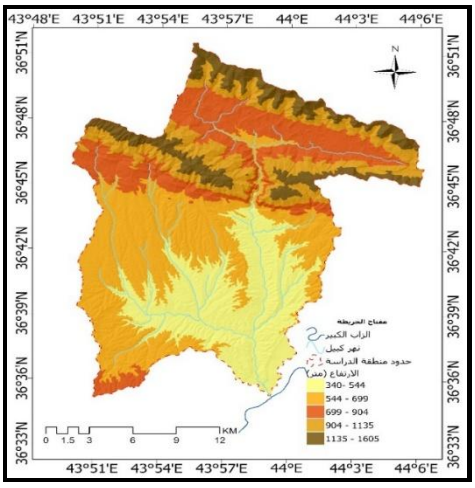
الشكل 3: التكوينات الجيولوجية في حوض كبيل

الجدول 1: التكوينات الجيولوجية ومساحاتها ونسبها المئوية في منطقة الدراسة.

ت	نوع التكوين	المساحة كم^2	النسب المئوية %
1	تكوين قمجوقة	30.1	7.44
2	تكوين عقرة – بخمة	51.89	12.82
3	تكوين كولوش	6.11	1.51
4	تكوين جركس	10.8	2.67
5	تكوين بلاسبي	28.91	7.14
6	تكوين انجانة	17.55	4.34
7	تكوين مقدادية	20.92	5.17
8	تكوين باي حسن	175.54	43.38
9	تكوين سرمورد، بالامبو، كراكو	4.68	1.16
10	ترسبات المراوح الغرينية	4.1	1.01
11	ترسبات المنحدرات	38.2	9.44
12	ترسبات السهل الفيضي	15.85	3.92
	المجموع	404.65	100

B. الخصائص التضاريسية للحوض

تؤثر الخصائص التضاريسية بشكل مباشر في الدراسات الهيدرولوجية، وينحصر تأثير التضاريس متمثلاً بالارتفاع والانحدار على التصريف المائي من زيادة أو نقصان في سرعة جريان المياه على سطح الأرض (Al-Shammari, 2023) والتضاريس عامل متحكم في حركة المياه السطحية، وكذلك كمية المياه المنصرفة وسرعتها، وكذلك التباين في وصول موجة التصريف من المنبع الى المصب (Hassan, 2023)تزداد سرعة جريان مياه الامطار في المناطق الشديدة الانحدار، وهذا يؤدي الى انخفاض طاقة الترشيح والتبخر. أما في المناطق ذات الانحدار الطفيف، فتتميز ببطء تدفق المياه، وبالتالي تزداد كميات الترشيح والتبخر (Karbal, 1986) وكذلك تعكس دراسة خصائص الانحدار والارتفاع أثر العناصر المناخية، لاسيما في كميات الامطار المتساقطة وقيم التبخر. تزداد كميات الامطار الساقطة وتنخفض درجات الحرارة مع الارتفاع عن مستوى سطح البحر، والعكس صحيح. أُجريت دراسة خصائص الارتفاع باستخدام نموذج الارتفاع الرقمي (DEM) بدقة تمييز(12.5) متراً باستخدام برنامج يوضح الشكل (4) والجدول (2) أن طوبوغرافية حوض كبيل تتراوح ما بين (340 م) كأدنى ارتفاع عند منفذ الحوض، وتصل إلى (1605 م) فوق مستوى سطح البحر في المناطق الشمالية والشمالية الشرقية. وتم تصنيف المنطقة إلى خمس فئات رئيسة بناءً على درجات الارتفاع: الفئة الأولى تتمثل بالمنطقة السهلية في الأجزاء الجنوبية الشرقية والمناطق الوسطى. تتميز أنواع الجريان في هذا المنطقة بأنها غير دائمة حيث يرتبط وجودها بالتساقطات المطرية والثلجية. تواجه هذه المناطق تدفقات مائية عالية خلال العواصف المطرية التي تتجاوز قدرة السطح على امتصاصها. اما الفئة الثانية، فتعد من اكثر الفئات التضاريسية مساحة وهي أكثر تموجا من الفئة السابقة، وهي تمثل أراضي التلال المنخفضة. الفئة الثالثة تمثل الأراضي المتموجة وتتصف بالتضرس وتعد من المناطق النشطة تعرويا. تتمثل الفئة الرابعة بأقدام الجبال التي تمتد بشكل شريطٍ طولي من اتجاه الشمال الشرقي الى الجنوب الشرقي وعلى جانبي كلي زنته .اما الفئة الخامسة، فتعد من أعلى مناطق الحوض ارتفاعاً إذ تقع ضمن المنطقة الشديدة الالتواء والمتمثلة بالجبال الشاهقة والوعرة. وتعد هذه الفئة ذات أقل انتشار مكاني من بين فئات الارتفاع الأخرى فهي تغطي قمم الجبال العالية.



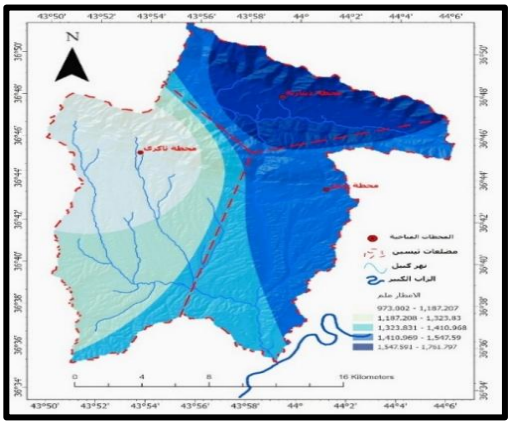
الشكل 4: خصائص الارتفاع لمنطقة الدراسة.

الجدول 2: مساحة ونسب الارتفاعات لحوض كبيل.

الفئة /متر	المساحة كم^2	النسبة المئوية %
340 – 455	101.27	25.03
544 – 699	128.61	31.78
699 – 904	78.43	19.38
904 – 1135	55.72	13.77
1135 – 1605	40.62	10.04
المجموع	404.65	100

C. الخصائص المناخية

اعتمدت الدراسة الحالية على بيانات هطول الأمطار المسجلة في عدة محطات داخل نطاق منطقة الدراسة، والتي تشمل محطات (ئاكرى ودينارته وبجيل)، فضلا عن استخدام طريقة مضلعات ثايسن (Thiessen Polygons) لحساب متوسط وتوزيع التساقط المطري التي تستند على الموقع الجغرافي للمحطات المطرية المؤثرة وكميات الهطول التي تستقبلها، حيث بلغ عدد الأيام الممطرة للسنة المائية (2023 – 2024) سبعة وخمسين يوماً ممطرًا. كما يتبين في الجداول (10 و 11 و 12) انه كان عدد الأيام الممطرة متطابقة في جميع المحطات الواقعة داخل حوض كبيل، إلا أن مجموع الامطار المسجلة لكل من محطة (ئاكرى ودينارته وبجيل) أظهر تباينًا ملحوظًا، إذ بلغ إجمالي الهطول المطري في محطة ئاكرى 994.9 ملم، بينما سجلت محطة دينارته 1761.8 ملم، و1502 ملم في بجيل كما هو مبين في الشكل (5) مما يشير إلى تفاوت كبير في كميات الهطول بين المحطات. بلغ مجموع حجم المياه الواصلة الى حوض كبيل للسنة المائية (2023–2024) حوالي 535746283 م^3 مكعب كما هو مبين في الجدول (13). على الرغم من أن الهطول المطري في دينارته هو الأعلى، إلا أن حجم المياه المتساقطة لم يتناسب بشكل مباشر مع هذه الكمية. ففي محطة دينارته، بلغ حجم المياه المتساقطة 155267434 م^3، بينما سجلت محطة بجيل 194223620 م^3، وأقل حجم كان في محطة ئاكرى بواقع 186255229 م^3. يعكس هذا التفاوت في حجم المياه المتساقطة الى الاختلاف في المساحات التي تغطيها كل محطة حسب تصنيف ثايسن.



الشكل 5: التوزيع المكاني لهطول الامطار على نطاق الحوض لسنة (2024–2023).

7. طريقة استخلاص رقم المنحنى للأحواض (CN)

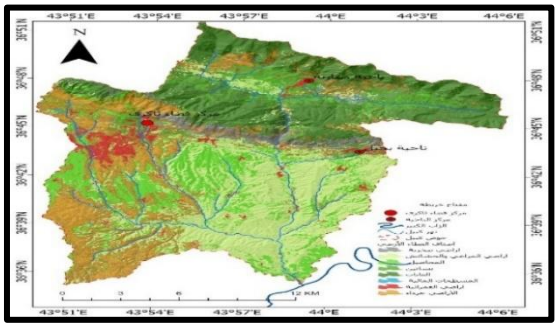
يعكس رقم المنحنى (Curve Number - CN) القيمة المعبرة عن الحالة الهيدرولوجية للتربة ومدى قدرتها على امتصاص المياه بالإضافة إلى تأثير الغطاء الأرضي. وهو مؤشر يُستخدم لمعرفة مدى استجابة حوض التجميع للجريان السطحي. وتعتمد طريقة رقم المنحنى (Curve Number) على مجموعة من المعادلات الرياضية التي تُبنى على المعلومات متاحة عن هيدرولوجية التربة وخصائص الغطاء الأرضي وأنماط استخدام الأرضي، بالإضافة إلى كمية الأمطار يُعد هذا الرقم أحد المدخلات الأساسية في معادلة الجريان السطحي التي طورتها خدمة الحفاظ على التربة (Hameed, 2013)، حيث يتيح تقدير الجريان السطحي بدقة من خلال دمج العوامل المشار اليها، ويساعد على فهم العلاقة بين الهطول والتسلل والجريان السطحي في منطقة الدراسة (Khalaf et al., 2020).

8. وصف الغطاء الأرضي Land Cover Description

يشير الغطاء الأرضي الى الخصائص الطبيعية من تربة وغطاء نباتي وموارد مائية بالإضافة إلى المعالم التي انشأها الانسان (Ahmed,2019). ان تحليل أصناف غطاء الأرض في حوض كبيل يوضح تأثيرها على قدرة الحوض على تشكل الجريان السطحي أو تغذية المياه الجوفية، اذ تتميز الأسطح المبينة في الحوض بقدرة عالية على تكوين السيول عند هطول الأمطار الغزيرة مقارنةً بالمناطق ذات التكوينات العالية المسامية التي تعزز تسرب المياه وتغذية الخزانات الجوفية (Al-Zarfi, 2021). فقد تم تصنيف الغطاء الأرضي إلى ثمانية اصناف بالاعتماد على المرئية الفضائية (Landsat 8,9) التي تم الحصول عليها من موقع الهيئة الجيولوجية الأمريكية(USGS) بدقة مكانية (30 متراً) بتاريخ (15/5/2024) وذلك باستخدام برنامج (Arc GIS Pro.3.0) وتطبيق أسلوب التصنيف الموجه(Supervised Classification) وتم إنتاج الشكل (6) الذي يُظهر الأصناف الثمانية الرئيسة من الغطاء الأرضي في حوض كبيل. ويبين الجدول (3) نسب توزيع الغطاء الأرضي بحسب التصنيف، فالأراضي الجرداء تمثل مجمل المناطق غير المستخدمة من الحوض، ويشغل هذا الصنف مساحة (50.18 كم^2) بما يعادل (12.4%) من إجمالي مساحة الحوض وتظهر الأراضي الجرداء تأثيراً واضحاً يتمثل في تعزيز سرعة الجريان السطحي(Al-Jabouri and Al - Douri, 2020) ويرجع ذلك إلى غياب الغطاء النباتي باستثناء الأراضي الرملية والحصوية تكون هذه الأراضي عادة غير متماسكة مما يسمح بمرور المياه. اما صنف الاراضي العمرانية فيشمل جميع مظاهر النمو الحضري مثل الاستخدامات السكنية والتجارية وطرق النقل والأرصفة بالإضافة إلى غيرها من الانشطة العمرانية. ولا تزيد مساحته عن (15.15 كم^2)، أي ما يساوي (3.74%) من المساحة الاجمالية للمنطقة .

وهيدرولوجياً تتميز أراضي هذا الصنف بمسامية منخفضة كونها مصمتة مما يمنع تسلل المياه إلى التربة ويُعزز من التدفق السطحي (Hassan, 2021).

وتشغل المنكشفات الصخرية مساحة تقدر ب(28.01 كم^2) أي ما يعادل (6.92%) من اجمالي مساحة المنطقة المدروسة. يظهر صنف المكشفات الصخرية بشكل متفرق ضمن منطقة الدراسة، يختلف هذا الصنف في صلابة الصخور المنكشفة وقابلية الترشيح وتتميز بضعف المسامية، مما يقلل من قدرة التربة على نفاذ المياه، باستثناء بعض المناطق التي تحتوي على شقوق وفواصل تسمح بتسرب كميات قليلة من المياه عبر الشقوق والفواصل الموجودة بين أجزائها عقب سقوط الأمطار. وتشمل اراضي المراعي والحشائش الطبيعية على الحشائش القصيرة والطويلة التي تغطي جزءاً كبيراً من منطقة الدراسة، وتعتبر ثاني أكبر صنف من حيث المساحة اذ يشغل حوالي (91.55 كم^2) بما يعادل (22.62%) من إجمالي مساحة حوض كبيل. يلعب الغطاء النباتي دوراً مهماً في تقليل حجم الجريان السطحي، وتختلف كثافة هذا الصنف من منطقة إلى أخرى داخل حوض كبيل، حيث تساهم زيادة الكثافة في تعزيز ترشيح المياه وتقليل كميتها المتدفقة على السطح (Khadir and Al -2024) والثانوية والبرك، بالإضافة إلى غيرها من المتجمعات المائية، وتُشكّل أقل نسبة من مساحة منطقة الدراسة حيث بلغت (0.28 كم^2) بما يعادل (0.069%) من إجمالي مساحة الحوض. اما صنف المحاصيل، فانه يشمل الأراضي المستخدمة للإنتاج الزراعي في حوض كبيل، والتي تشمل بشكل أساسي زراعة الحنطة والرز والماش والسمسم، ويشغل مساحة (107.03كم^2) التي تعادل (26.45%) من إجمالي مساحة حوض كبيل. يعمل هذا الصنف من الأراضي الأكثر استخداماً وانتشاراً ضمن حوض كبيل على إعاقة الجريان السطحي مما يعزز فرصة نفاذ المياه إلى باطن التربة، وبالتالي تنخفض القدرة على إحداث الجريان (Al-Ghamidh,2023) ويشمل صنف البساتين الأراضي الزراعية المتمثلة بالبساتين المختلفة، حيث بلغت مساحتها في الحوض (17.41كم^2) بما يعادل (4.3%) من إجمالي المساحة. تعمل البساتين على إعاقة الجريان السطحي، مما تعزز فرص نفاذ المياه وترشيحها داخل التربة. اما صنف الغابات، فانه يشغل مساحة تقدر بحدود (95.05 كم^2) وبنسبة (23.48%) من المساحة الكلية. ويتركز في شمال منطقة الدراسة. تسهم الغابات في تقليل الجريان السطحي، اذ تعمل جذورها على امتصاص المياه وتخزينها في التربة , مما يعزز قدرة الأرض على الاحتفاظ بالرطوبة وإعادة تغذية المياه الجوفية.



الشكل 6: استعمالات الأرض لحوض كبيل.

الجدول3: نسب ومساحات الغطاء الأرضي والاستعمالات.

الغطاء واستعمال الأرض	المساحة كم^2	النسبة المئوية %
المحاصيل	107.03	26.45
الاراضي الصخرية	28.01	6.92
المسطحات المائية	0.28	0.069
الأراضي العمرانية	15.15	3.74
الغابات	95.05	23.48
اراضي المراعي الطبيعية والحشائش	91.55	22.62
البساتين	17.41	4.3
الاراضي الجرداء	50.18	12.4
المجموع	404.65	100%

تعد نوعية التربة من العوامل الأساسية التي تؤثر بشكل كبير على كمية الجريان السطحي، وقد حددت طريقة (SCS-CN) أربع مجموعات هيدرولوجية رئيسة للتربة استناداً إلى معدل النفاذية بها، الذي يعتمد على معدل وسرعة انتقال المياه عبر التربة (Al-Nafie, 2010). وتنقسم هذه المجموعات إلى (A,B,C,D)، حيث يتميز كل نوع بخصائص فريدة تميزه عن الأنواع الأخرى، حيث تتميز المجموعة A بطبقات رملية عميقة ذات نفاذية عالية جداً ومحتوى منخفض من طين وغرين، مما ينتج جرياناً سطحياً منخفضاً. ومن أنواع التربة في هذه المجموعة التربة رملية والتربة المزيجية والتربة الرملية المزيجية، أما المجموعة B، فتضم طبقات رملية أقل عمقاً من المجموعة A مع معدل ارتشاح متوسط، وتشمل تربة مزيجية وتربة غرينية مزيجية، بينما تحتوي المجموعة C على طبقات طينية محدودة العمق ذات نفاذية منخفضة نسبياً، ومن أنواع التربة في هذه المجموعة التربة المزيجية الرملية الطينية. وتتميز المجموعة D بتربة طينية ذات نفاذية منخفضة جداً وجريان سطحي عالٍ، مع وجود طبقة سطحية ضحلة من تربة ناعمة، وتشمل هذه المجموعة الترب الطينية المزيجية والطينية الغرينية المزيجية كما هو مبين في الجدول (4) (USDA, 1986) .

الجدول 4: أصناف الترب الهيدرولوجية بحسب طريقة (SCS-CN).

المجاميع الهيدرولوجية للتربة	عمق الجريان	المجاميع الهيدرولوجية للتربة
A	قليل	طبقة رملية ذات عمق كبير تتخللها نسبة ضئيلة من الطين والغرين، تمثل (رملية – رملية مزيجية او مزيجية رملية)
B	متوسط	مع معدل تسرب متوسط بعد ترطيب التربة .(التربة مزيجية غرينية – مزيجية) (A) طبقة رملية اقل عمقاً من صنف.
C	عالٍ	طبقة طينية ذات عمق محدد، تتميز بمعدل ارتشاح أقل من المتوسط قبل أن تصل التربة إلى حالة التشبع. (مزيجية طينية رملية).
D	عالٍ جداً	طبقة طينية ذات قدرة انتفاخ مرتفعة، يعلوها طبقة سطحية ضحلة من التربة الغرينية ناعمة . تتنوع قوام التربة بين (مزيجية طينية – مزيجية رملية – وغرينية طينية).

تم رسم الشكل للترب الهيدرولوجية للحوض بناءً على التحليل المختبري لعينات التربة المأخوذة من منطقة الدراسة (Salim et al., 2025)، حيث وجد في منطقة الدراسة ثلاثة اصناف من الترب الهيدرولوجية (B,C,D)، بينما لم يظهر الصنف (A) من بين المجموعات الأربعة المعتمدة. وان مساحات وتوزيع هذه الترب في منطقة الدارسة يبيّنه الجدول (5) والشكل (7).

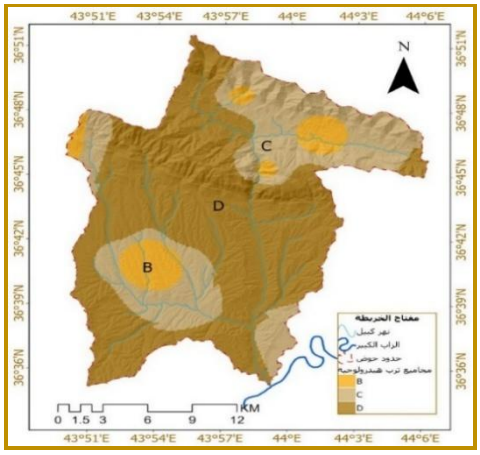
الجدول 5: اصناف الترب الهيدرولوجية.

الصنف	المساحة ($كم^2$)	النسبة %
B	29.69	7.33
C	123.54	30.53
D	251.42	62.13
المجموع	404.65	%100

1. الترب الهيدرولوجية (الصنف B): تضم هذه المجموعة الترب المزيجية – المزيجية الغرينية التي تتصف بنسيج خشن إلى متوسط والطبقة الرملية فيها اقل عمقاً من المجموعة (A)(Al-Saeedi and Al-Ajili, 2019). تساهم هذه المجموعة بجريان سطحي معتدل، إذ تؤثر بشكل مباشر على خصائص الجريان السطحي في المنطقة وتشغل مساحة (29.69) $كم^2$ بما يعادل (7.33%) من إجمالي المساحة الكلية لحوض كبيل.

2. الترب الهيدرولوجية (الصنف C): من ملاحظة الجدول (5) ، نجد ان ترب هذه المجموعة شغلت مساحة قدرها (123.54) $كم^2$، اي ما يعادل (30.53%) من إجمالي مساحة الحوض. تتكون هذه الترب من ترب مزيجية غنية بالغرين ذات نفاذية تتراوح بين الضعيفة والجيدة(Falih, 2023). تتميز هذه التربة بمعدل ارتشاح منخفض إلى متوسط، مما يؤدي إلى زيادة معدلات الجريان السطحي فوقها (Aftan and Hamid, 2023).

3. الترب الهيدرولوجية (الصنف D): تمثل هذه المجموعة أكبر المجموعات الهيدرولوجية مساحة، حيث تُقدر مساحتها بـ(251.42) $كم^2$ بما يعادل (62.13%) من إجمالي مساحة منطقة الدراسة وتُعد هذه الفئة من الترب الأقل كفاءة بين المجموعات الهيدرولوجية في امتصاص المياه حيث يتميز معدل تسربها بالانخفاض الشديد وتتسم بارتفاع الجريان السطحي مقارنة بالمجموعات الأخرى (Al-Samarrai and Al-Samarrai, 2024).



الشكل 7: الترب الهيدرولوجية لحوض كبيل.

9. الحالة المسبقة لرطوبة التربة

إن الحالة المسبقة لرطوبة التربة لها تأثير كبير في حجم الجريان السطحي، كما تشير إلى مستوى الرطوبة في التربة قبل بدء العاصفة المطرية (Al-Kanani and Al-Asadi, 2020). تم تصنيف الرطوبة المسبقة للتربة إلى ثلاث فئات رئيسة تُستخدم كمدخلات في رقم المنحنى (CN) (الجدول 6) (Gangodagamage and Aggarwal, 2012). الفئة الاولى (AMC I) تشير إلى الترب الجافة التي تمثل أدنى احتمالية للجريان السطحي، والفئة الثانية (AMC II) تشير إلى التربة الاعتيادية ذات الرطوبة المتوسطة، والفئة الثالثة (AMC III) تشير إلى التربة الرطبة مما يعكس أعلى احتمالية للجريان السطحي (Gangodagamage and Aggarwal, 2012). تم تخصيص قيمة (CN) خاصة بكل حالة من هذه الحالات لتحديد الجريان السطحي وفقاً لدرجة رطوبة التربة مما يسهم في تحليل تأثير حالة رطوبة التربة السابقة (AMC) على توليد الجريان السطحي. تُظهر البيانات أن تأثير الرطوبة السابقة على الجريان السطحي كان جوهريًا، وقد سَجّلت إحدى التساقطات 33 ملم دون تسجيل أي جريان سطحي بسبب جفاف التربة، في المقابل سُجل هطول قدره 31.2 ملم، ولكن نظرًا لوجود رطوبة مرتفعة في الخمسة أيام التي سبقت الزخة المطرية فتم تسجيل جريان سطحي بلغ 10.06 ملم، مما يؤكد أن الحالة السابقة لرطوبة التربة لها تأثير على توليد الجريان السطحي أكثر من كمية الهطول المطري بحد ذاتها. كما أظهرت البيانات أن أعلى قيمة للجريان

السطحي المسجلة بلغت 89.27 ملم عندما كان الهطول المطري 122.7 ملم، وكانت التربة في حالة رطبة جدًا. تم استخدام بيانات هطول الأمطار اليومية كمدخلات لحساب الجريان السطحي اليومي.

وبناءً على (CN) لظروف (AMC-I) تم اشتقاق قيم (CN) لكل من (AMC-I)(AMC-III) باستخدام المعادلتين (1 و 3).

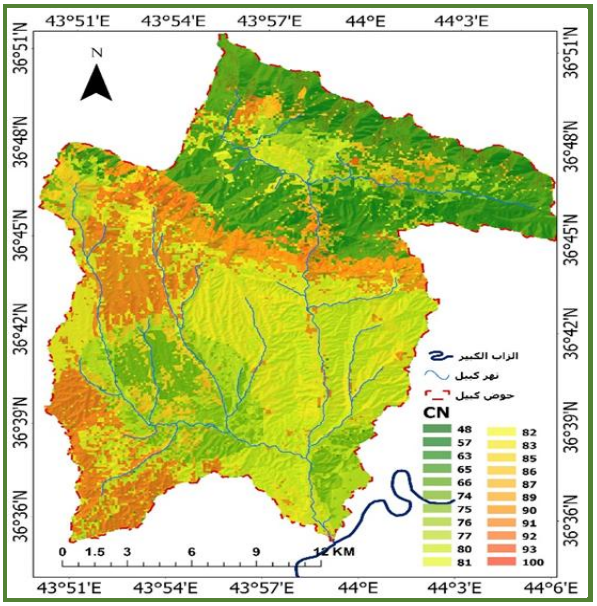
الجدول 6: تصنيف الحالة المسبقة لرطوبة التربة (AMC).

فئة AMC	مجموع الأمطار في الأيام الخمسة السابقة (ملم)		مجموع الأمطار في الأيام الخمسة السابقة (ملم)
	موسم النمو	موسم السكون	
AMC I	اصغر من 35	اصغر من 12.7	الجافة
AMC II	35 إلى 52.5	12.7 إلى 27.9	المعتدلة
AMC III	أكبر من 52.5	أكبر من 27.9	الغزيرة الأمطار

10. النتائج والمناقشة

استخراج قيم رقم المنحنى (CN)

تُعبر قيم (CN) عن الاستجابة المائية للأسطح التي تستقبل مياه الأمطار وتحويلها إلى جريان سطحي. تعتمد كمية الجريان وطبيعته على نفاذية التربة وخصائص الغطاء الأرضي، والتي يتم التعبير عنها من خلال قيم (CN) (Al- Kanani and Al- Asadi, 2020)، حيث تتراوح هذه القيم مابين (0 – 100). تشير قيمة (CN) القريبة من 0 إلى تربة ذات نفاذية عالية، مما يسمح بتسرب اكبر للمياه وتقليل الجريان السطحي، بينما تعكس قيمة (CN) القريبة من 100 إلى انخفاض كبير في النفاذية وهي الأكثر قدرة على توليد الجريان السطحي، وتمثل القيمة المتوسطة أسطحاً ذات نفاذية متوازنة (Muhammad, 2021). لحساب قيمة (CN) يتم دمج طبقتين هما طبقة استعمالات الأرض وطبقة التربة الهيدرولوجية باستخدام أداة (Combine) ضمن برنامج (Arc GIS Pro.3.0) (Khalaf et al. 2020). وبينت النتائج (الشكل 8 والجدول 7) وجود مجموعة شاملة تضم 24 قيمة لـ CN تتراوح ما بين 48 و 100. يعكس هذا النطاق تنوع نوعية الغطاء الارضي والتربة في المناطق المدروسة، مما يقدم لنا فهماً معمقاً لخصائص الجريان السطحي. تم حساب رقم المنحنى المرجح لحالة (AMC-II) باستخدام الصيغة المعتمدة وكانت القيمة الناتجة (77.49)، وباستخدام المعادلات التجريبية التي تم توضيحها في الجدول (8)، تم اشتقاق (CN) لكل من (AMC-I)(AMC-III) حيث بلغت القيم (60.06) و (88.06) على التوالي. بناءً على هذه القيم، وتم تقدير الحد الأقصى لقدرة التربة على الاحتفاظ بالمياه.



الشكل8: قيم CN لحوض كبيل.

الجدول7: قيم CN، المساحات والنسب المئوية

رقم المنحنى	مساحة	النسبة المئوية	(% مساحة X CN (موزون))
100	0.2	0.049	4.94
100	0.02	0.005	0.49
100	0.058	0.014	1.43
87	12.23	3.022	262.95
93	40.41	9.986	928.74

106.90	1.243	5.03	86
270.10	2.936	11.88	92
52.65	0.650	2.63	81
13.34	0.178	0.72	75
1257.38	15.717	63.6	80
348.01	4.703	19.03	74
47.05	0.554	2.24	85
609.53	9.675	39.15	63
690.79	12.119	49.04	57
46.50	0.969	3.92	48
497.00	5.462	22.1	91
121.63	1.367	5.53	89
69.39	0.771	3.12	90
145.30	1.772	7.17	82
142.74	1.878	7.6	76
45.14	0.694	2.81	65
194.58	2.948	11.93	66
520.06	6.754	27.33	77
1372.43	16.535	66.91	83
7749.07	100.000	404.65	المجموع

الجدول 8: معاملات CN وآلية الحساب والنتائج

معاملات CN	آلية حساب القيم	النتائج
CN II	موزون / 100	77.49
CN I	$CN(I) = \frac{4.1CN(II)}{10-0.058CN(II)}$	60.06
CN III	$CN(III) = \frac{23CN(II)}{10+0.13CN(II)}$	88.06

الجدول 9: معاملات SCS-CN لعام 2024.

معاملات	AMC I (جاف)	AMC II (معتدل)	AMC III (رطبة)
CN	60.06	77.49	88.06
S	168.91	73.78	34.44
Ia = 0.2S	33.78	14.76	6.89

استخلاص الامكانية القصوى لاحتفاظ التربة بالماء بعد بدء الجريان السطحي (S)

يمثل معامل الإمكانية القصوى للاحتفاظ بالماء (S) قدرة التربة على احتجاز الماء بعد حدوث الجريان السطحي (Potential Maximum Retention After Runoff)، حيث يُوضح حالة التربة عندما تكون في حالة تشبع تام بالماء بعد عملية التسرب. يتباين سمك طبقة التربة الممتلئة بالماء بتباين نوع التربة وقابليتها لامتصاص الماء أثناء فترة تساقط الأمطار، وبناءً على ذلك، يمكن التأكد أن هذا العامل له تأثير مباشر على نوع التربة والغطاء الأرضي السائد (Al-Saadi and Al-Jaberi, 2018)، كما أن الغطاء النباتي يلعب دوراً هاماً في تحسين قدرة التربة على الاحتفاظ بالماء، حيث تلعب النباتات على إعاقة جريان الماء وبالتالي زيادة التسرب إلى داخل التربة. كذلك يؤثر الانحدار في المنطقة على قدرة التربة على الاحتفاظ بالماء، حيث أن التربة في المناطق ذات الانحدار العالي قد تكون أقل قدرة على الاحتفاظ بالماء. تُعبر القيمة المرتفعة للمعامل (S) إلى قدرة أعلى للتربة على الاحتفاظ بالماء مما يقلل من نسبة الجريان السطحي، بينما تُشير القيم المنخفضة إلى انخفاض القدرة التخزينية للتربة للماء مما يؤدي إلى زيادة سرعة وكمية الجريان السطحي (Muhammad and Mahmoud, 2019).

تم تحليل قيم (S) لثلاث محطات (ئاكرى، دينارته، بجيل) بناءً على بيانات الهطول المطري لـ 57 يوماً، فأظهرت النتائج أن قيم (S) كما هو موضح في الجدول (9) تزداد مع انخفاض مستوى رطوبة التربة، حيث كانت (168.91 ملم) في الحالة الجافة، و(73.78 ملم) في الحالة المعتدلة، و(34.44 ملم) في الحالة الرطبة، مما يُظهر العلاقة العكسية بين تشبع التربة وقدرتها على امتصاص مياه الأمطار قبل بدء الجريان السطحي.

معامل الاستخلاص الأولي Initial Abstraction (Ia)

يُعتبر هذا المعامل من العناصر المهمة في تقدير كمية الجريان السطحي ويشير إلى الكمية المفقودة من المياه قبل بدء عملية الجريان السطحي نتيجة لعمليات التبخر والتسرب او عن طريق ما تحتجزه النباتات من مياه الأمطار. يرتبط معامل (Ia) بشكل وثيق بالتربة وغطاءات الأرض من خلال علاقته بالمعامل (S)، إذ تعادل قيمته خُمس قيمة الامكانية القصوى للاحتفاظ بالماء (S) (Al-ani et al., 2016). تشير القيم المنخفضة لمعامل (Ia) والتي تقترب من الصفر إلى قلة كمية الفواقد من مياه الأمطار قبل بدء الجريان السطحي وتساعد على توليد كميات كبيرة من الجريان السطحي. في حين يصبح معدل الاستخلاص الأولي (Ia) مساوياً لمعدل المياه الجارية في حال وصلت قيمة المعامل (50.8) ملم، أما إذا ارتفعت قيمة (Ia) عن قيمة الوسيط تزداد كمية الفاقد من مياه الأمطار وبالتالي تقل كمية المياه الجارية على السطح (Al-Obaidi, 2022). في إطار دراسة معامل الاستخلاص الأولي (Ia) لحوض كبيل في ثلاث محطات (ئاكرى، دينارته، بجيل) تم تحليل البيانات لـ57 يوماً ممطرًا، حيث تم تصنيف هذه الأيام إلى ثلاث حالات: جافة، معتدلة، ورطبة وفقاً لمعدلات هطول الأمطار المسجلة في كل محطة كما هو موضح في الجدول (9). حقق معامل الاستخلاص الأولى في الحالة الجافة (AMC I) ما مقداره (33.78) ملم مما يشير إلى قدرة التربة العالية على الاحتفاظ بالمياه. أما في

الحالة المعتدلة، فقد سجلت قيمة معامل الاستخلاص الأولى (AMC II) بمقدار (14.76) ملم مما يشير إلى انخفاض قدرة التربة على تخزين المياه مقارنة بالحالة الجافة. في هذه الحالة تزداد احتمالية الجريان السطحي عند حدوث هطول الامطار. وفي الحالة الرطبة (AMC III) كانت قيمة معامل الاستخلاص الأولى (6.89) ملم وهي الأدنى بين الحالات الثلاث، وتعكس هذه القيمة تشبع التربة بالمياه، مما يؤدي إلى ارتفاع معدلات الجريان السطحي نتيجة للعجز في قدرة التربة على استيعاب المزيد من المياه. تبرز هذه النتائج أهمية دراسة كل محطة بشكل مستقل بسبب اختلاف ايام سقوط الامطار وكمياتها وبالتالي الأيام المصنفة كجافة ومعتدلة ورطبة اختلفت في كل محطة وكذلك عمق وحجم الجريان السطحي كما هو مبين في الجداول (10) و (11) و (12).

الجدول 10: البيانات الهيدرولوجية لمحطة ناكرى: تاريخ سقوط العاصفة، كمية التساقط، حالة رطوبة التربة، وقيم CN وS وIa و Q و QV.

تاريخ سقوط العاصفة المطرية	كمية التساقط المطري /ملم	خمسة أيام متتالية	الحالة المسبقة لرطوبة التربة AMC	CN	(mm)S	Ia	(mm)Q	QV (^{3}m)
3/10/2023	5.4	0	I	60.06	168.91	33.78	0.00	0.00
4/10/2023	5.6	5.4	I	60.06	168.91	33.78	0.00	0.00
10/10/2023	4	1.2	I	60.06	168.91	33.78	0.00	0.00
16/10/2023	5.8	0.2	I	60.06	168.91	33.78	0.00	0.00
1/11/2023	3.2	0	I	60.06	168.91	33.78	0.00	0.00
3/11/2023	1.8	3.2	I	60.06	168.91	33.78	0.00	0.00
14/11/2023	3.2	0	I	60.06	168.91	33.78	0.00	0.00
15/11/2023	4	3.2	I	60.06	168.91	33.78	0.00	0.00
16/11/2023	14.6	7.2	I	60.06	168.91	33.78	0.00	0.00
17/11/2023	33	21.8	I	60.06	168.91	33.78	0.00	0.00
19/11/2023	64	55	III	88.06	34.44	6.89	35.63	6670292.30
20/11/2023	42	115.8	III	88.06	34.44	6.89	17.73	3319233.30
27/11/2023	13.2	0	I	60.06	168.91	33.78	0.00	0.00
9/12/2024	3.2	2.8	I	60.06	168.91	33.78	0.00	0.00
11/12/2024	4.4	6	I	60.06	168.91	33.78	0.00	0.00
12/12/2024	31.6	9.4	I	60.06	168.91	33.78	0.00	0.00
13/12/2024	4	41	III	88.06	34.44	6.89	0.00	0.00
21/12/2024	16.4	0.2	I	60.06	168.91	33.78	0.00	0.00
22/12/2024	19.4	16.6	II	77.49	73.78	14.76	0.27	50546.70
23/12/2024	27	35.8	III	88.06	34.44	6.89	7.41	1387226.10
24/12/2024	18.2	62.8	III	88.06	34.44	6.89	2.80	524188.00
4/1/2024	5.2	0.4	I	60.06	168.91	33.78	0.00	0.00
5/1/2024	20.2	5.6	I	60.06	168.91	33.78	0.00	0.00
9/1/2024	3.4	25.4	II	77.49	73.78	14.76	0.00	0.00
10/1/2024	5.4	23.6	III	88.06	34.44	6.89	0.00	0.00
11/1/2024	23.4	8.8	I	60.06	168.91	33.78	0.00	0.00
12/1/2024	14.4	32.2	III	88.06	34.44	6.89	1.35	252733.50
13/1/2024	67	46.6	III	88.06	34.44	6.89	38.22	7155166.20
14/1/2024	13.4	113.6	III	88.06	34.44	6.89	1.04	194698.40
23/1/2024	11	3.8	I	60.06	168.91	33.78	0.00	0.00
24/1/2024	11.8	14.8	II	77.49	73.78	14.76	0.00	0.00
26/1/2024	40.4	26.6	II	77.49	73.78	14.76	6.61	1237458.10
4/2/2024	24	3	I	60.06	168.91	33.78	0.00	0.00
5/2/2024	13.8	27	II	77.49	73.78	14.76	0.00	0.00
14/2/2024	74	0	I	60.06	168.91	33.78	7.73	1447133.30
15/2/2024	18.8	74	III	88.06	34.44	6.89	3.06	572862.60
16/2/2024	25.8	92.8	III	88.06	34.44	6.89	6.70	1254307.00
18/2/2024	7.4	119.2	III	88.06	34.44	6.89	0.01	1872.10
20/2/2024	11.8	52.8	III	88.06	34.44	6.89	0.61	114198.10
18/3/2024	25	3.6	I	60.06	168.91	33.78	0.00	0.00
19/3/2024	41.1	28.6	I	60.06	168.91	33.78	0.30	56163.00
20/3/2024	10.2	70	III	88.06	34.44	6.89	0.29	54290.90
21/3/2024	6	80.2	III	88.06	34.44	6.89	0.00	0.00
22/3/2024	31.2	86.2	III	88.06	34.44	6.89	10.06	1883332.60
23/3/2024	13.2	113.8	III	88.06	34.44	6.89	0.98	183465.80
24/3/2024	4.2	102	III	88.06	34.44	6.89	0.00	0.00
26/3/2024	21.4	54.6	III	88.06	34.44	6.89	4.30	805003.00
6/4/2024	2.6	0	I	60.06	168.91	33.78	0.00	0.00
7/4/2024	15.2	2.6	I	60.06	168.91	33.78	0.00	0.00
9/4/2024	25.4	22	I	60.06	168.91	33.78	0.00	0.00
30/4/2024	15.8	0	I	60.06	168.91	33.78	0.00	0.00
1/5/2024	17.2	15.8	I	60.06	168.91	33.78	0.00	0.00
2/5/2024	12.2	33	I	60.06	168.91	33.78	0.00	0.00

0.00	0.00	14.76	73.78	77.49	II	45.2	14	3/5/2024
0.00	0.00	6.89	34.44	88.06	III	59.2	7.2	4/5/2024
0.00	0.00	14.76	73.78	77.49	II	37	4.2	7/5/2024
0.00	0.00	33.78	168.91	60.06	I	2.4	13.6	21/5/2024

الجدول 11:البيانات الهيدرولوجية لمحطة ئاكرى: تاريخ سقوط العاصفة، كمية التساقط، حالة رطوبة التربة، وقيم CN وS وIa و Q و QV.

QV (^{3}m)	(mm)Q	Ia	(mm)S	CN	الحالة المسبقة لرطوبة التربة AMC	خمسة أيام متتالية	كمية التساقط المطري /ملم	تاريخ سقوط العاصفة المطرية
0.00	0.00	33.78	168.91	60.06	I	0	5.4	3/10/2023
0.00	0.00	33.78	168.91	60.06	I	5.4	5.6	4/10/2023
0.00	0.00	33.78	168.91	60.06	I	1.2	4	10/10/2023
0.00	0.00	33.78	168.91	60.06	I	0.2	5.8	16/10/2023
0.00	0.00	33.78	168.91	60.06	I	0	3.2	1/11/2023
0.00	0.00	33.78	168.91	60.06	I	3.2	1.8	3/11/2023
0.00	0.00	33.78	168.91	60.06	I	0	3.2	14/11/2023
0.00	0.00	33.78	168.91	60.06	I	3.2	4	15/11/2023
0.00	0.00	33.78	168.91	60.06	I	7.2	14.6	16/11/2023
0.00	0.00	33.78	168.91	60.06	I	21.8	33	17/11/2023
6670292.30	35.63	6.89	34.44	88.06	III	55	64	19/11/2023
3319233.30	17.73	6.89	34.44	88.06	III	115.8	42	20/11/2023
0.00	0.00	33.78	168.91	60.06	I	0	13.2	27/11/2023
0.00	0.00	33.78	168.91	60.06	I	2.8	3.2	9/12/2024
0.00	0.00	33.78	168.91	60.06	I	6	4.4	11/12/2024
0.00	0.00	33.78	168.91	60.06	I	9.4	31.6	12/12/2024
0.00	0.00	6.89	34.44	88.06	III	41	4	13/12/2024
0.00	0.00	33.78	168.91	60.06	I	0.2	16.4	21/12/2024
50546.70	0.27	14.76	73.78	77.49	II	16.6	19.4	22/12/2024
1387226.10	7.41	6.89	34.44	88.06	III	35.8	27	23/12/2024
524188.00	2.80	6.89	34.44	88.06	III	62.8	18.2	24/12/2024
0.00	0.00	33.78	168.91	60.06	I	0.4	5.2	4/1/2024
0.00	0.00	33.78	168.91	60.06	I	5.6	20.2	5/1/2024
0.00	0.00	14.76	73.78	77.49	II	25.4	3.4	9/1/2024
0.00	0.00	6.89	34.44	88.06	III	23.6	5.4	10/1/2024
0.00	0.00	33.78	168.91	60.06	I	8.8	23.4	11/1/2024
252733.50	1.35	6.89	34.44	88.06	III	32.2	14.4	12/1/2024
7155166.20	38.22	6.89	34.44	88.06	III	46.6	67	13/1/2024
194698.40	1.04	6.89	34.44	88.06	III	113.6	13.4	14/1/2024
0.00	0.00	33.78	168.91	60.06	I	3.8	11	23/1/2024
0.00	0.00	14.76	73.78	77.49	II	14.8	11.8	24/1/2024
1237458.10	6.61	14.76	73.78	77.49	II	26.6	40.4	26/1/2024
0.00	0.00	33.78	168.91	60.06	I	3	24	4/2/2024
0.00	0.00	14.76	73.78	77.49	II	27	13.8	5/2/2024
1447133.30	7.73	33.78	168.91	60.06	I	0	74	14/2/2024
572862.60	3.06	6.89	34.44	88.06	III	74	18.8	15/2/2024
1254307.00	6.70	6.89	34.44	88.06	III	92.8	25.8	16/2/2024
1872.10	0.01	6.89	34.44	88.06	III	119.2	7.4	18/2/2024
114198.10	0.61	6.89	34.44	88.06	III	52.8	11.8	20/2/2024
0.00	0.00	33.78	168.91	60.06	I	3.6	25	18/3/2024
56163.00	0.30	33.78	168.91	60.06	I	28.6	41.1	19/3/2024
54290.90	0.29	6.89	34.44	88.06	III	70	10.2	20/3/2024
0.00	0.00	6.89	34.44	88.06	III	80.2	6	21/3/2024
1883332.60	10.06	6.89	34.44	88.06	III	86.2	31.2	22/3/2024
183465.80	0.98	6.89	34.44	88.06	III	113.8	13.2	23/3/2024
0.00	0.00	6.89	34.44	88.06	III	102	4.2	24/3/2024
805003.00	4.30	6.89	34.44	88.06	III	54.6	21.4	26/3/2024
0.00	0.00	33.78	168.91	60.06	I	0	2.6	6/4/2024
0.00	0.00	33.78	168.91	60.06	I	2.6	15.2	7/4/2024
0.00	0.00	33.78	168.91	60.06	I	22	25.4	9/4/2024
0.00	0.00	33.78	168.91	60.06	I	0	15.8	30/4/2024
0.00	0.00	33.78	168.91	60.06	I	15.8	17.2	1/5/2024
0.00	0.00	33.78	168.91	60.06	I	33	12.2	2/5/2024
0.00	0.00	14.76	73.78	77.49	II	45.2	14	3/5/2024
0.00	0.00	6.89	34.44	88.06	III	59.2	7.2	4/5/2024
0.00	0.00	14.76	73.78	77.49	II	37	4.2	7/5/2024
0.00	0.00	33.78	168.91	60.06	I	2.4	13.6	21/5/2024

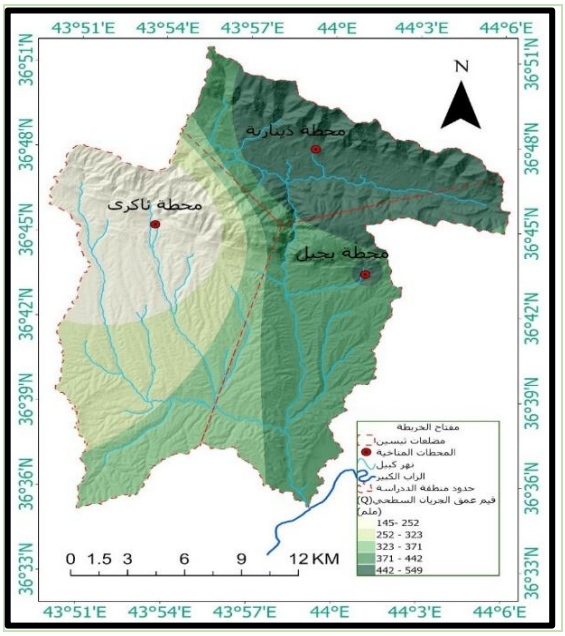
الجدول11: البيانات الهيدرولوجية لمحطة دينارته: تاريخ سقوط العاصفة، كمية التساقط ، حالة رطوبة التربة، وقيم CN وS وIa و Q و QV.

تاريخ سقوط العاصفة المطرية	كمية التساقط المطري /ملم	خمسة أيام متتالية	الحالة المسبقة لرطوبة التربة AMC	CN	(mm)S	Ia	(mm)Q	QV (^{3}m)
3/10/2023	3.5	0	I	60.06	168.91	33.78	0.00	0.00
4/10/2023	11.8	3.5	I	60.06	168.91	33.78	0.00	0.00
10/10/2023	10.3	1	I	60.06	168.91	33.78	0.00	0.00
16/10/2023	7.5	0	I	60.06	168.91	33.78	0.00	0.00
1/11/2023	7.2	0	I	60.06	168.91	33.78	0.00	0.00
3/11/2023	3	7.2	I	60.06	168.91	33.78	0.00	0.00
14/11/2023	6.6	0	I	60.06	168.91	33.78	0.00	0.00
15/11/2023	8.4	6.6	I	60.06	168.91	33.78	0.00	0.00
16/11/2023	18.2	15	I	60.06	168.91	33.78	0.00	0.00
17/11/2023	88	33.2	I	60.06	168.91	33.78	13.17	1161198.90
19/11/2023	120.5	121.2	III	88.06	34.44	6.89	87.18	7686660.60
20/11/2023	41	235.1	III	88.06	34.44	6.89	16.97	1496244.90
27/11/2023	17	0.7	I	60.06	168.91	33.78	0.00	0.00
9/12/2024	6.4	4.4	I	60.06	168.91	33.78	0.00	0.00
11/12/2024	8.6	10.8	I	60.06	168.91	33.78	0.00	0.00
12/12/2024	42.7	16.8	II	77.49	73.78	14.76	7.68	677145.60
13/12/2024	9.7	59.5	III	88.06	34.44	6.89	0.21	18515.70
21/12/2024	21.3	0	I	60.06	168.91	33.78	0.00	0.00
22/12/2024	44	21.3	II	77.49	73.78	14.76	8.30	731811.00
23/12/2-24	122.7	65.3	III	88.06	34.44	6.89	89.27	7870935.90
24/12/2024	39.5	188	III	88.06	34.44	6.89	15.86	1398376.20
4/1/2024	19.7	0	I	60.06	168.91	33.78	0.00	0.00
5/1/2024	51.2	19.7	II	77.49	73.78	14.76	12.05	1062448.50
9/1/2024	7	70.9	III	88.06	34.44	6.89	0.00	0.00
10/1/2024	7.8	58.2	III	88.06	34.44	6.89	0.02	1763.40
11/1/2024	57.2	14.8	I	60.06	168.91	33.78	2.85	251284.50
12/1/2024	38.3	72	III	88.06	34.44	6.89	14.98	1320786.60
13/1/2024	120.3	110.3	III	88.06	34.44	6.89	86.99	7669908.30
14/1/2024	11.8	230.6	III	88.06	34.44	6.89	0.61	53783.70
23/1/2024	17	5.8	I	60.06	168.91	33.78	0.00	0.00
24/1/2024	20.3	22.8	I	60.06	168.91	33.78	0.00	0.00
26/1/2024	86.5	43.1	II	77.49	73.78	14.76	35.37	3118572.90
4/2/2024	18.5	2	I	60.06	168.91	33.78	0.00	0.00
5/2/2024	20	20.5	II	77.49	73.78	14.76	0.35	30859.50
14/2/2024	121	0	I	60.06	168.91	33.78	29.70	2618649.00
15/2/2024	12.3	121	III	88.06	34.44	6.89	0.73	64364.10
16/2/2024	23.7	133.3	III	88.06	34.44	6.89	5.51	485816.70
18/2/2024	3.5	157	III	88.06	34.44	6.89	0.00	0.00
20/2/2024	12	43	II	77.49	73.78	14.76	0.00	0.00
18/3/2024	60.5	5.3	I	60.06	168.91	33.78	3.65	321820.50
19/3/2024	85.8	65.8	III	88.06	34.44	6.89	54.94	4844059.80
20/3/2024	13.3	151.6	III	88.06	34.44	6.89	1.01	89051.70
21/3/2024	9.5	164.9	III	88.06	34.44	6.89	0.18	15870.60
22/3/2024	62	174.4	III	88.06	34.44	6.89	33.92	2990726.40
23/3/2024	30.3	231.1	III	88.06	34.44	6.89	9.47	834969.90
24/3/2024	4.5	200.9	III	88.06	34.44	6.89	0.00	0.00
26/3/2024	36.2	106.3	III	88.06	34.44	6.89	13.48	1188531.60
6/4/2024	4.1	0	I	60.06	168.91	33.78	0.00	0.00
7/4/2024	17.8	4.1	I	60.06	168.91	33.78	0.00	0.00
9/4/2024	38.5	23.2	I	60.06	168.91	33.78	0.13	11462.10
30/4/2024	1.6	0	I	60.06	168.91	33.78	0.00	0.00
1/5/2024	40	1.6	I	60.06	168.91	33.78	0.22	19397.40
2/5/2024	14.5	41.6	II	77.49	73.78	14.76	0.00	0.00
3/5/2024	21.3	56.1	III	88.06	34.44	6.89	4.25	374722.50
4/5/2024	4.7	77.4	III	88.06	34.44	6.89	0.00	0.00
7/5/2024	19.5	48.3	II	77.49	73.78	14.76	0.29	25569.30
21/5/2024	11.5	1.6	I	60.06	168.91	33.78	0.00	0.00

تقدير عمق الجريان السطحي (Q)

يعبر عمق الجريان السطحي Q عن الناتج النهائي لتفاعل عاصفة مطرية معينة مع خصائص حوض التصريف. ويختلف هذا العمق بناءً على نوع الأغطية الأرضية ومستوى نفاذية التربة (Al-Zarfi and (Al-Taie, 2021 حيث تُعد أرقام المنحنى (CN) العامل المتغير الرئيس الذي يتحكم في تباين عمق الجريان السطحي

بين مختلف أجزاء الحوض (Salah and Mayas, 2023). في هذه الدراسة، تم تقدير عمق الجريان السطحي لمنطقة الدراسة كما هو مبين في الشكل (9) بالاعتماد على مكونات الغطاءات الأرضية ونوع التربة الهيدرلوجية إضافة إلى الأمطار اليومية الساقطة على أجزاء الحوض. سجلت محطة دينارته أعلى عمق جريان سطحي بواقع 549.36 ملم، تليها محطة بجيل بعمق 442.89 ملم، في حين كانت محطة ئاكرى الأقل تأثرًا بالجريان السطحي بواقع 154.11 ملم كما هو مبين في الجدول (12). وهذا يبين تأثير مقدار سقوط الامطار وحالة التربة بالإضافة الى الانحدار ونفاذية التربة.



الشكل 9: عمق الجريان السطحي (**Q**) لحوض كبيل.

تقدير حجم الجريان السطحي (QV)

تُعتبر دراسة حجم الجريان السطحي من الجوانب الهيدرولوجية المهمة لتقدير كمية الجريان في أحواض التصريف المائي، حيث يُعبر عنه بإجمالي المياه المتدفقة ضمن مساحة الحوض (Al-Darrat, 2020). تم تقدير حجم الجريان السطحي (QV) لحوض كبيل اعتماداً على عمق الجريان السطحي (Q) التي تم الحصول عليها وفقاً للمعادلة (6) المذكورة مسبقاً. بلغ مجموع الجريان السطحي في حوض كبيل 132851245.8 م^3 وبنسبة 24.8% من حجم السواقط على الحوض للسنة المائية (2023–2024) (الجدول 13).

الجدول 13: متوسط عمق الجريان وحجم الجريان السطحي لسنة (2023–2024) في حوض كبيل.

اسم المحطة	المساحة m^2	كمية الأمطار المتساقطة (mm)	حجم المياه المتساقطة (m^3)	عمق الجريان السطحي Q (mm)	حجم الجريان السطحي QV (m^3)	النسبة المئوية للجريان السطحي
محطة ئاكرى	187.21	994.9	186255229	145.11	27166043.1	%14.60
محطة دينارته	88.13	1761.8	155267434	549.36	48415096.8	%31.18
محطة بجيل	129.31	1502	194223620	442.89	57270105.9	%29.48
المجموع	404.65		535746283		132851245.8	%24.8

سجلت محطة دينارته 48415096.8 م^3 من المياه الجارية، في حين سجلت محطة بجيل اعلى جريان سطحي بقيمة 57270105.9 م^3، وأقل قيمة للجريان كانت في محطة ئاكرى حيث بلغت (27166043.1) م^3. بالنظر إلى النسبة المئوية لحجم الجريان السطحي نسبة الى حجم المياه الساقطة من خلال الامطار، سجلت محطة دينارته النسبة الأعلى بواقع 31.18%، تليها محطة بجيل بنسبة 29.48%، بينما سجلت محطة ئاكرى أدنى نسبة عند 14.60%. تعكس هذه النسب الفروقات في خصائص التربة والغطاء الأرضي بين المحطات الثلاثة كما هو مبين في الجدول (13) مما يتطلب تطوير استراتيجيات إدارة الجريان السطحي، لا سيما في المناطق ذات التصريف العالي باستخدام تقنيات الحصاد المائي وإنشاء السدود الصغيرة للتحكم في تدفق المياه وتقليل مخاطر الفيضانات.

العلاقات الارتباطية (Correlation Coefficient):

تم حساب معامل ارتباط بيرسون (r) في هذه الدراسة والذي هو مقياس إحصائي يعبر عن قوة واتجاه العلاقة بين متغيرين حيث تتراوح قيمته بين (+1) و (−1) باستخدام برنامج (Minitab 18). وتناولت

هذه الدراسة دراسة علاقة السيح السطحي في حوض كبيل مع مجموعة من المتغيرات والتي لها تأثير على السيح (Q) وتشمل الامطار (P) ورقم المنحنى (CN) ومعامل الاستخلاص الأولي (Ia) والمنسوب (E) والانحدار (LS) واستخدامات الارض (LCLU) بالإضافة الى تحديد نوع التربة (S)، وكذلك دراسة علاقات الارتباط بين هذه العوامل مع بعضها كما هو مبين في الجدول رقم (14).

الجدول 14: العلاقات الارتباطية بين السيح والمتغيرات الاخرى في حوض كبيل

	Q	P	CN	Ia	E	SL	LCLU
السيح (Q)	1						
الامطار (P)	0.931	1					
رقم المنحنى (CN)	-0.56	-0.569	1				
معامل الاستخلاص الأولي (Ia)	0.56	0.586	-0.988	1			
المنسوب (E)	0.313	0.407	-0.493	0.546	1		
الانحدار (LS)	0.222	0.268	-0.304	0.346	0.623	1	
استخدام الارض (LCLU)	-0.463	-0.467	0.675	-0.655	-0.353	-0.227	1
نوع التربة (S)	0.473	0.485	-0.438	0.429	0.081	0.042	-0.238

من خلال الجدول (14)، نلاحظ ان للسيح علاقات ارتباط موجبة وسالبة مع المتغيرات، حيث كانت علاقة الارتباط موجبة مع كل من الامطار (P) ومعامل الاستخلاص الأولي (Ia) والمنسوب (E) والانحدار (LS) ونوع التربة (S). وكانت اقوى علاقة ارتباط موجبة (r) كانت مع الامطار، اذ بلغت 0.93. بينما علاقة الارتباط السلبية كانت مع كل من رقم المنحنى (CN) واستخدامات الارض (LCLU) حيث بلغت قيمة (r) −0.56 و−0.46 على التوالي. اما بالنسبة لعلاقات الارتباط بين المتغيرات نفسها، فمن الجدول (14) ايضا نلاحظ وجود مختلف العلاقات الموجبة والسالبة والقوية والضعيفة فيها، فعلى سبيل المثال اقوى علاقة ارتباط موجبة كانت بين رقم المنحنى واستخدامات الارض (0.67) بينما اقوى علاقة ارتباط سالبة وعكسية كانت بين رقم المنحنى ومعامل الاستخلاص الاولي (−0.98).

11. الاستنتاجات

1 − بينت الدراسة وجود ثلاثة اصناف من التربة الهيدرولوجية وفق العينات المختبرية، وهي (B) و(C) و(D). وعلى ثمانية أصناف من الغطاء الأرضي داخل الحوض.

2− تم حساب رقم المنحنى للحالات المختلفة للرطوبة عن طريق حساب (CN) الموزون، حيث بلغ قيمة (CN) في الحالة الجافة بـ (60.06)، وفي الحالة المعتدلة بـ (77.49)، بينما بلغت قيمتها في الحالة الرطبة (88.06). وتعكس هذه القيم التفاوت في القدرة على الجريان السطحي.

3− أكدت الدراسة وجود تباين واضح في قيم عمق الجريان السطحي داخل الحوض، وذلك نتيجة لاختلاف الخصائص الهيدرولوجية للمحطات المدروسة، حيث سجلت محطة دينارته أعلى عمق جريان سطحي (549.36 ملم)، تلتها محطة بجيل بعمق (442.89 ملم)، بينما كانت محطة ئاكرى الأدنى بعمق جريان(145.11 ملم).

4− تم احتساب حجم الجريان السطحي في محطات منطقة الدراسة، حيث سجلت محطة بجيل أعلى حجم جريان بمقدار (57270105.9 م^3)، تليها محطة دينارته بحجم (48415096.8 م^3)، ثم محطة ئاكرى بأدنى حجم جريان بلغ (27166043.1 م^3). وبلغت النسبة المئوية للجريان السطحي في حوض كبيل 24.8% من حجم السواقط على الحوض. بينت الدراسة ان لمساحة الحوض تأثير على حجم الجريان السطحي اكثر من كمية الهطول المطري.

5− بينت الدراسة ان للسيح علاقات ارتباط موجبة وسالبة مع المتغيرات، حيث وجدت اقوى علاقة الارتباط موجبة (r) مع الامطار (P)، اذ بلغت قيمتها 0.93، في حين اعلى علاقة ارتباط سالبة (r) كانت مع رقم المنحنى (CN) حيث بلغت قيمتها 0.56−.

12. المراجع

Aften, L.S. and Hamid, L.S., 2023. Estimating the volume of surface runoff of the Bazian Basin in Sulaymaniyah Governorate, Madad Al-Adab Journal, (n.d.), p. 560.

Ahmed, I. H. 2022. Hydrological characteristics of the soils of Erbil basin, MSc Thesis, University of Mosul, College of Education for Humanities, p.16.

Ahmed, I. M.H. 2019. Representing the value of the water flow curve (CN) for the Tharthar Valley Basin using geographic information systems, Higher Diploma Thesis, College of Education for Humanities, University of Mosul, p. 43.

Al-Bahadli, K.K.J. 2021. Evaluation of the Tigris River for agricultural investment in Maysan Province. MSc Thesis, University of Maysan, College of Education, p.19.

Al-Kanani, H. M. Ha., and Al-Asadi, S. A. R. 2020. Estimating the depth of surface runoff in Wadi Abu Ghar using remote sensing techniques and geographic information systems. Journal of the College of Education, University of Wasit, (41): 138.

Al-Nafie, H.M. 2010. Estimating surface runoff and its flash flood risks in the upper basin of Wadi Arna, east of Makkah Al-Mukarramah, using remote sensing and geographic information systems. Master's thesis, Umm Al-Qura University, College of Social Sciences, p. 89.

Al-Obaidi, O.H.A. 2022. AStudy of Some Water Harvesting Indicators Using Remote Sensing and Geographic Information Systems Technologies in Al-Kathna and Najaf Governorates, PhD Thesis, Al-Muthanna University, College of Agriculture, p. 124.

Al-Saadi, H.K.H. and Al-Jaberi, A. H. 2018. Spatial Modeling of Water Harvesting in the Arar Valley Basin, Western Iraq, Using GIS and RS Techniques. Basra Journal of Humanities Research,43 (3): 317.

Al-Saeedi, A.J. and Al-Ajili, A.A. 2019. Hydrology of the Wadi Jada Basin in the Samawah Desert Using Geographical Technologies, Journal of Arts, 131(2):171.

Al-Samarrai, S.H.G. and Al- Samarrai, H. H. L. 2024. Estimating the surface runoff of the Shishin Valley basin using the (SC-SCS) method, Madad Al-Adab Journal, Samarra University, College of Education, (n-t), p. 756.

Al-Zarfi, N. Q. M. and Al-Taie, A. A. Fd. (2021). Estimating the volume of surface runoff in the Wadi al-Ghadari basin using the (CN) method. Uruk Journal of Humanities, 14(4):3122.

Al-Zarfi, N. Q. M. 2021. Hydrological Assessment of the Possibility of Rainwater Harvesting in the Muthanna Desert (Wadi Al-Ghadari - An Applied Study), Master's Thesis, Muthanna University, College of Education for Human Sciences, p. 102.

Falih, H. N. 2023. Hydrology of the Barada Valley Basin in Northeast Diyala, Journal of Arts 136: 407. https://doi.org/10.31973/aj.v1i136.1244

Gangodagamage, C. and Aggarwal, S. P. 2012. Integrating Satellite based Remote Sensing Observations with SCS Curve Number Method for Simplified Hydrologic Modeling in Ungauged Basins. Asian Journal of Geoinformatics, 12(3).

Hameed, H. M . 2013. Water harvesting in Erbil Governorate, Kurdistan Region, Iraq: Detection of Suitable sites using Geographic Information System and Remote Sensing, Department of Physical Geography and Ecosystem Science, Lund University, p. 23.

Hassan, A.A. and Al-Koran, B. M. M. 2012. Slope forms in Mount Aqra: A study in applied geomorphology. Journal of Basic Education Research,12(3),p.481.

Hassan, M.M. and Abdulsalam. M.M., 2023. Analysis of the hydrological characteristics of the basins of Sharbazir district, east of Sulaymaniyah province, using the CN-SCS method, Journal of Survey in Fisheries Sciences, 10(2):292

Al-Fahdawi, M.A. M. A. 2018. Geomorphometry of Karst forms between Anah and Haditha regions [Master 's thesis, University of Anbar, College of Education], p.25.

Al-Hayali, S. B. A. (2021). Hydrological hazards of water basins in Aqra area, PhD Thesis, College of Education for Humanities, University of Mosul.

Al-Koran, B. M. M. 2011. Slope forms in Mount Aqra: A study in applied geomorphology, MSc Thesis, Salahaddin University – Erbil, College of Arts, p.55.

Al-Sayyab, A., et al1982. Geology of Iraq. Mosul: Dar Al- Kutub for Printing and Publishing, p.124.

Al-Shammari, S.A.M.N. (2023). Analysis of morphometric and morphotectonic characteristics in Wadi Balkian basin, MSc Thesis, College of Education, Al-Mustansiriya University,p.26.

Al-Zubaidi, M. R. F. 2018. Hydrogeomorphological evaluation of the southeastern basins of Mount Birs and their impact on sustainable development, PhD Thesis, Al-Mustansiriya University, College of Education, p.8.

Al-ani et al. H.Z.A. 2016. Analyzing remote sensing and geographic information systems data in estimating surface runoff for watershed site selection (Jam Jamal Basin - Iraq as a case study), Journal of Arts, Design, Humanities and Social Sciences, 11:143.

Al-Birmani, D.B.R. 2019. The Impact of Climate on Hydrological Characteristics and Their Suitability for Different Uses in Babil Governorate, PhD Thesis, Department of Geography, College of Arts, University of Kufa, p. 20.

Al-Darrat, A. J. 2020. Quantitative Assessment of Surface Runoff in Wadi Al-Karath, Tobruk, Northern Libya: A Hydromorphometric Study, Sabratha University Scientific Journal, p. 62. https://www.jhs.sabu.edu.ly/index.php/hsjsu/article/view/138

Al-Ghamidh, A. 2023. A Study of Changes in Hydrological Conditions of the Amman-Zarqa Basin Using Progressive Climate Change Scenarios, a Soil and Water Assessment Model, and Geospatial Techniques. An-Najah University Journal for Research (Humanities), 37(5):949.

Ali, A.Y. and Hamad, N. J. 2023.Geomorphological evaluation of neotectonics in the basin of Wadi Jummah Sur – Southeast of Koysinjaq. Journal of Koya University, p.1012.

Al-Jabouri, D.K.H. and Al-Douri, R.S.H. 2020. Hydrological Analysis of the Application of Water Harvesting Technology in the Wadi Al-Laqlaq Basin Using the (CN-SCS) Method. Tikrit University Journal for Humanities, p. 221.https://doi.org/10.25130/jtuh.27.7.2020.11

Al-Kanani, H. M. H. and Al-Asadi, S.A.R. 2020. Estimating the depth of surface runoff in the Wadi Abu Ghar basin using remote sensing techniques and geographic information systems. Journal of the College of Education, 41(4): 316. .https://doi.org/10.31185/eduj.Vol4.Iss41.1931

Governorate, Using Contemporary Techniques. Journal of Historical and Civilizational Studies, 12(50):386.

Omar, I. S. A., 2022. Hydromorphometric study of the southern basins of Mount Biher in water harvesting, MSc Thesis. University of DUHOK, College of Humanities, Department of Geography.

Salah, B. M. N., and Mayas, M.A.H. 2023. Estimating Surface Runoff Volume Using the SCS (CN) Model in the Wadi Zabid Basin - Yemen, Sana'a University Journal of Humanities,4(1):123.https://doi.org/10.59628/jhs.v4i1.315.

Salim, J.I. 2016. Hydromorphometric characteristics of the Bakrman basin and their effects on sediment and nutrient transport, PhD Thesis, University of Mosul, College of Agriculture and Forestry, p.27.

Salim, J.I. et al., 2025. Application of RUSLE Model to Mapping the Soil Erosion Risk in Gebel Watershed, Iraqi National Journal of Earth Science, 25(1):123.Dol: 10.33899/earth.2024.143444.1146.

USDA Soil Conservation Service.1986.Urban Hydrology for Small Watersheds Technical Release:55.U.S.Department of Agriculture, Washington, p. 4.

Wang, D., and Qin, L.,2015. Application of SCS – CN Model in Runoff Estimation, International Symposium on Material, Energy and Environment Engineering, published by Atlantis. Press, p. 50. https://doi.org/10.2991/ism3e-15.2015.14.

Hassan, R.S.K. 2021. Modeling Flood Risks in Mosul City, Master's Thesis, College of Education for Humanities, University of Mosul, p. 78.

Hassan, I. J.D. 2023. Hydrology of valley basins and water harvesting west of Lake Sawa, MSc Thesis, University of Baghdad, College of Education for Women, p. 16. https://doi.org/10.31185/eduj.Vol4.Iss41.1931.

Karbal, A.R. 1986. Geomorphology: The science of landforms. University of Basrah, College of Arts, p.119.

Khadir, D.A.K. and Al-Jabouri, D.K.H. 2024. Estimating the volume of surface runoff of the Wadi Al-Qasr basin in Al-Sharqat district using the (CN-SCS) method, Tikrit Journal of Humanities, 31 (2), 248. https://doi.org/10.25130/jtuh.31.2.2024.13.

Khalaf, S. S. A,. et al,2022. Estimating the volume of surface runoff in Diyala Governorate using the soil conservation method (SCS-CN) and analyzing it using digital data from remote sensing and geographic information systems. Diyala Journal of Humanities Research, 92: 77. http://repo.uodiyala.edu.iq/handle/xmlui/5563.

Khalaf, S.S., et al. 2020. Integration of remote sensing data and geographic information systems in automated analysis for modeling hydrological characteristics (Diyala Governorate as a model), Journal of Arts, Humanities and Social Sciences 59: 287.

Hammed, R. A., and Mahmoud, L.M.(2019). Water harvesting and its investment mechanisms in the area west of the Tigriris between Al-Fatha and Tikrit using remote sensing data and geographic information systems. Al-Frahedis Arts Journal,11(3),233.

Muhammad, A.H. 2021. Modeling the Hydrological Map of the Wadi Al-Wilh Basin, West of Salah al-Din

Vol. 26, No. 04, 2026 (01-18) المجلة العراقية الوطنية لعلوم الأرض،

المجلة العراقية الوطنية لعلوم الأرض

www.earth.uomosul.edu.iq

Estimation of Surface Runoff in Gebel Watershed Using SCS-CN Model and Correlation Analysis with Watershed Characteristics

Nadya Sedeeq Ramadhan [1], **Jihad Ibrahim Salim**[2*]

nadiaramadha9@gmail.com jihad.salim@uod.ac

[1] *Department of Physical Geography, College of Humanities, University of Duhok, Duhok, Iraq.*
[2] *Department of Forestry, College of Agriculture Engineering Sciences, University of Duhok, Iraq.*
* *Correspondence author.*

Received: 25 May 2025 Received in revised form: 01 July 2025 Accepted: 18 August 2025
Available online: 01 October 2026

Abstract

Estimating surface runoff is a key factor in water resources management, especially in arid and semi-arid environments. This research aims to analyze the hydrological characteristics of the Gebel watershed, which has an area of 404.65 km^2, using the SCS-CN model. Three soil groups (B, C, D) are identified based on soil samples taken from the study area, and the land cover is classified into eight classes. Daily rainfall data for the year (2023-2024) are analyzed for three meteorological stations located within the study area (Akre, Dinarta, and Bajil). The Thiessen polygon method is used for spatial rainfall distribution, which contributes to improving the accuracy of the estimates. The amount of rainfall in Dinarata was (1761.8 mm), in Akre (994.9 mm), and in Bajil (1502 mm), while the surface runoff was (549.46 mm) in Dinarata, (145.11 mm) in Akre, and (442.89 mm) in Bajil; therefore, the volume of total runoff in Gebel watershed was (132851245.8 m³). The Bajil station portion is (57270105.9 m³), Dinarata has (48415096.8 m³), and Akre has (27166043.1 m³), with runoff percentages of (31.18%), (29.48%), and (14.60%), respectively. The study demonstrates that runoff has a positive correlation with precipitation (P), initial abstraction (Ia), elevation (E), slope (LS), and soil type (S). The strongest correlation is observed with precipitation (r = 0.931). In contrast, negative correlations are found with both the Curve Number (CN) and Land Cover and Land Use (LCLU), with correlation coefficients of -0.56 and -0.46, respectively. The results confirm that the SCS-CN model is an effective tool for accurately estimating surface runoff.

Keywords:

Surface flow, rainfall, watershed.

DOI: 10.33899/injes.v26i4.56210, ©Authors, 2026, College of Science, University of Mosul.

This is an open-access article under the CC BY 4.0 license (http://creativecommons.org/licenses/by/4.0/).

==========

المجلة العراقية الوطنية لعلوم الأرض، Vol. 26, No. 04, 2026 (19-25)

المجلة العراقية الوطنية لعلوم الأرض

www.earth.uomosul.edu.iq

تقييم صلاحية صخور الحجر الجيري في منطقة الشرقاط كمواد بناء وكركام لرصف السكك الحديدية/ شمالي العراق

لؤي موسى راوي[1]، نهاد سعود الجبوري[2]*، احمد ابراهيم محمد[1]

loaytaref@tu.edu.iq nihadsaoud@uomosul.edu.iq ahmed.moh@tu.edu.iq

[1] كلية التربية الأساسية الشرقاط، جامعة تكريت، تكريت، العراق.

[2] قسم هندسة التعدين، كلية هندسة النفط والتعدين، جامعة الموصل، الموصل، العراق.

* الباحث المراسل.

تاريخ الاستلام: 19 أيار 2025 تاريخ المراجعة: 02 تموز 2025 تاريخ القبول: 22 آب 2025

تاريخ النشر الالكتروني: 01 تشرين الأول 2026

الملخص

تُعد أحجار البناء من المواد الطبيعية المستخدمة في الإنشاءات، نظراً لما تتميز به من خصائص فيزيائية وميكانيكية ملائمة للأغراض الهندسية. يتم استخراج هذه الصخور وقصّها إلى كتل بأحجام محددة وفقًا للمعايير الهندسية (Dimension stone) (ASTM, C 119-02., 2004), من بين هذه الصخور، يُعد الحجر الجيري من أهم المواد المستخدمة في عدة صناعات، منها إنتاج كتل البناء، تصنيع الحصى المستخدم في الخرسانة، أنظمة الصرف الصحي كمرشحات، وفي الطرق وفي صناعة أحجار الزينة لتغطية الأرضيات والواجهات الداخلية والخارجية للمباني. تم دراسة صلاحية استخدام صخور الحجر الجيري لتكوين الفتحة الى الجنوب من قضاء الشرقاط الواقع شمال محافظة صلاح الدين لأغراض البناء وركام لرصف السكك الحديدية. اذ تمت نمذجة الحجر الجيري من اربع محطات ومن ثم إعدادها لإجراء الفحوصات المختبرية حسب المواصفات الأمريكية القياسية (ASTM, C 568 - 99, 2004). وأظهرت نتائج الفحوصات أن كثافة العينات تراوحت بين 2.07 و2.17 غم/سم³، كما تراوحت قيم نسبة الامتصاص ما بين (5.94- 6.41)، والمقاومة الانضغاطية اللامحصورة بين (15.6- 18.4) ميكاباسكال. وتراوحت مقاومة الانشاء (4.11- 6.53) ميكاباسكال. بينما تراوحت قيمة مقاومة سحج الركام بين (34.5- 41.7 %). أظهرت النتائج أن صخور الحجر الجيري في المنطقة المدروسة تُعد مناسبة للاستخدام كمواد بناء، وفقًا للمواصفة الأمريكية القياسية (ASTM, C 568-99, 2004)، وذلك في جميع محطات منطقة الدراسة. في المقابل، بيّنت الفحوصات عدم صلاحية الصخور في المحطات الاربعة لاستخدامها كركام رصف في خطوط السكك الحديدية.

الكلمات المفتاحية:

أحجار البناء، صخور الحجر الجيري، منطقة الشرقاط، ركام لرصف السكك الحديدية، مواد البناء.

DOI: 10.33899/injes.v26i4.61141, ©Authors, 2026, College of Science, University of Mosul.
This is an open-access article under the CC BY 4.0 license (http://creativecommons.org/licenses/by/4.0/).

==========

1. المقدمة

تُعد أحجار البناء نوعًا من الصخور التي تتواجد طبيعيًا وتمتلك خصائص فيزيائية وهندسية خاصة، حيث تُستخرج من المقالع وتُقطع إلى كتل منتظمة تُعرف بـ أحجار البناء المشكلة (Dimension Stone)، وذلك وفقًا للمواصفة الأمريكية (ASTM C119-02, 2004)

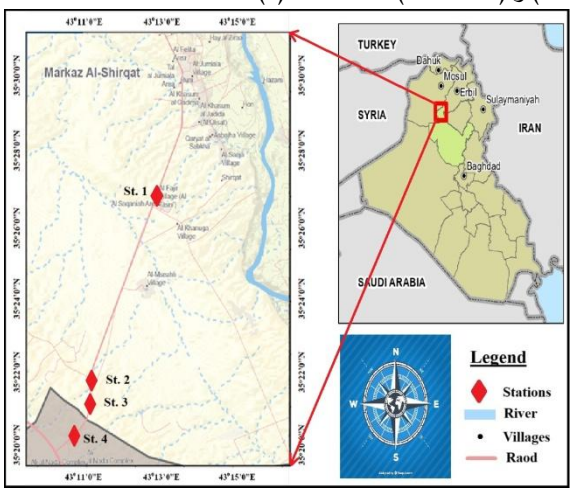
يعتبر الحجر الجيري من أهم الخامات المعدنية التي تُستخدم كمادة رئيسية أو مساعدة في العديد من التطبيقات. فهو يدخل في صناعة كتل البناء، والحصى المكسر، والخرسانة، كما يُستخدم في أنظمة الصرف الصحي كوسيط ترشيح، وفي رصف الطرق بعد مزجه بالقار، إضافة إلى استخدامه في إنتاج أحجار الزينة لتكسية الأرضيات والواجهات الداخلية والخارجية للمباني (Ayid and Abood, 2025 ; Guo et al., 2022(Al-Ali and Al-Khafaji, 2020; الحجر مصطلح عام يطلق على القطع الصخرية المستخرجة من المقالع (Haddad, 2003). عرف الحجر كمادة اساسية للبناء منذ فجر التاريخ وقد تميزت كل حضارة من الحضارات التي تعاقبت على أي بقعة من العالم بنمط خاص يميز مساكنها وقصورها ومعابدها وقد تركت اثارها بصمات واضحة على النمط المعماري الذي نحتت فيه

حجارة منشاتها او طريقة البناء او نوع الحجر (Al-Darsia, and Abdulhadi, 2011). حيث تكون الصخور الجيرية واسعة الانتشار في الطبيعة وتكون ما نسبة (20– 25%) من مجموع الصخور الرسوبية الكلي (Pettijohn, 1975) وعالميا تحتل صخور الحجر الجيري المرتبة الثالثة من مصادر المعادن والصخور المستخرجة (Flugel, 2004) يطلق على المواد الحبيبية تسمية الركام التي يتم الحصول عليها بعد عمليات تكسير الصخور وتتراوح حجومها من (5– 70) ملم ومن ضمنها يدخل الرمل والحصى وكسارة الصخور الصناعية. حيث يكون الركام المادة الرئيسية في اعمال الرصف بنسبة (70– 75%) من الحجم الكلي لمكونات طبقات الرصف اي ما يعادل (90– 95%) بالوزن، إن وظيفة الركام الاساسية والمهمة هي تحمل جميع الاجهادات المسلطة والمختلفة (Al-Darsia, and Abdulhadi, 2011).

يهدف البحث الى دراسة الخواص الجيوتكنيكية الفيزيائية والميكانيكية لصخور الحجر الجيري في منطقة الدراسة لمعرفة مدى صلاحيتها لمختلف أغراض البناء وكركام رصف في السكك الحديدية.

2. موقع منطقة الدراسة

تقع منطقة الدراسة ضمن قضاء الشرقاط الى الشمال من محافظة صلاح الدين/ شمالي العراق والتي تمتد من مفرق الشرقاط جنوب المدينة باتجاه مركز قضاء الشرقاط والمحددة بين خطي طول (43º 11' 0") و (43º 15' 0") شرقاً ، ودائرتي عرض (35º 20' 0"") و (35º 30' 0") شمالا , شكل (1).



الشكل 1: يبين موقع منطقة الدراسة.

3. طرق العمل:

1.3. العمل الحقلي:

شمل العمل الحقلي جولات حقليه للاطلاع على منطقة الدراسة ومن ثم تحديد محطات النمذجة الممثلة للمنطقة بواسطة ال (GPS) واخذ النماذج من الكتل الصخرية غير منتظمة الشكل (Irregular) تكون من غير المتجوية وكمياتها تكفي لإعداد جميع العينات لإكمال وإنجاز الفحوصات المختبرية التي على اساسها يتم أخذ القرار بشأن صلاحيتها لأغراض البناء وطبقا للمواصفة الامريكية القياسية الخاصة بالبناء(ASTM, C 568-99, 2004), اذ تمت النمذجة من اربع محطات تغطي المنطقة وكما موضح في شكل (1).

2.3. العمل المختبري

تضمنت أعمال المختبر، أولاً، إعداد وتجهيز نماذج مختلفة، نموذج لكل محطة تمثل منطقة الدراسة، وثانياً، إجراء الاختبارات. تم اختيار الاختبارات المطلوبة وفقاً للمواصفة القياسية الأمريكية (ASTM, C 568-99, 2004)، والتي تعتمد على معدل الامتصاص والكثافة ومقاومة الضغط غير المحصورة ومقاومة الانحناء. أجريت هذه الاختبارات في مختبر الصخور/كلية العلوم/جامعة تكريت، بالاعتماد على طريقة الوزن الثلاثي. تم اختبار معدل التآكل الميكانيكي (لوس أنجلوس) بالاعتماد على المواصفة القياسية (ASTM, C 131-96, 2004). تم إجراء الاختبار في مختبرات قسم الهندسة المدنية/كلية الهندسة/جامعة تكريت. صنفت هذه المواصفة أحجار البناء الطبيعية إلى ثلاث مجموعات كما هو موضح في الجدول 1، بالإضافة إلى المواصفات الميكانيكية والفيزيائية للركام المستخدم كحجر أرصفة للسكك الحديدية (Raymond,1979) (ORBD, 1999) الجدول 2.

الجدول 1: يبين اصناف وخواص الحجر الجيري الجيوتكنيكية حسب (ASTM, C 568, 2004).

الصنف	المتطلبات الفيزيائية		المتطلبات الهندسية	
	الامتصاص (%) بالكتلة	الكثافة (غم اسم^3)	المقاومة الأنضغاطية (ميكاباسكال)	مقاومة الانثناء (ميكاباسكال)
I	12<	> −1.76 2.16	28 > −12	> −2.9 3.4
II	12 > −7.5	> −2.16 2.56	55 > −28	− 3.4 6.9 >
III	7.5 > −3	2.56	55	6.9

الجدول 2: يوضح المواصفات للفحوصات الفيزيائية والميكانيكية لركام الحجر الجيري المستخدم كحجر لرصف السكك الحديدية (Raymond,1979; ORBD, 1999).

ت	المواصفات الخاصة بالركام الفيزيائية والميكانيكية	المدى المسموح به
1	قيمة الكثافة الجافة	يجب ان لا تقل عن 2.4 (غم\سم^3)
2	نسبة او مقدار امتصاص الماء	يجب ان لا تزيد عن 3%
3	المقاومة الانضغاطية اللامحصورة	لا تقل عن 80 ميكاباسكال
4	قيمة مقاومة السحج (التآكل) للركام	لا تزيد عن 25- 30 %

4. الفحوصات المختبرية

A. الكثافة الجافة (ρdry):

وهي نسبة وزن النموذج الجاف إلى حجمه الكلي الذي يشمل حجم المادة الصلبة و حجم الفجوات المتصلة والمغلقة ووحداتها (كغم/ م^3) او غم/ سم^3 (ASTM, C 127-01, 2004). وتم قياس كتلة وحدة الحجم للنماذج بطريقة الأوزان الثلاثة وفق المواصفة اعلاه وحسب المعادلة الاتية.

ρdry ={Wd / (Wsat. –Wsub.)} ρW ..... (1)

ρdry= الكثافة الجافة (gm.cm^3), Wd= وزن العينة الجافة (gm), Wsat= وزن العينة المشبعة (gm), Wsub= وزن العينة المغمورة بالماء (gm), ρW= كثافة الماء (gm.cm^3), وكما في جدول (3).

B. نسبة الامتصاص:

تمثل خاصية الامتصاص مقدار الزيادة في وزن الصخرة نتيجة تغلغل الماء إلى داخل مسامها خلال فترة محددة عادةً ما تمتد إلى 48 ساعة. هذا القياس لا يشمل الماء الموجود على السطح الخارجي، بل يقتصر فقط على ما تم امتصاصه فعليًا داخل البنية المسامية للصخر. ويُعبَّر عن هذه الخاصية بنسبة مئوية تمثل وزن الماء الممتص(Ww) إلى الوزن الجاف الكامل للصخرة (Wd) ، وفقًا للمعيار المعتمد (ASTM, C 170-09, 2010). تُعد خاصية الامتصاص من المعايير المهمة في تقييم كفاءة الصخور لأغراض البناء، إذ تشير القيم المنخفضة إلى مقاومة أعلى تجاه عوامل التعرية البيئية مثل التجمد والذوبان، إلى جانب التغيرات في الرطوبة والجفاف، مما يجعلها أكثر استقرارًا واستدامة في الاستخدامات الانشائية (Griffin, 2008). تم تطبيق المعادلة الخاصة بحساب نسبة الامتصاص على العينات المدروسة، والجدول (3) يبين نتائج فحص نسبة الامتصاص.

$$W.ab = (Ww/Wd) \quad X100 \quad \ldots\ldots\ldots\ldots\ldots\ldots (2)$$

C. المقاومة الأنضغاطية اللامحصورة (Unconfined Compressive Strength)

تُعد المقاومة الانضغاطية غير المحصورة من الخصائص الأساسية التي تعبّر عن قدرة الصخرة على تحمل الضغط العمودي المسلط عليها حتى لحظة الانهيار. ويُقصد بها مجموع القوى الناتجة عن تماسك الحبيبات أو البلورات التي تُكوّن الصخرة، والتي تُقاوم القوى الخارجية المؤثرة عليها بشكل عمودي (Al-Sultani, 1992). تم إجراء فحص هذه الخاصية باستخدام نماذج صخرية غير منتظمة، وذلك وفقًا للمواصفة القياسية (ASTM-D 2938-95, 2004) ، حيث تم اختبار أربعة نماذج تمثل الصخور في منطقة الدراسة. وقد تم توثيق النتائج المستخلصة في الجدول (4).

D. مقاومة الانثناء:

تمثل مقاومة الانثناء قدرة الصخرة على تحمل قوى الانحناء أو الانثناء، وتُعد من الخصائص المهمة في التطبيقات المعمارية، خصوصًا عند استخدام الصخور في العتبات العلوية للأبواب والنوافذ (Grisafe, D.A., 1976).

تم إجراء الفحص على النماذج الصخرية وهي بحالتها الطبيعية (Natural State)، وفقًا للمواصفة القياسية (ASTM, C 99-09, 2010). وتضمنت طريقة الفحص تثبيت العينة بحيث يكون سطحها البالغ أبعاده (203 ملم طولًا X 101 ملم عرضًا) في وضع أفقي على مسندين، مع تحديد مسافة 180 ملم بين المسندين، وبُعد متساوٍ عن نقطة التحميل المركزية. كما جرى التأكد من أن المساند الثلاثة كانت متوازية، بينما سُلط الحمل تدريجيًا بمعدل لا يتجاوز 4450 نيوتن/دقيقة حتى لحظة فشل العينة. تم حساب مقاومة الانثناء (R) لأربعة نماذج باستخدام المعادلة (3) وعُرضت نتائج الفحص في الجدول (5).

$$R = \frac{3Wl}{2bd^2} \quad \ldots\ldots\ldots\ldots\ldots\ldots (3)$$

حيث W يمثل الحمل عند لحظة الانهيار (N)، و l المسافة بين مسندي التحميل (mm)، و b عرض العينة (mm)، و d سُمك العينة (mm).

E. مقاومة التآكل الميكانيكي (السحج)

هي مؤشر نوعي لمصادر الركام المختلفة المتشابهة بالتركيب المعدني، وقد تَمَّ فحص العينات حسب المواصفة القاسية الأمريكية (ASTM, C,131-96, 2004) تم حساب النسبة المئوية للسحق من العلاقة رقم (4), ولقد تراوحت قيم مقاومة التآكل الميكانيكي ما بين (34.5– 41.7), حيث تم فحص اربع نماذج وبواقع نموذج لكل محطة كما في جدول (6).

$$Abr.\% = \{(A-B)/A\} \times 100 \quad \ldots\ldots\ldots\ldots\ldots\ldots (4)$$

A= كتلة النموذج قبل الفحص (g), B= كتلة النموذج الجاف (g), المتبقي على منخل قطر الفتحة Mm (1,7) بعد الفحص .

5. النتائج والمناقشة

أظهرت نتائج الفحوصات المختبرية تبايناً واضحاً في قيمها، اذ تراوحت قيم الكثافة لعينات الحجر الجيري التي تم فحصها بين 2.07 و2.17 غم/سم³ و قيم نسبة الامتصاص ما بين (5.94– 6.41%)، والجدول 3 يبين نتائج قيم الكثافة ونسبة الامتصاص، ومن ملاحظة الجدول وجد ان قيم الامتصاص مرتفعة وان هذه القيم تدل على ان حجم الفراغات كبير او هناك اتصال بين هذه الفراغات ببعضها البعض، وان لهذه الخاصية دور مهم في معرفة مقاومة الصخرة لظروف التجوية (عمليات الانجماد والذوبان) حيث تتباين مقاومة الصخرة مع هذه العمليات، إذ ان نسبة الامتصاص العالية تقلل مقاومة الصخرة للتجوية وبالعكس.

وكانت نتائج فحص المقاومة الانضغاطية اللامحصورة بين (15.6– 18.4) ميكا باسكال كما موضحة في الجدول 4، هذا التباين البسيط في قيم المقاومة الانضغاطية له علاقة كبيرة ووثيقة الصلة بخاصيتي المسامية والكثافة، اذ تزيد قيمها بزيادة الكثافة وتقل مع نقصان المسامية. وبنفس السياق مع قيم مقاومة الانثناء، اذ تراوحت قيم مقاومة الانثناء بين (4.11– 6.53) ميكا باسكال (جدول 5). وقد فسر هذا التباين في قيم مقاومة الانثناء (Flexural Strength) لصخور الحجر الجيري في المحطات المدروسة إلى مجموعة من العوامل الجيولوجية والفيزيائية والتركيبية مثل التركيب المعدني كونه متكون بشكل أساسي من معدن الكالسيت (CaCo3) ووجود الشوائب فيه مثل الكوارتز او الاطيان، والنسيج البنيوي اذ الحبيبات الدقيقة والمتماسكة تعطي مقاومة أعلى للانثناء كما ان وجود فواصل طبقية او شقوق دقيقة يضعف مقاومة الانثناء بشكل ملحوظ، كما فسر هذا التباين ايضاً بعلاقة الانثناء مع الكثافة والمسامية، اذا ان المسامية العالية والكثافة القليلة تعني مقاومة اقل للانثناء، كما ان تزايد المسامية يسمح بتكوين مناطق ضعف داخل العينة، مما يقلل من القدرة على تحمل الاحمال او الاجهادات. كذلك امتصاص الماء يقلل من مقاومة الانثناء، لأن الماء قد يضعف الروابط بين الحبيبات أو يؤدي إلى تليين المواد الطينية المصاحبة. بالإضافة الى الظروف الجيوميكانيكية والاتجاهات البلورية اذ ان اتجاه التحميل بالنسبة للتركيب الطبقي (خاصة إذا كان الحجر الجيري طبقي التكوين) يؤثر على النتائج، فمقاومة الانثناء تكون أكبر إذا كان التحميل عمودياً على مستويات التطبق.

بينما جدول 6 يبين نتائج فحص مقاومة سحج الركام والتي تراوحت قيمها بين (34.5– 41.7%)، وهذه النسب دلالة على أنْ هنالك نوعا من الترابط في البنية الداخلية للصخرة بحيث أصبحت لها

المقاومة للتآكل وأدت الى التقليل من كمية المواد الناعمة المتكونة اثناء الفحص بجهاز لوس انجلوس.

وبشكل عام يلاحظ فيها انخفاض كثافة الحجر الجيري وارتفاع نسبة الامتصاص والتي تعود إلى عدة عوامل جيولوجية وتركيبية، يمكننا تفسيرها بما يلي:

1. المسامية العالية:

تعني وجود فراغات داخلية في بنية الحجر، وهي المسؤولة عن انخفاض الكثافة لأن الكثافة تحسب ككتلة لوحدة الحجم، وإذا كان هناك فراغات يكون الوزن أقل بالنسبة للحجم، وكذلك مسؤولة عن ارتفاع نسبة الامتصاص (لأن هذه الفراغات تمتص الماء بسهولة).

2. نوع التكوين الجيولوجي:

بعض أنواع الحجر الجيري ومنها قيد الدراسة تتكون من فتات بيولوجي مما يجعل بنيته أقل تماسكًا وأكثر مسامية، كما ان التكوين قيد الدراسة يعتقد انه ترسب في بيئات بحرية ضحلة مما ادى إلى ترسيب مواد كربونية خفيفة وذات مسامية مثل الأصداف والشعاب المرجانية.

3. درجة التماسك:

عندما تكون عملية التلاحم بين الحبيبات ضعيفة أو غير مكتملة، تبقى فراغات بين الحبيبات، ما يساهم في انخفاض الكثافة وزيادة الامتصاص.

4. نوع المعادن المكونة:

وجود معادن طينية أو عضوية ضمن الحجر الجيري يزيد من امتصاص الماء، وكلما قلت نسبة الكالسيت النقي($CaCO_3$) ، زادت المسامية عادة.

5. التعرية أو التحلل الجزئي:

في الدراسة الحالية الحجر الجيري متعرض لتحلل جزئي (مثل الذوبان بفعل الأمطار الحمضية)، مما زاد من مساميته. كلما زادت المسامية، انخفضت الكثافة وارتفعت نسبة الامتصاص وهذا شائع في الأنواع المسامية أو الفتاتية من الحجر الجيري، ويقل في الأنواع الكثيفة كالحجر الجيري البلوري أو الرخام.

الجدول 3: قيم الكثافة الجافة ونسبة الامتصاص.

رقم المحطة	الفحوصات الفيزيائية	
	الامتصاص (%) بالكتلة	الكثافة (غم\سم^3)
1	6.12	2.17
2	5.94	2.07
3	6.41	2.11
4	5.63	2.14

الجدول 4: نتائج المقاومة الانضغاطية اللامحصورة.

رقم المحطة	المقاومة الأنضغاطية (ميكاباسكال)
1	17.2
2	15.6
3	18.4
4	15.9

الجدول 5: يبين نتائج مقاومة الانثناء.

رقم المحطة	مقاومة الانثناء (ميكاباسكال)
1	6.53
2	4.11
3	4.75
4	5.27

الجدول 6: يوضح نتائج مقاومة التآكل لصخور الحجر الجيري في منطقة الدراسة.

رقم المحطة	نسبة مقاومة التآكل %
1	41.7
2	34.5
3	37.2
4	39.4

6. تقييم صلاحية الحجر الجيري لأغراض البناء:

تم إجراء تقييم شامل لصلاحية صخور الحجر الجيري في المحطات الأربع الواقعة ضمن منطقة الدراسة لاستخدامها في أغراض البناء، وذلك من خلال مقارنة النتائج المختبرية للخواص الجيوتكنيكية لهذه الصخور مع القيم القياسية المعتمدة في المواصفة الأمريكية (ASTM, C 568-99, 2004). وقد صنّفت هذه المواصفة صخور الحجر الجيري المستخدمة في البناء إلى ثلاث درجات رئيسية استنادًا إلى خصائص مثل الكثافة، ونسبة الامتصاص، والمقاومة الانضغاطية، بالإضافة إلى مقاومة الانثناء. وتشمل هذه التصنيفات:

- الصنف الأول (I): مقبول (Accepted)
- الصنف الثاني (II): موصى به (Recommended)
- الصنف الثالث (III): موصى به بدرجة عالية (Highly Recommended)

وقد جرى تصنيف صخور الحجر الجيري في منطقة الدراسة بناءً على هذه الخواص، كما هو موضح في الجدول رقم (7).

الجدول 7: يبيّن مدى مطابقة صخور كل محطة للمواصفة القياسية، باستخدام علامة (+) للدلالة على المطابقة، وعلامة (–) لعدم المطابقة، مع تحديد الفئة التصنيفية لكل نوع من الصخور بحسب المواصفة.

رقم المحطة	نسبة الامتصاص %	الكثافة (كغم/م^3)	المقاومة الانضغاطية الغير محصورة (ميكاباسكال)	مقاومة الانثناء (ميكاباسكال)	التقييم النهائي
1	+(III)	+ (I)	+ (I)	+ (II)	ناجح
2	+(III)	+ (I)	+ (I)	+ (II)	ناجح
3	+(III)	+ (I)	+ (I)	+ (II)	ناجح
4	+(III)	+ (I)	+ (I)	+ (II)	ناجح

أظهرت نتائج فحوصات الامتصاص في جميع محطات الدراسة انخفاضًا في نسب الامتصاص، ويُعزى ذلك إلى قلة الفراغات بين الحبيبات المكونة للصخور، بالإضافة إلى طبيعتها المعدنية. ووفقًا لهذا الأداء، فقد صُنّفت هذه الصخور ضمن الصنف الثالث (III) بحسب المواصفة الأمريكية (ASTM, C 568-99, 2004)، مما يشير إلى مطابقتها للمديات المقبولة لاستخدام الحجر الجيري في أغراض البناء، كما هو موضح في الجدول (7). أما بالنسبة للكثافة، فقد بيّنت النتائج أن الصخور المدروسة تتمتع بكثافة منخفضة، ويرجع ذلك إلى اعتماد القياس على حجم المادة الصلبة وحده دون احتساب الحجم الكلي للصخرة. وفيما يخص المقاومة الانضغاطية، فقد صُنّفت صخور الحجر الجيري في جميع المحطات ضمن الصنف الأول (I) نظرًا لما أظهرته من قدرة معتدلة إلى قوية على مقاومة الضغط، وهي ضمن القيم

المسموح بها بحسب المواصفة ذاتها. كذلك سجلت الصخور قيمًا مرتفعة لمقاومة الانثناء، ويُحتمل أن يكون ذلك نتيجة لتأثير عمليات الدلمتة (Dolomitization)، التي أسهمت في تعزيز هذه الخاصية. وبشكل عام، حافظت جميع النماذج الصخرية على تكوينها الكتلي دون تدهور، ما يدل على متانة البنية الداخلية لها، وتُعد هذه الخصائص ضمن الحدود المقبولة وفق المواصفات الامريكية (ASTM, C 568-99, 2004) لاعتمادها في الأعمال البنائية.

7. تقييم الخواص الجيوتكنيكية لصخور الحجر الجيري لاستخدامها كركام رصف لخطوط السكك الحديدية

لمعرفة صلاحية صخور الحجر الجيري ومدى ملاءمتها للاستخدام كحجر رصف للسكك الحديدية يجب أ ن تمتلك الصخرة المواصفات الميكانيكية والفيزيائية المبينة في الجداول المذكورة سابقا (ORBD, 1999) و (Raymond,1979) تم ايجاد الخواص الجيوتكنيكية حسب المواصفات القياسية الامريكية الخاصة بكل فحص والمذكورة في الجداول انفا لصخور الحجر الجيري في منطقة الدراسة تم ادراج نتائج هذه الفحوصات كما موضح في الجدول (8). تراوحت قيمة الكثافة الجافة الحقيقية لصخور الحجر الجيري لمنطقة الدراسة ما بين (2.07– 2.17) غم/سم^3 وهي اقل من المدى المسموح به، اذ انَّ المدى المسموح به هو أن لا يقل عن (2.4) غم/سم3 اما نسبة الامتصاص تراوحت ما بين (5.63 – 6.41%) وهي اعلى من الحد المسموح به, وفيما يخص قيمة مقاومة السحق(التآكل) للركام تراوحت بين (34.5– 41.7%) حيث تعتبر هذه القيم اعلى من القيم التي حددتها المواصفة والتي يجب ان لا تتجاوز عن (25– 30%), وقد بينت الفحوصات انخفاض في المقاومة الانضغاطية اللا محصورة حيث تراوحت ما بين (15.6– 18.4) ميكاباسكال وهي اقل من القيمة المسموح بها التي يجب ان لا تقل عن (80) ميكاباسكال. وبعد مقارنة نتائج الفحوصات الجيوتكنيكية لصخور الحجر الجيري في منطقة الدراسة مع المواصفات الخاصة للحجر المستخدم كركام رصف للسكك الحديدية في الجدول السابقة (الكثافة الجافة الحقيقية، نسبة الامتصاص، المقاومة الانضغاطية، نسبة السحج) تبين ان صخور منطقة الدراسة لا تحقق المواصفات القياسية المطلوبة المذكورة في الجدول وبذلك تكون غير صالحة للاستخدام كركام رصف للسكك الحديدية وكما موضح في جدول (9). وتمت مقارنة نتائج الدراسة الحالية مع نتائج دراسات اخرى مثل دراسة صلاحية الحجر الجيري من نفس التكوين في جبل مكحول بالقرب من قرية النمل والى الشرق من موقع الدراسة الحالية (للباحثان مصطفى الشجيري ومحمد راشد عبود) واظهرت توافقاً بالنتائج اذ توصلت الى صلاحيتها لأغراض البناء وعدم صلاحيتها كحجر رصف للسكك الحديدية.

الجدول 8: يوضح نتائج الفحوصات الجيوتكنيكية التي تم قياسها والمستخدمة لتقييم صلاحية صخور الحجر الجيري كحجر رصف للسكك الحديدية.

رقم المحطة	الكثافة الجافة غم\ سم^3	نسبة او قيمة الامتصاص %	نسبة او قيمة مقاومة سحج الركام %	المقاومة الانضغاطية اللامحصورة (ميكاباسكال)
1	2.17	6.12	41.7	17.2
2	2.07	5.94	34.5	15.6
3	2.11	6.41	37.2	18.4
4	2.14	5.63	39.4	15.9

الجدول 9: يوضح نتائج صلاحية صخور الحجر الجيري في منطقة الدراسة لاستخدامه كحجر رصف للسكك الحديدية.

رقم المحطة	الكثافة الجافة (غم\ سم^3)	نسبة او قيمة الامتصاص %	نسبة او قيمة مقاومة سحج الركام %	المقاومة الانضغاطية اللامحصورة (ميكاباسكال)
1	-	-	-	-
2	-	-	-	-
3	-	-	-	-
4	-	-	-	-

(+) مطابق, (–) غير مطابق

8. الاستنتاجات:

1. من خلال مقارنة بعض الخواص المستحصلة مع المواصفة الامريكية القياسية (ASTM, C 568-99, 2004), تبين ملائمة استخدام صخور الحجر الجيري في جميع محطات منطقة الدراسة لأغراض البناء.
2. وجدت صخور المنطقة على انها صخور غير ملائمة لاستخدامها كركام رصف في السكك الحديدية لأنها لا تحقق المواصفات المطلوبة لهذا الغرض.

9. شكر وتقدير

يود المؤلفون الإعراب عن امتنانهم لكل من جامعة تكريت (تكريت، العراق)، وكلية هندسة النفط والتعدين بجامعة الموصل (الموصل، العراق)، وكلية الهندسة بجامعة تشوكوروفا (أضنة، تركيا)؛ وذلك لدعمهم في إنجاز هذا العمل.

10. تضارب المصالح

يُعلن المؤلفون أنه لا يوجد لديهم أي تضارب في المصالح.

11. بيان التمويل

لم يتلق هذا البحث أي تمويل خارجي.

12. المراجع

Al-Ali, N.A. and Al-Khafaji, S. J., 2020. Assessment of Limestone of Ibrahim Formation in Zurbatiya Area, Eastern Iraq for Ordinary Portland Cement Industry. Iraqi National Journal of Earth Science, 20(2), pp. 19–32. https://doi.org/10.33899/earth.2020.170358

Al-Darsia, M. A. and Abdulhadi, A. M., 2011. Building Materials, First Edition, Arab Community Library for Publishing and Distribution, Amman, 519 P. (in Arabic).

Al-Sultani, D.G., 1992. Geotechnical Properties and Surface Mining Assessment of Marble Rocks in the Khitai Area, Northern Iraq, Master's Thesis, College of Science - University of Mosul, 130 P. (in Arabic).

ASTM, C 119-02, 2004. Standard Terminology Relating to Dimension Stone1, 6 P.

ASTM, C 127-01, 2004. Standard Test Method for Density, Relative Density (Specific Gravity), and Absorption of Course Aggregate1.

ASTM, C 131-96, 2004. Standard test methods for Resistance to degradation of small- size coarse aggregate by abrasion and impact in the Los Angeles machine. P1- 4.

ASTM, C 568-99, 2004. Standard Specifications for Limestone Dimension Stone. 2 P.

ASTM, C 170-09, 2010. Standard Test Method for Compressive Strength of Dimension Stone, 3 P.

ASTM, C 99-09, 2010. Standard Test Method for Modulus of Rupture of Dimension Stone, 3 P.

ASTM, D 2938-95, 2004. Standard test methods for unconfined compressive strength of intact rock core specimens, 3 P.

Ayid, A.M. and Abood, M.R., 2025. Assessment of the Validity of Limestone Rocks in The Mishraq Area, North of Iraq, For Building Purposes and As a Railway Ballast Stone. Iraqi National Journal of Earth Science, 25(1), pp. 68–80.
https://doi.org/10.33899/earth.2024.145658.1204

Flugel, 2004. Microfacies of Carbonate Rocks. Analysis-Interpretation and Application, Springer-Verlag, Berlin, 976 P.

Grisafe, D.A., 1976. Kansas Building Limestone, Mineral Resources Series, K.G.S. University of Kansas.

Guo, Y., Xie, J., Fan, Z., Markine, V., Connolly, D. P., and Jing, G., 2022. Railway ballast material selection and evaluation: A review. Construction and Building Materials, 344 P.
https://doi.org/10.1016/j.conbuildmat.2022.128218 .

Haddad, K.M., 2003. Standard Methods for Quantity Preparation for Civil Engineering, Architectural, and Services Works, House of Wisdom, Baghdad, Iraq, 230 P. (in Arabic).

Griffin, J.A., 2008. Development of a rating classification for rock to be used as toe bench material, MSc Thesis, Kent State University, 131 P.

ORBD, 1999. Organization of Road and Bridge Design Department. Handbook for railway bridges, Iraq State Government,118.

Raymond, G.P., 1979. Design for railroad ballast and Subgrade support. Geotechnical Engineering Division, ASCE 104.No.GT, 45.

Pettijohn, F.J., 1975. Sedimentary Rocks, Harper Row Pub. 3rd Edition, New York, 628 P.

Vol. 26, No. 04, 2026 (19-25) *المجلة العراقية الوطنية لعلوم الأرض،*

المجلة العراقية الوطنية لعلوم الأرض

www.earth.uomosul.edu.iq

Evaluation of the suitability of Limestone rocks in the Sharqat area as construction materials and railway ballast / Northern Iraq

Loai Moussa RAWEE [1], Nihad Saoud ALJUBOORI [2*], Ahmed I. MOHAMED [1]

loaytaref@tu.edu.iq nihadsaoud@uomosul.edu.iq ahmed.moh@tu.edu.iq

[1] *Basic Education College, Tikrit University, Tikrit, Iraq.*

[2] *Department of Mining Engineering, College of Petroleum and Mining Engineering, University of Mosul, Mosul, Iraq.*

** Correspondence author.*

Received: 19 May 2025 Received in revised form: 02 July 2025 Accepted: 22 August 2025
Available online: 01 October 2026

ABSTRACT

Building stones are rocks that are found in natural form and have special specifications that are quarried and cut into rock blocks (dimension stone) (ASTM, C 119-02, 2004), and limestone is considered one of the most important mineral raw materials that refer to the main or secondary material in many fields, and limestone is used in the manufacture of building blocks because the classification of crushed gravel is final. After all, the classification of crushed gravel is final; limestone is considered one of the most important mineral raw materials as it refers to decorative stones for facades and interior facades. Brickwork for buildings .The suitability of using limestone rocks to form a trench in Salah al-Din Governorate/ Sharqat District for construction purposes and railway stabilization aggregate was studied. Limestone was sampled from four stations, and samples were prepared for the required laboratory tests according to the American Standard Specification (ASTM C568-99, 2004). Density values ranged between 2.07-2.17 gm/cm^3. Absorption values ranged between 5.94-6.41%, and unconfined compressive strength between 15.6-18.4 MPa. Flexural strength ranged between 4.11-6.53 MPa, while the abrasion resistance of the aggregate ranged between 34.5-41.7%. It was found that the limestone rocks present in the study area are suitable as building materials according to the American Standard Specification (ASTM, C568-99, 2004) in all stations in the study area, while at the same time the four stations are not suitable as railway aggregate

Keywords:

Building stones, Limestone rocks, Railway ballast, Sharqat area, construction materials

DOI: 10.33899/injes.v26i4.61141, ©Authors, 2026, College of Science, University of Mosul.

This is an open-access article under the CC BY 4.0 license (http://creativecommons.org/licenses/by/4.0/).

==========

المجلة العراقية الوطنية لعلوم الأرض، Vol. 26, No. 04, 2026 (26-37)

المجلة العراقية الوطنية لعلوم الأرض

www.earth.uomosul.edu.iq

تقييم استقرارية المنحدرات الصخرية على الجناح الشمالي الشرقي لطية مكحول المحدبة، شمالي العراق

رفل أمجد خضير[1*]، محمد راشد عبود[1]، عبد السلام مهدي ترف[1]

rafal.199593@gmail.com mrabood@tu.edu.iq abdulsalam_mehdi@tu.edu.iq

[1] قسم علوم الارض التطبيقية، كلية العلوم، جامعة تكريت، تكريت، العراق.

* الباحث المراسل.

تاريخ الاستلام: 28 تشرين الثاني 2024 تاريخ المراجعة: 02 شباط 2025 تاريخ القبول: 03 أيار 2025

تاريخ النشر الالكتروني: 01 تشرين الأول 2026

الملخص

تقع طية مكحول المحدبة على بعد حوالي 58 كم شمال شرقي مدينة تكريت، تم اختيار ست محطات فيها لهذا البحث وجميعها ضمن تكوين فتحة. واستخدم التحليل الحركي ونظام تصنيف كتلة المنحدر للبحث وتحليل المستوى المحتمل للاستقرار لكل منها، باستخدام برنامجي DIPS v6.008 و SMRTool v205. بناءً على التحليل الحركي. بأستخدام برنامج DIPS v6.008 وجد ان الأنزلاق المستوي يحدث في المحطات (1، 2، 5 و6)، والأنزلاق الأسفيني يحدث في جميع المحطات، أما الانقلاب المباشر فيحدث في المحطات (4 و 6)، والأنقلاب المائل يحدث في المحطة (6) ويعتبر اقل انواع الأنهيارات حدوثا في منطقة الدراسة. أما تقدير كتلة المنحدر وفقاً لنتائج برنامج(SMR- Tool) المنفصل والمستمر ظهر ان أسوأ حالة للأنزلاق المستوي تكون في المحطة (3) والتي تكون غير مستقرة بشكل كلي وتقع ضمن الفئة الخامسة (V) وبنسبة أنهيار 0.9، والمحطات التي تكون غير مستقرة هي للأنزلاق المستوي في المحطة (6) وللأنزلاق الاسفيني في المحطة (1)، وتكون ضمن الفئة الرابعة (IV) وبنسبة أنهيار (0.6)، والمحطات التي تكون مستقرة بشكل جزئي هي للأنزلاق المستوي في المحطة (1)، والانزلاق الاسفيني في المحطات (2، 3، 4، 5 و 6) والأنقلاب المباشر في المحطات (4 و 6) والأنقلاب المائل في المحطة (6)، وتقع ضمن الفئة الثالثة (III) وبنسبة انهيار (0.4).

الكلمات المفتاحية:

تكوين فتحة، الحجر الجيري، التحليل الحركي، الانهيار، جبسوم.

DOI: 10.33899/injes.v26i4.56126, ©Authors, 2026, College of Science, University of Mosul.
This is an open-access article under the CC BY 4.0 license (http://creativecommons.org/licenses/by/4.0/) .

==========

1. المقدمة

إن أحد المجالات المهمة لدراسة الجيولوجيا الهندسية هو استقرارية المنحدرات الصخرية. ويعد استقرار المنحدرات أمراً بالغ الأهمية لتقييم استقرار التضاريس الجبلية، حيث يتم تشييد العديد من المرافق الهندسية مثل المباني، الأنفاق، الطرق، قطع الصخور في المناجم والبناء بجميع أشكاله (Qader and Syan, 2021). وإن استقرارية المنحدرات الصخرية على طول المنحدرات المقطوعة بالطرق يشكل مصدر قلق كبير جداً (Al-Jawadi, 2021). وتعتبر الانهيارات الأرضية من أخطر الكوارث البيئية على سكان المناطق الجبلية، وعادة ما تحدث عندما تتوفر العوامل المسببة لها (Bayram et al., 2021).

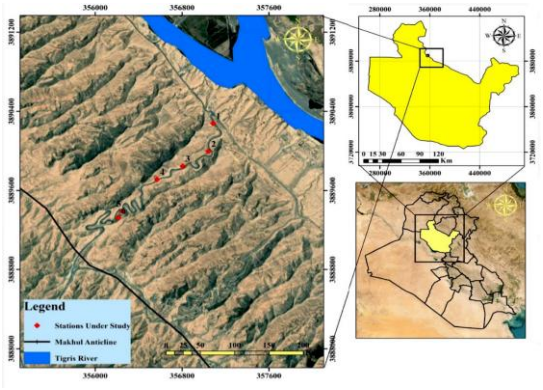
إن القوى التي تسبب الانهيارات او تعمل على زيادة احتمالية الانهيارات هي الرطوبة، التجمد، وذوبان الثلج، وكذلك التراكيب الصخرية التي تساعد على الانهيارات مثل الفواصل والشقوق. أهم العوامل المسببة لها هي قوة الجاذبية (Al-Jawadi et al., 2021). وبشكل عام، هناك ثلاثة أسباب رئيسة لعدم استقرار المنحدرات في المناطق الجبلية، وهي: (1) الأسباب الجيولوجية والبيئية (Al-Talib et al., 2021)، (2) الأسباب الجيومورفولوجية والديناميكية (Al-Jawadi et al., 2021) ، (3) الأنشطة البشرية (Al-Talib et al., 2021) ، مثل حفر المنحدرات والتفجير واستخدام الأراضي (Bayram et al., 2021). وقد قام العديد من العلماء مثل (Umrao et al.,

Siddique et al., 2015؛Sarkar et al., 2012 ؛2011 Saranaathan and Kannan, ؛Basahel and Mitri, 2017؛ 2017؛ Sharma et al., 2019 ؛Fattah et al., 2023 ؛Al-Jumili, 2024) بفحص استقرارية المنحدرات الصخرية بالقرب من قطع الطرق التي تربط المناطق النائية في الوديان أو على سفوح التلال والجبال.

تم اختيار ست محطات (مواقع المنحدرات) بناءً على المكاشف الصخرية والمحتمل حدوث انهيار فيها. تم استخدام التحليل الحركي ونظام تصنيف كتلة المنحدر (Slope Mass Rating, SMR) لبحث وتحليل المستوى المحتمل لاستقرارية كل منها من خلال برنامج (DIPS v6.008) (Rocscience, 2015) و(SMRTool v205) (Riquelme et al., 2014). يستخدم التحليل الحركي بشكل شائع للتنبؤ بالانهيارات المحتملة (الانزلاق المستوي، الانزلاق الاسفيني، الانقلاب) والاتجاه المحتمل لحدوث الانهيار على طول الفواصل باستخدام تقنية الإسقاط الشبكي المجسم. بالإضافة إلى ذلك، تم تسجيل قيم معامل تصنيف كتلة الصخور (Rock Mass Rating, RMR) لطريقة استقرارية المنحدر التي اقترحها (Bieniawski, 1989)، في حين تم تسجيل قيم معامل (SMR) باستخدام طريقة التصنيف التي اقترحها (Romana et al., 2003) و (Tomas et al., 2007).

2. موقع وجيولوجية منطقة الدراسة

تقع منطقة الدراسة ضمن الحدود الإدارية لمحافظة صلاح الدين في قضاء بيجي شمالي العراق في الجناح الشمال الشرقي لطية مكحول المحدبة وعلى بعد حوالي (58) كم شمال شرقي مدينة تكريت ضمن الاحداثيات (357085 – 356212) شرقاً و (3890278 – 3889325) شمالاً حسب نظام الاحداثيات التربيعية (UTM) كما في الشكل (1).



شكل 1: خارطة موقعية لمنطقة الدراسة موضح عليها المحطات المختارة.

ينكشف في منطقة الدراسة تكوين فتحة الذي يعود إلى عصر المايوسين الاوسط (Middle Miocene) وتكوين انجانة العائد إلى عصر المايوسين الاعلى (Upper Miocene) بالإضافة إلى ترسبات حديثة تعود إلى العصر الرباعي (Quaternary). يظهر تكوين فتحة على شكل مكاشف صخرية مكونة من صخور الحجر الجيري وصخور الجبس والمارل يصل سمكها الى حوالي (268) م في منطقة فتحة (Hussain, 2009)، ويتميز سمك تكوين انجانة بالتغاير من مكان الى أخر ويعود ذلك إما لحدوث تعرية في المناطق المرتفعة (Al-Naqib, 1959) و (Bellen et al., 1959). من الناحية التكتونية تقع منطقة الدراسة في نطاق الطيات الواطئة ضمن حزام حمرين – مكحول الذي يعتبر الحد الفاصل بين نطاق الرصيف المستقر والرصيف غير المستقر حسب تقسيمات (Buday and Jassim, 1987). حيث انه في عصر البلايوسين اصطدمت الصفيحة العربية بالصفيحتين التركية والايرانية ونتج الاصطدام مع الصفيحة الايرانية تكون جبال زاكروس ذات اتجاه (شمال غرب – جنوب شرق) والذي هو نفس اتجاه محور طية مكحول (Buday and Jassim, 1987). ومن الناحية التركيبية يوصف تركيب مكحول بأنه طية محدبة غير متناظرة وذات غاطس مزدوج (Asymmetrical Anticline Double Plunging) وزاوية ميل طرفها الشمالي الشرقي اعلى من زاوية ميل طرفها الجنوبي الغربي، واتجاه محور الطية (شمال غرب – جنوب شرق) بموازاة سلسلة جبال زاكروس (Al-Ansari, 1973).

تهدف الدراسة الحالية إلى تقييم استقرارية المنحدر الصخري في طية مكحول المحدبة الواقعة على بعد (58) كم شمال شرقي مدينة تكريت، والتي تعتبر بالغة الأهمية بسبب التأثير المحتمل لعدم استقرار المنحدرات الصخرية على الطرق في المناطق الوعرة.

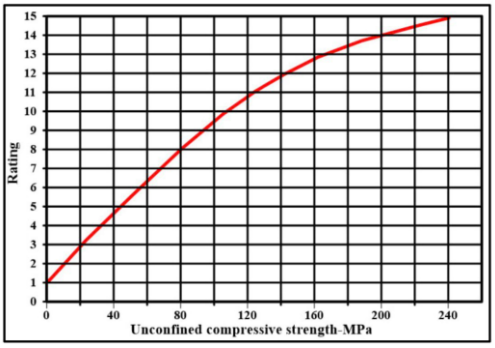
3. منهجية البحث

تم إجراء مسح جيولوجي هندسي على فترات متقطعة من (23) شباط إلى (28) نيسان 2024 ، لست محطات على الطرف الشمالي الشرقي لطية مكحول المحدبة ممثلة منطقة الدراسة على الطريق الواصل بين بغداد والموصل وموقع سد مكحول وضمن تكوين فتحة. وشملت القياسات التي أجريت في الحقل قياس وضعية الطبقات والانقطاعات متمثلة بقيم الميل واتجاه الميل واتجاه المنحدر وزاوية ميل المنحدر بواسطة البوصلة الجيولوجية، واجراء مسح مفصل للانقطاعات من حيث طبيعة سطوحها، انواعها، وضعيتها، ترددها، المسافات بين الانقطاعات، مدى انفتاحها وامتداداتها على اسطح التطبق، لما لها من دور كبير في استقرارية الكتل الصخرية وعملية القلع.

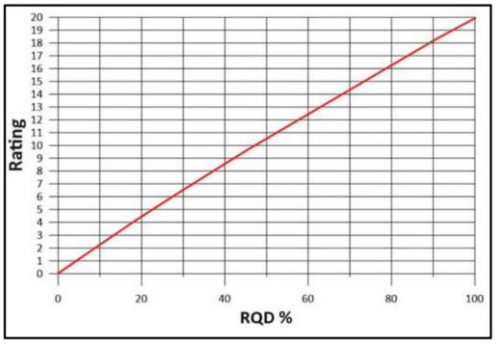
تم إجراء الفحص المختبري وفقاً للطريقة المقترحة من قبل (ISRM, 1985) لقياس مؤشر القوة من اختبار حمل النقطة. وتم تصنيف المقاومة الانضغاطية حسب (Anon, 1977). في هذه الدراسة، يتم استخدام التحليل الحركي جنبًا إلى جنب مع أنظمة (SMR) و (CSMR) لتحليل استقرار المنحدرات الصخرية. التحليل الحركي هو تحليل احتمالية حدوث الانهيار فيما يتعلق بمجموعات الفواصل، ومستوى التطبق، وزاوية الاحتكاك الداخلي، يمكن استخدام التحليل الحركي بسهولة لتحديد الانهيارات المحتملة. ان الانواع الرئيسة

للانهيارات الارضية هي (الانزلاق المستوي، الانزلاق الاسفيني، الانقلاب، السقوط الصخري) (Hock and Bray, 1981).

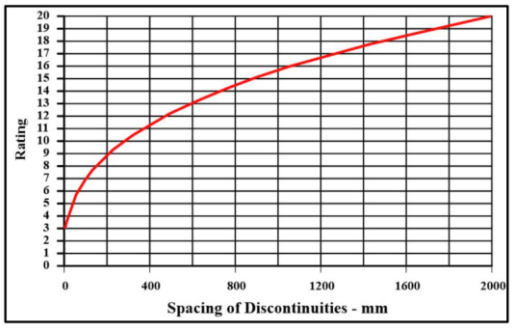
يوضح برنامج (DIPS v6.008) البيانات التي تم الحصول عليها بشكل مجسم (Rocscience, 2015). ويجب ان يكون التماسك عبر الانقطاعات صفراً، ويجب ان تكون زاوية الاحتكاك الداخلي هي العامل الوحيد الذي يحدد قوة القص. حيث تم استخدام طريقة الإمالة لحساب زوايا الاحتكاك الداخلي (Bruce et al., 1989). اقترح (Romana, 1985) نظام تصنيف كتلة المنحدر (SMR) لتصنيف استقرار منحدر الصخور. كما اقترح (Bieniawski, 1989) نظام تصنيف كتلة الصخور (RMR). هناك ست معاملات ضرورية لإيجاد (RMR) هي: (1) المقاومة الانضغاطية غير المحصورة؛ (2) مؤشر جودة الصخور (RQD)؛ (3) المسافة بين الانقطاعات؛ (4) حالة المياه الجوفية؛ (5) حالة الانقطاعات؛ (6) اتجاهات أو وضعية الانقطاعات. يمكن الحصول على تصنيف هذه المعاملات من (Bieniawski, 1989) كما في الاشكال (2، 3 و 4)، حيث يتم جمع قيم هذه العوامل لإعطاء قيمة RMRb (RMR_{1989}).



شكل 2: تصنيف المقاومة الانضغاطية غير المحصورة (UCS).



شكل 3: تصنيف جودة كتلة الصخور (RQD).



شكل 4: تصنيف المسافة بين الانقطاعات.

أن (SMR) يتم حسابه عن طريق جمع (RMR) مع ثلاثة عوامل تصحيح، أحدها هو عامل طريقة الحفر. تم تعديل SMR إلى حد ما يشمل الانهيار الإسفيني والانزلاق المستوي والانقلاب (Anbalagan et al., 1992). قام (Tomás et al., 2007) بتعديل نهج رومانا المنفصل (SMR) وإنشاء SMR المستمر (Contiuous Slope Mass Rating, CSMR)، على عكس المنفصل (SMR)، الذي يقدم نطاقًا لكل عامل تعديل. ويقدم (CSMR) قيمة فريدة لكل منها. توضح المعادلة (1) كيف يتم حساب (SMR) باستخدام (RMRb) بالإضافة إلى عوامل التعديل التي اقترحها (Romana, 1985) والتي تمثل مدى ثبات المنحدر، كما في المعادلة الأتية:

SMR=RMRb +(F1. F2.F3) +F4…… (1)

تم أجراء تعديل لقيمة (SMR) المنفصل إلى قيمة (CSMR) المستمر والتي تكون قيم الناتجة أكثر دقة، حيث يتم حساب عوامل التصحيح (F1,F2,F3) عن طريق المعادلات التالية (Tomás et al., 2007):

F1= (16/25) -(3/500) Arctan [(1/10) (|A|-17)] ……..(2)

إذ إنَّ: |A|=| αj - αs | للأنزلاق المستوي.

|A|=| αi - αs | للأنزلاق الأسفيني.

|A|=| αj - αs |-180 للأنقلاب.

أن (αj) هي اتجاه ميل للفواصل، وأن (αs و αi) تمثل اتجاه المنحدر وأتجاه الغاطس لخط تقاطع مستويين فاصلين

(يستخدم للأنزلاق المستوي والأسفيني)

F2=(9/16)+(1/195) Arctan [(17/100)B-5] ….(3)

(يستخدم للانقلاب) *F2=1*……(4)

أن قيمة (B) تمثل ميل الفاصل (ßj) في الأنزلاق المستوي والأنقلاب وتمثل خطوط التقاطع في الأنزلاق الأسفيني.

(يستخدم للأنزلاق المستوي والأسفيني) *F3=-30+(1/3) Arctan (C)* …….(5)

(يستخدم للأنقلاب) F3=-13-(1/7) Arctan (C- 120) ……(6)

أن قيمة (C) تمثل الأنزلاق المستوي في الأختلاف الزاوي لميل الفاصل والمنحدر (ßj, ßs)، وتمثل قيمة (C) في الأنزلاق الأسفيني بأنه الفرق بين ميل خط التقاطع وميل للمنحدر (C= ßj- ßs)، وتمثل

قيمة (C) في الأنقلاب بأنه مجموع ميل الفاصل وميل المنحدر (C= ßj +ßs).

تم تثبيت عامل التعديل لطريقة حفر المنحدر الصخري F4 تجريبياً (Anbalagan et al., 1992). هذه القيم ذات صلة أيضًا بتصنيف (CSMR). باستخدام (SMRTool-v205 (Riquelme et al., 2014، الذي يستخدم قيم (RMRb)، تم تنفيذ عدم الاستمرارية، وموقف المنحدر، (SMR) لـ (Romana, 1985) ، وتقييم كتلة المنحدر المستمر (CSMR) لـ (Tomas et al. 2007) باستخدام هذا النوع من حفر المنحدر لجميع محطات المنحدر المقطوعة في الصخر.

4. النتائج والمناقشة

في هذه الدراسة، تم مسح المنحدر في ست محطات والتي تختلف في خصائص الصخور الجيولوجية والجيومورفولوجية والتركيبية وأنماط اسطح الانقطاعات. تتكون المنحدرات في منطقة الدراسة من الناحية الصخارية في المحطة رقم (1) من الجبسوم ذي اللون الابيض مع طبقات من الحجر الجيري ذي اللون الاصفر الفاتح، وفي المحطة رقم (2) من طبقات من الجبسوم ذي اللون الابيض مع طبقات من الحجر الجيري المارلي، وفي المحطات (3، 4، 5 و 6) طبقات من الحجر الجيري ذي اللون الأصفر الفاتح مع طبقات من الحجر الجيري المارلي ذي اللون الرصاصي الى الاخضر الفاتح وطبقات من الجبسوم. ويتراوح ميل المنحدرات الصخرية من (°30-°90) كما هو مبين في الجدول (1).

جدول (1) معلومات المحطات في منطقة الدراسة (أسم التكوين ووضعية كل من المنحدرات ومستويات التطبق والانقطاعات وكذلك زاوية الاحتكاك الداخلي).

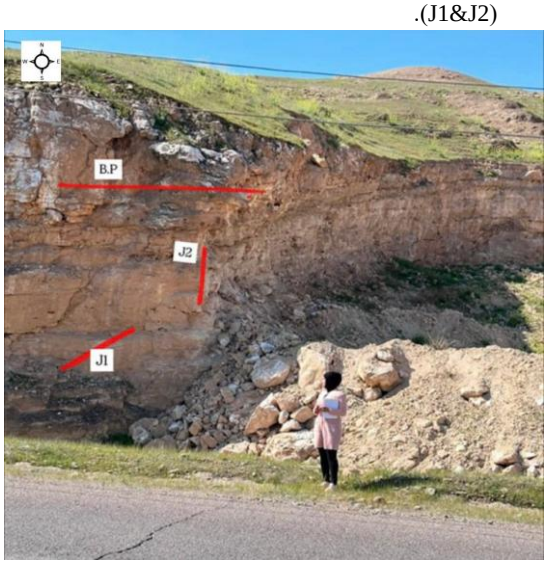
رقم المحطة	التكويـن	اتجاه ميل / قيمة ميل					زاوية الاحتكاك الداخلي (Ø)
		المنحدر Slope	الطبقات Bedding	مجموعة الفواصل (J1)	مجموعة الفواصل (J2)	مجموعة الفواصل (J3)	
1	فتحة	90°/030°	22°/030°	70°/160°	88°/140°	-----	38°
2		90°/030°	20°/030°	84°/030°	88°/150°	-----	40°
3		90°/150°	45°/064°	70°/220°	74°/020°	-----	35°
4		90°/150°	18°/020°	90°/290°	70°/250°	-----	32°
5		84°/120°	18°/030°	90°/210°	90°/108°	-----	30°
6		90°/120°	90°/040°	88°/20°	90°/120°	60°/200°	30°

5. التحليل الحركي

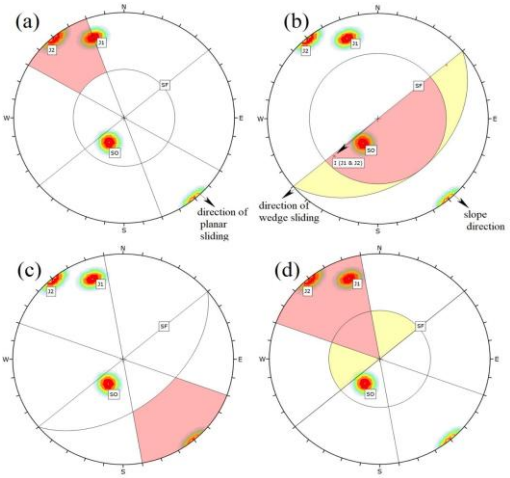
أجري التحليل الحركي لمنحدرات منطقة الدراسة اعتماداً على اختبار ماركلاند باستخدام برنامج (DIPS v6.008) (Rocscience, 2015) وباستخدام زاوية الاحتكاك الداخلي ووضعية الانقطاعات للصخور وكذلك قيمة اتجاه الميل وقيمة الميل للمنحدر للكشف عن أي انهيار محتمل، يتم عرض منطقة الانهيار المحتملة باللون الوردي لكل من المحطات الست (الاشكال 5,6,7,8,9,10)، وكما موضح في اللوحات (1,2,3,4,5,6).

وكانت النتائج كما يلي:

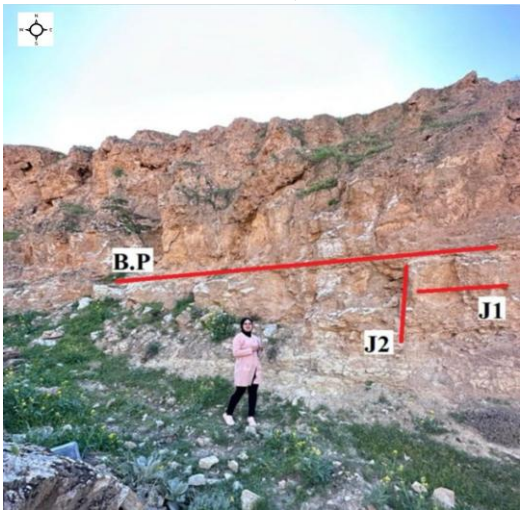
1. امكانية حدوث الأنزلاق المستوي في المحطات (1، 2، 5 و 6) حيث يحدث الأنزلاق المستوي على الأنقطاع (J1) في المحطات (1، 2 و 5)، وعلى الأنقطاع (J2) في المحطتين (6 و1).
2. امكانية حدوث الأنزلاق الأسفيني في جميع محطات منطقة الدراسة حيث يحدث من تقاطع (J1&J2) في المحطات (1، 2، 4 و 5) ومن تقاطع (SO&J2) في المحطة رقم (3)، ومن تقاطع (SO&J1) في المحطة رقم (6).
3. امكانية حدوث الأنقلاب المباشر في المحطتين (4 و 6)، حيث يحدث من تقاطع (SO&J2) في المحطة رقم (4)، ومن تقاطع (SO&J1) و (J1&J3) في المحطة رقم (6).
4. امكانية حدوث الإنقلاب المائل في المحطة رقم (6) من تقاطع (J1&J2).



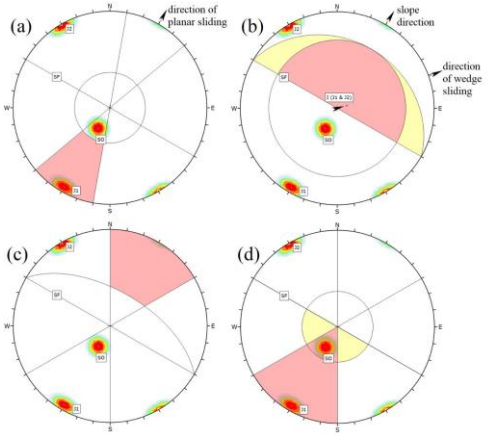
اللوحة 1: منحدر المحطة رقم (1)، موضحا فيها الانقطاعات، سطح التطبق، اتجاه التصوير (شمال–غرب).



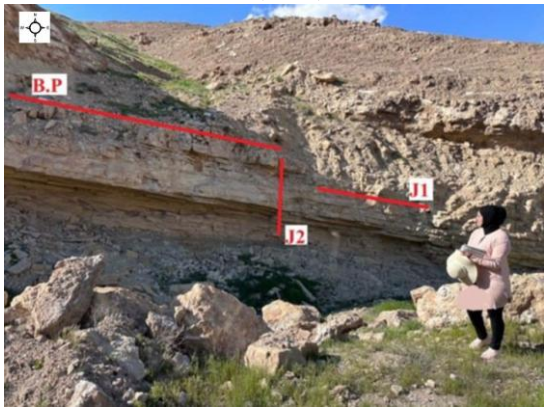
شكل 5: نتائج التحليل الحركي للمحطة (1)، (a) احتمال انزلاق مستوي حول اقطاب الانقطاع (j2 , j1). (b) احتمال حصول انزلاق اسفيني من تقاطع j1 مع j2. (c) لا يوجد احتمال حصول انقلاب ثنائي. (d) لا يوجد احتمال حصول انقلاب مباشر، حيث (SF) وجه المنحدر، (SO) مستوى التطبق، (J1 ,J2) مجاميع الفواصل.



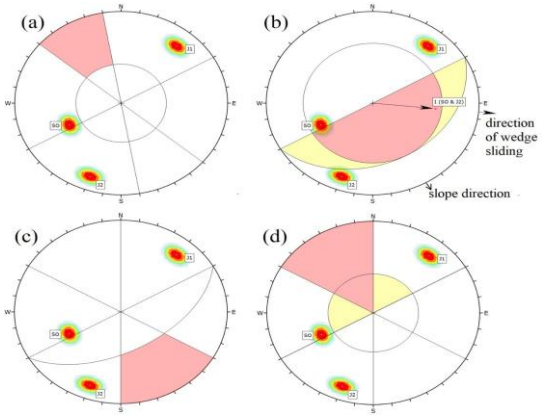
اللوحة (2) منحدر المحطة رقم (2)، موضحا فيها الانقطاعات، سطح التطبق، اتجاه التصوير (شمال–غرب).



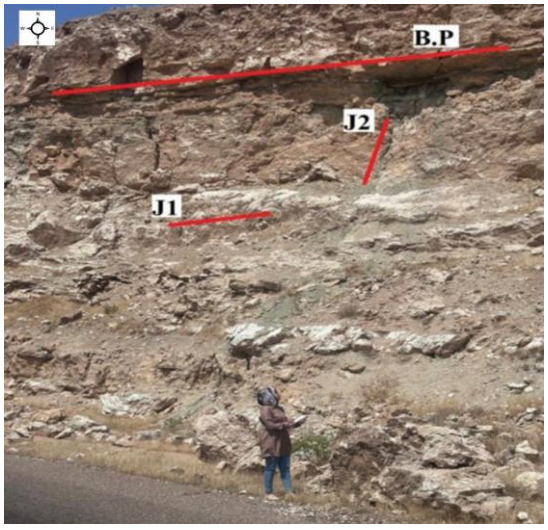
الشكل 6: نتائج التحليل الحركي للمحطة رقم (2)، الشكل (a) أحتمال أنزلاق مستوي حول قطب الانقطاع (J1) (b) أحتمال حصول أنزلاق أسفيني من تقاطع (J2 & J1) (c) لا يوجد أحتمال حصول أنقلاب أنثنائي (d) لا يوجد أحتمال حصول أنقلاب مباشر، حيث أن (SF) وجه المنحدر، (SO) مستوى التطبق، مجاميع الفواصل (J2, J1).



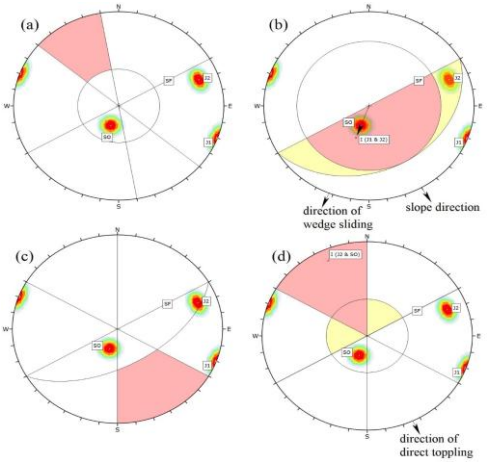
اللوحة (3) منحدر المحطة رقم (3)، موضحا فيها الانقطاعات، سطح التطبق، اتجاه التصوير (شمال–غرب).



الشكل (7) نتائج التحليل الحركي للمحطة رقم (3)، الشكل (a) لايوجد أحتمال أنزلاق مستوي (b) أحتمال حصول أنزلاق أسفيني من تقاطع (J2 & SO) (c) لا يوجد أحتمال حصول أنقلاب أنثنائي (d) لا يوجد أحتمال حصول أنقلاب مباشر، حيث أن (SF) وجه المنحدر، (SO) مستوى التطبق، مجاميع الفواصل (J2, J1).



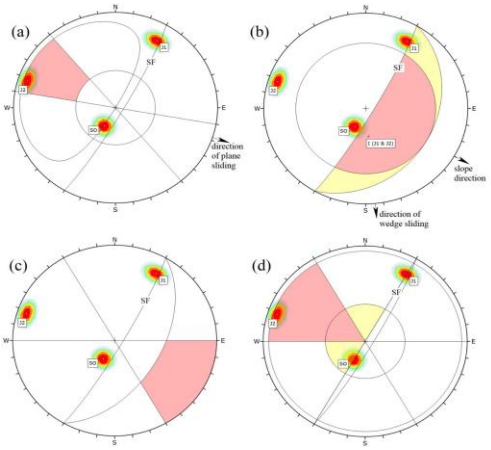
اللوحة (4) منحدر المحطة رقم (4)، موضحا فيها الانقطاعات، سطح التطبق، اتجاه التصوير (شمال–غرب).



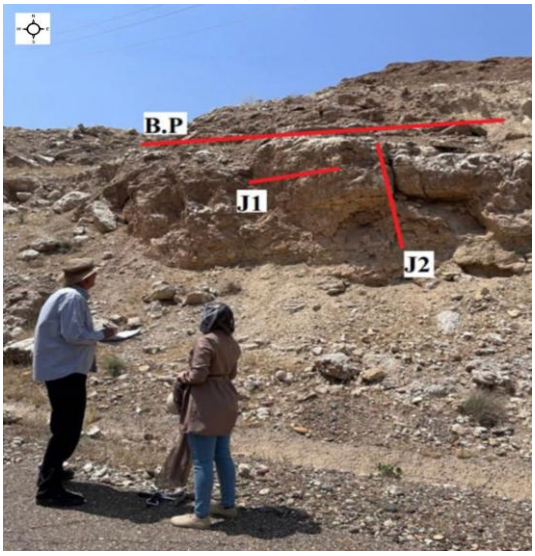
الشكل (8) نتائج التحليل الحركي للمحطة رقم (4)، الشكل (a) لايوجد أحتمال أنزلاق مستوي (b) أحتمال حصول أنزلاق أسفيني من تقاطع (J1 & J2)، (c) لا يوجد أحتمال حصول أنقلاب أنثنائي (d) أحتمال حصول أنقلاب مباشرمن تقاطع (J2 & SO)، حيث أن (SF) وجه المنحدر، (SO) مستوى التطبق، (J2, J1) مجاميع الفواصل.



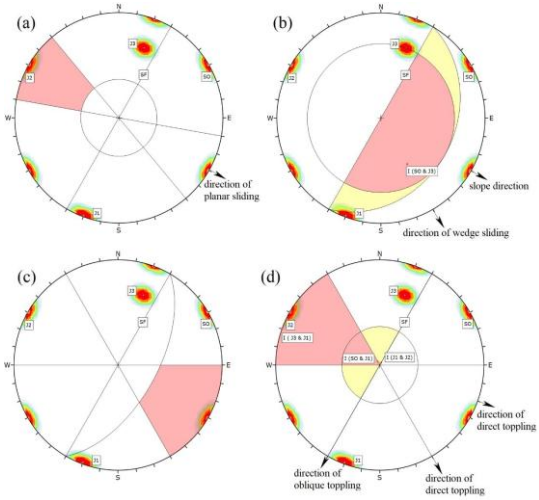
اللوحة (5) منحدر المحطة رقم (5)، موضحا فيها الانقطاعات، سطح التطبق، اتجاه التصوير (شمال–غرب).



الشكل (9) نتائج التحليل الحركي للمحطة رقم (5)، الشكل (a) أحتمال أنزلاق مستوي حول قطب الانقطاع (J1) (b) أحتمال حصول أنزلاق أسفيني من تقاطع (J1 & J2) (c)لا يوجد أحتمال حصول أنقلاب أنثنائي (d)لا يوجد أحتمال حصول أنقلاب مباشر، حيث أن (SF) وجه المنحدر، (SO) مستوى التطبق، (J2, J1) مجاميع الفواصل.



اللوحة (6) منحدر المحطة رقم (6)، موضحا فيها الانقطاعات، سطح التطبق، اتجاه التصوير (شمال–غرب).



الشكل 10: نتائج التحليل الحركي للمحطة رقم (6)، الشكل (a) أحتمال أنزلاق مستوي حول قطب الانقطاع (J2) (b) أحتمال

حصول أنزلاق أسفيني من تقاطع (J3 & SO) (c)لا يوجد أحتمال حصول أنقلاب أنثنائي (d) أحتمال حصول أنقلاب مباشرمن تقاطع (J2 J1)، (J1& SO) ، (J3 &J1) حيث أن (SF) وجه المنحدر، (SO) مستوى التطبق، (J2, J1) مجاميع الفواصل.

6. نظام تصنيف كتلة المنحدر (SMR)

تم استخدام التحليل الحركي لتحديد اربع أنماط فشل رئيسة للمنحدرات الصخرية هي (أنزلاق مستوٍ، أنزلاق أسفيني، انقلاب مباشر، انقلاب مائل) كما هو موضح في الجدول (2)، وتم تطبيق هذه النتائج على نظام تصنيف كتلة المنحدر(SMR). ومن ثم تحديد (RMRb) وفقاً لاقتراح (Bieniawski, 1989). تم حساب المقاومة الانضغاطية غير المحصورة (UCS) من اختبارات حمل النقطة من خلال معادلات

والتي تم إجراؤها وفقًا (ISRM, 1985)، ويوضح الجدول (3) قيم (UCS) وتتراوح القيم من (7.61) إلى (27.9) ميكا باسكال. تم استخدام العلاقة بين عدد الفواصل الحجمية (Jv) و(RQD) كما في المعادلة (7) لحساب قيمة (RQD) (Palmstrom, 2005) :

RQD =110-2.5 (Jv) …….. (7)

والتي تتراوح مابين (93.68%) الى (78.33%)، وتتراوح قيمة متوسط التباعد لجميع الانقطاعات من (459.55mm) الى (mm 236)، كما هو مبين في الجدول (5). ويبين الجدول (6) معاملات (RMR) المستخدمة لوصف الكتلة الصخرية للمحطات في منطقة الدراسة. وأن قيمة (RMRb) والتي يتم حسابها عن طريق حساب خواص الكتلة الصخرية بما تمثله من قيم من الاشكال (2) و (3) و (4) ثم تضاف التقديرات لتعطي قيمة (RMRb) ومن ثم الحصول على قيم (1989)RMRb لكل محطة، كما هو موضح في الجدول (7).

جدول 2: نتائج التحليل الحركي للمنحدرات الصخرية باستخدام برنامج (DIPv-6.008).

التكوين Formation	المحطات Stations	الانزلاق المستوي Plane sliding, failure probability, and trend	الانزلاق الاسفيني Wedge Sliding, failure probability, and trend	انقلاب ثنائي Flexural Toppling, failure probability, and trend	انقلاب مباشر Direct Toppling, failure probability, and trend	انقلاب مائل
فتحة	1	140°, 160°	228°	-------	-------	-------
	2	30°	74°	-------	-------	-------
	3	-------	96°	-------	-------	-------
	4	-------	203°	-------	155°	-------
	5	108°	175°	-------	-------	-------
	6	120°	150°	-------	110°,150°	210°

جدول 3: نتائج فحص حمل النقطة وقيمة المقاومة الانضغاطية غير المحصورة (UCS) لنماذج منطقة الدراسة.

التكوين Formation	المحطة Stations	D (mm)	W (mm)	F (Kn)	F (Mn)	A	f	De^2 (m^2)	IS	$IS_{(50)}$	UCS*
فتحة	1	110.7	50.8	2.05	0.0021	5623.6	1.267	0.007	0.286	0.363	7.616
	2	110.5	30.7	1.8	0.0018	3392.4	1.131	0.004	0.417	0.471	9.893
	3	110.6	60.4	7.73	0.0077	6680.2	1.317	0.0085	0.908	1.1966	25.128
	4	80.6	50.2	5.54	0.0055	4046.1	1.176	0.0051	1.0748	1.2649	26.562
	5	120.2	62	9.35	0.0094	7452.4	1.350	0.009	0.985	1.330	27.925
	6	110.2	55.2	7.9	0.0079	6083	1.290	0.008	1.019	1.315	27.615

* UCS: Unconfined compressive strength

جدول 4: عدد الفواصل الحجمي (JV)، (RQD) ومعدل التباعد للمحطة رقم (1).

Discontinuities (Joints and Bedding plane)	Set spacing and frequency Spacing (m) Min.	Max.	Average spacing (m)	Average frequency
Bedding plane (So)	0.05	0.70	0.375	2.6
(J1)	0.2	1.2	0.7	1.428
(J2)	0.20	0.60	0.4	2.5
Jv= Σ Frequencies (Joints/m^3) 6.528				
RQD = 93.68				
Average frequency of all discontinuities =Jv/3 2.176				
Average frequency of all discontinuities (m) = (1 / Average frequency) 459.55mm				

جدول 5: عدد الفواصل الحجمي (JV) عامل جودة الصخور (RQD) ومعدل التباعد للانقطاعات لجميع محطات منطقة الدراسة.

Formation	Stations	Jv (Joint/m3)	RQD	Average spacing of all discontinuities (m)
فتحة	1	6.528	93.68	0.45
	2	9.260	86.838	0.324
	3	10.302	84.245	0.2912
	4	7.8023	90.495	0.384
	5	10.434	83.915	0.287
	6	12.666	78.335	0.236

جدول 6: وصف الكتلة الصخرية (RMR) في المحطات.

Formation	Stations	Uniaxial compressive strength (UCS)(MPa)	RQD	Average spacing of all discontinuities (m)	Condition of discontinuities	Groundwater condition
فتحة	1	7.616	93.68	0.45	Persistence <1m, separation > 5, Smooth, no infilling, slightly weathered.	Wet
	2	9.893	86.838	0.324	Persistence < 1 m, separation > 5, Smooth, no infilling, slightly weathered.	Wet
	3	25.1288	84.245	0.2912	Persistence < 1 m, separation > 5mm, Smooth, no infilling, Moderately weathered.	Wet
	4	26.56	90.495	0.384	Persistence < 3-10 m, separation < 0.1mm, Smooth, no infilling, slightly weathered.	Wet
	5	27.925	83.915	0.287	Persistence < 3-10 m, separation < 0.1mm, Smooth, no infilling, slightly weathered.	Wet
	6	27.615	78.335	0.236	Persistence <1m, separation > 5, Smooth, no infilling, slightly weathered.	Wet

جدول 7: توصيف معاملات كتلة الصخور (RMR) وقيم RMRb(1989) للكتل الصخرية في محطات منطقة الدراسة.

Formation	Stations	Rating of parameters					RMR_b (1989)
		Uniaxial compressive strength (UCS)	RQD	Average space in all Discontinuities	Condition of discontinuities	Ground water	
فتحة	1	1.7	19	11.9	18	7	57.6
	2	1.3	16.5	10.7	18	7	53.5
	3	3.2	17	10.3	16	7	53.5
	4	3.3	18.2	10.2	19	7	57.7
	5	3.5	16.9	10.2	19	7	56.6
	6	3.5	15.6	9.5	23	7	58.6

الجدول 8: نتائج تصنيف كتلة المنحدر (SMR) المنفصلة باستخدام برنامج (SMRTool).

Stations	Slope attitude	RMRb	Failure type	Failure Direction	F1	F2	F3	F4	F1. F2. F3	SMR value	SMR class/ Stability
1	030°/90°	57.6	PS	140°	0.15	1	-25	0	-3.75	53	lll / Pasta
			PS	160°	0.15	1	-25	0	-3.75	53	lll / Pasta
			WS	228°	0.7	1	-25	0	-17.5	40	lV / Unsta
2	030°/90°	53.5	PS	30°	1	1	-50	0	-50	3	V / CUnsta
			WS	74°	0.15	1	-50	0	-7.5	46	lll / Pasta
3	150°/90°	53.5	WS	96°	0.15	0.85	-60	0	-7.65	45	lll / Pasta
4	150°/90°	57.7	WS	203°	0.15	1	-6	0	-0.9	56	lll / Pasta
			DT	155°	0.85	1	0	0	0	57	lll / Pasta
5	120°/84°	56.6	PS	108°	0.7	1	-6	0	-4.2	52	lll / Pasta
			WS	175°	0.15	1	-6	0	-0.9	55	lll / Pasta
6	120°/90°	58.6	PS	120°	1	1	-25	0	-25	33	lV/ Unsta
			WS	150°	0.15	1	-60	0	-9	49	lll / Pasta
			DT	150°	0.15	1	-25	0	-3.75	54	lll / Pasta
			DT	110°	0.7	0.15	-60	0	-6.3	52	lll / Pasta
			OT	150°	0.15	1	-25	0	-3.75	54	lll / Pasta

Where: PS=Planar sliding, WS=Wedge sliding, FT=Flexural toppling, DT=Direct toppling, F1, F2andF3 are adjustment factors of SMR, Sta=Stable, Pasta=Partially stable, Unsta=Unstable, Cunsta=Completely unstable.

الجدول 9: نتائج قيمة (CSMR) المستمرة باستخدام برنامج (SMRTool).

Stations	Slope attitude	RMRb	Failure type	Failure Direction	F1	F2	F3	F4	F1. F2. F3	SMR value	(CSMR) class/ Stability
1	030°/90°	57.6	PS	140°	0.20115	1	-25.6526	0	-5.16	52	lll / Pasta
			PS	160°	0.16411	1	-25.716	0	-4.2202	53	lll / Pasta
			WS	228°	0.60812	1	-25.3434	0	-15.4118	42	lll / Pasta
2	030°/90°	53.5	PS	30°	0.99721	0.9925	-56.8459	0	-562618	0	V /CUnsta
			WS	74°	0.22252	0.99113	-57.7073	0	-12.7272	40	lV/ Unsta
3	150°/90°	53.5	WS	96°	0.19053	0.87884	-59.6155	0	-9.9825	43	lll / Pasta
4	150°/90°	57.7	WS	203°	0.31093	1	-4.0731	0	-1.2664	56	lll / Pasta
			DT	155°	0.93846	1	-0.62322	0	-0.5848	57	lll / Pasta
5	120°/84°	56.6	PS	108°	0.79939	0.9956	-3.1541	0	-2.5103	54	lll / Pasta
			WS	175°	0.24666	0.9956	-3.1541	0	-0.77458	55	lll / Pasta
6	120°/90°	58.6	PS	120°	0.99721	0.9956	-30	0	-29.7646	28	lV/ Unsta
			WS	150°	0.32541	0.9343	-59.5446	0	-18.1035	40	lV/ Unsta
			DT	150°	0.32541	1	-25.7133	0	-8.364	50	lll / Pasta
			DT	110°	0.84995	0.15896	-59.7878	0	-8.0779	50	lll / Pasta
			مائل	150°	0.1466	1	-25.716	6	-3.7751	54	lll / Pasta

Where: PS=Planar sliding, WS=Wedge sliding, FT=Flexural toppling, DT=Direct toppling, F1, F2andF3 are adjustment factors of SMR, Sta=Stable, Pasta=Partially stable, Unsta=Unstable, Cunsta=Completely unstable.

لتقييم أستقرارية المنحدرات الصخرية في جميع المحطات، تم حساب نظام تصنيف كتلة المنحدر(SMR) لـ (Romana, 1985) ونظام تصنيف كتلة المنحدر المستمر(CSMR) لـ (Tomas et al., 2007) عن طريق استخدام برنامج (SMRTool v205) (Riquelme et al., 2014)، حيث أن البرنامج يحتوي على نظامين هما نظام كتلة المنحدر المنفصل (SMR) ونظام كتلة المنحدر المستمرة (CSMR).

تم حساب قيمة (RMRb) من تغيرات في صفات كتلة الصخور، وأن هذه القيمة تستخدم لأيجاد (SMR) في كل المحطات، وأن قيم (F2, F3, F1) يتم حسابها من خلال البرنامج (SMRTool v205) وذلك اعتمادا على الأتجاه النسبي للفواصل نسبة إلى المنحدر، وأن قيمة (F4) تعتمد على طبيعة ونوع المنحدر، وبما أن المنحدر ناتج من الحفر عن طريق وسائل ميكانيكية، فأن قيمته هي صفر (0).

من خلال برنامج (SMR Tool) تمت ملاحظة أن أقل قيمة لتصنيف كتلة المنحدر لـ (SMR) المنفصل والمستمر للأنزلاق المستوي تكون في المحطة (3) والتي تتراوح قيمها (0–3) والتي تكون غير مستقرة بشكل كلي (Completely unstable) وتقع ضمن الفئة الخامسة (V) وبنسبة أنهيار (0.9)، والمحطات التي تكون غير مستقرة (Unstable) وتكون ضمن الفئة الرابعة (IV) والتي تتراوح قيمها (28–42) وبنسبة أنهيار (0.6) للأنزلاق المستوي هي محطة (6) وللأنزلاق الاسفيني هي المحطة (1)، والمحطات التي تكون مستقرة بشكل جزئي (Partially stable) وتقع ضمن الفئة الثالثة (III) وبنسبة انهيار 0.4 والتي تتراوح قيمها ما بين (43 – 57) للأنزلاق المستوي هي في المحطة (1)، والانزلاق الاسفيني في المحطات (2، 3، 4، 5 و 6) والأنقلاب المباشر في المحطات (4 و 6) والأنقلاب المائل في المحطة (6).

من خلال مقارنة النتائج ما بين الـ (SMR) و الـ (CSMR) وجد هنالك اختلاف في بعض المحطات، حيث ان الأنزلاق الأسفيني في المحطات (2، 6) لـ (SMR) كانت مستقرة بشكل جزئي (Partially stable) وتقع ضمن الفئة الثالثة (III)، اما الأنزلاق الاسفيني لنفس المحطات لـ (CSMR) فتكون غير مستقرة (Unstable) وضمن الفئة الرابعة (IV).

7. الاستنتاجات

تبين من خلال نتائج التحليل الحركي بأستخدام برنامج (DIPS v6.008) ان اكثر انواع الأنهيار حدوثاً هي من نوع الأنزلاق الأسفيني حيث يحدث في جميع محطات منطقة الدراسة، اما الأنهيار الأخر فهو انهيار الأنزلاق المستوي والذي يحدث في المحطات (1، 2، 5 و 6)، والأنقلاب المباشر يحدث في المحطات (4 و 6)، اما اقل انواع الأنهيارات حدوثا فهو الأنقلاب المائل والذي يحدث في المحطة (6). وفقاً لنتائج برنامج (SMR Tool) المنفصلة والمستمرة، فإن أسوأ حالة للأنزلاق المستوي تكون في المحطة (3) والتي تكون غير مستقرة بشكل كلي وتقع ضمن الفئة الخامسة (V) وبنسبة أنهيار 0.9، والمحطات التي تكون غير مستقرة هي للأنزلاق المستوي في المحطة (6) وللأنزلاق الاسفيني في المحطة (1)، وتكون ضمن الفئة الرابعة (IV) وبنسبة أنهيار (0.6)، والمحطات التي تكون مستقرة بشكل جزئي هي للأنزلاق المستوي في المحطة (1)، والانزلاق الاسفيني في المحطات (2، 3، 4، 5 و 6) والأنقلاب المباشر في المحطات (4 و 6) والأنقلاب المائل في المحطة (6)، وتقع ضمن الفئة الثالثة (III) وبنسبة انهيار 0.4.

8. الشكر والتقدير

شكري وتقديري إلى الاساتذة المشرفين على مساعدتهم السخية ومعلوماتهم القيمة.

9. تضارب المصالح

يُعلن المؤلفون أنه لا يوجد لديهم أي تضارب في المصالح.

.

10. بيان التمويل

لم يتلق هذا البحث أي تمويل خارجي.

11. المصادر

Al-Jawadi, A.S., 2021.Theoretical Models of Slope Stability Analysis in The Maqlub Mountain Rock Cut Routes, North Iraq, 2021, The Iraqi Geological Journal, 54 (1A), pp. 55-68. https://doi.org /10.46717/igj.54.1A.6Ms-2021-01-27 .

Al-Jawadi, A.S., Al-Dabbagh, Th.H., and Dawlat, M.S., 2021, Slope Assessment and Suggested Slope Design of the Bekhme Residential Complex in North Iraq, Indian Geotechnical Journal, pp. 1-11, Springer India. https://doi.org /10.1007/s40098-020-00497-1 .

Al-Jumili, A.I., 2024. "Assessment of Rock Slope Stability along the Qaywan-Mokba Road in Sulaymaniyah Governorate / Northeastern Iraq." Iraqi Geological Journal. 44 P.

Al-Naqib, K.M., 1959. Geology of the Southern area of Kirkuk Liwa, Iraq. IPC. Technical pub. London, internal report.

Al-Talib, S.A., Al-Jawadi, A.S., and Al-Sanjari, A.A., 2021. Impact of Gercus Formation Erosion and Rock Sliding on Duhok Dam Reservoir – Northern Iraq, Iraqi Journal of Science, Vol. 62, No. 5, pp. 1562-1569. https://doi.org /10.24996/ijs.2021.

Anbalagan, R., Sharma, S. and Raghuvanshi, T.K., 1992, June. Rock mass stability evaluation using modified SMR approach. In Rock Mechanics Proceedings of the Sixth National Symposium on Rock Mechanics, 258–268.

Anon., 1977: The description of rock masses for engineering purposes, Report by the Geological Society Engineering Group Working Party, Quarterly Journal of Engineering Geology, Vol.10, pp.355-388.

Bayram, A.F., Mohamed, A.I. and Othman, A.A., 2021. Stability and sustainability assessment for the surface failure of various rock slopes excavated along the Konya-Alanya Road segment, Turkey. Kuwait Journal of Science, 48(4), 1-15.

Bellen, Van R.C., Dunnington, H.W., Wetzel, R., Morton, D.M., 1959. Lexique stratigraphique international, V.3, Iraq, Asie, Paris, Internet Geol. Cong. Comm. Strat. Pt.,333 P

Bieniawski, Z.T., 1989. Engineering rock mass classifications: a complete manual for engineers and geologists in mining, civil, and petroleum engineering. John Wiley and Sons, 251.

Bruce, I.G., Cruden, D.M. and Eaton, T.M., 1989. Use of a tilting table to determine the basic friction angle of hard rock samples. Canadian Geotechnical Journal, 26(3), 274-279.

Buday, T. and Jassim, S.Z., 1987. The Regional Geology of Iraq. Vol.2, Tectonism, Magmatism and Metamorphism, Edited by Kassab, I.I and Abbas, M.J. Baghdad, Iraq, 352 p.

Fattah, M.B., AL-Zubaydi, J.H., and Zainy, M.T., 2023. Structural Analysis for Slope Stability Assessment of Selected Sites at Shurshirin Valley, Zurbatiyah Region, Eastern Iraq. Iraq Geological Journal, 56(2F),290-300. https://doi.org/10.46717/igj.56.2F.19ms-2023-12-25.

Hoek, E. and Bray, J.W., 1981. Rock Slope Engineering, 3rd ed., Institution of Mining and Metallurgy, London, 358 P.

Hussain, A. I., 2009. Morphotectonic Study of Jabil Makhul Area by Using Satellite Images, Remote Sensing Unit, College of Science, University of Tikrit. Tikrit-Iraq. P.15. In Arabic.

ISRM, J.A., 1985, April. Suggested method for determining point load strength. In International Journal of Rock Mechanics and Mining Sciences and Geomechanics Abstracts, 22(2), 51-70.

Palmstrom, A., 2005. Measurements of and correlations between block size and rock quality designation (RQD). Tunnelling and Underground Space Technology, 20(4), 362–377. https://doi.org/10.1016/j.tust.2005.01.005 .

Qader, R.M., Syan, S.H.A., 2021. Rock slope stability assessment along main road, Kurdistan Region, The Iraqi Geological Journal,79-93.

https://doi.org/10.46717/igj.54.1B.7Ms-2021-02-25 .

Riquelme, A., Abellán, A. and Tomás, R., 2014. SMRTool beta. A calculator for determining slope mass rating (SMR). Universidad de Alicante. Website:http://personal.ua.es/en/ariquelme/smrtool.html (07/05/2014). License: Creative Commons BY-NC-SA.

Romana, M., 1985, September. New adjustment ratings for application of Bieniawski classification to slopes. In Proceedings of the International Symposium on the Role of Rock Mechanics, Zacatecas, Mexico, 49-53.

Saranaathan, S.E. and Kannan, M., 2017. SMR and Kinematic analysis for slope instability along Bodi-Bodimettu ghat section, Tamil Nadu. Journal of the Geological Society of India, 89(5), 589-599.

Sarkar, S., Kanungo, D.P. and Kumar, S., 2012. Rock mass classification and slope stability assessment of road cut slopes in Garhwal Himalaya, India. Geotechnical and Geological Engineering, 30(4), 827-840.

Sharma, M., Sharma, S., Kumar, M. and Singh, S.K., 2019. Analysis of slope stability of road cut slopes of Srinagar, Uttarakhand, India. International Journal of Applied Engineering Research, 14(3), 609-615.

Siddique, T., Alam, M.M., Mondal, M.E.A. and Vishal, V., 2015. Slope mass rating and kinematic analysis of slopes along the National Highway 58 near Jonk, Rishikesh, India. Journal of Rock Mechanics and Geotechnical Engineering, 7(5), 600-606.

Tomás, R., Delgado, J., Gáñez, S. and Bernardo, J., 2007. Modification of slope mass rating (SMR) by continuous functions. International Journal of Rock Mechanics and Mining Sciences, 44(7), 1062-1069.

Umrao, R. K., Singh, R., Ahmad, M. and TN, S., 2011. Stability analysis of cut slopes using continuous slope mass rating and kinematic analysis in Rudraprayag district, Uttarakhand. Geomaterials, 1(3), 79-87. DIO.

Vol. 26, No. 04, 2026 (26-37) *المجلة العراقية الوطنية لعلوم الأرض،*

المجلة العراقية الوطنية لعلوم الأرض

www.earth.uomosul.edu.iq

Evaluation of Rock Slope Stability on the Northeastern Limb of Makhul Anticline, Northern Iraq

Rafal A. Khudier [1*], Mohameed R. Abood [1], Abdalsalam M. Tarif [1]

rafal.199593@gmail.com mrabood@tu.edu.iq abdulsalam_mehdi@tu.edu.iq

[1] *Department of Applied Geology, College of Science, University of Tikrit, Tikrit, Iraq.*
** Correspondence author.*

Received: 28 November 2024 Received in revised form: 02 February 2025 Accepted: 03 May 2025
Available online: 01 October 2026

Abstract

Makhul anticline is about 58 km long in the northeast of Tikrit City, where six slope site stations within the Fatha Formation are selected for this investigation. Kinematic analysis and the slope mass classification system are used to search and analyze the potential level of stability by applying two packages (DIPS v6.008 and SMRTool v205). Based on the kinematic analysis using the DIPS v6.008 system, it is found that plane sliding occurs at stations (1, 2, 5, and 6), wedge sliding occurs at all stations, direct toppling occurs at stations (4 and 6), and oblique toppling occurs at station (6) that is considered the least frequent type of failure in the study area. As for estimating the mass of the slope according to the results of the separate SMR-Tool program and the continuous CSMR program, it is shown that the worst case of flat slide is at station (3), which is completely unstable and falls within the fifth category (V) with a failure rate of 0.9. The unstable stations are the plane sliding at station (6) and the wedge sliding at station (1), and both are within the fourth category (IV) with a failure rate of 0.6, whereas the partially stable stations are the plane sliding at station (1) and the wedge sliding at stations (2, 3, 4, 5, and 6), the direct toppling at stations (4 and 6), and the oblique toppling at station (6), which fall within the third category (III) with a failure rate of 0.4.

Keywords:

Fatha Formation, Limestone, kinematic analysis, failure, Gypsum.

DOI: 10.33899/injes.v26i4.56126, ©Authors, 2026, College of Science, University of Mosul.

This is an open-access article under the CC BY 4.0 license (http://creativecommons.org/licenses/by/4.0/).

==========

البحوث باللغة الانكليزية

Arabic Section

IRAQI NATIONAL JOURNAL OF EARTH SCIENCE

Vol. 26 **October 2026** **No. 04**

Editor-in- Chief

Prof. Dr. Rayan Ghazi Thannoun

Managing Editor

Assistant Prof. Dr. Azealdeen Salih Al-Jawadi

Editorial Board

Prof. Dr. Majid Majdi Al- Mutwali
Prof. Dr. Moez Ben Fadhel (Tunisia)
Prof. Dr. Haji Rahab (Algeria)
Prof. Dr. Sherif Farouk (Egypt)
Prof. Dr. Ezzadin N. Baban
Prof. Dr. Basem Sayed Nabawy (Egypt)
Prof. Dr. Alain Preat (Belgium)
Prof. Dr. Masdouq M. Al-Taj (Jordan)
Prof. Dr. Sawsan Hameed Faisal Al-Hazaa
Prof. Dr. Sattar Gabar Rasheej Al-khafagi
Prof. Dr. Rafee Ibraheem Al Hamedi
Assistant Prof. Dr. Aahed Younis Al-Mallah
Assistant Prof. Dr. Mohammed Fawzy Omer
Assistant Prof. Dr. Namam Mohammed Saleh
Assistant Prof. Dr. Omar Abdullah Ismail
Assistant Prof. Dr. Falah Abed M. Al-Miamary
Dr. Haitham I. Hamid
Assistant Prof. Dr. Saddam Essa Al-khatony
Assistant Professor Dr. Mehdi Rahnama (Iran)
Assistant Professor Dr. Rashid Pourmirzaei (Iran)
Assistant Professor Dr. Bashar Aziz Mahmoud

Managing the Electronic System of the Magazine

Assistant Prof. Dr. Saddam Essa Al-Khatony

Technical Affairs, Coordination, and Publication

Assistant Lecturer Myasar Samir Mahmoud Al-Siraj
Research Assistant Azhar Nazar Idres Al-kallo

Management Coordinator: Assistant Lecturer Hiba Esam Thannon

Published by: College of Science / University of Mosul
p-ISSN: 1682-3222
e-ISSN: 2664-2816

E-mail: injes@uomosul.edu.iq
Website: http://www.iasj.net
https://earth.uomosul.edu.iq/
Mobile: 009647701610916

contents

Paragenesis and Multi-fracture System in Jurassic Barsarin Formation: Implications from Various Burial Settings, NE-Iraq
Rayan Fattah, Namam Salih , Alain Préat 1
Hydrogeological Evaluation of Groundwater Vulnerability Assessment Using the DRASTIC and Pesticide DRASTIC Model: A Case Study from the Qushtapa and Shamamik Area, within Erbil Basin, Kurdistan Region, Iraq
Seber M. M. Ameen , Rebwar N. Dara 19
GIS to Create Maps Based on the Bergsma Model for Gully Erosion Estimation Using DEM: A Case Study for Qarahanjeer, Kirkuk, Iraq
Suzan I. Baez, Fawzi M. Omar , Mustafa R. Mezaal 31
Integrated Reservoir Characterization and Petrophysical Assessment of the Kurra Chine Formation in the Peshkhabir Oil Field, Northern Iraq
Mahdi Khairi Aswad, Sazan Mohammed Ali 40
Water Suitability for Paddy Field Irrigation in Tropical Watershed Dominated by Ancient Volcanic Rocks and Limestones, Indonesia
Ahmad Cahyadi , Indra Agus Riyanto , Marselli Nabila Putri, Rizka Novi Ramadhan.....54
Petrography, Facies Analysis, and Depositional Environment of the Sargelu Formation (Middle Jurassic), in a Selected Section, Northeastern Iraq
Noor T. Al-Taee 68
Calcareous Nannofossil Biostratigraphy of Sarmord Formation (Lower-Upper Cretaceous) in Bekhme Anticline, Kurdistan Region – Northeastern Iraq
Inas H. Al-Khafaf , Majed M. Al-Mutwali 81
Petrophysical Properties and Sedimentology of the Palani Formation (Late Eocene-Early Oligocene) from Kirkuk Oil Field, Northeastern Iraq
Ezzat I. Al-Fandi , Zaid A. Malak, Rafee Ibraheem AL-Hamidi 98
Environmental Applications of Marine Foraminifera and Ostracoda Assemblage in Faw Town, South of Iraq
Badria Ali Hussain, Abbas Hameed Mohammed 108
Deep Insights for Optimizing Hydraulic Fracturing Designs to Maximize Productivity in Horizontal Wells within Unconventional Reservoirs
Huda J. TH. AL-Hillali, Faleh H. M. Almahdaw.....122
Reservoir Evaluation of Nahr Umr Formation at Abu-Amood Oil Field, Southern Iraq
Mhammed Q. Abd Talib, Mohammd S. Al-Jawad 130
Assessment of Heavy Metal Pollution and Sources Identification in Urban Soil Using Pollution Indices and Statistical Analysis, Mosul, Iraq
Ruqaya B. Mohammed , Hazim J. Mahmood 138
An Assessment of Heavy Metal Pollution in Roadside Dust: A Case Study from Basrah Governorate, Southern Iraq
Iqbal O. Al-Taie, Hanan A. Darweesh , Yasmin I. Al Fraji 151
Hydromorphometric Analysis of the Koya Basin in the Kurdistan Region of Iraq.
Ala Qader, Shwan Seeyan 161
Study of Radon Concentration in Well Water in the Districts of Kirkuk Governorate
Lana H. Mohammed , Alyaa H. Mohammed, Ebtihal G. Khidher, Mohammed Ahmed Omar.....175

Three-dimensional Slope Stability Evaluation Under Seismic Load: A Case Study in Balaroa, Central Sulawesi, Indonesia
Rahmat Yusup Borman, Busthan Azikin, Hendra Pachri 184
Reservoir Quality Assessment of Subsurface Sections Across Jurassic Period (Mus and Sargelu) Formations in Duhok Governorate, Kurdistan Region, Iraq
Parween Ramadhan Abid, Rzger Abdulkarim Abdula..... 193
Analysis of the Morphometric Characteristics and Their Relationship with the River Network Properties of Valley Al-Amghar Basin, Southwestern Al-Muthanna Desert: An Applied Statistical Study
Hader M. A. Al-Kafari, Safaa A. Al-Asadi 206
Comprehensive Review of Meteorological Drought in Iraq
Sura B. Idrees, Omar M.A. Mahmood Agha 219
Late Middle Miocene (Serravallian) of the Fat'ha Formation, Northern Iraq: Palynofloral Evidence
Ahmed S. Qulmani , Maha A. Al-Hasson 235
Utilizing Shear Wave Velocity Techniques for Identifying Engineering Challenges in 6th October City, Egypt
Diaa Hamed 244
Measurement of Magnetic Intensity Using Three Different Sensor Levels and Three Vertical Gradient Determinations to Detect Subsurface Engineering Utilities.
Ahmad S. Al-Banna , Hayder H. Majeed , Fitian R. Al- Rawi , Tariq Safa Aldin 257
Groundwater Overdraft and Climate-Driven Land Subsidence in the Sulaimani-Sharazoor Basin, Iraq: Insights from InSAR Techniques
Shahrayar Tawfeeq San, Dara Hama Amin 263
Assessing the Drinking Water Quality Index in Arid Areas: An Analysis of the El Hadjeb Region in Biskra, Southeastern Algeria.
Warda Chaib, Farida Bettiche, Nora Salemkour, Asma Rezeg , Halima Mancer, Khadidja Bouzid , Nora Bouchahm 283
Microfacies Analysis and Depositional Environment of the Ibrahim, Azkand and Anah Formations in Selected Oil Fields of Northern Iraq.
Abdulla Ahmed Abid, Faris Nejres Hassan Al Jubory, Saad Ahmed Mahmood 293
Sewage Sludge and Sediment Analyses as Indicators of Regional Heavy-Metal Pollution: A Case Study in El-Harrach, Algeria
Amina Bousseliou , Issam Boudraa , Smaine Chellat , Brahim Kebabi 309
Model for Hazard Mapping and Disaster Management of Land Degradation Using Geospatial Techniques in Iraq: A Review
Mohammed H. Azeez, Hisham M. Jawad Al Sharaa, Abdul Razzak T. Ziboon..... 323

Iraqi National Journal of Earth Science, Vol. 26, No. 04, 2026 (01-18)

Iraqi National Journal of Earth Science

www.earth.uomosul.edu.iq

Paragenesis and Multi-fracture System in Jurassic Barsarin Formation: Implications from Various Burial Settings, NE-Iraq

Rayan Fattah [1], **Namam Salih** [2*], **Alain Préat** [3]

rayanmhamadfatah99@gmail.com namam.salih@soran.edu.iq alain.preat@ulb.be

[1] *Department of Petroleum Geosciences, Science Faculty, Soran University, Erbil, Soran-44008, Iraq*
[2] *Department of Petroleum Engineering and Mining, Engineering Faculty, Soran University, Soran-Erbil, 44008, Iraq*
[3] *Res. Grp., Biogeochemistry and Modelling of the Earth System, Université Libre de Bruxelles, 1050 Brussels, Belgium*
[*] *Corresponding author*

Received: 23 January 2025 Received in revised form: 20 March 2025 Accepted: 13 May 2025
Available online: 01 October 2026

Abstract

Generation of fracture systems and geofluid evolution in shallow and subsurface environmental conditions play a critical role in various geological processes and petroleum applications. This paper evaluates comprehensive data to provide a deep understanding of multi-fracturing systems dissolved/filled by various cement phases related to different tectonic settings and the influx of diagenetic fluids in near-surface and subsurface settings. This study utilized intensive field observation and an optical microscope to track the paragenesis of the targeted formation and fracture stages in the Jurassic interval. The study recognizes five main types of fractures: (1) FI generated during surface or near surface conditions; the timing of initiating FI is not older than low-amplitude stylolite (LAS) (2) FII formed in shallow burial diagenesis and was coeval with late diagenetic stage, (3) FIII in-situ fractures formed in the subsurface conditions coinciding with high-amplitude stylolitization (HAS), (4) FIV fracture filled by calcite cement with plenty of solid bitumen fluid inclusions; and (5) FV-filled dolomite cements. The characteristics and appearance of dolomite crystals, corrosion, suture contact between saddle dolomite/calcite grains, and tightly compacted grains are directly linked to the increasing burial weight of overlying sedimentary rocks during the "Mesogenesis Phase". In summary, the findings add new insight as the fractures act as essential conduits and barriers in hydrocarbon migration and accumulation through various geological processes, from their formation during deposition to their evolution and the fracturing significant in post-depositional settings. The recognition of how these fractures originated enables more effective exploration and production strategies in hydrocarbon reservoirs.

Keywords:

Fracturing; Petrography; Dolomitization; Upper Jurassic Carbonate rocks; Stylolitization; Paleo-fluids Evolution; Shallow and deep-burial diagenesis.

DOI: 10.33899/injes.v26i4.60916, ©Authors, 2026, College of Science, University of Mosul.
This is an open-access article under the CC BY 4.0 license (http://creativecommons.org/licenses/by/4.0/).

==========

1. Introduction

Fractures show mechanical failures of the rock strength to natural geological stresses such as tectonic movement, lithostatic pressure variations, thermal stresses, high fluid pressure, and even fluid withdrawal, since fluid also partially supports the weight of the overburden rock (Tiab and Donaldson, 2003). Fractures are essential for hydrocarbon storage and act as conduits for fluid flow (Xu et al., 2016; Peacock et al., 2016). Fractures are recognized as significant migration paths for hydrothermal fluids, which contribute to the formation of saddle dolomite (Tiab and Donaldson, 2033) and hydrothermal dolostone reservoirs (Zhao et al., 2012; Jiang et al., 2016). Fracture effectiveness often refers to the condition when natural fractures are open, facilitating efficient fluid flow under reservoir conditions (Lu et al., 2018; Oyedokun and Schubert, 2017). The effectiveness of fractures can be analyzed by examining the filling time of paleo-fluid, the period of fracture development, the time of cement breaking, and the subsequent dissolving time (Ren et al., 2019; Amirjan and Bozorg, 2018). Natural fractures can substantially influence the flow of

formation and production fluids, particularly in low-permeability rock formations (Weisenberger et al., 2019). They establish conduits between organic-rich source layers and matrix pores during hydrocarbon charging, as well as between matrix pores, hydraulic fractures, and the wellbore during extraction (Warpinski and Lorenz, 2008).

The presence of cement in fractures, whether cemented or cement-lined, along with the topology of fracture cement and porosity, can greatly affect fracture permeability, impacting well productivity and reservoir performance (Landry et al., 2016, Wennberg et al., 2016). The diagenetic condition of cracks may affect fluid flow on a basin scale (Fischer et al., 2009, Bjørlykke and Jahren, 2012). The kind and quantity of fracture cement can impact fracture spacing (Hooker and Katz, 2015)and**,** among other variables, cement in pre-existing fractures can influence subsequent fracture propagation (Virgo et al., 2014, Lee et al., 2018). Comprehending the mechanisms of cement accumulation in fractures is crucial for forecasting the flow and storage characteristics of these rocks (Weisenberger et al., 2019). Cements convey insights into the physical and chemical conditions of the reservoir during various diagenetic stages, as well as fluid composition, so yielding information that would otherwise be inaccessible from voids (Baqués et al., 2020). Significant variables influencing the diagenesis of carbonate rocks include fluctuations in sea levels linked to tectonic events and climatic variations, as well as sedimentary diagenesis (Bathurst, 1972). Therefore, the rocks rapidly respond to diagenetic processes such as cementation, dissolution, porosity, and neomorphism that lead to the destruction of the sedimentary textures, skeletal grains, and groundmass (Boggs, 2006). Compaction is a detrimental factor in carbonate rocks, resulting from significant lithostatic pressure, which decreases porosity (Rasool et al., 2023). Dissolution can also occur due to meteoric and organic acids, as well as high-temperature and magnesium-rich fluids (Baqués et al., 2020). Dissolution surfaces and stylolites are generated due to pressure solution (Jiayu, 1999). Stylolites arise from heightened overburden sedimentation or tectonic pressure, influencing the grains in carbonate rock, facilitating disintegration, and extending seams (André et al., 2010). Dolomitization is a significant diagenetic event in the Jurassic strata and **is** characterized by broad and pervasive dolomitization exhibiting various crystal sizes (Rasool et al., 2023).

Numerous natural fractures that developed under moderate to profound burial conditions throughout geological time scales are lined or sealed with mineral cement (Laubach, 2003). The extent of fill is influenced by the fracture size, the rate of fracture opening, heat exposure, geochemical conditions, and the reactivity and composition of the fracture-vertical rock formations (Lander and Laubach, 2014). Therefore, several scholars have studied the timing and generation of fracture systems based on the geometry of the rock, paragenesis, and staging of fractures by cross-cutting or direct dating using U-Pb radiogenic isotopes (Salih et al., 2019a, Shen et al., 2019, Shen et al., 2022, Xu et al., 2025).

During the deposition phase, the mechanical properties of sediment are influenced by the accumulation of layers, leading to load-induced fracturing. This is evident in carbonate systems, where the early cementation of sediments can generate stress within the sediment column, resulting in brittle fracturing. For instance, McNeill and Eberli (2009) observed that the rapid progradation of carbonate margins can lead to early fracturing due to the load from overlying sediments (McNeill and Eberli, 2009). The presence of different cement types, such as dolomite or calcite, in these fractures further complicates the interaction between deposition and fracturing, influencing fluid pathways critical for diagenetic processes, as shown by (Budd et al., 2013).

In a syn-depositional environment, fractures can serve as conduits for fluid movement and chemical exchanges, significantly affecting the diagenetic evolution of the sediments. For example, syn-depositional fractures in high-relief carbonate platforms can facilitate the migration of diagenetic fluids, enhancing the permeability of these structures (Berra and Carminati, 2012). Studies by Léveillé et al. (2014) suggested that cements can fill fractures during this stage, which provides insights into past aqueous activity (Léveillé et al., 2014). These can effectively alter reservoir characteristics by influencing mineral precipitation and fluid dynamics during the early stages of sedimentary formation.

Furthermore, the fracturing system during post-deposition continues to evolve the interaction between fractures and cementation, with existing

fractures potentially sealed by subsequent cementation, altering flow pathways through the rock. Fracturing often precedes or coincides with cementation processes, with fracture fills affecting the mechanical integrity of the rock and consequently its reservoir quality. Gale et al. (2004) noted that the characteristics of dolostone reservoirs can reflect the geological interplay between fracturing and the growth of cements that seal these fractures (Gale et al., 2004). The timing of fracture growth relative to cementation is vital, as it determines how fractures accommodate fluid migration within the diagenetic landscape (Salomon et al., 2020). Moreover, the type and degree of cementation are influenced by several factors, including sedimentology, the chemical composition of pore fluids, and mechanical stability. The distribution of fractures is not uniform and can depend on lithology and other sedimentologic characteristics, suggesting a predictive model for understanding fracture networks based on these controls (Sonntag et al., 2014).

Therefore, in carbonate systems, the mechanical and diagenetic interactions show that the observed fractures can provide significant insights into past sedimentary environments and tectonic activities, which is valuable for hydrocarbon exploration and other geological applications. However, there is not enough data about the timing of the fracture system based on the type of cementation that originated from various paleo-fluid sources. Therefore, the novelty of this work is to understand the timing and staging of the fracture system within the Upper Jurassic formation based on the type of cement that requires not less than 1Ma to accumulate inside the pore spaces of these fractures.

2. Aims and objectives of the study area

The main aim and objective of this work is to conduct an in-depth investigation and analysis of the fracture systems that are produced from the source rocks of the Barsarin Formation, with a particular emphasis on understanding their paragenetic sequence. Analyzing and understanding the sequence of their chronological sequence of fracture systems, their characteristics, and their distribution will provide insight into the migration and accumulation of hydrocarbons within the geological framework. Therefore, understanding the fracture systems is essential and can significantly impact reservoir quality by facilitating fluid flow and influencing the mechanical behavior of source rocks during hydrocarbon generation and migration processes.

This study will involve a detailed evaluation of the various types of fractures, including their cementation and paragenetic sequence, as well as petrographic observation of the different phases of dolomite formation and stylolitization, LAS, and HAS, to study the characteristics of petrography and paragenesis under various settings. Thus, the sequence of various cement formation associated with the fracture stages, and providing insights into the diagenetic history of the source rocks as well, will be provided in this study.

3. Geological setting

The Upper Jurassic Barsarin Formation occurs in the High Folded, Imbricated, and northern Thrust Zones of Iraq (Fig. 1), and probably continues in the same structural zones towards Turkey and Iran (Buday, 1980). Resulting from the tectonic activity of the Arabian plate and the development of the southern Neo-Tethys ocean (Jassim and Goff, 2006). This ocean had sea level variations that influenced evaporitic sabkhas in the basin during the Jurassic-Cretaceous period (Salih et al., 2021). NE Iraq established an euxinic basin isolated from the Neo-Tethys by a rifted basin where shallow-water carbonates occurred (Jassim and Goff, 2006). The type locality and type section of the Barsarin Formation are situated in the Balambo-Tanjero zone in Barsarin village, northeast of the Rowanduz district in Iraq. Buday (1980) examined the contacts of the Barsarin Formation in the type locality; they seem to be conformable; nonetheless, the base of this formation in the northern thrust zone was characterized by the presence of ferruginous and detrital strata. The initial occurrence of stromatolites signifies the beginning of the Barsarin Formation as observed at the outcrop (Salae, 2001).

The formation reported previously as it contains limestones and dolomitic limestones, characterized by lamination, some with a fluffy texture, locally cherty, alternating between normal layers and crumbled, brecciated, and contorted beds Buday (1980), represented by basin-floor evaporite facies (Sadooni, 1997). The brecciated

strata exhibit a combination of marl and shale (Buday, 1980). The dissolution of anhydrite layers is the origin of the breccia formations (Bellen et al., 1959).

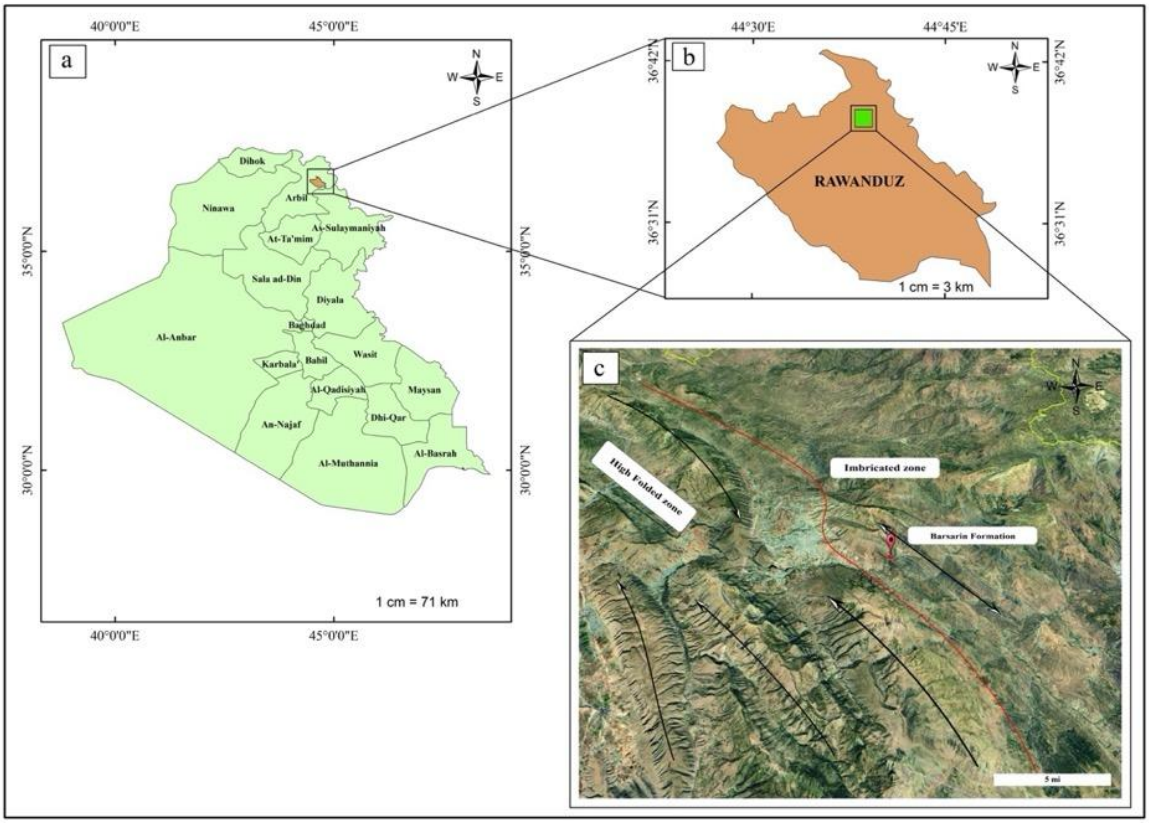


Fig. 1: (a) Simplified general map of Iraq; (b-c) location map and satellite image of the studied area.

4. Materials and Methods

Detailed fieldwork was conducted at the studied section (Fig.1); a total of twenty-seven samples were collected from the outcrop of the Barsarin Formation, specifically from dolomitic and dolomitic limestone at various litho-stratigraphic levels, with sampling predominantly following a NW-SE orientation. Thirty-three samples were prepared for thin-section examination in the laboratory. A slab was initially extracted from each rock sample via a diamond saw to accommodate a microscope slide. After drying on a hot plate, the lapped face of the slab was bonded to a glass slide using epoxy resin. The slab was sectioned with a thin-section saw, with cuts made close to the slide, and further reduced on a thin-section grinder. The section was subsequently final lapped using 600-grit carborundum on a glass plate, with an optional fine grinding phase employing 1000-grit carborundum before polishing. Polishing was conducted on a nylon cloth using diamond paste and a polishing equipment to attain a surface appropriate for meticulous microscopic analysis. The produced thin sections were subsequently examined using a LEICA DM2700P polarized optical microscope, concentrating on the identification of various carbonate phases, the geometric correlations of fractures and veins, and the analysis of cementation types and origins (Fig. 2).

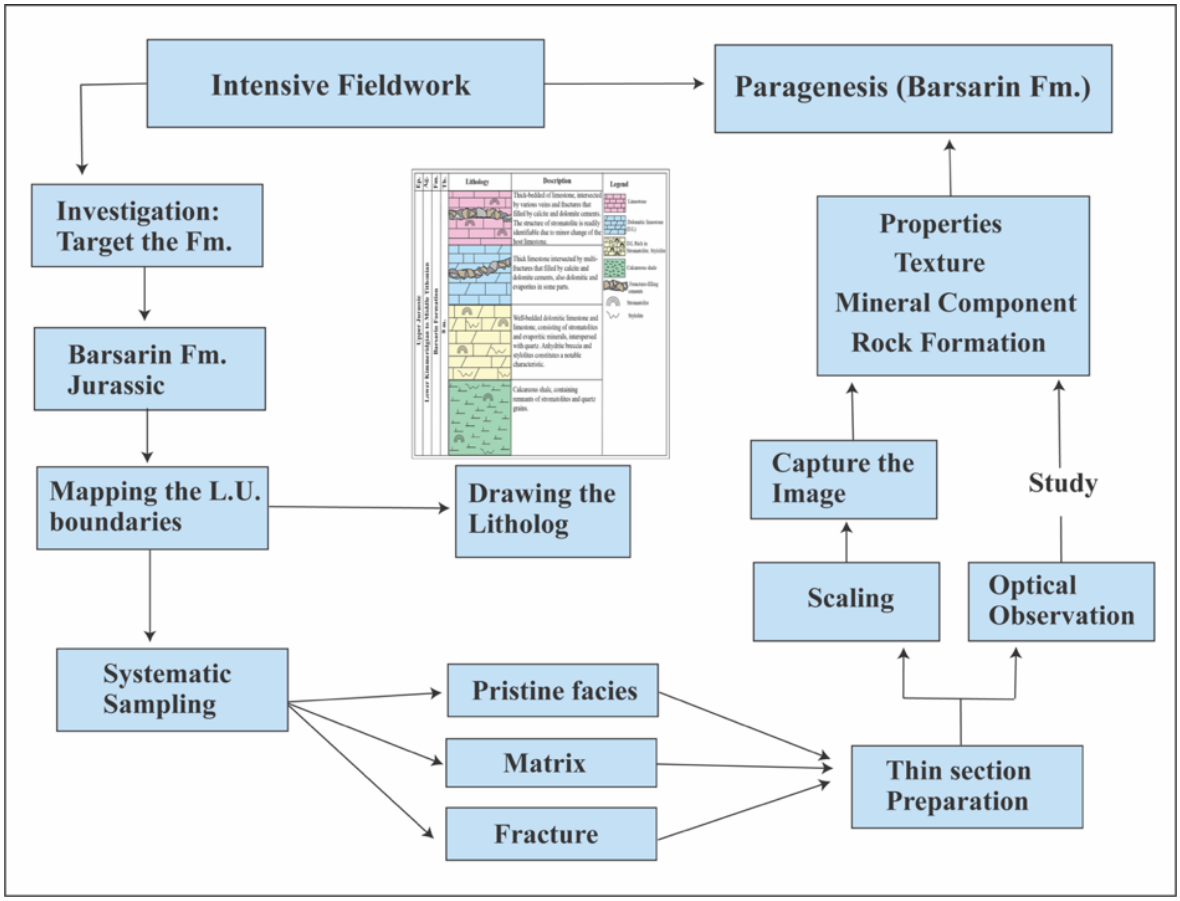


Fig. 2: Flow diagram illustrating the process of the work plan starting from fieldwork to the final stage of paragenesis of the Barbarian Formation.

5. Results and Discussions

A. Field observation

The lower part of the Barsarin Formation consists of decimeter-thick layers less than 30 centimeters with stromatolites and evaporites. Alternation of well-bedded dolomitic and shaly limestones is well recognized in the field. The upper part of the formation consists of distinctive limestones and dolomitic limestones. The thickness of the succession in the examined section type is around 8 meters. Fossils are absent in surface and subsurface rocks due to extensive dolomitization and recrystallisation. The formation has been dated to the Kimmeridgian-Early Tithonian using stratigraphic position, with the underlying Late Tithonian Chia Gara Formation and overlying Kimmeridgian-Oxfordian Naokelekan Formation (Jassim and Goff, 2006). In the study area, some layers in the upper part show two white and dark grey alternating bands. The dark grey band corresponds to the matrix of the rock, varies from mm to cm in width, while the white band is mostly represented by a fracture-filling cement, ranging from mm to cm in size. These banded layers are usually arranged in parallel and oblique directions corresponding to the bedding plane. Additionally, hard dolomitic rocks filling the fractures are also recognized in the field (Figs. 3 and 4).

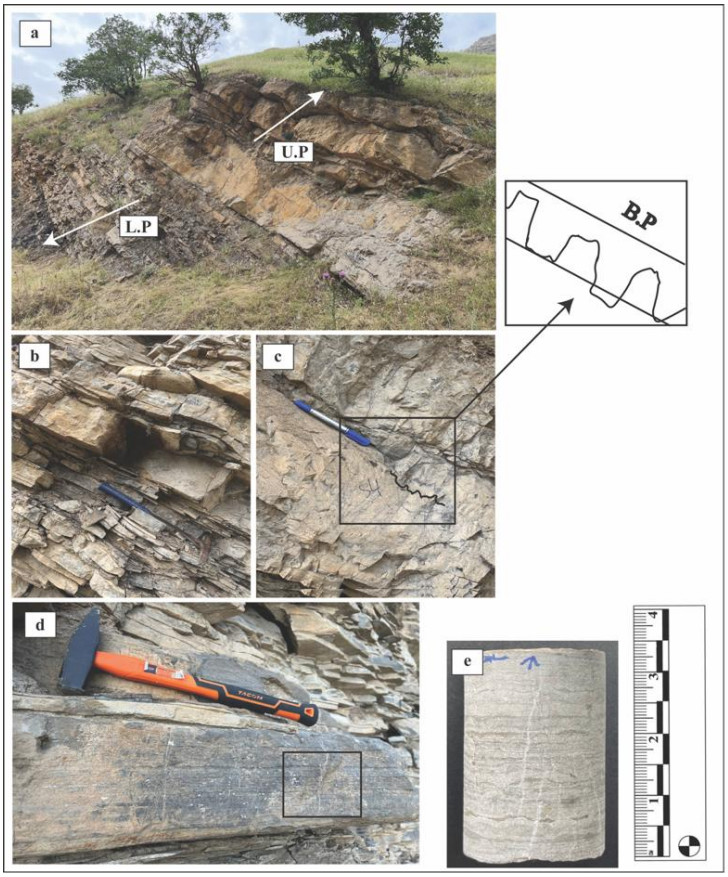


Fig. 3: Field photographs showing the studied section: (a) the lower (L.P) and upper parts (U.P) represented by thin well-bedded and massive layers, respectively (Not to scale), (b) thin-layered rocks, Sample 2. Not to scale. (c) thick-layered rocks, close up the high amplitude stylolite lined in parallel to bedding plane (B.P). Sample 4. (d) thick-layered stromatolite. Sample 10, (e) core sample obtained from a stromatolitic bed. Sample 10.

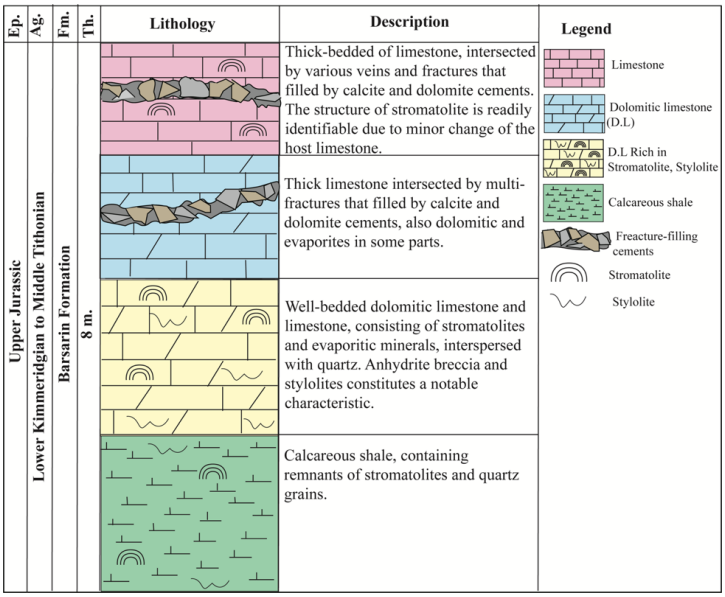


Fig. 4: Litho-log section illustrating the detailed description of the Barsarin Formation in the field.

B. Petrographical Observations

I. non-diagenetic phase "Pristine facies"

a. Stromatolitic boundstone

The main distinctive feature in the depositional facies is the stromatolitic boundstone, considered the original facies of the Barsarin Formation (Fig. 5). In places, stromatolites underwent partial to intensive alteration due to

multi-diagenetic stage processes (Fig. 5a, b). Due to physical compaction, stromatolites suffered textural distortion (Fig. 5c). The sizes of the stromatolites varied from mm- to cm. Sub- to euhedral dolomite crystals are well developed and follow the horizontal laminae of the stromatolite (See Fig. 5d). Associated with this boundstone is a clayey mudstone, with microscopic clay particles (smaller than 0.05mm) that are invisible to the naked eye. These small particles can accumulate in calm, low-energy environments such as lakes, tidal flats, and the deep ocean. The latter facies is partly micritic, with coatings around the grains; the matrix is also microsparitic due to earlier diagenesis. Cyanobacteria are the main organisms that contribute to the formation of microbial mats, previously referred to as 'algal' mats, and are consequently significant in producing laminated carbonate deposits that are called stromatolites (Adams and MacKenzie, 1998). During the depositional environment, these particles comprise organic-rich microbial mats layered with layers of sediment that have precipitated or been deposited on the mat surface (Adams and MacKenzie, 1998). Stromatolites are present throughout the geological record, but they are considered a significant fossil in the Precambrian time because they are utilized for stratigraphic correlation (Tucker, 1981). The most basic kinds of stromatolites, known as "stromatolitic boundstone," are typically located in confined tidal flat environments (Sardarabadi et al., 2016). The amplitude of stromatolites would increase with burial depth. Flat stromatolites are predominantly found in low-energy situations such as supratidal or upper intertidal zones (Sardarabadi et al., 2016). Flat laminated and low- to high-amplitude stromatolites are the predominant features in the current study. The term stromatolite refers to layered microbial deposits (Riding, 1999). Stromatolitic lamination has the greatest impact on weathered surfaces, exhibiting greater irregularity and less development on steep-sided columns (Riding and Tomas, 2006). The association of bedded dolomite with stromatolite structures would probably be indicative of the supratidal and intertidal environments. To support this origin, the evaporite minerals are dominant in the early diagenetic stage. The same case has been documented in various sedimentary structures that can be considered as the direct key for the environmental conditions in the supratidal and intertidal environments in which evaporation would likely occur, and evaporation and stromatolite are associated with bedded dolomites (Prothero and Schwab, 2004).

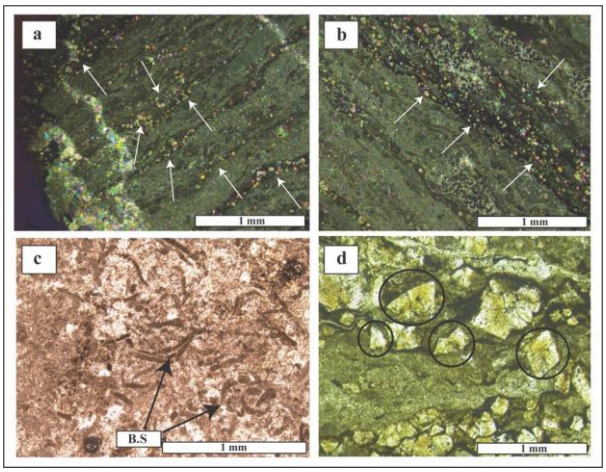


Fig. 5: Photomicrographs show the compaction detected in the thin sections (a, b) the white arrows shows that the stromatolite undergone extensive dolomitization, close up the dolomite grains that arranged in-line with stromatolite distribution, suggesting that stromatolite and dolomite formed at the same time, sample (J1), (c) black arrows show the floating and breaking fragments of stromatolite (B.S) into different pieces due to increasing of compaction associated with stress, sample (J2). (d) black circles show the rhombohedral to subhedral dolomitic crystals, sample (J3).

b. Fenestrae pore-space and Microspar

These two features are considered to be earlier alteration in the studied section, or shortly after deposition. Fenestrae are pore spaces that exceed the typical size of grain-supported voids; they originate from a combination of desiccation and the entrapment of gas bubbles inside the sediment (Adams and MacKenzie, 1998). Fenestral porosity predominantly arises in

carbonate mud-rich sediments of tidal flats, frequently linked to the decomposition of organic matter from cyanobacterial mats (Adams and MacKenzie, 1998). Porosity in carbonate rocks is essential for understanding diagenetic processes and highly significant in evaluating the reservoir rocks. Fenestral porosity in carbonate rocks is fabric selective (Fig. 6a). Fenestral porosity will not constitute effective reservoir rocks unless the fenestrae are interconnected to provide adequate permeability.

Furthermore, microspar is recognized by fine, crystalline calcite comprising crystals from 4–10μm, produced through the recrystallisation of micrite (Bourouni et al., 2017). These fine-grained crystals produced micropore intercrystalline networks filled by hydrocarbons and probably could be associated with fine-grained dolomitization. Accumulation of hydrocarbons in pore space and in-between microspar has also been recognized under an optical microscope (Fig. 6b).

c. Silicification

Silicification is the process where the original skeletal material is replaced by the simultaneous dissolution of calcium carbonate and the precipitation of silica (Butts, 2014). The processes may be facilitated by the nucleation of silica onto organic matter surrounding the mineral crystallites, for example within a shell Butts (2014), or may occur during early or late diagenesis "silicification". The process involves the selective replacement of fossils or the formation of chert layers and nodules, as shown in the Barsarin Formation (Salih et al., 2021). Siliceous skeletal grains, providing a silica supply, comprise sponge spicules in shelf environmental conditions, as well as diatoms and radiolarians in deeper seas. The silicification phase is one of the prominent features in most of the marine facies and diagenetic fluids (Fig. 6c, d). The abundant growth of pyramidal quartz crystals highlights a 'pervasive' silicification and crosscuts the bioclasts and the stylolites or pressure solution joints, as also observed under an optical microscope.

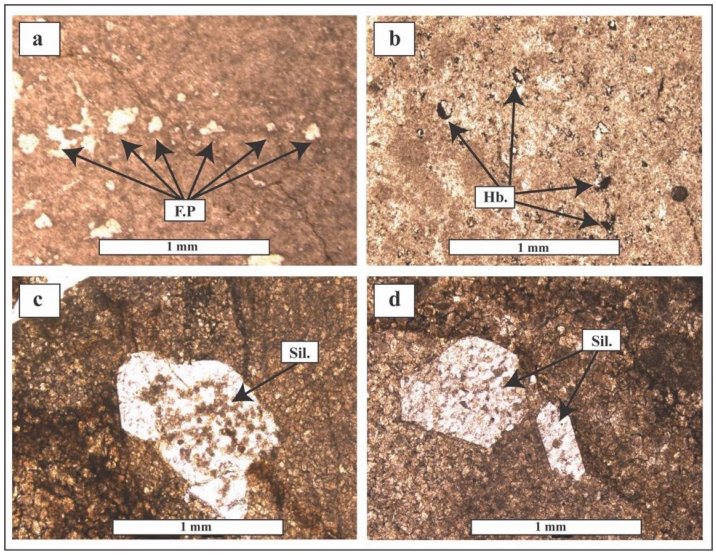


Fig. 6: (PPL) photomicrographs showing (a) Fenestral porosity, sample (J4), (b) micropore filled by hydrocarbon (Hb) also hydrocarbon (Hb) between microsparitoc- pore space, sample (J5), (c-d) silicification (Sil.), samples (J6 and J7).

II. Diagenetic Phase-early, near-surface, and late deep-burial diagenesis

Six different types of dolomites were recognized based on their characteristics and physical properties under two different environmental settings:

a. Dolomite Brecciation (DB) and anhedral-subhedral dolomite (DA)

In situ brecciation of dolomites and floating of dolomite grains within anhydrite bodies (leaching of anhydrite) is a distinctive feature of early diagenesis (Salih et al., 2021). This kind of feature is similar to brecciated texture (Fig. 7a). Anhydrite cements offer the clearest indication of the date of matrix dolomitization in relation to early diagenesis (Adams and Diamond, 2017). Anhydrite cementation is a prevalent characteristic that may be linked to seepage reflux dolomites (Ruppel and Cander, 1988; Rahimpour-Bonab et al., 2010). Calcium ions released during dolomitization interact with sulfate-rich refluxing

brines Machel (2004), and the region of maximum anhydrite cementation typically coincides with the dolomitization process. This area is unstable and susceptible to alteration by following fluids (Jones and Xiao, 2005; Al-Helal et al., 2012).

The anhedral-subhedral dolomite (D_A) is characterized by sub-planar crystals, tightly packed crystals, with persisting micrite products that predate this phase "D_A", and the crystals commonly have a unit extinction under cross-nicols. Therefore, both dolomite phases probably could be linked to early diagenesis and near-surface conditions since the collapse of mimic dolomite still preserved the pristine facies (Fig. 7b).

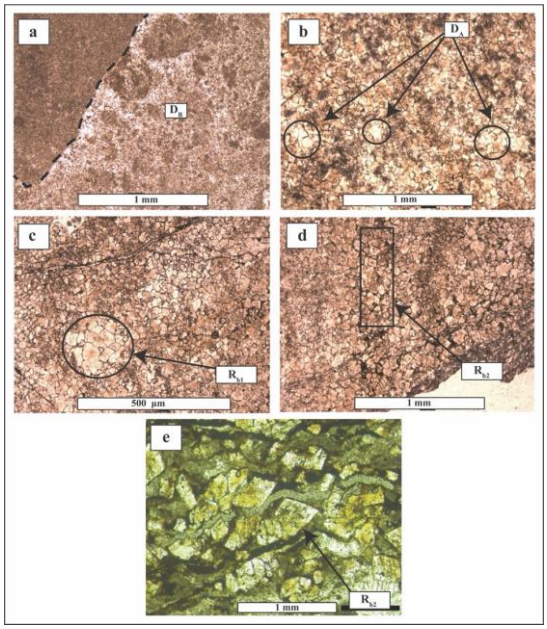


Fig. 7: Photomicrographs illustrating (a) brecciation of dolomite; D_B shows a dolomite brecciation in close contact with micrite facies, sample (J8). The area above the dotted line represents the early paragenetic sequence and predates D_B; (b) show the aggregation of dolomite from anhedral, small-sized dolomite to subhedral large size dolomite crystals (see black circles), (J9), (c-e) dolomitization phases, Samples: (J10, J10, J11). (c) The black circle shows semi-rhombohedral dolomite (Rb_1), Sample (J10). (d) The black rectangle shows rhombohedral dolomite (Rb_2), Sample (J10). (e) The black arrow shows rhombohedral dolomite (Rb_2), Sample (J11).

b. Semi-Rhombohedral Dolomites (Rb1)

This type of dolomite is characterized by semi-rhombohedral crystals (5µm-110µm) and completely rhombohedral crystals (Fig. 7c) within a tight textural appearance. The dolomite crystals show a partial preservation of pristine facies (micrite preservation), suggesting an early replacement process (Elias Bahnan et al., 2021). Fine crystalline dolomite (Rb_1) is related to one of the initial stages of dolomitization that impacted the mudstone facies. Rb_1 could also be linked to stylolite formation as it coincides with early stylolitization. The origin of Mg-rich fluids suggests that Rb_1 may have originated as a result of evaporation; the same case has been reported by Zhang et al. (2022). Fine-crystalline dolomite microcrystals (Rb_1) typically exhibit sub-planar rhombic textures, signifying that Rb_1 formed at comparatively low temperatures during the first shallow burial phase (Sibley and Gregg, 1987).

c. Rhombohedral Dolomite (Rb_2)

Rb_2 dolomite consists of coarse crystalline, planar euhedral dolomite, in places with a distinct zonation with a clear rim and cloudy core (Fig. 7d, e). The rim of crystals is clear, displaying a white color indicating a higher replacement exchange. Rb_2 substitutes for Rb_1 in the most permeable regions, yielding non-mimetic, medium to coarse planar euhedral crystal mosaics, and characterized by high porosity and permeability compared to Rb_1 dolomite. The primary distinctions between these two phases of dolomites in the literature are based on the increased crystal size and the occurrence of zonation within late dolomitic crystals (Gomez-Rivas et al., 2022). This suggests that rhombohedral dolomite cements were found under higher temperatures than those of semi-rhombohedral dolomite (Gregg and Sibley, 1984, Gregg and Shelton, 1990). Rd_2 dolomites have larger crystal sizes compared to Rd_1 and display an interconnected mosaic of planar to anhedral shapes.

d. Radiaxial calcite-filling fractures (R_X)

Radiaxial cement (R_X) consists of large, elongate calcite crystals, forming a single phase in a multi-fracturing system. Fracture-filling R_X cement has two sets of cleavages arranged at an acute angle (Fig. 8a, b). These cleavages show a curved surface, which usually might give a sweepy extinction, and twin planes under crossed nicols. In the literature, radiaxial cements have been represented by fibrous calcite cement and considered as a marine or replacement cement (Kim and Lee, 2003). Radiaxial cements are widespread pore-filling cements in ancient limestones, characterized by a unique combination of curved twins, convergent optic axes, and divergent sub-crystals inside a singular crystal (Davies, 1977; Saller, 1986). Other scholars added

that radiaxial fibrous calcite is a substitution for fibrous aragonite or high-Mg calcite (Bathurst, 1972; Kendall and Tucker, 1973), that it can form through the precipitation of low-Mg and high-Mg calcite, and that crystal development is asymmetric (James and Jones, 2015). High-Mg calcite types might be replaced by low-Mg calcite during burial. Primary pores and subsequent fractures are typically bordered with turbid crystals of radiaxial fibrous calcite (Kendall, 1985). Radiaxial fibrous calcite typically constitutes the initial production of pore-lining cement, and radiaxial fibrous calcite is viewed as the original calcite cement that formed during shallow burial in marine pore fluids (Bishop et al., 2014). However, the radiaxial dolomite cement in our study requires different environmental conditions than those previously documented in the literature. The twisted cleavage of R_X and the associated stylolitic features with R_X cement, and sweepy extinction of these crystals under crossed nicols definitely require higher temperature conditions than those reported previously. Therefore, paragenetically, the radiaxial calcite-filling fractures predate saddle dolomite formation.

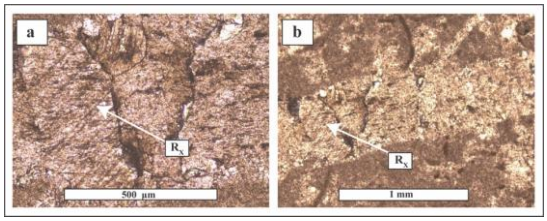


Fig. 8: (PPL) photomicrographs (a-b) white arrows show a single crystal of radiaxial cement inside the fracture, Sample (J12).

e. Saddle Dolomite (SD)

Saddle dolomites have larger crystal sizes (up to 650µm) than those of D_B, D_A, Rb_1, and Rb_2, and develop a typical curved habit with a sweepy extinction. All these properties indicate that SD may have developed from the fast precipitation of high temperatures with magnesium-rich fluids during diagenesis. The same case has been reported by (Machel, 2004, Davies and Smith Jr, 2006). The homogenization temperature from microthermometry analyses and fluid inclusions suggests that SD can originate from hydrothermal fluids, higher than >200°C (Zhang et al., 2022). A large number of saddle dolomite assemblages consist of anhedral crystals in mosaic aggregates with uneven borders (Yu et al., 2019). However, the literature does not give information about the petrographic composition between burial hydrothermal dolomitization (BHD) and shallow hydrothermal dolomitization (SHD). The primary characteristics of BHD are the corrosion boundaries between the attached grains, which could be linked to high pressure or the compaction process during burial. Furthermore, the dissolution process occurred later during burial diagenesis, likely at depths over 2km inside the late burial diagenesis of SD-filling fractures. Dissolution of carbonates, or burial corrosion, is a predominant phenomenon in the subsurface that frequently develops near transtensional active faults and serves as channels for hydrothermal fluids that evolve, potentially resulting in various forms of mineralization and dissolution (Smith, 2013). Furthermore, the zigzag boundaries between the SD grains, "suture contacts," are another indicator of BHD (Fig. 9a-f).

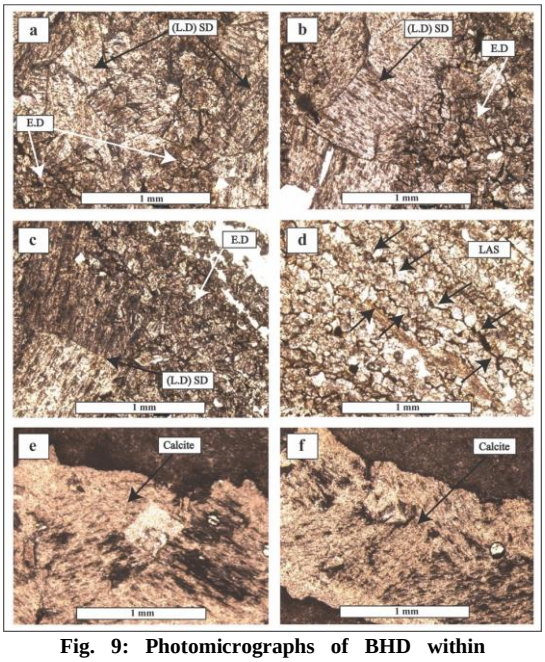


Fig. 9: Photomicrographs of BHD within saddle dolomites illustrating: (a - c) black arrows show Late Dolomitization (L.D.) coarse crystals of saddle dolomite (SD. White arrows show Early Dolomitization (E.D), fine-sized crystals of saddle dolomite. (d) LAS Low Amplitude Stylolization, sample (J13). (e,f) black arrows show calcite formation filling the fracture, sample (J14).

III Mechanical stylolitization controlled by increasing burial depth

Stylolitization provides preferential pathways for large-scale fluid flow, resulting in spatial and temporal variations of reservoir heterogeneities in

carbonate successions (Morad et al., 2018). During the diagenetic features of carbonate rocks and the tectonic compression phase in foreland basins, stylolites are considered conduits for the flow of hydrocarbons and hot basinal brines (Paganoni et al., 2016). These brines can lead to the precipitation of minerals such as saddle dolomite, calcite, fluorite, and sphalerite, characteristic of hydrothermal ore deposits, adjacent to and within the proximity of stylolites (Vandeginste and John, 2013; Mansurbeg et al., 2016). They are believed to arise from pressure-induced dissolution caused by overburden stress or tectonic compression (Ameen et al., 2010). The function of stylolites is as conduits as well as obstructions for fluid movement (Baron and Parnell, 2007; Heap et al., 2014). Some scholars have reported that the dissolution of limestone along the stylolite may provide dolomitization through the movement of Mg-rich fluids or hydrocarbons (Tondi et al., 2006; Merino and Canals, 2011). Consequently, fine-crystalline dolomite cements linked to stylolite may occur concurrently with or after stylolite development (Dunnington, 1954). Stylolite was generated through chemical compression and exhibits varied scales and dimensions. Certain researchers have reported that pressure dissolution appeared at depths of 610 to 914 meters, forming stylolites (Dunnington, 1954), which can potentially be observed in a profound burial environment (Tang, 2007). Over the past few years, researchers have suggested that stylolites develop at depths ranging from 500 meters to 1 kilometer (Beaudoin et al., 2016). Different and distinctive types of bedding-parallel stylolites were identified in the research area, suggesting that the Barsarin Formation experienced varying vertical stress as a result of mechanical compaction and vertical overburden stress.

Two types of stylolites are recognized in the studied area. The low amplitude stylolites (LAS) are associated with microspar and anhedral dolomitization, while the high amplitude stylolites (HAS) are usually associated with radiaxial cement (Fig. 10a, b), burial dolomitization and calcite formation, and postdate the LAS (Fig. 10c, d). Therefore, LAS suggest early subsidence or shallow burial diagenesis of the Barsarin Formation, while HAS strongly favors the continuous increasing of burial depth. The key indicators for increasing the vertical stress due to increasing burial depth are: (i) increase in the distance between the crest and the trough of stylolite (amplitude), (ii) LAS synchronizes with early diagenetic fluids, while HAS synchronizes with late diagenetic fluids, (iii) HAS is associated with a vertical multi-fracturing system parallel to burial depth, while LAS does not coincide with any fracture system, in places crosscut by the early fracturing stage. Furthermore, both stylolites lack any evidence of shearing deformation, and this is an indication that these stylolites formed due to continuous increasing of burial weight of overlying sequence formations.

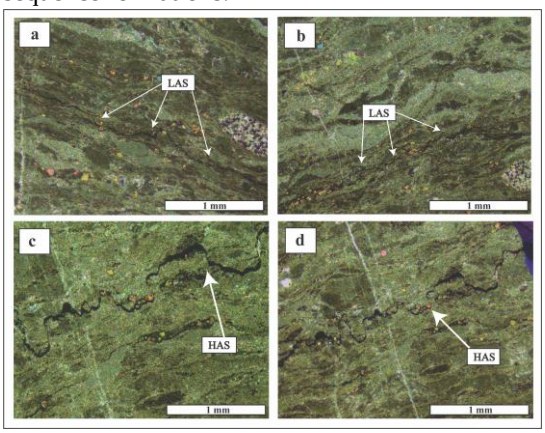


Fig. 10: Photomicrographs (a, b). White arrows show Low-amplitude stylolite (LAS) post-dated Rb_1 fabric. (c, d) white arrows show high-amplitude stylolite (HAS), Sample (J15).

IV Staging of multi-fracture system in Upper Jurassic source rock

In addition to the depositional and early diagenetic facies, the following multi-fracture stages were recognized under an optical microscope:

Fracture I (FI): The earliest fracture formation was identified in the Barsarin Formation, a fracture filled by calcite cement with variable-sized crystals in a mosaic shape (Fig. 11). The FI-filled calcite cement crosscuts the early stylolite. The early stylolites were characterized by a low amplitude pattern (LAS) and usually followed the stromatolitic facies pattern (Fig. 10a-b). However, the late stylolite was characterized by a high amplitude pattern (HAS) developed also within the various matrix facies.

Fracture II (FII): This fracture type is also filled by calcite crystals and post-dates the FI and the initial bedding-parallel stylolite (LAS). The crystal shape was characterized by an anhedral-subhedral crystal shape within a compacted texture.

Fracture III (FIII): This type of fracture is characterized by euhedral to subhedral grains with variable sizes of calcite crystals, usually with the medium-sized crystals formed close to the fracture wall and the size growing toward the fracture core.

Fracture IV (FIV): FIV is the largest fracture filled by elongate shapes of calcite crystals in a complex set of fractures. It is usually filled by radiaxial calcite crystals, likely formed from re-opening of an earlier fracture. The re-opened fracture extends through host limestone/dolomite matrix facies. The re-opening fracture was likely formed under high pressure and deep burial conditions due to the corrosive and dissolution surface of the radiaxial cement and the sweepy/curved shapes of the crystals filling this fracture. The development of suture contact, compacted zigzag shapes between dolomite crystals, and dissolution features support deep burial diagenesis.

Fracture V (FV): This fracture is associated with saddle dolomite formation and contains disturbed solid bitumen inclusions, likely hydrocarbon inclusions (Fig. 12). Suture contact between previous dolomitization and fracture-filled saddle dolomite, corrosion, and compacting of SD crystals are likely linked to increasing subsidence rate and overlying sedimentary rocks. The diagenetic setting of the last phase of dolomitization is similar to that of the deep diagenetic "Mesogenesis Phase". Saddle dolomite formation and its mechanism can be recognized by their appearance and features under deep conditions.

Burial corrosion is a form of selective dissolution that occurs in the burial diagenetic environment, characterized by significant selective dissolution following cementation and pressure solution, with distinguished zigzag wall of dolomite crystals that is consistent with stylolite occurrence. Stylolites that separate two dolomites function as conduits for fluids or hydrocarbons. It is most likely formed under high pressure/temperature because the crystals of dolomite have a sweepy texture that gives a curved shape. There are two different cement formations, formed by two different fluid sources, suggesting a spanning of cementation time intervals.

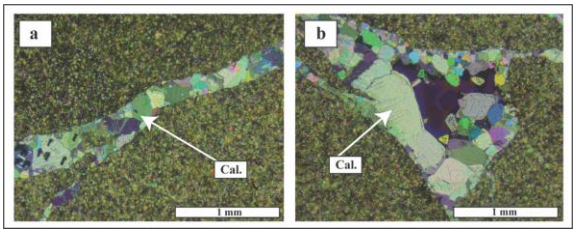


Fig. 11: Microphotographs. (a, b) illustrating fracture-filling calcite cement (FI), Cal. = calcite, Sample (J16).

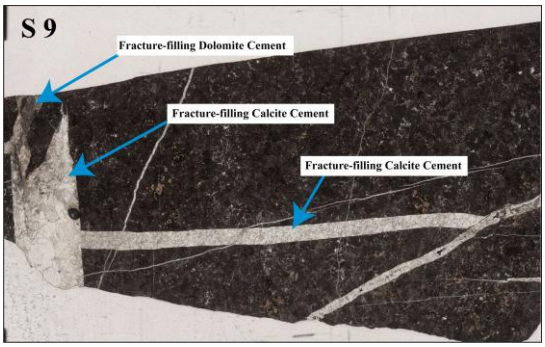


Fig. 12: Image scanning of thin section showing multi-fractures that are filled by various types of cements, sample (J17).

V Timing of fracturing and diagenetic fluids

Fractures can be categorized as structural and dissolution fractures based on their origin (Yang et al., 2004; Zhao et al., 2012). The deformation stress facilitates the development of structural fractures, encompassing low-angle, oblique, and high-angle fractures (Zhang et al., 2022). Since the diagenetic fluids have primarily dissolved the structural fractures or unstable rocks, curved and smooth fracture edges will be produced (Salih et al., 2023; Salih, 2023). Hydrothermal minerals and black residual bitumen in the dissolution fractures suggest that the dissolution fluid may be either hydrothermal or organic acid fluid (Salih et al., 2019a, b). The extent of fill is influenced by the fracture size (a smaller volume relative to surface area facilitates the sealing of narrower fractures, assuming other factors remain constant) and the rate at which the fracture opened (Lander and Laubach, 2014). Thermal exposure, geochemical conditions, and the reactivity and composition of the fracture wall rocks could be involved in the length and size of fracture opening. One facet of fracture diagenesis is the ability of the host rock to supply reactants through localized dissolution and diffusion (Gale et al., 2014). Certain fractures exhibit planes with many host-rock inclusions aligned parallel to the fracture wall, resulting from the crack-seal mechanism during fracture propagation. Some cracks comprise multiple

minerals (Gale et al., 2014). The series of fractures can be categorized based on the intersecting and geometrical relationships. In the early stage of fracturing, the low-angle and oblique fractures predominantly developed and were subsequently filled with calcite cements. In the final stages, high-angle, re-opening, subsequent, and vertical fractures developed, subsequently filled with medium- to coarse-crystalline calcite and saddle dolomite (SD). Several scholars classified and identified the timing of fractures utilizing various methods or based on various parameters, like cross-cutting of fractures, U-Pb direct dating, fluid inclusion and microthermometry, etc. (Zhang et al., 2022). In addition to using the cross-cutting relationship and geometrical distribution of natural fractures, our study adds a type of fracture-filled cementation that required enough time for the dissolution-cementation/replacement process. Some natural fractures that developed under moderate to profound burial conditions throughout geological time scales are lined or sealed with mineral cement (Laubach, 2003). White-colored, coarse crystalline calcite cement is found in the fracture (FIII). This type of fracture was also associated with a complex set of fractures and was parallel to the amplitude of late stylolites. These fractures probably coincided with the formation of the stylolitization process. The fractures terminated at the wider end of the stylolite, called tension gash. These tension gashes support the mechanical overburden stress due to further increase of burial depth and vertical stress during this stage (Salih et al., 2020).

6. Conclusion

The detailed data and analysis presented in this study provide valuable insights into the generation and evolution of the fracture systems and fluid evolution in shallow and subsurface environmental conditions within the Upper Jurassic Barsarin Formation. The results contribute significantly to the understanding of critical geological processes, petroleum formation, and petroleum applications. Through systematic investigation, four main types of fractures (FI, FII, FIII, FIV, and FV) are recognized. The fracture-filled cements show a distinct characteristic based on their formation conditions, age dynamics, and paragenetic sequence. The identification of these fractures provides a paragenetic sequence of various fracturing stages for future developments in exploration for hydrocarbon source rock and reservoirs. The paragenesis for the different stages of fracture is recognized as follows:

1. FI fractures: formed at surface or near-surface conditions, having an age no older than early stylolite formation (LAS).
2. FII fractures: developed during burial diagenesis, and coeval with later stages of diagenesis.
3. FIII fractures: in-situ fractures formed under subsurface conditions, coinciding with high-amplitude stylolitization.
4. FIV fractures: filled by calcite cement with abundant solid bitumen fluid inclusions, reflecting the increasing burial weight of overlying sedimentary rocks during the "mesogenesis phase."
5. FV-filled dolomite cement, and in places associated with calcite cement.

The FIII and FIV fractures cover a large volume among the other types of fractures, and show a complex history of fracture formation under different re-opening systems, with targeted features and textures indicating a deep burial influence on calcite-cement formation. Fracture V coincides with saddle dolomite formation that is characterized by distinct hydrocarbon inclusions under hot diagenetic conditions. The evolution of the geo-chronological stages of these fractures reveals a significant interaction between fluid movement and pristine facies, particularly under varying pressure and thermal regimes during shallow/deep burial conditions. The distinctions between shallow/deep settings provide a valuable framework for understanding similar geological formations and their respective hydrocarbon potentials.

The findings obtained from this study not only enrich the geological understanding of the Barsarin Formation but also add a new insight into future exploration of similar fractured reservoirs. The recognition of these diagenetic and textural features emphasizes the need for further studies that examine the implications for hydrocarbon accumulation, fluid movement, and sedimentary basin evolution. In brief, such detailed and enhanced studies may lead to more efficient exploration and extraction strategies in the future of natural resources.

7. Future Recommendation

Given the significant implications of the findings from this study, several ways for future research and exploration can be recommended:

1. Utilizing advanced Laser Ablation U-Pb dating using ICP-MS for obtaining absolute, meaningful ages and direct dating of the fracture system within the Barsarin Formation.
2. Future studies could benefit from the integration of advanced imaging technologies such as micro-CT scanning (Computed Tomography) to provide a 3D view of fracture geometries and connectivity within subsurface environments. Such approaches could enhance the accuracy of fracture network models and improve predictions for fluid flow behavior.
3. Detailed petrophysical and geochemical analyses (major, minor, and trace elemental analyses; REE; mineralogical components) could provide the specific processes that governed their formation and how these processes vary across different geological settings.
4. Using a sophisticated technique to determine the paleo-temperature and paleo-pressure of any trapped fluids with each stage of fracture type by utilizing fluid inclusion and microthermometry.
5. Future research should focus on evaluating the environmental impact of utilizing geological formations for reservoir storage, ensuring that methods used align with sustainability aspects.

8. Conflict of Interest

The authors declare that they have no known competing financial interests or personal relationships that could have appeared to influence the recent work.

9. Funding Statement

This research received no external funding.

10. References

Adams, A. and Diamond, L. W. 2017. Early diagenesis driven by widespread meteoric infiltration of a Central European carbonate ramp: A reinterpretation of the Upper Muschelkalk. Sedimentary Geology, 362, 37-52.

Adams, A. and MacKenzie, W. S. 1998. Carbonate sediments and rocks under the microscope: A Colour Atlas, CRC Press, 184 P.

Al-Helal, A. B., Whitaker, F. F. and Xiao, Y. 2012. Reactive transport modeling of brine reflux: dolomitization, anhydrite precipitation, and porosity evolution. Journal of Sedimentary Research, 82, 196-215.

Ameen, M. S., Buhidma, I. M. and Rahim, Z. 2010. The function of fractures and in-situ stresses in the Khuff reservoir performance, onshore fields, Saudi Arabia. AAPG Bulletin, 94, 27-60.

Amirjan, M. and Bozorg, M. 2018. Properties and corrosion behavior of Al based nanocomposite foams produced by the sintering-dissolution process. International Journal of Minerals, Metallurgy, and Materials, 25, 94-101.

André, L., Azaroual, M. and Menjoz, A. 2010. Numerical simulations of the thermal impact of supercritical CO2 injection on chemical reactivity in a carbonate saline reservoir. Transport in porous media, 82, 247-274.

Baqués, V., Ukar, E., Laubach, S. E., Forstner, S. R. and Fall, A. 2020. Fracture, Dissolution, and Cementation Events in Ordovician Carbonate Reservoirs, Tarim Basin, NW China. Geofluids, 2020, 9037429.

Baron, M. and Parnell, J. 2007. Relationships between stylolites and cementation in sandstone reservoirs: Examples from the North Sea, UK and East Greenland. Sedimentary Geology, 194, 17-35.

Bathurst, R. G. 1972. Carbonate sediments and their diagenesis. Elsevier. 1-658 p.

Beaudoin, N., Koehn, D., Lacombe, O., Lecouty, A., Billi, A., Aharonov, E. and Parlangeau, C. 2016. Fingerprinting stress: Stylolite and calcite twinning paleopiezometry revealing the complexity of progressive stress patterns during folding—The case of the Monte Nero anticline in the Apennines, Italy. Tectonics, 35, 1687-1712.

Bellen, R. C., Dunnington, H. V., Wetzel, R. and Morton, D. 1959. Lexique stratigraphique international: Asie. Iraq. Vol. 3C, Centre national de la recherche scientifique. 330 P.

Berra, F. and Carminati, E. 2012. Differential compaction and early rock fracturing in high-relief carbonate platforms: numerical modelling of a Triassic case study (Esino Limestone, Central Southern Alps, Italy). Basin Research, 24, 598-614.

Bishop, J., Montañez, I. and Dy, S. 2014. Meteoric diagenesis and fluid-rock interaction in the Middle Permian Capitan backreef: Yates Formation, Slaughter Canyon, New Mexico. American Association of Petroleum Geology, 98, 1495–1519.

Bjørlykke, K. and Jahren, J. 2012. Open or closed geochemical systems during diagenesis in sedimentary basins: Constraints on mass transfer during diagenesis and the prediction of porosity in sandstone and carbonate reservoirs. AAPG Bulletin, 96, 2193-2214.

Boggs, S. 2006. Principles of Sedimentology and Stratigraphy, Pearson Prentice Hall, 662 P.

Bourouni, P., Tsikouras, B. and Hatzipanagiotou, K. 2017. Petrological investigation of carbonate rocks from the Ionian zone (Etoloakarnania, western Greece). Bulletin of the Geological Society of Greece, 43, 2540.

Buday, T. 1980. The Regional Geology of Iraq, Vol 1: Stratigraphy and Paleogeography. Publications of Geological Survey of Iraq, Baghdad, 445 p.

Budd, D. A., Frost III, E. L., Huntington, K. W. and Allwardt, P. F. 2013. Syndepositional deformation features in high-relief carbonate platforms: long-lived conduits for diagenetic fluids. Journal of Sedimentary Research, 83, 12-36.

Butts, S. H. 2014. Silicification. The Paleontological Society Papers, 20, 15-34.

Davies, G. R. 1977. Former magnesian calcite and aragonite submarine cements in upper Paleozoic reefs of the Canadian Arctic: A summary. Geology, 5, 11-15.

Davies, G. R. and Smith Jr., L. B. 2006. Structurally controlled hydrothermal dolomite reservoir facies: An overview. AAPG Bulletin, 90, 1641-1690.

Dunnington, H. V. 1954. Stylolite development post-dates rock induration. Journal of Sedimentary Research, 24, 27-49.

Elias Bahnan, A., Pironon, J., Carpentier, C., Barré, G. and Gaucher, E. C. 2021. The diagenetic history of the giant Lacq gas field, witness to the Aptian- Albian rifting and the Pyrenean orogeny, revealed by fluid and basin modeling. Marine and Petroleum Geology, 133, 105250.

Fischer, M. P., Higuera-Díaz, I. C., Evans, M. A., Perry, E. C. and Lefticariu, L. 2009. Fracture-controlled paleohydrology in a map-scale detachment fold: Insights from the analysis of fluid inclusions in calcite and quartz veins. Journal of Structural Geology, 31, 1490-1510.

Gale, J. F. W., Laubach, S. E., Marrett, R. A., Olson, J. E., Holder, J. and Reed, R. M. 2004. Predicting and characterizing fractures in dolostone reservoirs: using the link between diagenesis and fracturing. Geological Society, London, Special Publications, 235, 177-192.

Gale, J. F. W., Laubach, S. E., Olson, J. E., Eichhubl, P. and Fall, A. 2014. Natural fractures in shale: A review and new observations. AAPG Bulletin, 98, 2165-2216.

Gomez-Rivas, E., Martín-Martín, J. D., Bons, P. D., Koehn, D., Griera, A., Travé, A., Llorens, M.-G., Humphrey, E. and Neilson, J. 2022. Stylolites and stylolite networks as primary controls on the geometry and distribution of carbonate diagenetic alterations. Marine and Petroleum Geology, 136, 105444.

Gregg, J. M. and Shelton, K. L. 1990. Dolomitization and dolomite neomorphism in the back reef facies of the Bonneterre and Davis formations (Cambrian), southeastern Missouri. Journal of Sedimentary Research, 60, 549-562.

Gregg, J. M. and Sibley, D. F. 1984. Epigenetic dolomitization and the origin of xenotopic dolomite texture. Journal of Sedimentary Research, 54, 908-931.

Heap, M. J., Baud, P., Reuschlé, T. and Meredith, P. G. 2014. Stylolites in limestones: Barriers to fluid flow? Geology, 42, 51-54.

Hooker, J. N. and Katz, R. F. 2015. Vein spacing in extending, layered rock: The effect of synkinematic cementation. American Journal of Science, 315, 557-588.

James, N. P. and Jones, B. 2015. Origin of Carbonate Sedimentary Rocks, John Wiley and Sons, 446 P.

Jassim, S. Z. and Goff, J. C. 2006. Geology of Iraq, DOLIN, SRO, distributed by Geological Society of London.

Jiang, L., Cai, C., Worden, R. H., Crowley, S. F., Jia, L., Zhang, K. and Duncan, I. J. 2016. Multiphase dolomitization of deeply buried Cambrian petroleum reservoirs, Tarim Basin, north-west China. Sedimentology, 63, 2130-2157.

Jiayu, G. 1999. Characteristics and evolutional models of karst reservoirs of lower Ordovician carbonate rocks in the Lunnan area of Tarim Basin. Chinese journal of arid land research, 12, 317-324.

Jones, G. D. and Xiao, Y. 2005. Dolomitization, anhydrite cementation, and porosity evolution in a reflux system: Insights from reactive transport models. AAPG Bulletin, 89, 577-601.

Kendall, A. C. 1985. Radiaxial Fibrous Calcite: A Reappraisal, 59-77. In: Schneidermann, N. and Harris, P. M. (eds.) Carbonate Cements: Based on a Symposium Sponsored by the Society of Economic Paleontologists and Mineralogists. SEPM Society for Sedimentary Geology.

Kendall, A. C. and Tucker, M. E. 1973. Radiaxial fibrous calcite: a replacement after acicular carbonate. Sedimentology, 20, 365-389.

Kim, Y. and Lee, Y. I. 2003. Radiaxial fibrous calcites as low-magnesian calcite cement precipitated in a marine-meteoric mixing zone. Sedimentology, 50, 731-742.

Lander, R. H. and Laubach, S. E. 2014. Insights into rates of fracture growth and sealing from a model for quartz cementation in fractured sandstones. GSA Bulletin, 127, 516-538.

Landry, C. J., Eichhubl, P., Prodanović, M. and Wilkins, S. 2016. Nanoscale grain boundary channels in fracture cement enhance flow in mudrocks. Journal of Geophysical Research: Solid Earth, 121, 3366-3376.

Laubach, S. E. 2003. Practical approaches to identifying sealed and open fractures. AAPG Bulletin, 87, 561-579.

Lee, H. P., Olson, J. E. and Schultz, R. A. 2018. Interaction analysis of propagating opening mode fractures with veins using the Discrete Element Method. International Journal of Rock Mechanics and Mining Sciences, 103, 275-288.

Léveillé, R. J., Bridges, J., Wiens, R. C., Mangold, N., Cousin, A., Lanza, N., Forni, O., Ollila, A., Grotzinger, J. and Clegg, S. 2014. Chemistry of fracture-filling raised ridges in Yellowknife Bay, Gale Crater: Window into past aqueous activity and habitability on Mars.

Journal of Geophysical Research: Planets, 119, 2398-2415.

Lu, Y., Lü, H., Cui, Y. and Chen, H. 2018. Method for fracture effectiveness evaluation based on 3D Mohr Circle and its application. Acta Petrolei Sinica, 39, 564.

Machel, H. G. 2004. Concepts and models of dolomitization: a critical reappraisal. Geological Society, London, Special Publications, 235, 7-63.

Mansurbeg, H., Morad, D., Othman, R., Morad, S., Ceriani, A., Al-Aasm, I., Kolo, K., Spirov, P., Proust, J. N., Preat, A. and Koyi, H. 2016. Hydrothermal dolomitization of the Bekhme formation (Upper Cretaceous), Zagros Basin, Kurdistan Region of Iraq: Record of oil migration and degradation. Sedimentary Geology, 341, 147-162.

McNeill, D. F. and Eberli, G. P. 2009. Early Load-Induced Fracturing in a Prograding Carbonate Margin. Perspectives in carbonate geology: A tribute to the career of Robert Nathan Ginsburg, 327-336.

Merino, E. and Canals, A., 2011. Self-accelerating dolomite-for-calcite replacement: Self-organized dynamics of burial dolomitization and associated mineralization. American Journal of Science, 311, 573 - 607.

Monty, C. L. V. 1976. The origin and development of cryptalgal fabrics. Developments in sedimentology. Elsevier, 193-249.

Morad, D., Nader, F. H., Morad, S., Al Darmaki, F. and Hellevang, H. 2018. Impact of stylolitization on fluid flow and diagenesis in foreland basins: Evidence from an Upper Jurassic carbonate gas reservoir, Abu Dhabi, United Arab Emirates. Journal of Sedimentary Research, 88, 1345-1361.

Oyedokun, O. and Schubert, J. 2017. A quick and energy consistent analytical method for predicting hydraulic fracture propagation through heterogeneous layered media and formations with natural fractures: The use of an effective fracture toughness. Journal of Natural Gas Science and Engineering, 44, 351-364.

Paganoni, M., Al Harthi, A., Morad, D., Morad, S., Ceriani, A., Mansurbeg, H., Al Suwaidi, A., Al-Aasm, I. S., Ehrenberg, S. N. and Sirat, M. 2016. Impact of stylolitization on diagenesis of a Lower Cretaceous carbonate reservoir from a giant oilfield, Abu Dhabi, United Arab Emirates. Sedimentary Geology, 335, 70-92.

Peacock, D. C. P., Nixon, C. W., Rotevatn, A., Sanderson, D. J. and Zuluaga, L. F. 2016. Glossary of fault and other fracture networks. Journal of Structural Geology, 92, 12-29.

Prothero, D. R. and Schwab, F. 2004. Sedimentary geology, Macmillan, 600 P.

Rahimpour-Bonab, H., Esrafili-Dizaji, B. and Tavakoli, V. 2010. Dolomitization and anhydrite precipitation in permo-triassic carbonates at the South Pars gas field, offshore Iran: controls on reservoir quality. Journal of Petroleum Geology, 33, 43-66.

Rasool, R. H., Ali, S. A. and Al-Juboury, A. I. 2023. Petrography and diagenesis of the Middle to Upper Jurassic succession from Sargelu section, northeastern Iraq. Al-Kitab Journal for Pure Sciences, 7, 153-172.

Ren, Q., Jin, Q., Feng, J. and Li, M. 2019. Simulation of stress fields and quantitative prediction of fractures distribution in upper Ordovician biological limestone formation within Hetianhe field, Tarim Basin, NW China. Journal of Petroleum Science and Engineering, 173, 1236-1253.

Riding, R. 1999. The term stromatolite: towards an essential definition. Lethaia, 32, 321-330.

Riding, R. and Tomas, S. 2006. Stromatolite reef crusts, Early Cretaceous, Spain: bacterial origin of in situ-precipitated peloid microspar? Sedimentology, 53, 23-34.

Ruppel, S. C. and Cander, H. S. 1988. Dolomitization of shallow-water platform carbonates by sea water and seawater-derived brines: San Andres Formation (Guadalupian), west Texas in V. Shukla and P. A. Baker, eds., Sedimentology and geochemistry of dolostones: SEPM Special Publication 43, 245–262 P.

Sadooni, F. N. 1997. Stratigraphy and petroleum prospects of Upper Jurassic carbonates in Iraq. Petroleum Geoscience, 3, 233-243.

Salae, A. 2001. Stratigraphy and sedimentology of the Upper Jurassic succession, NE Iraq. University of Baghdad, M Sc thesis, 95 pp.

Salih, N. M. 2023a. The Impact of Hydrothermal Fluids on Porosity Enhancement and Hydrocarbon Migration in Qamchuqa Formation, Lower Cretaceous, Kirkuk Oil Company. Minerals, 13(3), 377. https://doi.org/10.3390/min13030377

Salih, N. M., Al-Majmaie, S. M., and Muhammad, Z. A. 2023. The Porous–Permeable Zones in Heterogeneous Carbonate Reservoirs: A Case Study from Amara Oilfield, Iraq. Proceedings, 87(1), 35. https://doi.org/10.3390/IECG2022-13965

Salih, N., Mansurbeg, H., Kolo, K., Gerdes, A. and Préat, A. 2019a. In situ U-Pb dating of hydrothermal diagenesis in tectonically controlled fracturing in the Upper Cretaceous Bekhme Formation, Kurdistan Region-Iraq. International Geology Review, 62, 2261-2279.

Salih, N., Mansurbeg, H., and Préat, A. 2020. Geochemical and Dynamic Model of Repeated Hydrothermal Injections in Two Mesozoic Successions, Provençal Domain, Maritime Alps, SE-France. Minerals, 10(9), 775. https://doi.org/10.3390/min10090775

Salih, N., Mansurbeg, H., Kolo, K. and Préat, A. 2019b. Hydrothermal carbonate mineralization, calcretization, and microbial diagenesis associated with multiple sedimentary phases in the Upper Cretaceous Bekhme Formation, Kurdistan Region-Iraq. Geosciences, 9, 459.

Salih, N., Préat, A., Gerdes, A., Konhauser, K. and Proust, J.-N. 2021. Tracking the Origin and Evolution of Diagenetic Fluids of Upper Jurassic Carbonate Rocks in the Zagros Thrust Fold Belt, NE-Iraq. Water, 13, 3284.

Saller, A. H. 1986. Radiaxial calcite in lower Miocene strata, subsurface Enewetak Atoll. Journal of Sedimentary Research, 56, 743-762.

Salomon, E., Rotevatn, A., Kristensen, T. B., Grundvåg, S. A., Henstra, G. A., Meckler, A. N., Albert, R. and Gerdes, A. 2020. Fault-controlled fluid circulation and diagenesis along basin-bounding fault systems in rifts – insights from the East Greenland rift system. Solid Earth, 11, 1987-2013.

Sardarabadi, S., Jahani, D. and Ghadimvand, N. 2016. Facies, Depositional Environment and Diagenesis of the Qom Formation in Rameh Section (Northeastern Garmsar). Open Journal of Geology, 6, 1240-1256.

Shen, A., Hu, A., Cheng, T., Liang, F., Pan, W., Feng, Y. and Zhao, J. 2019. Laser ablation in situ U-Pb dating and its application to diagenesis-porosity evolution of carbonate reservoirs. Petroleum Exploration and Development, 46, 1127-1140.

Shen, A., Luo, X., Hu, A., Qiao, Z. and Zhang, J. 2022. Dolomitization evolution and its effects on hydrocarbon reservoir formation from penecontemporaneous to deep burial environment. Petroleum Exploration and Development, 49, 731-743.

Sibley, D. F. and Gregg, J. M. 1987. Classification of dolomite rock textures. Journal of Sedimentary Research, 57, 967-975.

Smith, T. 2013. Subsurface corrosion of calcite dissolution and dolomite by fault-sourced hydrothermal fluids, AAPG Annual Convention and Exhibition, Pittsburgh, Pennsylvania, May 19-22, 2013, Search and Discovery Article #50918.

Sonntag, R., Evans, J. P., Pointe, P. L., Deraps, M., Sisley, H. and Richey, D. 2014. Sedimentological controls on the fracture distribution and network development in Mesaverde Group sandstone lithofacies, Uinta Basin, Utah, USA. Geological Society, London, Special Publications, 374, 23-50.

Tang, J. 2007. The Diagenesis of the Upper Paleozoic Carbonate Rocks in the Southeast Xiang Depression. Journal-Southwest Petroleum Institute, 29, 43.

Tiab, D. and Donaldson, E. 2003. Petrophysics: Theory and Practice of Measuring Reservoir Rock and Fluid Transport Properties: Second Edition, Gulf Professional Publishing - Elsevier, 1008 P.

Tondi, E., Antonellini, M., Aydin, A., Marchegiani, L. and Cello, G. 2006. The role of deformation bands, stylolites and sheared stylolites in fault development in carbonate grainstones of Majella Mountain, Italy. Journal of Structural Geology, 28, 376-391.

Tucker, M. E. 1981. Sedimentary petrology: an introduction. Geoscience Texts. England, 252, 252 P.

Vandeginste, V. and John, C. M. 2013. Diagenetic implications of stylolitization in pelagic carbonates, Canterbury Basin, offshore New Zealand. Journal of Sedimentary Research, 83, 226-240.

Virgo, S., Abe, S. and Urai, J. L. 2014. The evolution of crack seal vein and fracture networks in an evolving stress field: Insights from Discrete Element Models of fracture sealing. Journal of Geophysical Research: Solid Earth, 119, 8708-8727.

Warpinski, N. R. and Lorenz, J. C. 2008. Analysis of the multiwell experiment data and results: Implications for the basin-centered gas model. Vail Hedberg Conference: AAPG Hedberg Series, no. 3, p. 157-176.

Weisenberger, T. B., Eichhubl, P., Laubach, S. E. and Fall, A. 2019. Degradation of fracture porosity in sandstone by carbonate cement, Piceance Basin, Colorado, USA. Petroleum Geoscience, 25, 354-370.

Wennberg, O. P., Casini, G., Jonoud, S. and Peacock, D. C. P. 2016. The characteristics of open fractures in carbonate reservoirs and their impact on fluid flow: a discussion. Petroleum Geoscience, 22, 91-104.

Xu, H., Guo, X., Cao, Z., Alves, T. M., Tao, Z., Wang, B., Chen, J., Zuo, G., Zhang, X. and Luo, T. 2025. Petroleum-charge history of Paleozoic carbonates in the Tahe oil field, Tarim Basin, northwestern China: Insights from oil geochemistry, fluid inclusion, and U-Pb dating. AAPG Bulletin, 109, 57-84.

Xu, J., Zhang, B., Qin, Y., Cao, G. and Zhang, H. 2016. Method for calculating the fracture porosity of tight-fracture reservoirs. GEOPHYSICS, 81, IM57-IM70.

Yang, N., Lü, X. and Pan, W. 2004. Features of fracture development in Ordovician carbonate reservoirs of the Lunnan buried hill. Journal of Xi'an Shiyou University (Natural Science Edition), 19, 40-43.

Yu, K., Qiu, L., Cao, Y., Sun, P., Qu, C. and Yang, Y. 2019. Hydrothermal origin of early Permian saddle dolomites in the Junggar Basin, NW China. Journal of Asian Earth Sciences, 184, 103990.

Zhang, X., Li, Q., You, X., Ma, L., Jing, A., Tian, W. and Wen, L. 2022. Characteristics and formation mechanism of the lower Paleozoic dolomite reservoirs in the Dongying depression, Bohai Bay Basin. Energies, 15, 2155.

Zhao, W., Anjiang, S., Suyun, H., Wenqing, P., JianFeng, Z. and Zhan Feng, Q. 2012. Types and distributional features of Cambrian-Ordovician dolostone reservoirs in Tarim Basin, northwestern China. Acta Petrologica Sinica, 28, 758-768.

Iraqi National Journal of Earth Science, Vol. 26, No. 04, 2026 (01-18)

Iraqi National Journal of Earth Science

www.earth.uomosul.edu.iq

الترتيب ونظام الكسور المتعددة في تكوين البارسارين الجوراسيك: الآثار المترتبة على مواقع الدفن المختلفة، شمال شرق العراق

ريان فتاح [1]، نمام صالح[2]*، الان بريات[3]

rayanmhamadfatah99@gmail.com namam.salih@soran.edu.iq alain.preat@ulb.be

[1] قسم علوم الأرض البترولية، كلية العلوم، جامعة سوران، سوران، أربيل، 44008، العراق.

[2] قسم هندسة البترول والتعدين، كلية الهندسة، جامعة سوران، سوران، أربيل، 44008، العراق.

[3] مجموعة أبحاث الكيمياء الحيوية الجيولوجية ونمذجة نظام الأرض، الجامعة الحرة في بروكسل، 1050، بروكسل، بلجيكا.

* الباحث المراسل.

تاريخ الاستلام: 23 كانون الثاني 2025 تاريخ المراجعة: 20 آذار 2025 تاريخ القبول: 13 أيار 2025

تاريخ النشر الالكتروني: 01 تشرين الأول 2026

الملخص

يلعب تكوّين نظام الكسور وتطور السوائل الجيولوجية في الظروف البيئية الضحلة والعميقة دورًا حاسمًا في مختلف العمليات الجيولوجية وتطبيقات البترول. تُقيّم هذا البحث البيانات الشاملة لتوفير فهم معمق لنظام الكسور المتعددة، الذي تملأه مراحل التماسك/الذوبان المختلفة المرتبطة بسوائل مختلفة قرب السطح وتحته. استخدمت هذه الدراسة مجهرًا ضوئيًا ورصدًا ميدانيًا مكثفًا لتتبع التكوين المستهدف ونظام الكسور اللاحقة في العصر الجوراسيك. حددت الدراسة خمسة أنواع رئيسية من الكسور: (1) FI الناتج عن ظروف سطحية أو قريبة من السطح، حيث بدأت تكوين الكسور ليس أحدث من توقيت ستيلوليت منخفض السعة. (2) الكسور FII المتشكل في دفن ضحل، وكان متزامنًا مع ستيلوليت منخفض السعة "الستيلولايت المبكر". (3) FIII الكسور المتشكل في ظروف تحت سطحية متزامنة مع ستيلوليت عالي السعة(4) الكسور الرابعة (FIV) المملوءة بأسمنت الكالسيت مع وجود كميات وفيرة من شوائب سائل البيتومين الصلب؛ و(5) الكسور الخامسة (FV) المملوءة بأسمنت الدولوميت. ترتبط خصائص ومظهر بلورات الدولوميت، والتآكل، والتلامس الخيطي بين حبيبات الدولوميت السرجي، والحبيبات المضغوطة بإحكام ارتباطًا مباشرًا بزيادة وزن دفن الصخور الرسوبية العلوية "مرحلة التولد المتوسط". باختصار، تُضيف هذه النتائج رؤيةً جديدةً، إذ تُشكّل الكسور قنواتٍ وحواجزَ أساسيةً لهجرة الهيدروكربونات وتراكمها عبر عملياتٍ جيولوجيةٍ مُتنوعة، بدءًا من تكوّنها أثناء الترسيب وصولًا إلى تطورها وأهميتها في بيئات ما بعد الترسيب. ويُمكّن فهم آلية عمل هذه الكسور من وضع استراتيجياتٍ أكثر فعاليةً للاستكشاف والإنتاج في مكامن الهيدروكربون.

الكلمات المفتاحية:

الكسور، علم الصخور، الدولوميت، الصخور الكربونية في العصر الجوراسيك العلوي، الستيلوليت، تطور السوائل القديمة، التشخيص الدفن الضحل والعميق

DOI: 10.33899/injes.v26i4.60916, ©Authors, 2026, College of Science, University of Mosul.

This is an open-access article under the CC BY 4.0 license (http://creativecommons.org/licenses/by/4.0/)

Iraqi National Journal of Earth Science, Vol. 26, No. 04, 2026 (19-30)

Iraqi National Journal of Earth Science

www.earth.uomosul.edu.iq

Hydrogeological Evaluation of Groundwater Vulnerability Assessment Using the DRASTIC and Pesticide DRASTIC Model: A Case Study from the Qushtapa and Shamamik Area, within Erbil Basin, Kurdistan Region, Iraq

Seber M. M. Ameen[1,2,*], **Rebwar N. Dara**[2,3]

sebarameen@gmail.com rebwar.dara@su.edu.krd

[1] *General Directorate of Divan, Ministry of Agriculture and Water Resources, Kurdistan Region, Erbil, Iraq*
[2] *Department of Earth Sciences and Petroleum, College of Science, University of Salahaddin - Erbil, Erbil, Iraq*
[3] *Department of Petroleum Engineering, College of Engineering, University of Knowledge, Erbil, Iraq*
* *Correspondence author.*

Received: 16 June 2025 Received in revised form: 23 August 2025 Accepted: 14 September 2025
Available online: 01 October 2026

Abstract

Groundwater is a vital freshwater resource. Evaluating its vulnerability to contamination has emerged as a powerful tool for preventing and managing groundwater pollution. This study applied GIS-based standard DRASTIC and Pesticide DRASTIC models to the Qushtapa and Shamamik area to evaluate and delineate groundwater sensitivity zones. The DRASTIC index ranges from 74 to 130, while the Pesticide DRASTIC index ranges from 96 to 168. According to both methods, the examined area is classified into four classes: very low, low, moderate, and high vulnerability zones. The results show that the low vulnerability class for both models occupy the largest area, which is approximately 45.92% and 53.47% of the total area. Additionally, sensitivity analysis for a single parameter has shown that for DRASTIC, the vadose zone is the most effective impact parameter of the vulnerability index, while for Pesticide, the DRASTIC soil media parameter has the most impact on the vulnerability index. The models are validated with NO_3 concentration that ranges between 12-43 mg/l in Qushtapa area and 18-44 mg/l in Shamamik area. The findings show that Pesticide DRASTIC has a higher coefficient of determination R^2 of about 0.62 than DRASTIC, which is about 0.58, indicating that Pesticide DRASTIC is a more precise model for evaluating aquifer vulnerability in the study area.

Keywords:

Hydraulic Conductivity, Sensitivity Analysis, Soil Media, Nitrate.

DOI: 10.33899/injes.v26i4.56020, *©Authors, 2026, College of Science, University of Mosul.*
This is an open-access article under the CC BY 4.0 license (http://creativecommons.org/licenses/by/4.0/) .

==========

1. Introduction

Groundwater is a crucial naturally occurring freshwater resource that is vital for human well-being, economic growth, and ecological processes (Arya et al., 2020; Paul and Das, 2021). Groundwater pollution is a significant and escalating issue in many large urban and agricultural regions, as aquifers are naturally vulnerable to contamination from land use and human activities (Saidi et al., 2011). Erbil Basin, as part of Iraq, is similar to other arid and semi-arid areas because of its limited surface water supplies, or its unsuitability renders groundwater the sole water supply; however, groundwater contamination has emerged as a progressively severe issue, especially in regions where fertilizers are extensively used in agriculture. Groundwater is directly threatened by numerous human activities, including overexploitation, population growth, rapid urbanization, intensive agriculture, increased food production, and alteration in land use, while indirect threats arise from seawater intrusion, global warming, and climate change (Haritash et al., 2017; Ncibi et al., 2020). Moreover, the widespread use of chemical fertilizers exacerbates the critical issue of nitrate contamination in aquifers. According to Haritash et al. (2016), Houria et al. (2020), and Kirlas et al.

(2022), the Environmental Protection Agency (EPA) of the United States uses nitrate content as an index for assessing groundwater quality degradation and defining susceptible regions. Currently, assessment of aquifer vulnerability is conducted in nearly all developed countries in regions where water resources face difficulties resulting from urbanization, industrial, and agricultural activities. The remediation of contaminated aquifers is excessively expensive and sometimes unfeasible. In this context, acknowledging the necessity for effective methods to safeguard groundwater resources against prospective contamination, resource managers and researchers have attempted to establish aquifer vulnerability evaluation methods to predict which areas are more susceptible to contamination due to surface activities. Groundwater vulnerability mapping is crucial for effectively mitigating groundwater pollution (Oke, 2020). It assesses the likelihood of groundwater contamination across various sizes and administrative tiers. DRASTIC (Aller et al., 1987) is one of the most prevalent subjective techniques employed in porous aquifers, recognized for its popularity, reliability, and extensive application as an empirical rank-based index approach. It serves as a model to spatially and comparatively illustrate areas of high vulnerability to low vulnerability concerning groundwater pollution potential (Dixon, 2005). The primary benefit of the model lies in its simplicity and adaptability across many hydrogeological contexts and pollution sources, including agricultural, urban, and industrial influences (Ahmed et al., 2015). To validate the precision of a vulnerability approach for a particular aquifer, a relationship between groundwater vulnerability values and chemical parameters is frequently employed. The predominant chemical measure utilized for validation is nitrate content since it is strongly linked to several human activities, including agricultural activities (Khosravi et al., 2018). Pesticide DRASTIC is a specialized variation of the classic DRASTIC that assesses groundwater sensitivity to a particular contaminant. In contrast to the classic DRASTIC, it employs specific parameter weight values for the factors, while the factor ratings remain the same. Saha and Alam (2014), Saida et al. (2017), and Kirlas et al. (2022) all assert that P-DRASTIC has a superior correlation coefficient, signifying its greater appropriateness for regions characterized by agricultural practices and significant chemical fertilizer application. The study area is the Qushtapa and Shamamik area, which is part of the Erbil plain, characterized by intensive agricultural and industrial activities. It's the area within the Erbil Basin that faces the greatest water shortage and groundwater decline due to over-exploitation and land-use change, in addition to climate change. The escalating contamination of freshwater from agricultural, industrial, and urban sources in the region is causing water pollution issues in water resources to reach alarming levels. Smail and Dişli (2023) applied the original and two modified DRASTIC models to the central Erbil sub-basin. Their results showed that the depth to groundwater (D) parameter and vadose zone (I) have the most impact on groundwater vulnerability. Later, Hamed et al. (2024) applied the standard DRASTIC model focusing on a dumpsite, which is part of the central sub-basin. Their findings revealed that vadose zone (I) and aquifer media (A) parameters are the most influential factors in groundwater vulnerability. Although previous studies applied the model to significant areas within the Erbil Basin, there is still a clear gap in assessing the groundwater vulnerability in areas that practice intensive agriculture and industry and are directly influenced by the remnants of human activities.

2. Aim of Study

This study aims to assess the vulnerability of the aquifer in Qushtapa and Shamamik areas using standard DRASTIC and Pesticide DRASTIC, and to identify the effect of each factor or applied parameter on the aquifer vulnerability. To accomplish these aims, many GIS analysis and mapping frameworks are employed using the ArcMap 10.8 version to create a vulnerability map of the region. These vulnerability maps serve as key instruments to attract the attention of authorities. Groundwater pollution vulnerability maps are among the most effective tools for notifying policymakers about potential future polluting activities.

3. Materials and Methods

Study Area

The study area is situated in the Erbil basin, Iraqi Kurdistan Region. Geographically located to the south of Erbil City between latitudes (35° 43'

50" to 36° 14' 01" N) and longitudes (43° 40' 42" to 44° 17' 55" E) as shown in Fig. (1). It encompasses an area of about 1,302 km2. Its climate is categorized as dry to semi-arid. The topographical variability of the Erbil Basin influences the depth of the water table (Gardi, 2017). Consequently, it exhibits fluctuating water table levels over short distances. The major geological formation outcrop units in the study area are Recent alluvium, Lower Bakhtiari (Mukdadiya), and Upper Bakhtiari (Bai Hassan) formations (Fig. 2). According to Shekhmamundy and Surdashy (2022) and Mohammed et al. (2013), the alluvium and Upper Bakhtiari (Bai Hassan) Formation are composed of conglomerate, gravel, sand and clay, while the Lower Bakhtiari (Mukdadiya) Formation is composed of thin layers of gravelly sandstone, siltstone and claystone.

DRASTIC Parameters Data

DRASTIC is an acronym representing seven important hydrogeological parameters, including: (D) depth to groundwater, (R) net recharge, (A) aquifer media, (S) soil media, (T) topography, (I) impact of vadose zone, and finally (C) hydraulic conductivity. Each parameter is allocated a weight between 1 and 5 based on its significance. The least significant parameter is assigned a weight of 1, whilst the most significant parameter is assigned a weight of 5 (Salih and Al-Manmi, 2021).

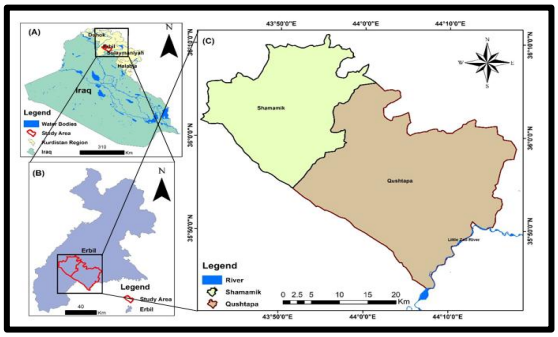


Fig. 1. Location map of the study area in Erbil Governorate.

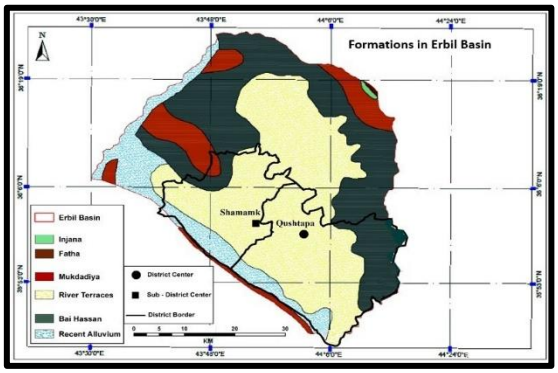


Fig. 2: Geological map of the Erbil Basin showing the study area boundary (modified after Mustafa and Mawlood, 2024).

The classic DRASTIC is applicable for regular settings, whereas the Pesticide DRASTIC is utilized in agricultural regions characterized by significant pesticide and fertilizer application, resulting in distinct weight categorization (Aller et al. 1987). Additionally, the rating of the parameters is dependent upon their relative importance for pollution potential, with ratings ranging from 1 to 10 (Table 1), where 10 indicates the greatest pollution potential, and 1 signifies the smallest pollution potential. Most parameters are assigned a single rating per range; however, some factors, such as impact of vadose zone (I), soil media (S), and aquifer media (A), get ratings informed by location-specific knowledge (Pórcel et al., 2014).

Table 1: Range/type, weight, and ratings of parameters in DRASTIC and Pesticide DRASTIC (modified from Aller et al., 1987).

Parameters	Range or Type	Rating	Standard Weight	Pesticide Weight
D	17-20	9	5	5
	20-30	8		
	30-40	7		
	40-50	6		
	50-60	5		
	60-70	4		
	70-80	3		
	80-90	2		
	90-131	1		
R	3-5	1	4	4
	5-7	3		
	7-9	5		
	9-11	8		
	11-13	10		
A	Massive Shale	2	3	3
	Metamorphic/ Igneous	3		
	Weather Metamorphic/ Igneous, clay with sand	4		
	Glacial till, clay with gravel	5		
	Bedded sandstone, shale sequence, massive sandstone, massive limestone	6		
	Sand	7		
	Sand and Gravel	8		

	Basalt	9		
	Karst limestone	10		
S	No Shrinking Clay	1	2	5
	Muck	2		
	Clay loam	3		
	Silty loam	4		
	Loam	5		
	Sandy loam	6		
	Shrinking Clay	7		
	Peat	8		
	Sand	9		
	Gravel	10		
T %	0-2	10	1	3
	2-6	9		
	6-12	5		
	12-18	3		
	>18	1		
I	Confining layer	1	5	4
	Silt/Clay	2		
	Shale	3		
	Limestone	4		
	Sandy Clay	5		
	Sandstone	6		
	Sand, gravel, and silt	7		
	Sand and gravel	8		
	Basalt	9		
	Karst limestone	10		
c	0.04074-4.074	1	3	2
	4.074-12.222	2		
	12.222-28.518	4		
	28.518-40.74	6		
	40.74-81.48	8		
	>81.48	10		

The DRASTIC and Pesticide DRASTIC models have been implemented based on transdisciplinary data. This study utilizes a methodology consisting of the following steps:

1. Collection of raw data.
2. All DRASTIC parameters are converted into a raster layer using ArcGIS 10.8 with IDW spatial analysis interpolation. According to previous research, IDW is one of the simplest and most commonly applied techniques, and it has been effectively used in hydrogeological assessments (Chakraborty et al., 2022; Kirlas et al., 2022; Hamed et al., 2024).
3. Construction of a rating map for each parameter by reclassifying each raster based on the rating criteria developed by Aller et al. (1987), which correspond to local conditions.
4. Preparation of vulnerability maps for each model by applying the DRASTIC standard weights, and the final index is calculated with the weighted overlay approach.
5. Conducting a sensitivity analysis to compare effective and theoretical parameter weights.
6. Validation of vulnerability maps against nitrate concentration.

The parameters are outlined as follows:

Depth to water (D)

This denotes the distance between the ground surface and the groundwater level (Witczak et al., 2014). It is determined by measuring the static water level during October 2024 from 20 wells in cooperation with the Erbil Groundwater Directorate. It is classified into 9 classes, rated from 9 to 1, from shallow to deep (Table 1 and Fig. 3). A shallow water level indicates a higher chance of pollution. The rating is conducted based on rating criteria developed by Aller et al. (1987) to reflect the local hydrogeological condition, following Sener et al. (2009), Khan and Jhariya (2019), Kirlas et al. (2022), and Hamed et al. (2024).

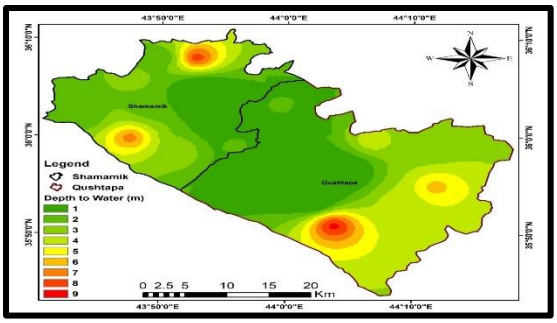


Fig. 3: Depth to groundwater rating map.

Net Recharge (R)

This denotes the volume of surface water that permeates through soil into the subsurface, ultimately reaching the aquifer system. Infiltration is crucial for the transfer of surface contaminants into groundwater. Consequently, elevated infiltration values enhance pollution potential (Aller et al., 1987). The map of this parameter is prepared by applying the Piscopo (2001) method as shown in Equation (1), which incorporates three different interpolated maps for soil permeability, rainfall, and slope.

Recharge Value=Slope+Rainfall+Soil permeability……..... (1)

The slope is derived from the digital elevation model (DEM) of the study area; rainfall data are estimated from a previous study for the Erbil Basin, which has an average rainfall of 467 mm/year from 2000-2020 (Hamad, 2022); and the soil permeability is determined by conducting infiltration capacity tests in 20 sites, which is moderate to high. Table 2 shows the standard values for the Piscopo method (Piscopo, 2001), whose weights are integrated with the previous interpolated maps to produce the recharge value index. The method has been applied by other researchers, including Awawdeh et al. (2015), Yankey et al. (2021), and Kirlas et al. (2022). The net recharge value for eastern and eastern-south was 6-7, and the rest was 7-9, which explains why the recharge rate was 3 and 5, respectively (Fig. 4).

Table 2: Net Recharge rating (Piscopo, 2001).

	Range	Factor
Slope %	<2	4
	2-10	3
	10-33	2
	>33	1
Rainfall mm/year	>850	4
	700-850	3
	500-700	2
	<500	1
Soil Permeability	High	5
	Moderate-High	4
	Moderate	3
	Slow	2
	Very low	1
Recharge Value	11-13	10
	9-11	8
	7-9	5
	5-7	3
	3-5	1

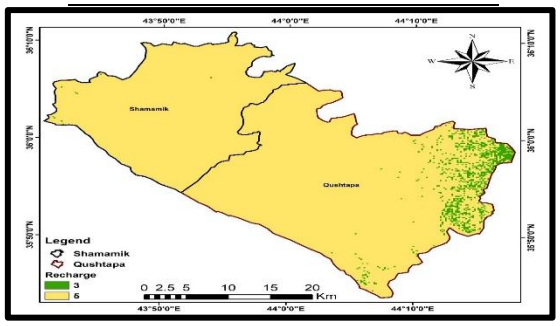


Fig. 4: Recharge rating map.

Aquifer Media (A)

This relates to the characteristics of the geological formation, including consolidated rocks and non-consolidated materials, whereby groundwater is retained inside its pores (Saha and Alam, 2014; Zghibi et al., 2016). According to the geological profile of the wells obtained from the Erbil surrounding water directorate, the lithology of the aquifers varied from conglomerate to clay. Generally, larger grain size leads to higher vulnerability due to its higher permeability, which means gravel has higher effectiveness in groundwater vulnerability; therefore, rated 8 compared to sandy clay rated 4 (Fig. 5).

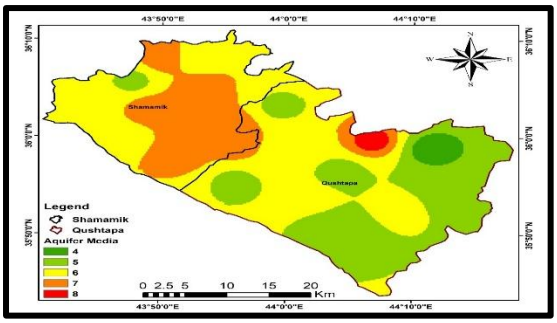


Fig. 5. Aquifer media rating map.

Soil Media (S)

This pertains to the most exposed stratum in the unsaturated zone. The soil layer can significantly influence the transport of potential contaminants (Ifediegwu and Chibuike, 2021). The soil media is detected by grain size analysis for 20 soil samples to a depth of 30 cm. Fine-textured soil is less sensitive than coarse-textured soil due to the accelerated movement of contaminants into the aquifer system. The soil media in the study area are divided into two types: areas with slightly coarse-textured soil, which is gravely silty sand, and the rest are silty sand soil. The classification of the soil is determined using GRADISTAT software based on the Folk and Ward (1957) classification. The soil is classified into two classes and rated as 7 and 8, representing gravely silty sand and silty sand soil, respectively (Fig. 6).

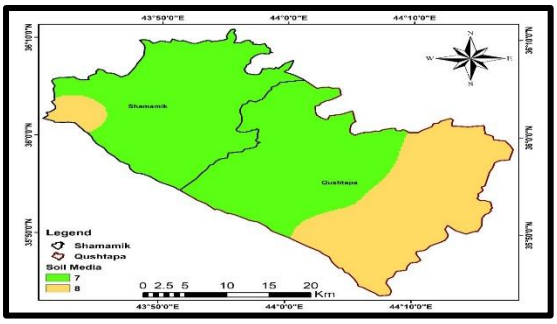


Fig. 6: Soil media rating map.

Topography (T)

This denotes the variety of land surface slope. Generally, low slope regions have increased susceptibility to groundwater contamination. The

topography is extracted from the DEM of the study area with 12.5m resolution. The slope% ranges between 0 and 43%; therefore, the topography is classified into 5 classes (Table 1). The low slope area is rated as 10, and the steep slope area is rated as 1 (Fig. 7).

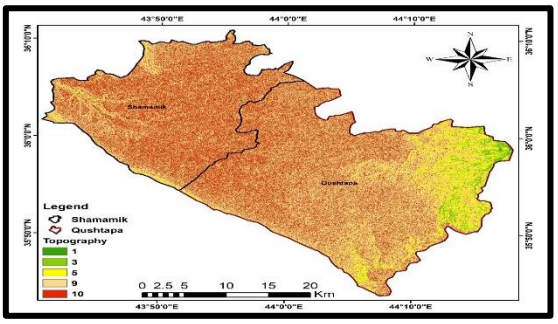


Fig. 7: Topography rating map.

Impact of Vadose Zone (I)

This refers to the distance between the soil media and the water table, representing the unsaturated zone. Similarly, as aquifer media, it is derived from the geological profile of the wells. Generally, larger grain size in materials correlates with increased susceptibility. From the geological profile of the wells, the component of this zone varies from gravel to clay; therefore, it is classified into 6 classes. The coarse-grain size materials, such as gravel, have a higher impact; that's why rated as 8, and the fine-textured material, such as clay, is rated as 3 (Fig. 8).

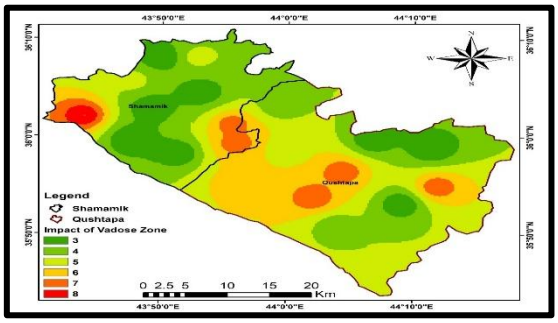


Fig. 8: Vadose Zone rating map.

Hydraulic conductivity (C)

This denotes the capacity of water-bearing formation materials to transmit groundwater. Therefore, the migration of contaminants is contingent upon this parameter (Aller et al., 1987). Decreased C indicates a lower risk of groundwater contamination, since contaminants may traverse the aquifers more slowly. In this study, the data for hydraulic conductivity are derived from the pumping test data obtained from the Erbil Surrounding Water Directorate. It varied from 0.0021 to 0.72 m/day. For all 20 wells, C is less than 4 m/day; therefore, it is rated as 1 (Table 1 and Fig. 9).

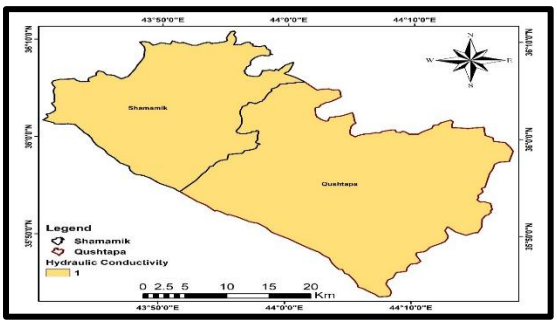


Fig. 9: Hydraulic conductivity rating map.

After generating a separate rating map for each parameter with ArcMap, by a numeric arrangement including weighting and rating, the DRASTIC Vulnerability Index (DI) value can be derived using equation (2).

$$DI=DrDw+RrRw+ArAw+SrSw+TrTw+IrIw+CrCw \quad \text{.....(2)}$$

Where: D, R, A, S, T, I, and C stand for the seven parameters, and w and r represent the weight and rating of the parameters, respectively.

A larger DI value means greater aquifer vulnerability. The rating maps for both DRASTIC and Pesticide DRASTIC are the same since both use the same rating, and only the weights of the parameters will be different. Different DIs will be calculated for each model by inserting the theoretical weights of the parameters in Equation (2). The vulnerability values commonly vary between 23 and 230 for standard DRASTIC, as well as 26 and 256 in the Pesticide DRASTIC. Notably, based on Aller et al. (1987), there is no specific or formal categorization for vulnerability categories, and so the index is interpreted according to the relative distribution of values throughout the research area.

Sensitivity Analysis

Sensitivity analysis generally assesses the robustness and degree of uncertainty of output findings derived from multiple methodologies. The current study has used a single-parameter sensitivity test to evaluate the effect of each parameter on the last vulnerability index DI. It compares the given (theoretical) weight with the actual (effective) weight (Napolitano and Fabbri, 1996; Oke, 2020; Kirlas et al., 2022). It enables the researcher to assess the significance of subjective aspects in vulnerability methodologies (Gogu et al., 2003; Noori et al., 2019). The actual (effective)

weight for all seven parameters is derived by equation (3).

$$W=((P_r P_w)/V)*100 \quad \ldots\ldots\ldots\ldots\ldots\ldots (3)$$

Where: *W* denotes the actual weight of each parameter; *Pr* and Pw represent the rate and weight for each parameter, whereas *V* signifies the total vulnerability index (Ouedraogo et al., 2016).

When a parameter possesses an effective (actual) weight higher than the theoretical (given) weight, it exerts greater influence on the outcomes of the vulnerability model.

Validation Test

Validation test is a crucial process to ascertain the findings of the applied models and to choose the most suitable and reliable model for the study area (Saidi et al., 2011; Khan and Jhariya, 2019; Kirlas et al., 2022). The test employed to assess the reliability of the applicable model is the calculation of the coefficient of determination (R2) between the DI value of DRASTIC and Pesticide DRASTIC and the Nitrate (NO3) concentration in 20 groundwater samples in October 2024 (Table 3).

Table 3: Nitrate concentration in Qushatpa and Shamamik for validation.

Sampling Location	NO_3 (mg/l)	Sampling Location	NO_3 (mg/l)
Qucha Blbas	24	Shekh Sherwan	38
Kardiz	29	Pirdawd	18
Dushiwan	25	Helawa	44
Dola Bakra	25	Jdida lak	21
Sebiran Ado	12	Awena	41
Dolaza	15	Sorbash Hawez	18
Grda Sor	21	Beryat	19
Grd Lanka	43	Bnberz	42
Grd Mala	24	Daldaghan	19
Sherawa	39	Dhemat	23

4. Results and Discussion

Standard DRASTIC Vulnerability Map

The final DRASTIC vulnerability map (Fig. 10) for the Qushtapa and Shamamik area is produced by integrating the rating maps of all factors inside the ArcGIS environment. It is classified according to the natural breaks of the Jenks (1967) approach. Numerous researchers employed this strategy, including regional researchers (Hamed et al., 2024) and foreign investigators such as Thapa et al. (2018), Wei et al. (2021), and Krlas et al. (2022). This signifies the method's reliability and applicability across many geographical regions. Qushtapa and Shamamik are categorized into four classes according to the DI values, which range between 74 and 130. A high DRASTIC index value signifies an increased risk level in the region. Usually, a DI value higher than 200 is regarded as very highly vulnerable (Ncibi et al., 2020). The proportions for each DI class to the total area are presented in Table (4).

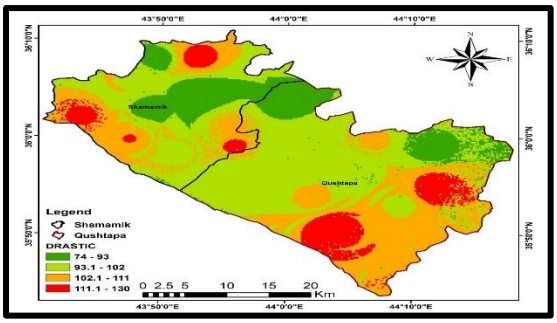


Fig. 10: DRASTIC Vulnerability map of Qushtapa and Shamamik.

The results show that the northwest and central regions of the Qushtapa and Shamamik area are characterized by elevated groundwater depth, exhibiting reduced vulnerability; similarly, locations with less permeable unsaturated zones are likewise less susceptible to contamination. Furthermore, the steep slope region, particularly the northeastern part of the research area with topography above 18%, exhibits reduced vulnerability. Regions with shallow groundwater depth and aquifer media consisting of porous materials like sand and gravel are more susceptible, particularly those with a mild slope of 2-12%.

Pesticide DRASTIC Vulnerability Map

The Pesticide DRASTIC map (Fig. 11) is also produced by integrating the rating maps of the same parameters using different weights. The region is categorized using the natural breaks of the Jenks (1967) approach, similar to a classic DRASTIC model. The area is categorized into four classes based on the DI value for the Pesticide DRASTIC map. The DI ranges between 96 and 168 and is classified into four classes. Aller et al. (1987) didn't propose an exact categorization for Pesticide DRASTIC. The proportions for each DI class to the total area are presented in Table (4). The vulnerability index (DI) value exceeding the classic or standard DRASTIC is consistent with the findings of Al-Abadi et al. (2017) and Kirlas et al. (2022).

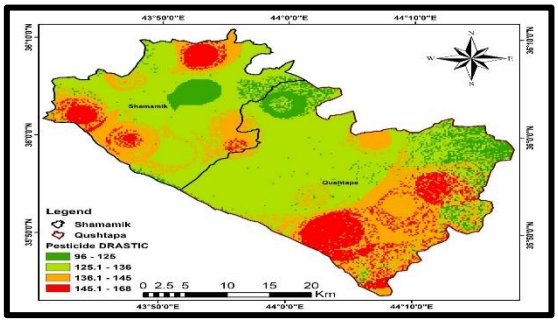


Fig. 11: Pesticide DRASTIC Vulnerability map of Qushtapa and Shamamik.

The distinction between the two produced maps lies in the fact that, for Pesticide DRASTIC, the region exhibiting low and high vulnerability classes has a broader expanse compared to the standard DRASTIC, while the categories of very low and moderate vulnerability classes occupy smaller areas. The discrepancies result from the differing weights assigned to the parameters. The sensitivity analysis is conducted to illustrate the degree of dependability. Current research has examined the influence of a single parameter.

Table 4: Classification of the study area according to Vulnerability classes.

Vulnerability Class	DRASTIC		Pesticide DRASTIC	
	DI value	Occupied Area	DI value	Occupied Area
Very Low	74-93	15.65%	96-125	9.81%
Low	93.1-102	45.92%	125.1-136	53.47%
Moderate	102.1-111	29.16%	136.1-145	25.05%
High	111.1-130	9.27%	145.1-168	11.67%

Single parameter influence of weight-rating parameters on DRASTIC and Pesticide DRASTIC models

A sensitivity analysis using a single parameter is performed for all seven components of both models. The effective weight of the parameters in both models depends on the given theoretical weight. Babiker et al. (2005) revealed the weight and its reciprocal effect on the other parameters in each approach. The efficiency of the components in DRASTIC is presented in Table (5). The findings reveal inconsistencies between the theoretical weight and the actual effective weight identified in this study. In DRASTIC, the vadose zone (I) has the most effective weight of approximately 23.45% rather than 21.74%. This outcome is consistent with previous studies, including Şener and Şener (2015); Ouedraogo et al. (2016); Oke (2020); and Kirlas et al. (2022). The net recharge (R) and Aquifer media (A) exhibit a greater effective weight; however, they remain within the same efficiency rank. This observation aligns with previous research, including Neshat and Pradhan (2017) and Kirlas et al. (2022). The two main parameters that dramatically indicate reduced effectiveness in weight are depth to water (D) and hydraulic conductivity (C), which demonstrate 13.07 % and 2.98 % rather than 21.73% and 13.043%, respectively. The DRASTIC result highlights the importance of the factors affecting groundwater vulnerability in the order of (I>R>A>S>D>T>C), as opposed to a theoretical order (I~D > R > A~C > S > T).

Table 5: Statistical evaluation of DRASTIC Single-Parameter sensitivity test.

Parameters	Theoretical weight	Theoretical Weight%	Mean Effective Weight	Mean Effective Weight%
D	5	21.74	3.00	13.07
R	4	17.39	4.51	19.60
A	3	13.04	4.01	17.44
S	2	8.69	3.35	14.56
T	1	4.35	2.04	8.88
I	5	21.74	5.40	23.46
C	3	13.04	0.68	2.98

On the other hand, in the Pesticide DRASTIC evaluation (Table 6), the soil media emerges as the most influential parameter, exhibiting a theoretical weight of approximately 27.7% rather than 19.23%. The second most significant parameter is topography (T), which demonstrates an effective weight of around 19.88% rather than 11.54%. The depth to groundwater (D) and hydraulic conductivity (C) parameters have a minimal impact exhibiting effective weights of around 9.75% and 1.48% respectively; in contrast to theoretical weights of 19.23% and 7.69%, instead of 19.23% and 7.69% respectively. This finding aligns with the findings of Kirlas et al. (2022). This study investigates the influence of parameters in Pesticide DRASTIC in the order of (S>T>R>I>A>D>C), in contrast to a theoretical order (S>D>I>R>T>A>C).

Table 6: Statistical evaluation of Pesticide DRASTIC Single-Parameter sensitivity test.

Parameters	Theoretical weight	Theoretical Weight%	Mean Effective Weight	Mean Effective Weight%
D	5	19.23	2.54	9.76
R	4	15.38	3.80	14.63
A	3	11.54	3.39	13.02
S	5	19.23	7.07	27.18
T	3	11.54	5.17	19.89
I	4	15.38	3.64	14.00
C	2	7.69	0.39	1.48

Validation Test

The Pearson correlation results indicate that the coefficient of determination R^2 for the standard

DRASTIC is 0.58, but for the Pesticide DRASTIC model it is 0.62 (Figs. 12 and 13). A stronger correlation with NO_3 concentration provides a more effective and accurate model of vulnerability (Kilrals et al., 2022). The results show that a Pesticide DRASTIC is superior and more precise than a standard DRASTIC model for evaluating groundwater vulnerability in the study area.

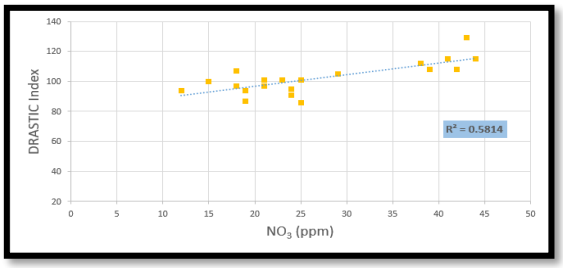


Fig. 12: Correlation of DRASTIC index with NO_3 values.

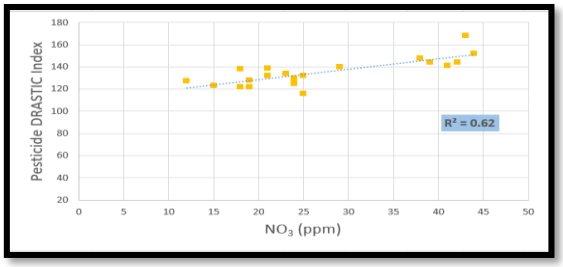


Fig. 13: Correlation of Pesticide DRASTIC index with NO_3 values.

5. Conclusion

The GIS-based DRASTIC and Pesticide DRASTIC models have been applied to assess the aquifer vulnerability in the Qushtapa and Shamamik areas. The results show that:

1. The aquifer in Qushtapa and Shamamik is situated within zones of varying vulnerability ranging from very low to high.
2. The Original DRASTIC index value ranges from 74-130, while the Pesticide DRASTIC index value ranges from 96-168.
3. The sensitivity analysis indicates that the essential vulnerability of Qushtapa and Shamamik areas for the DRASTIC model mostly arises from the vadose zone, whereas for the Pesticide DRASTIC model it mostly arises from the soil media.
4. The hydraulic conductivity parameter for both models show the least effective weight.
5. The vulnerability maps validation with nitrate concentration reveals that Pesticide DRASTIC is a more accurate predictive method than the standard DRASTIC.

6. Acknowledgements

The authors gratefully acknowledge the staff of the Erbil Groundwater Directorate and the Erbil Surrounding Water Directorate for their cooperation and for granting access to wells for field data collection and sampling.

7. Conflict of Interest

The authors declare that they have no conflict of interest.

8. Funding Statement

This research received no external funding.

9. Author Contributions

Seber M.M. Ameen: Collected the data for the study, analyzed and prepared the DRASTIC layers and maps, and prepared the first draft of the manuscript.

Rebwar N. Dara: Contributed to the research methodology, participated in fieldwork and data collection, supervised the study, and reviewed the first draft.

10. References

Ahmed, I., Nazzal, Y., Zaidi, F. K., Al-Arifi, N. S., Ghrefat, H. and Naeem, M., 2015. Hydrogeological vulnerability and pollution risk mapping of the Saq and overlying aquifers using the DRASTIC model and GIS techniques, NW Saudi Arabia. Environmental Earth Sciences, 74, pp. 1303-1318. https://doi.org/10.1007/s12665-015-4120-5

Al-Abadi, A. M., Al-Shamma'a, A. M. and Aljabbari, M. H., 2017. A GIS-based DRASTIC model for assessing intrinsic groundwater vulnerability in northeastern Missan governorate, southern Iraq. Applied Water Science, 7, pp. 89-101. https://doi.org/10.1007/s13201-014-0221-7

Aller, L., Bennett, T., Lehr, J., Petty, R. J. and Hackett, G., 1987. DRASTIC: A standardized system for evaluating groundwater pollution potential using hydrogeologic settings. US Environmental Protection Agency. Washington, DC, 455.

Arya, S., Subramani, T., Vennila, G. and Roy, P. D., 2020. Groundwater vulnerability to pollution in the semi-arid Vattamalaikarai River Basin of South India through DRASTIC index evaluation. Geochemistry, 80(4), 125635. https://doi.org/10.1016/j.chemer.2020.125635

Awawdeh, M., Obeidat, M. and Zaiter, G., 2015. Groundwater vulnerability assessment in the vicinity of Ramtha wastewater treatment plant, North Jordan. Applied Water Science, 5, pp. 321-334. https://doi.org/10.1007/s13201-014-0194-6

Babiker, I. S., Mohamed, M. A., Hiyama, T. and Kato, K., 2005. A GIS-based DRASTIC model for assessing aquifer vulnerability in Kakamigahara Heights, Gifu Prefecture, central Japan. Science of the Total Environment, 345(1-3), pp. 127-140. https://doi.org/10.1016/j.scitotenv.2004.11. 005

Chakraborty, B., Roy, S., Bera, A., Adhikary, P. P., Bera, B., Sengupta, D., and Shit, P. K., 2022. Groundwater vulnerability assessment using GIS-based DRASTIC model in the upper catchment of Dwarakeshwar River basin, West Bengal, India. Environmental Earth Sciences, 81(1), 2. https://doi.org/10.1007/s12665-021-10002-3

Dixon, B., 2005. Groundwater vulnerability mapping: a GIS and fuzzy rule based integrated tool. Applied Geography, 25(4), pp. 327-347. https://doi.org/10.1016/j.apgeog.2005.07.002

Folk, R. L. and Ward, W. C., 1957. Brazos River bar [Texas]; a study in the significance of grain size parameters. Journal of Sedimentary Research, 27(1), pp. 3-26.

Gardi, S. Q., 2017. Integrated use of geoelectrical resistivity and geochemical analysis to assess the environmental impact on soil and groundwater at Erbil dumpsite, west of Erbil City, Iraqi Kurdistan Region. ARO-The Scientific Journal of Koya University, 5(2), pp. 19-31. https://doi.org/10.14500/aro.10192

Gogu, R. C., Hallet, V. and Dassargues, A., 2003. Comparison of aquifer vulnerability assessment techniques. Application to the Néblon river basin (Belgium). Environmental Geology, 44, pp. 881-892.

Hamad, R., 2022. Erbil Basin Groundwater Recharge Potential Zone Determination Using Fuzzy-Analytical Hierarchy Process (AHP) in North Iraq. Tikrit Journal for Agricultural Sciences, 22(3), pp. 175-190. https://doi.org/10.21203/rs.3.rs-1315621/v1

Hamed, M. H., 2024. Groundwater vulnerability assessment using a GIS-based DRASTIC method in the Erbil Dumpsite area (Kani Qirzhala), Central Erbil Basin, North Iraq. Journal of Groundwater Science and Engineering. https://doi.org/10.26599/JGSE.2024.9280003

Hamed, M. H., Toma, J. J., Karimkhan, K. and Hanna, A. M., 2024. Application of Geographical Information System–Water Quality Index Techniques for Evaluating the Groundwater Quality in Kaniqirzhala Landfill, Kurdistan Region, Iraq. The Iraqi Geological Journal, pp. 296-315. https://doi.org/10.46717/igj.57.2C.20ms-2024-9-28

Haritash, A. K., Gaur, S. and Garg, S., 2016. Assessment of water quality and suitability analysis of River Ganga in Rishikesh, India. Applied Water Science, 6, pp. 383-392. https://doi.org/10.1007/ s13201-014-0235-1

Haritash, A. K., Mathur, K., Singh, P. and Singh, S. K., 2017. Hydrochemical characterization and suitability assessment of groundwater in Baga–Calangute stretch of Goa, India. Environmental Earth Sciences, 76, pp. 1-10. https://doi.org/10.1007/s12665-017-6679-5

Houria, B., Mahdi, K. and Zohra, T. F., 2020. Hydrochemical characterisation of groundwater quality: Merdja plain (Tebessa town, Algeria). Civil Engineering Journal, 6(2), pp. 318-325. https://doi.org/10.28991/cej-2020-03091473

Ifediegwu, S. I. and Chibuike, I. E., 2021. GIS-based evaluation of shallow aquifer vulnerability to pollution using DRASTIC model: a case study on Abakaliki, southeastern Nigeria. Arabian Journal of Geosciences, 14(23), 2534.https://doi.org/10.1007/s12517-021-08811-8

Jenks, G. F., 1967. The data model concept in statistical mapping. International Yearbook of Cartography, 7, pp. 186-190.

Khan, R. and Jhariya, D. C., 2019. Assessment of groundwater pollution vulnerability using GIS based modified DRASTIC model in Raipur City, Chhattisgarh. Journal of the Geological Society of India, 93(3), pp. 293-304. https://doi.org/10.1007/s12594-019-1177-x

Khosravi, K., Sartaj, M., Tsai, F. T. C., Singh, V. P., Kazakis, N., Melesse, A. M. and Pham, B. T., 2018. A comparison study of DRASTIC methods with various objective methods for groundwater vulnerability assessment. Science of the Total Environment, 642 P. 1032-1049. https://doi.org/10.1016/j.scitotenv.2018.06.130

Kirlas, M. C., Karpouzos, D. K., Georgiou, P. E. and Katsifarakis, K. L., 2022. A comparative study of groundwater vulnerability methods in a porous aquifer in Greece. Applied Water Science, 12(6), 123. https://doi.org/10.1007/s13201-022-01651-1

Mohammed, F. A., Smail, S. Q. and Kettanah, Y. A., 2013. Environmental significance of major and trace elements in the soils of selected areas in Erbil City, Kurdistan Region, Northern Iraq. Iraqi National Journal of Earth Science, 13(2), 15-0.

Mustafa, J. S. and Mawlood, D. K., 2024. Assessment of the Groundwater in Erbil Basin with Support of Visual MODFLOW. Journal of Ecological Engineering, 25(4). https://doi.org/10.12911/22998993/184184

Napolitano, P. and Fabbri, A. G., 1996. Single-parameter sensitivity analysis for aquifer vulnerability assessment using DRASTIC and SINTACS. IAHS Publications-Series of Proceedings and Reports-Intern Assoc Hydrological Sciences, 235(235), pp. 559-566.

Neshat, A. and Pradhan, B., 2017. Evaluation of groundwater vulnerability to pollution using DRASTIC framework and GIS. Arabian Journal of Geosciences, 10, pp. 1-8. https://doi.org/10.1007/s12517-017-3292-6

Ncibi, K., Chaar, H., Hadji, R., Baccari, N., Sebei, A., Khelifi, F., and Hamed, Y., 2020. A GIS-based statistical model for assessing groundwater susceptibility index in

shallow aquifer in Central Tunisia (Sidi Bouzid basin). Arabian Journal of Geosciences, 13(2), 98. https://doi.org/10.1007/ s12517-020-5112-7

Noori, R., Ghahremanzadeh, H., Kløve, B., Adamowski, J. F., and Baghvand, A., 2019. Modified-DRASTIC, modified-SINTACS and SI methods for groundwater vulnerability assessment in the southern Tehran aquifer. Journal of Environmental Science and Health, Part A, 54(1), pp. 89-100.

Oke, S. A., 2020. Regional aquifer vulnerability and pollution sensitivity analysis of drastic application to Dahomey Basin of Nigeria. International Journal of Environmental Research and Public Health, 17(7), 2609. https://doi.org/10. 3390/ijerph17072609

Ouedraogo, I., Defourny, P. and Vanclooster, M., 2016. Mapping the groundwater vulnerability for pollution at the pan African scale. Science of the Total Environment, 544, pp. 939-953. https://doi.org/10.1016/j.scitotenv. 2015.11.135

Paul, S. and Das, C. S., 2021. An investigation of groundwater vulnerability in the North 24 parganas district using DRASTIC and hybrid-DRASTIC models: A case study. Environmental Advances, 5, 100093. https://doi.org/10. 1016/j.envadv.2021.100093

Piscopo, G., 2001. Groundwater vulnerability map explanatory notes Castlereagh Catchment. NSW Department of Land and Water Conservation, Australia.

Pórcel, R. A. D., Schüth, C., De León-Gómez, H., Hoppe, A. and Lehné, R., 2014. Land-use impact and nitrate analysis to validate DRASTIC vulnerability maps using a GIS platform of Pablillo River Basin, Linares, NL, Mexico. International Journal of Geosciences, 5(12), 1468. https://doi.org/10.4236/ijg.2014.512120

Saha, D. and Alam, F., 2014. Groundwater vulnerability assessment using DRASTIC and Pesticide DRASTIC models in intense agriculture area of the Gangetic plains, India. Environmental Monitoring and Assessment, 186, pp. 8741-8763. https://doi.org/10.1007/s10661-014-4041-x

Saida, S., Tarik, H., Abdellah, A., Farid, H. and Hakim, B., 2017. Assessment of groundwater vulnerability to nitrate based on the optimised DRASTIC models in the GIS environment (case of Sidi Rached Basin, Algeria). Geosciences, 7(2), 20. https://doi.org/10.3390/geosciences7020020

Saidi, S., Bouri, S. and Ben Dhia, H., 2011. Sensitivity analysis in groundwater vulnerability assessment based on GIS in the Mahdia-Ksour Essaf aquifer, Tunisia: a validation study. Hydrological Sciences Journal–Journal des Sciences Hydrologiques, 56(2), pp. 288–304. https://doi.org/10.1080/02626667.2011.552886

Salih, A. O. and Al-Manmi, D. A., 2021. DRASTIC model adjusted with lineament density to map groundwater vulnerability: a case study in Rania basin, Kurdistan, Iraq. Environmental Science and Pollution Research, 28(42), pp. 59731-59744. https://doi.org/10.1007/s11356-021-14912-4

Sener, E., Sener, S. and Davraz, A., 2009. Assessment of aquifer vulnerability based on GIS and DRASTIC methods: a case study of the Senirkent-Uluborlu Basin (Isparta, Turkey). Hydrogeology Journal, 17(8), 2023.https://doi.org/10.1007/s10040-009-0497-0

Şener, E. and Şener, Ş., 2015. Evaluation of groundwater vulnerability to pollution using fuzzy analytic hierarchy process method. Environmental Earth Sciences, 73, pp. 8405-8424. https://doi.org/10.1007/ s12665-014-4001-3

Shekhmamundy, I. H. and Surdashy, A. M., 2022. Geomorphological analysis and distribution of landform of Erbil Masterplan Layout. The Iraqi Geological Journal, pp. 197-211. https://doi.org/10.46717/igj.55.2F.14ms-2022-12-29

Smail, R. Q. S. and Dişli, E., 2023. Assessment and validation of groundwater vulnerability to nitrate and TDS using based on a modified DRASTIC model: a case study in the Erbil Central Sub-Basin, Iraq. Environmental Monitoring and Assessment, 195(5), 567. https://doi.org/10.1007/s10661-023-11165-1

Witczak, S., Duda, R., and Zurek, A., 2014. The Polish concept of groundwater vulnerability mapping. Groundwater Vulnerability Assessment and Mapping: IAH-Selected Papers, volume 11, 45.

Yankey, R. K., Anornu, G. K., Osae, S. K. and Ganyaglo, S. Y., 2021. Drastic model application to groundwater vulnerability elucidation for decision making: the case of south western coastal basin, Ghana. Modeling Earth Systems and Environment, 7, pp. 2197-2213.

Zghibi, A., Merzougui, A., Chenini, I., Ergaieg, K., Zouhri, L. and Tarhouni, J., 2016. Groundwater vulnerability analysis of Tunisian coastal aquifer: an application of DRASTIC index method in GIS environment. Groundwater for Sustainable Development, 2, pp. 169-181. https://doi.org/10.1016/j.gsd.2016.10.001

Iraqi National Journal of Earth Science, Vol. 26, No. 04, 2026 (19-30)

Iraqi National Journal of Earth Science

www.earth.uomosul.edu.iq

التقييم الهيدروجيولوجي لقابلية تلوث المياه الجوفية باستخدام نموذج DRASTIC ونموذج DRASTIC للمبيدات: دراسة حالة من منطقة قوشتبة وشمامك، ضمن حوض أربيل، إقليم كوردستان، العراق

سيبر محسن محمد أمين[1،2]* ، ريبوار ناصر دارا [2،3]

sebarameen@gmail.com rebwar.dara@su.edu.krd

[1] المديرية العامة للديوان، وزارة الزراعة و الموارد المائية، اربيل، اقليم كوردستان، العراق.

[2] قسم علوم الارض و النفط، كلية العلوم، جامعة صلاح الدين–اربيل، اربيل، اقليم كوردستان، العراق.

[3] قسم هندسة النفط، كلية الهندسة، جامعة نوليج، أربيل، العراق.

* الباحث المراسل.

تاريخ الاستلام: 16 حزيران 2025 تاريخ المراجعة: 23 آب 2025 تاريخ القبول: 14 أيلول 2025

تاريخ النشر الالكتروني: 01 تشرين الأول 2026

الملخص

المياه الجوفية مورد حيوي للمياه العذبة. وقد برز تقييم قابليتها للتلوث كأداة قوية للوقاية من تلوث المياه الجوفية وإدارته. وقد طبقت هذه الدراسة نموذجي DRASTIC ونموذج DRASTIC للمبيدات القياسيين القائمين على نظم المعلومات الجغرافية على منطقة قوشتبة وشمامك لتقييم وتحديد مناطق حساسية المياه الجوفية. يتراوح مؤشر قابلية DRASTIC للتعرض ما بين 74 و130، بينما يتراوح مؤشر قابلية DRASTIC للمبيدات ما بين 96 و168. ووفقًا لكلا الطريقتين، تم تصنيف منطقة الدراسة إلى أربع فئات: مناطق قابلية تعرض منخفضة للغاية ومنخفضة ومتوسطة وعالية. توضح النتيجة أن فئة القابلية المنخفضة للتعرض لكلا النموذجين احتلت أكبر مساحة والتي تبلغ حوالي 45.92٪ و53.47٪ من المساحة الإجمالية. بالإضافة إلى ذلك، أظهر تحليل الحساسية لمتغير واحد أن لـ DRASTIC منطقة غير مشبعة هي المتغير الأكثر فعالية لمؤشر القابلية للتعرض، بينما بالنسبة لـ DRASTIC للمبيدات الحشرية، فإن وسائط التربة هي المتغير الأكثر فعالية لمؤشر القابلية للتعرض. تم التحقق من صحة النماذج باستخدام تركيز NO_3 الذي يتراوح ما بين 12–43 مغم/لتر في منطقة قوشتبة، وبين 18–44 مغم/لتر في منطقة شامامك. أظهرت النتائج أن DRASTIC للمبيد الآفات يظهر علاقة أعلى بنحو 0.62 من DRASTIC والتي تبلغ نحو 0.58، مما يشير إلى أن DRASTIC للمبيد الآفات هو النموذج الأكثر دقة لتقييم ضعف طبقة المياه الجوفية في منطقة الدراسة.

الكلمات المفتاحية:

الموصلية الهيدروليكية، تحليل الحساسية، وسائط التربة، نترات.

DOI: 10.33899/injes.v26i4.56020, ©Authors, 2026, College of Science, University of Mosul.

This is an open-access article under the CC BY 4.0 license (http://creativecommons.org/licenses/by/4.0/).

==========

Iraqi National Journal of Earth Science, Vol. 26, No. 04, 2026 (31-39)

Iraqi National Journal of Earth Science

www.earth.uomosul.edu.iq

GIS to Create Maps Based on the Bergsma Model for Gully Erosion Estimation Using DEM: A Case Study for Qarahanjeer, Kirkuk, Iraq

Suzan I. Baez [1*], **Fawzi M. Omar** [1], **Mustafa R. Mezaal** [1]

suzanibrahimgis@gmail.com fawzialbeyati@yahoo.com Mostafa.redha@ntu.edu.iq

[1] *Department of Surveying Engineering, College of Technical Engineering Kirkuk, University of Northern Technical, Mosul, Iraq.*
[2] *Department of Surveying Engineering, College of Technical Engineering Mosul, University of Northern Technical, Mosul, Iraq.*
***** *Correspondence author.*

Received: 03 July 2025 Received in revised form: 18 September 2025 Accepted: 07 November 2025
Available online: 01 October 2026

Abstract

Gully erosion is a serious environmental problem that threatens soil sustainability, especially in arid and semi-arid regions like Qarahanjeer in Kirkuk, which spans an area of 676 km². The main research problem is the lack of studies and effective methods to determine the extent of gully erosion. To meet this challenge, this study used the Bergsma (1986) model and GIS techniques to estimate gully erosion based on digital elevation model (DEM) data from the ALOS PALSAR program. The main objective of the study is to evaluate the applicability of the Bergsma model in mapping gully erosion risk areas in the Qarahanjeer region and to verify its effectiveness using field observations. The results revealed the levels of gully erosion. High erosion was the predominant category, comprising 54.692% of the research area, represented by categories from 1501 to 2700. Moderate erosion (21%) occurred in transitional zones, characterized by augmented fluvial energy and vegetative cover (1001 to 1500). Despite very limited areas (12.47%) categorized (2701 to 3700), severe erosion (0.69 %) categories (3701 to 4700) assessments signify significant degradation, as these operations disrupt natural drainage patterns. Also, recommended that depressions be dug in the basin estuaries to collect water, particularly surface runoff for use, and to utilize high-resolution spatial data to estimate erosion. Applying research and recording geomorphological changes with GIS and remote sensing.

Keywords:

Digital Elevation Model Dem, Bergsma Model, Gully Erosion, Qarahanjeer.

DOI: 10.33899/injes.v26i4.56023, ©Authors, 2026, College of Science, University of Mosul.
This is an open-access article under the CC BY 4.0 license (http://creativecommons.org/licenses/by/4.0/) .

==========

1. Introduction

Landforms are subject to change over time, and erosion is one of the most important aspects affecting these morphological changes on the Earth's surface (Kirkby and Bracken, 2009). One of the complexities of soil erosion studies in Kirkuk is the lack of information on the location of gullies and the reliance on traditional methods to study this type of erosion. The study is limited to the Qarahanjeer area in the north-eastern Governorate of Kirkuk. It focuses on a specific time frame for the digital elevation model (DEM) and analysis using GIS techniques. Streams are formed from the confluence of minor watercourses, making them wider and longer. Therefore, the amount of running water increases, which increases the likelihood of their ability to erode, which works to deepen and widen these streams, which makes the running water capable of carrying boulders and small pieces of rock (Wang et al., 2014).

Gullies, in general, are active in the absence of plants on the sides that work to stabilize them. Gully or water-induced soil erosion is a prevalent kind of land degradation due to its detrimental on-site effects on landforms, such as the reduction of soil productivity and quality, as well as off-site cumulative impacts from several erosion control elements, including rainfall erosion, soil erodibility, and slope (Ismaeel et al., 2021). Soil is also one of the basic factors that provide the basic needs of humans. Unfortunately, every year,

millions of tons of soil are exposed to environmental hazards and human activities (Zhang et al., 2015). Water erosion contributes about 56% of these sediments. During the past two decades, many methods have been used to estimate the area of erosion in water basins. These methods are also tools for estimating sediments in water basins. Among the methods used to estimate erosion are those related to land use changes and how to employ this to determine sedimentation volume (Feng et al., 2010). The study successfully utilized Geographic Information Systems (GIS) and Remote Sensing (RS) technologies to map the areas most susceptible to gully erosion within the Mamran Basin. This mapping is crucial for understanding the spatial distribution of erosion risks (Jawad and Baqer, 2024). Other researchers utilized satellite data to identify gully erosion and created corresponding maps of this erosion type (Giordano and Marchisio, 1991). Gully erosion is considered one of the problems that all regions suffer from, especially the eastern region of Misan. It is the most dangerous type of erosion and is widespread due to its impact on fertile lands. Suitable for crops, the Bergsma method is employed to assess soil erosion rates in the Wadi Al-Rahba basin located in the East Governorate of Misan, where it quantified erosion levels from extremely low to moderate, ranging from 750 to 1400 m^2/km^2. (Al-Saadi, 2023). Recently, the Kalar District of Sulaymaniyah Governorate covers the 314,746 km^2 Mamran Basin, a watershed with numerous streams. Their analysis used 1990–2020 Sulaymaniyah station rainfall data. The northwest and southeast of the research area have 0.6% moderately active erosion, whereas 15.3% has considerable erosion in dispersed areas. Basin erosion is severe in 3.6% and high in 80.5% (Jawad and Baqer, 2024). The study's importance lies in highlighting geomorphology's role in revealing the extent of erosion in Qarahanjeer and identifying active gully erosion sites, measuring erosion intensity, and assessing associated risks through spatial analysis and mapping to support land management decisions and mitigate environmental degradation. Due to the effect of the study area on the effectiveness of water erosion, which results in geomorphological risks, we will therefore address the forms of water erosion as follows:

Rain erosion: It is the process resulting from the sudden and heavy collision of raindrops with soil and rock fragments, especially those concentrated on steep slopes, which causes the fragments to fly into the air due to the rain. They then descend to a new position due to the force of gravity, where the drops work to separate the soil particles and fine detrital materials through the pressure resulting from the direct collision of these raindrops with the particles, causing quantities of soil to be scattered in the air. Some of it moves many times, leading to the erosion of sediments from their original locations. The activity of rain depends on its kinetic energy, the duration of rain, the quality of vegetation cover, and the cohesion of soil particles (Almashhadani and Al-Hasanay, 2023).

Sheet erosion: The mechanism of this type of erosion involves the thin-layer removal of soil by the action of shallow surface flow and raindrops. It is usually evenly distributed on an even slope and remains unnoticeable until a significant portion of valuable topsoil is lost, and then deposition of soil occurs at the slope bottom (Ismaeel et al., 2021).

Rill's erosion: Stream erosion develops due to the accumulation of runoff as the laminar flow transforms from a diffuse flow into a concentrated flow that moves along slopes with varying slopes. It is the stage that follows the laminar flow stage, as it takes the form of a fine network of streams resulting from heavy rainfall, as they form strips of flow that have an excellent capacity for surface erosion and appear parallel to the sides of the slopes. Their depth does not exceed a few centimeters. Their appearance coincides with the rainy season, and their features become clearer in areas where grooves, depressions, and gaps are widespread, as their activity increases with the increase in the slope and the amount of water (Li et al., 2025), as shown in Figure (1).



Fig. 1: Field investigation of stream erosion (20/06/2025).

Gully erosion: Gully erosion is one of the geomorphological processes caused by surface running water through erosion processes, when certain conditions are available in terms of depth, slope, and suitable rock. Gully erosion is an advanced stage of torrent erosion, and the underlying energy of running water in the gullies increases with increasing distance from the watershed line and increasing slope. The gradual deepening of the streams forms gully erosion, as the gullies take on different shapes and sizes, and their cross-section takes the shape of the Latin letter (V), as shown in Figure (2). These are narrow channels, whose edges often have very steep sides reflecting the action of vertical erosion. As for the transverse ridges, the shape of their course resembles the letter (U), where horizontal erosion is superior to vertical erosion (Almashhadani and Al-Hasanay, 2023).



Fig. 2: Gully erosion morphology: Field study conducted on June 20, 2025, at Coordinates (E 467237, N 3927907).

2. Study Area

Qarahanjeer district, located in Kirkuk City, northern Iraq, occupies an area of about 676 km² and consists of 30 small towns. Qarahanjeer district lies between longitudes (44° 30' - 44° 50' E) and latitudes (35° 23' - 35° 41' N). Sulaymaniyah City borders it to the east, while Markaz Kirkuk, Shawn, and Laylan districts border Qarahanjeer to the west, north, and south, respectively (Fig. 3). The climate of Qarahanjeer is part of the Kirkuk climate, which is warm and semi-arid, with an intensive increase in temperature in summer and rainy with low temperatures in winter (Shareef et al., 2019). A wavy topography characterizes Qarahanjeer, with the lowest and highest points being about 395 m and 991 m, respectively. The Khassa River passes through Qarahanjeer from east to west and ends at Khassa Lake.

The study aims to highlight the role of geomorphology in revealing the extent of erosion and assessing hazards through spatial analysis and mapping to inform land management decisions and reduce environmental degradation effects in Qarahanjeer, focusing on the Muqdadiya and Bai Hassan formations, which cover the area of study.

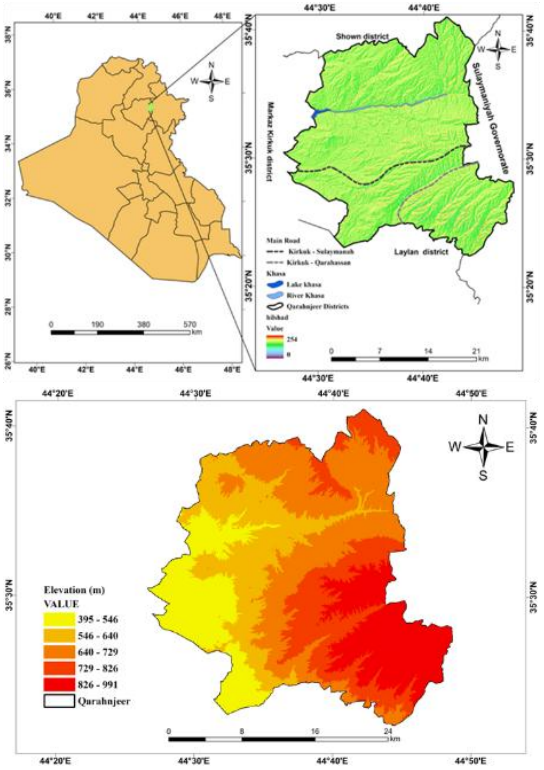


Fig. 3: Location of the study area (Qarahanjeer).

3. Geological and soil data

Soil types and their distribution are essential for regulating the infiltration of surface runoff. Soil with low infiltration rates rapidly accumulates water, increasing soil degradation. Consequently, it is essential to comprehend both the distribution of soil types and the geological and lithological distribution of sediments within the studied area. Geological factors significantly influence erosion

as they govern erosional processes (Ali et al., 2016). The lithological properties of land are crucial in gully erosion (Casalí et al., 1999; El Maaoui et al., 2012; Golestani et al., 2014). Lithological features are associated with geomorphological landforms (Dai et al., 2001; Zinck et al., 2001; Gorum et al., 2008; Zhu et al., 2014). To achieve this objective, theme layer maps were used to provide a comprehensive overview of the soil distribution and types within the research region, and the initial geology map (GM) illustrates the predominant lithology of the strata, revealing two formations present in the research area (Mukdadiya and Bai Hassan formations) (Fig. 4a). Mukdadiya is composed of pebbly sandstone, sandstone, and mudstone deposits, whereas Bai Hassan consists of conglomerate, sandstone, and claystone. Furthermore, alluvial deposits consist of sediments including sand, silt, and clay. The second thematic map is the soil type map (ST) (Fig. 4b). Only limited sections of the research region comprise soil containing sand and gypsum.

4. Gully Erosion according to the Bergsma method

The tool is named 'Gully Erosion' by the Bergsma method, which contains six parameters (Input stream feature, input basin feature, input cell size width, input cell size height, output grid parameter, and output gully erosion), through which the user can control the modeling of gully erosion.

Two essential key layers need to be acquired to apply gully erosion (the stream feature and the basin feature of the study area). This study has implemented an adaptive method for measuring

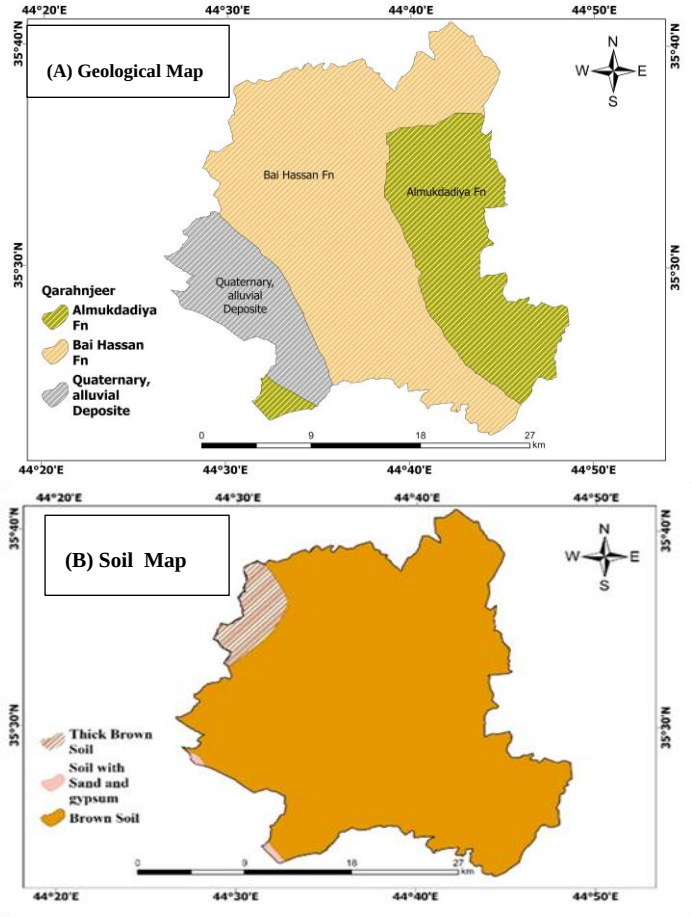


Fig. 4. (A) Geological map and (B) Soil map.

Gully erosion was assessed using a Python method published by Ismaeel et al. (2021), as shown in Figure 5. This tool helps to make figuring out erosion in the study area faster and more accurate.

The design of the tool highlights the specifications for data input and output, along with the geomorphological principles it utilizes. It evaluates gully erosion via the Bergsma approach, examining stream capacity and density, and it accepts Shapefile inputs and stores Feature Class outputs in a Geodatabase, shown as an isopleth map that changes depending on the research area's representation and on whether erosion levels are increasing or decreasing

5. Materials and Methods

The method employed for calculating gully erosion through digital elevation model analysis is a procedure for finding erosion across extensive areas.

Stream network extraction in GIS relies on hydrologic analysis of Digital Elevation Models (DEMs) through systematic geospatial processing. First, the DEM undergoes preprocessing to fill sinks and ensure seamless flow direction calculations. Using GIS hydrology tools (Flow

Direction), flow paths are calculated for the steepest downward slope of each cell. Subsequently, a Flow Accumulation raster quantifies upstream contributing areas, where higher cell values indicate concentrated flow. Stream channels are then delineated using a user-defined threshold (value >1,000 cells) to distinguish active streams from intermittent flows. The resulting binary raster is converted to vector polylines using tools like Stream to Feature, generating a topological stream network as shown in Figure (6). Optional steps include stream ordering (Strahler method) to classify channel hierarchies and smoothing to enhance cartographic representation. This method is widely applied in erosion modeling, as demonstrated in studies like the Bergsma model for gully erosion prediction.

After extracting streams and calculating areas, the Bergsma equation is as follows:

$$AE = \sum \frac{L}{A}$$

Where: AE is the erosion rate per square, L is the stream length in each square, and A is the area of one square in km².

Consequently, due to its functionality, the instrument was designated as Gully Erosion by the Bergsma Method, which includes input stream feature, input basin feature, input cell size width, input cell size height, output grid parameter, and output gully erosion. It comprises six factors that enable the user to regulate the modelling of gully erosion. These parameters are crucial for its functionality within the ArcGIS Desktop environment and enable comprehensive control over the gully erosion modeling process, allowing for detailed analysis and mapping. The parameters are:

1. Input the study area as a shapefile or feature class.
2. Input a stream of a shape file or feature class.
3. Input the cell size width. The default value for the length of a quarter of a square rib is 1000 square meters, meaning that the tool sets 1000 square meters according to what Bergsma saw when dividing the lengths of waterways by the area of the squares.
4. Input Cell Size Height parameter, from which the height of the square is specified in meters.
5. The output grid parameter generates a square grid file in Shapefile format, which is then used to calculate gully erosion.
6. Finally, Output Gully Erosion saves the Gully Erosion file as a Shapefile in the computer's memory, as shown in Figure 7.

6. Results and Discussion

The Qarahanjeer area is a dynamic geological model for examining the effects of accelerated erosion processes on sedimentary deposits. The Muqdadiya and Bai Hassan Formations are in danger of quickly falling apart due to water infiltration and a weak geological structure with faults and folds that cause soil subsidence and gullies.

The majority of the research region is brown soil. The timeframe for this study is 2024.

Gully erosion stages are classified using the Bergsma method of natural geomorphic factors (steepness of slopes and hydrology). The Bergsma method ensures the classification of gully erosion at levels in a study area according to gully length per unit area. The results show that a 2.301% area of (15573607.408 m^2) is affected by very minor erosion, followed by light erosion (8.83%) area of (59752225.981m^2), moderate erosion (21.000%)

area of (142159214.599 m2), high erosion (54.692 %), very high erosion (12.47%) area of (84412599.999 m^2), and severe erosion (4.678,400.00 m^2), at a density of 2701 to 3700 m/km^2.

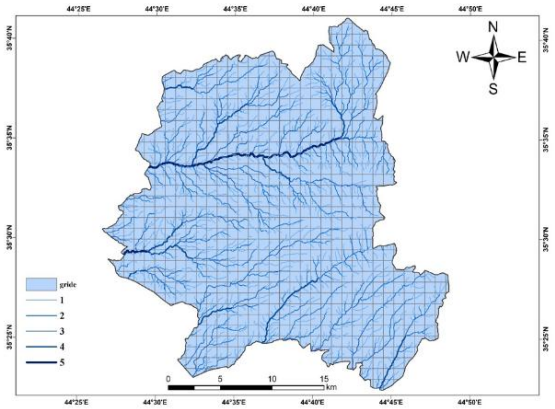


Fig. 6: Stream network of the study area generated by the researcher using ArcGIS 10.8

High erosion is the dominant class, covering (370,082,414.60 m^2) of the area. The spatial distribution of gully erosion in the study area is primarily attributed to the spatial heterogeneity of geomorphological and hydrological dynamics, as illustrated in Figure 7 and Table 1.

Table 1: Classification of intensity of gully erosion according to Bergsma equation

Class gully erosion levels	Area (km^2)	Area (m^2)	Percentage %	category
Very light erosion	15.573607	15573607.408	2.301	0 - 400
light erosion	59.752226	59752225.981	8.830	401 - 1000
Moderate erosion	142.159215	142159214.599	21.000	1001 - 1500
High erosion	370.082415	370082414.603	54.692	1501 - 2700
Very high erosion	84.4126	84412599.999	12.47	2701 - 3700
Severe erosion	4.6784	4678400.000	0.6913	3701 - 4700
Total area	676.639	676658462.4	100.000	

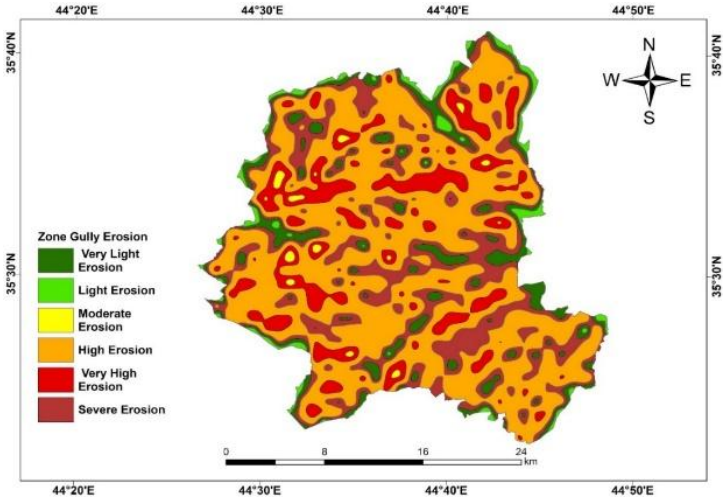


Fig. 7: Results of gully erosion levels in the study area

More than half (54%) are centered in low-lying areas or along stream valleys, which have high fluvial forces and are prone to erosion. Also, a chart shows the variations in areas (Fig. 8). This deep incision and lengthening of gullies cause them to become denser and yield more sediment. High elevational or watershed-divide areas experience low erosivity in response to slope steepness, water concentration, and landscape resistance. The lowest risk areas are classified as no erosion zones covering 40% of the area, followed by moderate risk areas.

Erosion zones (21%) represent transitional zones with increasing fluvial energy but are buffered due to high vegetation cover reducing the

impact and preventing excessive gully development.

Other erosion classes show only degraded processes, such as extreme erosion, which occupy 12.47% and 0.691% (very high value), respectively, indicating a very advanced erosion process. Validation of field data ensures accuracy. Gully erosion by human activity, such as agriculture, road construction, and quarrying, disrupts natural drainage patterns and removes vegetation cover. These processes become even more important with the increasing susceptibility of soil and steep headwaters and a disproportionate increase in produced sediment for the high erosion zones. Mitigation relies on enhancing water drainage and stabilizing inclines.

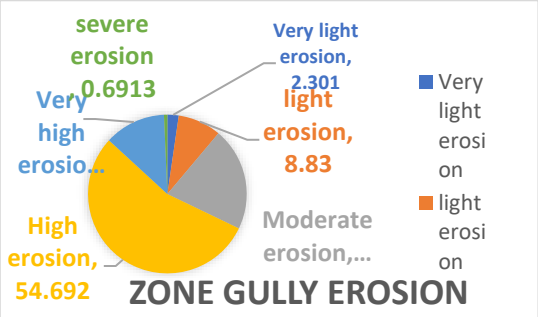


Fig. 8: Shows the area of Gully erosion

7. Conclusion

This study employed GIS tools to analyze gully erosion in Qarahanjeer utilizing DEM data. A new GIS tool is called Gully Erosion by Bergsma, which has six parameters

(input stream feature, input basin feature, input cell size width, input cell size height, output grid parameter, and output gully erosion).

Using the results of this tool is needed to make a gully map for any area. The research results show that most of the study area was affected by erosion, with an area forming approximately 54.692% of the total area in the study region, specifically within the categories of 1501 – 2700. The study concludes that the results match the researcher's findings from the field study and his observations of the impact of gully erosion on the study area. It becomes clear that the slope factor and the study area's geology directly impact the extent of erosion through their effect on surface runoff, and hydrological processes dominated the regional variability of gully erosion, highlighting the need for targeted mitigation measures. Intensive and accelerated development outcomes should include restoration management, the configuration of a new and advanced drainage system, slope stabilization techniques, and significant vegetation restoration to reduce the impact of erosion and ensure a positive impact on the developed landscape.

The following suggestions are important for future research:

1. Benefit from the water quantities, especially surface runoff, through the process of water harvesting by creating depressions in the basin estuaries.
2. Investing in the area due to its proximity to the Khassa Dam by encouraging residents to engage in ecotourism in the study area.
3. Investing in the area for industry, which is characterized by a high percentage of gravel.

8. Conflict of Interest

The authors declare that they have no conflict of interest.

9. Funding Statement

Research received no external funding.

10. Author Contributions

Suzan I. Baez, draft writing, methodology, data collecting, analysis

Fawzi M. Omar, Supervising, Revising, Grammarian Reviewing

Mustafa R. Mezaal, Supervising, Revising, Grammarian Reviewing

11. References

Ali, S., Al-Umary, F.A., Salar, S.G., Al-Ansari, N. and Knutsson, S., 2016, GIS based soil erosion estimation using EPM method, Garmiyan Area, Kurdistan Region, Iraq, Journal of Civil Engineering and Architecture, 10(3), pp. 291–308.

Almashhadani, A.A. and Al-Hasanay, Z.K., 2023, Water erosion hazards for the Basin Zah Rizi region in Sulaymaniyah Governorate, Al-Adab Journal, 3(144), pp. 225–236. https://doi.org/10.31973/aj.v3i144.4079

Al-Saadi, M.W.H.H., 2023, Analysis and modeling of drought effects based on drought indicators in the eastern region of Missan, Journal of Sustainable Studies, 5(2).

Bergsma, E., 1986, Aspects of mapping units in the rain erosion hazard catchment survey, in Land evaluation for land use planning and conservation in sloping areas, International Institute for Land Reclamation and Improvement, pp. 84–105.

Casalí, J., López, J.J. and Giráldez, J.V., 1999, Ephemeral gully erosion in southern Navarra (Spain), Catena, 36(1–2), pp. 65–84. https://doi.org/10.1016/S0341-8162(99)00013-2

Dai, F.C., Lee, C.F., Li, J. and Xu, Z.W., 2001, Assessment of landslide susceptibility on the natural terrain of Lantau Island, Hong Kong, Environmental Geology, 40(3), pp. 381–391. https://doi.org/10.1007/s002540000163

El Maaoui, M.A., Felfoul, M.S., Boussema, M.R. and Snane, M.H., 2012, Sediment yield from irregularly shaped gullies located on the Fortuna lithologic formation in semi-arid area of Tunisia, Catena, 93, pp. 97–104. https://doi.org/10.1016/j.catena.2012.02.004

Feng, X., Wang, Y., Chen, L., Fu, B. and Bai, G., 2010, Modeling soil erosion and its response to land-use change in hilly catchments of the Chinese Loess Plateau, Geomorphology, 118(3–4), pp. 239–248. https://doi.org/10.1016/j.geomorph.2010.01.004

Giordano, A. and Marchisio, C., 1991, Analysis and correlation of the existing soil erosion maps in the Mediterranean basin, Vol. 3, pp. 97–132.

Golestani, G., Issazadeh, L. and Serajamani, R., 2014, Lithology effects on gully erosion in Ghoori Chay Watershed using RS and GIS, International Journal of Biology, 4(2), pp. 71–76. https://doi.org/10.12692/ijb/4.2.71-76

Gorum, T., Gonencgil, B., Gokceoglu, C. and Nefeslioglu, H.A., 2008, Implementation of reconstructed geomorphologic units in landslide susceptibility mapping: The Melen Gorge (NW Turkey), Natural Hazards, 46(3), pp. 323–351. https://doi.org/10.1007/s11069-007-9190-6

Ismaeel, O.A., Thannoun, R.G. and Yahya, B.M., 2021, Developing an active tool in GIS to determine gully erosion levels depending on the Bergsma method, Uruk Journal for Humanity Science, 14(3), pp. 2464–2466. https://doi.org/10.52113/uj05/021-14/2456-2467

Jawad, M. and Baqer, S.M., 2024, Evaluation of the gully erosion risks in the Mamran Basin within Sulaymaniyah Governorate using GIS and RS, Pakistan Journal of Life and Social Sciences, 22(1), pp. 3211–3225. https://doi.org/10.57239/PJLSS-2024-22.1.00234

Kirkby, M.J. and Bracken, L.J., 2009, Gully processes and gully dynamics, Earth Surface Processes and Landforms, 34(14), pp. 1841–1851. https://doi.org/10.1002/esp.1866

Li, Y., Zhang, J., Hu, Y., Zhao, J. and Tang, P., 2025, Contributions of flow discharge, slope gradient, and scouring time on rill erosion: A quantitative study of exposed slopes in the loess region, International Journal of Sediment Research, 40(30), pp. 500–511. https://doi.org/10.1016/j.ijsrc.2025.03.001

Shareef, M. A., Hassan, N. D., Hasan, S. F., & Noori, A. M. (2019). Integrating of GIS and fuzzy multi-criteria method to evaluate land degradation and their impact on the urban growth of Kirkuk city, Iraq. International Journal of Advanced Science and Technology, 28(15), 800-815.

Wang, T., He, F., Zhang, A., Gu, L., Wen, Y., Jiang, W. and Shao, H., 2014, A quantitative study of gully erosion based on object-oriented analysis techniques: A case study in Beiyanzikou Catchment of Qixia, Shandong, China, The Scientific World Journal, 2014, 417325. https://doi.org/10.1155/2014/417325

Zhang, W., Zhou, J., Feng, G., Weindorf, D.C., Hu, G. and Sheng, J., 2015, Characteristics of water erosion and conservation practice in arid regions of Central Asia: Xinjiang, China as an example, International Soil and Water Conservation Research, 3(2), pp. 97–111. https://doi.org/10.1016/j.iswcr.2015.06.002

Zhu, H., Tang, G., Qian, K. and Liu, H., 2014, Extraction and analysis of gully head of Loess Plateau in China based on digital elevation model, Chinese Geographical Science, 24(3), pp. 328–338. https://doi.org/10.1007/s11769-014-0663-8

Zinck, J.A., López, J., Metternicht, G.I., Shrestha, D.P. and Vázquez-Selem, L., 2001, Mapping and modelling mass movements and gullies in mountainous areas using remote sensing and GIS techniques, International Journal of Applied Earth Observation and Geoinformation, 3(1), pp. 43–53. https://doi.org/10.1016/S0303-2434(01)85020-0

Iraqi National Journal of Earth Science, Vol. 26, No. 04, 2026 (31-39)

Iraqi National Journal of Earth Science

www.earth.uomosul.edu.iq

نظم المعلومات الجغرافية لأنشاء خرائط بناء على طريقة Bergsma لتقدير تآكل الاخاديد باستخدام نموذج الارتفاع الرقمي: دراسة حالة في قره هنجير، كركوك، العراق

سوزان إبراهيم بايز [1*] ، فوزي مردان عمر [1] ، مصطفى رضا مزعل [1]

suzanibrahimgis@gmail.com fawzialbeyati@yahoo.com Mostafa.redha@ntu.edu.iq

[1] قسم هندسة المساحة، كلية التقنية الشمالية كركوك، جامعة التقنية الشمالية، الموصل، العراق.

[2] قسم هندسة المساحة، كلية التقنية الشمالية موصل، جامعة التقنية الشمالية، الموصل، العراق.

** الباحث المراسل*

تاريخ الاستلام: 03 تموز 2025 تاريخ المراجعة: 18 أيلول 2025 تاريخ القبول: 07 تشرين الثاني 2025

تاريخ النشر الالكتروني: 01 تشرين الأول 2026

الملخص

يُعد تآكل الأخاديد مشكلة بيئية خطيرة تهدد استدامة التربة، لا سيما في المناطق القاحلة وشبه القاحلة مثل منطقة قره هنجير في كركوك التي تبلغ مساحتها676 كم². وتكمن المشكلة البحثية الرئيسة في نقص الدراسات وعدم توفر طرق فعالة لتحديد معدلات تآكل الأخاديد بدقة. لمواجهة هذا التحدي، اعتمدت هذه الدراسة على نموذج Bergsma وتقنيات نظم المعلومات الجغرافية لتقدير تآكل الأخاديد باستخدام بيانات النموذج الرقمي للارتفاعات. وتهدف الدراسة بشكل أساسي إلى تقييم مدى فعالية نموذج Bergsma في رسم خرائط مناطق خطر تآكل الأخاديد في قره هنجير، مع التحقق من دقة النتائج من خلال الملاحظات الميدانية. وأظهرت النتائج تصنيف تآكل الأخاديد إلى عدة مستويات، حيث كان التآكل العالي هو الفئة السائدة، حيث شمل 54.692% من منطقة الدراسة، وذلك ضمن نطاق قيم تتراوح مابين 1501 و2700. أما التآكل المتوسط (21%)، والذي يقع ضمن فئة 1001 إلى 1500، فقد ظهر في المناطق الانتقالية حيث تقلل الغطاءات النباتية جزئياً من تأثير طاقة التدفق المائي. وعلى الرغم من محدودية المساحات المتأثرة بالتآكل الشديد جداً (12.47%) ضمن فئة 2701 إلى 3700، إلا أن المناطق التي تعاني من تآكل حاد (0.69%) ضمن فئة 3701 إلى 4700 تشير إلى تدهور بيئي كبير، حيث تعمل هذه العمليات على تعطيل أنماط التصريف الطبيعي. كما أوصت الدراسة بحفر منخفضات في مصبات الأحواض لتجميع المياه، وخاصة الجريان السطحي، للاستفادة منها في ري الأراضي. بالإضافة إلى ذلك، شددت على أهمية استخدام بيانات مكانية عالية الدقة لتحسين تقديرات التآكل، وتطبيق البحوث وتسجيل التغيرات الجيومرفولوجية باستخدام نظم المعلومات الجغرافية والاستشعار عن بعد...

الكلمات المفتاحية:

النموذج الارتفاع الرقمي، طريقة Bergsma ، التعرية الاخدودية، قره هنجير.

DOI: 10.33899/injes.v26i4.56023, ©Authors, 2026, College of Science, University of Mosul.

This is an open-access article under the CC BY 4.0 license (http://creativecommons.org/licenses/by/4.0/).

Iraqi National Journal of Earth Science, Vol. 26, No. 04, 2026 (40-53)

Iraqi National Journal of Earth Science

www.earth.uomosul.edu.iq

Integrated Reservoir Characterization and Petrophysical Assessment of the Kurra Chine Formation in the Peshkhabir Oil Field, Northern Iraq

Mahdi Khairi Aswad [1*], **Sazan Mohammed Ali** [2]

mahdi.aswad@su.edu.krd sazan.mohammed91@gmail.com

[1] *Department of Earth Sciences and Petroleum, College of Science, University of Salahaddin -Erbil, Kurdistan Region, Iraq.*

[2] *Department of Civil Engineering, College of Engineering, Salahaddin University -Erbil, Kurdistan Region, Iraq.*

** Correspondence author.*

Received: 12 July 2025 Received in revised form: 01 September 2025 Accepted: 24 October 2025
Available online: 01 October 2026

Abstract

The Kurra Chine Formation, a Triassic unit, is a prominent unit in the subsurface of northern Iraq and a key target for hydrocarbon exploration because of its complex lithology and reservoir potential. However, few studies have fully characterized its petrophysical properties and reservoir quality, necessitating further investigation. This research aims to enhance understanding of the formation's hydrocarbon potential by conducting a comprehensive reservoir characterization and petrophysical evaluation at Peshkhabir Well-6 (PKH-6). To achieve this goal, an integrated approach was employed, combining wireline log interpretation, core sample analysis, and petrographic analysis. The total thickness of the formation is 546 m, with key reservoir intervals exhibiting an average shale volume of 9%. Lithologic analysis indicates dolomite, anhydrite, shale, limestone, and sandstone, with dolomite identified as the primary flow unit. Petrophysical evaluation indicates an average effective porosity of 6%, permeability reaching 24 mD, and average Water and hydrocarbon saturation of 21% and 79%, respectively. Petrographic observations confirmed hydrocarbon-filled pores, reinforcing the viability of the formation as a productive reservoir. These findings offer new insights into the reservoir quality, hydrocarbon distribution, and flow characteristics of the Kurra Chine Formation, contributing to improved exploration and field development strategies for Triassic reservoirs in northern Iraq.

Keywords:

Kurra Chine Formation, Northern Iraq, Peshkhabir Oil Field, Petrophysical and Reservoir Characterization

DOI: 10.33899/injes.v26i4.56026, ©Authors, 2026, College of Science, University of Mosul.
This is an open-access article under the CC BY 4.0 license (http://creativecommons.org/licenses/by/4.0/).

==========

1. Introduction

The Kurdistan region of northern Iraq is part of the prolific Zagros Fold Thrust Belt, which has numerous oil and gas fields. One of the key stratigraphic units within this region is the Kurra Chine Formation, which belongs to the Upper Triassic carbonate system in northern Iraq (Koshnaw et al., 2019). The Kurra Chine Formation is considered a complete petroleum system because it contains the key elements of reservoir, source, and cap rock. Evaluating the properties of carbonate reservoirs is essential for estimating hydrocarbon volume and improving reservoir management. Wireline logging remains widely used to address subsurface uncertainty, providing quantitative petrophysical properties and lithological characteristics. Unlike clastic reservoirs, carbonate reservoirs are more complex, with significant reservoir heterogeneity in porosity and permeability arising from diagenetic processes and the distribution of clay minerals within reservoir units (Lucia, 2007).

In the reservoir and pay zones of northern Iraq, conditions such as high-volume water saturation necessitate detailed formation evaluation and petrophysical property analysis to identify the underlying causes of fluid volume changes (Aswad, 2020). Well-logging techniques, joined with petrographic interpretation and core sample analysis, enable the determination of reservoir quality and zone characteristics, as well

as subsurface formation characterization (Shalaby et al., 2023; Radwan et al., 2023). Additionally, advanced petrophysical tools and petrographic interpretation facilitate the identification of carbonate pore types and their relationships with reservoir quality (Teillet et al., 2021). Well logging tools play an important role in identifying hydrocarbon source rock and in reservoir description in drilled wells (Olorunniwo et al., 2019; Al Adwani, 2022). The Kurra Chine Formation, which comprises various carbonate lithologies, has demonstrated prolific hydrocarbon potential in drilled wells in northern Iraq. Wetzel (1959) provided an initial description of this formation and highlighted its composition of limestone, papery shale, and dolomitic limestone with a maximum thickness of 834 m (Bellen et al., 1959). The Kurra Chine Formation is characterized by haematite in the lower part (Balaky and Tamar-Agh, 2017). Numerous studies have investigated this Formation (Table 1).

Table 1: Previous studies of the Kuraa Chine Formation regarding the reservoir and hydrocarbon potential

Authors	Description
Sadooni (1995)	Studied the source rock of the Kurra Chine Formation and determined the main lithology
Ameri et al. (2009)	Identified kerogen types I and II, indicating maturation level within the Kurra Chine Formation
Aqrawi et al. (2010)	Divided the formation into four lithological units, including two carbonate units and two evaporite units
Al-Hamdani et al. (2019)	Evaluated the effects of diagenetic processes on porosity in multiple wells across northeastern Iraq
Edilbi et al. (2019)	Studied the level of maturation of the source rock of the Kurra Chine Formation
Lunn (2020)	Divided the formation into (A, B, and C) on the basis of sea level fluctuations and the maximum flooding surface.
Al-Dolaimy et al. (2021a)	Studied biomarkers of the Kurra Chine Formation, identifying pristine (pr) and phytane (ph) Pr/Ph ratios
Baban and Ahmed (2021)	Studied only unit A of the formation in the Shaikhan oil field
Al-Dolaimy et al. (2021b)	Studied pyrolysis analysis and indicated a low hydrocarbon generation potential
Al Dabagh et al. (2021a)	Studied the petrography and microfacies analysis of the Kurra Chine Formation to determine its depositional environment
Al Dabagh et al. (2021b)	Studied the effects of total and effective porosities on permeability in three wells,
Balaky et al. (2022)	Highlighted the heterogeneity of the shale units in a reservoir
Aswad et al. (2023a)	Examined the pyrolysis analysis of the Kurra Chine Formation in the Tawke Oil Field
Aswad et al. (2023b)	Examined the porosity types and petrography of the Kurra Chine Formation in the Tawke Oil Field
Aswad et al. (2024a)	Examined the palynofacies of the Kurra Chine Formation in the Tawke Oil Field
Aswad et al. (2024b)	Formation evaluation of the Kurra Chine Formation in the Tawke Oil Field
AL Khafaji et al., (2025)	Studied organic geochemistry and thermal history modeling Of the upper part of the Kurra Chine Formation from Butmah-15 well, northwestern Iraq
Aswad (2025)	Studied the source rock evaluation of the Kurra Chine Formation

2. Aim of study

The Formation is the thickest Triassic unit in northern Iraq, and plays an important role in oil and gas exploration and production. Its complex lithology, comprising dolomite, anhydrite, shale, limestone, and sandstone, presents challenges for reservoir characterization and fluid distribution analysis. While previous studies have investigated formations in various oil fields, detailed petrophysical evaluation of Peshkhabir Well-6 (PKH-6), a significant well in the Peshkhabir Oil Field, is lacking. This study addresses this gap by conducting a comprehensive formation evaluation through wireline log interpretation, core sample analysis, and petrographic investigations. Unlike conventional studies that rely primarily on log-based assessments, this research integrates quantitative analysis of porosity, permeability, and hydrocarbon saturation to determine reservoir quality and producibility.

The overall aim of this study is to evaluate the reservoir characteristics and hydrocarbon potential of the Kurra Chine Formation in Well PKH-6.

Specific Objectives

- To quantify the petrophysical properties (porosity, permeability, shale volume, and hydrocarbon saturation).
- To identify the primary reservoir flow zones and assess the dominance of dolomite as the main reservoir lithology.
- To evaluate hydrocarbon-filled porosity and confirm reservoir potential through petrographic evidence.

- To provide insights into regional hydrocarbon distribution within the Kurra Chine Formation to support future exploration strategies.

3. Location and Tectonic Setting of the Studied Area

The studied well is located in Zakho, within the Peshkhabir Oil Field, Northern Iraq. This study focuses on analyzing cuttings from Well-6 of the Peshkhabir Oil Field. The coordinates of the studied well are 37º 05' 04" N and 42º 31' 01" E (Fig. 1). Structurally, the study area lies within the highly folded zone and is part of the Taurus fold and thrust belt (Fig. 1b). Tectonic activity in this region is related to the collision between the Eurasian and Arabian plates, which produced a foreland basin. The foreland basin corresponds to the Zagros fold belt in Iraq (Aqrawi, 1998). Tectonically, Iraq is located northeast of the Arabian plate, where ongoing convergence between the plates has shaped the regional geological features. The lower and upper parts of the Kurra Chine Formation are unconformable and conformable with the Baluti and Galikhana Formation, respectively (Balaky, 2022). The thickness of the Formation is 834 m at the type locality, and the main lithology includes limestone, thick- bedded dolomite, and brecciated clasts (Bellen, 1959).

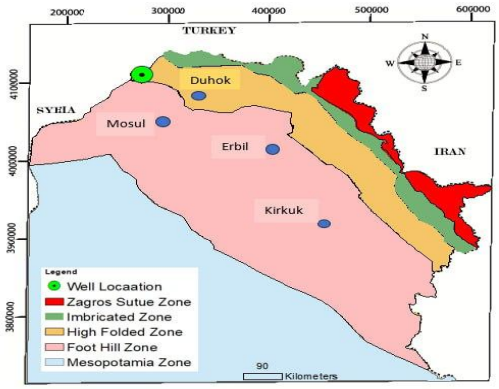


Fig.1: Location of the studied well and tectonic map of the studied area (after Edilbi et al., 2019).

4. Materials and Methods

Well Logging

Well- logging analysis was conducted using Tech-Log software to evaluate shale volume at different depths. The Well Logs were used to determine petrophysical properties.

Lithology was evaluated using the Neutron-Density (N-D) cross-plot method.**Shale volume**: According to Asquith and Krygowski (2004), shale volume in the reservoir can be rapidly estimated using Larionov and Linear GR methods

$$IGr = \{GRlog-GRmin\}/\{GRmax-GRmin\}$$

$$Vsh = 0.33*(2^{2\ *IGR} -1) \quad Larionov\ method$$

Porosity: - refers to the ratio of the pore volume to the bulk volume. According to Al-Dolaimy et al. (2021a),

Total porosity: N - D cross plots are used to determine porosity for the current study.

$$Øt = \{ØN+ØD\}/2$$

Effective porosity: represents the interconnected pores and is calculated by $Øe = Øt * (1-Vsh)$.

Permeability: represents the ability of rock to pass through fluids. It was estimated from wireline logs using the Wyllie-Rose equation. K = {100 Ø 2.25/ Swi}2

Water saturation is the fraction of the pore space filled with water.

Archie equation: applied in intervals less than 15% shale (Archie, 1942).

$$Sw = \{(F*Rw)/Rt\}-n\ 12 \qquad F = a/Øm$$

Simandoux equation (1963) is used for shale-rich zones, which contain more than 10% shale

$$Sw = \{(-Vsh/Rsh) +/- \sqrt{(Vsh/Rsh)2 + (4Øm/wart)\}/ (2Ø2 /aRw)}$$

Hydrocarbon saturation (Sh): is crucial for hydrocarbon reservoir evaluations (Edilbi et al., 2019). Was calculated as. Sh = 1-Sw

Movable hydrocarbon saturation: refers to the fraction of hydrocarbon that can be produced.

$$MHS = \{Sxo- Sw\}* Øe$$

Residual Hydrocarbon Saturation (RHS): represents the hydrocarbon trapped in the rock matrix. RHS = (1-Sxo)

Hydrocarbon index: defined as the ratio of movable to residual hydrocarbons, MHS/RHS. All abbreviations are mentioned in (Table 2).

Flow Zone Indicator (FZI): The FZI method (Porras and Campos, 2001) was used to categorize flow units with similar flow capacities. This approach enhances the understanding of reservoir quality and flow behavior, enabling the identification of zones with optimal productivity potential.

Core samples: Fifty core samples were taken from the Kurra Chine Formation. The lithology of core samples was described in the wellsite report and provided with a mud log. Conventional core analysis (CCA) was carried out on 50 core plugs by Emirates Link Reslab LCC in Abu Dhabi (UAE). Core samples were used to recognize the lithology and then used for petrographic descriptions (Fig. 2)

Petrography: Thirty-five thin section slides were prepared from core plugs of the Kurra Chine Formation.

These plugs were cut and oriented perpendicular to the bedding plane, then stained with Alizarin Red S (ARS) to distinguish calcite from dolomite, following the procedure of Friedman (1959).

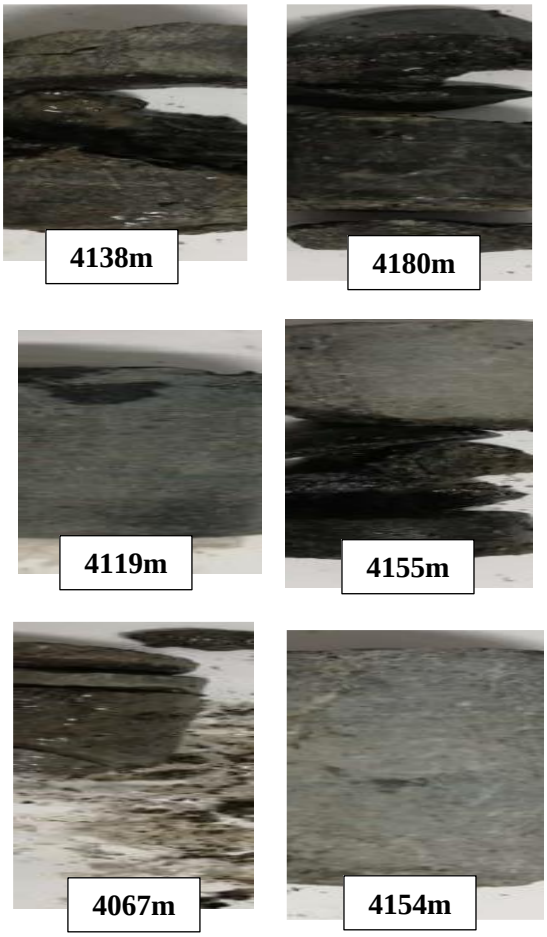


Fig. 2: Lithologic description of core samples indicates dolomite, fractures, veins, and fragments of anhydrite

Table 2: Abbreviations of the formulas were used in this study

Symb/Abbr	Description	Symb/Abbr	Description
IGR	Index Gamma Ray	Rw	Formation water resistivity
GRlog	Gamma-ray log value in zone of interest, API unit	Rt	True resistivity
GRmax	Gamma-ray log value in shaly bed, API	Rsh	Shale resistivity
GRcln	Gamma-ray value in clean zone, API	K	Permeability
Vsh	Volume of shale	Swi	Irreducible water saturation
ϕn	Neutron porosity	F	Formation factor
ϕt	Total porosity	Sw	Water saturation
ϕe	Effective porosity	MHS	Movable hydrocarbon saturation
Shc	Hydrocarbon saturation	RHS	Residual hydrocarbon saturation
a	Tortuosity factor = 1	Sxo	Flushed zone saturation
m	Cementation exponent = 2	n	Saturation exponent = 2

5. Results

Lithology

In this study, the lithology of the Kurra Chine was identified through an integrated analysis of wireline logging data, core samples and petrographic slides. The cross-plot lithology comprises dolomite, anhydrite, shale, limestone, and minor sandstones (Fig.3). Additionally, based on core samples, the main lithologies are dolomite, anhydrite, and shale. Further confirmation from petrographic analysis indicates that the dominant lithologies are dolomite, anhydrite, and shale.

Shale Volume

Shale volume is determined from Larionov (1969) formula. Shale volume varies from zone to zone. Overall, average shale volumes of the rock, reservoir, and pay zones are approximately 15%, 10%, and 9%, respectively (Table 3 and Fig. 4).

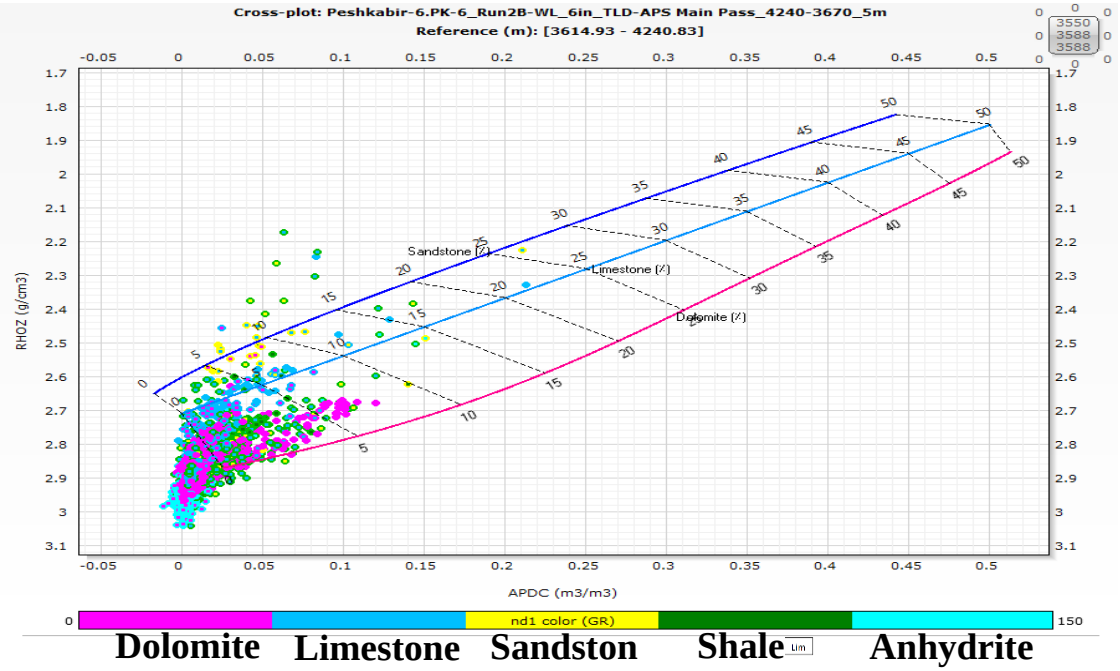


Fig. 3: Cross-plots of the parameters labeled N and D are used to identify the lithology of the Peshkhabir Oilfield. The description further explains that the bottom legend provides evidence for the lithology types shown in the figure, from left to right, namely, dolomite (pink), limestone (light blue), anhydrite (light), shale (green), and sandstone (yellow). These lithology types are the main ones found in the wireline logs

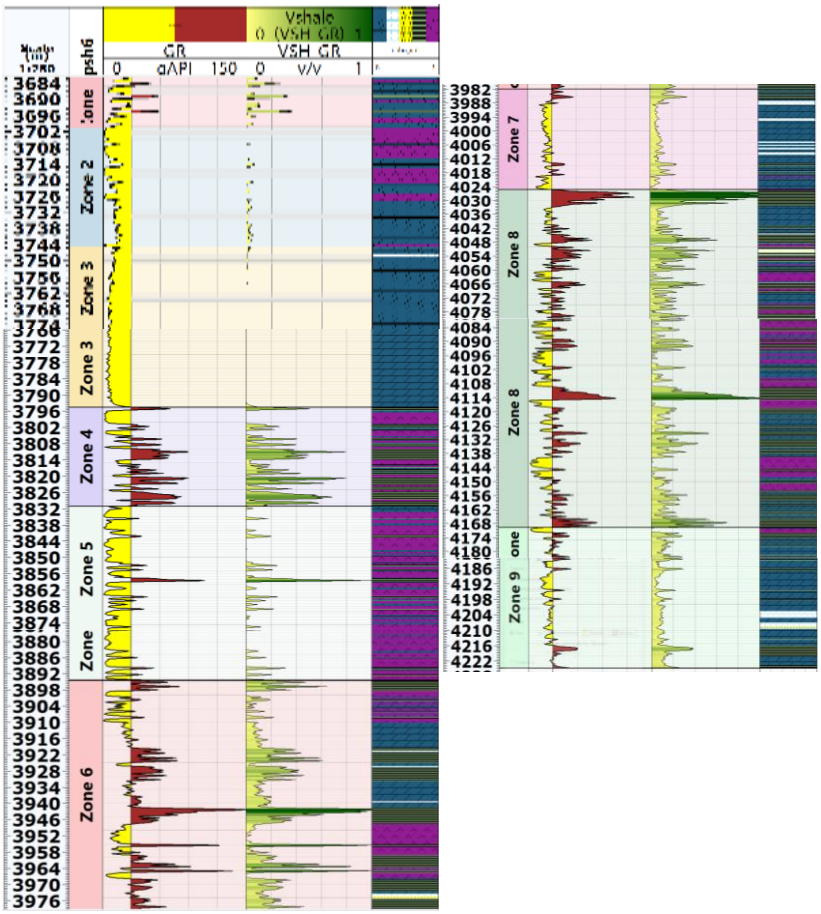


Fig. 4: The borehole depth, GR, and shale volume information from the Larionov method and stratigraphic column. The figure specifically highlights the presence of shale at different depths via the Larionov method at Peshkhabir Oil Field

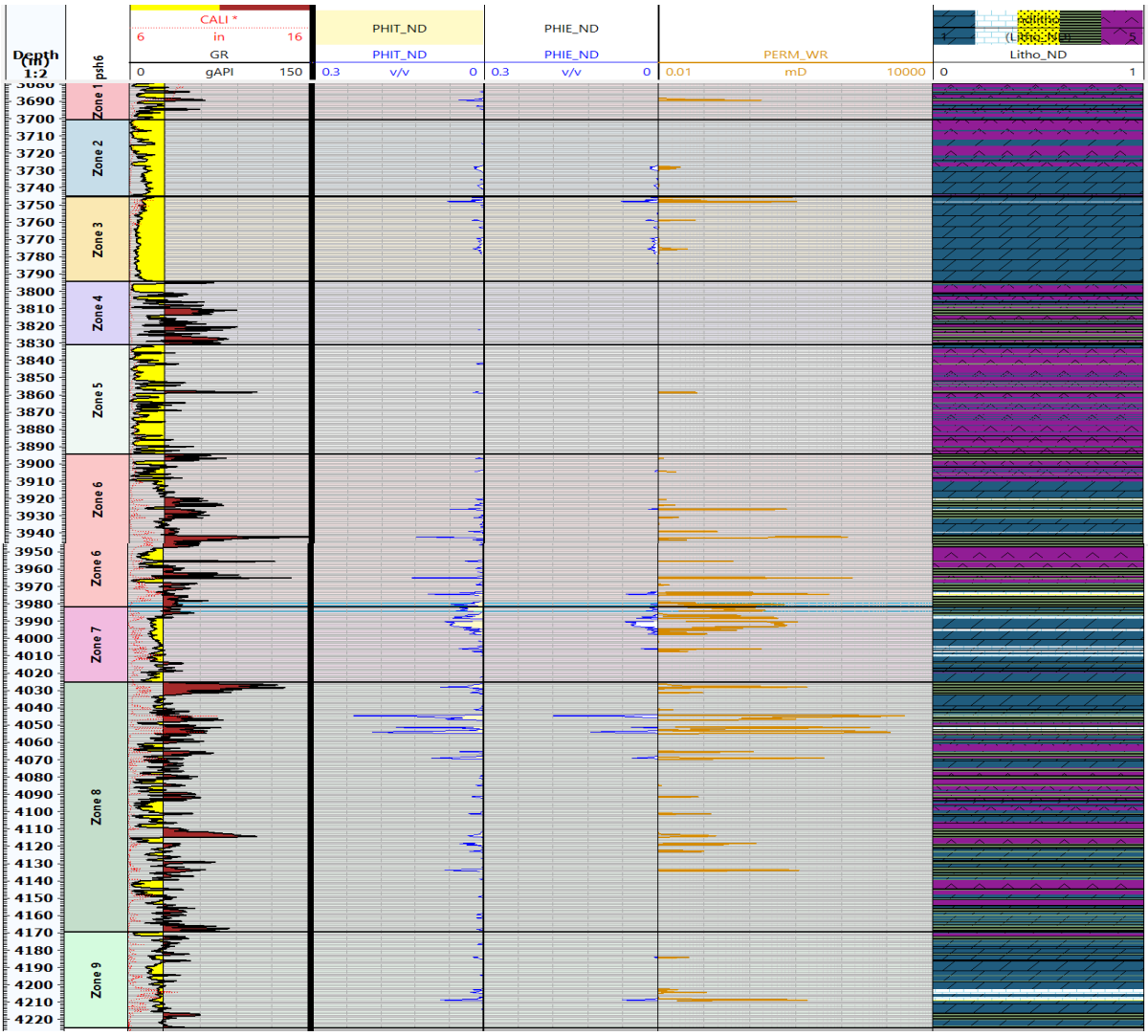


Fig. 5: N-D cross plots, density log (PHIE_D), sonic log (PHIE_S), and (PHIE_ND), data with a specific focus on measuring the effective porosity. The description addition

Porosity and Permeability

Porosity of the Kurra Chine varies significantly across zones and units, indicating low values at certain intervals. The higher total and effective porosity of the Kurra Chine Formation is 20% and 18%, respectively. Permeability also varies across depths and is controlled primarily by the pore- throat structure. The average porosity and permeability values for the rock, reservoir, and pay zones are approximately (0.013% and 13 mD), (0.014% and 1mD), and (0.046% and 24 mD), respectively (Table 3; Fig. 5).

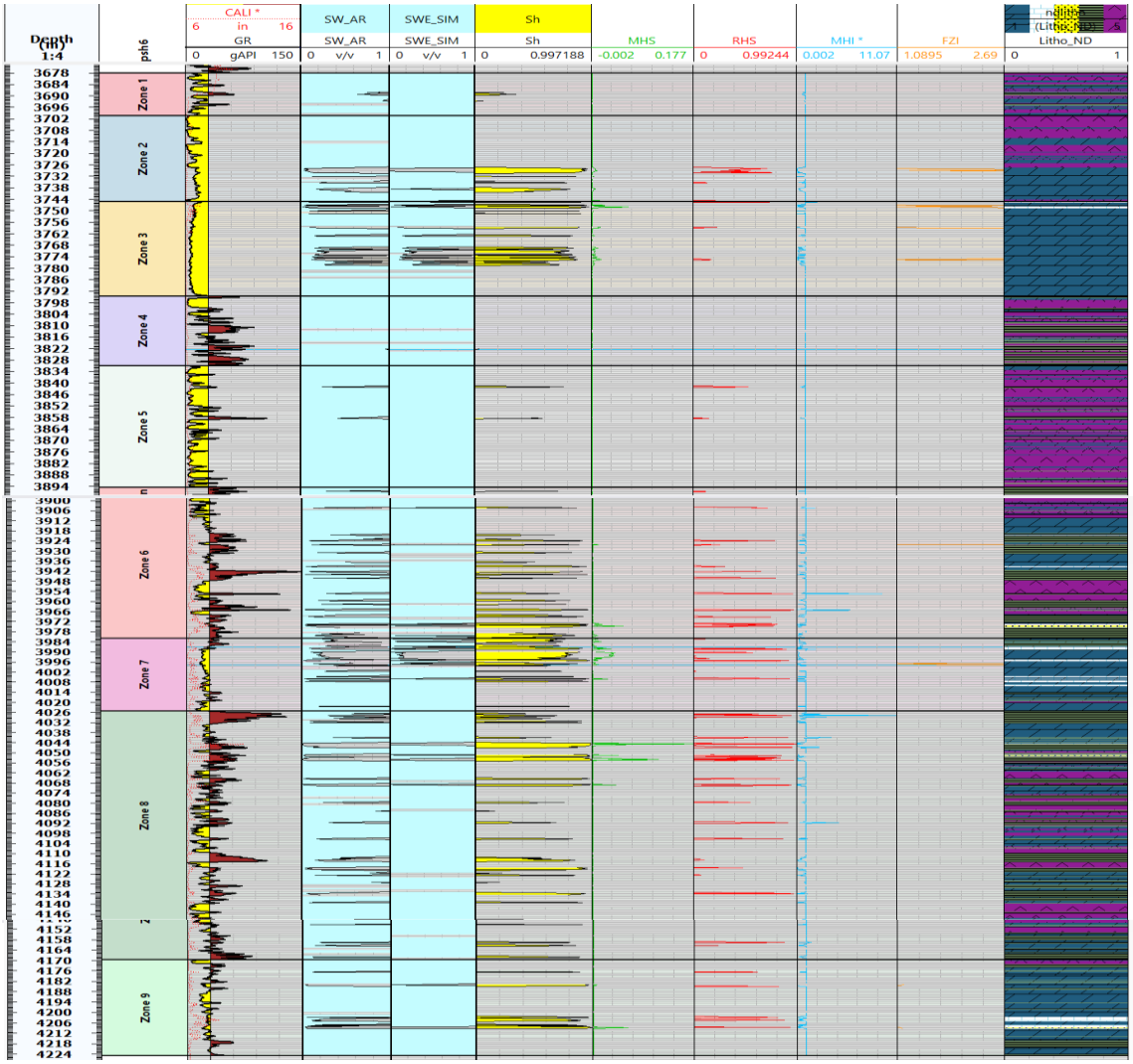


Fig. 6: Water saturation (Sw) volumes were determined via both Archie's and Simandoux equations. Moreover, it refers to hydrocarbon saturation (Sh), especially movable and residual hydrocarbon saturation. Additionally, the flow zone indicator (FZI) was used. The caption clarifies that the yellow, green, red, blue, and orange columns represent the hydrocarbon saturation.

Water and hydrocarbon saturation

The average water content within the formation is approximately 70%, whereas hydrocarbon content accounts for about 30%. The average values for movable and residual hydrocarbons, and flow zone indicators in these three zones are about 40%, 60%, and 90%, respectively (Fig. 6). Reservoir and pay zones. The gross thickness of the formation is 546 m, whereas the pay zone is only 58 m thick. This limited pay zone thickness is attributed to the influence of clay and anhydrite within the dolomite and reservoir units, which reduce the effective reservoir quality. Overall, the formation has low porosity and medium permeability. The main parameters of the net-to-gross ratio are explained in Fig. 7 and Table 3. Notably, dolomite is the only lithology containing pay zones within the formation.

Net-to-gross and pay zones

Kurra Chine Formation is classified into rock, reservoir, and pay zones. The gross thickness of the formation is 546 m, whereas the pay zone is only 58 m thick. This limited pay zone thickness is attributed to the influence of clay and anhydrite within the dolomite and reservoir units, which reduce the effective reservoir quality.

Overall, the formation has low porosity and medium permeability. The main parameters of the net-to-gross ratio are explained in Fig. 7 and Table 3. Notably, dolomite is the only lithology containing pay zones within the formation.

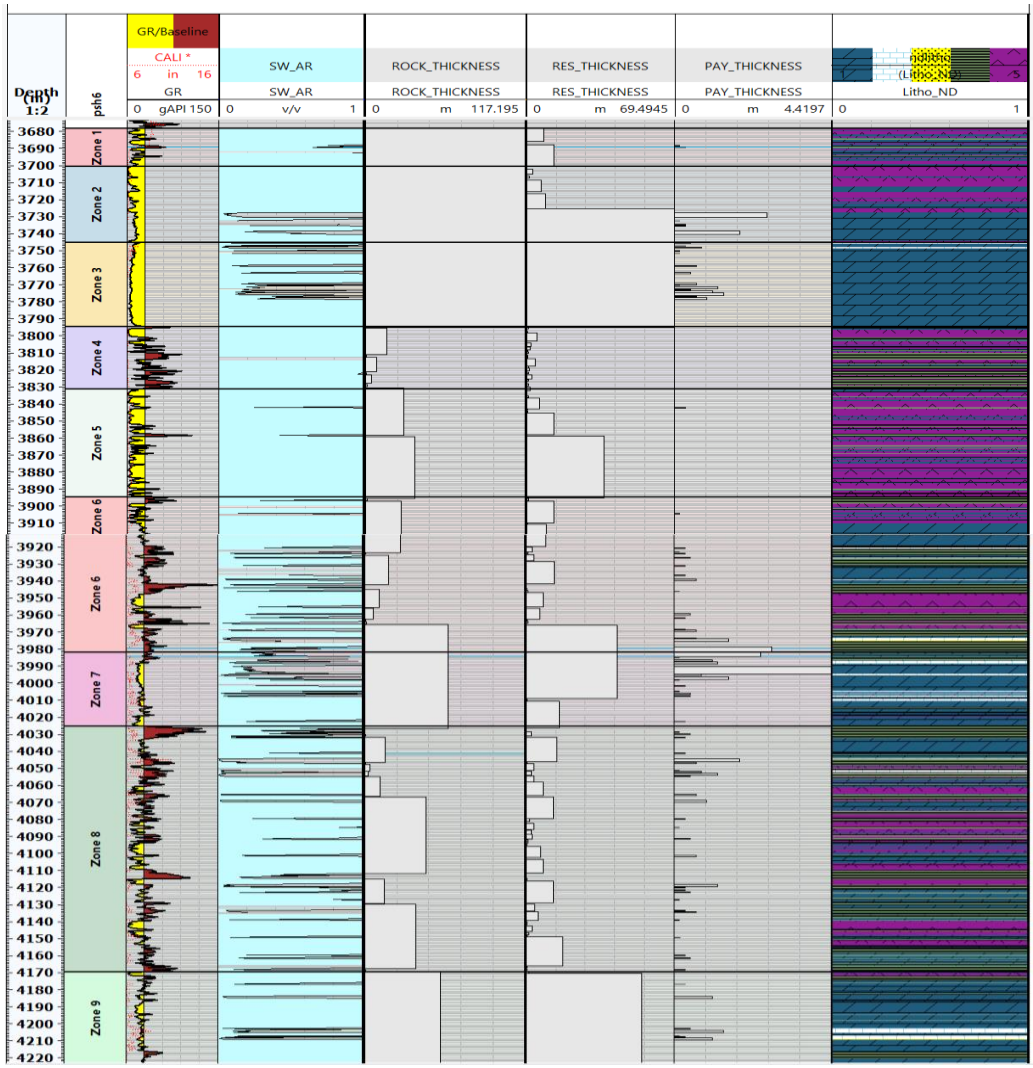


Fig. 7: Rock thickness, reservoir thickness, and pay thickness. This figure emphasizes the main reservoir thickness and pay thickness of the dolomite lithology. The figure provides information on the lithology associated with depth.

Table 3: Explanation of the parameters used for petrophysical properties

Flag names	Top (m)	Bottom (m)	Gross	Net	Not Net	NTG	AV. Sh %	AV. Ø%	AV. Sw %	AV. K mD
Rock	3678	4224	546	527	19	0.96	0.15	0.013	0.67	13
Res	3678	4224	546	500	47	0.91	0.10	0.014	0.67	15
Pay	3678	4224	546	58	468	0.106	0.09	0.046	0.21	24

Core samples and petrography

This section of slides represents the dolomite with high porosity and hydrocarbon content at some depths. Most pores in dolomite units are filled with hydrocarbons (Fig. 2). Core samples and petrographic analysis play important roles in identifying the porosity and lithology of the Kurra Chine Formation. Detailed information regarding the core plug and thin sections is presented in Table 4. Petrographic images of the Kurra Chine A carbonates reveal two significant findings: lithology identification and residual hydrocarbons occluding intercrystalline pores.

6. Discussion

The Kurra Chine Formation, located within the structurally active Taurus Fold Belt, is a key carbonate reservoir in the Kurdistan region. This formation has been shaped by complex tectonic events, including the collision between the Eurasian and Arabian plates, which created accommodation space for thick intervals of the Jurassic formations (Khoshnaw et al., 2019). The petrophysical analysis of Well PKH-6 provides insights into the reservoir quality and heterogeneity of the Kurra Chine Formation. The

lithology, shale volume, porosity, permeability, flow zone indicator, water and hydrocarbon saturations, and core and petrographic analysis of the Middle Triassic carbonate succession provide important insights into reservoir properties of the Kurra Chine Formation. The thickness of the formation varies slightly across different field and study areas. The thickness of the Formation at this Well is 540m. According to Bellen (1959), the lithology of this Formation is reported as limestone, shale, dolomite, and anhydrite.

The lithology of the Kurra Chine Formation in this field, based on the neutron–density cross–plot, was dolomite, anhydrite, shale, limestone, and minor sandstones. This lithology was emphasized by core samples and petrographic descriptions.

Shale volume was determined from Larionov's (1969) formula. The ratios of the Kurra Chine Formation in the Peshkhabir Oil Field differ. The clean zones are present, and most zones contain less than 60% shale, with the exception of Zone four, which is 8010 to 8030m. The Kurra Chine Formation comprises three shale-free zones, namely Zone 2, Zone 3, and Zone 5, which are identified as the main reservoir zones within the formation. In contrast, Zones 4, 6 and 8 present significant shale content, with average shale volumes of 60%, 40%, and 20% respectively. These shale zones are likely to serve as source rocks, potentially generating hydrocarbons that migrated to upper reservoir units. The overall average shale volumes of the rock, reservoir, and pay zones are approximately 15%, 10%, and 9%, respectively (Table 3 and Fig. 4). Total and effective porosity, for example, Zone 7 has total and effective porosities of approximately 9% and 6%, respectively. Most pores in this zone are filled with clay materials, which, along with anhydrite fragments, exert a significant influence on porosity reduction, with values of 20% and 18%, respectively. Permeability of the formation, anhydrite, and clay materials significantly influences the pore- throat geometry and fluid flow behavior. However, the dolomite units consistently display higher permeabilities across all the zones, with an average permeability of approximately 25 mD (Fig. 5). This highlights dolomite lithology as the key reservoir unit within the Kurra Chine. A comprehensive understanding of porosity and permeability is vital for active reservoir development and increasing production rate. Fluid saturation of the formation, the pore size in these units are relatively small, the total hydrocarbon volume is modest, and the connectivity of the pores and the presence of open flow lines significantly influence fluid. This directly impacts the daily production rate, as the interconnected pore structure and open flow lines enable efficient hydrocarbon extraction from the reservoir. Hydrocarbons, both movable and residual, are mainly concentrated in the dolomite units (Fig. 6). The flow zone indicator (FZI) is associated primarily with dolomite units and is notably observed in zones two, three, and seven. This suggests that 40% of the hydrocarbons are movable and can flow within the reservoir. The FZI further indicates that flow lines within the dolomite units are open, facilitating hydrocarbon migration within the reservoir. Core descriptions, faults, and fractures significantly influence the reservoir quality of carbonate rocks by allowing greater capacities of fluids to be filtered and migrate upward (Gumati, 2024) (Fig. 8). These hydrocarbons are likely residual hydrocarbons, or more plausibly, bitumen. All the samples were subjected to chemical cleaning before conventional reservoir core analysis (RCA) was conducted. While most normal hydrocarbons were removed during this process, sticky and insoluble bitumen may have remained trapped in the samples. There are several potential explanations for the presence of residual hydrocarbons. This may represent residual oil left behind after hydrocarbon migration from the formation to another stratigraphic level. The residual oil was degraded over time, leaving behind black, sticky, bitumen-like substances. At one point, the Kurra Chine functioned as an oil-filled reservoir. However, subsequent geological events, seal breaches, or further structural development could ha have caused hydrocarbons to migrate to another part of the reservoir (Fig. 7). These findings highlight the complex history of hydrocarbon migration and trapping within the formation. Further details are illustrated in Fig. 9. The petrographic images from the Kurra Chine B carbonates reveal no traces of residual hydrocarbons or bitumen. All the intercrystalline pore spaces appear open, as shown by the blue stain in the images. These observations suggest several possibilities: the Kurra Chine B Formation may have never been charged with hydrocarbons or was not part of a hydrocarbon migration

pathway. Alternatively, the formation may have contained normal hydrocarbons that were successfully removed during the sample cleaning process. However, the test results indicate that no oil was present in this formation. This evidence supports the conclusion that the Kurra Chine B Formation likely played a minimal role in hydrocarbon accumulation or migration. A small amount of preserved vuggy and fracture porosity. The pores have been partly occluded by anhydrite (A) and dolomite (arrow). (d) Dolostone (D) with a small amount of preserved intercrystalline porosity (blue stain). (e) Dolostone (D) with small amount of preserved vuggy and fracture porosity (Fig. 9).

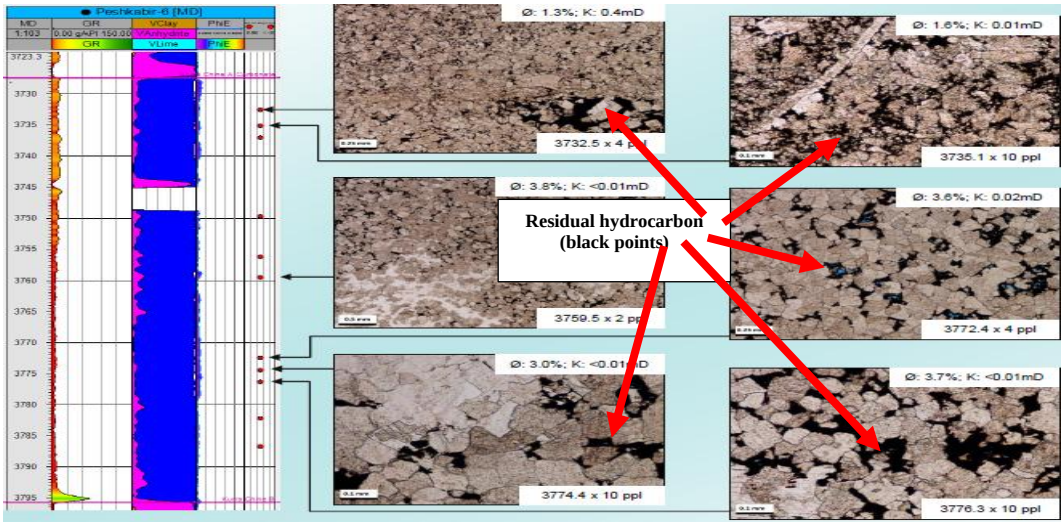


Fig. 8: Photomicrographs under plane polarizers of 10ppl and 4ppl. Shows the dolomite pores, and is filled with hydrocarbons. The petrographic images from the Kurra Chine A Carbonates have two things in common: the lithology of the Kurra Chine Formation and common residual hydrocarbons, which occlude almost all the intercrystalline pores.

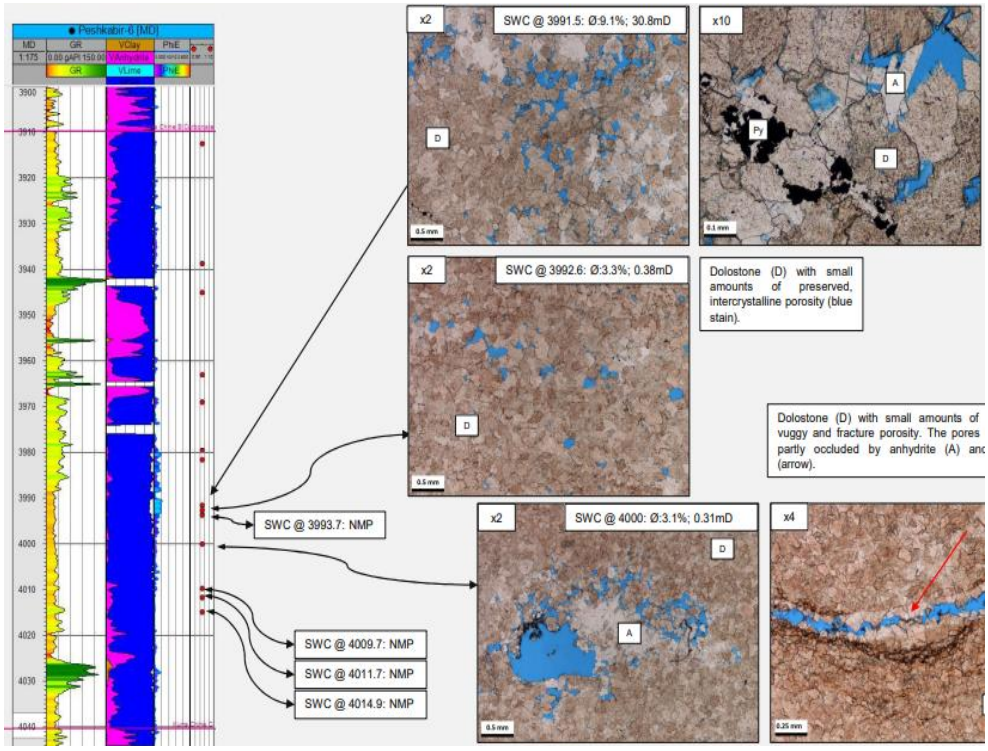


Fig. 9: (a) Dolostone (D) with common anhydrite cement (A) and small amounts of pyrite. Intercrystalline pores are present but are partly occluded by cement. (b) Dolostone (D) with a small amount of preserved intercrystalline porosity (blue stain). (c) Dolostone (D) with a long vein. (D) Dolostone with intercrystalline porosity. (e) Dolostone with vugs and fractures

Table 4: Depth of the core plug numbers and thin section slides of the Kurra Chine Formation

Formation	Well No.	Depth	Thin section	Core Plug No.
Kurra Chine	PKH-6	3732.5	2	
		3735.1	2	
		3737	1	
		3749.7		
		3756.2	2	
		3759.5	2	
		3772.4	1	
		3774.4	2	
		3776.3	2	
		3782.2		
		3786.7	2	
		3811.3	1	
		3822.7	1	
		3825	1	
		3826.1		
		3895.7		
		3912.5		
		3938.7		
		3945		
		3963	2	
		3969		
		3979.5	2	
		3981.6	1	
		3991.5	2	
		3992.6	1	
		3993.7		
		4000	2	
		4009.7		
		411.7		
		4014.9		
		4052.7		
		4067.6	2	
		4073.3		
		4084.6		
		4091.4		
		4099.7		
		4112	1	
		4119		
		4128		
		4131.4		
		4138.6		
		4154.5	1	
		4155.4	2	
		4180.4		
		4199.8		
		4206		
		4220		

7. Conclusions

This study provides a comprehensive analysis of the petrophysical properties of the Kurra Chine Formation at Peshkhabir Well-6 (PKH-6), offering new insights into reservoir quality and hydrocarbon distribution. The integration of wireline logs, core sample analysis, and petrographic investigations has enabled a more detailed assessment of porosity, permeability, and hydrocarbon saturation than previously available methods.

Key findings include the following:

- The total formation thickness is 546 m, with pay zones averaging 9% shale volume.
- Dolomite was identified as the primary reservoir lithology and flow zone, with a regular permeability of 24 mD and a porosity of 6%.
- The average hydrocarbon saturation was 79%, confirming the formation's economic potential.
- Petrographic analysis confirmed the hydrocarbon-filled porosity, reinforcing the importance of the dolomite reservoir.

The novelty of this research lies in its integrated petrophysical evaluation approach,

which improves reservoir characterization accuracy and exploration efficiency. These findings provide valuable data for future field development, reservoir modeling, and hydrocarbon production strategies in the Triassic formations of northern Iraq.

8. Acknowledgements

The authors sincerely thank the Department of Earth Sciences and Petroleum for supporting this research. The authors also thank the Ministry of Natural Resources (MNR) and DNO-Genel Energy Ltd. for supplying the necessary data.

9. Conflict of Interest

The authors confirm that there are no financial or personal conflicts of interest that could have influenced the outcomes presented in this paper.

10. Funding Statement

This research received no external funding.

11. References

Al-Adwani N.S., 2022. Evaluation of the hydrocarbon source rock and the reservoir characterization of the Minagish Formation using wireline logs, Heliyon 8 (6) https://doi.org/10.1016/j.heliyon.2022.e09797.

Al-Ameri, T.K., Al-Dolaimy, Q.H., Al-Khafaji, A.J., 2009. Palynofacies and hydrocarbon generation potential of the upper Triassic Kurrachine Formation and lower part of the Baluti Formation, Mosul Block, Northwestern Iraq. Arabian Journal of Geosciences 2, 273_283. https://doi.org/10.1007/s12517-009-0041-5.

Al-Dabagh, M.M., Ali, M.S. and Al-Hamdani, A.M., 2021a. Microfacies valuation of Kurra Chine Formation (Triassic) and scenario of depositional basin development in northern and northwestern Iraq. _*Journal of Petroleum Research and Studies*, (33). DOI: http://doi.org/10.52716/jprs.v11i4.56

Al-Dabagh, M.M. and Ali, M.S., 2021b. The Impact of Primary and Effective Porosities on the Permeability of the Kurra Chine Formation Successions (Late Triassic) in Selected Wells-Northern Iraq. *Journal of Petroleum Research and Studies* (30). https://jprs.gov.iq/index.php/jprs/article/view/439/359

Al-Dolaimy, A.M., Al-Beyati, F.M. and Al-Mallah, A.Y., 2021a. Distribution of Steranes and Triterpanes Biomarkers as an Indication of Depositional Environment and Maturity of Sargelu and Kurrachine Formations in Different Wells Northern Iraq. *The Iraqi Geological Journal*, pp.87-100. https://doi.org/10.46717/IGJ.54.1C.7MS-2021-03-27

Al-Dolaimy, A.M., Al-Mallah, A.Y., Abdel-Fattah, M.I. and Al-Beyati, F.M., 2021b. Source Rock Characteristics of Sargelu and Kurrachine Formations from the Selected Wells in Northern Iraq. *The Iraqi Geological Journal*, pp.60-74. https://doi.org/10.46717/igj.54.2A.5Ms-2021-07-26

Al-Hamdani, A.M., Ali, M.S. and Aldabagh, M.M., 2019. Diagenetic Effects on Porosity Development of Reservoir Rocks of Kurra Chine Formation in Northern and North Western Iraq. DOI: 10.13140/RG.2.2.16285.84967

Aqrawi, A.A., Goff, J.C., Horbury, A.D. and Sadooni, F.N., 2010. *The petroleum geology of Iraq* (Vol. 424). Beaconsfield, UK: Scientific Press.

Aqrawi, A.A.M., 1998. Paleozoic Stratigraphy and Petroleum Systems of the Western and Southwestern Deserts of Iraq. GeoArabia 3, 417–418. https://doi.org/10.2113/geoarabia0302417

Archie, E., 1942. The electrical resistivity log as an aid in determining some reservoir characteristics: Petroleum Transactions, AIME, 146, (1), 54 – 62. https://doi.org/10.2118/942054-G

Asquith, G. and Krygowski, A., 2004. Basic Well Log Analysis, Second Edition, AAPG Methods in Exploration Series, No.16, The American Association of Petroleum Geologists, Tulsa, ISBN: 0-89181-667-4 https://archives.datapages.com/data/specpubs/method16/me16ch00/me16ch00.htm

Aswad M.K., 2020. Estimation of water and hydrocarbon saturation based on wireline logs in carbonate rocks of the Sargelu Formation (Middle Jurassic) from the Kurdistan region, Iraq, Iraqi Bulletin of Geology and Mining 16 (2) 95–108. file:///C:/Users/max/Downloads/419-Article+Text-946-990-10-20201116%20(2).pdf

Aswad, M.K., Naqshabandi, S.F., and Omer, M.F., 2023a. Kurra Chine Formation: Evaluation of Source Rock Based on Rock-Eval Pyrolysis Analysis Integrated by Selected Wells and Outcrop Samples in Iraq's Kurdistan Region. Iraqi Geological Journal. 56(2B) 37-50. http://dx.doi.org/10.46717/igj.56.2B.3ms-2023-8-31

Aswad, M.K., Naqshabandi, S.F. and Omer, M.F., 2024b. Palynofacies analysis and depositional environment of the Upper Triassic Kurra Chine Formation: integrated by samples from Sarta and Tawke oil fields and outcrop samples from Sirwan Valley in the Kurdistan Region, northern Iraq. IOP Conf. Series: Earth and Environmental Science. https://doi.org/10.1088/1755-1315/1300/1/012033

Aswad, M.K., Omer, M.F. and Naqshabandi, S.F., 2024a. Unlocking the hydrocarbon potential: Formation evaluation and petrophysical properties of the Upper Triassic Kurra Chine Formation in Sarta Oil Field, Kurdistan Region, Northern Iraq. Heliyon, 10(3). https://doi.org/10.1016/j.heliyon.2024.e25173

Aswad, M.K., Omer, M.F. and Naqshabandi, S.F., 2023b, Examining the impact of cement on porosity evolution in the upper Triassic Kurra Chine Formation of Sirwan Valley, Kurdistan region, Iraq: a study integrating cathodoluminescence and scanning electron microscopy, Kuwait Journal of Science https://doi.org/10.1016/ j.kjs.2023.07.013

Baban D.H. and Ahmed S.M., 2021. Source Rocks' Potentiality of the Sargelu Formation (Middle Jurassic) in the Taq Taq Oilfield, Kurdistan Region, Iraq, The Iraqi Geological Journal, 59–85. https://doi.org/10.46717/igj.54.2E.5Ms-2021- 11-21.

Balaky S.M., Tamar-Agha M.Y., 2017. Sedimentology and stratigraphy of Geli Khana Formation (Anisian–Ladinian), a contourite depositional system in the northeastern passive margin of the Arabian Plate, northern Iraq-Kurdistan region, Arabian Journal of Geoscience. 10 (5), 1–20. http://dx.doi.org/10.1007/s12517-017-2952-x

Balaky, S.M., Al-Dabagh, M.M., Asaad, I.S., Tamar-Agha, M., Ali, M.S., Radwan, A.E., 2022. Sedimentological and petrophysical heterogeneities control on reservoir characterization of the Upper Triassic shallow marine carbonate Kurra Chine Formation, Northern Iraq: Integration of outcrop and subsurface data. Marine and Petroleum Geology, 106085.https://doi.org/10.1016/j.marpetgeo.2022.106085

Bellen, R.C., Dunnington, H.V., Wetzel, R. and Morton, D.M., 1959. Lexique stratigraphique international Asia, fascicule 10a, Iraq. *Centre national de la recherche scientifique*, *Paris*, *33*. https://www.abebooks.com/Stratigraphic-Lexicon-Iraq-R.C-Bellen-H.V/32131811905/bd

Choquette, P.W. and Pray, L.C., 1970. Geologic nomenclature and classification of porosity in sedimentary carbonates. *AAPG Bulletin*, *54*(2), 207-250. https://doi.org/10.1306/5D25C98B-16C1-11D7-8645000102C1865D

Choquette, P.W., Hiatt, E.E., 2008. Shallow-burial dolomite cement: A major component of many ancient sucrose dolomites. Sedimentology 55, 423–460. https://doi.org/10.1111/j.1365-3091.2007.00908.x

Edilbi, A.N., Kolo, K., Muhammed, N.R., Yasin, S.R., Mamaseni, W.J. and Akram, R., 2019. Source rock evaluation of shale intervals of the Kurra Chine Formation, Kurdistan Region-Iraq: An organic geochemical and basin modeling approach. *Egyptian Journal of Petroleum*, *28*(4), 315-321. https://doi.org/10.1016/j.ejpe.2019.06.003

El Sharawy, M.S. and Nabawy, B.S., 2019. Integration of electrofacies and hydraulic flow units to delineate reservoir quality in uncored reservoirs: A case study, Nubia Sandstone Reservoir, Gulf of Suez, Egypt. *Natural Resources Research*, *28*, 1587-1608.https://doi.org/10.1016/j. heliyon. 2024.e25173

Friedman, G.M., 1959. Identification of carbonate minerals by staining methods. J. Sediment. Res. 29, 87–97.

Gumati, M.S., 2024. Fluid and lithology discrimination using integrated facies, petrophysical modelling and (AI and vp/vs) rock physics template analysis derived from well data in the carbonate fault-controlled reservoir: A case study from the North Beda Field, Amin High, Sirt Basin, Libya. *Acta Geophysica*, 1-22 https://doi.org/10.1007/s11600-024-01447-8

Koshnaw, R.I., Stockli, D.F. and Schlunegger, F., 2019. Timing of the Arabia-Eurasia continental collision—Evidence from detrital zircon U-Pb geochronology of the Red Bed Series strata of the northwest Zagros hinterland, Kurdistan region of Iraq. *Geology*, *47*(1), pp.47-50. https://doi.org/10.1130/G45499.1

Larionov v.v., 1969. Borehole Radiometry, U.S.S.R., Moscow. Nedra, 127P.

Lucia F.J., 2007. Carbonate Reservoir Characterization. An Integrated Approach, Springer-Verlag Berlin Heidelberg, 2007, 336. https://doi.org/10.2118/82071-JPT

Lunn, G.A., 2020. Dating and correlation of the Baluti Formation, Kurdistan, Iraq: Implications for the regional recognition of a Carnian "marker dolomite", and a review of the Triassic to Early Jurassic sequence stratigraphy of the Arabian Plate. *Journal of Petroleum Geology*, *43*(1), 109-125. https://doi.org/10.1111/jpg.12752.

Olorunniwo I., Olotu S.J., Alao O.A., 2019. Adepelumi A.A., Hydrocarbon reservoir characterization and discrimination using well-logs over "AIB-EX" Oil Field, Niger Delta, Heliyon 5 (5) https://doi.org/10.1016/j.heliyon.2019.e01742.

Porras, J.C. and Campos, O., 2001. March. Rock typing: a key approach for petrophysical characterization and definition of flow units, Santa Barbara Field, Eastern Venezuela Basin. In *SPE Latin America and Caribbean Petroleum Engineering Conference* (pp. SPE-69458). SPE. https://doi.org/10.2118/69458-MS

Radwan A.A., Nabawy B.S., Kassem A.A., Elmahdy M., 2023. An integrated workflow for seismic interpretation, petrophysical and petrographical characterization for the clastic Mangahewa reservoir in Pohokura gas field, Taranaki Basin, New Zealand, Geoenergy Science and Engineering 229, 212117, https://doi.org/ 10.1016/j.geoen.2023.212117

Sadooni, F.N., 1995. Petroleum prospects of Upper Triassic carbonates in northern Iraq. *Journal of Petroleum Geology*, *18*(2), 171-190..https://doi.org/10.1111/j.1747-5457.1995.tb00896.x

Shalaby M.R., Thota S.T., Norsahminan D.N.P., Kamalrulzaman, K.N., Matter W.S., Al-Awah H., 2023. Reservoir quality evaluation using petrophysical, well-log analysis and petrographical description: a case study from the Carboniferous-Permian Kulshill group formations, southern Bonaparte Basin, Australia, Geoenergy Science and Engineering 226, 211738, https://doi.org/10.1016/j.geoen.2023.211738.

Simandoux, P., 1963. Dielectric measurements on porous media: application to the measurement of water saturation, study of the behaviour of argillaceous formations: Revue de l'Institut Français du Pétrole, 18, S1, 193 – 215.

Teillet T., Fournier F., Zhao L., Borgomano J., Hong F., 2021, Geophysical pore type inversion in carbonate reservoir: integration of cores, well logs, and seismic data (Yadana field, offshore Myanmar), Geophysics 86 (3), B149–B164. https://doi.org/10.1190/geo2020-0486.1

Iraqi National Journal of Earth Science, Vol. 26, No. 04, 2026 (40-53)

Iraqi National Journal of Earth Science

www.earth.uomosul.edu.iq

التوصيف المتكامل للمكمن والتقييم البتروفيزيائي لتكوين كُرّا تشين في حقل بيشكخابور النفطي، شمال العراق

مهدى خيرى أسود [1] ، سازان محمد على [2]

Mahdi.aswad@su.edu.krd sazan.mohammed91@gmail.com

[1] قسم علوم الارض و النفط، كلية علوم، جامعة صلاح الدين، اربيل، العراق.

[2] قسم الهندسة المدنية، كلية الهندسة، جامعة صلاح الدين، اربيل ، العراق.

* الباحث المراسل.

تاريخ الاستلام: 12 تموز 2025 تاريخ المراجعة: 01 أيلول 2025 تاريخ القبول: 24 تشرين الأول 2025

تاريخ النشر الالكتروني: 01 تشرين الأول 2026

الملخص

تكوين كورا تشين، الذي يعود إلى العصر الترياسي، يُعد من الوحدات البارزة في الطبقات التحت سطحية في شمالي العراق، يعد هدفًا رئيسيًا لاستكشاف الهيدروكربونات بسبب تعقيد ليثولوجيته وإمكاناته كمكمن. ومع ذلك، فإن عددًا قليلاً من الدراسات قد قامت بوصف خواصه البتروفزيائية وجودة المكمن بشكل كامل، مما يستدعي إجراء المزيد من البحوث . يهدف هذا البحث إلى تعزيز فهم الإمكانات الهيدروكربونية للتكوين من خلال تنفيذ تصنيف مكمني شامل وتقييم بتروفيزيائي في بئر بيشخابير رقم 6 (PKH-6). ولتحقيق هذا الهدف، تم اعتماد نهج تكاملي يجمع بين تفسير سجلات الآبار السلكية، وتحليل عينات اللباب، والتحليلات البتروغرافية. تم تحديد السماكة الكلية للتكوين بـ 546 مترًا، حيث أظهرت الفواصل المكمنية الرئيسية متوسط حجم طمي يبلغ 9%. وكشف التحليل الصخاري عن وجود مكونات من الدولومايت، والأنهيدرايت، والطين الصفحي، والحجر الجيري، والحجر الرملي، مع تحديد الدولومايت بوصفه الوحدة الأساسية لتدفق الموائع. وأظهر التحليل البتروفيزيائي متوسط مسامية كلية وفعالة تبلغ 6%، ونفاذية تصل إلى 24 مليدارسي، ومتوسط تشبع هيدروكربوني يبلغ 79%. وأكدت الملاحظات البتروغرافية وجود مسامات مملوءة بالهيدروكربونات، مما يعزز من صلاحية التكوين كمكمن منتج. توفر هذه النتائج رؤى جديدة حول جودة المكمن، وتوزيع الهيدروكربونات، وخصائص التدفق في تكوين كورا تشين، مما يسهم في تحسين استراتيجيات الاستكشاف وتطوير الحقول للمكامن الثلاثية في شمال العراق.

الكلمات المفتاحية:

كوين كورا تشين، شمال العراق، حقل نفط بيشكخابور، التوصيف البتروفيزيائي وتوصيف المكمن

DOI: 10.33899/injes.v26i4.56026, *©Authors, 2026, College of Science, University of Mosul.*

This is an open-access article under the CC BY 4.0 license (http://creativecommons.org/licenses/by/4.0/).

==========

Iraqi National Journal of Earth Science, Vol. 26, No. 04, 2026 (54-67)

Iraqi National Journal of Earth Science

www.earth.uomosul.edu.iq

Water Suitability for Paddy Field Irrigation in Tropical Watershed Dominated by Ancient Volcanic Rocks and Limestones, Indonesia

Ahmad Cahyadi [1*], Indra Agus Riyanto [2], Marselli Nabila Putri [1], Rizka Novi Ramadhania [1]

ahmad.cahyadi@ugm.ac.id indra.agus.r@gmail.com marselli.nabila2103@mail.ugm.ac.id rizka.novi.ramadhania@mail.ugm.ac.id

[1] *Department of Environmental Geography, Faculty of Geography, Universitas Gadjah Mada, Yogyakarta, Indonesia.*
[2] *PT Pelsart Tambang Kencana, Jakarta, Indonesia.*
* *Correspondence author.*

Received: 15 July 2025 Received in revised form: 03 September 2025 Accepted: 04 October 2025
Available online: 01 October 2026

Abstract

Proper water quality for plant growth is important to ensure high productivity in food production. However, the hydrological and geological characteristics of a region cause distinctive characteristics that need to be understood in order to carry out proper agricultural practices. The purpose of this study was to determine the temporal variation of Tesih River water suitability for irrigation. This research is expected to provide an overview of the temporal variation of water suitability for irrigation in a watershed dominated by ancient volcanic rocks and limestone that have formed karst areas. On the other hand, this study is expected to provide an overview of the influence of climatological conditions controlled by tropical climate and the characteristics of the Asian-Australian monsoon winds at the study site that are strong on water suitability for irrigation. Methods used: Percent Sodium (Na%), Sodium Adsorption Ratio (SAR), Wilcox diagram, USSL diagram, Hardness (H), Magnesium Hazard (MH), Kelly's ratio (KR), Permeability Index (PI), and Residual Sodium Carbonate (RSC). The water suitability methods used were percentage of sodium (Na%), sodium adsorption ratio (SAR), Wilcox diagram, USSL diagram, hardness (H), magnesium hazard (MH), Kelly's ratio (KR), permeability index (PI), and residual sodium carbonate (RSC). The analyses showed that the river water was good (based on Na%, USSL diagram, and RSC), very good (SAR and PI), excellent (the Wilcox diagram), or suitable for irrigation (H, MH, and KR). Overall, the river has the physical and chemical qualities suitable for supporting crop growth without damaging soil properties.

Keywords:

Paddy Field Irrigation, Karst, Ancient Volcanic Rock, Water Quality, Hydrogeochemistry.

DOI: 10.33899/injes.v26i4.56030, ©Authors, 2026, College of Science, University of Mosul.
This is an open-access article under the CC BY 4.0 license (http://creativecommons.org/licenses/by/4.0/).

==========

1. Introduction

Irrigation is the key component of agricultural practices (Döll and Siebert, 2002; Šimunić et al., 2021; Mohammed et al., 2025). Irrigated farmlands account for an estimated 20% of the global agricultural area, contributing approximately 40% of annual food production (Mohtar and Fares, 2022). However, irrigation is perceived as one of the most uneconomical forms of water utilisation. On average, the agricultural sector constitutes around 70% of freshwater needs worldwide and almost 90% in developing countries (FAO, 2017). It is therefore encouraged to implement increasingly productive cultivation systems that use water efficiently (Al-Obeidi et al., 2025).

The need for irrigation water rises every year (Abdoulaye *et al*., 2019) as a result of population growth and changes in lifestyle, with inevitably increasing food demand (Telteu *et al*., 2021; Salem *et al*., 2022). In line with this, Day (2019) calculated that the global water needs in 2050 would be 55% greater than in 2000. For irrigation water, supplies can come from rainwater, surface water (including rivers, lakes and swamps) and groundwater (Starr *et al*., 2014; Samardžić et al.,

2022). However, rivers have long been the most common and main source of irrigation (Tickner *et al*., 2017), comprising 60% of total irrigated land that produces around 24% of global food supplies.

To determine suitability for controlled watering of farmlands, water sources are usually evaluated for their quantity and quality before distribution (Šoškĭć *et al*., 2001; Al-Saffah and Al-Mashhadany, 2025). Water quantity analysis incorporates infrastructure and total land area to be irrigated, whereas water quality assessment aims to ensure farm productivity and effective plant treatment (Šoškĭć *et al*., 2001; Tanaskovikj *et al.*, 2014; Kateb and Al-Youzbakey, 2025) while preventing land or soil deterioration (Paruch et al., 2015; Ismail et al., 2019; Hafiane *et al*., 2020). The latter is, however, conducted less frequently than the former. Water with unsuitable chemical and physical qualities can lead to suboptimal crop growth and even crop failure and soil damage in some cases (Abbasian *et al*., 2014; Ibrahim and Al-Youzbakey, 2024).

Indonesia is an agrarian country where the agricultural sector produces a considerable amount of food and plays a crucial role in its economy (Maat, 2014), with around 14% contribution to the country's gross domestic product (GDP) (Barichello and Patunru, 2009). This further affirms the importance of monitoring and fulfilling irrigation water needs, which have been found to constantly increase by about 20% between 2000 and 2020 (Tirtalistyani *et al*., 2022). This upward trend has also been predicted to continue as a result of farmland expansion to achieve food self-sufficiency (Fulazzaky, 2017; Ma'Mun *et al*., 2021). Like the research trend worldwide, many studies have been performed on water quantity or availability for irrigation in Indonesia (Mediawan *et al*., 2021; Khasanah *et al*., 2021), but only a few have been conducted on water quality and its multitemporal variations. A multitemporal study can shed light on the hydrogeochemical characteristics of water, which are closely related to the seasons and change over time as a result of contact or interaction between groundwater and rocks.

In line with this, the research uses the Tesih Watershed as an example because (1) it is situated in a rural region where rice fields and dry farmlands occupy most of its area and (2) it has unique geological features. The watershed is 12.22 km2 and lies on ancient volcanic rocks and limestones that form karst landscapes in Sawahan and Tambakromo Villages, Ponjong District, Gunungkidul, Indonesia (Fig. 1). Geologically, it is located on the Semilir and Wonosari Formations composed of reef limestones (Rahardjo, 1995). Semilir Fm of the Early Miocene age covers the largest area of the watershed (9.78 km^2). It consists of lapilli tuffs with intrusive tuffs and tuff clays, tuff sandstones, pebbly sandstones, and pumice breccia. Wonosari Fm (2.44 km^2) was formed in the Middle to Late Miocene and consists of layered limestones, massive limestone, marl-tuff, and sandstones (Adji *et al*., 2019). Wonosari Fm is part of the Gunungsewu Karst Area in the Ponjong Hydrogeological Subsystem (Kusumayudha, 2009). In addition, the watershed receives about 2,000–3,000 mm of rainfall per year (Cahyadi *et al*., 2021).

This research aimed to analyse the suitability of water in the Tesih Watershed for irrigation multi-temporally. It collected water samples every two weeks for one year to describe the temporal variations of water quality in a watershed on ancient volcanic rocks and karstic limestones. It also explains the influence of tropical climate controls and the strong Asian-Australian monsoon winds (Cahyadi *et al*., 2021) on the water's suitability. The Asian-Australian monsoon winds have contrasting characteristics: wet in the rainy season and very dry in the dry season (Riyanto *et al*., 2020).

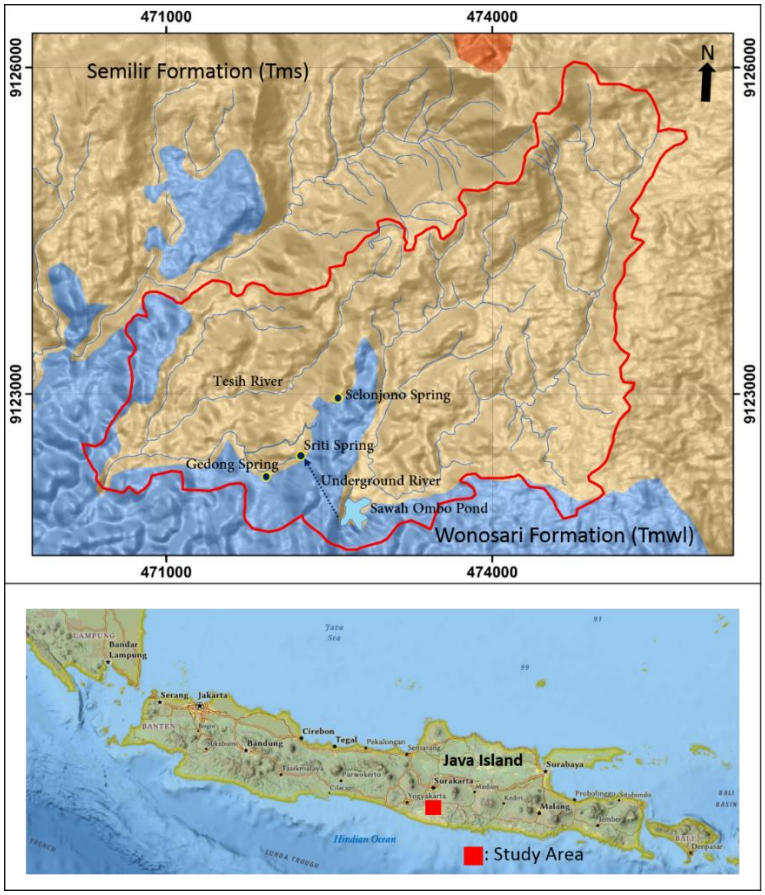


Fig. 1: Location of the Tesih Watershed on Java Island, Indonesia (Sources: Topographic Map in 1:25,000 scale from the Geospatial Information Agency, Geological Map in 1:50,000 scale from the Geological Agency, and maps provided by https://esri.com/natgeomapmaker)

2. Materials and Methods

From 2020 to 2021, twenty-five water samples were collected from the Tesih River during the dry and rainy (wet) seasons, with a sampling interval of two weeks. Samples therefore represent the different seasonal conditions and influences throughout the year (Dragović, 2012). In the field, a water quality test kit was used to measure temperature, pH, electrical conductivity (EC), and total dissolved solids (TDS), and an alkalinity test kit to analyse HCO3- by titration. Further, the samples were tested in the laboratory to determine Ca2+, Mg2+, Na+, K+, Cl- and SO42- concentrations.

Table 1 details the equation and classification of nine different methods used to assess water suitability for irrigation. Comparing multiple methods can determine their respective degrees of sensitivity to data variation because they use different parameters and equations (Wilcox, 1955; McGeorge, 1954; Bhat *et al*., 2018; Cahyadi *et al*., 2023a). Besides, it allows cross-evaluation or validation of one method with another, particularly in analysing water suitability for irrigation that incorporates numerous aspects of water quality, plant productivity, and preventive measures against crop failure (Mohammed, 2021). The water suitability analysis also factors in land cultivation, fertilisation and the addition of certain elements for effective, efficient and target-specific soil enrichment (Nishanthiny *et al*., 2010; Ayers and Westcot, 1985). K+ and Cl- were not included in the assessment, but both ions were input into the charge-balance error (CBE) equation to ensure the quality of the hydrogeochemical data used in this research.

Table 1: Water quality equations for irrigation purposes.

Method	Equation	Classification (C)
Na%	$\frac{(Na+K)100}{(Ca+Mg+Na+K)}$	S1 < 20 Excellent (E) S2 20–40 Good (G) S3 40–60 Permissible (Pe) S4 60–80 Doubtful (D) S5 >80 Unsuitable (Un)
Sodium adsorption ratio (SA)	$\frac{Na}{\sqrt{1}/2(Ca+Mg)}$	S1 <10 Excellent (E) S2 10–18 Good (G) S3 18–26 Fair (F) S4 >26 Poor (Po)
Wilcox	Diagram-based, correlating two parameters: Na% and EC	Excellent to Good (EG) Good to Permissible (GP) Doubtful to Unsuitable (DU) Unsuitable (Un)
USSL	Diagram-based, correlating two parameters: SAR and conductivity	C1S1 Good (G) C1S2 Moderate to Good (MG) C1S3 Moderate (M) C1S4 Moderate to Poor (MP) C2S1 Moderate to Good (MG) C2S2 Moderate (M) C2S3 Moderate to Poor (MP) C2S4 Poor (P) C3S1 Moderate (M) C3S2 Moderate to Poor (MP) C3S3 Poor (P) C3S4 Very Poor (VP) C4S1 Moderate to Poor (MP) C4S2 Poor (P) C4S3 Very Poor (VP) C4S4 Unusable (U)
Hardness/H ($CaCO_3$)	2.5 (Ca)+4.1(Mg)	<75 Soft (Sf) 75–150 Moderate (M) 150–300 Hard (H) >300 Very Hard (VH)
Magnesium hazard (MH)	$\frac{Mg}{Ca+Mg}\times 100$	≤50% Suitable (S) >50% Unsuitable (Un)
Kelly's ratio (KR)	$\frac{Na}{Ca+Mg}\times 100$	≤1 Suitable (S) ≥3 Unsuitable (Un)
Permeability index (PI)	$\frac{Na+\sqrt{HCO_3}}{Ca+Mg+Na}\times 100$	<25% Unsuitable (Un) >25% Good (G)
Residual sodium carbonate (RSC)	(HCO_3+ CO_3) - (Ca+ Mg)	(-) Very Good (Vg) 0–1.39 Good (G) >1.39 Unsuitable (Un)

Source: Cahyadi *et al.* (2023a)

3. Results and Discussion

Table 2 presents the chemical analysis results of the river water samples, including CBE values and major ion concentrations on each day of measurement. The CBE varied from -9.6 to 12.4 with an average of <10%, meaning the data obtained using the field analysis kits and laboratory tests are acceptable for further hydrogeochemical analysis to evaluate water suitability for irrigation. As the table shows, the major ions in the study area formed different patterns of temporal variations throughout the year. Calcium and bicarbonate ions were detected at larger concentrations than the other ions. This particularly illustrates the substantial influence of karst aquifers even though karst landforms occupied only 20% of the Tesih Watershed area.

Fig. 2 shows that calcium and bicarbonate tended to have lower concentrations in the wet season than in the dry season. The trend is closely related to dilution by rain and interaction between water and rock (Pratama *et al*., 2021), especially the limestone of Wonosari Fm. This effect was also seen from the drastic increases in calcium and carbonate concentrations in the dry season, during

which only the water carrying both ions from the karst aquifer fed the Tesih River. Ancient volcanic rocks are generally not good aquifers as they partition most rainwater into surface runoff. As a result, surface water drains quickly during the wet season without seeping into the soil, often leaving little to no groundwater storage during months of no rain. Accordingly, instead of rain and surface runoff, water from three perennial karst springs (Cahyadi *et al*., 2023b) recharges the Tesih River in the dry season. These springs are Selonjono, Gedong, and Sriti (see Fig. 1). Sriti is a resurgence of an underground river (Cahyadi *et al*., 2022a), while Selonjono and Gedong are epikarst springs (Cahyadi *et al*., 2022b).

Fig. 3 shows that, unlike calcium and bicarbonate, the concentrations of the other major ions (magnesium, potassium, sodium, chloride, and sulphate) varied less considerably or did not show a substantial change over the observation period. An exception was identified in sulphate ions, whose concentration rose drastically at the beginning of the second wet season (October-November 2020). This condition likely results from anthropogenic pollution, especially from agricultural lands that are usually left bare or uncultivated in this period. It leads to runoff with high erosion rates that easily removes and carries soil particles and chemical elements typical of farming practices, such as sulphate, downstream, increasing their presence in the waters (Huebsch *et al*., 2014; Chen *et al*., 2020). As crops grow, their roots retain more residues and eventually decrease sulphate concentrations in the river.

Table 2: Water quality equations for irrigation purposes.

Date	Ca^{2+}	Mg^{2+}	Na^{+}	K^{+}	Cl^{-}	HCO_3^{-}	SO_4^{2-}	CBE
17/02/2020	37.41	3.87	5.00	1.00	3.00	134.24	2.00	2.1
09/03/2020	32.00	16.52	8.00	1.00	3.50	213.56	14.00	-7.8
16/03/2022	62.09	7.89	10.00	1.00	3.00	244.06	12.00	-1.5
30/03/2020	49.00	7.74	7.00	2.00	2.50	231.86	14.00	-9.5
13/04/2020	52.80	9.72	9.00	2.00	4.50	219.66	12.00	-1.3
28/04/2020	56.62	11.60	16.00	2.00	5.00	231.86	15.00	3.1
12/05/2020	50.15	15.47	9.00	2.00	5.00	219.66	9.00	3.6
28/05/2020	55.72	12.09	13.00	2.00	6.00	213.56	18.00	4.1
06/06/2020	105.20	18.46	9.00	1.00	3.50	396.60	7.50	6.3
22/06/2020	106.27	15.72	11.00	1.00	3.25	433.21	6.00	-4.2
06/07/2020	104.80	11.18	11.00	1.00	3.75	405.76	6.00	-1.8
20/07/2020	114.40	10.94	9.00	1.00	3.75	427.11	17.00	-2.7
03/08/2022	111.04	11.37	7.00	1.00	3.25	424.06	4.00	0.9
18/08/2022	116.58	13.44	6.00	1.00	3.50	414.91	9.50	-1.6
31/08/2022	115.20	10.21	6.00	1.00	3.50	408.81	7.00	-5.9
19/09/2020	107.34	12.96	5.00	1.00	3.50	445.42	6.50	-9.6
26/09/2020	82.00	16.77	7.00	1.00	3.00	408.81	6.50	-0.3
12/10/2020	85.17	13.54	3.00	1.00	3.40	335.59	6.50	-4.2
26/10/2020	100.80	6.08	6.00	1.00	8.90	363.05	7.00	12.4
09/11/2020	32.00	16.04	9.00	3.00	4.00	128.13	28.00	9.5
26/11/2020	34.00	6.36	11.00	2.00	4.50	85.42	38.00	8.5
07/12/2020	39.60	5.40	9.00	2.00	4.50	128.13	20.00	4.0
21/12/2020	46.87	2.95	12.00	2.00	4.50	164.74	21.00	-1.7
04/01/2021	30.25	6.29	7.00	1.00	3.50	122.03	23.00	-4.5
19/01/2021	48.00	14.58	6.00	2.00	4.00	207.45	9.00	2.7

Notes: Major ion concentrations are expressed in mg/L and CBE in %
Source: Direct measurements in the field and laboratory analyses

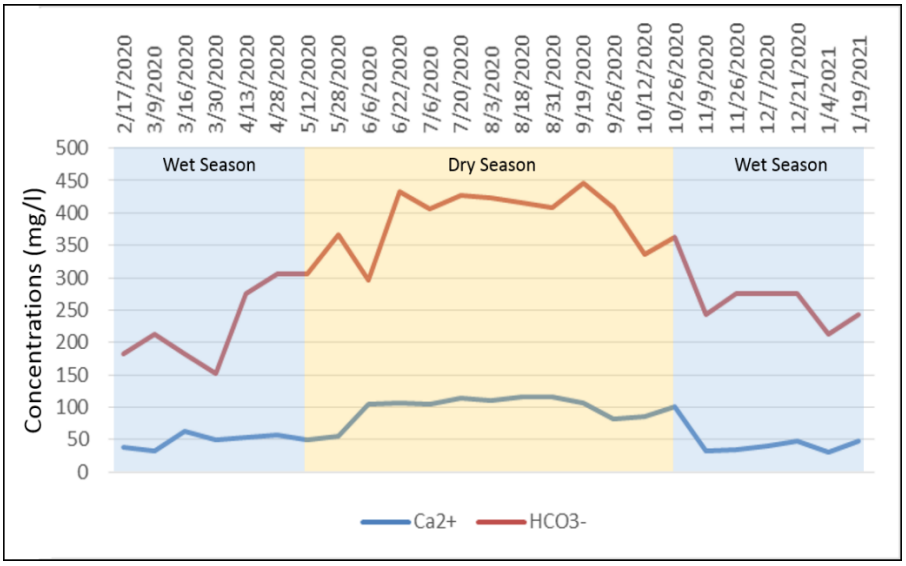


Fig. 2: Temporal variations of calcium and bicarbonate ions in the Tesih River

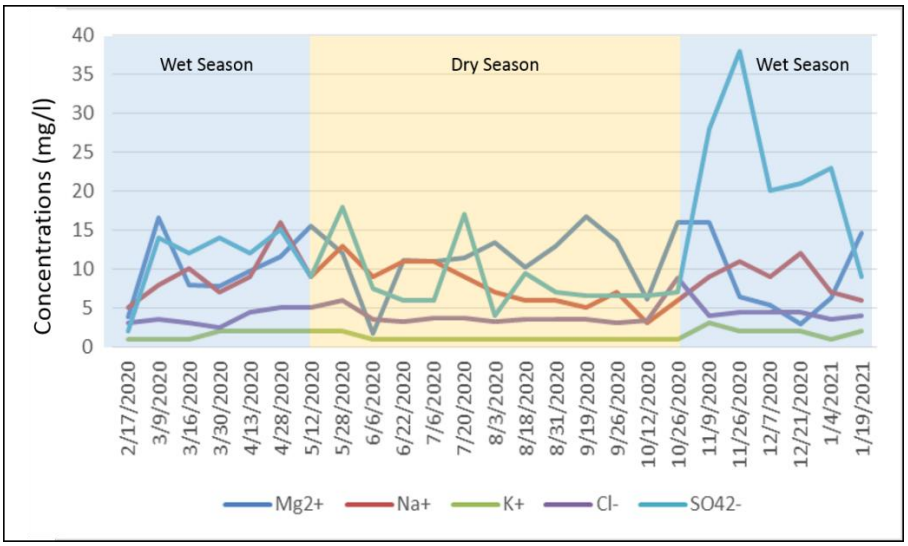


Fig. 3: Temporal variations of magnesium, sodium, potassium, chloride and sulphate in the Tesih River

Table 3 shows the physical analysis results of the water samples, including pH, TDS, temperature, SAR and Na%. The data obtained indicate that pH, EC and TDS had the same temporal pattern, where their concentrations tended to be higher in the dry season than the wet season. Similar to major ions, this pattern results from dilution by rain during the wet season and intensified water-rock interaction that is predominant during the dry season (Ramadhan et al., 2021).

The pH levels were in the range of 6.29–8.76 (mean=7.63) in the wet season and 7.91–8.62 (mean = 8.21) in the dry season. Despite the temporal variation, these data suggest alkaline water and thus indicate the dominant effect of karst aquifers, which generally have high pH (Adji *et al.*, 2017; Pratama *et al*., 2021; Mahrizkhal *et al*., 2022). This finding further supports the chemical analysis results that identified the presence of calcium and bicarbonate ions in the river, which are indicative of water flowing in and from a karst hydrogeological system. The EC levels varied from 190 to 355 µS/cm (mean=288.25 µS/cm) in the wet season and from 338 to 594 µS/cm (mean = 507.77 µS/cm) in the dry season. TDS was detected at 100–180 ppm (mean=288.25 ppm) in the wet season, or lower than in the dry season, 169–315 ppm (282.31 ppm). Even though the EC and TDS levels tended to be higher during the dry season, they were still considered very suitable (excellent to good) for agricultural irrigation, according to the Wilcox method (Wilcox, 1955).

Table 3: Physical parameters, sodium adsorption ratio (SAR) and percentage of sodium (Na%)

Date	pH	TDS (ppm)	Temp. (°C)	SAR	C	Na%	C
17/02/2020	8.76	110	27.8	0.21	E	10.	E
09/03/2020	7.68	153	29.2	0.29	E	11.2	E
16/03/2022	8.05	175	26.9	0.32	E	10.9	E
30/03/2020	8.02	174	28.0	0.25	E	10.9	E
13/04/2020	7.73	170	28.1	0.30	E	11.4	E
28/04/2020	8.15	178	30.8	0.51	E	16.5	E
12/05/2020	8.12	174	27.3	0.28	E	10.5	E
28/05/2020	7.91	169	30.4	0.41	E	14.0	E
06/06/2020	8.62	292	27.1	0.21	E	5.8	E
22/06/2020	8.23	310	26.7	0.26	E	7.1	E
06/07/2020	8.21	310	26.0	0.27	E	7.6	E
20/07/2020	8.16	310	26.6	0.22	E	5.9	E
03/08/2022	8.01	315	25.1	0.17	E	4.8	E
18/08/2022	8.07	310	28.0	0.14	E	4.0	E
31/08/2022	8.35	315	27.0	0.14	E	4.2	E
19/09/2020	8.33	310	26.0	0.12	E	3.6	E
26/09/2020	8.24	310	26.5	0.18	E	5.7	E
12/10/2020	8.15	250	26.4	0.08	E	2.8	E
26/10/2020	8.30	295	26.3	0.16	E	4.9	E
09/11/2020	6.78	120	28.4	0.32	E	13.8	E
26/11/2020	7.50	140	27.3	0.42	E	16.8	E
07/12/2020	7.29	140	26.5	0.36	E	15.5	E
21/12/2020	6.29	150	26.4	0.46	E	18.2	E
04/01/2021	7.61	100	26.1	0.30	E	14.0	E
19/01/2021	7.64	180	26.2	0.19	E	8.0	E

Notes: C (Classification) and E (Excellent)

Wet Season Dry Season

Source: Direct measurements in the field and laboratory analyses

As seen in Table 3, the SAR of the Tesih River was in the range of 0.19–0.46 (mean=0.33) in the wet season and 0.19–0.41 (mean = 0.31) in the dry season. Na% varied from 8.0 to 18.2 (mean=13.1) in the wet season and from 2.8 to 14.0 (mean=11.8) in the dry season. Both parameters had very similar temporal patterns: their levels were higher in the wet than in the dry season (Fig. 4), which can be linked to the presence of calcium. Intensive water-rock interaction during the dry season increases calcium levels, thus reducing SAR and Na%. Several other karst springs in the Ponjong Hydrogeological System of the Gunungsewu Karst Area, namely Selonjono, Gedong and Beton, also show the same temporal variation (Cahyadi *et al*., 2020a; 2020b; Cahyadi *et al*., 2022; 2023b). Despite their wide range of values, SAR and Na% were relatively low and were thus categorised as excellent throughout the year. Low SAR and Na% mean the river water is less likely to damage soil properties, harden soil, disrupt infiltration, or decrease hydraulic conductivity, aggregate stability, and drainage capacity when used for irrigation (Naseem *et al*., 2010; Dragović et al., 2012; Shah and Mistry, 2013; Patil and Nagarajan, 2015).

The Wilcox diagram analysis revealed that all the water samples of the Tesih River were categorised as Excellent to Good (Fig. 5), which is the best grade in the classification. This means that even though the Wilcox diagram incorporates EC and Na%, the results are the same as the suitability classification using Na% alone. The USSL analysis categorised the water samples into Moderate to good (C2S1) and Good (C1S1); both are also the highest levels in the USSL classification (Fig. 6). The USSL diagram has the most classes (16) among the nine methods used in this research and thus provides more detailed results. In this case, what appears to be 'Excellent to good' in the Wilcox classification can be further divided into 'Moderate to good' and 'Good'.

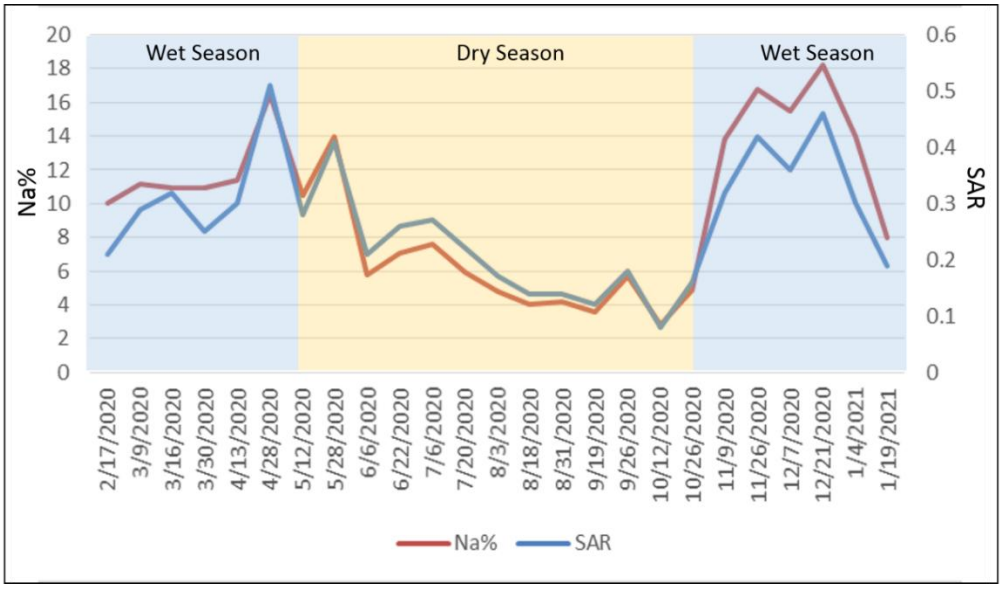


Fig. 4: Temporal variations of Na% and SAR in the Tesih River

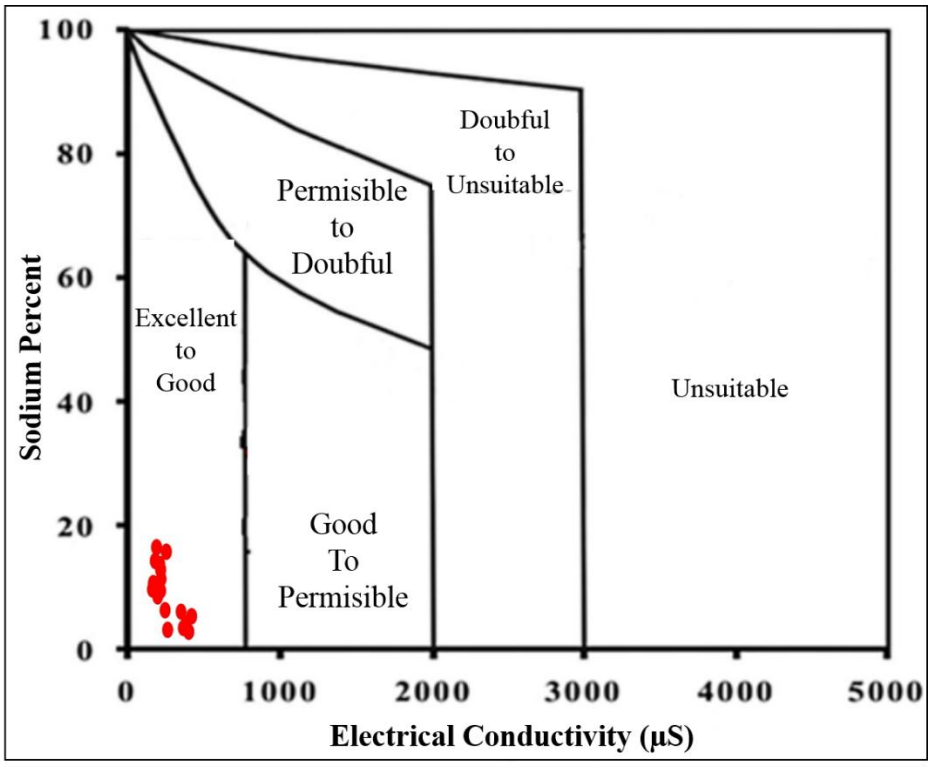


Fig. 5: Wilcox diagram of the Tesih River

Table 4 shows the results of water suitability analysis for irrigation using residual sodium carbonate (RSC), permeability index (PI), magnesium hazard (MH), Kelly's ratio (KR), and hardness (H). Only RSC and H showed variations in the water suitability classification. PI, MH, and KR analyses placed the river water into Good and Suitable, while the RSC method categorised it into two: Good and Very good. Based on the H values, the water fell into three categories: Hard, Very hard and Moderate. PI, MH, and KR only have two classes and are thus less sensitive to hydrogeochemical variations, even though they use similar parameters as RSC and H. On the contrary, RSC and H have more water suitability classes for irrigation, three and four, respectively. Moreover, their parameters fit the conditions of the study area, i.e., the influence of karst aquifers with dominant calcium and bicarbonate ions in the water.

Table 4: Water suitability analysis of the Tesih River for irrigation based on RSC, PI, MH, KR and H

Date	RSC	C	PI	C	MH	C	KR	C	H	C
17/02/2020	0.015	G	70.8	G	14.6	S	0.10	S	109.4	H
09/03/2020	0.544	G	67.1	G	46.0	S	0.12	S	147.7	H
16/03/2022	0.252	G	58.2	G	17.3	S	0.12	S	187.6	H
30/03/2020	0.718	G	66.6	G	20.7	S	0.10	S	154.2	H
13/04/2020	0.165	G	59.8	G	23.3	S	0.11	S	171.9	H
28/04/2020	0.020	G	59.1	G	25.3	S	0.18	S	189.1	H
12/05/2020	-0.175	VG	54.9	G	33.7	S	0.10	S	188.8	H
28/05/2020	-0.275	VG	56.1	G	26.4	S	0.15	S	188.9	H
06/06/2020	-0.268	VG	41.1	G	22.4	S	0.06	S	338.7	VH
22/06/2020	0.504	G	44.4	G	19.6	S	0.07	S	330.1	VH
06/07/2020	0.500	G	46.1	G	15.0	S	0.08	S	307.8	VH
20/07/2020	0.391	G	43.4	G	13.6	S	0.06	S	330.8	VH
03/08/2022	0.474	G	43.4	G	14.4	S	0.05	S	324.2	VH
18/08/2022	-0.123	VG	39.9	G	16.0	S	0.04	S	346.5	VH
31/08/2022	0.111	G	41.6	G	12.7	S	0.04	S	329.8	VH
19/09/2020	0.878	G	44.0	G	16.6	S	0.03	S	321.5	VH
26/09/2020	1.228	G	50.1	G	25.2	S	0.06	S	273.7	H
12/10/2020	0.136	G	45.1	G	20.8	S	0.02	S	268.4	H
26/10/2020	0.420	G	46.6	G	9.0	S	0.05	S	276.9	H
09/11/2020	-0.816	VG	55.6	G	45.3	S	0.13	S	145.8	M
26/11/2020	-0.82	VG	61.6	G	23.6	S	0.22	S	111.1	M
07/12/2020	-0.32	VG	65.5	G	18.4	S	0.16	S	121.1	M
21/12/2020	0.118	G	69.8	G	9.4	S	0.20	S	129.3	M
04/01/2021	-0.027	VG	73.7	G	25.5	S	0.15	S	101.4	M
19/01/2021	-0.195	VG	54.6	G	33.4	S	0.07	S	179.8	H

Notes: C (Classification), G (Good), VG (Very Good), S (Suitable for Irrigation), H (Hard), VH (Very Hard), and M (Moderate)

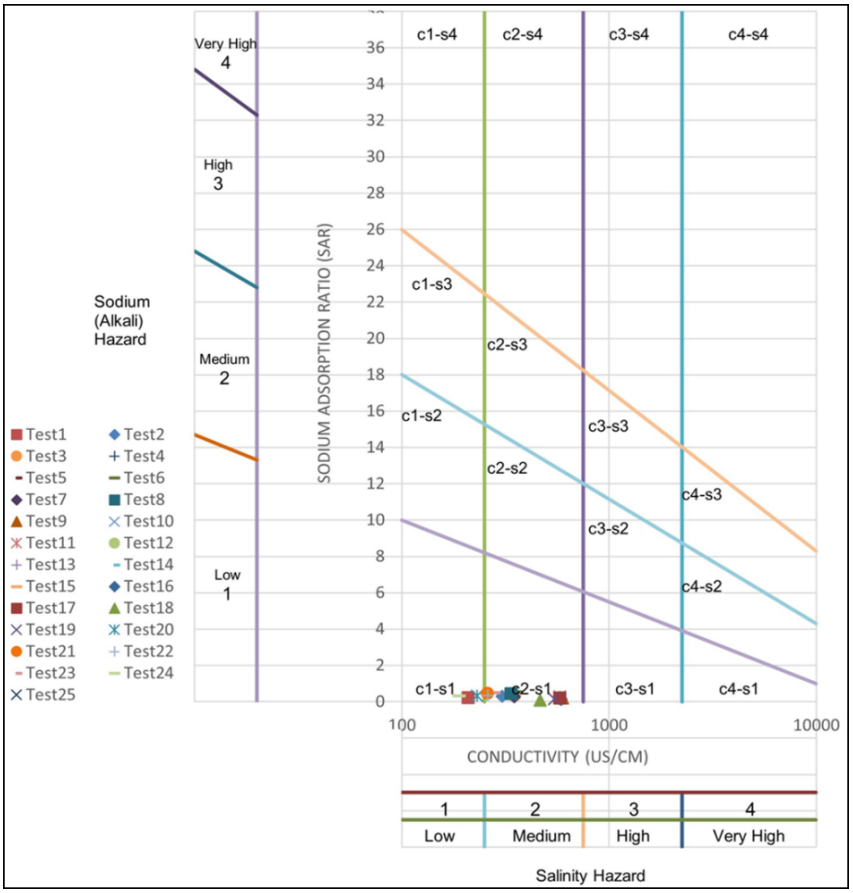


Fig. 6: USSL diagram of the Tesih River

4. Conclusion

This research confirms that seasons and geological conditions strongly influence the suitability of a water body for irrigation. During months of no substantial rain, little to no water flows from the ancient volcanic aquifer in the Tesih Watershed. This means only water from the karst aquifer feeds the Tesih River. Consequently, karstic characteristics such as calcium and bicarbonate ions dominate the water's hydrogeochemistry as a result of intensified water-rock interaction. In contrast, these ions decrease during months of rain because dilution by rainwater is the predominant process influencing their presence during the wet season. Furthermore, the river water samples are classified as Good and Very good (based on Na%, SAR, RSC and PI), Excellent to good (Wilcox diagram), Moderate to good and Good (USSL diagram), and Suitable for irrigation (MH, KR and H). From these results, it can be inferred that the influence of seasonal and geological conditions on hydrogeochemical variations does not change the classification of the water suitability for irrigation.

Hydrogeochemical analysis results should be considered in selecting the methods of water suitability assessment for irrigation. This is to find those with parameters fitting to and, thus, more sensitive to hydrogeochemical changes in the study area. In addition, methods with more classes can explain variations in water suitability better and are more practical for agricultural land and crop management.

5. Acknowledgements

This research is part of the Independent Research Grant awarded to the Faculty of Geography, Universitas Gadjah Mada, Indonesia, for the year 2025, Batch 1, and is conducted based on the Decree of the Dean of the Faculty of Geography, Universitas Gadjah Mada, Number 109/UN1/GE/KPT/2025. The authors would like to thank the people of Sawahan and Tambakromo Villages (Ponjong, Gunungkidul, Indonesia) for granting the research permit. Gratitude is also extended to Lili Ismangil for his invaluable assistance during the data collection.

6. Conflict of Interest

The authors declare no conflict of interest.

7. Funding Statement

This research received no external funding.

8. Author Contributions

Ahmad Cahyadi: Conceptualization, Methodology, Data Curation, Software, Writing-Original draft preparation

Indra Agus Riyanto: Data curation, software, validation

Marseli Nabila Putri: Data curation, writing-reviewing and editing, manuscript layout

Rizka Novi Ramadhania: Data curation, writing-reviewing and editing

The authors confirm that these statements accurately represent their respective contributions to the work and that all authors have reviewed and approved the final version of the manuscript.

9. References

Abbasian, A., Mohaddesi, A., Aminpanah, H., Ghasemi, S.M.S., Javadi, M. and Ebrahimian, M. 2014. Evaluation of Rice Cultivars in Different Irrigation Treatments Based on Sensitive and Tolerance Indices. Agriculture and Forestry, 60(2), pp. 251-259. https://www.agricultforest.ac.me/paper.php?journal_id=182andid=2299

Abdoulaye, A.O., Lu, H., Zhu, Y., Hamoud, Y.A. and Sheteiwy, M. 2019. The global trend of the net irrigation water requirement of maize from 1960 to 2050. Climate, 7(10), pp. 1-19. https://doi.org/10.3390/cli7100124

Adji, T.N., Haryono, E., Fatchurohman, H. and Oktama. R. 2017. Spatial and temporal hydrochemistry variations of karst water in Gunung Sewu, Java, Indonesia. Environmental Earth Sciences, 76(20). https://doi.org/10.1007/s12665-017-7057-z

Adji, T.N., Haryono, E., Mujib, A., Fatchurohman, H. and Bahtiar, I.Y. 2019. Assessment of aquifer karstification degree in some karst sites on Java Island. Indonesia. Carbonates and Evaporites, 34(1), pp. 53–66. https://doi.org/10.1007/s13146-017-0403-0

Al-Obeidi, Y.F.G., Al-joboury, M.A.J. and Ismael, A.A. 2025. Hydrochemical Assessment of Groundwater for Irrigation and Drinking Water in Al-Kubba and Sherikhan Area, Northwest of Mosul City. Iraqi National Journal of Earth Science, 25(3), pp. 214-225. https://doi.org/10.33899/earth.2024.140285.1083

Al-Saffah, A.M.R. and Al-Mashhadany, M.H.S. 2025. Evaluation of Groundwater in Makhmur District for Irrigation Purposes Using Artificial Intelligence. Iraqi National Journal of Earth Science, 25(3), pp. 123-134. https://doi.org/10.33899/earth.2024.147722.1245

Ayers, R.S. and Westcot, D.W. 1985. Water Quality for Agriculture. Rome, Food and Agriculture Organization of the United Nations (FAO).

Barichello, R. and Patunru, A. 2009. The magazine of food, farm, and resource issues. Agriculture in Indonesia: Lagging Performance and Difficult Choices, 24(2). http://www.choicesmagazine.org

Bhat, A.M., Wani, S.A., Singh, V.K., Sahoo, J., Tomar, D. and Sanswal, R. 2018. An Overview of the Assessment of Groundwater Quality for Irrigation. Journal of Agricultural Science and Food Research, 9(1), pp. 1-9.

Cahyadi, A., Adji, T.N., Haryono, E., Widyastuti, M., Aji, A.P.K., Naufal, M. and Riyanto, I.A. 2020a. Temporal Variation of Tropical Karst Groundwater Suitability for Irrigation in Gremeng Resurgence, Gunungsewu Karst Area. Indonesia. E3S Web of Conferences, 202. https://doi.org/10.1051/e3sconf/202020204004

Cahyadi, A., Haryono, E., Adji, T.N., Widyastuti, M., Riyanto, I.A., Aji, A.P.K., Fatchurohman, H., Tastian, N.F. and Muhammad, D.T.N. 2020b. Temporal variation of water suitability for paddy irrigation needs at karst springs influenced by allogenic recharge in Gunungsewu Karst Area, Indonesia. E3S Web of Conferences, 200. https://doi.org/10.1051/e3sconf/202020002024

Cahyadi, A., Haryono, E., Adji, T.N., Widyastuti, M., Riyanto, I.A., Muhammad, D.T.N. and Tastian, N.F. 2021. Rainfall variability in Gunung Sewu Karst Area, Java Island, Indonesia. Indonesian Journal of Forestry Research, 8(1), pp. 23–35. https://doi.org/10.20886/IJFR.2021.8.1.23-35

Cahyadi, A., Adji, T.N., Haryono, E., Widyastuti, M. and Agniy, R.F. 2022a. Tracing Flow Directions of the Pentung Allogenic River in Gunungsewu Karst Area, Gunungkidul, using Artificial Tracer Test. IOP Conference Series: Earth and Environmental Science, 1098(1), 012048. https://doi.org/10.1088/1755-1315/1098/1/012048

Cahyadi, A., Haryono, E., Adji, T.N., Widyastuti, M., Riyanto, I.A., Acintya, R. and Qushoyyi, N.F. 2022b. Hydrogeochemical characteristics and water quality of karst springs in Selonjono Karst Gunungsewu Special Region of Yogyakarta (Karakteristik hidrogeokimia dan kualitas air pada mata air karst Selonjono Karst Gunungsewu Daerah Istimewa Yogyakarta). Jurnal Geodika, 6(2), pp. 175-185. (in Indonesian) https://doi.org/10.29408/geodika.v6i2.6100

Cahyadi, A., Riyanto, I.A., Ramadhan, F., Widyastuti, M., Fatchurohman, H. and Adji, T.N. 2023a. Multitemporal water quality analysis of an epikarst spring for agricultural irrigation in the Gunungsewu Karst Area, Indonesia. AIP Conference Proceedings, 2683. https://doi.org/10.1063/5.0145414

Cahyadi, A., Riyanto, I. A., and Adji, T. N. 2023. Suitability of Water from Tropical Epikarst Spring for Irrigation in the Gunungsewu Karst Area, Indonesia. IOP Conference Series: Earth and Environmental Science, 1268(1). https://doi.org/10.1088/1755-1315/1268/1/012008

Chen, J., Luo, M., Ma, R., Zhou, H., Zou, S. and Gan, Y. 2020. Nitrate Distribution Under the Influence of Seasonal Hydrodynamic Changes and Human Activities in Huixian Karst Wetland, South China. Journal of Contaminant Hydrology, 234, 103700. https://doi.org/10.1016/j.jconhyd.2020.103700

Day, A. 2019. World Water Demand Will Increase 55% by 2050. https://savethewater.org/waterdemand-to-increase-55-globally-by-2050/

Döll, P. and Siebert, S. 2002. Global modeling of irrigation water requirements. Water Resources Research, 38(4), pp. 1–10. https://doi.org/10.1029/2001wr000355

Dragović, S. 2012. Effect of Irrigation on Field Crops Yield under the Variable Agro-climatic Condition of Serbia. Agriculture and Forestry, 54(08), pp. 25-40. https://www.agricultforest.ac.me/paper.php?journal_id=157andid=2016

Dragović, S., Spalević, V., Radojević, V., Cicmil, M. and Uščumlić, M. 2012. Importance of Chemical and Microbiological Water Quality for Irrigation in Organic Food Production. Agriculture and Forestry, 55(09), pp. 83-102. https://www.agricultforest.ac.me/paper.php?journal_id=158andid=2037

Food and Agriculture Organization of the United Nation (FAO). 2017. Water for Sustainable Food and Agriculture: A Report Produced for the G20 Presidency of Germany. Roma, FAO.

Fulazzaky, M.A. 2017. Participation of farmers in irrigation water management in Indonesia: a review. In Irrigation and Drainage, 66(2), pp. 182–191. John Wiley and Sons Ltd. https://doi.org/10.1002/ird.2085

Hafiane, F.Z., Tahri, L., Nouayti, N., el Jarmouni, M., Arifi, K., Elamrani Idrissi, A. and Fekhaoui, M. 2020. Assessment of spatial and seasonal nitrate variation of groundwater in the irrigated perimeter (Tadla plain, Morocco). Agriculture and Forestry, 66(1), pp. 203–214. https://doi.org/10.17707/AgricultForest.66.1.19

Huebsch, M., Fenton, O., Horan, B., Hennessy, D., Richards, K.G., Jordan, P., Goldsceider, N., Butcher, C. and Blum, P. 2014. Mobilisation or Dilution? Nitrate Response of Karst Springs to High Rainfall Events. Hydrology and Earth System Science, 18(11), pp. 4423-4435. https://doi.org/10.5194/hess-18-4423-2014

Ibrahim, I.F. and Al-Youzbakey, K.T. 2024. Water Quality Evaluation of the Main Valley for Agricultural Uses on the Left Side of Mosul City. Iraqi National Journal of Earth Science, 24(1), pp. 62-89. https://doi.org/10.33899/earth.2023.141188.1098

Ismail, A.H., Shareef, M.A. and Alatar, F.M. 2019. Hydrochemistry of Groundwater and its Suitability for Drinking and Irrigation in Baghdad. Iraq. Environmental Processes, 6(2), pp. 543–560. https://doi.org/10.1007/s40710-019-00374-x

Kateb, A.S. and Al-Youzbakey, K.T. 2025. Sulphate Suggested Guide Groundwater Quality for Irrigation in the Eastern Regions of Nineveh Governorate. Iraqi National Journal of Earth Science, 25(1), pp. 70-86. https://doi.org/10.33899/earth.2024.143216.1142

Khasanah, N., Tanika, L., Pratama, L.D.Y., Leimona, B., Prasetiyo, E., Marulani, F., Hendriatna, A., Zulkarnain, M.T., Toulier, A. and van Noordwijk, M. 2021.

Groundwater-extracting rice production in the Rejoso watershed (Indonesia) reducing urban water availability: Characterisation and intervention priorities. Land, 10(6). https://doi.org/10.3390/land10060586

Kusumayudha, S.B. 2009. Detecting springs in the coastal area of the Gunungsewu Karst Terrain, Yogyakarta Special Province. Indonesia. Using fractal geometry analysis. IPTEK Journal of Science and Technology, 2(4), pp. 1–12. https://doi.org/10.12962/j20882033.v20i4.86

Ma'Mun, S.R., Loch, A. and Young, M.D. 2021. Sustainable irrigation in Indonesia: A case study of Southeast Sulawesi Province, Land Use Policy, 111. https://doi.org/10.1016/j.landusepol.2021.105707

Maat, H. 2014. Agriculture in Indonesia. In Encyclopaedia of the History of Science, Technology, and Medicine in Non-Western Cultures, 1–5. Netherlands: Springer. https://doi.org/10.1007/978-94-007-3934-5_10229-1

Mahrizkhal, D.S., Priambada, A.P., Al-Ghozali, M.Q., Rahmawati, A.I., Cahyadi, A., Haryono, E. and Adji, T.N. 2022. Variation of Saturation Indices (SIcal) with respect to Calcite Mineral at Kalisirah and Jumbleng Springs, South Gombong Karst, Central Java, Indonesia. IOP Conference Series: Earth and Environmental Science, 1039(1). https://doi.org/10.1088/1755-1315/1039/1/012001

McGeorge, W.T. 1954. Diagnosis and improvement of saline and alkaline soils. Soil Science Society of America Journal, 18(3), pp. 348.

Mediawan, Y., Montarcih, L., Soetopoi, W. and Prayogo, T.B. 2021. Water balance supporting the irrigation water demand in Java Island, Indonesia. Indonesian Journal of Geography, 53(1), pp. 9–19. https://doi.org/10.22146/IJG.59102

Mohammed, M.N. 2011. Quality Assessment of Tigris River by Using Water Quality Index for Irrigation Purpose. European Journal of Scientific Research, 57, pp. 15-28.

Mohammed, A.H., Mohammed, A.A., Salih, S.A. and Salih, A.M. 2025. Hydro-morphometric and Hydrochemical Criteria to Select the Optimal Location for Small Dam in Um Al-Shibabit Valley, Al-Shirqat, Northern Iraq. Iraqi National Journal of Earth Science, https://doi.org/10.33899/earth.2025.145119.1186

Mohtar, R.H. and Fares, A. 2022. The Future of Water for Food. Frontiers in Sustainable Food Systems, 6, 880767. https://doi.org/10.3389/fsufs.2022.8880767

Naseem, S., Hamza, S. and Bashir, E. 2010. Groundwater Geochemistry of Winder Agricultural Farms, Balochistan, Pakistan and Assessment for Irrigation Water Quality. European Water, 31, pp. 21–32. http://ewra.net/ew/pdf/EW_2010_31_03.pdf

Nishanthiny, S.C., Thushyanthy, M., Barathithasan, T. and Saravanan, S. 2010. Irrigation Water Quality Based on Hydrochemical Analysis, Jaffna, Sri Lanka. American-Eurasian Journal of Agricultural and Environmental Sciences, 7, pp. 100-102.

Opperman, J. 2023. Managing Rivers as Systems to Maintain Irrigation and Other Benefits. https://www.forbes.com/sites/jeffopperman/2023/06/29/managing-rivers-as-systems-to-maintain-irrigation-and-other-benefits/?sh=19cf819d82c5

Paruch, A.M., Mæhlum, T. and Robertson, L. 2015. Changes in Microbial Quality of Irrigation Water under Different Weather Conditions in Southeast Norway. Environmental Processes, 2(1), pp. 115–124. https://doi.org/10.1007/s40710-014-0054-2

Patil, S.K. and Nagarajan, R. 2015. Geospatial Assessment of Irrigation Water Potential for Black Soil Salinization. Agriculture and Forestry, 61(2), pp. 189-199. https://www.agricultforest.ac.me/paper.php?journal_id=190andid=2425

Pratama, A.D., Dwiputra, D.S., Nurkholis, A., Haryono, E., Cahyadi, A., Agniy, R.F. and Adji, T.N. 2021. Factors Affecting Hydrochemistry of Karst Springs and their Relationship to Aquifer Development. Environmental Processes, 8(4), pp. 1379–1413. https://doi.org/10.1007/s40710-021-00547-7

Rahardjo, W., Sukandarrumidi and Rosidi, H.M.D. 1995. Geological map of the Yogyakarta sheet Java. Bandung, Geological Research and Development Centre.

Ramadhan, F., Riyanto, I.A., Cahyadi, A., Naufal, M., Widyastuti, M. and Adji, T.N. 2021. Impact of Tropical Cyclone Savannah on Stream Hydrogeochemical Characteristics of Guntur Spring, Gunungsewu Karst Area. (Dampak Siklon Tropis Savannah Terhadap Karakteristik Hidrogeokimia Aliran pada Mata Air Guntur, Kawasan Karst Gunungsewu). Jurnal Geografi : Media Informasi Pengembangan dan Profesi Kegeografian, 18(2), pp. 90–96. (in Indonesian) https://doi.org/10.15294/jg.v18i2.30293

Riyanto, I.A., Widyastuti, M., Cahyadi, A., Agniy, R.F. and Adji, T.N. 2020. Groundwater Management Based on Vulnerability to Contamination in the Tropical Karst Region of Guntur Spring, Gunungsewu Karst, Java Island, Indonesia. Environmental Processes, 7(4), pp. 1277–1302. https://doi.org/10.1007/s40710-020-00460-5

Salem, H.S., Pudza, M.Y. and Yihdego, Y. 2022. Water Strategies and Water–Food Nexus: Challenges and Opportunities Towards Sustainable Development in Various Regions of the World. Sustainable Water Resources Management, 8(14). https://doi.org/10.1007/s40899-022-00676-3

Samardžić, S., Pejić, B., Bajić, I., Ćirić, V., Aksić, M. and Vojnov, B. 2022. Water–yield relations of processing potato under surface and shallow subsurface drip irrigation in temperate climatic environment. Agriculture and Forestry, 68(4), pp. 89–105. https://doi.org/10.17707/AgricultForest.68.4.08

Shah, S.M. and Mistry, S.M. 2013. Groundwater Quality Assessment for Irrigation Use in Vadodara District, Gujarat, India. Engineering and Technology, 23, pp. 7-23. https://zenodo.org/record/1087474/files/16547.pdf

Šimunić, I., Likso, T., Husnjak, S., Orlović-Leko, P. and Bubalo, K.M. 2021. Analysis of climate elements in the northeastern region of Croatia for the purpose of determining irrigation requirements of maize and soybean on drained soil. Agriculture and Forestry, 67(2), pp. 7–20. https://doi.org/10.17707/AgricultForest.67.2.01

Šoškĭć, S., Spalević, V. and Kužel, S. 2001. Analiza Eksploatacije Zalivnog Polja U Uslovima Navodnjavanja Sistemom za Vještačko Kišenje na Ćemovskom Polju. Poljoprivreda Šumarstvo, 47(1-2), pp. 29-37. http://www.agricultforest.ac.me/data/20200207-00%20Content112.pdf

Starr, G. and Levison, J. 2014. Identification of Crop Groundwater and Surface Water Consumption Using Blue and Green Virtual Water Contents at a Subwatershed Scale. Environmental Processes, 1(4), pp. 497–515. https://doi.org/10.1007/s40710-014-0040-8

Tanaskovikj, V., Cukaliev, O., Markoski, M., Srdjevic, B., Spalevic, V., Simunic, I., Moteva, M. and Djurovic, N. 2014. The Influence of Irrigation and Drip Fertigation Regime on Specific Water Consumption and Evapotranspiration Coefficient in Tomato Crop Production, Agriculture and Forestry, 60(4), pp. 243-254. https://www.agricultforest.ac.me/paper.php?journal_id=185andid=2359

Telteu, C.E., Müller, S.H., Burek, P., Liu, X., Eric, S.B.J., Seaby, A.L., Grillakis, M., Newland, S., Satoh, Y., Rakovec, O., Stacke, T., Chang, J., Wanders, N., Lovekumar, S.H., Trautmann, T., Mao, G., and Herz, F. 2021. Understanding each other's models: a standard representation of global water models to support improvement. intercomparison. and communication. Water Geoscientific Model Development, 14(6), pp. 1-56, https://doi.org/10.5194/gmd-2020-367

Ticker, D., Parker, H., Moncrieff, C.R., Oates, N.E.M., Ludi, E. and Acreman, M. 2017. Managing Rivers for Multiple Benefits – a Coherent Approach to Research, Policy and Planning. Frontiers in Environmental Science, 15, 4. https://doi.org/10.3389/fenvs.2017.00004

Tirtalistyani, R., Murtiningrum, M. and Kanwar, R.S. 2022. Indonesia Rice Irrigation System: Time for Innovation. In Sustainability, 14(19). https://doi.org/10.3390/su141912477

Wilcox, W.T. 1955. Classification and use of irrigation waters. United States, Department of Agriculture, 21, pp. 696.

Iraqi National Journal of Earth Science, Vol. 26, No. 04, 2026 (54-67)

Iraqi National Journal of Earth Science

www.earth.uomosul.edu.iq

مدى ملاءمة المياه لري حقول الأرز في حوض مائي استوائي تسوده صخور بركانية قديمة وحجر جيري (إندونيسيا)

أحمد كاهيادي[1*]، إندرا أغوس ريانتو[2]، مارسيللي نابيلا بوتري[1]، ريزكا نوفي رامادانيا[1]

ahmad.cahyadi@ugm.ac.id indra.agus.r@gmail.com marselli.nabila2103@mail.ugm.ac.id

rizka.novi.ramadhania@mail.ugm.ac.id

[1] قسم الجغرافيا البيئية، كلية الجغرافيا، جامعة غادجاه مادا، يوجياكارتا، إندونيسيا.

[2] شركة بي تي بيلسارت تامبانغ كينسانا، جاكرتا، إندونيسيا.

** الباحث المراسل.*

تاريخ الاستلام: 15 تموز 2025 تاريخ المراجعة: 03 أيلول 2025 تاريخ القبول: 04 تشرين الأول 2025

تاريخ النشر الالكتروني: 01 تشرين الأول 2026

الملخص

تُعد جودة المياه المناسبة لنمو النباتات أمراً بالغ الأهمية لضمان إنتاجية عالية في مجال إنتاج الغذاء. ومع ذلك، فإن الخصائص الهيدرولوجية والجيولوجية للمنطقة تضفي عليها سمات مميزة تتطلب فهماً دقيقاً لتطبيق الممارسات الزراعية السليمة. هدفت هذه الدراسة إلى تحديد التباين الزمني في مدى ملاءمة مياه نهر "تيسيه" (Tesih) لأغراض الري. ومن المتوقع أن يقدم هذا البحث لمحة عامة عن التباين الزمني في ملاءمة المياه للري داخل حوض مائي تسوده صخور بركانية قديمة وتكوينات من الحجر الجيري التي شكلت مناطق كارستية. وعلاوة على ذلك، تهدف الدراسة إلى تسليط الضوء على تأثير الظروف المناخية –التي يحكمها المناخ الاستوائي وخصائص الرياح الموسمية الآسيوية–الأسترالية في موقع الدراسة– على مدى ملاءمة المياه للري. الطرق المستخدمة: النسبة المئوية للصوديوم (%Na)، ونسبة امتزاز الصوديوم (SAR)، ومخطط ويلكوكس (Wilcox)، ومخطط USSL، وعسر الماء (H)، ومخاطر المغنيسيوم (MH)، ونسبة كيلي (KR)، ومؤشر النفاذية (PI)، وكربونات الصوديوم المتبقية (RSC). وقد أظهرت التحاليل أن مياه النهر كانت جيدة (استناداً إلى %Na ومخطط USSL وRSC)، أو جيدة جداً (وفقاً لـ SAR وPI)، أو ممتازة (وفقاً لمخطط ويلكوكس)، أو مناسبة للري (وفقاً لـ H وMH وKR). وبشكل عام، يتمتع النهر بخصائص فيزيائية وكيميائية ملائمة لدعم نمو المحاصيل دون الإضرار بخصائص التربة.

الكلمات المفتاحية:

ري حقول الأرز، الكارست (التضاريس الكارستية)، صخور بركانية قديمة، جودة المياه، الهيدروجيوكيمياء.

DOI: 10.33899/injes.v26i4.56030, *©Authors, 2026, College of Science, University of Mosul.*

This is an open-access article under the CC BY 4.0 license (http://creativecommons.org/licenses/by/4.0/)

Iraqi National Journal of Earth Science, Vol. 26, No. 04, 2026 (68-80)

Iraqi National Journal of Earth Science

www.earth.uomosul.edu.iq

Petrography, Facies Analysis, and Depositional Environment of the Sargelu Formation (Middle Jurassic), in a Selected Section, Northeastern Iraq

Noor T. Al-Taee [1*]

noortalal@uomosul.edu.iq

[1] *Department of Geology and Petroleum, College of Science, University of Mosul, Mosul, Iraq.*
** Correspondence author.*

Received: 02 October 2025 Received in revised form: 28 December 2025 Accepted: 02 February 2026
Available online: 01 October 2026

Abstract

The study deals with the sedimentology of the Middle Jurassic Sargelu Formation and its implications for facies analysis and depositional environment. The studied section is located in Sulaymaniyah City, between the Sargelu and Goshan villages, within the Highfolded zone, northeastern Kurdistan Region of Iraq. In the study area, the Formation is characterized by a succession of limestone interbedded with thin beds of dolomite and thin shale. It overlies the Sehkaniyan Formation and underlies the Naokelekan Formation. Twenty-two thin sections from the limestone succession were chosen for petrographic analysis using a polarizing microscope to determine their petrographic constituents. The petrographic study of carbonate units showed that they consist mainly of skeletal grains (calcospheres, radiolaria, pelecypods, planktonic foraminifera, and ostracods). The successions were affected by several diagenetic processes such as recrystallization, dolomitization, compaction, and Pyritization. Three different microfacies were recognized that showed a wide range of facies associations. These are further subdivided into eight sub-microfacies, suggesting the deposition of the Sargelu Formation in the deep shelf and deep marine basinal environments.

Keywords:

Facies analysis, Jurassic, Deep marine, Sargelu Formation, Iraq.

DOI: 10.33899/injes.v26i4.55951, ©Authors, 2026, College of Science, University of Mosul.

This is an open-access article under the CC BY 4.0 license (http://creativecommons.org/licenses/by/4.0/).

==========

1. Introduction

The Sargelu Formation is a Middle Jurassic carbonate succession, deposited in the Unstable Shelf of northeastern Iraq, between the High and some nearby Low Folded Zones (Buday, 1980; Jassim and Goff, 2006). Given the importance of hydrocarbons, it is necessary to define their environment in previously unstudied locations to provide a comprehensive overview, especially for the current study site. The first description of the Sargelu Formation was done by Wetzel (1948 in Bellen et al., 1959) in Sulaymaniyah City (Surdash anticline). Previous studies on the formation have been conducted using various surface and subsurface detectors and have described the mineralogical, field, and lithological characteristics (Bitman et al., 2004; Al-Ahmad, 2006; English et al., 2015; Al-Trim et al., 2022; Rasoul et al., 2024). All sedimentological and stratigraphic studies of the formation suggest that the Sargelu Formation was deposited in an open, deep marine shelf environment extending to the slope and basin (Buday, 1980; Koutsoukos, 1985; Abdullah et al., 2015). This study aims to identify the main petrographic components, diagenetic processes, facies associations, and to reconstruct the depositional environment of the Sargelu Formation in the studied area.

2. Geological setting and location

The studied section is located in Sulaymaniyah City, lying between the Sargelu and Goshan villages, in the northeastern Kurdistan Region of Iraq. The latitude is 35°17'46.1"N and the longitude is about 45°22'49.6"E.

Tectonically, the investigated section belongs to the Western Zagros Fold–Thrust Belt in northern Iraq. It occupies the transitional area between the High Folded and Low Folded zones of the Unstable Shelf as defined (Buday, 1980; Jassim and Goff, 2006). According to Fouad (2015), the succession is located at the High Folded Zones-Thrust Zone boundary, which arose in the northeast, forming the Zagros Fold-Thrust-Belt (Figure 1A and B).

The Sargelu Formation is part of the Arabian Plate (AP7) Tectonostratigraphic Megasequence, which started from the Late Toarcian-Early Tithonian (Mid- Late Jurassic) (Sharland et al., 2001). During the Permian and Triassic, the Neo-Tethys opening began and continued to its maximum width during the Late Triassic to Middle Jurassic (Saadouni and Al-Sharhan, 2004). Sedimentation then occurred in a limited, deep aquatic environment during the Middle Jurassic, and the basin During the Kimmeridgian–Early Tithonian, progressive basin restriction promoted widespread evaporitic conditions (Jassim and Goff, 2006; Tobia, 2019). Wetzl (1948 in Bellen et al., 1959) described the lithologic composition of the Sargelu Formation in the Surdash anticline, and the Sargelu–Naokelekan contact as sharp and conformable, transitioning from thin bituminous black shales with chert bands into well-bedded grey stromatolitic limestone.

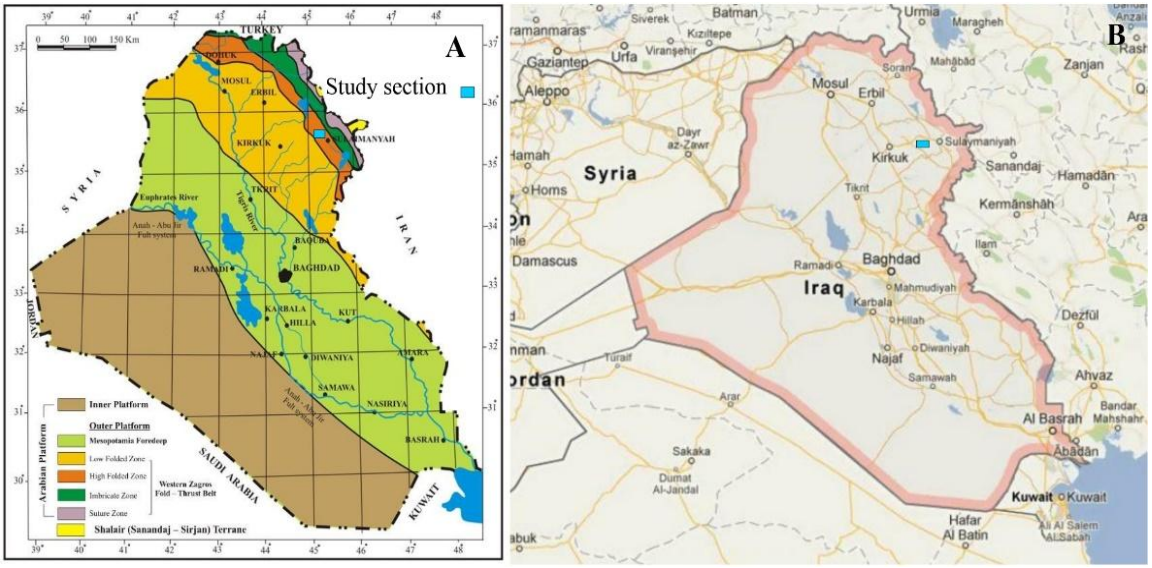


Fig. 1: A. Tectonic division, from Fouad (2015) of Iraq, showing the location of the section. B.Geographical location of Iraq

The Middle Jurassic Sargelu Formation of Iraq accumulated during the development of the Mesopotamian intra-shelf basin, which became separated from the Neo-Tethys Ocean as a consequence of rifting along the northeastern margin of the Arabian Plate (Jassim and Boday 2006).

3. Lithostratigraphy

The Sargelu succession attains a thickness of approximately 78 m in the studied section. Both its basal and upper boundaries are conformable, with gradual transitions to the underlying (Sehkanyan Formation) and the overlying (Naokelekan Formation)(Fig. 2A, B). The Sargelu Formation begins with 10 m-thick yellowish-white bioturbated limestone, followed by a sequence of alternate limestone beds (not exceeding 1m) with shale beds (30 cm – 1m), this sequence reaches about 53 meters thick. Then, followed by a succession of yellowish-white limestone and dolomitic limestone beds reaching 10 meters thick. After that, the yellowish-white limestone beds continue, with shale beds 1m thick between them. Finally, the limestone continues to the end of the studied section, with thin chert layers interspersed with dolomitic limestone beds, which ends with limestone of the Naokelekan Formation (Figure 2).



Fig. 2: The contact of the Sarjelo Formation, A: the lower contact with the underlying Sehkanyan Formation, and B: the Upper contact with the overlying Naokelekan Formation

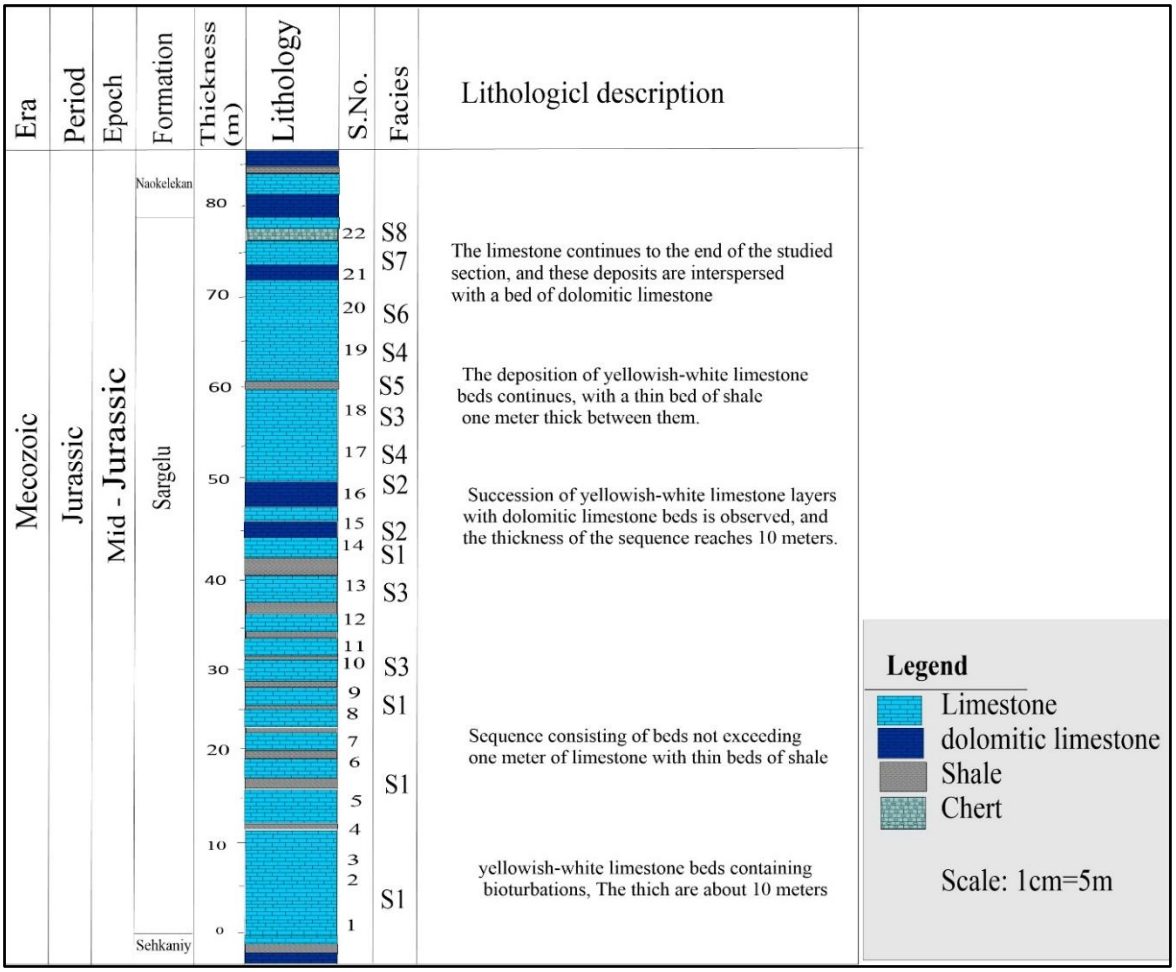


Fig. 3: Lithological column of the Sargelu Formation

4. Petrography

The Sargelu Formation is characterized by well-preserved fossils that enable researchers to identify different facies and infer the depositional environments. The skeletal grains include both whole and/ or biogenic debris in various shapes and sizes. The diverse fossil assemblage includes the following:

Pelecypods characterized by their long and curved forms, with particularly common filaments, indicative of Aalenian - Bathonian age, and representing pelagic Posidonia shells “Posidonia sp”. (Murry,2006). They are observed as thin,

curved shells ranging from 170 μm to 3 mm in length (Pl. 1-A). They often exhibit a wavy appearance due to physical compaction (Pl. 1-B). Posidonia was interpreted as filaments (Flügel, 1982). Whereas the formation of coral limestone referred to Bositra (Pl. 1-A, 1-C). The latter is distinguished by its curved shell structure; they occur in both shallow- and deep-marine settings (Kuhry, 1976).

Calcispheres are typically less than 0.5 mm in diameter and are generally spherical in shape (Horowitz and Potter, 1971; Tucker, 2003). Their origin remains uncertain; some authors interpret them as chambers of foraminifera (Flügel, 1982). However, Mesozoic calcispheres are particularly abundant in pelagic limestones, especially in basinal and basin-margin settings (Wilson, 1975; Flügel, 2010, 2004). In the present study, calcispheres are recognized by their small size and oval to spherical shape, which are filled with sparry calcite (Pl. 1-D, 2-C).

Foraminifera identified occur as skeletal grains, such as planktonic forms, typically with small size, spherical chambers, and commonly filled with calcite or pyrite, like Globigerina (Pl. 1-E). Most of the specimens were affected by diagenetic changes, including recrystallization and compaction. Ammonites possess a planispiral coiled shell in the larval stage; their shell are often large (Benton and Harper, 1997). They are commonly found in pelagic, relatively deep-sea water deposits (Tucker, 1981; Wilson, 2002). In the Sargelu Formation, large but poorly preserved ammonite shells are found on the lower parts of the formation (Pl. 1-F). Their shells were commonly affected by dissolution, which was subsequently filled with sparry calcite cement.

Radiolarians are planktonic fauna that inhabit deep-basin marine environments and were found in pelagic limestones (Bishop, 1972; Kuhry et al., 1976). In the Sargelu Formation, the radiolarians are observed particularly in the lower parts. They exhibit spherical shapes; post-depositional dissolution processes often result in the preservation of empty molds of radiolarians, which are occasionally infilled by pyrite during subsequent diagenetic stages (Pl. 2-B).

Bioclasts are fossil fragments formed through the breakdown of skeletal remains; they provide information about the type of water energy (Flügel, 2004). In the Sargelu Formation, the bioclasts primarily consist of reworked skeletal fragments of Posidonia, foraminifera, ostracods, and radiolarians (Pl. 2-C).

Ostracods are characterized by their bivalve, oval-shaped calcareous shells and are known to inhabit a wide range of environments (Abawi et al., 2000; Awadeesian, 2015). In the studied samples, ostracods occur in moderate proportions and often show post-depositional diagenetic modification, such as recrystallization or partial dissolution (Pl. 2-D).

The overall pelagic microfaunal assemblage includes radiolarians, calcispheres, planktonic foraminifera, and pelagic ostracods, collectively reflecting deposition within a deep marine, low-energy environment. These microfossil components provide valuable paleoenvironmental and paleoecological information about the sedimentary conditions of the Sargelu Formation. The examined rocks are dominated by micrite between and within the grains and microfractures of the rock (Pl. 1-D). The presence of micrite indicates deposition in low-energy marine environments (Friedman, 1985; Boggs, 2006). One of the prominent features observed in the Sargelu Formation carbonates is the presence of sparry calcite, which commonly fills pores, groundmass, and fossils (Pl. 2-E).

The formation was affected by many diagenetic processes, which are as follows:

Bioturbation: the Sarglo Formation deposits exhibit varying levels of bioturbation, particularly within the limestone and bituminous shale layers. These bioturbations are characterized by faint to moderate intensity due to the deep, semi-reduced depositional environment, which limited the abundance of organisms capable of remobilizing the sediments (Pl. 3-D).

Compaction: the process that occurs at burial depths up to 1000 meters (Flügel, 2010). In carbonate sediments, compaction leads to a decrease in sediment thickness and a reduction in intergranular porosity (Meyers, 1980; Lingman,1980). Cementation plays a key role in regulating the magnitude of compaction (Bathurst,1975), which can limit or inhibit further compaction (Flügel, 2010). Both mechanical and chemical compaction played important roles in modifying the formation deposits. Variations in mechanical compaction are reflected by observable textural features. by the presence of elongated shells, deformed bioclastic shells, shell debris, microfractures, and elongation of limestone

clasts (Pl. 3-A). Chemical compaction is indicated by dissolution, as increased matrix porosity and fractures, resulting from diagenetic processes represented by stylolites (Pl. 2-A).

Cementation: refers to the precipitation of calcium carbonate from saturated solutions, occurring in or between grains, pores, and fractures, resulting in the development of sparry calcite crystals that enhance rock cohesion (Larsen and Chilingar, 1979). Although cementation is not the dominant diagenetic process throughout the Sargelu Formation, several distinct types of carbonate cement have been identified:

Drusy Cement: Consists of calcite crystals growing progressively from pore walls toward the center. This cement type was observed in the lower stratigraphic parts of the study section (Pl. 3-B). It forms under vadose or phreatic freshwater conditions (Flügel, 1982; Bathurst, 1975; Scholle and Ulmer-Scholle, 2003).

Granular Cement: Composed of euhedral to subhedral calcite crystals found in voids within fossils and channels (Pl. 3-C). This type is commonly deposited in vadose, freshwater phreatic, and burial environments (Flügel, 1982; Bathurst, 1975; Flügel, 2004; Scholle and Ulmer-Scholle, 2003).

Blocky Cement: Made up of large, equant calcite crystals lacking preferred orientation. It forms following the dissolution of grains or earlier cement and is abundant within the Sargelu Formation deposits, filling channels, fossils, and voids (Pl. 3-D). This cement type commonly forms in aerated phreatic, vadose, and deep burial settings (Flügel, 2004; Scholle and Ulmer-Scholle, 2003).

Dissolution: Partial dissolution in the Sargelu Formation leads to the formation of various types of secondary porosity. Vuggy porosity develops due to dissolution processes during diagenesis (Tucker, 2001; Machel, 2004). It influences both grains and the micritic matrix and is noted in the middle beds of the formation (Pl. 1-E). Fracture porosity: This type results from a combination of dissolution, compaction, and tectonic activity. It occurs predominantly in the lower beds of the Sargelu Formation (Pl. 1-C).

Neomorphism is the process by which a mineral phase changes from one crystalline form to another (Lingman,1980), accompanied by alterations in crystal size, shape, and structure (Flügel, 2004). This process may result in either an increase or a decrease in crystal size (Bathurst, 1975). The transformation of micrite into microspar. These features are especially notable in association with Posidonia shells “halobiid bivalves" (Pl. 2-F).

Pyritization: Authigenic minerals produced under reducing conditions (Edgar,2013). Reducing conditions are necessary for pyrite formation (Larsen and Chilingar, 1979). This typically occurs in the early stages of burial and is formed by local chemical reactions (Wilkin et al 1997). Consequently, the lack of oxygen promotes the development of a reducing environment in deep marine settings, leading to dolomitization by removing sulfates from seawater (Berner, 1971). In the Sargelu Formation, two types of pyrite were found as patches and framboidal (Pl. 1-F,1-C).

Dolomitization: it occurs in many ancient carbonate rocks as a mosaic of anhedral crystals with irregular intercrystalline boundaries (Land, 1973; Blatt et al., 1980). Two main dolomite type textures have been observed in the Sargelu Formation (Randazzo and Zachos, 1984):

Floating-rhomb porphyrotopic fabric: This texture forms during early stages of heterogeneous dolomitization and appears variably throughout the studied section (Pl. 2-B).

Sutured mosaic texture: It is characterized by late, homogeneous dolomitization of compacted limestone rocks, accompanied by dissolution of the structural components, tightly packed, relatively large, anhedral dolomite crystals arranged in a mosaic pattern. This texture results from dolomitization of micritic limestone or dolomitization with associated skeletal dissolution (Randazzo and Zachos, 1984). This type of fabric is found in different beds of the formation (Pl. 3-A).

5. Facies analysis

Detailed petrographic analysis of the Sargelu Formation. It is observed that the lithofacies in the studied section are characterized by a limestone facies containing fragmented ammonite and Posidonia shell debris; however, these components could not be fully documented hard to reach and to the presence of broken fragments resulting from scraping processes within the exposed section. Additionally, a shale (mudstone) facies was identified, which represents one of the most prominent lithofacies within the studied interval. A detailed microfacies analysis enables dividing the

facies into three major microfacies and eight sub-microfacies, which are as follows:

A. Lime - Mudstone Microfacies

This microfacies represents one of the least abundant facies within the formation deposits. It is present in the lower stratigraphic part of the succession and consists of micrite with a minor proportion of skeletal grains, which constitute less than 10% of the total facies components. This microfacies corresponds to (SMF3) (Wilson, 1975; Flügel, 2004), and represents deposition within the deep basin zone (FZ1) on the deep basinal water zone. This facies includes:

Bositra Lime-mudstone Sub microfacies (S1)

It occurs in the lower interval of the formation and is dominated by micritic material with filament remains of Bostirea. (Pl. 1-C). It was affected by crystallization, physical compaction, and cementation processes.

Radiolarian Dolomitic Mudstone Submicrofacies (S2)

This microfacies, composed of bituminous dolomite with radiolarians, appears in the middle-lower stratigraphic parts of the succession (Pl. 2-B). It is influenced by dolomitization, showing floating and mosaic dolomite textures (Randazzo and Zachos,1984).

B. Lime - Wackestone Microfacies

This facies consists of allochems around 10% to less than 50% of the microfacies components and micritic matrix. The allochems are composed of Posidonia remains, planktonic foraminifera, filament elements, and Calcispheres with associated debris, forming about 10% of the total components. Petrographic criteria allow this microfacies to be further classified into:

Posidonia/ Foraminifera Wackestone Submicrofacies (S3)

This submicrofacies is composed of planktonic foraminifera (Globigerina) as the dominant skeletal grains, along with filminte (Posidonia). Additionally, some calcispheres and ostracods are also present (Pl. 1-E). It is identified within the lower stratigraphic part of the succession. The micritic matrix contains a significant amount of organic matter and shows evidence of diagenetic alterations, including crystallization, physical compaction, and cementation. This microfacies is comparable to the SMF3 category defined by (Wilson, 1975; Flügel, 2004) and represents deposition within the deep basin facies zone (FZ1) in the deep basinal water zone.

Filament Wackestone Submicrofacies (S4)

This microfacies is composed of filamentous material with some pelecypod, planktonic foraminifera, and ostracod shells. This microfacies is affected by recrystallization, granular cementation, and physical compaction, resulting in few fractures (Pl. 3-C). This microfacies characterizes the upper succession of the formation and can be correlated with SMF3(Wilson, 1975; Flügel, 2004) standard microfacies. The depositional setting corresponds to the Facies Zone (FZ1) in the deep basinal water zone.

Bioclastic- Lime Wackestone Submicrofacies (S5)

This microfacies consists of bioclastic debris composed of filamentous, pelecypod, Posidonia, and ostracode debris. It is affected by recrystallization and compaction, with small amounts of pyrite (Pl. 2-C). This microfacies occurs within the middle stratigraphic part of the section. This microfacies is composed of grains that may constitute up to 40% of the rock composition. This microfacies can be correlated with the standard microfacies SMF10 (Wilson,1975; Flügel, 2004), and the depositional setting corresponds to the Facies Zone (FZ2) on the deep shelf as

C. Lime - Packstone Microfacies

This microfacies consists of allochems within the micrite substrate, which constitute between 50% and 90% of the facies composition. These grains are represented by various shells, including filamentous, pelecypod, Posidonia, calcispheres, planktonic foraminifera, and ostracods. This microfacies is affected by both physical and chemical compaction and dissolution, as well as dolomitization, as follows:

Filaments-Bositra Lime Packstone Submicrofacies (S6)

This microfacies consists of a high concentration of compacted Bositra shells with smaller proportions of filamentous shells. This shell makes up approximately 50% of the microfacies. Diagenetic processes affecting this

microfacies include recrystallization, intragranular cementation, and physical and chemical compaction of the shells (Pl. 1-A). This microfacies occurs in the upper part of the formation and can be correlated with the standard microfacies SMF1 (Wilson, 1975; Flügel, 2004) and was deposited within the deep shelf (FZ1).

Filaments -Lime Packstone Submicrofacies (S7)

This microfacies consists of a high concentration of filamentous shells only. This shell makes up exceed 70% of the microfacies. Diagenetic processes affecting this microfacies include recrystallization, pyritization, and physical-chemical compaction of the shells (Pl. 1-B). This microfacies occurs in the upper stratigraphic part of the succession. This microfacies corresponds to SMF1 (Wilson,1975; Flügel, 2004) and was deposited within Facies Zone1 (FZ1) (wilson on the deep basinal water zone.

Bioclastic Lime Packstone Submicrofacies (S8)

This microfacies consists of filamentous, Posidonia, and ammonite, as well as planktonic foraminifera bioclastic debris. It is affected by recrystallization and compaction. This microfacies occurs within the middle part of the studied section. (Pl. 3-D), composed of grains that may constitute up to 60% of the rock composition. This microfacies s can be correlated with the standard microfacies SMF10 (Wilson, 1975; Flügel, 2004) and was deposited in the setting of Facies Zone2 (FZ2) on the deep shelf.

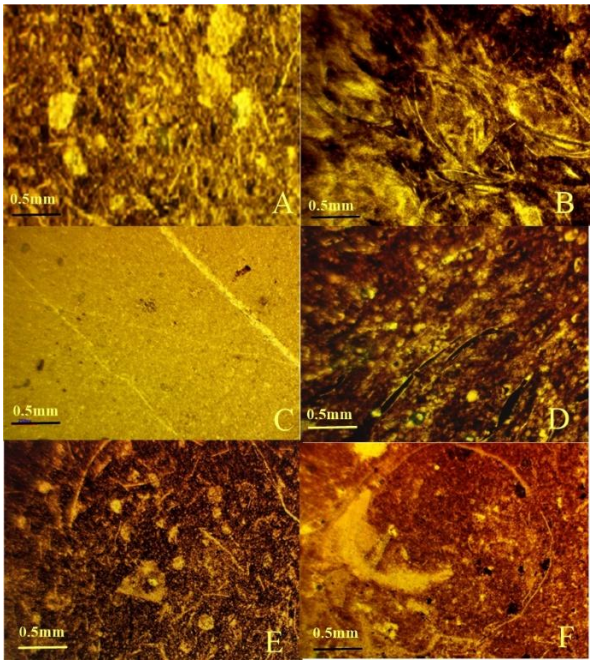


Plate1: A: Pelecypods is represented by Filaments–Bositra Lime Packstone Submicrofacies affected by Recrystallization, pyrite and dolomitization in the upper stratigraphic of section, B: Filaments-Lime Packstone Submicrofacies Diagenetic affecting this facies include recrystallization, pyritization, and physical-chemical compaction of the shells in the upper part of the formation, C: Bositra Lime-mudstone Submicrofacies effected by Dissolution, Pyritization, facies filled by granular cement, present in the lower stratigraphic part of the formation, D: Calcispheres filled with sparry calcite, radiolarian, micrite between and within the grains, vuggy porosity, framboidal pyrite, E: Posidonia Foraminiferal Wackestone Submicrofacies, Vuggy porosityis, Presence of Compaction features and pyrite mineralization, F: Ammonite, Pyritization Pyritization replacement in the central region of the ammonite.

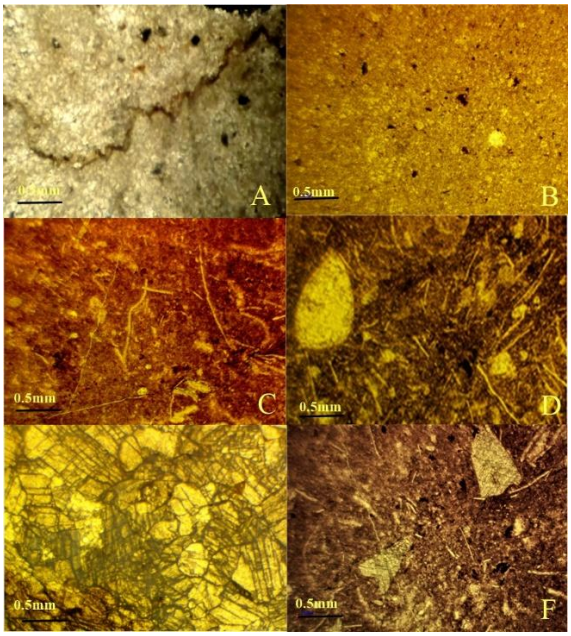


Plate2: A: Pyritization, stylolites Result of chemical compression found in the central part section, B: Radiolarian Dolomitic Mudstone Submicrofacies, showing floating and mosaic dolomite textures, Pyritization,dissolution, cementation in Radiolarian grain in the middle stratigraphic and lower part of the section, C: Bioclastic- Lime Wackestone Submicrofacies, filamentous, pelecypod, Posidonia, and ostracode debris. It is affected by recrystallization and compaction, with small amounts of pyrite. This facies restricted to the central part of the investigated section: D: Ostracoda Recrystallization, vuggy porosity, framboidal pyrite, pelagic pelecypod, in the upper part of the section; (E) sparry calcite, F: Posidonia shells—neomorphism in the central parts of the section.

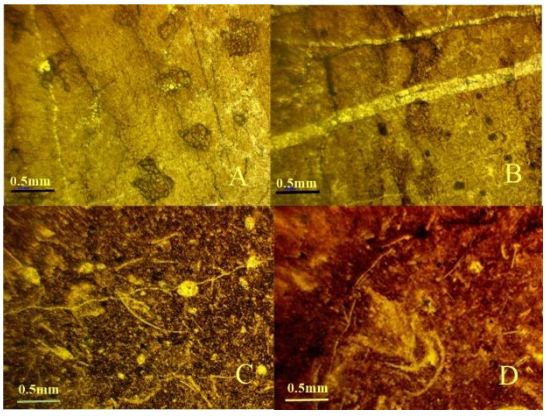


Plate3: A: Sutured Mosaic Texture, elongation of limestone clasts, compaction, Framboidal Pyrite, Microfractures, Pyritization, Partial Recrystallization, Fracturing, Compaction, B: Drusy Cement, Pyritization, C: Filament Wackestone Submicrofacies, Granular Cement, D: Bioclastic Lime Packstone Submicrofacies, fossils, and voids filled by Blocky Cement.

6. Depositional Environment

Numerous lines and/or evidence have been used to interpret the Sargelu Formation's depositional environment. There was a noticeable variation in the microfacies types along the studied section. According to Dunham (1962), packstone microfacies represent the dominant facies, followed by wackestone microfacies, whereas mudstone microfacies were the least frequently encountered.

A. Big transition from S7 what interpretation

As paleontological evidence, the microfacies contain Bositra, which is considered an indicator of Middle Jurassic deep environments (Friedman and Sanders, 1978; Nichols, 1999; Scholle and Ulmer–Scholle, 2003)

Similarly, the presence of Radiolaria indicates semi-anoxic deep marine environments (Kuhry et al., 1976; Friedman and Sanders, 1978; Tucker, 2001). Poor preservation of these fossils is noted due to intense diagenetic alteration. Posidonia is observed throughout the formation, indicating deep marine conditions adapted to low oxygen levels (Krumbein and Sloss, 1963; Kauffman and Sageman, 1990), and is dated to the Middle Jurassic (Aalenian–Bajocian) based on (Murray, 2006). Posidonia appears as monovalved specimens in the studied microfacies, suggesting slow and quiet deposition, which allowed shells to embed into the seafloor (Al-Tarim et al., 2022).

Planktonic foraminifera, such as Globigerina, are also present alongside Posidonia (Haq and Boersma, 1978), typically small in size and affected by recrystallization and dissolution. Their presence supports deposition in deep basinal marine environments (Murray, 2006). The scarcity of benthic foraminifera is evidence of an anoxic environment (Al- Taee et al., 2024).

Ammonite shells are rare within the formation evidence of deep water, and show signs of diagenetic alteration, including recrystallization and compaction, which have obscured details of their internal structures. These shells typically represent deposits from deep marine settings (Benton and Harper, 1997). Calcispheres are also present in the Sargelu Formation and are often associated with planktonic foraminifera and Radiolaria. This association makes it difficult to distinguish between the calcareous spheres and calcified Radiolaria. Most of the unstructured calcareous spheres likely originated from calcified spherical Radiolaria (Wilson, 1975).

The shale present in the middle and upper stratigraphic section suggests a decrease in current strength, along with the presence of horizontal lamination and absence of other sedimentary structures, supporting the interpretation of a deep marine basinal depositional environment.

Moreover, the presence of various forms of pyrite serves as an indicator of low-oxygen conditions (Hudson, 1982; Al-Taee et al.,2024), indicating deposition under open deep-marine conditions. As shown in Figure 4, the sea level is constant at the beginning of the formation's deposition in the Deep Basin environment, then it fluctuates to end in the Deep Shelf environment. Based on the identification of biotic components, analysis of sedimentary facies, and environmental interpretations, a depositional model was developed to represent the sedimentary setting of the Sargelu Formation at the studied locality (Figure 5).

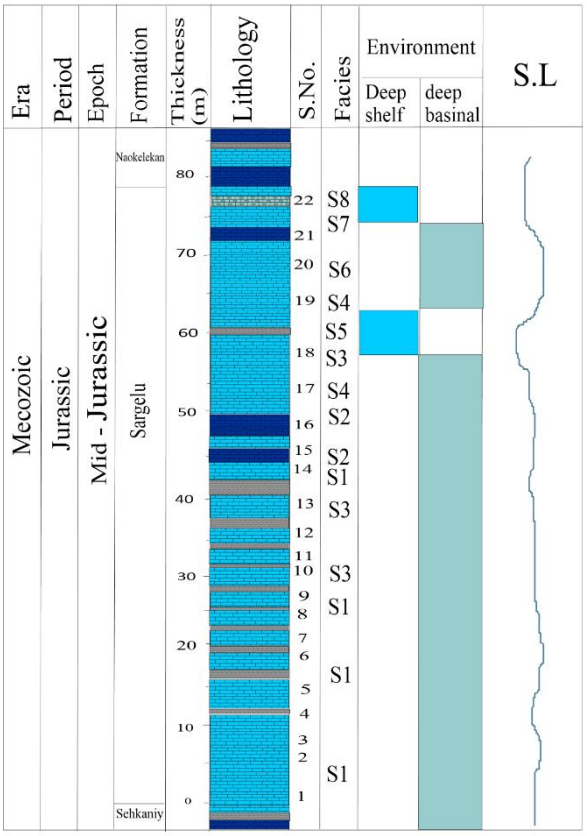


Fig. 4: Sedimentary log showing Microfauna sites and environments with sea-level (S.L.) changes of the study section

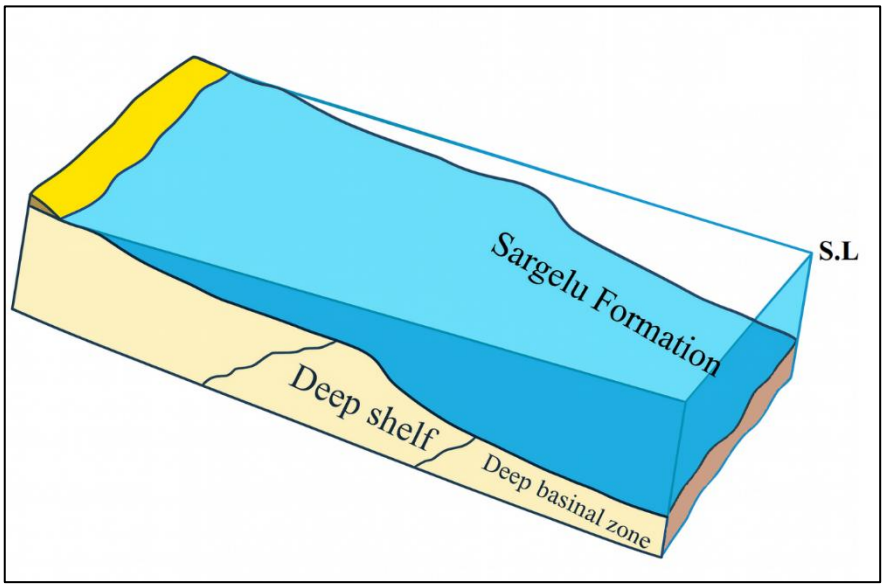


Fig. 5: Depositional model of the Sargelu Formation in the studied area

7. Conclusions

The total thickness of the Sargelu Formation in the section is approximately 78 meters, mainly composed of limestone deposits accompanied by shale interbeds and dolomitic limestone layers.

Petrographically, pelagic organisms such as filaments, Bositra, pelagic Posidonia shells, Ammonites, radiolarians, calcispheres, planktonic foraminifera, and pelagic ostracods exhibit evidence of multiple diagenetic modifications (Recrystallization, dissolution, Cementation, compaction effects, and Dolomitization).

Three main microfacies, including lime mudstone, lime wackestone, and lime packstone, were further classified into eight secondary types after comparing them with the standard facies.

Facies and paleontological evidence indicate that the Sargelu Formation accumulated within a deep-water realm, extending from deep-shelf environments to deep basin waters.

8. Conflict of Interest

The authors declare that they have no conflict of interest.

9. Funding Statement

This research received no external funding.

10. References

Abawi, T.S., Nader, A.D., Khalaf, S.K., 2000. Micropaleontology, Dar Al-Kutub for Printing and Publishing, University of Mosul, 416 P.

Abdula, R.A., Balaky, S.M., Nurmohamadi, M.S., and Piroui, M., 2015. Microfacies analysis and depositional environment of the Sargelu Formation (Middle Jurassic) from Kurdistan Region, northern Iraq. Donnish Journal of Geology and Mining Research, 1(1), pp. 001–026.

Al-Ahmed, A., 2006. Organic Geochemistry Palynofacies and hydrocarbon potential of Sargelu Formation (Middle Jurassic) Northern Iraq. Ph.D. Thesis, Unpublished, Baghdad University, 120 P.

Al-Taee, N.T., Al-Juboury, A.I., Ghafor, I.M., Rowe, H., Zanoni, G., and Dettman, D.L., 2024. Mineralogical and Geochemical Variations Across the Paleocene-Eocene Sinjar Formation, Dokan Area, Northeastern Iraq.Iraqi National Journal of Earth Science, Vol. 24, No. 2, pp. 125-139. DOI:10.33899/earth.2023.142953.1138

Al-Taee, N.T., Ghafor, I.M., Al-Juboury, A.L., and Dettman, D.L., 2024 b: Biostratigraphy and paleoecology of the Sinjar Formation (Late Paleocene-early Eocene) in Dokan and Sinjar areas, Iraq, Iraqi Geol. J. 57(1A): 221-249. Doi: 10.46717/igj.57.1A.17ms-2024pp.1-28

Al-Tarim, H.A.F., and Al-Shakiri, A.J. 2022. Field Description and Lithostratigraphic Study of Sargelu Formation in Rania and Sargelu sections, Northern Iraq. Iraqi Journal of Science, pp. 583-595.

Awadeesian, A.M.R., Al-Jawed, S.N.A., Sale, H.A.H., Sherwani, G.H., 2015. Mishrif carbonates facies and diagenesis glossary, South Iraq microfacies investigation technique: types, classification, and related diagenetic impacts. Arab J Geosci [Internet]. 8(12): pp.

10715–37. http://dx.doi.org/10.1007/s12517-015-1954-9.

Bathurst, R.G.C., 1975. Carbonate sediments and their diagenesis. Development in Sedimentology-12, Elsevier Scientific Publ. Amsterdam, 658 P.

Bellen, V.R.C., Dunnington, H. V., Wetzel, R. and Morton, D.M., 1959. Lexique Stratigraphique International. V. III, Asie, Fascicule, 10a, Iraq, Central National deal Recherches Scientifiques, Paris, 333 P.

Benton, M. and Harper, D., 1997. Basic paleontology. Longman Asia Limited, Hong Kong, 342 P.

Berner, R.A., 1971.Principles of Chemical Sedimentology. McGraw-Hill Book Company.

Bishop, B.A., 1972. Petrography and origin of Cretaceous limestones – Sierra De Picachos and Vicinity, Nuevo Leon, Mexico. Journal of Sedimentology Petroleum, 42(2), pp. 270-286.

Boggs, S.J., 2006. Principles of Sedimentology and Stratigraphy (4th ed.), Pearson Prentice-Hall, 662 P.

Buday, T., 1980. The regional geology of Iraq, Vol. 1, stratigraphy and paleogeography, Mosul, Iraq, Dar Al-Kutub Publishing House, University of Mosul, 445 P.

Dunham, R.J., 1962. Classification of Carbonate Rocks According to Depositional Texture. In: Ham, W.E. (eds.), Classification of Carbonate Rocks, AAPG. Mem. - 1, Tulsa, Okla., pp. 108-121.

Edgar, K., Bohaty, S., Gibbs, S., Sexton, P., Norris, R., Wilson, P., 2013. Symbiont "bleaching" in planktic foraminifera during the Middle Eocene Climatic Optimum. Geology. 41(1): pp.15–8.

English, J.M., Lunn, G.A., Ferreira, L. and Yacu, G. 2015. Geologic evolution of the Iraqi Zagros, and its influence on the distribution of hydrocarbons in the Kurdistan region. AAPG Bulletin, 99 (2), pp.231-272.

Flügel, E., 1982. Microfacies Analysis of Limestone, Springer Verlag, Berlin, 633 P.

Flügel, E., 2004. Microfacies of carbonate rocks: analysis, interpretation and application, Springer Verlag: 984 P.

Flügel, E., 2010. Microfacies of carbonate rocks: analysis, interpretation and application, 2nd ed. Springer, Berlin: 929 P.

Fouad, S. ,2015. Tectonic map of Iraq, scale 1: 1000 000, 3rd edition. Iraqi Bulletin of Geology and Mining, Vol. 11, pp. 1-7.

Friedman, G. M. and Sanders, J.E., 1978. Principles of Sedimentology, John Wiley and Sons, New York, pp. 722.

Friedman, G.M., 1985. The term micrite or micrite cement is a contradiction–discussion of micritic cement in microborings is not indicator. J.S.P., Vol. 55, pp. 777-784.

Haq, B.U., and Boersma, A., 1978. Introduction to marine micropaleontology. Elsevier, New York, 376 P.

Horowitz, A.S. and Potter, P.E., 1971, Introductory petrography of fossils. Springer-Verlag, Berlin.pp. 302.

Hudson, J.D., 1982. Pyrite in ammonite–bearing shales from the Jurassic of England and Germany. Sedimentology, Vol. 29, No. 5, pp. 639-667.

Jassim, S.Z., and J. C. Goff, 2006. Geology of Iraq, Prague and Moravian Museum, Brno: 341 P.

Kauffman, E.G. and Sageman, B.B., 1990, Biological sensing of benthic environments in dark shales and related oxygen–restricted facies. In: Ginsburg, R.N. and Beaudoin, B., eds., Cretaceous resources, events and rhythms: background and plans for research. Kluwer Academic Publishers. London, 352 P.

Krumbein, W.C. and Sloss, L.L., 1963. Stratigraphy and sedimentation, 2nd edition, San Francisco, 660 P. Koutsoukos, E.A.M., 1985. Distribuicao paleobatimetrica de foraminiferos bentonicos do Cenozoic: Margen continent altantica. Brazil, Combase. Congresso Brasileiro de Geol., Vol. 2, pp. 685-696.

Kuhry, B., Declercq, S.W.G., Dekker, L. 1976. Indications of current action in Late Jurassic limestones, Radiolarian limestones, Saccocoma limestones, and associated rocks from the Subbetic of SE-SPAIN. Jour Sed Geology. 15: pp.235–58.

Land, L.S., 1973. Holocene meteoric dolomitization of Pleistocene limestone, north Jamaica. Sedimentology, Vol. 20, pp. 411-422.

Lingman, M.W., 1980. Carbonate diagenetic textures from upper near surface diagenetic environment. A.A.P.G. Bull., 64(4): pp.461-486.

Larsen, G. and Chilingar, G.V., 1979. Introduction diagenesis of sediments and rocks, in Larsen, G. and Chilingar, G.V., eds., Diagenesis in sediments and sedimentary rocks. Development in Sedimentology 25 A. Elsevier Publ. Co., Amsterdam, pp. 1-29.

Machel, H.G., 2004. The geometry and petrogenesis of dolomite hydrocarbon reservoirs. Brathwaite C.J.R., Rizzi G, Darke G, editors. Vol. 235. Geo. Soc. Lond. Spec.

Meyers, W.J., 1980. Compaction in Mississippian skeletal limestones, Southwestern New Mexico. Jour. Sed. Pet., Vol. 50, No. 2, pp. 457-474.

Murray, J.W., 2006.Ecology and Applications of Benthic Foraminifera, Cambridge University Press UK, 426 P.

Nichols, G., 1999. Sedimentology and Stratigraphy. Blackwell Science Ltd., Oxford, 355 P.

Pitman, J.K., Steinshouer, D., Lewan, M.D., 2004. Petroleum generation and migration in the Mesopotamian Basin and Zagros Fold Belt of Iraq: results from abasin-modeling study, GeoArabia, Gulf PetroLink. Vol. 9. Bahrain.

Randazzo, A.F. and Zachos, L.G., 1984. Classification and description of dolomite fabrics of rocks from the Floridan aquifer, USA. Jour. Sed. Geology, Vol. 37, pp. 151-162.

Rasool, R.H., Ali, S.A., Al-Juboury, A.I., 2023. Mineralogy of the middle to upper Jurassic succession from Sargelu section, northeastern Iraq, Iraqi National Journal of Earth Science.

Sadooni, F.N. and AlShahran, A.S., 2004. Stratigraphy, lithofacies distribution and petroleum potential of the Triassic sediment's strata in the northern parts of the Arabian Plate. AAPG Bull., 88, pp.515–538. DOI:10.33899/earth.2023.143790.1155

Scholle, P.A. and Ulmer– Scholle, D.S., 2003. A Color Guide to the Petrography of Carbonate Rocks: Grains, Textures, Porosity, Diagenesis, AAPG. Memoir 77, Tulsa, Oklahoma, U.S.A., 474 P.

Sharland, P.R., Archer, R., Casey, D.M., Davis, R.B., Hall, S.H., Heward, A. P., Horbury, A. D., and Simmons, M.D., 2001. Arabian Plate Sequence Stratigraphy. GeoArabia, Special Publication, No. 2, pp. 372.

Tucker, M.E., 1981. Sedimentary Petrology: An Introduction, Vol. 3, Blackwell Scientific Publishing, Oxford, 252 P.

Tucker, M.E., 2001. Sedimentary petrology: An introduction to the origin of sedimentary rocks. Blackwell Science, Oxford and Northampton. 262 P.

Tucker, M.E., 2003. Sedimentary Rocks in the Field, Wiley, England, 234 P.

Wilson, J.L., 1975. Carbonate Facies in Geologic History, Springer- Verlag, New York, 475 P.

Wilkin, R.T., Barnes, H.L., 1997. Formation processes of framboidal pyrite. Geochim Cosmochim Acta [Internet]. 61(2): pp. 323–39. Available from: http://dx.doi.org/10.1016/s0016-7037(96)00320-1.

Wilson, M., Evans, M. 2002. Sedimentology and diagenesis of Tertiary carbonates on the Mangkalihat Peninsula, Borneo: Implications for subsurface reservoir quality. Marine and Petroleum Geology - MAR PETROL GEOL. Vol. 19, pp. 873-900. DOI:10.1016/S0264-8172(02)00085-5

Iraqi National Journal of Earth Science, Vol. 26, No. 04, 2026 (68-80)

Iraqi National Journal of Earth Science

www.earth.uomosul.edu.iq

البتروغرافية، السحنات الدقيقة والبيئة الترسيبية لتكوين سارجيلو (الجوراسي الأوسط)، في مقطع مختار من شمال شرقي العراق

نور طلال الطائي [1*]

noortalal@uomosul.edu.iq

[1] قسم علوم الارض والنفط، كلية العلوم، جامعة الموصل، الموصل، العراق.

* الباحث المراسل.

تاريخ الاستلام: 02 تشرين الأول 2025 تاريخ المراجعة: 28 كانون الأول 2025 تاريخ القبول: 14 شباط 2026

تاريخ النشر الالكتروني: 01 تشرين الأول 2026

الملخص

تناولت هذه الدراسة رسوبيات تكوين سارجيلو الجوراسي الأوسط، من خلال تحليل السحنات والبيئة الترسيبية. يقع المقطع المدروس في مدينة السليمانية بين قريتي سارجيلو وكوشان ضمن نطاق الطيات العالية، شمال شرق إقليم كردستان في العراق. يتميز التكوين في منطقة الدراسة بتتابعات من الحجر الجيري وطبقات رقيقة من الدولومات والصخر الزيتي الرقيق. يكون حد التماس العلوي مع تكوين ناوكليكان وحد التماس السفلي مع تكوين سهيكانيان. دُرست 22 شريحة رقيقة من تتابع الحجر الجيري لتكوين سارجيلو من الناحية البتروغرافية باستخدام المجهر المستقطب لتحديد مكوناتها الصخرية. أظهرت الدراسة الصخرية للوحدات الجيرية بانها تتألف بشكل رئيس من الحبيبات الهيكلية التي اشتملت على الكرات الكلسية، الراديولاريا، فاسية القدم، الفورامنيفيرا الطافية والاوستراكود. فضلا عن تأثر صخور التكوين والعديد من العمليات التحويرية مثل إعادة التبلور والدلمتة والضغط، وتأثرها بالبيريت. تم التعرف على ثلاث سحنات دقيقة مختلفة أظهرت مجموعة واسعة من الارتباطات السحنية، التي قسمت بدورها إلى ثماني سحنات دقيقة فرعية، تشير إلى ترسيب تكوين سارجيلو في بيئات الرصيف العميق ونطاق المياه البحرية الحوضية العميقة.

الكلمات المفتاحية:

تحليل السحنات، الجوراسي، الحوض العميق، تكوين سارجيلو، العراق.

DOI: 10.33899/injes.v26i4.55951, ©Authors, 202*6*, College of Science, University of Mosul.

This is an open-access article under the CC BY 4.0 license (http://creativecommons.org/licenses/by/4.0/)

Iraqi National Journal of Earth Science, Vol. 26 No. 04, 2026 (81-97)

Iraqi National Journal of Earth Science

www.earth.uomosul.edu.iq

Calcareous Nannofossil Biostratigraphy of Sarmord Formation (Lower-Upper Cretaceous) in Bekhme Anticline, Kurdistan Region – Northeastern Iraq

Inas H. Al-Khafaf [1*], **Majed M. Al-Mutwali** [2]

Inasalkhafaf7@uomosul.edu.iq majidmutwaly@uomosul.edu.iq

[1] *Department of Environmental Science, College of Environmental Sciences, University of Mosul, Mosul, Iraq*

[2] *Department of Petroleum and Refining Engineering, College of Petroleum and Mining Engineering, University of Mosul, Mosul, Iraq .*

* *Correspondence author.*

Received: 13 March 2025 Received in revised form: 02 May 2025 Accepted: 17 June 2025
Available online: 01 October 2026

Abstract

The calcareous nannofossil biostratigraphy has been studied in the Sarmord Formation (Lower - Upper Cretaceous) at an exposed section in the southern limb of the Bekhme anticline, Kurdistan Region, northeastern Iraq. Lithologically, the formation consists of marl, marly limestone, and limestone represented by 52 samples. These rocks contain inadequate benthic foraminiferal fauna, green algae, echinoderms, and some bioclasts. 83 species of nannofossils belonging to 37 genera were identified. The relative abundance of calcareous nannofossils throughout the section varied from moderate to good. Six distinct zones and two subzones can be identified based on the stratigraphic distribution of the calcareous nannofossils. These are from ancient to recent:
Speetonia colligate Interval Zone (Part) (CC4)
Lithraphidites bollii Interval Zone (CC5)
Micrantholithus hoschulzii Partial range Zone (CC6)
Chiastozygus litterarius Interval Zone (CC7)
Hayesites irregularis Interval Subzone (CC7a)
Rhagdiscus angustus Interval Subzone (CC7b)
Prediscosphaera columnata Interval Zone (CC8)
Eiffellthus turriseiffeli Interval Zone (CC9)
The Calcareous nannofossil zones have been correlated with other zonal schemes extending from the late Early Hauterivian to the Early Cenomanian.

Keywords:

Biostratigraphy, Calcareous nannofossil, Sarmord Formation, Bekhme anticline.

DOI: 10.33899/injes.v26i4.56104, ©Authors, 2026, College of Science, University of Mosul.
This is an open-access article under the CC BY 4.0 license (http://creativecommons.org/licenses/by/4.0/).

==========

1. Introduction

The sedimentary sequence included in the present study crops out at the core of the Berat anticline within the High Folded zone exposed beside the main road to Bekhma Dam tunnel. The section is chosen at Bekhme Gorge, approximately 90 Km northeast of Erbil City at Latitude 36˚ 41′ 46″ N and Longitude 44˚ 17′ 08″ E (Fig. 1). The studied sequences are restricted between the Chia Gara Formation at the bottom and the Qamchuqa Formation at the top. There has been some debate regarding the classification of these sequences in terms of lithostratigraphy. They have been attributed either to the Balambo Formation in some studies (Al-Hamdani, 1991; Abdullah, 2022), or to the Sarmord Formation by others (e.g., Ali, 2010), or even referred to by a compound name like the Balambo-Sarmord Formation (Balaki, 2019). In our current study, we have chosen to refer to these sedimentary sequences as the Sarmord Formation.

This decision is made because the sequences lack fossils indicating deep marine sedimentation, and instead, the fossil components suggest sedimentation in marine shelf environments.

The Sarmord Formation was initially defined by Wetzel (1950) in Bellen et al. (1959) in the northern Iraqi region of the Surdash Anticline in Sulaimani Governorate. Lithologically, it is composed of marly neritic limestones, buff weathering, and brown and bluish marls. It has a thickness of approximately 455 m and is assigned an age of Valanginian-Aptian.

Karim et al. (2021) reported that the Sarmord Formation requires further study due to ambiguity surrounding its definition, age, and stratigraphic and territorial distribution. They conducted their study in the Qaywan section and determined that the Formation is of Valanginian to Barremian age. Al-Abassi et al. (2023) noted that the Chia Cara Formation underlies the Sarmord Formation unconformably in the Amadia and Barsarin sections, while the Balambo Formation underlies it conformably in the Gara section. Additionally, they found that the upper boundary of the Sarmord Formation is conformable with the Qamchuqa Formation in the Gara and Amadia sections, and with the Balambo Formation in the Barsarin section.

Regarding the study section, it has a thickness of about 164 m. The lower part consists of medium to thick bedded brownish marly limestone, alternating rhythmically with thin to medium beds of marl and friable shale. The middle part is composed of medium to thick bedded yellow limonitic limestone interbedded with friable shale, with some marl and marly limestone. This interval is followed by medium-grained, medium to thick-bedded limestone, intercalated with shale and some marl beds.

The modern sequences of the formation comprise crushed limestone that contains Thalassinoides intercalated with green marl (Fig.7). The Thalassinoides consist of branches of cylindrical or (Y) shape burrow system with unlined sharp walls, straight or curved commonly penetrate in firm, unlithified substrates (Myrow, 1995), the average length of each burrow system is 5-10cm with a diameter range between 1-2 cm, these structures remained open after being vacated by the tracemaker, thus allowing material from subsequent depositional events to accumulate therein (MacEachern et al., 2007), so it was observed that there is a clear difference like sediment fillings the burrows from the sediments surrounding it. The ichnogenus Thalassinoides exemplifies the Glossifungites Ichnofacies, which reflects the colonization of firm substrates. Firm grounds were formed when semi-consolidated muds were exhumed by mass wasting and erosive bottom currents (Sávra et al., 2001).

Stratigraphically, the lower boundary of the Sarmord Formation is seen to be gradational and conformable with the Chia Cara Formation, which is exposed near the deepest cut of the river in the Bekhme Gorge with no field evidence of unconformity (Balaki, 2019). The upper boundary is conformable with the Qamchuqa Formation. Additionally, several studies have emphasized the importance of investigating this formation to confirm its stratigraphic status, as it is one of the less explored formations in Iraq

The goal of this work is to identify the main calcareous nannofossil zones and compare them to regional and international standards and to determine morphology, biostratigraphic distributions, and abundances. As a result, the proposal of new chronostratigraphic and biostratigraphic frameworks for the Sarmord Formation was suggested.

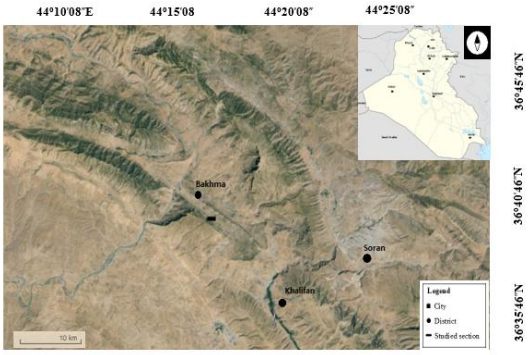


Fig. 1: Location map of studied section

2. Field Description of the Studied Section

In the area under investigation, the Sarmord Formation typically consists of limestone, marl, and marly limestone successions with varying thicknesses. The lower part is composed of medium to thick-bedded brownish marly limestone, which alternates rhythmically with thin to medium beds of marl and friable shale (Fig. 2). The middle part contains medium-thick beds of limestone interbedded with friable shale, marl, and marly limestone (Figs. 3 and 4).

The upper part of the formation is characterized by reddish limestone intercalated with shale and some marl beds (Fig. 5), along with dark gray

marly limestone and crushed limestone containing Thalassinoides at its uppermost part (Fig. 7).



Fig. 2. Field photograph showing bedded brownish marly limestone alternating with thin beds of marl and friable shale at the bottom of the Sarmord Formation in Bekhme Gorge.



Fig. 3: Marly limestone beds within the middle part of the studied Sarmord Formation



Fig. 4: Thick limestone beds, interbedded with friable shale, marl, and marly limestone within the central part of the studied section of the Sarmord Formation



Fig.5: Field photograph showing reddish medium to thick bedded limestone, intercalated by shale and some marl beds in the upper part of the studied section of the Sarmord Formation



Fig. 6: Field photograph showing the location of the top contact of the Sarmord Formation (grey marl) alongside the Qamchuqa Formation (thick brownish limestone beds) at the northeastern part of the Bekhme Gorge.



Fig. 7. Field photograph showing:?? Trace fossils (Thalassinoides) at the uppermost marly limestone bed of the Sarmord Formation at its upper contact with the Qamchuqa Formation

3. Methodology

Fifty-two samples were collected from the studied section with an inter-sample distance ranging between 2 and 5 meters. These samples were processed using the simple smear slide technique. These smear slides were viewed at 1000x magnification using a polarizing microscope.

4. Results

Calcareous nannofossils are valuable tools for biostratigraphy; they provide a comprehensive framework for biostratigraphy from the Lower Cretaceous succession being studied. As a result, they are effective for chronostratigraphic correlation. Additionally, calcareous nannofossils are useful for biostratigraphically correlating marine strata over long distances. A total of 83 species of calcareous nannoplankton from 37 genera were identified through biostratigraphic analysis of treated samples from the research area. The distribution chart of these species is displayed in Fig. 8. All identified species are shown in plates (1-8).

The biostratigraphy of the measured sections is based on the ranges and assemblages of calcareous nannoplankton datum events. In this study, six zones and two subzones are identified through the stratigraphic distribution of calcareous nannofossils depending on the CC zonation of Sissingh (1977). These biozones have been compared with worldwide biozones (Fig. 9) and local studies (Fig. 10). The biozones are listed below from ancient to recent:

1- Speetonia colligate Interval Zone (CC4) (Part)

Definition and Correlation: The lower boundary of this subzone is not determined in this study, while the upper boundary is determined by the late appearance of Speetonia colligate, with a thickness of 14 meters represented by samples (1-5). This zone is equivalent to the Speetonia colligate subzone (CC4b) of (Sissingh, 1977) and coincides with NC4b according to (Roth, 1978). Additionally, it is correlated with BC8, BC9, and the lower part of BC10 (Bowen et al., 1998). This subzone belongs globally to the Cretarhabdus loriei Interval Zone and defines the interval as late Early Hauterivian to Late Hauterivian.

Discussion: This zone is characterized by the prevalence of the following species (*Cyclagelosphaera argoensis, Eiffellithus striatus, Eprolithus antiquus, Helenea quadrata, Lithraphidites bollii, Rucinolithus windleyae).* The presence of these species is an indicator of the Hauterivian.

As for the formation's contact boundaries, the lower contact with the Chia Cara Formation is conformable.

2- Lithraphidites bollii Interval Zone (CC5)

Definition and Correlation: The biostratigraphic interval is defined by the range of the nominated taxon between the last appearance of Speetonia colligate at the bottom and the last occurrence of Cacicalathina oblongata at the top. This interval has a thickness of 23 meters, represented by samples (5-13). This zone coincides with the Lithraphidites bollii Interval Zone (CC5) of (Sissingh, 1977) and is also correlated with NC5a by (Roth, 1978); it is correlated with the upper part of BC10, BC11, BC12, BC13, and the lower part of BC14 by (Bowen et al., 1998). This interval has been defined as the Early Barremian.

Discussion: This zone is characterized by the prevalence of *Assipetra infracretacea, Assipetra terebrodentarius, Calcicalathina oblongata, Cyclagelosphaera deflandrei, Ellipsagelosphaera supergesta, Haqius circumradiatus, Helenea chiastia, Nannoconus minutus, Pickelhaube furtiva.*

3- *Micrantholithus hoschulzii* Partial range Zone (CC6)

Definition and Correlation: The biostratigraphic interval is characterized by the partial range of the nominated taxon between the last occurrence of Cacicalathina oblongata at the base and the first occurrence of Hayesites irregularis at the top. This zone is recorded with a thickness of 16 meters, represented by samples (13-16); it is equivalent to the Micrantholithus hoschulzii Partial Range Zone (CC6) of (Sissingh, 1977) and coincides with NC5b of (Roth, 1978). It is correlated with the upper part of BC14, BC15, BC16, and BC17 (Bowen et al., 1998). The Late Barremian is the interval defined by this zone.

Discussion: This zone is characterized by the prevalence of *Diazomatolithus lehmanii, Nannoconus minutus, Rhagodiscus asper, Watznaueria barnesiae, Watznaueria biporta, and Watznaueria fossacincta.*

4- *Chiastozygus litterarius* Interval Zone (CC7)

Definition and Correlation: There are two subzones within this zone depending on the subzonal marker. The first is the *Hayesites irregularis* Interval Subzone (CC7a), which represents the interval from the first occurrence of the nominated taxon *Hayesites irregularis* at the base to the first occurrence of *Eprolithus floralis* at the top. It has a thickness of 27 meters, represented by samples (16-23). This subzone coincides with the *Hayesites irregularis* Interval Subzone (CC7a) by Sissingh (1977) and coincides with NC6 by Roth (1978). it is correlated with the BC18, BC19, and the lower part of BC20 by (Bowen et al., 1998). This subzone has defined the interval as the early Aptian.

Discussion: This subzone is characterized by the prevalence of *Assipetra terebrodentarius*, *Braarudosphaera batilliformis*, *Cretarhabdus conicus*, *Cretarhabdus delicatus*, *Cyclagelosphaera margerelii*, *Diazomatolithus lehmanii*, *Haqius circumradiatus*, *Hayesites irregularis*, *Microstaurus chiastius*, *Micrantholithus hoschulzii*, *Micrantholithus obtusus*, and Barremian/Aptian boundary is also marked by the beginning of first occurrence of *Nannoconus truittii frequens* and *Nannoconus troelsenii*.

The second subzone is the *Eprolithus floralis* Interval Subzone (CC7b), which represents the duration between the initial appearance of *Eprolithus floralis* and the initial appearance of *Prediscosphaera columnata*. With a thickness of 12 meters, it is represented by samples (23-28). This subzone coincides with the *Rhagodiscus angustus* Interval Subzone (CC7b) according to (Sissingh, 1977) and also aligns with NC7 according to (Roth, 1978). Additionally, it is compatible with the upper part of BC20, BC21, and the lower part of BC22 according to (Bowen et al., 1998). This subzone is defined from the Late Aptian.

Discussion: This subzone is characterized by the prevalence of *Assipetra terebrodentarius*, *Diazomatolithus lehmanii, Eprolithus floralis, Haqius circumradiatus, Micrantholithus hoschulzii, Nannoconus minutus*, *Nannoconus elongatus, and Watznaueria barnesiae*.

5- *Prediscosphaera columnata* Interval Zone (CC8)

Definition and Correlation: The interval zone determined by the first appearance of *Prediscosphaera columnata* to the first appearance of *Eiffellithus turriseiffeli*, with a thickness of 26 meters, represented by samples (28-39). This zone corresponds to the *Prediscosphaera columnata* Interval Zone (CC8) as defined by Sissingh (1977) and coincides with NC8 and NC9 as defined by Roth (1978), as well as being compatible with the upper part of BC22, BC23, BC24, BC25, and BC26 as defined by Bowen et al. (1998). This zone represents an Early to Late Albian age.

Discussion: This subzone is characterized by the prevalence of Assipetra terebrodentarius, Braarudosphaera pseudobatilliformis, Calcicalathina alta, Cyclagelosphaera margerelii, Nannoconus steinmannii, Nannoconus troelsenii, and Prediscosphaera columnata.

6- Eiffellithus turriseiffeli Interval Zone (CC9)

Definition and Correlation: The lower boundary of this zone is defined by the first occurrence of Eiffellithus turriseiffeli to the initial appearance of *Lithraphidites acutus*. It has a thickness of 46 meters, as represented by samples (39-50). This zone corresponds to the Eiffellithus turriseiffeli Zone (CC9) as described by Sissingh (1977) and aligns with the lower part of NC10 according to Roth (1978). Additionally, it correlates with BC27a and, as noted by Bowen et al. (1998), indicates a Late Albian to Early Cenomanian age.

Discussion: This subzone is characterized by the prevalence of *Assipetra terebrodentarius*, *Calcicalathina alta*, *Diazomatolithus lehmanii*, *Eiffellithus turriseiffelii*, *Eprolithus floralis, Hayesites albiensis, Hayesites irregularis, Nannoconus dislocates*, Nannoconus *minutus, Pickelhaube furtiva, Watznaueria barnesiae.*

As for the upper contact is conformable with the Qamchuqa Formation.

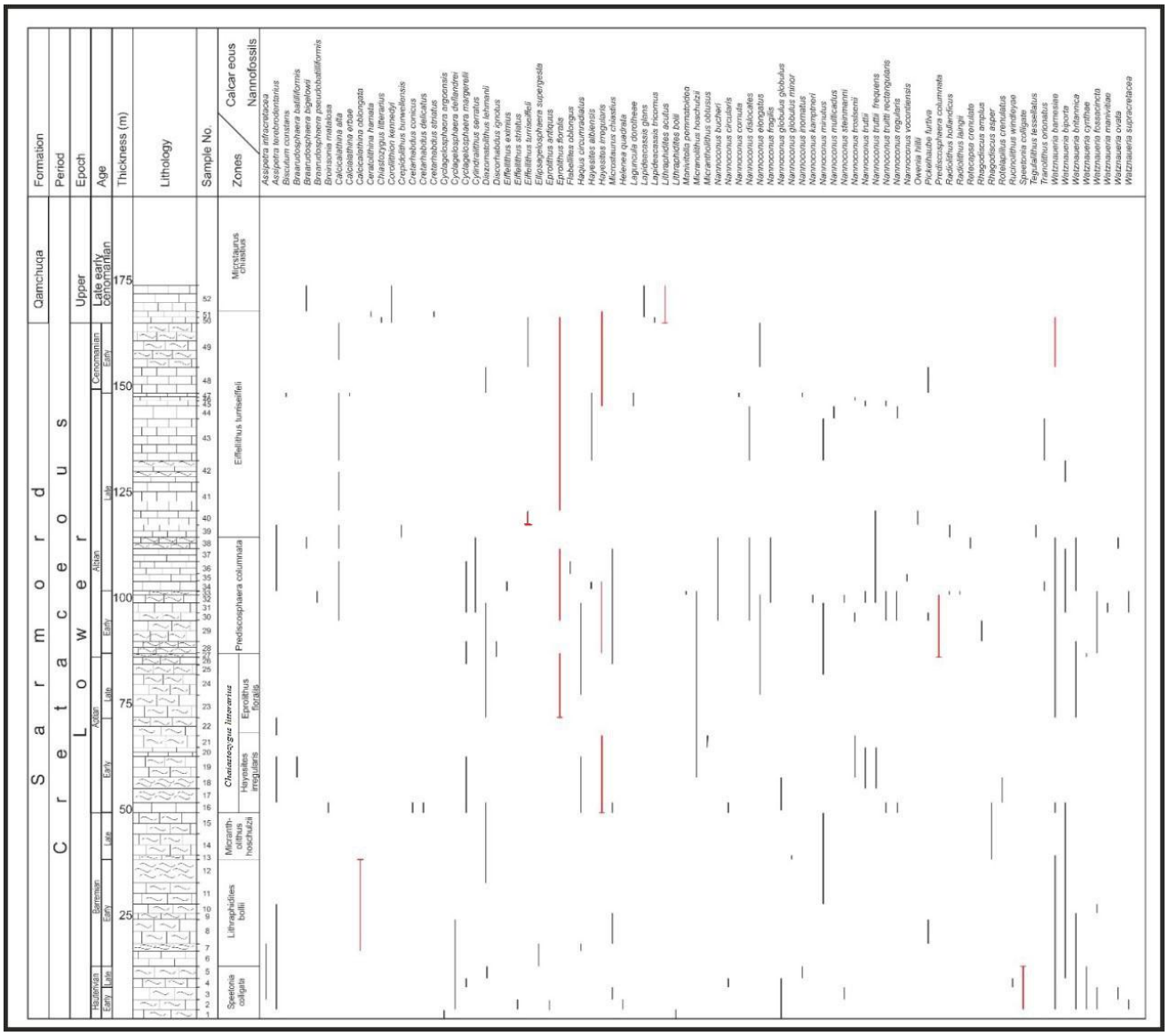


Fig. 8: Distribution of calcareous nannofossils in the Sarmord Formation on the Bekhme Anticline.

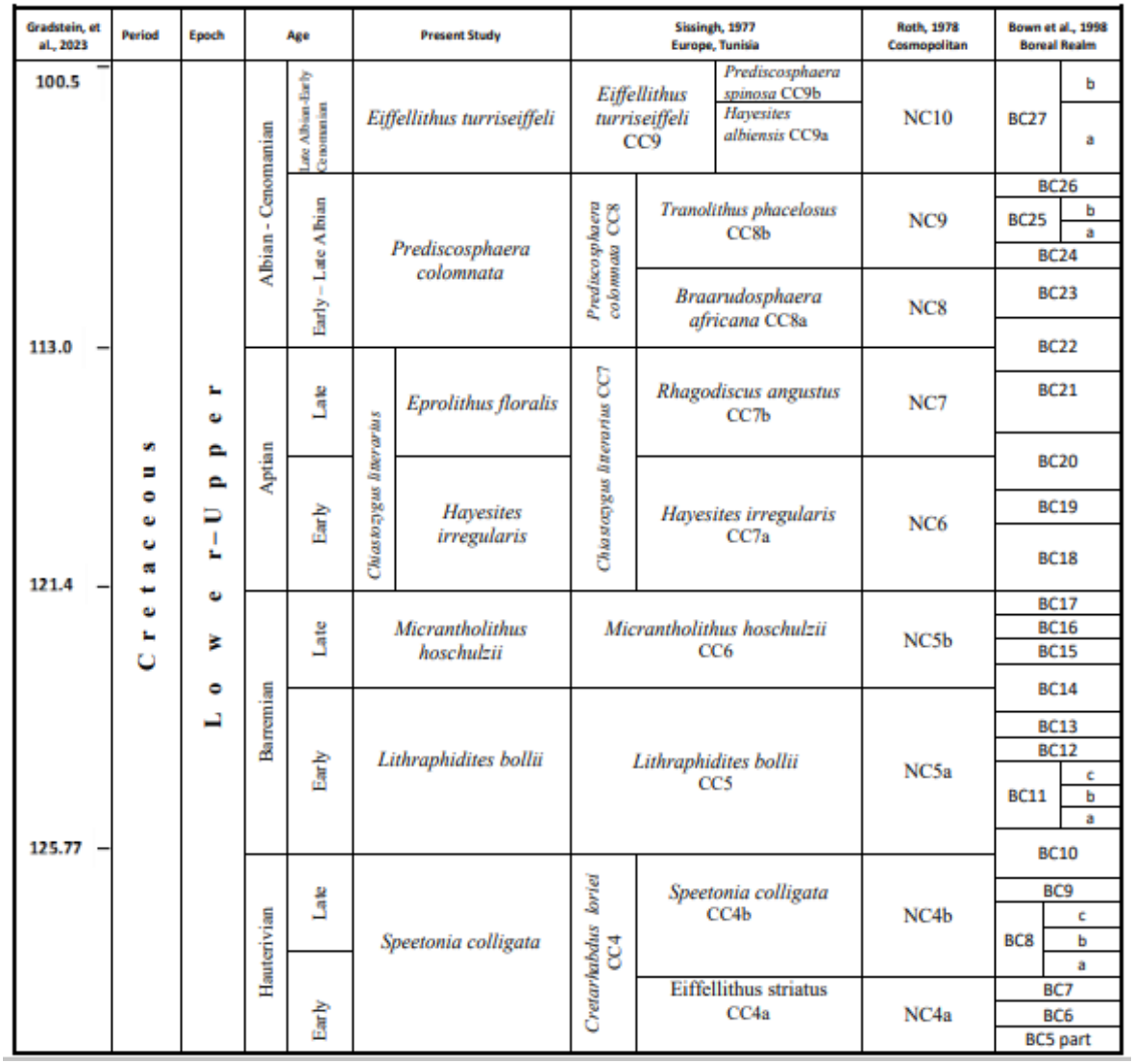


Fig. 9: The calcareous nannofossil biostratigraphic correlation of the Sarmord Formation with other worldwide zonal schemes.

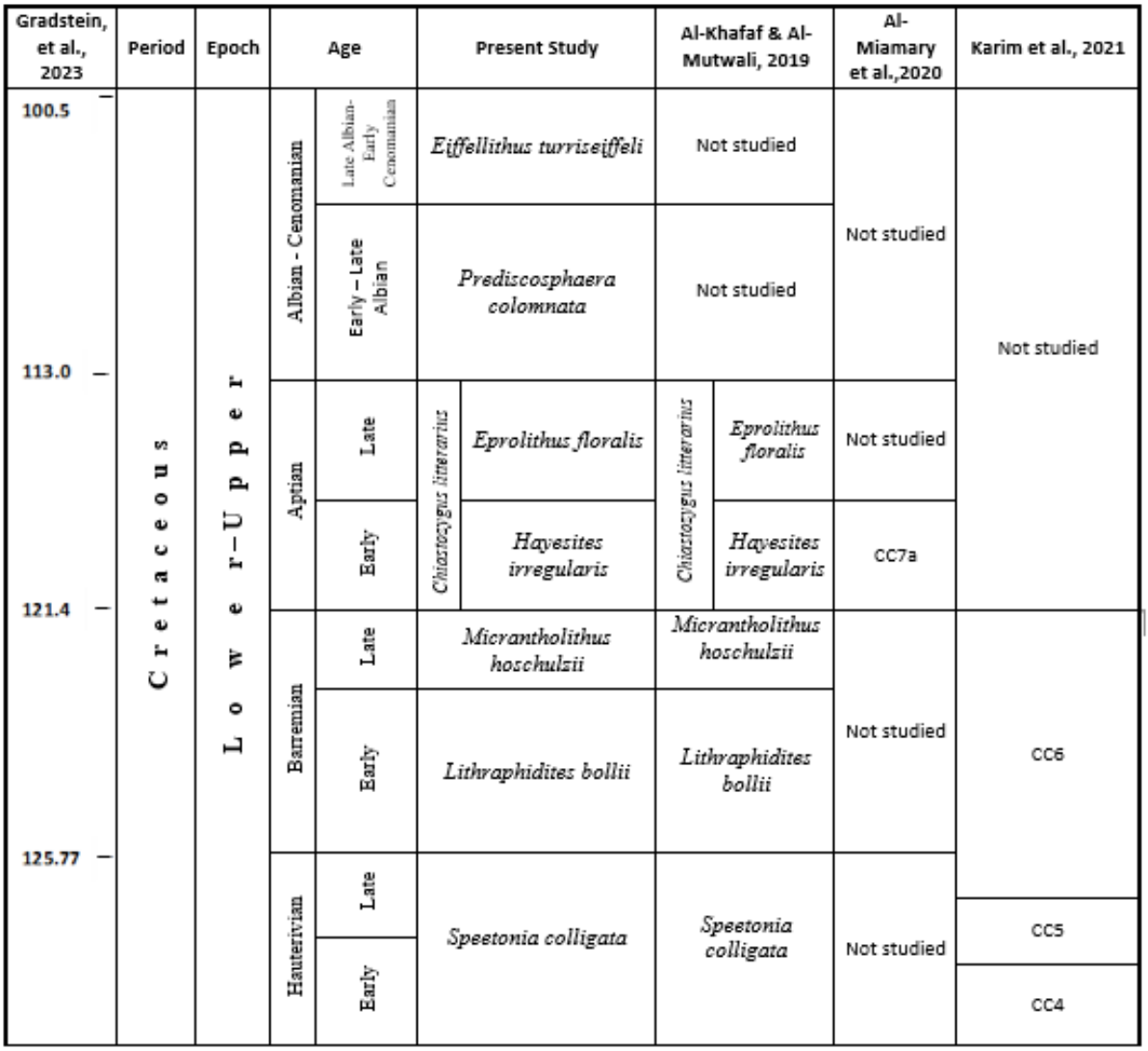


Fig. 10: Calcareous nannofossil biostratigraphic correlation of the Sarmord Formation with other local studies.

5. Conclusion

The current study focuses on the Sarmord Formation in the Bekhme Anticline. This formation is comprised of marl, marly limestone, and limestone. Through biostratigraphic study, the identification of 83 species of calcareous nannoplankton from 37 genera was achieved. The age of the formation, extending from the Late Early Hauterivian to the Early Cenomanian, was determined by finding six zones and two subzones. These are from ancient to recent:

Speetonia colligate Interval Zone (Part) (CC4), Lithraphidites bollii Interval Zone (CC5), Micrantholithus hoschulzii Partial range Zone (CC6), Chiastozygus litterarius Interval Zone (CC7), *Hayesites irregularis* Interval Subzone (CC7a), *Rhagdiscus angustus* Interval Subzone (CC7b), Prediscosphaera columnata Interval Zone (CC8), Eiffellthus turriseiffeli Interval Zone (CC9).

6. Conflict of Interest

The authors declare that they have no conflict of interest.

7. Funding Statement

This research received no external funding.

8. Author Contributions

Inas H. Al-Khafaf: First Author: Conception of the research idea; writing the complete research methodology, including the conclusions; preparation of the figures and plates presented in the research paper.

Co-Author: Majid M. Al-Mutwali Second Author: Conception of the research idea; writing the introduction; review and supervision.

9. References

Abdullah, A.O., 2022. Sedimentology and Stratigraphy of Balambo Formation (Valanginian-Cenomanian) in Two Different Tectonic Zones, Zagros Foreland Basin, Kurdistan Region, Northeastern Iraq. Unpublished M. Sc. Thesis, Salahaddin University,120 pp.

Ali, D.O., 2010. Sedimentology and Stratigraphy of Bekhme Formation (Upper Cretaceous) in Selected Sections in Kurdistan Region, Iraq. Unpublished M. Sc. Thesis, Salahaddin University,132 pp.

Al-Abbasi, M., Al-Mutwali, M., and Al-Banna, N., 2023. Biostratigraphy and Chronostratigraphy of Late Jurassic–Early Cretaceous in Selected Areas in Kurdistan Region, Northern Iraq. Iraqi Bulletin of Geology and Mining, 19 (1), 29-48. https://doi.org/10.59150/ibgm1901a03

Al-Hamdani, R.K., 1991. Stratigraphy and structure of the south-Eastern part of Perat anticline (Bekhme area, NE of Iraq). Unpublished M.Sc. Thesis, Uni. of Mosul, 109 pp.

Al-Khafaf, E. and Al-Mutwali, M., 2019. Calcareous nannofossils biostratigraphy of the Lower Part of Balambo Formation (Lower Cretaceous) in Azmir Anticline, Northeastern Iraq. *Iraqi National Journal of Earth Science*, 19(1), 19-38.

Al-Miamary, F.A., Al-Badrani, O.A., and Al-Juboury, A. I., 2020. Calcareous nannofossils and chemostratigraphy of the Early Aptian Oceanic Anoxic Event 1a from Northern Iraq. *Bulletin of the Iraq Natural History Museum (P-ISSN: 1017-8678, E-ISSN: 2311-9799)*, *16*(1), 95-111. https://doi.org/10.26842/binhm.7.2020.16.1.0095

Balaki, H.G., 2019. Structural Evolution of the Bradost, Pirs, Berat and Maqloub- Barda Rash Anticlines in the Zagros Fold Thrust Belt, Kurdistan Region, NE Iraq. Unpublished Ph.D. Thesis, Salahaddin University, Erbil, Iraq. 241 pp.

Bellen, R.C.V., Dunnington, H., Wetzel, R., and Morton, D., 1959. Lexique Stratigraphique. Asie, Iraq, 333.

Bown, P.R., Rutledge, D.C., Crux, J.A., and Gallagher, L.T., 1998. Lower Cretaceous. In Bown, P.R. (Ed.), *Calcareous Nannofossil Biostratigraphy*, Kluwer Academic Publishers, Dordrecht, 86-131.

Gradstein, F.M., Ogg, J.G., Smith, A.G., and Ogg, G. M., 2023. Geological Time Scale 2012, Cambridge Univ. Press, 1176 P. Drafted by K.M. Cohen, D.A.T. Harper, P.L. Gibbard, N. Car (c) International Commission on Stratigraphy, September 2023.

Karim, K.H., Al-Dulaimy, S.I., Ahmad, P.M., and Al-Badrani, O., 2021. Stratigraphy and Nannofossil Biozonation of Sarmord Formation on the Qaywan Anticline in Sulaymaniyah Governorate, Northern Iraq. *The Iraqi Geological Journal*, 75-86. https://doi.org/10.46717/igj.54.2D.6Ms-2021-10-25

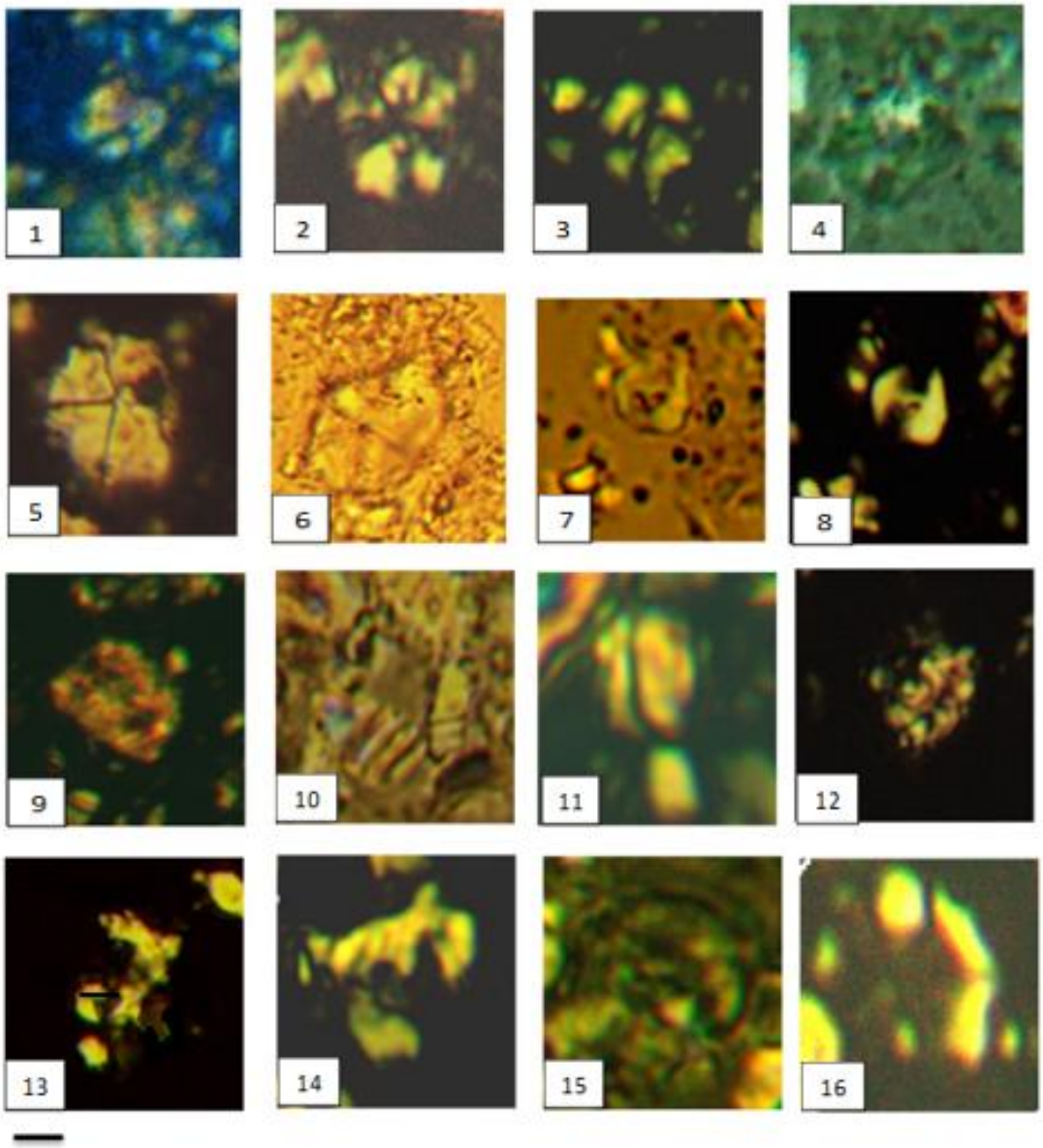
Mac_Eachern, J.A., Pemberton, S.G., Gingras, M.K., Bann, K.L. and Dafoe, L.T., 2007. Uses of Trace Fossils in Genetic Stratigraphy. In Trace Fossils: Concepts, Problems, Prospects, Miller, W. (ed.), Elsevier, pp. 110-134. https://doi.org/10.1016/B978-044452949-7/50133-9

Myrow, P.M., 1995. *Thalassinoides* and the Enigma of Early Paleozoic Open-Framework Burrow Systems. Palaios, Vol. 10, pp. 58-74, https://doi.org/10.2307/3515007

Roth, P.H., 1978. Cretaceous nannoplankton biostratigraphy and oceanography of the Northwestern Atlantic Ocean. *Initial Reports of Deep Sea Drilling Project*, 44, 731-659.https://doi.org/10.2973/dsdp.proc.44.134.1978

Savrda, C.E., Browning, J.V., Krawinkel, H., and Hesselbo, S.P., 2001. Firmground ichnofabrics in deep-water sequence stratigraphy: Tertiary clinoform- toe deposits. New Jersey Slope. Palaios 16, pp. 294-305. https://doi.org/10.1669/0883-1351(2001)016%3C0294:FIIDWS%3E2.0.CO;2

Sissingh, W., 1977. Biostratigraphy of Cretaceous calcareous nannoplankton. Geological Mining, 56, 37-65.



Calcareous nannofossils from the Sarmord Formation, cross-polarized light (XPL) and plane-polarized light (PPL). The magnification is 1000X. The Scale bar is 5µm.

Plate 1- *1-Assipetra infracretacea* (Thierstein, 1973) Roth, 1973, sample 6, 2- *Assipetra terebrodentarius* (Applegate et al. *in* Covington and Wise, 1987) Rutledge and Bergen *in* Bergen, 1994, sample 2, 3- *Biscutum constans* (Górka, 1957) Black *in* Black and Barnes, 1959, sample 30, 4- *Braarudosphaera batilliformis* Troelsen Quadros, 1971, sample 19, 5- *Braarudosphaera bigelowii* (Gran and Braarud, 1935) Deflandre, 1947, sample 38, 6- *Braarudosphaera pseudobatilliformis* Alves et al. 2017, sample 32, 7,8- *Broinsonia matalosa* (Stover, 1966) Burnett in Gale et al., 1996, sample 16, 9,10 *Calcicalathina alta* Perch-Nielsen, 1979, sample 30, 50, 11- *Calcicalathina erbae* Bergen 1998, sample 47, 12- *Calcicalathina oblongata* (Worsley, 1971) Thierstein, 1971, sample 12, 13,14 *Ceratolithina hamata* Martini, 1967, sample 51,50, 15- *Chiastozygus litterarius* (Górka, 1957) Manivit, 1971, sample, 50, 16- *Corollithion kennedyi* Crux, 1981, sample 50.

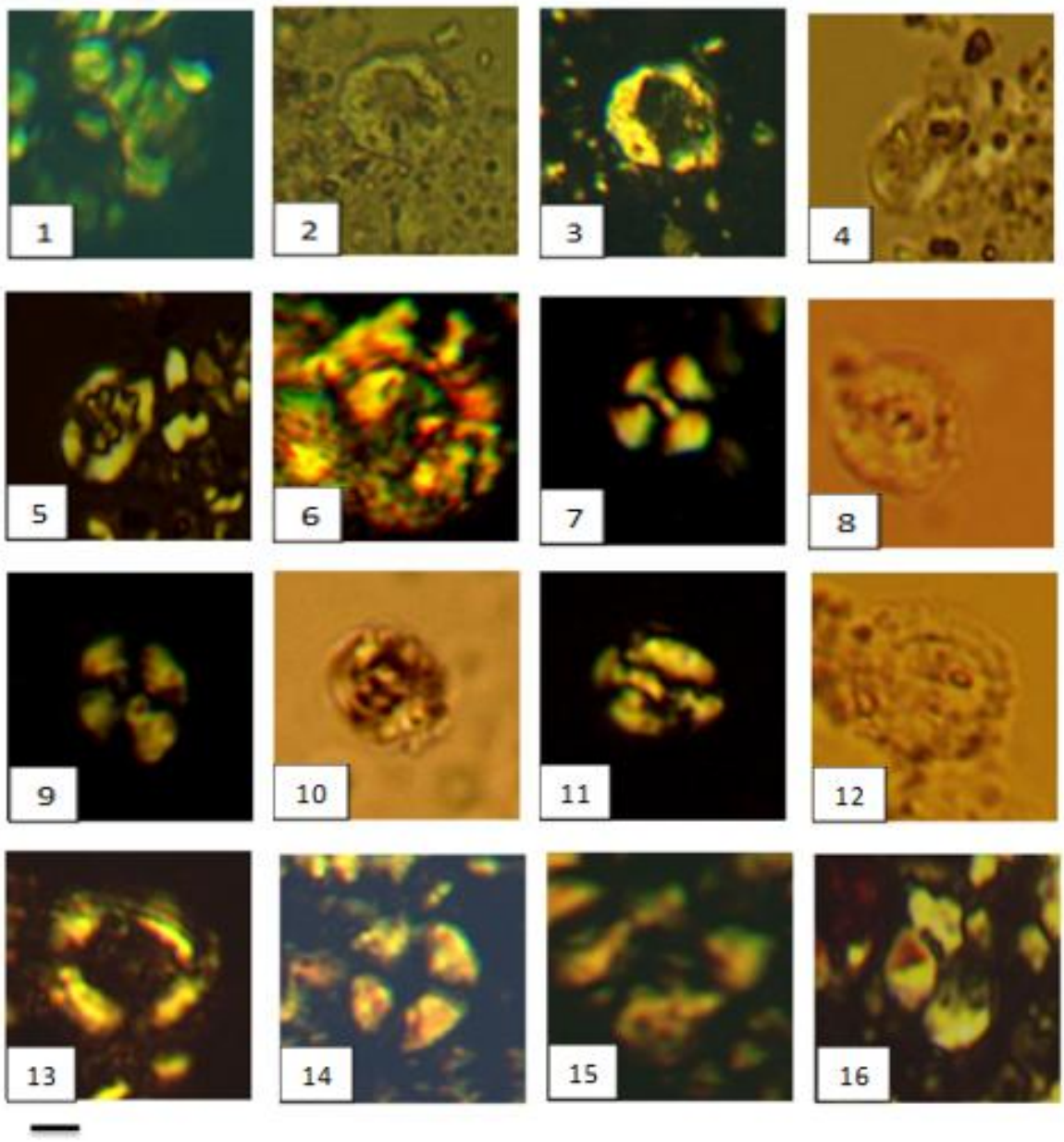


Plate 2. The Scale bar is 5µm 1- *Crepidolithus burwellensis* Black 1972, sample 39, 2,3- *Cretarhabdus conicus* Bramlette and Martini, 1964, sample 16, 4,5- *Cretarhabdus delicatus* Applegate, Covington, and Wise in Covington and Wise, 1987, sample 16, 6- *Cretarhabdus striatus* (Stradner, 1963) Black, 1973, sample 50, 7- *Cyclagelosphaera argoensis* Bown, 1992, sample 1, 8,9- *Cyclagelosphaera deflandrei* (Manivit, 1966) Roth, 1973, sample 2, 10,11- *Cyclagelosphaera margerelii* Noël, 1965, sample 28, 12,13- *Cylindralithus serratus* Bramlette and Martini, 1964, sample 31, 14- *Diazomatolithus lehmanii* Noël, 1965, sample, 28, 15- *Discorhabdus ignotus* (Górka, 1957) Perch-Nielsen, 1968, sample, 28, 16- *Eiffellithus eximius* (Stover, 1966) Perch-Nielsen, 1968, sample, 34.

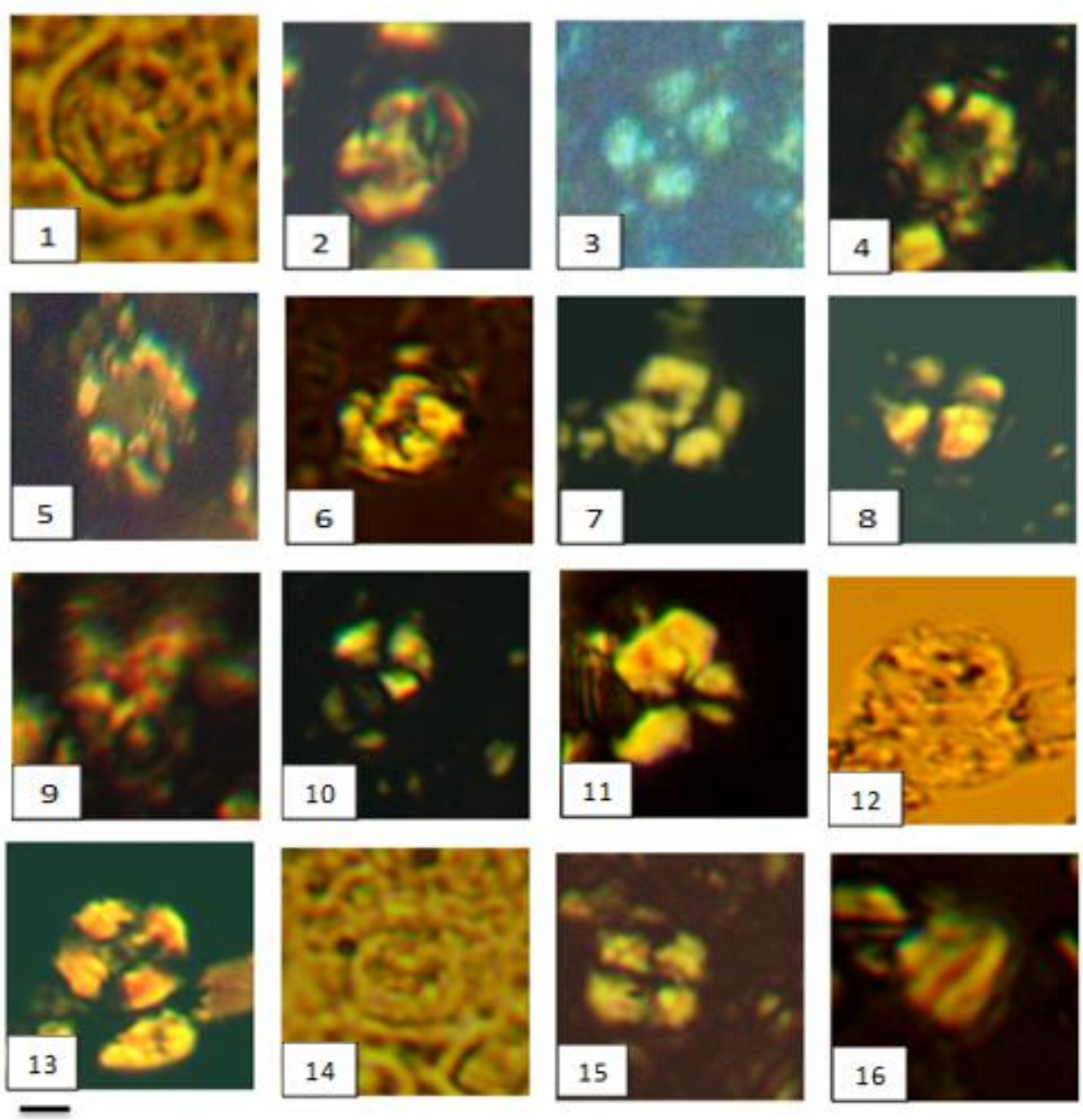


Plate 3. The Scale bar is 5µm 1- *Eiffellithus striatus* (Black, 1971) Applegate and Bergen, 1988, sample 2, 2- *Eiffellithus turriseiffelii* (Deflandre *in* Deflandre and Fert, 1954) Reinhardt, 1965, sample 39, 3- *Ellipsagelosphaera supergesta* Varol and Bowman 2019, sample 6, 4- *Eprolithus antiquus* Perch-Nielsen, 1979, sample 2, 5,6- *Eprolithus floralis* (Stradner, 1962) Stover, 1966, sample 23, 37, 7- *Flabellites oblongus* (Bukry, 1969) Crux *in* Crux et al., 1982, sample 36, 8- *Haqius circumradiatus* (Stover, 1966) Roth, 1978, sample 30, 9- *Hayesites albiensis* Manivit, 1971, sample 43, 10,11- *Hayesites irregularis* (Thierstein *in* Roth and Thierstein, 1972) Applegate et al. *in* Covington and Wise, 1987, sample 16,51, 12,13- *Microstaurus chiastius* (Worsley, 1971) Grün in Grün and Allemann 1975 emend. Bralower et al. 1989 sample 31, 14,15- *Helenea quadrata* (Worsley, 1971) Rutledge and Bown *in* Bown et al., 1998, sample 2, 16- *Lapideacassis glans* Black, 1971, sample 40.

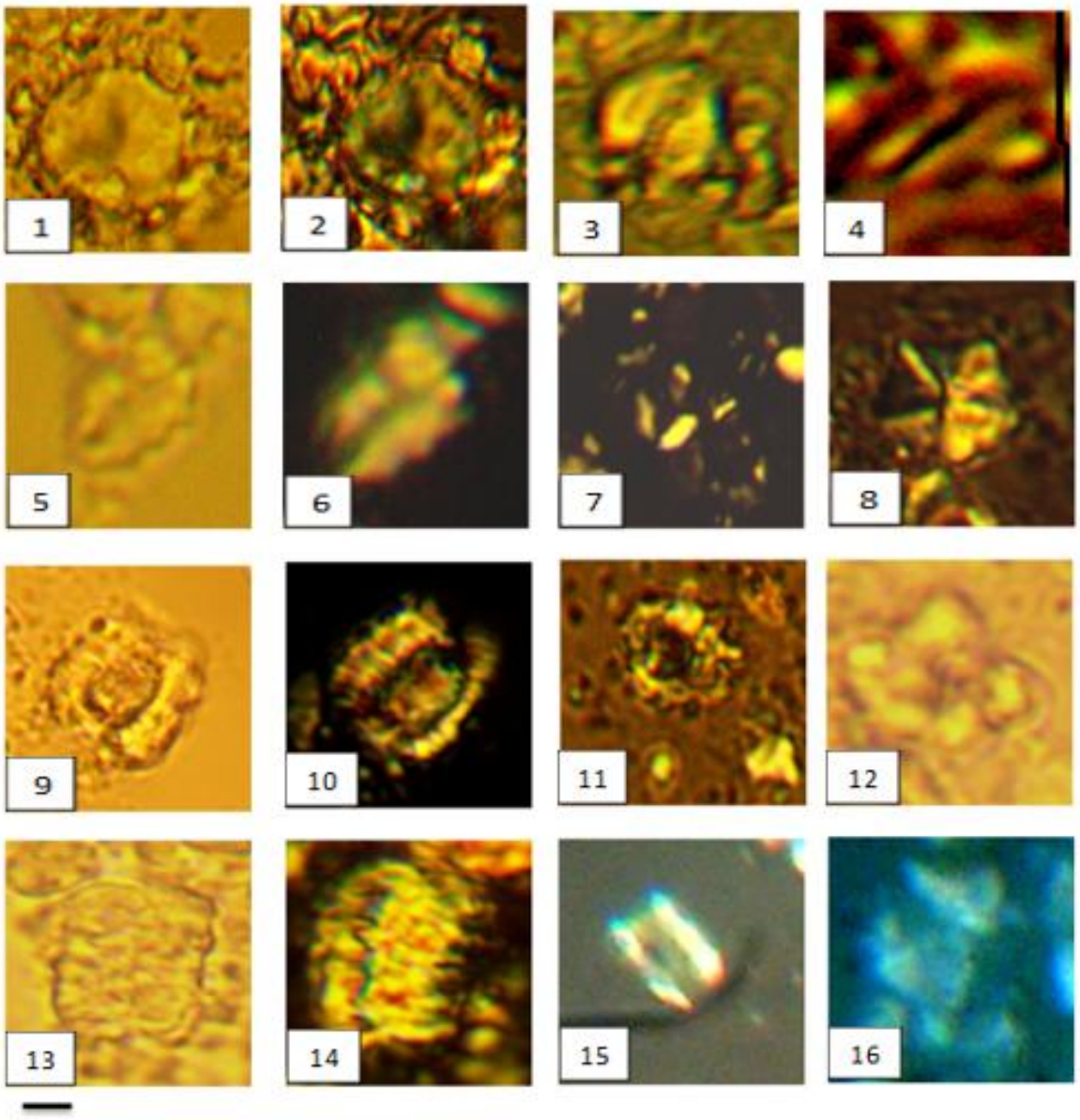


Plate 4. The Scale bar is 5µm 1,2- *Laguncula dorotheae* Black, 1971, sample 46, 3- *Lapideacassis tricornus* Wind and Wise *in* Wise and Wind, 1977, sample 50, 4- *Lithraphidites acutus* Verbeek and Manivit *in* Manivit et al., 1977, sample 50, 5,6- *Lithraphidites bollii* (Thierstein, 1971) Thierstein, 1973, sample 1, 7- *Manivitella pemmatoidea* (Deflandre *in* Manivit, 1965) Thierstein, 1971, sample 33, 8- *Micrantholithus hoschulzii* (Reinhardt, 1966) Thierstein, 1971, sample 33, 9,10- *Nannoconus bucheri* Brönnimann, 1955, sample 38, 11- *Nannoconus circularis* Deres and Achéritéguy, 1980, sample 16, 12- *Nannoconus cornuta* Deres and Achéritéguy 1980, sample 47, 13,14- *Nannoconus dislocatus* Perch-Nielsen, 1988, sample 37, 15- *Nannoconus elongatus* Brönnimann, 1955, sample 23, 16- *Micrantholithus obtusus* Stradner, 1963, sample 21.

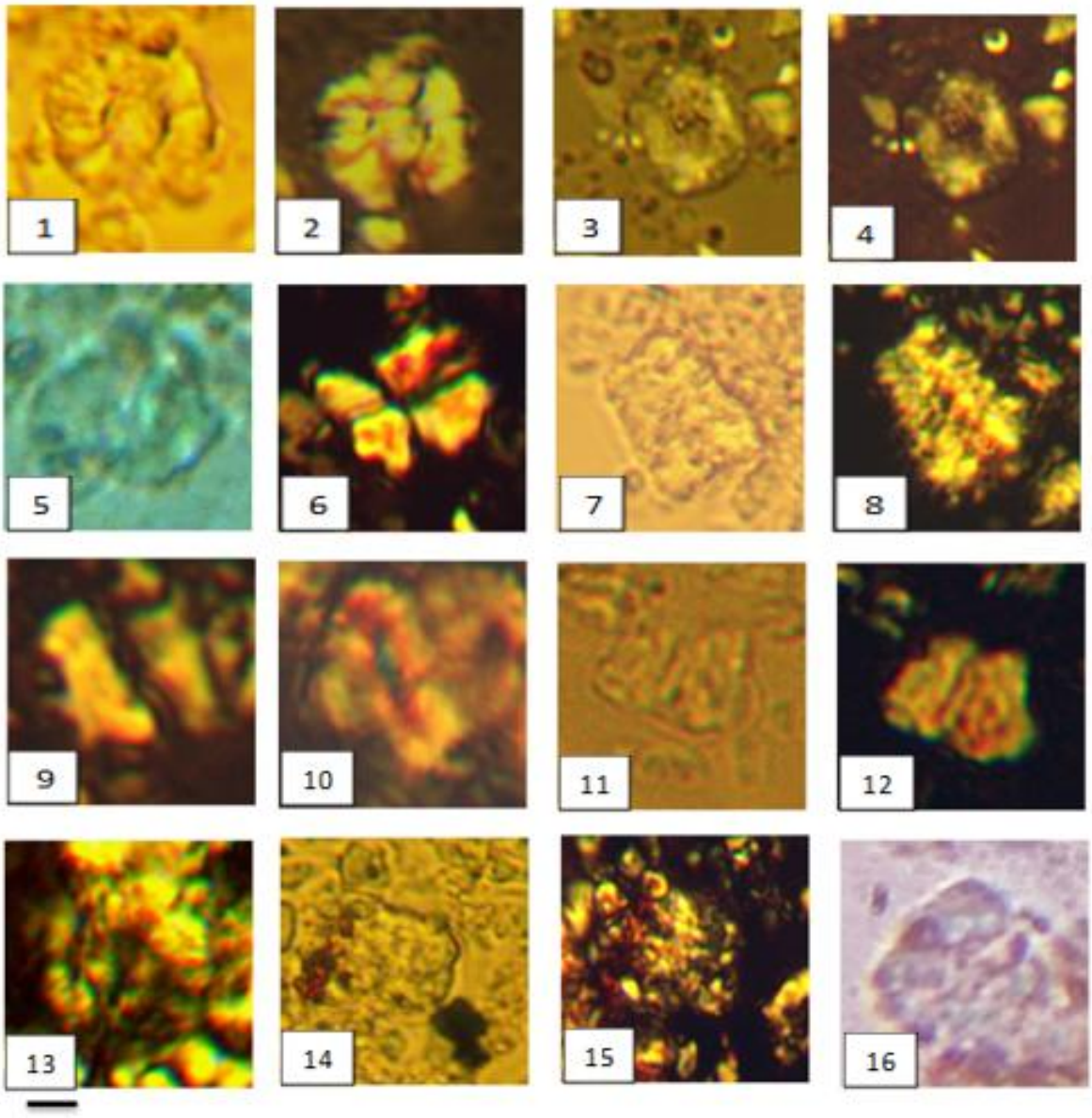


Plate 5. The Scale bar is 5µm 1,2- *Nannoconus fragilis* Deres and Achéritéguy, 1980, sample 38, 3,4- *Nannoconus globulus globulus* Brönnimann, 1955, sample 16, 5- *Nannoconus globulus minor* Bralower *in* Bralower et al., 1989, sample 13, 6- *Nannoconus inornatus* Rutledge and Bown, 1996, sample 47, 7,8- *Nannoconus kamptneri* Brönnimann, 1955, sample 32, 9- *Nannoconus minutus* Brönnimann, 1955, sample 29, 10- *Nannoconus multicadus* Deflandre and Deflandre-Rigaud, 1959, sample 29, 11,12- *Nannoconus steinmannii* Kamptner, 1931, sample 3, 13- *Nannoconus troelsenii* Alves, Lima and Shimabukuro 2017, sample 46, 14,15- *Nannoconus truittii* Brönnimann, 1955, sample 32, 16- *Nannoconus truittii frequens* DeresandAchéritéguy, 1980, sample 18.

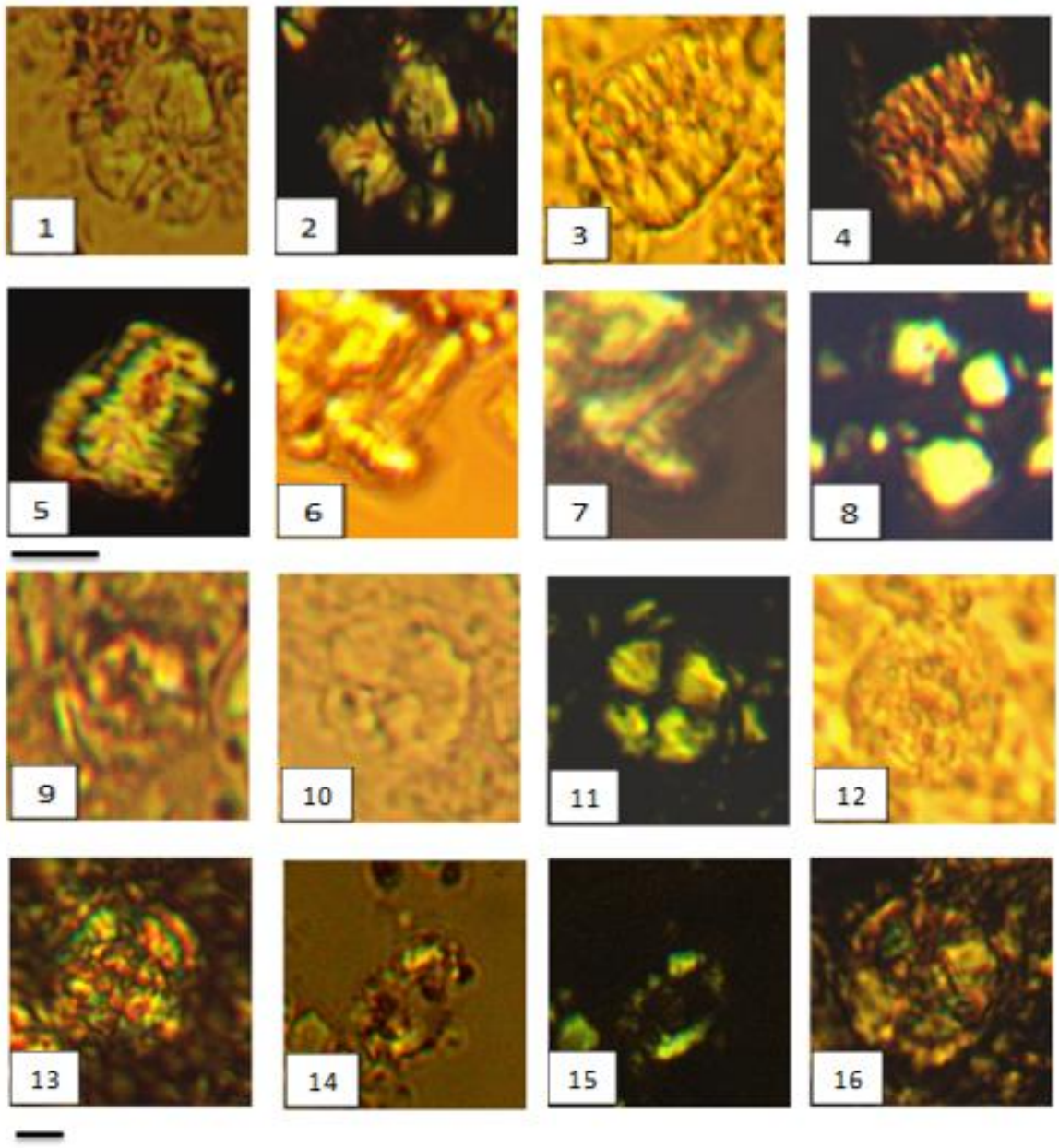


Plate 6. The Scale bar is 1-8 (7µm), 9-16 (5µm) 1,2- *Nannoconus truittii rectangularis* Deres Achéritéguy, 1980, sample 16, 3,4- *Nannoconus regularis* Deres and Acherit, sample 32, 5- *Nannoconus vocontiensis* Deres and Achéritéguy, 1980, sample 35, 6,7- *Owenia hillii* Crux, 1991, sample 40, 8- *Pickelhaube furtiva* (Roth, 1983) Applegate et al. *in* Covington and Wise, 1987, sample 48, 9- *Prediscosphaera columnata* (Stover, 1966) Perch-Nielsen, 1984, sample 28, 10,11- *Radiolithus hollandicus* Varol, 1992, sample 33, 12,13- *Radiolithus laingii* Varol, 1992, sample 33, 14,15- *Retecapsa crenulata* (Bramlette and Martini, 1964) Grün *in* Grün and Allemann, 1975, sample 13, 16- *Rhagodiscus amplus* Bown, 2005, sample 29.

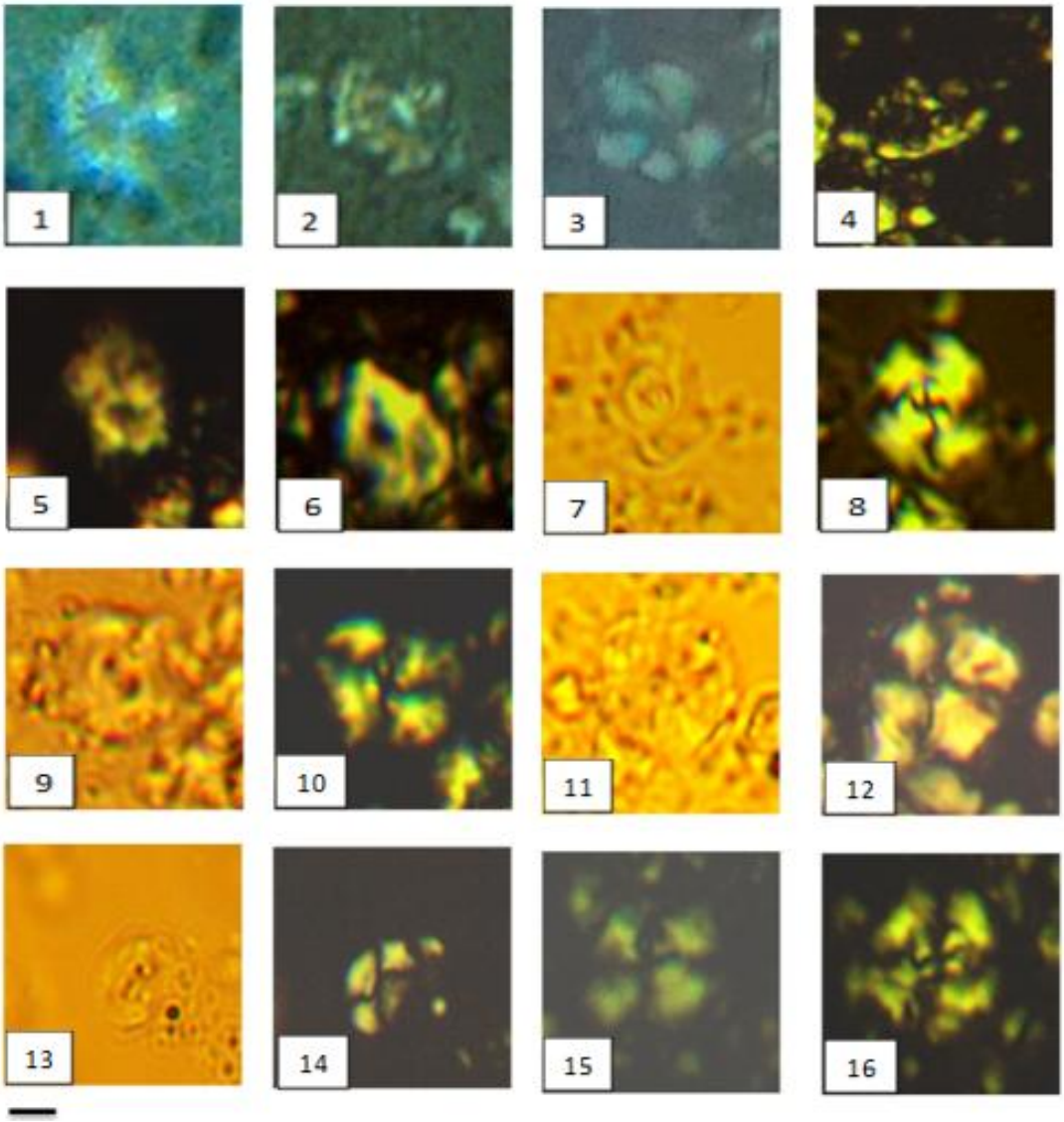


Plate 7. The Scale bar is 5µm 1- *Rhagodiscus asper* (Stradner, 1963) Reinhardt, 1967, sample 16, 2- *Rotelapillus crenulatus* (Stover, 1966) Perch-Nielsen, 1984, sample 18, 3- *Rucinolithus windleyae* Rutledge and Bown, 1996, sample 4, 4- *Speetonia colligata* Black, 1971, sample 5, 5- *Tegulalithus tessellatus* (Stradner *in* Stradner et al., 1968) Crux, 1986, sample 39, 6- *Tranolithus orionatus* (Reinhardt, 1966a) Reinhardt, 1966b, sample 34, 7,8- *Watznaueria barnesiae* (Black *in* Black and Barnes, 1959) Perch-Nielsen, 1968, sample 37, 9,10- *Watznaueria biporta* Bukry, 1969, sample 38, 11,12- *Watznaueria britannica* (Stradner, 1963) Reinhardt, 1964, sample 37, 13,14- *Watznaueria cynthae* Worsley, 1971, sample 5, 15- *Watznaueria fossacincta* (Black, 1971) Bown *in* Bown and Cooper, 1989, sample 28, 16- *Watznaueria manivitiae* Bukry 1973, sample 21

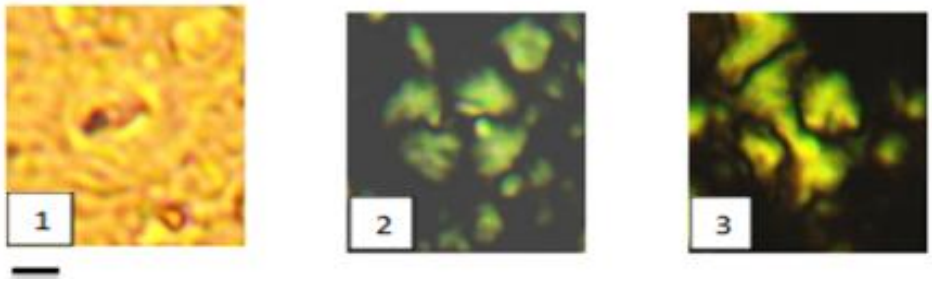


Plate 8. The Scale bar is 5µm 1,2- *Watznaueria ovata* Bukry, 1969, sample 38, 3- *Watznaueria supracretacea* (Reinhardt, 1965) Wise and Wind, 1977, sample 31.

Iraqi National Journal of Earth Science, Vol. 26 No. 04, 2026 (81-97)

Iraqi National Journal of Earth Science

www.earth.uomosul.edu.iq

الطباقية الحياتية لمتحجرات النانو الجيرية لتكوين سارمورد (الكريتاسي الأسفل – الأعلى) في طية بخمة، إقليم كردستان – شمال شرقي العراق

إيناس حازم حميد الخفاف[1]* ، **ماجد مجدي عبد المجيد المتولي[2]**

inasalkhafaf7@uomosul.edu.iq majidmutwaly@uomosul.edu.iq

[1] قسم علوم البيئة، كلية العلوم البيئية، جامعة الموصل ، الموصل، العراق.

[2] قسم هندسة النفط و التكرير، كلية هندسة النفط والتعدين، جامعة الموصل، الموصل، العراق.

* الباحث المراسل.

تاريخ الاستلام: 13 آذار 2025 تاريخ المراجعة: 02 أيار 2025 تاريخ القبول: 17 حزيران 2025

تاريخ النشر الالكتروني: 01 تشرين الأول 2026

الملخص

تمت دراسة الطباقية الحياتية لمتحجرات النانو الجيرية لتكوين سارمورد (الكريتاسي الاسفل – الاعلى) في المقطع المكشوف في الجناح الجنوبي لطية بخمة، إقليم كردستان – شمال شرقي العراق. يتألف التكوين صخارياً من المارل، الحجر الجيري المارلي والحجر الجيري والمتمثلة بحوالي 52 نموذجاً. حيث لوحظ ان هذه الطبقات الصخرية كانت مفتقرة لمتحجرات الفورامنيفرا القاعية والطحالب الخضراء، وشوكيات الجلد، بالإضافة إلى بعض بقايا الكائنات الأخرى، تم تشخيص83 نوعا تعود الى 37 جنسا من متحجرات النانو الجيرية حيث كانت الوفرة النسبية لها تتراوح ما بين المتوسطة الى الجيدة ومن خلال التوزيع الطباقي لمتحجرات النانو الجيرية تم تحديد ستة انطقة طباقية حياتية واثنان تحت نطاق. وهي من الاقدم الى الاحدث:

Speetonia colligate Interval Zone (Part) (CC4)
Lithraphidites bollii Interval Zone (CC5)
Micrantholithus hoschulzii Partial range Zone (CC6)
Chiastozygus litterarius Interval Zone (CC7)
Hayesites irregularis Interval Subzone (CC7a)
Rhagdiscus angustus Interval Subzone (CC7b)
Prediscosphaera columnata Interval Zone (CC8)
Eiffellthus turriseiffeli Interval Zone (CC9)

تمت مضاهاة هذه الانطقة مع مجموعة من الانطقة الطباقية العالمية والمحلية ومن خلال ذلك تم تحديد عمر التكوين الممتد من الهاتروفيان المبكر والى السينومينيان المبكر.

الكلمات المفتاحية:

الطباقية الحياتية، متحجرات النانو الجيرية، تكوين سارمورد، طية بخمة

DOI: 10.33899/injes.v26i4.56104, ©Authors, 2026, College of Science, University of Mosul.

This is an open-access article under the CC BY 4.0 license (http://creativecommons.org/licenses/by/4.0/)

Iraqi National Journal of Earth Science, Vol. 26, No. 04, 2026 (98-107)

Iraqi National Journal of Earth Science

www.earth.uomosul.edu.iq

Petrophysical Properties and Sedimentology of the Palani Formation (Late Eocene-Early Oligocene) from Kirkuk Oil Field, Northeastern Iraq

Ezzat I. Al-Fandi [1*], Zaid A. Malak [1], Rafee Ibraheem AL-Hamidi [1]

ezzatalfandi@uomosul.edu.iq zaidmalak@uomosul.edu.iq rafeegeo66@uomosul.edu.iq

[1]*Department of Geology and Petroleum, College of Science, University of Mosul, Mosul, Iraq.*
** Correspondence author.*

Received: 05 September 2024 Received in revised form: 29 October 2024 Accepted: 30 December 2024
Available online: 01 October 2026

Abstract

The Oligocene sequences in northeastern Iraq encompass nine formations collectively referred to as the Kirkuk Group. This study emphasizes the Palani Formation within the Kirkuk oil field, specifically at well (KX16) located in the Baba Dome. The Palani Formation, dating to the late Eocene to early Oligocene, is predominantly composed of limestone and marly limestone. Its thickness measures approximately 29 meters, spanning depths of 768 to 797 meters. Petrophysical analyses, including Gamma Ray (GR), Neutron, and Density Logs, reveal a significant shale content (V-Shale up to 1.0) and variable porosity across zones. The formation is subdivided into four zones based on reservoir potential: Zone A (poor reservoir rocks), Zone B (moderate porosity), Zone C (poor reservoir rocks), and Zone E (good reservoir rocks with high productivity). Mineralogical identification through cross-plots underscores the limestone dominance, which is crucial for reservoir characterization and secondary porosity assessment. Additionally, the Palani Formation features fine-grained sediments and reflects deposition in a low-energy basinal environment. These findings underscore the importance of detailed petrophysical and mineralogical studies in enhancing the understanding of hydrocarbon reservoirs and evaluating their potential productivity in the context of regional geology.

Keywords:

Kirkuk oil field; Palani Formation; limestone; High porosity; Petrophysical analyses

DOI: 10.33899/injes.v26i2.56115, ©Authors, 2026, College of Science, University of Mosul.
This is an open-access article under the CC BY 4.0 license (http://creativecommons.org/licenses/by/4.0/) .

==========

1. Introduction

The study of Tertiary sequences in Iraq is of great significance, encompassing some of the most crucial oil-bearing strata in Iraq and the Middle East, particularly within the Kirkuk Governorate in northeastern Iraq, specifically in the Kirkuk Oil fields. Over the past four decades, this area has garnered substantial attention, marked by active exploration activities that employ various modern methods and techniques for hydrocarbon exploration (Oil Exploration Company, 2019). A significant portion of these efforts has been undertaken by Iraqi researchers, complemented by the involvement of foreign companies operating in the region. These endeavors have yielded a wealth of critical and essential field data regarding the surface and subsurface geology of the area. The abundance of formations deposited during the Eocene to Oligocene, along with the various tectonic movements that occurred, further expresses the importance of this era. Moreover, numerous oil reservoirs are situated within the formations of this period, distinguished by their substantial hydrocarbon content (Jassim and Goff, 2006).

The Palani Formation has been described in various subsurface profiles with a single outcrop at Qara Chauq by Bellen (1956). Within the Kirkuk oil field, the formation exists within the Targil Dome at well Kirkuk-85. The Palani Formation comprises dolomitized globigerinal limestone (Jassim and Goff, 2006). Ditmar et al. (1971) proposed a late Eocene age for the formation; others, such as Bellen (1956), Kharajiany (2008), Banna (2008), and Al-Jwaini (2015), suggested an early Oligocene age, based on its stratigraphic context between the late Eocene Jaddala Formation and the early Oligocene Sheikh Alas Formation.

The stratified sequence of the Oligocene in the Sinjar region of Northern Iraq was studied by Al Banna et al. (2010), they indicated that the Oligocene sequences are incompatible with the formation of Jaddala with the age of the Eocene, and are compatible and sometimes incompatible with the formations of Anah and Ibrahim (early Miocene) age. Al-Tamimi (2011) studied the stratigraphy and reservoir properties in Oligocene sequences in the Kirkuk region, identified four depositional environments from this sequence, and pointed out that the Palani Formation represents the deep basin environment (basinal environment). Ghafur (2012) conducted a study of the characteristics of sediments and reservoirs of the Kirkuk Group in Northern Iraq (Oligocene – early Miocene). The formations of the Kirkuk Group were studied to determine the lithostratigraphic and biostratigraphic frameworks, in addition to identifying the diagenetic processes, types of carbonate platforms, and the depositional environment. The study stated that the environment of the Palani Formation is deep (basinal), characterized by fine-grained sediments, low-energy conditions, and deposition primarily in a pelagic or hemipelagic setting. Ghafur also highlighted the role of tectonic activity during the Oligocene and early Miocene in shaping the depositional patterns and influencing the distribution of facies within the Kirkuk Group. According to the study of Al-Bayati (2023), the depositional environment of the Palani Formation in central and northern Iraq is represented by an outer slope. Al-Hamdany (2023) conducted a study on the Palani and Sheikh Allas formations in wells K-218 and K-246 within the Kirkuk Oilfield. The study focused on microfacies analysis, petrophysical properties, and reservoir evaluation. The results indicated that the Palani Formation is of Early Oligocene age and was deposited in a deep marine outer shelf environment, whereas the Sheikh Allas Formation was deposited in a reef environment. The study also showed that the Sheikh Allas Formation has higher porosity and permeability than the Palani Formation.

The aim of the current research on the Palani Formation is to achieve the following:

Study the Petrophysical Properties of the formation to determine its significance as a reservoir and its role in preserving hydrocarbons.

Evaluate production potential for oil exploration to assess the production potential of the Palani Formation by utilizing data analyzed and interpreted through the Petrophysics v3.6 program. This includes calculating porosity and other key properties to classify reservoir zones.

Classify sedimentary patterns: To divide the Palani Formation into areas with varying porosity characteristics based on data analysis results.

2. Location of the Study Area

The study area is situated in the Northeastern part of Kirkuk Governorate, within the Kirkuk oil field. The Kirkuk oil field spans approximately 100 km in length and 4.5 km in width (Figure 1). This research focuses on the Palani Formation, utilizing data from the well KX16, which is positioned in the Baba Dome, a segment of the Kirkuk oil field. The Palani Formation has a thickness of roughly 29 meters, between depths of 768 and 797 meters.



Fig. 1: Map showing the location of the studied well (AL-Tamimi, 2011).

3. Methods and Materials

The current research was conducted on Well KX16 in the Kirkuk oil field, utilizing available logs from the Northern Oil Company to study the petrophysical characteristics. The gamma-ray log was employed for porosity volume calculation, while neutron and density logs were used to calculate the total and effective porosity. These log data were input into a scanner and then converted from their paper or image format to digital data in a lase file format, easily manageable through the Neuralog V 2010.11 computer program. Subsequently, petrophysical properties were studied, involving porosity calculations using the Interactive Petrophysics v3.6 program. Petrophysical analysis was conducted primarily through common mathematical equations and some standard charts (Schlumberger) applied to

log data, following sensor studies (Schlumberger, 1997).

At Kirkuk well KX16, the Palani Formation is about 29 meters thick, spanning depths from 768 to 797 meters (Figure2). It is composed predominantly of gray, robust limestone and marly limestone, occasionally interbedded with very thin bands of marl. It contains foraminifera fossils and assorted bioclastic fragments. The Palani Formation is underlain unconformably by the Jaddala Formation and overlain conformably by the Sheikh Alas Formation (Figure 2).

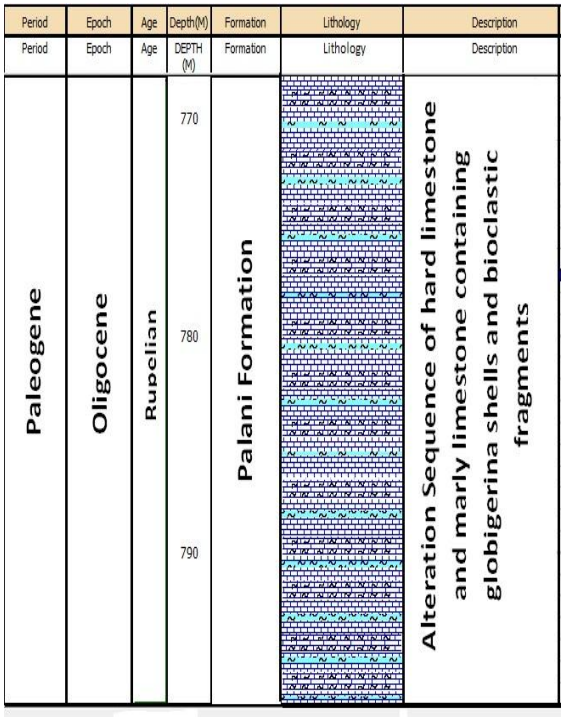


Fig. 2: lithological column of the Palani Formation at well KX16.

4. Geological setting and Stratigraphy

Iraq is divided into three zones: the Mesopotamian Zone, the Foot Hill Zone, and the High Folded Zone. The current research area is situated in the northeastern part of Iraq within the Foot Hill Zone, in the Hamrin-Makhul subzone. This zone is characterized by narrow, asymmetrical, longitudinal anticlines separated by broad synclinal depressions, and it features a thick sedimentary cover (Jassim and Goff, 2006).

The Kirkuk oil field consists of three main domes: the Northern dome (Khurmala), which is gas-bearing; the central dome (Avanah), which contains Eocene strata suitable for oil reservoirs; and the third dome (Baba), which is located within the study area and contains the Tertiary strata. The area of study lies in the northeastern part of the field within the Kirkuk Governorate and is intersected by the Kirkuk reverse fault (Sayab, 1982).

Due to the significance of the Kirkuk oil field, its stratigraphy has been thoroughly examined (Henson,1950; Bellen,1956; Dunnington,1958). Subsequent studies have been conducted by foreign companies, employees of the North Oil Company, and numerous researchers (such as Al-Hashimi, 1975; Al-Jubouri, 1982; Zaki, 1990).

The Tertiary formations are particularly important from a reservoir perspective, especially the so-called Main Limestone, due to its high permeability and porosity, making it a distinguished field in the Middle East (Dunnington, 1958). The sedimentary sequences of the Tertiary period range from the late Paleocene to the late Miocene. The Tertiary deposits are divided into seven depositional cycles, with the reservoir rocks belonging to the Oligocene cycle, dating back 25-35 million years. The Oligocene deposits in Iraq are characterized by their limited extent and distribution, disappearing in most parts of Iraq but appearing in the Kirkuk area, the Ana area (Tatar, 1988), the Sinjar uplift (Ismail, 2006), and Mount Ashtagh (Kharajiany, 2008). Their thickness is also reduced, and there are some issues regarding the stratigraphy of the boundaries of this cycle, including unclear boundaries due to ambiguous or transitional contacts, evidence of erosion and unconformities complicating depositional continuity, lateral facies variability making correlation across regions challenging, structural deformation disrupting the stratigraphic record, diagenetic overprinting altering the original sedimentary characteristics, biostratigraphic uncertainties due to ambiguous fossil records, and incomplete data sets hindering precise interpretations (Buday, 1980).

The Oligocene sequences comprise nine formations: Shurau, Sheikh Alas, Palani, Bajwan, Baba, Tarjil, Anah, Azkand, and Ibrahim. This group is known as the Kirkuk Group, a term introduced by Henson (1950), which established the foundational stratigraphic framework and reef concepts, dividing them into reefs, fore-reefs, and back-reefs within the Kirkuk oil field.

Bellen (1956) studied the stratigraphy of the so-called Main Limestone in the structures of Kirkuk, Bai Hassan, and Qara Chauq Dagh. He

concluded that the formations comprising this cycle are bounded by unconformities at the top and bottom and suggested the presence of Lower, Middle, and Upper Oligocene beds. Later, Bellen et al. (1959) further divided the Oligocene deposits into nine formations within three sequences, corresponding to the Early, Middle, and Late Oligocene ages (Jassim and Goff, 2006).

However, (Ditmar et al., 1971) and (Bellen,1956) revised this classification, reducing it to two sequences instead of three, based on lithostratigraphic correlations and well log records.

The stratigraphic sequences of the Tertiary period show a transition from deep basin formations (Ibrahim, Palani, Tarjil) to shallower formations (Sheikh Alas, Baba), followed by even shallower formations (Shurau, Bajwan). This progression leads to restricted lacustrine environments, represented by the Fat'ha Formation, and ultimately to environments with continental deposits, as seen in the Injana and Mukdadiya formations. This study focuses on the examination of the first depositional cycle of the early Oligocene for well KX16, represented by the Palani Formation.

5. Shale Volume Determination

The first step involved employing a Gamma Ray (GR) log to calculate the shale volume (V-Shale) for the Palani Formation, impacting porosity values, water saturation, and hydrocarbon presence. The initial action was extracting the Gamma Ray Index (IGR) using the following equation

$$I_{GR} = \frac{GR_{\log} - GR_{\min}}{GR_{\max} - GR_{\min}} \quad \text{..... (1)}$$

Where:

IGR ……. Gamma ray index.

GRLog……..Gamma ray reading of formation.

GRmin……. Maximum gamma ray.

GRmax….(Shale) Maximum gamma ray Shale.

This facilitated the calculation of shale volume values in selected cross-sections, enabling their representation with depth and illustrating their vertical distribution within the formation sequences. Figure (3) illustrates the gamma ray values for well KX16, ranging from GR Clean at 17.22 API to GR Clay at 47.95 API. Figure (4) depicts the determined shale volume in the Palani Formation, indicating a maximum V. sh. value of 1.0, signifying high shale content. Figure (5), on the other hand, illustrates the relationship between GR and V. Sh. in the Palani Formation.

The second step involved applying the Larionov equation (1969) for post-Cretaceous sequences, specifically Tertiary rock :

$$V\text{-}Shale = 0.083 * (2^{(3.7*IGR)} - 1) \quad \text{..... (2)}$$

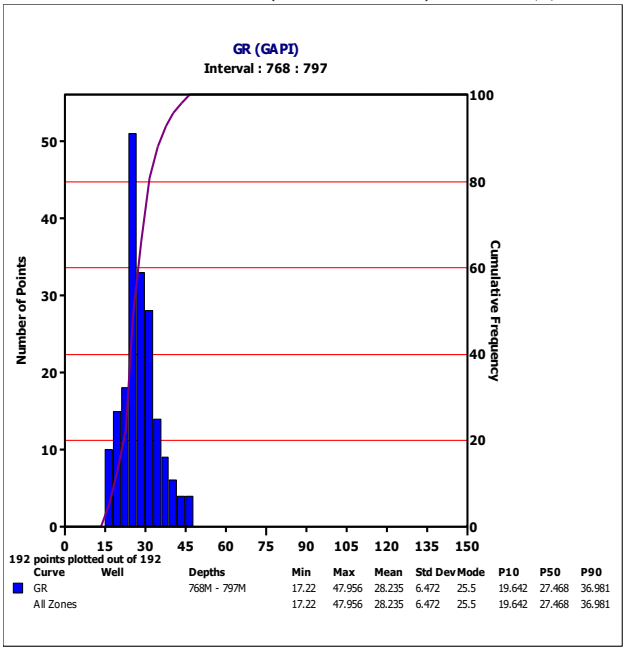


Fig. 3: A histogram illustrates the highest and lowest Gamma Ray (GR) values for well KX16 between the depths 797-768 in the Palani Formation.

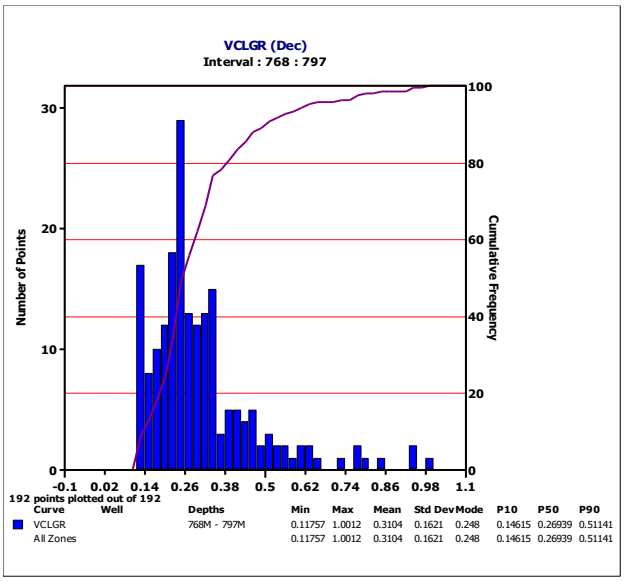


Fig. 4: A histogram illustrates the highest and lowest values for shale volume (V.sh.) in well KX16 between the depths 768-797 in the Palani Formation.

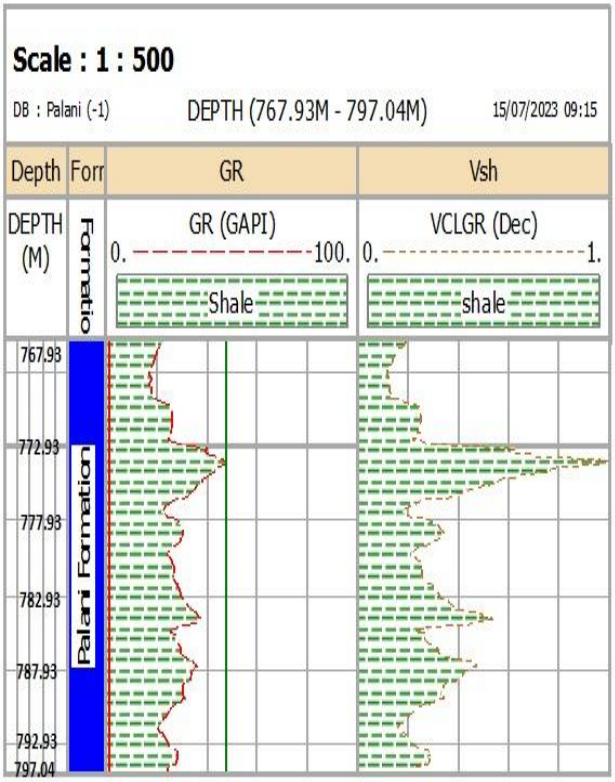


Fig. 5: Illustrates the relationship between Gamma Ray (GR) and shale volume (Vsh) for the Palani Formation in well KX16.

6. Porosity Estimation

Porosity, expressed as the percentage of rock pore volume to its total volume (Figure 6), is estimated using the formula of Schlumberger (1984) and Schlumberger (1997):

$$porosity\ \emptyset\ (\%) = \frac{Vb - Vgr}{Vb} \times 100 = \frac{Vp}{Vb} \times 100$$

Porosity is commonly measured indirectly using well-logging tools such as the Neutron Log and Density Log, combining their results with the equation:

$$\emptyset\, t = \frac{\emptyset D + \emptyset N}{2} \ldots\ldots\ldots\ldots\ldots\ldots\ldots\ldots (3)$$

Where:

Øt: total porosity

ØD: porosity from Density Log

ØN: porosity from Neutron Log

This technique indirectly measures rock porosity by logging rock density and utilizing it in the porosity calculation:

$$\phi_\rho = \frac{(\rho_{ma} - \rho_b)}{(\rho_{ma} - \rho_f)} \ldots\ldots\ldots\ldots\ldots\ldots (4)$$

Where:

$Ø\rho$: Porosity by density log

ρ_{ma}: Matrix density

ρ_b: Bulk density from log

ρ_f: Fluid density

For Palani Formation limestone, (ρma) is calculated as 2.71 gm/cm^3, and the fluid density ρ f for drilling mud (salt mud) is\ (1.1 gm/cm^3).

The neutron log is directly calculated from the tool using Equation … (3)

Effective Porosity (Øe) representing the connected pore volume to the total rock volume occupied:

by clay or shale, is calculated by:

$$Øe = Øt^{\times}(1\text{-}Vsh) \ldots\ldots\ldots\ldots (4)$$

Secondary Porosity, formed within the reservoir after deposition, such as cavities in carbonate rocks resulting from dissolution or fractures in reservoirs, can be calculated using the Secondary Porosity Index (SPI):

$$SPI = Øt\text{-}ØS \ldots\ldots\ldots\ldots\ldots\ldots\ldots (5)$$

Where:

Øt: Total Porosity.

ØS: Porosity from Sonic Log

To calculate Sonic Porosity (Øs) using the Sonic Log, changes in lithology for the studied formations in well K-216 are considered, and the following equation is applied: Wyllie Typical values (µsec/ft)

Matrix Δt: 51-55 SS; 47.5 LS; 43.5 DOL

Fluid Δt: 189 (salt water)

$$Øs = \Delta tlog - \Delta tma\ /\Delta tfl - \Delta tma \ldots\ldots\ldots\ldots (6)$$

Where:

Δtlog: Sonic log travel time; Δtma: Matrix travel time

Δtfl: Fluid travel time for the Palani Formation limestone (Δtma 47.5 µsec/ft).

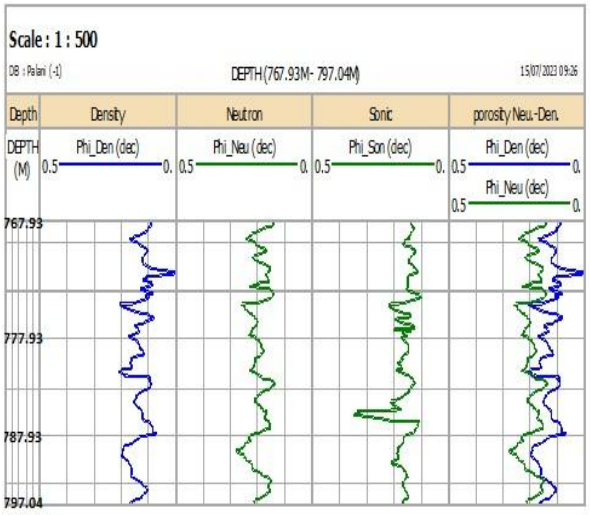


Fig. 6: Relationship between Density – Neutron and Sonic and Porosity in the well KX16.

7. Reservoir Zonation:

Based on the calculated porosity values for the selected formation using indirect methods (well-logging tools) and relying on effective porosity. The Palani Formation is composed of limestone. It has a thickness of approximately 29 meters, ranging between depths of 797 and 768 meters in well KX16. This zone was subdivided into several subzones (Figure 7):

Palani Zone A:

This subzone represents the rock sequences of the Palani Formation, consisting of limestone. It has a thickness of about 8 meters, ranging between depths of 776 and 768 meters in well KX16.

The porosity of the rocks in this zone is described as weak (6-10%), earning them the traditional classification of poor reservoir rocks according to conventional exploration literature.

Palani Zone B:

This zone comprises the rock sequences of the Palani Formation, characterized by limestone. It has a thickness of approximately 7.3 meters, ranging between depths of 783.8-776 meters in well KX16. The porosity of the rocks in this zone is described as ranging from weak to moderate (8-15%). Accordingly, according to traditional exploration literature, these rocks are classified as intermediate reservoir rocks with moderate productivity.

Palani Zone C:

This zone represents the rock sequences of the Palani Formation, consisting of limestone. It has a thickness of around 6.7 meters, ranging between depths of 790-783.8 meters in well KX16. The porosity of the rocks in this zone is characterized as weak (9-10%). Thus, following conventional exploration literature, these rocks are classified as poor reservoir rocks with low productivity.

Palani Zone E:

This zone represents the rock sequences of the Palani Formation, composed of limestone. It has a thickness of approximately 7 meters, ranging between depths of 797-790 meters in well KX16. The porosity of the rocks in this zone is characterized as very good (15-16%). According to traditional exploration literature, these rocks are classified as good reservoir rocks with high productivity.

It is noteworthy that the total porosity values do not show significant differences compared to the accepted effective porosity values in some small units due to shale volume. Zone B is characterized as having moderate productivity, while Zone E is classified as having good productivity. Zones C and A are characterized as having poor productivity due to a high shale volume in these zones.

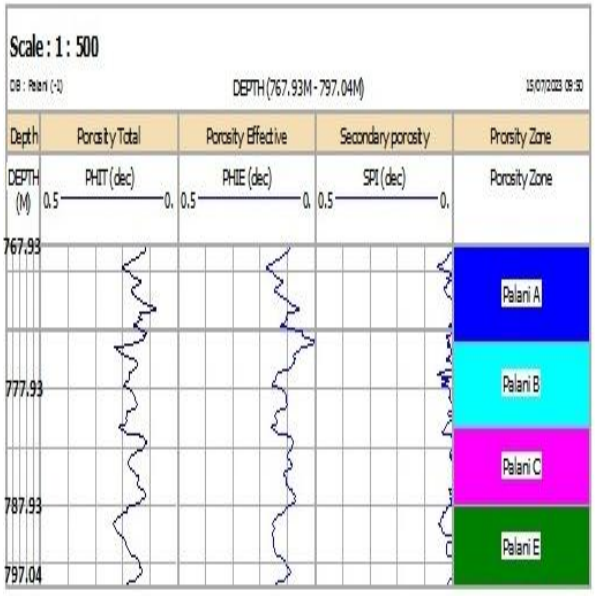


Fig. 7: Reservoir zonation of the Palani Formation depicting total and effective porosity along with secondary porosity in well KX16.

8. Identification of lithology and mineralogy

The identification of the lithology of the formation is crucial for reservoir characterization since the physical and chemical properties of rocks, including the presence of hydrocarbons or water, impact the estimation of formation properties. In the case of the studied Palani Formation, the density, neutron, and sonic logs were utilized for lithology identification.

- ***Neutron –Density Cross Plot for lithology identification***

The Neutron-Density Cross Plot method was employed for lithology identification. This method relies on the intersection of the pb vs Neutron plots (Schlumberger, 1989), primarily representing the cross-plot values of both derived porosity and total density. This allows for obtaining porosity values resulting from their interaction. The plots exhibited

a scattered distribution of values, reflecting variations in the formation's lithology. Figure (8) illustrates that most of the Palani Formation sequences fall within the limestone range based on the points plotted on the cross-plot. Density-neutron and sonic logs.

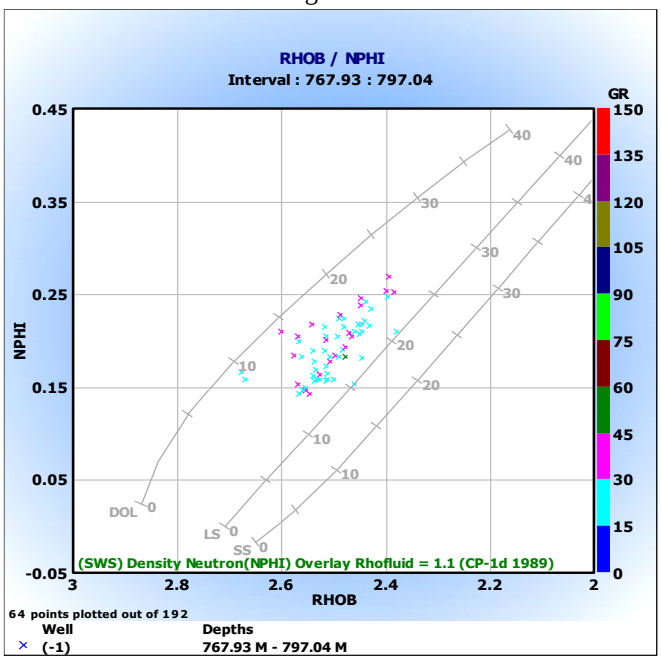


Fig. 8: The Pb vs Neutron cross-plot exhibits a scattered distribution of values, indicating variations in the lithology of the Palani Formation sequences in well KX16.

- ***M-N Cross Plot for mineral identification***

For complex mineralogical identification of lithology, the M-N Cross Plot provides a dual- and triple-mineral mixture chart Schlumberger, 1997). This chart includes values for individual minerals such as calcite, dolomite, sandstone, gypsum, sulfur, gas, and secondary porosity zones. By plotting M-N values and selecting a cross-section, mineral composition for the chosen formation is determined. It is observed that the formation consists of a mixture of limestone and secondary porosity by intersecting the M-N plot with the Pb vs. ØN porosity cross-plot, as depicted in Figure (9).

$$M = \frac{\Delta tf - \Delta tlog}{\Delta tlog - \Delta tlog} \text{.....(7)}$$

Where:

Δt log: transit travel time from sonic log μsec/ft.

Δtf: transit travel time of the formation fluid equal to 189 μsec/ft.

ρb: bulk density from density log g/cc.

ρf: bulk density of the formation fluid equal to 1.1 g/cc.

Øn log: porosity from neutron log.

ØNf: porosity for the formation fluid equal to 1.1

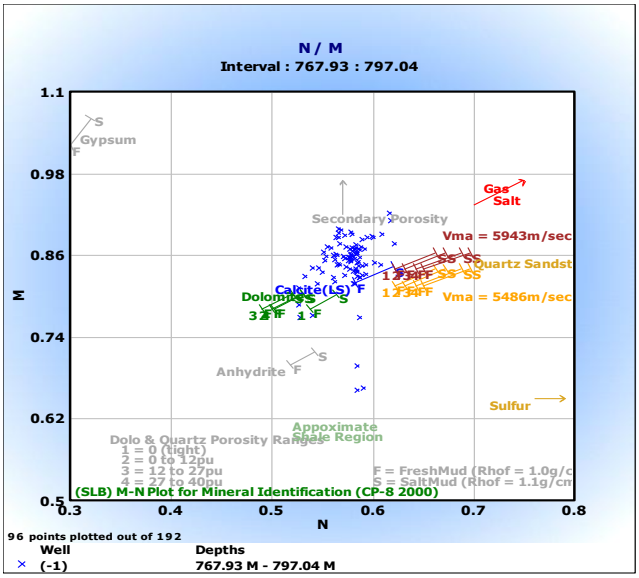


Fig. 9: Mineralogical Identification of the Palani Formation in well KX16.

9. Conclusions

The Palani Formation at well KX16 is situated between the Jaddala Formation (late Eocene) and Sheikh Alas Formation (early Oligocene) and is predominantly composed of limestone and marly limestone. Its thickness is approximately 29 meters, extending from depths of 768 to 797 meters.

Shale volume within the Palani Formation was determined by using a Gamma Ray (GR) sensor and the Larionov equation, revealing significant shale content with V-Shale reaching up to 1.0 in some sections. Porosity, a critical parameter for reservoir characterization, was estimated indirectly using well-logging tools such as the Neutron Log and Density Log. Effective porosity (Øe) calculations considered the presence of shale, impacting the reservoir's productivity potential across different zones.

Based on porosity values derived from these methods, the Palani Formation was divided into several subzones within:

-Palani Zone A: Thin, with weak porosity (6-10%), classified as poor reservoir rocks.

-Palani Zone B: Moderate thickness, exhibiting moderate porosity (8-15%), categorized as intermediate reservoir rocks.

-Palani Zone C: Limited thickness with weak porosity (9-10%), also classified as poor reservoir rocks.

-Palani Zone E: Substantial thickness, showcasing very good porosity (15-16%), categorized as good reservoir rocks with high productivity potential.

Mineralogical identification, crucial for understanding the formation's composition and its implications for hydrocarbon exploration, was performed using cross-plots such as the Neutron-Density and M-N plots. These plots indicated a predominant composition of limestone within the Palani Formation, essential for determining reservoir characteristics and potential secondary porosity zones.

10. Acknowledgements

The authors are very grateful to the College of Science, University of Mosul, for their provided facilities, which helped to improve the quality of this work. The authors are very grateful to the Editor-in-Chief Prof. Dr. Rayan Ghazi, the editorial board members, and the technical editors for their great efforts and valuable comments.

11. Conflict of Interest

The authors declare that they have no conflict of interest.

12. Funding Statement

This research received no external funding.

13. Author Contributions

I, Ezzat I. Al-Fandi, as the first and corresponding author, conducted the main petrophysical analysis and interpretation of the well-log data using Interactive Petrophysics (IP) v3.6. I was responsible for the interpretation and analysis of the petrophysical data, including shale-volume determination, porosity estimation, reservoir zonation, lithological and mineralogical identification, interpretation of cross-plots, and the overall scientific interpretation of the results. I also contributed substantially to the preparation and writing of the manuscript.

Dr. Zaid A. Malak contributed to the preparation and organization of the data and models, data processing, literature research, and revision and editing of the manuscript.

Dr. Rafee Ibrahim Al-Hamidi contributed to the scientific review, proofreading, and final checking of the manuscript.

The authors confirm that these statements accurately represent their respective contributions to the work and that all authors have reviewed and approved the final version of the manuscript.

14. References

Al-Banna, N.Y., 2008. Stratigraphic Note: Oligocene/Miocene boundary in northern Iraq, Geo Arabia-Manama, 13,187. http://dx.doi.org/10.2113/geoarabia1302187

Al-Banna, N.Y., Al-Mutwali, M.M. and Ismail, N.R., 2010. Oligocene stratigraphy in the Sinjar Basin, northwestern Iraq. Geo Arabia, 15(4), 17-44. http://dx.doi.org/10.2113/geoarabia150417

Al-Bayati, Y.K.J., 2023. Sedimentology and Sequence Stratigraphy of Oligocene Succession in Selected Sites of Iraq, Ph.D. Thesis (unpublished), University of Tikrit, Iraq, 191 P. http://dx.doi.org/10.33899/earth.2023.139106.1059

Al-Hamdany, D.M.I., 2023. Microfacies Analysis and Petrophysical Properties of Palani and Sheikh Allas Formations (Lower Oligocene) in Two Selected Wells of Kirkuk Oilfield, Northeastern Iraq. Unpublished M.Sc. Thesis, College of Science, University of Mosul, Mosul, Iraq, 119 P. (In Arabic)

Al-Hashimi, M. H. 1975. Geological Investigations of the Kirkuk Oil Field. Journal of Petroleum Geology, 22(2), pp. 189-210.

Al-Jubouri, J. R. 1982. Stratigraphy and Oil Potential of the Kirkuk Basin. Iraq Geological Society, 11(3), pp. 212-229.

AL-Jwaini, Y.S.K., 2015. Sequence Stratigraphy and Reservoir Characterization of the Late Paleogene - Early Neogene Succession in Kirkuk Area" Ph. D. Thesis (unpublished), University of Baghdad, Iraq, 230 P.

AL-Tamimi, A.M., 2011. Stratigraphy and Reservoir Characterization of the Oligocene Succession, Kirkuk Area, M.Sc. Thesis, University of Baghdad. http://dx.doi.org/10.26842/binhm.7.2022.17.1.0049

Bellen, V.R.C., 1956. The stratigraphy of the Main Limestone of the Kirkuk, Bai Hassan and Qara Chauq Dagh structures in Northern Iraq. Journal of the Institute of Petroleum, 42, pp. 233- 263.

Bellen, V.R.C., Dunnington, H.V., Wetzel, R. and Morton, D.M., 1959. Lexique Stratigraphique International. V. III, Asia, Fascicule, 10a, Iraq, Central National deal Recherche's Scientifique, Paris, 333 P.

Buday, R.T., 1980. The regional geology of Iraq, 1, stratigraphy and paleogeography, Kassab, I. I. M. Jassim, S.Z. (ed). SOM, Baghdad, 445

Ditmar, V. Iraq-Soviet Team, 1971. Geology conditions and hydrocarbon prospects of the Republic of Iraq (Northern and Central parts).

Dunnington, H.V., 1958. Generation, migration, accumulation and dissipation of oil in northern Iraq. In Weeks, G.L. (Ed), Habitat of oil, symposium. American Association of Petroleum Geologists, pp. 1194- 1251.

Ghafur, A.A., 2012. Sedimentology and reservoir characteristics of the Oligocene Miocene carbonates (Kirkuk Group) of Southern Kurdistan, Ph.D. Thesis, 324 P. http://dx.doi.org/10.13140/RG.2.2.27521.30565

Henson, F.R.S., 1950. Cretaceous and Tertiary reef formations and associated sediments in Middle East. American Association of Petroleum Geology Bulletin, 34, pp. 215–238.

Ismail, N.R., 2006. Biostratigraphy and Sequence Stratigraphy of the Oligocene-Early Miocene Formations in the Sinjar Basin, Northwest Iraq. Unpublished Ph.D. Thesis, College of Science, University of Mosul, 222 P.

Jassim, S.J. and Goff, J.C., 2006. Geology of Iraq, published by Dolin, Prague and Moravian Museum, Brno, First Edition, 318 P.

Kharajiany, S.O.A., 2008. Sedimentary facies of Oligocene rock units in Ashdagh mountain-Sangaw District-Kurdistan region, NE Iraq, Unpublished M.Sc. thesis, College of Science, University of Sulaymania, 137 P.

Larionov, V.V., 1969. Borehole Radiometry, Moscow, U.S.S.R., Nedra, 127 P.

Oil Exploration Company (OEC) Y., 2019. B. Study of the structural image of the Tertiary formations in Ismail field, unpublished study.

Schlumberger, 1972. Log Interpretation, Volume I - Principles, Schlumberger Limited, U.S.A., 113.

Schlumberger, 1979. Log Interpretation Charts. Schlumberger Wireline and Testing, Houston, Texas, 193 P.

Schlumberger, 1984. Well Evaluation Conference, India. Schlumberger Limited, 263 P.

Schlumberger, 1989. Interpretation Principles and Applications. Schlumberger Limited, U.S.A.

Schlumberger, 1997. Log Interpretation Charts, Schlumberger Wireline and Testing, Houston, Texas, 195 P.

Siab, A., 1982. Geology of Iraq, Dar Al-Kutub Printing and Publishing House, University of Mosul, 280 P.

Tatar, Y.A., 1988. Subsurface Sedimentary Study of Some Tertiary Formations in the Western Desert Region - Iraq, Unpublished MSc. Thesis, University of Mosul, College of Science, 176 P.

Zaki, K. 1990. Petrophysical Properties of the Kirkuk Field Reservoirs. Iraqi Journal of Earth Sciences, 7(4), pp. 250-263.

Iraqi National Journal of Earth Science, Vol. 26, No. 04, 2026 (98-107)

Iraqi National Journal of Earth Science

www.earth.uomosul.edu.iq

الخصائص البتروفيزيائية والرسوبية لتكوين بلاني (الايوسين المتأخر– الأوليجوسين المبكر) من حقل كركوك النفطي ، شمال شرق العراق

عزت ابراهيم خضر علي الفندي[1*] ، **زيد عبدالوهاب ملاك [1]** ، **رافع إبراهيم عبدالله حميدي [1]**

ezzatalfandi@uomosul.edu.iq zaidmalak@uomosul.edu.iq rafeegeo66@uomosul.edu.iq

[1] *قسم علوم الارض والنفط، كلية العلوم، جامعة الموصل، الموصل، العراق.*

* *الباحث المراسل.*

تاريخ الاستلام: 05 أيلول 2024 تاريخ المراجعة: 29 تشرين الأول 2024 تاريخ القبول: 30 كانون الأول 2024

تاريخ النشر الالكتروني: 01 تشرين الأول 2026

الملخص

تشمل تتابعات الأوليجوسين في شمال شرق العراق تسعة تكوينات تُعرف مجتمعة باسم مجموعة كركوك. ركزت هذه الدراسة على تكوين بالاني ضمن حقل كركوك النفطي، وتحديدًا في البئر (KX16) الواقع في قبة بابا. يعود تاريخ تكوين بالاني إلى فترة الأيوسين المتأخر حتى الأوليجوسين المبكر، وهو يتألف بشكل رئيسي من الحجر الجيري والحجر الجيري الصلصالي. يبلغ سمك التكوين حوالي 29 مترًا ويمتد بين أعماق 768 إلى 797 متراً. تؤكد التحليلات البتروفيزيائية، باستخدام سجلات أشعة جاما (GR) والنيوترون والكثافة، عن وجود نسبة عالية من الطفل (V-Shale تصل إلى 1.0) ومسامية متفاوتة عبر تتابعات التكوين. تم تقسيم التكوين إلى أربع انطقة بناءً على القدرة المكمنية : نطاق أ (صخور مكمنية فقيرة)، المنطقة ب (مسامية معتدلة)، المنطقة ج (صخور مكمنية فقيرة)، والمنطقة د (صخور مكمنية جيدة ذات إنتاجية عالية). تشير التحاليل المعدنية باستخدام مخططات المتقاطعة هيمنة الحجر الجيري، مما يعد أمراً بالغ الأهمية لتوصيف المكمن وتقييم المسامية الثانوية. بالإضافة إلى ذلك، يتميز تكوين بالاني برواسب دقيقة الحبيبات ويعكس بيئة ترسيب حوضية منخفضة الطاقة. تؤكد هذه النتائج أهمية الدراسات البتروفيزيائية والمعدنية المفصلة في تعزيز فهم المكامن الهيدروكربوناتية وتقييم إمكانياتها الإنتاجية في سياق الجيولوجيا الإقليمية.

الكلمات المفتاحية:

حقل كركوك النفطي، تكوين بلاني، الحجر الجيري، مسامية عالية، تحليلات البتروفزيائية.

DOI: 10.33899/injes.v26i2.56115, ©Authors, 2026, College of Science, University of Mosul.

This is an open-access article under the CC BY 4.0 license (http://creativecommons.org/licenses/by/4.0/).

==========

Iraqi National Journal of Earth Science, Vol. 26, No. 04, 2026 (108-121)

Iraqi National Journal of Earth Science

www.earth.uomosul.edu.iq

Environmental Applications of Marine Foraminifera and Ostracoda Assemblage in Faw Town, South of Iraq

Badria Ali Hussain [1*], **Abbas Hameed Mohammed** [1]

ali.b.h.1989.sa@gmail.com doctorabbas71@yahoo.co.in

[1] *Department of Geology, College of Science, University of Basrah, Basrah, Iraq.*

* *Correspondence author.*

Received: 27 May 2025 Received in revised form: 20 July 2025 Accepted: 27 August 2025
Available online: 01 October 2026

Abstract

In this paper, we present surface and subsurface sample from (50) cm by using grab instrument to (21) m by diver variations of ostracoda and foraminifera assemblage from (15) samples (5) shallow whereas (10) subsurface along Arabian Gulf at Al-Faw (Kaser Al- Muge) in the Basrah city south of Iraq, Surface and subsurface sediments variation in ostracoda and foraminifera assemblage. Totally (15) sample were sorted under the binocular microscope (24) species of the Ostracoda taxa belonging to (21) genera, (4) subfamilies, (17) families, (8) super families and (4) suborders and 51 species of the foraminifera taxa belonging to (19) genera, have been identified. With increasing depth of the depositional environments, the prevalent genera in ostracoda are Cyprideis, Tanella, Actinocythereis, and Neocytheromorpha, while the prevalent foraminiferal taxa are Ammonia, Elphidium, Quinqloculina, and Spiroloculina. In all studied samples the predominant genera of the surface sample belonging to tidal and marine environments which characterized by low saline water and mud flat condition, while the other genus indicate marine environment which characterized by high saline conditions, in addition, to that environments are affected by sea level changes. Ostracoda and foraminifera along Al-Faw beach were studied by sampling surface and subsurface sediments from the marine shelf and upper slope to understand recent ostracoda and foraminifera assemblages and Systematics. Grain size analysis and organic matter were also determined.

Keywords:

Ostracoda and foraminifera assemblage, Al Faw beach, Kaser Al-muge, Grain size and organic matter, South of Iraq.

DOI: 10.33899/injes.v26i4.56156, *©Authors, 2026, College of Science, University of Mosul.*
This is an open-access article under the CC BY 4.0 license (http://creativecommons.org/licenses/by/4.0/).

==========

1. Introduction

(Kaser Al-Muge) Al-Faw beach in southern Iraq is one of the most important study areas, comprising geographical units and forming a complex ecological system. Therefore, paleontological and sedimentological studies are important for determining sedimentary environments based on specific types of invertebrate fossils (ostracods and foraminifera). Ostracoda and foraminifera have received great importance in determining environments in different geological ages, including the modern era. Ostracoda and foraminifera have a long geological range, as they were found in sediments ranging in age from the Upper Cambrian to the Recent era (Al- Meshlab and Mohammed,2012; Al-Shawi et al., 2019; Al-Ali et al., 2020). Ostracoda and foraminifera are found in almost all mixed aquatic environments (marine, brackish, fresh) and are characterized by their large numbers; a few of them live on the surface of the water, and others spread throughout the water column. A large number of their species are benthic, and their spread is affected by salinity, temperature, substrate texture, and depth. Ostracoda and foraminifera are of great importance in stratigraphic comparison and identification of the ancient environment and ancient geography. In addition to being an important tool for oil exploration, they have also been utilized in research on environmental contamination (Al-Hilli, 1977). Irrigation-related man-made marine environments had a significant impact on the floodplain sediments of southern Iraq during the late Holocene, and irrigation water carried reworked sands and silts, resulting in widespread

contamination (Al Meshlab and Mohammed, 2012). The sediment region is made up of sand, silt, and clay, with the silt content being the most prevalent and the sand grain size being extremely small. At a depth of between 16 and 17 m, there is a distinctive thin layer of silty clay that is dark gray in color, which is characterized by the absence of fossils. This layer, which was represented by a pyritization, may represent the upper part of the Al-Hammar Formation (Sabah, 2010).

2. Study Area

The reason for selecting the Al-Faw (Kaser Al-Muge) region and the goal of the study is because the ecological study of the ostracoda and foraminifera fauna from that area has not yet been conducted. The purpose of the study is to determine the distribution of the ostracoda and foraminifera assemblage, attempt to match their distribution with the observed environment, and assess the ecology of the widespread and abundant ostracoda and foraminifera taxa. The necessary equipment for collecting the samples, such as a motor launch, mud grab, and water sampler, is also included in the choice of location and purpose of the study. The study area is investigated in southern Iraq, Al- Faw (Kaser Al-Muge). Figs. (1,2 and 3) and Table (1) were prepared using UTM GIS (Universal Transverse Mercator). The systematics of recent ostracoda and foraminifera depend on the sediment sample. This work includes many stations in Basrah city, Al- Faw (Kaser Al-Muge). Five surface samples by grab at 50 cm, and ten subsurface samples (down-sampled sediment) were collected by a diver at 21m. The study area lies south of Mesopotamia (Tectonically). It is one of the important areas for geological studies, which represents the largest body of water in Iraq.

Table 1: Location of the study area (TP 01 to TP 06) in the (Al- Faw-Kaser Al-Muge)

Name (Tern Point)	X (Longitude)	Y(Latitude)
TP 01	253379.8024	3308055.293
TP 02	251364.341	3310736.183
TP 03	240570.6423	3319262.927
TP 04	233964.1125	3323563.385
TP 05	222545.9978	3326135.924
TP 06	206223.3991	3327520.188

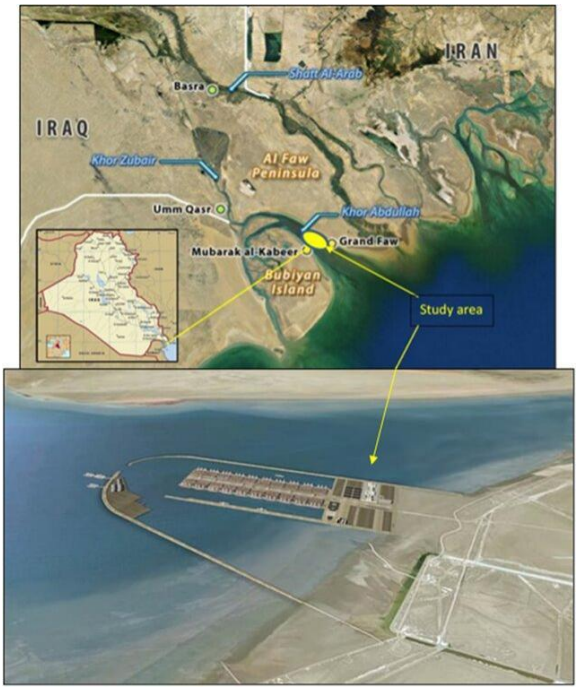


Fig. 1: Satellite image of the study area in southern Iraq, Basrah, Al-Faw beach. Eastern breakwater, western breakwater, and inner basin.

3. Materials and Methods

Total Fifteen sediment samples collected for two different location surface and subsurface in June, 2024 the coastal and marine environments of the study area along the A-Faw coastal in Basrah (Kaser Al-Muge), southern Iraq. The surface sediments sample by the author herself taking necessary precautions, making use of samples collected at depth (50) cm Petern grap (Betjeman, 1969), and the down-sample or subsurface by the diver is collected sediment samples in depth (21) m. Extreme care was taken to retrieve the sediment samples from sites that are not presently affected by modern-day tidal processes. All the sediment samples collected from the study area were brought to the laboratory and recorded, including details such as colour. The composition of the sediment and related substances included shell fragments of gastropoda, pelecypoda, wood pieces, coal fragments, etc. Prior to analyzing a sample, its location, depth, and surroundings were also recorded. We took 50 grams from each of the samples after cutting and weighing them on the balance. The sample was air-dried after being well cleaned. To break up the flocculated clay particles and dissolve any tiny salt that might have been trapped between the finer grains, a (0. 025) sodium hexametaphosphate solution was typically utilized

(Shepared and Moore, 1955; Barnes, 1959; Jayraju, 1993). To extract ostracoda, the fossil specimens were cleaned using an ASTM (230) mesh sieve (0. 063 mm opening) to remove the smaller particles (silt and clay mud) for viewing under the stereo binocular microscope. The residue, which contained sand and fossils, was placed in a ceramic eyelid and dried in an oven between (50°) C and (60°) C. Under a binocular microscope, benthic ostracoda and foraminifera specimens were chosen and separated from the residue using a (0. 001) mm winder and Newton sable hairbrush. The ostracoda and foraminifera were carefully distributed, and in this way, they were indexed on a single (24) chamber cardboard microfaunal slide. To make a slide, the typical species chosen from the slide are maintained in a slide with several chambers. Every species is identified and selected from these using a binocular microscope, and at the (TP 01, TP 02, TP 03, TP 04, TP 05, and TP 06) levels, the genus and species were processed for ostracoda and foraminifera research (Fig. 3 and Table 1). Offshore shallow water sediments are often composite materials made up of particles ranging in size from sand to clay in various combinations. The moisture content of each sample was first removed by thoroughly drying it in a hot air oven to determine the proportions of sand, silt, and clay. Following that, the samples were disseminated overnight with a 0. 025 N sodium hexametaphosphate solution for disaggregation in the right amounts. The material was then disaggregated and rinsed through a phosphor bronze wire mesh with a (230) ASTM sieve mesh (opening = 0. 063) until clear water came through, making sure the washings were less than (1000) cc. The weight of the substance coarser than (1/16) mm, i.e., sand, and the fine material (silt and clay) were determined by weighing the dried material that was retained on the sieve; the washings were analyzed by the pipette method in accordance with the procedure adopted by (Krumbein and Pettijohn, 1938). The suspension passing through the sieve was collected in a 1-liter graduated measuring jar. If the suspension collected in the jar, after complete washing, is less than (1000) cc, the already prepared sodium hexametaphosphate solution was added to make it up to (1000) cc. The suspension in the measuring jar was well agitated using a stirring device to have a uniform distribution of the particles in the suspension. As soon as the agitation stopped, the time was noted. Exactly after (2) hours and (3) minutes, a (20-cc) pipette was used to draw the sample out of the area using consistent suction after being gradually introduced into the solution to a depth of 10 cm. After being pipetted out, the sample was placed in a (50) cc beaker and dried in an oven. Measures were taken to avoid boiling and splitting. The residue's weight was determined after it was completely dry. The weights of sand, silt, and clay were transformed into weight percentages and displayed on a trilinear diagram. The species were identified and organized in accordance with the categorization proposed by (Moore and Pitrat, 1961; Harthman and Puri, 1974; Loeblich and Tappan, 1988). All species have been kept in the Paleontology Laboratory of the College of Science, Department of Geology, Basrah University.

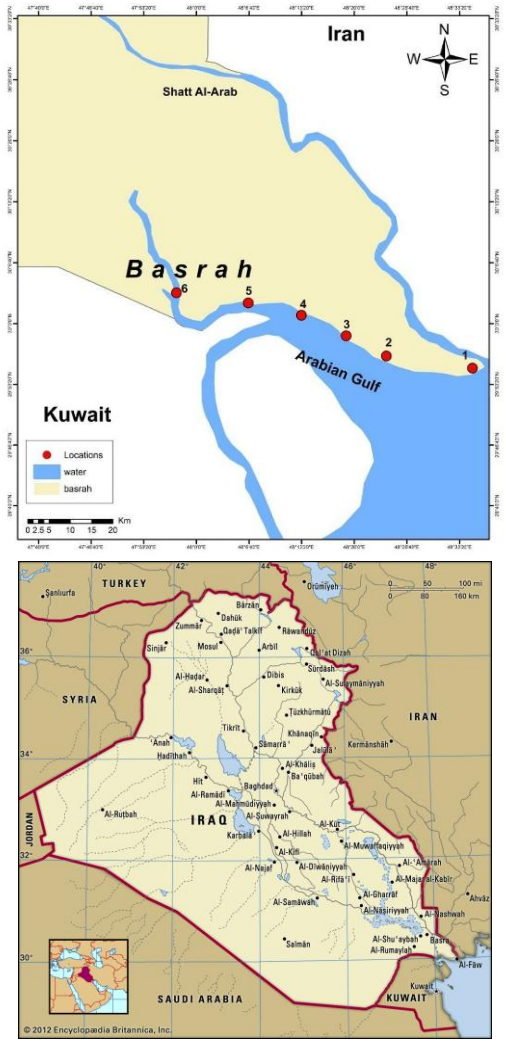


Fig. 2: Location of the study area in southern Iraq, Basrah, Al-Faw beach, the six sites (TP 01 to TP 06)

4. Results

1. Grain size analysis

Sand -Silt- Clay Ratio estimation:

The sediments were characterized in the current investigation using (Trefethen's, 1950) textural terminology. Using (Folk, 1974), the triangular diagram (Fig. 5) shows the percentage distribution of sand, silt, and clay fractions in surface and subsurface sediment samples. The percentage sediment texture is shown below for each region in the coastal and marine environments, as classified by the plot sediments. The percentages of clay, silt, and sand in the sediment components of Al- Faw beach are listed in Table 2. The results clearly indicate that the sediments are mainly composed of silt in the regions. We also note the presence of a difference in the percentages of sediment components of clay and sand. The sand percentage was low in areas, ranging at Al-Faw beach (eastern Kaser Al-Muge) between 8 and 39, with the highest value recorded at a depth at sample station (5) and the lowest value at a depth at station (9). In western Kaser Al-Muge, its clay ranged between 14 and 25 percent, with the highest value recorded at a depth of station (4) and the lowest value recorded at station (12).

Table 2: Results of volumetric analysis using the pipette method according to (Folk, 1974) and percentages of sediment components of clay, silt, and sand in (Kaser Al-Muge)

No.	Sample name	Sand%	Silt%	Clay%	Particle Size Distribution Classification
1	1	20	61	19	slightly clayey sandy silt
2	2	25	56	19	Slightly clayey sandy silt
3	3	23	59	18	slightly clayey sandy silt
4	4	12	63	25	slightly sandy clayey silt
5	5	39	44	17	slightly clayey sandy silt
6	15	13	66	21	slightly sandy clayey silt
7	6	21	62	17	slightly clayey sandy silt
8	7	18	67	15	slightly sandy, slightly clayey silt
9	8	8	70	22	slightly sandy clayey silt
10	12	14	62	24	slightly sandy clayey silt
11	10	14	65	21	slightly sandy clayey silt
12	11	25	61	14	slightly clayey sandy silt
13	13	11	64	25	slightly sandy clayey silt
14	14	16	62	22	slightly sandy clayey silt
15	9	17	68	15	slightly sandy, slightly clayey silt

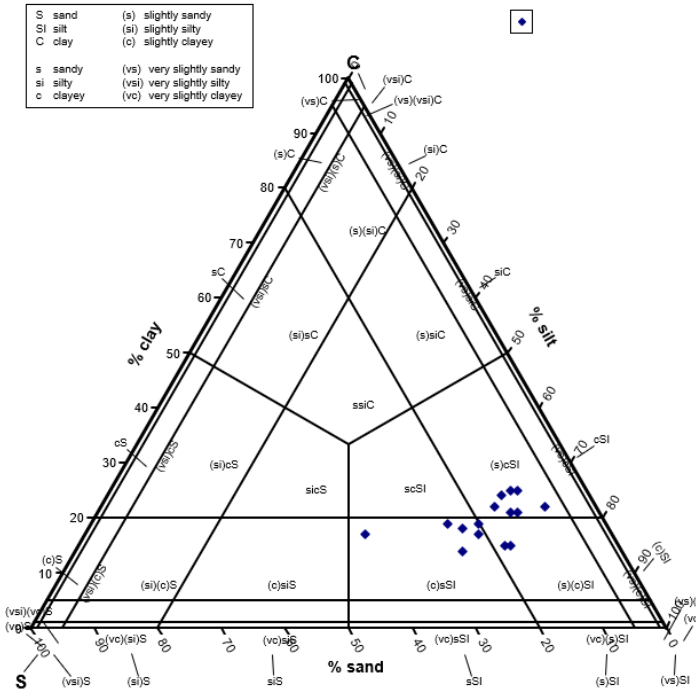


Fig. 3: Grain size analysis in the study area according to (Folk, 1974).

2. Organic Matter

The term organic matter refers to the decomposable matter accumulated in a sediment through organic activity and excludes shells and other hard skeletal parts originating from organisms. Most organic matter in coastal sediments is derived from benthic material which has been trapped between finer particles of the inorganic sediments. The organic matter in the sediment was determined by ignition (Davies, 1974). The recorded values are tabulated below. The OM values in the study area ranged from 1.42 to 1.60 in the surface sample, while in the deeper sample they ranged from 1.56 to 3.21. The only way to directly ascertain organic matter is by using a strong hydrogen peroxide solution to oxidize the sediment organic matter and measuring the resulting loss as an indicator of organic matter. The organic material, though, is often determined by its organic carbon concentration. Dry combustion, wet combustion, and titrimetric techniques may be used to estimate this with high accuracy. The dry combustion techniques are excessively expensive and don't differentiate between various kinds of carbon, like coal, charcoal, graphite, etc. The wet combustion techniques are excessively labor-intensive (Kumar, 1988).

Table 3: Percentage of Organic matter (OM)

Surface	Deep
1.45	2.68
1.60	2.78
1.53	3.01
1.52	2.08
1.42	2.67
	1.89
	2.32
	3.21
	1.56
	2.38

3. Identification of Ostracoda and Foraminifera

The ostracoda identified in the present study are under Suborder Podocopina according to (Moore and Pitrat, 1961; Harthman and Puri, 1974). The benthic ostracoda are most dominant group is suborder Podocopina, represented by (24) species belonging to (21) genera. The variation of ostracoda assemblages with depth showed the abundant presence of *Cypreidis*, *Tanella*, *Actinocythereis*, and *Neocytheromorpha*, with different (TP 01, TP 02, and TP 03) indicating high saline conditions. Nevertheless, in the sample, the presence of *Cypreidis* and *Tanella* suggests a marine environment characterized by mud flats and low salinity. Four benthic Ostracoda species, *Cypreidis torosa, Tanella gracilis, Actinocythereis scutiger, and Neocytheromorpha sp. cf. N. indoarabic*, were found in all the samples. The benthic Ostracoda have been abundant in four samples, and these are:

TP 01: *Cypreidis, Tanella, Actinocythereis, Neocytheromorpha, Parakrithe and Candona neglecta*.

TP 02: *Cypreidis, Tanella, Actinocythereis and Neocytheromorpha, Xestoleberis variegata and Miocyprideis sp.1*.

TP 03: *Cypreidis, Tanella, Actinocythereis and Neocytheromorpha, Keijia demissa and Kalingella*.

TP 04: *Cyprideis, Tanella, Actinocythereis and Neocytheromorpha, ALocopocyt-here reticulate and* Neocyprides sp.

TP 05: *Cyprideis, Tanella, Actinocythereis and Neocytheromorpha, Calliostoma coppingeri and Lankacythere coralloide*.

TP 06: *Cyprideis, Tanella, Actinocythereis and Neocytheromorpha, Dohukia fossulata and Heterocypris giesbrechtii*)

The foraminiferal assemblage that identified in the present study can be grouped into four suborders (Loeblich and Tappan, 1988): Textulariina, Milioliina, Rotaliina and Lagenina (Table 2). The most dominant group of foraminifera is Milioliina, represented by (6) genera and (23) species, whereas the other groups are: Textulariina and Lagenina appear few and rare. In the present study, only two species, *Ammonia* and *Elphidium* species, are abundant and have occurred since the early Holocene period for Rotaliina. *Quinqueloculina, Triloculina,* and *Spiroloculina* also occur in abundance for Milioliina.

The sediment sample variation of foraminifera with depth revealed the abundant presence of *Ammonia beccarii*, *Elphidium*, and *Quinqueloculina seminulum*, with fluctuations (TP 01, TP 02, and TP 03) indicating high salinity. However, in the specimen, the presence of *Ammonia* and *Elphidium* suggested a marine environment with low salinity and mudflat conditions. The four benthic foraminiferal species are *Ammonia beccarii, Ammonia tepida,*

Elphidium advenum, and *Elphidium crispum*, were found in all the samples. The benthic Foraminifera have been abundant in four samples, and these are:

TP 01: *Ammonia beccarii*, *Elphidium craticulatum*, *Quinqueloculina seminulum*, *Spiroloculina communis* and *Triloculina trigonula*.

TP 02: *Ammonia beccarii*, *Elphidium spl*, *Quinqueloculina seminulum*, *Quinqueloculina seminulum*, *Spiroloculina communis* and *Triloculina trigonula*.

TP 03: *Ammonia beccarii*, *Elphidium advenum*, *Elphidium sp*. *Nonionoides elongatum*, *Quinqueloculina seminulum Spiroloculina communis* and *Triloculina trigonula*.

TP 04: *Ammonia beccarii*, *Elphidium hispidulum* and *Elphidium sp*., *Spiroloculina communis* and *Triloculina trigonula*.

TP 05: *Ammonia beccarii*, *Elphidium hispidulum* and *Elphidium excavatum* **,** *Spiroloculina communis* and *Triloculina trigonula*.

TP 06: *Ammonia beccarii*, *Elphidium hispidulum* and *Elphidium excavatum*, *Spiroloculina communis* and *Triloculina trigonula)*

However, the foraminiferal assemblages do not exhibit high diversity. The agglutinated group is few fauna. The dominant groups are Miliolida and Rotaliina.

Studies of Foraminifera from the surface and subsurface sediments collected off (Kaser Al-Muge) in Faw Town have led to the recognition of benthonic species, (12) subfamilies, and (9) superfamilies. Out of the total (51) species, (17) species fall under suborder Rotiliinae; (5) species under suborder Textulariina; (28) species under suborder Millioliinae; and the remaining (1) species under suborder Laginiae.

Table 4: Foraminifera species that are found in the study area, according to Loeblich and Tappan 1988.

Suborder	Superfamily	Family	Subfamily	Genus	Species
Rotaliina	Rotollacea	Rotalidac	Rotaliinae	*Ammonia*	*Ammonia beccarii*
	Rotalioidea	Ammoniidae	Ammoniinae	*Ammonia*	*Ammonia tepida*
	Rotalioidea	Ammoniidae	Ammoniinae	*Ammonia*	*Ammonia dentata*
	Rotalioidea	Elphidiidae	Elphidiinae	*Elphidium*	*Elphidium advenum*
	Rotalioidea	Elphidiidae	Elphidiinae	*Elphidium*	*Elphidium incertum*
	Rotalioidea	Elphidiidae	Elphidiinae	*Elphidium*	*Elphidium crispum*
	Rotalioidea	Elphidiidae	Elphidiinae	*Elphidium*	*Elphidium excavatum*
	Rotalioidea	Elphidiidae	Elphidiinae	*Elphidium*	*Elphidium lessonii*
	Rotalioidea	Elphidiidae	Elphidiinae	*Elphidium*	*Elphidium selseyense*
	Rotalioidea	Elphidiidae	Elphidiinae	*Elphidium*	*Elphidium discoidale*
	Rotalioidea	Elphidiidae	Elphidiinae	*Elphidium*	*Elphidium gerthi*
Rotaliina	Rotalioidea	Elphidiidae	Elphidiinae	*Elphidium*	*Elphidium poevanum*
	Rotalioidea	Elphidiidae	Elphidiinae	*Elphidium*	*Elphidium macellum*
	Calcarinoidea	Calcarinidae	Pararotaliinae	*Pararotalia*	*Pararotalia nipponica*
	Calcarinoidea	Calcarinidae	Pararotaliinae	*Pararotalia*	*Pararotalia calcar*
	Bolivinitoidea	Bolivinitidae	Bolivinitinae	*Brizalina*	*Brizalina striatula*
	Rotalioidea	Rotalioidea	Notorotaliidae	*Parrellina*	*Parrellina hispidula*
	Nonionoidea	Nonionidae	Nonioninae	*Nonionoides*	*Nonion elongatum*
	Nonionoidea	Nonionidae	Nonioninae	*Nonion*	*Nonion fabric*
	Nonionoidea	Nonionidae	Nonioninae	*Nonionella*	*Nonionella stella*
	Nonionacea	Nonionidae	Nonioninae	*Florilus*	*Florilus grateloupi*
	Planorbulinoidea	Cibicididae	Cibicidinae	*Cibicides*	*Cibicides refulgens*
Textulariina	Textularioidea	Textulariidae	Textulariinae	*Textularia*	*Textularia sagittula*
Textulariina	Textularioidea	Textulariidae	Textulariinae	*Textularia*	*Textularia earlandi*
Textulariina	Textularioidea	Textulariidae	Textulariinae	*Textularia*	*Textularia agglutinans*
Textulariina	Textularioidea	Textulariidae	Textulariinae	*Textularia*	*Textularia candelana*
Textulariina	Textularioidea	Textulariidae	Textulariinae	*Textularia*	*Textularia aura*
Ammodiscina	Ammodiscoidea	Ammodiscidae	Ammodiscinae	*Ammodiscus*	*Ammodiscus incertus*
Miliolina	Milioloidea	Spiroloculinidae		*Spiroloculina*	*Spiroloculina communis*
Miliolina	Milioloidea	Spiroloculinidae		*Spiroloculina*	*Spiroloculina laevigata*
Miliolina	Milioloidea	Spiroloculinidae		*Spiroloculina*	*Spiroloculina nitida*
Miliolina	Milioloidea	Spiroloculinidae		*Spiroloculina*	*Spiroloculina sp.*
Miliolina	Milioloidea	Spiroloculinidae		*Spiroloculina*	*Spiroloculina depressa*
Miliolina	Soritoidea	Peneroplidae		*Spirolina*	*Spiroculina acicularis*
Miliolina	Milioloidea	Miliolidae	Miliolinae	*Rupertianella*	*Rupertianella rupertiana*
Miliolina	Milioloidea	Hauerinidae	Miliolinellinae	*Triloculina*	*Triloculina trigonula*
Miliolina	Milioloidea	Hauerinidae	Tubinellinae	*Articulina*	*Articulina funalis*
Miliolina	Milioloidea	Hauerinidae	Haueininae	*Quinqueloculina*	*Quinqueloculi-na sp*
		Hauerinidae			*Quinqueloculi-na agglutinans*
Miliolina	Milioloidea	Hauerinidae	Haueininae	*Quinqueloculina*	*Quinqueloculi-na lamarckiana*
Miliolina	Milioloidea	Hauerinidae	Haueininae	*Quinqueloculina*	*Quinqueloculi-na oblonga*
Miliolina	Milioloidea	Hauerinidae	Haueininae	*Quinqueloculina*	*Quinqueloculi-na polygona*
Miliolina	Milioloidea	Hauerinidae	Haueininae	*Quinqueloculina*	*Quinqueloculi-na reticulata*
Miliolina	Milioloidea	Hauerinidae	Haueininae	*Quinqueloculina*	*Quingueloculi-na stalkeri*
Miliolina	Milioloidea	Hauerinidae	Haueininae	*Quinqueloculina*	*Quinqueloculi-na seminulum*
Miliolina	Milioloidea	Hauerinidae	Haueininae	*Quinqueloculina*	*Quinqueloculi-na rameswarensis*
		Hauerinidae		*Quinqueloculina*	*Quinqueloculi-na tenagos*
Miliolina	Soritoidea	Soritidae	Soritinae	*Sorites*	*Sorites marginalis*
Miliolina	Milioloidea	Hauerinidae	Miliolinellinae	*Pyrgo*	*Pyrgo elongata*
Allogromoidea		Allogromiidae	Argillotubinae	*Micatuba*	*Micatuba*
	Nodosariacea	Lagenidae		*Lagena*	*Lagena setigera*

Plates of foraminifera species

Species of Foraminifera
Plate 1
1.*Ammonia beccarii*, 40 x
2.*Ammonia tepida*, 40 x
3.*Ammonia dentata*, 40 x
4.*Elphidium advenum*, 40 x
5.*Elphidium incertum*, 40 x
6.*Elphidium crispum*, 40 x

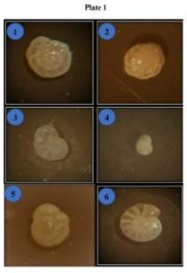


Plate 2
1.*Elphidium excavatum*, 40 x
2.*Elphidium lessonii*, 40 x
3.*Elphidium selseyense*, 40 x
4.*Elphidium discoidale*, 40 x
5.*Elphidium gerthi*, 40 x
6.*Elphidium poeyanum*, 40 x

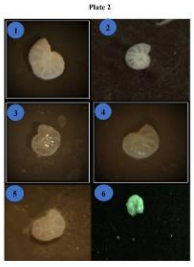


Plate 3

1.*Elphidium macellum*, 40 x
2.*Pararotalia nipponica*, 40 x
3.*Pararotalia calcar*, 40 x
4.*Brizalina striatula*, 40 x
5.*Parrellina hispidula*, 40 x
6.*Nonion elongatum*, 40 x

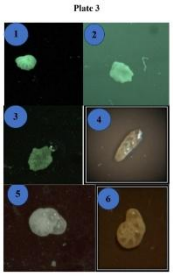


Plate 4

1.*Nonion fabric*, 40 x
2.*Nonionella stella*, 40 x
3.*Florilus grateloupi*, 40 x
4.*Cibicides refulgens*, 40 x
5.*Textularia sagittula*, 40 x
6.*Textularia earlandi*, 40 x

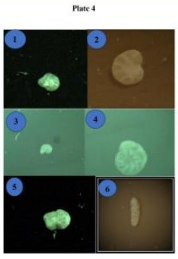


Plate 5

1.*Textularia agglutinans*, 40 x
2.*Textularia candelana*, 40 x
3.*Textularia aura*, 40 x
4.*Ammodiscus incertus*, 40 x
5.*Spiroloculina communis*, 40 x
6.*Spiroloculina laevigata*, 40 x

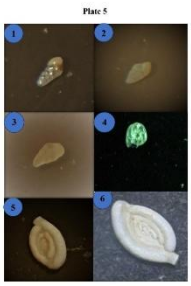


Plate 6

1.*Spiroloculina nitida*, 40 x
2.*Spiroloculina* sp., 40 x
3.*Spiroloculina depressa*, 40 x
4.*Spiroculina acicularis*, 40 x
5.*Rupertianella rupertiana*, 40 x
6.*Triloculina trigonula*, 40 x

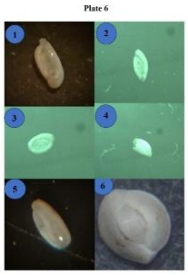


Plate 7

1.*Articulina funalis*, 40 x
2.*Quinqueloculina* sp., 40 x
3.*Quinqueloculina agglutinans*, 40 x
4.*Quinqueloculina lamarckiana*, 40 x
5.*Quinqueloculina oblonga*, 40 x
6.*Quinqueloculina polygona*, 40 x

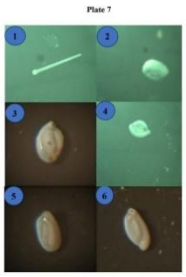


Plate 8

1.*Quinqueloculina reticulata*, 40 x
2.*Quinqueloculina stalkeri*, 40 x
3.*Quinqueloculina seminulum*, 40 x
4.*Quinqueloculina rameswarensis*, 40 x
5.*Quinqueloculina tenagos*, 40 x
6.*Sorites marginalis*, 40 x

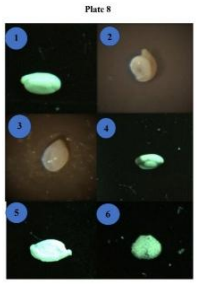


Plate 9

1.*Pyrgo elongata*, 40 x
2.*Micatuba* sp., 40 x
3.*Lagena setigera*, 40 x

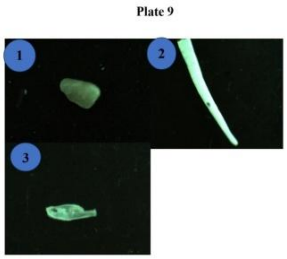


Table 5: Classification of ostracoda species in the study area according to (Moore and Pitrat, 1961; Howe, 1962; Harthman and Puri, 1974

Sub order	Super family	Family	Subfamily	Genus	Species
Podocopina		Cytherideae	Cytheracea	*Cyprideis*	*Cyprideis* sp.
		Cytherideae	Cytheracea	*Cyprideis*	*Cyprideis torosa*
	Cytheracea	Cytherideidae		*Miocyprideis*	*Miocyprideis* sp.1
		Cytherideidae		*Neocyprides*	*Neocyprides* sp.
		Cytherace	Cytherideinae	*Cytherlloidea*	*Cytherlloidea* sp.
	Cytheracea	Krithidae		*Parakrithe*	*Parakrithe*
	Cytheroidea	Xestoleberididae		*Xestoleberis*	*Xestoleberis variegata*
		Cytherellidae		*Cytherelloidea*	*Cytherelloidea praecipua*
			Pterygocyterinae	*ALocopocyt-here*	*ALocopocyt-here reticulate*
		Candonidae	Candoninaae	*Candona*	*Candona neglecta*
		Schizocytheridae		*Neomonocer-atina*	*Neomonoceratina iniqua*
		Schizocytheridae		*Neomonocer-atina*	*Neomonoceratina porocostata*
		Leptocytheridae		*Tanella*	*Tanella gracilis*
	Cypridacea	Cyprididae	Cypridinae	*Heterocypris*	*Heterocypris giesbrechtii*
	Bairdioidea	Bairdiidae		Bairdoppilata	*Bairdoppilata alcyonicola*
		Bairdiidae	Bairdiinae	*Bairdia*	*Bairdoppilat carinata*
	Bairdiace	Pectocytherida		*Keijia*	*Keijia Demiss*
		Trachyleberididae		*Actinocythereis*	*Actinocythereis scutiger*
		Trachyleberidida		*Carinocytherei*	*Carinocythereis hamat*
		Trachyleberidida		*Asymmetricyther*	*Asymmetricythere reticulata* sp
				Lankacyther	*Lankacythere coralloide*
			Arculacythereina	*Neocytheromorph*	*Neocytheromorpha sp. cf. N. indoarabic*
		Unertai		*Kalingell*	*Kalingell*
		Leptocytherida		*Dohuki*	*Dohukia fossulat*

Plates of ostracoda species

Species of Ostracoda
Plate 10
1.*Cyprideis* sp., 40 x
2.*Cyprideis torosa*, 40 x
3.*Miocyprideis* sp., 40 x
4.*Neocyprides*, 40 x
5.*Cytherlloidea* sp., 40 x
6.*Parakrithe* sp., 40 x

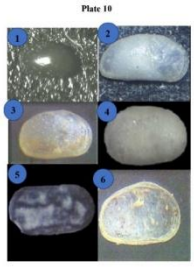


Plate 11
1.*Xestoleberis variegata*, 40 x
2.*Cytherelloidea praecipua*, 40 x
3.*ALocopocythere reticulate*, 40 x
4.*Candona neglecta*, 40 x
5.*Neomonoceratina iniqua*, 40 x
6.*Neomonoceratina porocostata*, 40 x



Plate 12
1.*Tanella gracilis*, 40 x
2.*Heterocypris giesbrechtii*, 40 x
3.*Bairdoppilata alcyonicola*, 40 x
4.*Bairdoppilata carinata*, 40 x
5.*Keijia Demissa*, 40 x
6.*Actinocythereis scutigera*, 40 x

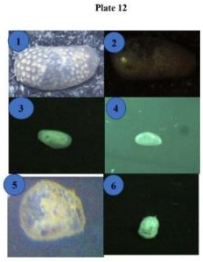
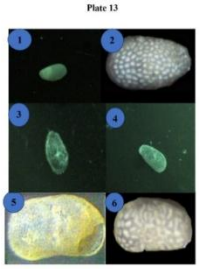


Plate 13
1.*Carinocythereis hamata*, 40 x
2.*Asymmetricythere reticulata* sp., 40 x
3.*Lankacythere coralloides*, 40 x
4.*Neocytheromorpha indoarabica*, 40 x
5.*Kalingella*, 40 x
6.*Dohukia fossulata*, 40 x



5. Discussion

The most important characteristic of ostracoda and foraminifera is their sensitivity to environmental change. Our knowledge of modern species indicates that many species have well-defined ecological ranges, and therefore changes in fossils assemblage through reflect changing environmental conditions, which can be reconstructed if the ecological tolerances of the

species are known (Haslett, 2002). The variations in salinity determine the composition and diversity of the ostracoda, and there are well-defined assemblages, each dominated by just four species: Cyprideis, Tanella, Actinocythereis and Neocytheromorpha (Boomer and Eisenhauer, 2002). There are some species that prefer muddy substrate, and some that prefer sandy substrate. In some environments, ostracod assemblages are dominated by a single taxon. The study was characterized by a high abundance of ostracod communities, which showed great diversity and were widespread, indicating that the organisms are sensitive to environmental changes (Hemidawi, 2020). The presence of certain ostracod communities in a particular region reflects the type of environment in which these communities and their significant environment impact have lived in the size, shape, and ornamentation of ostracod shells. So, the study of ostracod taxonomy gives clues to the environments (Alkaabi, 2001). Ostracod communities are environmentally controlled by factors such as temperature, water depth, sediment nature, volumetric gradient, and nutrient availability that reflect the direct impact of the environment. The high abundance of ostracoda in the study area, which showed largely varied sizes and shapes that indicates the original environment of ostracoda, which was not transferred from another region. The important species in the study are Cypreidis, Tanella, Actinocythereis and Neocytheromorpha, which have been shown the availability of this species in marine and brackish environments (Morkhoven, 1962 and 1963). The presence of Cypreidis, Tanella, Actinocythereis, and Neocytheromorpha in all the samples suggests their wide range of tolerance to the observed environmental parameters (Mohammed, 2006). The genera Cypreidis, Tanella, Actinocythereis, and Neocytheromorpha, and especially the species Tanella gracilis, are widely distributed in the Indo-Pacific and Atlantic, including the Caribbean and also in my study area. The wide geographic distribution of this cosmopolitan species in primary through passive transport by ships (Zhao and Whatley, 1989; Witte, 1993), and this species has been found to occur very widely throughout the Faw Coastal. In the present study, an attempt was made to identify the same in all the sediment samples taken off Faw Coastal (Kasar Al-Muge) due to the fact that the abundance of ostracoda in the sediments is reflected by the organic content and substrate characteristics. The primary origin of the organic matter found in the sediments. This is a kind of vegetation that flourishes either on land, in the surface waters of the sea, or in both. The majority of the organic matter in marine water sediments comes from terrigenous plant material, whereas the main source of organic matter for the ocean as a whole is the benthic photosynthetic organisms. In both instances, the amount of organic material in sediments is determined by the rate at which organic material is deposited and by an ample supply of organic material. The table above demonstrates that the organic matter is steadily rising and that it has the greatest average values (1. 423. 21) in both the surface and subsurface. The table shows that the amount of organic material increases with the particle size of the sediment, which explains why finer sediments absorb organic material (Kunenen, 1950). The categorization of the sediments and heavy minerals is also briefly discussed, along with how they help in understanding the provenance and depositional environment.

The majority of the sediment is unconsolidated and contains varying amounts of sand, silt, clay, shell pieces from gastropods, pelecypods, echinoids, wood chips, pieces, laterite fragments, coal chips, and foraminifera.

Foraminifera are microscopic, singled celled organisms that build themselves a shell (or test) and live both in the surface layers of the sediment and in the water column (planktonic) (Phleger, 1960); (Murray, 1980); (Maziqa, 2023) and (Shareef, 2023).

Foraminifera in surface and subsurface (down samples) differ in both size and species types of the species from those observed deep in (Kaser Al-Muge) (Faw Town). Foraminifera from deep depths (TP 01, TP 02, TP 03, TP 04, TP 05 and TP 06) are larger in size, while in shallow depths the foraminifera size is small. Different foraminiferal species exhibit responses to changes in salinity; for example, Ammonia beccarii has been reported from very low-salinity surface to higher-salinity marine environments (Hameed and Achuthyan, 2011). (Phleger and Parkar, 1951) report Ammonia beccarii living at salinity between 44% and 46%. Certain forms of foraminifera, especially agglutinated foraminiferal genera, like Textularia agglutinans, and calcareous genera like Elphidium, are much more tolerant of low salinity

conditions (Hameed and Achuthyan, 2011). Miliolid species that are found in the present study occur in marine water in all samples (TP 01 to TP 06). Many species such as Quinqueloculina seminulum, Sproloculina communis and Triloculina laevigata are found in all samples (TP 01 to TP 06).

The generic composition of agglutinated foraminifera such as Reophax and Ammobaculites does not exhibit any variation in the palaeoecological conditions. Their occurrence indicates a hyposaline to normal marine depositional environment, ranging in intertidal marine settings (Hameed and Achuthyan, 2011). They are assigned to the foraminiferal assemblage generally associated with the marginal marine environment. The above-mentioned genera also indicate the type of substrate that existed, reflecting the muddy layers. The generic composition further reflects the tropical waters. Thus, the agglutinated foraminifera characterize the studied sediments from the hypo- saline to normal marine water regime assignable to the tropical marginal marine environment of deposition. The calcareous group shows high diversity as compared to the other. (Murray, 1971).

In the present study, the calcareous foraminifera form the most dominant percentage of the fauna studied. Among these, the genus Elphidium has the maximum number of species. The genus Elphidium is the most common shallow-water marine foraminifera occurring throughout the world. It occurs in almost all shallow-water marine environments, from the supratidal region to the shelf, encompassing tropical, subtropical, and temperate environments. Elphidium has two principal forms. In the studied assemblage, keeled and nonkeeled forms were observed. According to Murray (1973), keeled forms occur mostly in the inner shelf with salinity 35.50%e, while the nonkeeled forms occur in hyposaline to hypersaline tidal marshes, lagoons, and nearshore environments. Bathymetrically, both the forms and the species exhibit a depth range of (0 to 50) m. Frerichs (1970) has noted the depth range of Elphidium crispum between (77) and (225) m in the Andaman Sea and Bay of Bengal. The species presented in this study are typical of al-Faw beach species commonly found along the eastern breakwater, western breakwater, and inner basin, pointing towards a relatively more stable environment. The occurrence of these tests in this area is due to transportation by waves and tidal currents, and for benthic foraminiferal production, oxygen was always available at the sediment-water interface.

The high percentage of Rotaliina and Miliolina indicates that the studied sites were very close to the mouth of the estuary. The absence of Miliammina fusca, another characteristic foraminifer, and the high percentage of calcareous and porcelaneous species from the six sites indicate that the sites were very near the mouth of the estuary and rule out their position far inland from the mouth. (Kumar, 1988).

The case studies show that foraminifera can be used to interpret environmental change, whether natural or anthropogenic, over time scales ranging from a few years or decades to thousands of years. Natural environmental changes are linked to the climate/ocean system. Because many modern forms were already present in the Holocene, it is possible to make detailed environmental reconstructions that far back in time. Foraminifera are good indicators of changes in salinity, temperature, availability of dissolved oxygen (Haslett, 2002), food supply, eutrophication, and changes in sea level. They can be used to document the effects of various types of pollution (organic, hydrocarbons, heavy metals). In contemporary polluted environments, pre-pollution conditions can be reconstructed from the foraminiferal assemblages preserved in the pre-pollution sedimentary record. Where pollution is diminishing, they can be used to monitor recovery, including recolonisation of previously defaunated substrates, or recolonization by the more sensitive species in areas where the impact did not kill off the entire Foraminiferal fauna (Haslett, 2002)

6. Conclusion

Integration of benthic ostracoda assemblage (21) genera age from the (15) samples (surface and down surface) allows drawing the following conclusions:

Fifteen sediment samples were analyzed for ostracoda assemblage variations, and the study yielded a total of (24) species belonging to (21) genera. The present study reveals that the Al-Faw coast is in the city of Basrah, south of Iraq. Sea level fluctuated locally, and the rise and fall of sea level have been much smaller since the middle current estuaries and tidal zones date from the Holocene, and they overlie the older accumulation

in the subsidence zones. Species were documented in the study area for the first time, along with one new species and one new variety: Heterocypris giesbrechtii.

Cypreidis, Tanella, Actinocythereis, and Neocytheromorpha are the most abundant and common species. are low in the study area.

Based on the investigation carried out on the coast of Faw in Basrah city (Kasar Al-Muge) in the study area, it can be concluded that the ostracod assemblage appears to be more suitable and congenial, and further, from the present study it can be inferred that the south coast is more congenial for the production, diversity, and distribution of ostracoda.

The sediments are divided into three categories: somewhat clay sandy silt, somewhat sandy clay, and somewhat sandy slightly clay silt. It is crucial to understand the environment.

The organic material is currently heavily confined in the finer sediment types.

Integration of benthic foraminiferal assemblages from the (15) samples studied allows us to draw the following conclusions:

Fifteen sediment samples were analyzed for foraminiferal assemblage variations, and the study yielded that, out of the total (51) species, (17) species fall under suborder Rotiliinae; (5) species under suborder Textulariinae; (28) species under suborder Millioliinae; and the remaining (1) species under suborder Laginiae occur in all the fifteen samples since the early Holocene period. The present study reveals that the Al-Faw coast in the city of Basrah, south of Iraq, sea level fluctuated locally and that the rise and fall of sea level have been much smaller since the middle Current estuaries and tidal zones date from the Holocene, and they overlie the older accumulation in the subsidence zones.

Out of the (51) species that have been identified in (18) genera, there are calcareous porous, calcareous porcelaneous, and arenaceous agglutinated. Lagena setigera, a new species of Articulina funalis, has been discovered, and (30) species have been recorded for the first time in the research area. The species are: Elphidium gerthi, Elphidium poeyanum, Pararotalia nipponica, Pararotalia calcar, Nonion elongatum, Nonion fabric, Nonionella stella, Florilus grateloupi, Cibicides refulgens, Textularia sagittula, Textularia earlandi, Textularia candelana, Textularia aura, Ammodiscus incertus, Spiroloculina nitida, Spiroloculina depressa, Spirolina acicularis, Rupertianella rupertiana, Articulina funalis, Quinqueloculina sp., Quinqueloculina agglutinans, Quinqueloculina oblonga, Quinqueloculina reticulata, Quinqueloculina stalkeri, Quinqueloculina rameswarensis, Quinqueloculina tenagos, Sorites marginalis, Pyrgo elongata, Micatuba, and Lagena setigera.

Ammonia beccarii is the most abundant and common species. Hyaline and agglutinated forms are found to occur in moderate to low abundance in the study area.

Based on the investigation carried out on the coast of Faw in Basrah city in (Kaser Al-Muge) in the study area, it can be concluded that the foraminifera assemblage appears to be more suitable and congenial, and further, from the present study it can be inferred that the south coast is more congenial for the production, diversity, and distribution of foraminifera.

7. Acknowledgments

From observation, it may be inferred that the rate of two authors is one of the authors, Assistant Prof. Muqdad Taher Sedkhan, for going through fieldwork, and to Assistant Prof. Dr Ali Khlaid Abbas, Head of the Department of Geology, College of Science, University of Basrah, Basrah, Iraq, for the encouragement and for their valuable suggestions in this work. The authors are thankful to the Ministry of Transport, General Company for Ports of Iraq, and Al-Saraj Company for support and technical help.

8. Conflict of Interest

The authors declare that they have no conflict of interest.

9. Funding Statement

This research received no external funding.

10. Author Contributions:

Badria Ali Hussein: Conceptualization, methodology, sample collection, formal analysis, data curation, investigation, visualization (figures and tables), writing – original draft, and writing – review & editing.

Abbas Hameed Mohammed: Conceptualization, supervision, sample collection, and formal analysis.

11. References

Al-Ali, R.A., Al-Shaikhli, Al-Marsoumi, S.S., and Hassoun, A., 2010. Study of Foraminifera species in the recent sediments of the Shatt Al-Arab coast, Khor Abdullah and Khor Al-Zubair, southern Iraq. Basra Research Journal (Operations), Issue (36), Part (4).

Al-Meshlab N.F.S.A., and Mohammed, A.H., 2012. Study Distribution of Ostracoda in the Recent Sediments in Al-Huizah Marshes-Amarah. Basrah Journal of Science (Bas J Sci), 30 (In Arabic).

Al-Ali, R.A., Mahdi, M.M. and Mohammed, A.H., 2020. Biostratigraphy of Khasib Formation by using planktonic foraminifera at selected wells in Rumila oil field, southern Iraq. The Iraqi Geological Journal, pp. 53-67.

Al-Hemidawi, F.N., 2020. Recent Fauna (Ostracoda, Foraminifera and Mollusca) and Geochemical Study of Al-Delmaj Marsh Area, Iraq, 186 P.

Al-Hilli, M.R., 1977. Study of the plant ecology of Ahwar region in southern Iraq. Ph.D. thesis, Univ. Cairo, 477 P.

Al-Ka'abi, 2001. Study of the paleoecology of Quaternary deposits within selected Archaeological sites in Baghdad and Babylon Governorates. M.Sc. Thesis, University of Baghdad, 211 P.

Al-Shawi, Z.A.A., Mahdi, M.M. and Mohammed, A.H., 2019. New records of planktonic foraminifera in the Shuaiba Formation (Aptian Age), Mesopotamian plain, South of Iraq. Iraqi Journal of Science, pp. 1322-1335.

Barnes, H., 1959. Apparatus and methods of oceanography, George Allen and Unwin Ltd., 341 P.

Betjeman, K.J., 1969. Recent foraminifera from the western continental shelf of Western Australia, Contr. Cushman Found. Foram. Res., Vol. 20, pt. 4, pp. 119-138, pls. 18-20.

Boomer, I. and Eisenhauer, G., 2002. Ostracod faunas as paleoenvironmental indicators in marginal marine environments. Geophysical Monograph Series, 131, pp. 135-149.

Davies, B.E., 1974. Loss on ignition as an estimation of sediment organic matter. Soil Sci. Soc. Am. Proc., vol. 38, pp. 150-151.

Folk, R.L., 1974. Petrology of Sedimentary Rocks, Hemphill Publishing Company, Austin, Texas, 183 P.

Frerichs, W.E., 1970. Distribution and ecology of benthonic foraminifera in the sediments of the Andaman Sea. Contribution Cushman.

Hameed, A. and Achyuthan, H.E.M.A., 2011. Benthic foraminiferal assemblages from the estuary and tidal zones along the east coast of Tamil Nadu, India: Deciphering Holocene sea-level change. Journal of the Palaeontological Society of India, 56, pp. 195-200.

Haslett, S.K., 2002. Quaternary Environmental Micropaleontology. First published in Great Britain in 2002 by Arnold, a member of the Hodder Headline Group, 338 Euston Road, London NW1 3BH. http://www.arnoldpublishers.com .

Jayaraju, N., 1993. Ecosystem and Population dynamics of Benthic Coastal and Foraminifera from Sediments Kovalam Estuarine Kanniyakumari Tuticorin of South India, Ph.D. Thesis, Sir Venkateswara University, Tirupati, India, 117 P.

Krumbein, W.C. and Pettijohn, F.J., 1938. Manual of sedimentary Petrography, New York, D. Appleton Century Co., Inc., 549 P.

Kuenen, Ph.H., 1950. Marine Geology, John Wiley and Sons, New York, 568 P.

Kumar, V., 1988. Ecology Distribution and Systematics of Recent Benthic Foraminifera from the Palk Bay, off Rameswaram, Tamil Nadu. Ph.D. Thesis, Bharathidasan University. Tiruchirapalli, India, 240 P.

Loeblich, A.R. and Tappan, H., 1988. Foraminiferal genera and their classification. Von Nostrand Reinhold, New York.

Mohammed, A.H., 2006. The vertical distribution of recent benthic ostracoda in Marakkanam and Odinur, east coast, South India. Barsch J Sci, 24(1), 103-111.

Moore, RS. and Pitrat, C.W., 1961. Treatise on Invertebrate Paleontology, Arthropoda, (Crustacea Ostracoda), 442 P., 334 figs. Geol. Soc. Amer. and Univ. of Kiel, fig. 334, 442 P.

Morkhoven, 1962. Post- Paleozoic Ostracoda: their morphology, taxonomy and economic use: Elsevier Publishing Company, Amsterdam, Vol. 1, 204 P.

Morkhoven, 1963. Post-Paleozoic Ostracoda: their morphology, taxonomy and economic use. Elsevier Publishing Company, Amsterdam, Vol. 1, pp. 2.

Murray, J.W., 1971. An atlas of British Recent foraminiferids. Heinemann Educational Books, London.

Murray, J.W., 1973. Distribution and ecology of living benthic foraminifera. Heinemann, London, 274 P.

Phleger, F.B. and Parker, F.L., 1951. Ecology of foraminifera north- west Gulf of Mexico, Pt. II, Foraminifera species. Geological Society of American Memoirs, 46: 46.

Quanhong, Z., and Whatley, R., 1989. Recent podocopid ostracoda of the Sedili River and Jason Bay, southeastern Malay Peninsula. Micropaleontology, pp. 168-187.

Sabah, Y.Y., 2010. Stratigraphy of the Mesopotamia plain. Iraqi Bull. Geol. Min. Special Issue, No.4, 2011: Geology of the Mesopotamia Plain, pp. 47-82.

Shepard, F.P. and Moore, D.G., 1955. Central Texas coast sedimentation: Characteristics of sedimentary environments, recent history, and diagenesis. Amer. Assoc. Petro. Geol. Bull., vol. 39, pp. 1463-1592.

Trefethen, J.M., 1950. Classification of sediments. Amer. Jour. Sci., Vol. 248, pp. 55-62.

Witte, L.J. 1993. Taxonomy and origin of modern West African shallow marine Ostracoda. Reprinted from the journal Scientific Journal of the Netherlands Academy of Sciences, 39; pp. 13-105, pls. 1-11.

Iraqi National Journal of Earth Science, Vol. 26, No. 04, 2026 (108-121)

Iraqi National Journal of Earth Science

www.earth.uomosul.edu.iq

التطبيقات البيئية لتجمعات الفورامينيفرا والأستراكودا البحرية، في مدينة الفاو، جنوبي العراق

بدرية علي حسين [1*]، **عباس حميد محمد** [1]

ali.b.h.1989.sa@gmail.com doctorabbas71@yahoo.co.in

[1] قسم علوم الأرض، كلية العلوم، جامعة البصرة، البصرة، العراق.

* الباحث المراسل.

تاريخ الاستلام: 27 أيار 2025 تاريخ المراجعة: 20 تموز 2025 تاريخ القبول: 27 آب 2025

تاريخ النشر الالكتروني: 01 تشرين الأول 2026

الملخص

في الدراسة الحالية، تم اخذ عينات سطحية وتحت سطحية من عمق (50) سم باستخدام أداة الجرافة إلى عمق (21) مترًا بواسطة الغواص لدراسة الاختلافات في مجموعة الأوستراكودا والفورامينيفرا من (15) عينة، (5) منها ضحلة و(10) تحت سطحية على طول الخليج العربي في الفاو (كاسر الأمواج) في مدينة البصرة جنوب العراق لدراسة اختلافات الرواسب السطحية وتحت السطحية في مجموعة الأوستراكودا والفورامينيفرا. تم دراسة (15) عينة تحت المجهر الثنائي. تم تحديد اربعة وعشرون نوعًا من تصنيفات الأوستراكودا تنتمي إلى (21) جنسًا وأيضًا واحد وخمسون نوعًا من انواع الفورامينيفرا تنتمي إلى (19) جنسًا. توصلت الدراسة الحديثة الى ان هناك الأوستراكودا مع العمق عن وجود وفير من Cypreidis و Tanella و Actinocythereis و Neocytheromorpha كذلك ازدياد في الأنواع العائدة للاجناس التالية من الفورامنفرا مع ازدياد العمق Ammonia و Elphidium و Quingloculina و Spiroloculina في جميع العينات وهي السائدة بينما تتوفر بقية الأجناس والأنواع بنسب متفاوتة في جميع العينات. تشير الأجناس السائدة في العينة السطحية إلى بيئات المد والجزر والمسطحات الطينية البحرية ذات الملوحة المنخفضة وحالة الطين المسطح بينما تشير باقي الأجناس الأخرى في العينات بأكملها إلى البيئة البحرية وظروف الملوحة العالية اضافة إلى تأثير التغاير في مستوى سطح البحر. تم أخذ عينات من الرواسب السطحية وتحت السطحية من الجرف البحري والمنحدر العلوي لفهم تجمعات الأوستراكودا والفورانيفيرا الحديثة وتصنيفها. كما تم إجراء وقياس تحليل حجم الحبيبات والمادة العضوية.

الكلمات المفتاحية:

تجمعات الأوستراكودا والفورامينيفيرا، شاطئ الفاو، كاسر الامواج، حجم الحبيبات والمادة العضوية، جنوب العراق.

DOI: 10.33899/injes.v26i4.56156, ©Authors, 2026, College of Science, University of Mosul.

This is an open-access article under the CC BY 4.0 license (http://creativecommons.org/licenses/by/4.0/)

Iraqi National Journal of Earth Science, Vol. 26, No. 04, 2026 (122-129)

Iraqi National Journal of Earth Science

www.earth.uomosul.edu.iq

Deep Insights for Optimizing Hydraulic Fracturing Designs to Maximize Productivity in Horizontal Wells within Unconventional Reservoirs

Huda J. TH. AL-Hillali [1*], **Faleh H. M. Almahdawi** [1]

huda.jaleel2208@coeng.uobaghdad.edu.iq dr.f.h.m.almahdawi@coeng.uobaghdad.edu.iq

[1] *Department of Petroleum Engineering, College of Engineering, University of Baghdad, Baghdad, Iraq.*
** Correspondence author.*

Received: 12 May 2025 Received in revised form: 10 August 2025 Accepted: 30 November 2025
Available online: 01 October 2026

Abstract

This study investigates the impact of various reservoir and fracture parameters on the productivity of horizontal wells using Schlumberger's PIPESIM software to conduct a comprehensive numerical simulation. The parameters analyzed include fracture length, width, porosity, permeability, and number of fractures. A series of simulations is conducted to systematically examine the effects of each parameter. The results show that fracture half-length and permeability have the greatest positive impact on well productivity, with the optimal fracture length being 4921.3ft and the optimal fracture permeability being 1000md. These two factors enhance the reservoir's ability to efficiently absorb and transport fluids, thus enhancing production rates. Additionally, fracture width and porosity show a moderate impact on productivity, highlighting their role in fluid flow dynamics. Interestingly, the number of fractures exhibits a nonlinear relationship with productivity, indicating that increasing the number of fractures initially leads to higher production rates; however, diminishing returns occur after a certain threshold is reached. The optimal number of fractures is 250, beyond which diminishing returns occur. These results provide valuable insights for improving hydraulic fracturing designs to maximize productivity in horizontal wells, especially in unconventional reservoirs, and to support more informed decision-making in field applications.

Keywords:

Hydraulic fracturing, Horizontal wells, Halfaya oil field.

DOI: 10.33899/injes.v26i4.56130, ©Authors, 2026, College of Science, University of Mosul.

This is an open-access article under the CC BY 4.0 license (http://creativecommons.org/licenses/by/4.0/).

==========

1. Introduction

Hydraulic fracturing, often referred to as "fracking", has generated a lot of attention lately. This process involves creating new or enhancing existing cracks in rock formations to extract oil and gas, or petroleum hydrocarbons. The fractures created in the rock serve as pathways that allow oil and gas to flow from the rock into the well for production (Fig. 1).

Simulations and computer models predict the expected dimensions (length and height), azimuth orientation, and distribution of fractures resulting from different techniques designed to create the most effective and cost-efficient fracture system (Abbas et al., 2022; Hamid et al., 2023; Abd-almohi et al., 2025). Accurate post-fracture assessments of production rates over time generate economic margins, based on accumulated experience, that inform future fracture treatments (Abdulmajeed and Awadh, 2022). Evaluating the overall performance of current wells helps determine the best locations for future wells in the formation to maximize production efficiency (Al-Bazali et al., 2008; Al-Delfi et al., 2023; AlHusseini and Hamed-Allah, 2023).

Hydraulic fracturing and horizontal wells are long-standing technologies in the oil and gas sector. The initial fracturing experiment occurred in 1947, with the process gaining commercial acceptance by 1950 (Bell, 2003). Horizontal wells were introduced in the 1930s, and by the late 1970s, they had become widely used (El-Dessouky et al., 1995; Faidhllah and Hamd-Allah, 2023; Faraj and Abdul Hussein, 2023).

The Saadi Formation (Late Turonian-Early Campanian) sequence, which is the thickest and most extensive formation in the Halfaya oil field (Al-adliy et al., 2024), is studied in the current research. The Saadi Formation consists of two distinct units: the non-reservoir Saadi A and the reservoir Saadi B, which is the primary tight oil reservoir of the field and 77 meters thick (Bell, 2003). It is located above the Tanuma Formation and below the Hartha Formation, and is mostly made up of limestone (Farman and Abdulamir, 2014).

This study aims to determine the effect of length, width, and number of hydraulic fractures on the productivity of a horizontal well in the Halfaya oil field.

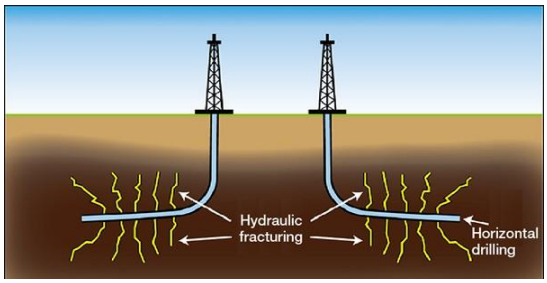


Fig. 1: Fracturing the rock formation for production (Farman and Abdulamir, 2014).

2. Geological Setting

The Halfaya oilfield is located about 35 km southeast of Amarah City (the center of the Missan Governorate) and 320 km southeast of Baghdad as shown in figure (3). Found in 1976, it covers an approximate area of 288 km² (Jreou, G. N. 2012). The youngest, thickest and most extensive formation of the Late Turonian-Early Campanian sequence is the Saadi Formation located within this area. The type section of the formation was originally defined on well Zubair-3 by Owen and Nasr (1958). Subsequently, Chatton and Hart (1961) and Ditmar and the Iraqi-Soviet team (1971 and 1972) modified its definition and age, the latter including in the Saadi Formation exposures of the Pilsner Formation. The Saadi Formation is composed of 300 m of white chalky argillaceous and globigerinal limestone capped by a well-developed 60 m thick marl bed. Distal to the type section, the upper part of the formation also includes organo-detrital limestone (Bellen et al., 1959; Farouk and Al-Haleem, 2022; Holditch, 2006; Jreou, 2012). The Halfaya field is an anticline oriented in a northwest-southeast direction and only covers an area of around 30 km in length by 10 km in width (Khalili and Ahmadi, 2023; King, 2012; Mansourizadeh et al., 2016).

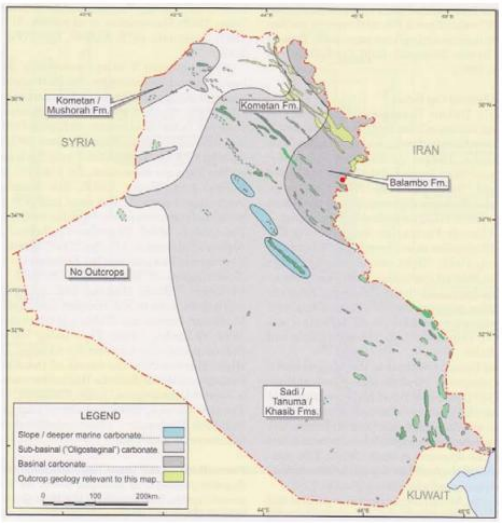


Fig. 2: Late Turonian-early Campanian palaeogeography of Iraq (Mansourizadeh et al., 2016).

3. Methodology

Data from the HF007 in Iraq's Halfaya oilfield are analyzed to determine optimal hydraulic fracture parameters for enhancing horizontal well productivity using Pipesim software. The study incorporated the following datasets:

1. Wellbore Design and Geometry

Total Wellbore Length: Combined vertical and horizontal sections from the surface to the reservoir.

Horizontal Section Length: Portion of the wellbore traversing the productive reservoir zone enhancing exposure to fractures.

Depth: Total distance from the surface to the well's bottom including vertical segments.

Wellbore Radius: Internal diameter influencing pressure dynamics, flow rates and fracture dimensions.

True Vertical Depth (TVD): Vertical measurement from the surface to the reservoir aiding in assessing vertical reach.

Deviation/Inclination: Angles of the horizontal wellbore section affecting fracture geometry and fluid flow.

2. Tubing and Casing Configuration

Casing Diameter: Size of the pipe stabilizing the wellbore and isolating formations.

Tubing Diameter: Inner pipe size impacting production fluid flow and friction losses.

Perforation Details: Location, density and type of casing perforations enabling reservoir-to-well fluid transfer.

3. Hydraulic Fracture Parameters

Fracture Length: Extent of fractures within the reservoir, directly influencing reservoir contact area.

Fracture Width: Opening size dictated by proppant volume and injection rates affecting flow capacity.

Fracture Conductivity: Efficiency of fluid transport through fractures, determined by proppant type, width and rock permeability.

Proppant Properties: Type (e.g., sand, ceramic) and quantity injected to hold fractures open, impacting conductivity.

Injection Data: Pressure and rate profiles during fracturing operations, critical for simulating fracture propagation.

4. Reservoir Characteristics

Reservoir Pressure/Temperature: Key drivers of fluid flow and viscosity.

Permeability/Porosity: Rock properties governing fluid mobility and hydrocarbon storage capacity.

Oil: API gravity, viscosity and composition.

5. Production Metrics

Production Rates: Initial and declining hydrocarbon output over time.

Pressure Data: Bottomhole (BHP) and wellhead pressures, critical for flow and reservoir health monitoring.

Fluid Composition: Oil, gas and water ratios to diagnose production challenges.

Decline Trends: Long-term production patterns guiding stimulation strategies.

6. Completion Design

Completion Type: Open-hole, cased-hole, or perforated configurations influencing fluid entry and fracture initiation.

Completion Tools: Packers, safety valves and tubing ensuring operational integrity.

7. Methodology Workflow

Pipesim software integrated these datasets to model fracture-wellbore-reservoir interactions. Sensitivity analyses tested fracture dimensions prioritizing configurations that maximized productivity while balancing economic and operational constraints. Historical production data validated model accuracy ensuring realistic optimization outcomes (Sissakian et al., 2023).

This structured approach aimed to reduce trial-and-error in fracture design offering actionable insights for the Halfaya field's development.

4. Results and Discussion

A. Effect of fracture half- length

It is observed that increasing length of fractures significantly enhances productivity due to the increased surface area for the fluid to invade fracture. However, the incremental gain diminishes beyond a certain length due to pressure drop along the wellbore and flow resistance. Therefore, an optimal length must be determined based on economic and technical factors (Savari et al., 2020).

When increasing fracture length (XF) as shown in figure (3), it essentially:

- will increase surface area for the fluid to invade the fracture.
- shortens the distance, so the slow and constrained oil must flow through dense stone.

So initially:

- a little XF goes a long way in achieving higher flow rates and pressure.
- getting an access to new and untapped reservoir that was never connected before.

However, after a certain XF (e.g. >3000 ft), the fracture has already linked most of the productive area.You've depleted the rock tone with the least overhead. New XF extensions may only extend to low-permeability or tight rock. That additional length might not be booking much new oil.

Reservoir depletion and interference

The farther out from the reservoir, the weaker the pressure support is. It takes time for those far-flung spots to contribute flow not always fast enough to matter at high rates. Longer fractures can also develop internal pressure losses.

After a certain point, the benefit of greater contact is offset by lower pressure in the fracture itself and diminishing returns. While continue to spend money and effort to lengthen the fracture, as the amount of additional fluid you obtain per foot of fracture decreases, it becomes economically inefficient.

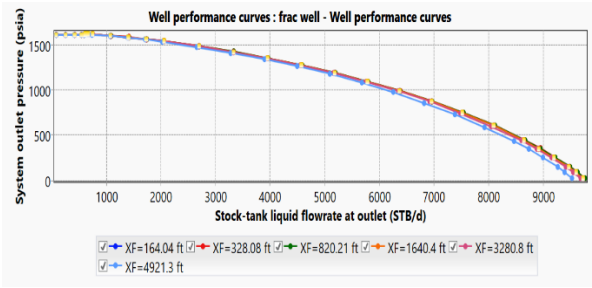


Fig. 3: Effect of fracture half- length

B. Effect of Fracture Width

The results of horizontal well performance curves as shown in figure (4) when changing fracture width indicate that this variable is a key factor in increasing production rates. In cases where fracture width is very small (for example, 0.019685 inches), pressure drops rapidly, and production decreases to very limited quantities, not exceeding tens of barrels per day. This reflects the limited flow path and high flow resistance. When width increases to intermediate values (0.03937 and 0.19685 inches), the well's production capacity improves significantly as the achievable flow rates increase at the same pressure levels, although the improvement remains less than that of larger widths.

In the case of larger widths (0.31496 and 0.3937 inches), performance shows a significant improvement with production rates exceeding 500 barrels per day, with a slower gradual decrease in pressure compared to previous cases. This indicates that fracture width provides better paths for fluid flow and enhances hydraulic communication between the well and the reservoir reducing pressure loss within the fracture and increasing recovery efficiency.

From these observations, it can be concluded that the relationship between fracture width and productivity is directly proportional. However, the effect of increasing width does not persist to the same degree. The improvement is significant when moving from very small to medium values, while the effect decreases as the value increases, which is consistent with the concept of diminishing returns. This also confirms that fracture width, despite its importance, is not the only factor determining performance. Length, extension and the number of fractures may play a greater role when width reaches high levels.

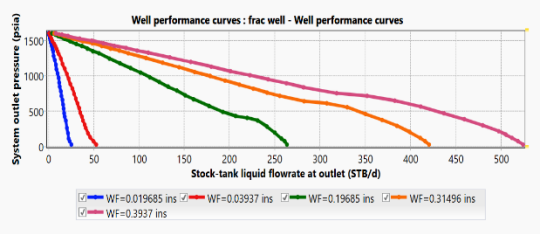


Fig. 4: Effect of Fracture Width.

C. Effect of fracture Porosity

Porosity has a secondary impact compared to permeability or fracture characteristics. It primarily determines the reservoir's storage capacity rather than its flow capacity. Thus, in tight formations, even high porosity does not guarantee good productivity without effective stimulation techniques (Mezaal et al., 2023).

In Figure (5), porosity variation (between 0.05 and 0.2) has little effect on well performance. The performance curves are almost identical indicating that porosity has a little effect on flow rate and pressure behavior in this scenario. In contrast, factors such as permeability and fracture properties have a greater impact.

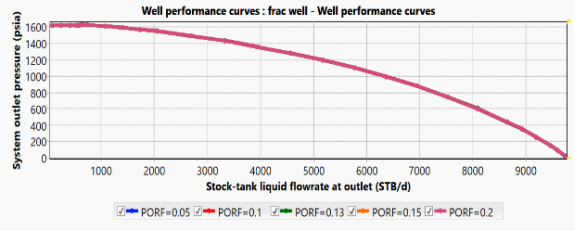


Fig. 5: Effect of fracture Porosity.

D. Effect of fracture Permeability

Permeability is found to be one of the most influential parameters for productivity. It directly governs the reservoir's ability to transmit fluids to the wellbore. Higher permeability results in increased production rates making it a key performance indicator, especially in conventional reservoirs (Khalili and Ahmadi, 2023).

In figure (6), the effect of KF (fracture permeability) is revealed.

Low KF (50–100 md): Bad performance, sudden drop of pressure and low flowrate.

Moderate KF (250–500 md): Massive improvement, way better flow and ability to handle pressure.

High KF (800–1000 md): Super performance, but returns begin to flatten out → little return.

Higher fracture permeability gives a better production, but the added benefit becomes trivial after a certain point (about 800 md).

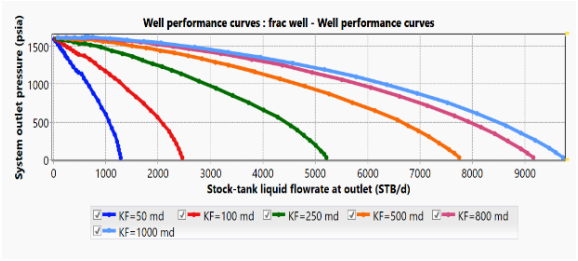


Fig. 6: Effect of fracture Permeability.

E. Effect of Number of Fractures

The analysis shows that increasing the number of hydraulic fractures significantly improves productivity by stimulating a larger reservoir volume and creating more drainage paths. However, excessive fracture density may result in fracture interference reducing the overall efficiency. Hence, optimized spacing and distribution are critical (Hussain and Al Mahdawi, 2019).

In figure (7), as the number of fractures (NF) increases (from 10 up to 2000), the well can deliver higher flowrates with less pressure loss.

The performance boost is noticeable at first, especially between NF = 10 and 100, but the curves begin to converge beyond NF = 500.

More fractures = more flow paths = better reservoir drainage.

Each added fracture improves fluid access to the wellbore and enhancing production.

After around 500–1000 fractures, performance gains slow down.

Additional fractures contribute less likely due to overlapping drainage zones and flow interference.

Between NF = 10 and 100, there's a major performance jump.

Between NF = 500 and 2000, the improvement is less dramatic.

Increasing fracture count significantly enhances production at first, but after a certain point (around NF = 500–1000), the impact levels off as fractures begin to interact and their effectiveness reduces.

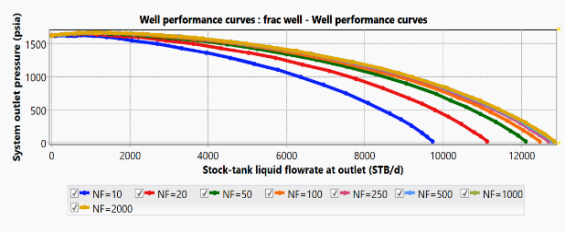


Fig. 7: Effect of Number of Fractures.

Summary of results as shown in Table 1 below

Table 1: Summary of results

Parameter	Impact on Productivity	Technical Notes
Horizontal Well Length	~35%	Diminishing returns beyond optimum
Fracture Width	~20%	Limited by stability and proppant flow
Fracture Porosity	~10%	Affects storage, not flow capacity
Fracture Permeability	~25%	Directly influences fluid flow
Number of Fractures	~30%	Spacing must be optimized

5. Conclusion

Increasing fracturing length increases reservoir contact and improves production, especially in low-permeability rocks.

Fracturing width is directly related to permeability within the fracture, which affects the rate of fluid flow into the well.

The number of fracturing units must be carefully selected to avoid interference and ensure effective reservoir coverage.

Permeability within a fracture is the primary factor in fluid transport and flow efficiency.

Porosity plays a supporting role in temporary fluid storage and takes on additional importance when natural fractures are present.

Optimal design requires a careful balance between these factors, based on a detailed geological assessment of each reservoir.

6. Conflict of Interest

The authors declare that they have no conflict of interest.

7. Funding Statement

This research received no external funding.

8. Author Contributions

Huda J. TH. AL-Hillali, conceived the manuscript and wrote the paper; took the samples and analyzed the data; prepared figures and tables.

Faleh H. M. Almahdawi, provided the writing ideas and supervised the study.

9. References

Abbas, M. A., Ismail, A. S., Zakaria, K., El-Shamy, A. M., and El Abedin, S. Z. 2022. Adsorption, thermodynamic, and quantum chemical investigations of an ionic liquid that inhibits corrosion of carbon steel in chloride solutions. Scientific Reports, 12(1), 1–13. https://doi.org/10.1038/s41598-022-16755-6

Hamid, A.A.A., Seddik, S. H., Hassan, M., and Hamid, H.M.A., 2023. Geology, Petrography, and Geochemistry of Younger Granites and Related Radioactive Pegmatite from Gabal El Urf Area, North Eastern Desert, Egypt: Implications for the Evolution of the NYF-Type Rare-Elements Granitic Pegmatite. Iraqi Geological Journal, 56(2), 1–18. https://doi.org/10.46717/igj.56.2E.1ms-2023-11-6

Abd-almohi, H. H., Alismaeel, Z. T., and M-Ridha, M. J. 2025. Inspection the impact of mixing and external resistance on the Microbial Desalination Cell for electricity generation and desalination efficiency by using Macroalgae as a bio-cathode. Journal of the Indian Chemical Society, 102(1), 101543. https://doi.org/10.1016/J.JICS.2024.101543

Abdulmajeed, R. K., and Awadh, S. M. 2022. A Predictive Model for Estimating Unconfined Compressive Strength from Petrophysical Properties in the Buzurgan Oilfield, Khasib Formation, Using Log Data. Iraqi Geological Journal, 55(2E), 140–151. https://doi.org/10.46717/igj.55.2E.9ms-2022-11-23

Al-adliy, S. H., Al-mahdawi, F. H. M., Mohammed, E. M. A. and Mukhtar, Y. M. F. (2024). Comparison Different Techniques of Optimum Location for Infill Well Drilling. Iraqi Journal of Chemical and Petroleum Engineering, 25(1), 75–81. https://doi.org/10.31699/ijcpe.2024.1.7

Al-Bazali, T., Zhang, J., Chenevert, M. E. and Sharma, M. M. 2008. Experimental and numerical study on the impact of strain rate on failure characteristics of shales. Journal of Petroleum Science and Engineering, 60, 194–204. https://doi.org/10.1016/j.petrol.2007.09.001

Al-Delfi, A. K., Al-Mahdawi, F. H. M., Mukhtar, Y. and Bagadi, Y. E. 2023. Experimental Study to Investigate the Effect of Polyacrylamide Gel to Reduce the Lost Circulation. Iraqi Journal of Chemical and Petroleum Engineering, 24(1), 79–88. https://doi.org/10.31699/ijcpe.2023.1.9

AlHusseini, A. K. and Hamed-Allah, S. M. 2023. Estimation Pore and Fracture Pressure Based on Log Data; Case Study: Mishrif Formation/Buzurgan Oilfield at Iraq. Iraqi Journal of Chemical and Petroleum Engineering, 24(1), 65–78. https://doi.org/10.31699/ijcpe.2023.1.8

Bell, J. S. 2003. Practical methods for estimating in situ stresses for borehole stability applications in sedimentary basins. Journal of Petroleum Science and Engineering, 38(3–4). https://doi.org/10.1016/S0920-4105(03)00025-1

El-Dessouky, H., Shaban, H. I. and Al-Ramadan, H. 1995. Steady-state analysis of multi-stage flash desalination process. Desalination, 103(3), 271–287. https://doi.org/10.1016/0011-9164(95)00080-1

Faidhllah, D. K. and Hamd-Allah, S. M. 2023. Prediction of Hydraulic Flow Units for Jeribe Reservoir in Jambour Oil Field Applying Flow Zone Indicator Method. Iraqi Journal of Chemical and Petroleum Engineering, 24(2), 65–70. https://doi.org/10.31699/ijcpe.2023.2.7

Faraj, A. K. and Abdul Hussein, H. A. 2023. Application of Finite Element Technique: A Review Study. Iraqi Journal of Chemical and Petroleum Engineering, 24(1), 113–124. https://doi.org/10.31699/IJCPE.2023.1.13

Farman, G. M. and Abdulamir, M. R. 2014. Formulation of New Equation to Estimate Productivity Index of Horizontal Wells. Iraqi Journal of Chemical and Petroleum Engineering, 15(2), 61–73. https://doi.org/10.31699/ijcpe.2014.2.7

Farouk, A. K. and Al-Haleem, A. A. 2022. Integrating Petrophysical and Geomechanical Rock Properties for Determination of Fracability of the Iraqi Tight Oil Reservoir. Iraqi Geological Journal, 55(1F), 81–94. https://doi.org/10.46717/igj.55.1F.7Ms-2022-06-22

Holditch, S. A. 2006. Tight Gas Sands. Journal of Petroleum Technology, 58(6), 86–93. https://doi.org/10.2118/103356-JPT

Hussain, N. F. and Al Mahdawi, F. H. M. 2019. Prediction of Fracture Pressure Gradient in Halfaya Oilfield. Iraqi Journal of Chemical and Petroleum Engineering, 20(1), 1–7. https://doi.org/10.31699/ijcpe.2019.1.1

Jreou, G. N. 2012. Increasing of Oil Field Productivity by Implementation of Re-entry Horizontal Injection Well, Case study. Iraqi Journal of Chemical and Petroleum Engineering, 13(3), 17–34. https://doi.org/10.31699/ijcpe.2012.3.3

Khalili, Y. and Ahmadi, M. 2023. Reservoir Modeling and Simulation: Advancements, Challenges, and Future Perspectives. Iraqi Journal of Chemical and Petroleum Engineering, 57(2), 343–364. https://doi.org/10.22059/JCHPE.2023.363392.1447

King, G. E. 2012. Hydraulic fracturing 101: What every representative, environmentalist, regulator, reporter, investor, university researcher, neighbor and engineer should know about estimating frac risk and improving frac performance in unconventional gas and oil wells. SPE Hydraulic Fracturing Technology Conference, 651–730. https://doi.org/10.2118/152596-ms

Mansourizadeh, M., Jamshidian, M., Bazargan, P. and Mohammadzadeh, O. 2016. Wellbore stability analysis and breakout pressure prediction in vertical and deviated boreholes using failure criteria – A case study. Journal

of Petroleum Science and Engineering, 145, 482–492. https://doi.org/10.1016/j.petrol.2016.06.024

Mezaal, G. F., Khwedim, K. and Abdulzahra, I. K. 2023. Mineralogical and Geochemical Characteristics of Clay Deposits, Bussaya Area, Southern Iraq. Iraqi Geological Journal, 56(2), 69–81. https://doi.org/10.46717/igj.56.2E.5ms-2023-11-10

Savari, S., Butcher, J. and Al-Hulail, M. 2020. Managing lost circulation in highly fractured, vugular formations: Engineered usage of high fluid loss squeeze and reticulated foam lost circulation materials. SPE/IADC Drilling Conference. https://doi.org/10.2118/199635-MS

Sissakian, V. K., Al-Ansari, N., Abdullah, L. H. and Laue, J. 2023. Neotectonic Indications from the Western and Southern Deserts of Iraq. International Journal of Geosciences, 14, 427–436. https://doi.org/10.4236/ijg.2023.145022

Iraqi National Journal of Earth Science, Vol. 26, No. 04, 2026 (122-129)

Iraqi National Journal of Earth Science

www.earth.uomosul.edu.iq

رؤى متعمقة لتحسين تصميمات التكسير الهيدروليكي لتحقيق أقصى قدر من الإنتاجية في الآبار الأفقية داخل الخزانات غير التقليدية

هدى جليل ثجيل الهلالي [1*] ، **فالح حسن محمد المهداوي [1]**

huda.jaleel2208@coeng.uobaghdad.edu.iq dr.f.h.m.almahdawi@coeng.uobaghdad.edu.iq

[1] قسم هندسة النفط، كلية الهندسة، جامعة بغداد، بغداد، العراق.

**الباحث المراسل.*

تاريخ الاستلام: 05 أيار 2025 تاريخ المراجعة: 10 آب 2025 تاريخ القبول: 30 تشرين الثاني 2025

تاريخ النشر الالكتروني: 01 تشرين الأول 2026

الملخص

تبحث هذه الدراسة في تأثير مختلف مَعلَمات المكمن والكسور على إنتاجية الآبار الأفقية باستخدام برنامج PIPESIM من شركة شلمبرجير لإجراء محاكاة رقمية شاملة. تشمل المعلمات التي تم تحليلها طول الكسر وعرضه ومساميته ونفاذيته وعدد الكسور. أُجريت سلسلة من عمليات المحاكاة لفحص آثار كل مَعلَمة بشكل منهجي. أظهرت النتائج أن طول الكسر ونفاذيته لهما التأثير الإيجابي الأكبر على إنتاجية البئر حيث افضل طول للكسر هو 4921.3 قدم، وافضل نفاذية للكسر هي 1000 ملي دارسي . يعزز هذان العاملان قدرة المكمن على امتصاص ونقل السوائل بكفاءة، مما يعزز معدلات الإنتاج. بالإضافة إلى ذلك، أظهر عرض الكسر والمسامية تأثيرًا معتدلًا على الإنتاجية، مما يبرز دورهما في ديناميكيات تدفق السوائل. ومن المثير للاهتمام أن عدد الكسور أظهر علاقة غير خطية مع الإنتاجية، مما يشير إلى أن زيادة عدد الكسور تؤدي في البداية إلى ارتفا ع معدلات الإنتاج. ومع ذلك، يحدث تناقص في العائدات بعد تجاوز حد معين وان افضل عدد للكسور هو250، وبعد تجاوز هذا الحد يحدث تناقص في العائدات. وتقدم هذه النتائج رؤى قيمة لتحسين تصاميم التكسير الهيدروليكي لتحقيق أقصى قدر من الإنتاجية في الآبار الأفقية، وخاصة في الخزانات غير التقليدية، ودعم اتخاذ قرارات أكثر استنارة في التطبيقات الميدانية.

الكلمات المفتاحية:

التكسير الهايدروليكي، الابار الافقية، حقل الحلفاية النفطي.

DOI: 10.33899/injes.v26i4.56130, ©Authors, 2026, College of Science, University of Mosul.

This is an open-access article under the CC BY 4.0 license (http://creativecommons.org/licenses/by/4.0/)

Iraqi National Journal of Earth Science, Vol. 26, No.04, 2026 (130-137)

Iraqi National Journal of Earth Science

www.earth.uomosul.edu.iq

Reservoir Evaluation of Nahr Umr Formation at Abu-Amood Oil Field, Southern Iraq

Mhammed Q. Abd Talib [1*], **Mohammd S. Al-Jawad** [2]

m.murad1708@coeng.uobaghdad.edu.iq mjawad@coeng.uobaghdad.edu.iq

[1] *Department of Petroleum Engineering, College of Engineering, University of Al-Farabi, Baghdad, Iraq.*
[2] *Department of Petroleum Engineering, College of Engineering, University of Baghdad, Baghdad, Iraq.*
** Correspondence author.*

Received: 27 May 2025 Received in revised form: 01 September 2025 Accepted: 02 December 2025
Available online: 01 October 2026

Abstract

This study presents the first comprehensive evaluation of the Nahr Umr Formation in Abu-Amood Oil Field, southern Iraq, addressing a critical research gap. Using well log data, the formation is divided into five lithological units. Key steps include depth correction of logs, shale volume calculation, and porosity-permeability estimation via neutron-density and sonic methods. Water saturation is computed using Archie (clean zones) and Indonesia (shaly zones) equations. The results have identified Unit 3 (clean sandstone) as the primary reservoir with high average porosity, permeability, and oil presence above the oil-water contact (OWC) at 3120 m. Units 1 and 5 exhibit low porosity and high-water saturation, while Unit 2 has suffered from data gaps due to borehole instability. The study highlights Nahr Umr's potential as a hydrocarbon reservoir and underscores challenges in shaly zones. These findings provide foundational insights for future exploration and development, emphasizing the need for improved core recovery and advanced modeling to reduce uncertainties in heterogeneous formations.

Keywords:

Abu-Amood, Formation Evaluation, Nahr Umr.

DOI: 10.33899/injes.v26i4.56157, *©Authors, 2026, College of Science, University of Mosul.*
This is an open-access article under the CC BY 4.0 license (http://creativecommons.org/licenses/by/4.0/).

==========

1. Introduction

The process of preparing a comprehensive study for a potential reservoir model usually starts with well log interpretation; then the results of interpretation will help in building an accurate model for the purpose of the study.

Abu-Amood oil field is located in Dhi Qar province, approximately 16 km north of the Qall'at Sukkar area and 26 km north of Refa'i, with an adjacency of only 17 km southwest of the Dejaila field as shown in Figure (1) (Khorshid and Khaleel, 2017a). The field is around 22 Km long and 6 Km wide with an azimuth of N65°W. The field primarily consists of several formations with high production potential.

Nahr Umr Formation at the Abu-Amood oil field is primarily characterized by sandstone rocks. According to the available geological reports, the formation top is at a depth of 3025 m below sea level, with an average thickness of 139 m. No faults are recognized in the formation, indicating a stable geological structure (Khorshid and Khaleel, 2017b).

Several studies have investigated the Abu Amood oil field, exploring different formations. The Mishrif, Zubair, and Yamama formations took center stage, with researchers analyzing them for petrophysical interpretation and geological modeling (Al-Baldawi, 2021; Hussain et al., 2021; Mahdi and Farman, 2023b, 2023a; Nasser et al., 2021). Beyond specific formation, other studies covered the entire field. They addressed various aspects, such as designing seismic surveys (Khorshid and Khaleel, 2017a), assessing the thermal maturity of source rocks (Abdullah et al., 2018), and designing an optimum completion method (Hameed and Al-Jawad, 2020). It is worth highlighting that, while the Nahr Umr Formation has received attention, the scrutiny has been

primarily centered on a structural and stratigraphic study only (Khorshid and Khaleel, 2017b).

Up to the present moment, no research attempts have been undertaken to study the Nahr Umr Formation at the Abu Amood oil field. Consequently, the primary objective of this study is to present the first reservoir evaluation for the Nahr Umr Formation. As a result, a knowledge gap in the existing research landscape has been filled. This study stands as an essential step toward enhancing our understanding of the reservoir within the Abu Amood oil field, particularly about the Nahr Umr Formation.

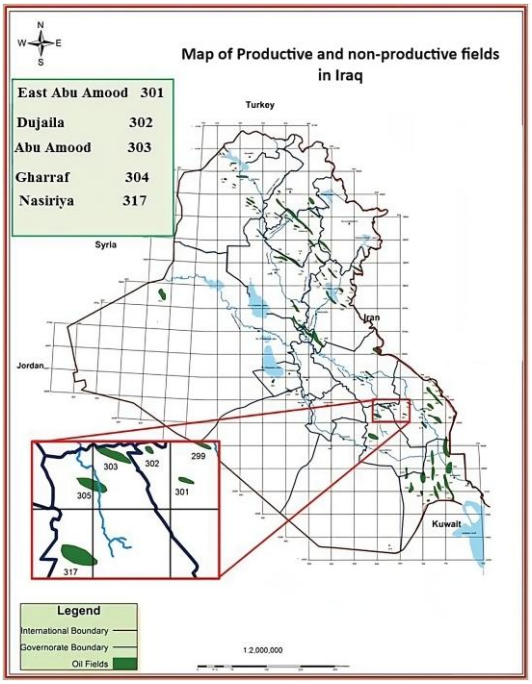


Fig. 1: Abu-Amood oil field location (Odeh, 2021).

2. Methodology

A. Log Depth Shifting

Different logging tools have different setting arrangements inside the borehole. Some are set up centrally in the borehole (e.g., resistivity logs), and others are pushed against the borehole wall (e.g., density log), and this results in off-depth errors in some tools due to drag, which makes the cable stretch, which in turn makes the readings inconsistent (Bassiouni, 1994).

The gamma-ray logging tool in the resistivity set is used as a reference to correlate the readings of other logging tools. The built-in Techlog shifting algorithm is used to make the shifting for all logs.

B. Shale Volume

The calculation of shale volume is important as it contributes to the calculations of effective porosity, which in turn is used in building the dynamic model of the reservoir.

Before computing the shale volume, a correction for the Gamma Ray log (GR) was conducted for mud weight. The mud weight, as well as the minimum and maximum gamma ray reading for each well, is shown in Table (1).

Table 1: Mud weight, minimum and maximum gamma ray reading for each well.

Wells	AAM-1	AAM-2	AAM-3	AAM-4	AAM-5
Mud weight (g/cm^3)	1.26	1.3	1.3	1.28	1.31
MIN GR corrected, GAPI	14.5	14.3	15.5	14.6	12.7
MAX GR corrected, GAPI	155.2	202.4	233	199	245

After correcting the gamma-ray readings, the volume of shale is computed using the Clavier equation (2) (Bassiouni, 1994). The result is illustrated in Figure (2).

$$GR_{Index} = \frac{GR - GR_{min}}{GR_{max} - GR_{min}} \quad (1)$$

$$V_{SH} = 1.7 - \sqrt{3.38 - (GR_{Index} + 0.7)^2} \quad (2)$$

Where: GR_Index: Gamma-ray index; GR: Gamma-ray reading from log; GR_min: Gamma-ray reading in a clean rock; GR_max: Gamma-ray reading in shale rock; V_SH: Volume of shale

C. Zonation

Zonation is a crucial step in well log interpretation for dividing the formation into similar rock lithologies and characteristics and using the equations fit for that lithology, as each equation has different parameters depending on the rock type under study.

As there are no previous works that investigate the Nahr Umr Formation in the Abu-Amood oil field, there is no prior zonation for it. The zonation of the formation is based on cutting reports of wells AAM-1 and AAM-3 found in the Final Geological Report (FGR), as well as GR, caliper, and deep resistivity log deflections as depicted in Figure (2). A summary of cutting reports of both wells is shown in Tables (2 and 3), respectively.

Table 2: Summary of cutting report for well AAM-1.

Depth interval, m	Details
3025 - 3027	Shale, slightly hard
3027 – 3046	Limestone, compact, moderately hard
3046 – 3050	Sandstone
3050 – 3068	Shale with beds of limestone, compact
3068 – 3100	Sandstone, medium Coarse
3100 – 3140	Sandstone, medium Coarse
3140 – 3143	Siltstone, slightly hard
3143 – 3162.6	Sandstone, slightly hard

Table 3: Summary of cutting report for well AAM-3.

Depth interval, m	Details
3046 – 3065	Limestone, compact, moderately hard
3065 – 3081	Sandstone, slightly hard, fine-grained
3081 – 3100	Sandstone, fine - medium grain
3100 – 3127	Sandstone, slightly hard, medium – coarse grain
3127 – 3163	Sandstone, fine – medium grain
3163 – 3188	Mix siltstone and sandstone, fine – medium grain

Nahr Umr Formation is divided into five units: unit-1 (mix of limestone and shale with a high proportion of limestone), unit-2 (mainly shale and its features with high caving approaching 23 inches in AAM-1), unit-3 (clean sandstone), unit-4 (shale), and unit-5 (clean sandstone).

D. Porosity

Porosity is a dimensionless quantity that describes the capacity of the rock to store fluids. Two types of porosity are calculated using different logging tools (i.e., density, sonic, and neutron logs); the first is the total porosity, which, as the name suggests, is the total porosity of the rock; the second type is the effective porosity, which is the total porosity minus the clay-bound water that is usually stored in the shale rocks (Bassiouni, 1994). Effective porosity is generally calculated using equation (3):

$$\phi_{effecitve} = \phi_{total} - V_{shale}\,\phi_{shale} \qquad (3)$$

According to the well log headers, the mud used in drilling well AAM-1 was FCL-CL mud, while lime mud was used in the rest; Thus, all the equations used to calculate the porosities took into consideration the fluid properties of fresh water-based mud for AAM-1 and brine water for the other wells.

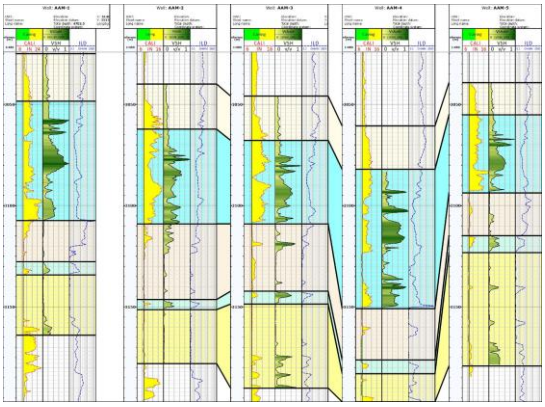


Fig. 2: Caliper, shale volume, deep resistivity and zonation of wells.

For each unit, different logging tools and equations are used depending on the unit's characteristics and rock type. All units' porosities are calculated using the neutron-density method (equation (4), except unit-2, which is calculated using the sonic log only due to the excessive caving in unit-2 as indicated by the caliper log.

$$\phi_{ND} = \sqrt{\frac{\phi_D^2 + \phi_N^2}{2}} \qquad (4)$$

Where: ϕ_{ND}: Neutron-Density porosity; ϕ_D: Porosity from density log; ϕ_N: Porosity from neutron log

After calculating the porosity of the formation, a calibration of the calculated porosity with the core porosity is needed, but due to the low recovery of some cores, there is an uncertainty in the depth-value data provided from the cores; a summary of core data is shown in Table).

Table 4: Summary of core data.

Property	Porosity, %	Permeability, mD
Mean	24.6	1596
S. D.	3.7	1216
Minimum	13.8	1.1
Maximum	34.7	6299
Count	62	63

A program written in Python is used to shift the core data to get a better match with the porosity log. The program takes the core data, log data, and the top and bottom interval of the core as input and calculates the optimum upward shift value that gives the lowest root mean square error (RMSE). The core details and the optimum shift value are shown in Table).

Table 5: Core description.

Well	Core	Recovery, %	Top interval, m	Bottom interval, m	Shift value, m
AAM-1	Core:4	53	3099	3115	6.15
AAM-2	Core:2	64	3113	3122	0.19

AAM-3	Core:3	94	3105	3113	0
	Core:4	64	3117	3126	0.1
	Core:5	79	3126	3135	0
	Core:6	66	3135	3145	0.19
AAM-5	Core:2	13.3	3096	3111	0.44
	Core:3	63.5	3111	3126	0.26

After shifting the cores, a cross plot is made between the porosity log and the shifted core porosity to get an equation that modifies the porosity log to make a better correlation with core data. Fig. 3 shows the cross plot as well as the equation used to modify the porosity.

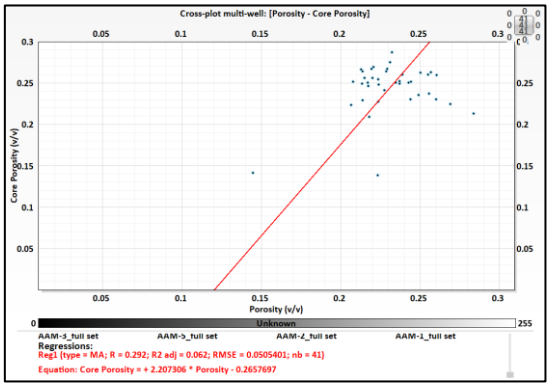


Fig. 3: Cross plot between computed porosity and core porosity.

E. Water Saturation

Water saturation is one of the most important results that can be calculated from well logs, as it reflects fluid content in a pore, whether hydrocarbon or water. Additionally, it's one of the parameters used when estimating the original oil in place (OOIP) (Bassiouni, 1994).

Unlike porosity, there is no direct log tool that can be used to calculate water saturation in a rock. Consequently, a range of empirical correlations is used with different parameters taken from other logs such as the deep resistivity log and the calculated porosity log, and used to estimate the water saturation of the rock (Bassiouni, 1994). The Archie equation (5) and Indonesia equation (6) are used to calculate the water saturation of the formation.

$$S_{w_{Archi}} = \left(\frac{a\,R_w}{\phi^m\,R_t}\right)^{\frac{1}{n}} \qquad (5)$$

$$S_{w_{Indonesia}} = \left(\frac{\sqrt{\frac{1}{R_t}}}{\left(\frac{V_{sh}^{(1-0.5\,V_{sh})}}{\sqrt{R_{sh}}}\right)+\sqrt{\frac{\phi_e^m}{a\,R_w}}}\right)^{\frac{2}{n}} \qquad (6)$$

Where: S_w: Water saturation; a: Tortuosity factor; m: Cementation exponent; n: Saturation exponent; R_w: Formation's water resistivity; R_t: Formation's resistivity; V_{sh}: Shale volume; R_{sh}: Shale resistivity; ϕ : Porosity, ϕ_e : Effective porosity.

Formation water resistivity (R_w) is an important parameter used to estimate water saturation. There are many methods to determine R_w if there is no water analysis is conducted.

For this case, a water analysis is conducted for a sample taken from well AAM-2. The reported R_w (0.0591 ohm.m) is at 22℃; so, equation (7) is used to convert the reported R_w to reservoir temperature, which is 94.4℃ (Bassiouni, 1994).

$$R_{res} = R_{lab}\frac{T_{lab}+6.77}{T_{res}+6.77} \qquad (7)$$

Where: R_{res}: Water resistivity at reservoir temperature; R_{lab}: Water resistivity at reference temperature; T_{lab}: reference temperature, °F; T_{res}: Reservoir temperature, °F

The computed formation's water resistivity is 0.022 ohm.m at reservoir temperature 94.4 ℃.

The rest of the required parameters (i.e., a, m and n) are determined using the Pickket plot. After the water zone is determined from FGR, the selected points are used in Pickket plot. Fig. 4 illustrates Pickket plot, and Table shows Archi parameters for Nahr Umr Formation.

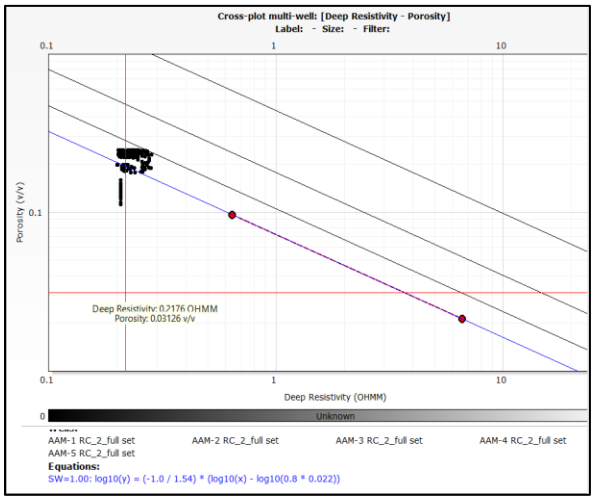


Fig. 4: Pickket plot for water zone data points.

Table 6: Archie parameters for Nahr Umr Formation in Abu-Amood oil field.

Parameter	Value
R_w ohm.m	0.022
m	1.54
a	0.8
n	2

The Archie equation is used to calculate the water saturation for units (1, 3, and 5). In contrast, the Indonesia equation is used for units (2 and 4). This is due to the presence of shale, as the Archie

equation is used for clean formations. For unit-1, default Archi parameters ($a = 1,\ m = 2,\ n = 2$) are used since the obtained parameters were for sandstone formation and not for limestone.

F. Permeability

Permeability is a rock property that describes how easily a fluid can flow through a rock. There are many methods in the literature to calculate the permeability of the rock, ranging from empirical correlation to machine learning techniques (Lazim et al., 2018; Matinkia et al., 2023). Due to the low number of core data, using the advanced methods in the literature is impractical. A cross plot between porosity and the logarithm of permeability, as shown in Fig. , was created to formulate an equation to predict the permeability.

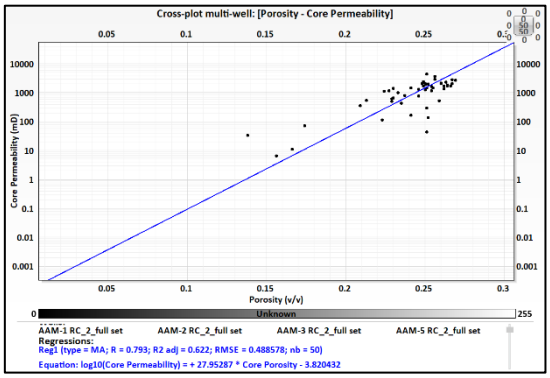


Fig. 5: Cross plot between porosity permeability for Nahr Umr Formation.

G. Oil-Water Contact

Oil-water contact (OWC) is an important parameter to determine since it is involved with the calculation of original oil in place. Two depths are found for OWC in the final geological reports of wells AAM-1 and AAM-5, which are 3120 m and 3126.75 m, respectively. The depth used in this work is 3120 m, as it's aligned with the interpretation of the logs.

3. Results and Discussion

The interpretation results are shown in Figs. 6 to 10, and each figure is divided into four sections. The first section represents the lithology, where the first track shows the lithology with depth, the second track is the caliper log, the third is the spontaneous potential (SP) log, and the last track shows the volume of shale. The second section shows the Neutron, density, and sonic logs, while the third section shows the deep and shallow resistivity logs, and the last section shows the results, where the first track is the porosity, the second track is the permeability, and the last track is water saturation, while the red line shows the OWC depth (i.e., 3120 m).

Unit-1 likely appears as a transition zone between the Nahr Umr Formation and the carbonate Mauddud Formation above it, which is characterized by low porosity approaching zero, low permeability, and high-water saturation, and it can be assumed that this unit acts as a caprock for the Nahr Umr Formation.

Unit-2 is the most ambiguous unit in the formation because of the lack of information about it due to the excessive caving that happened in the unit. As a result of the caving, most logging tools record the information of the mud instead of the formation. It is characterized by high caliper and high gamma-ray readings.

The most promising unit in the formation is Unit 3; it is a clean sandstone rock. It's characterized by high porosity and high permeability, and the uppermost part of the unit has oil, as indicated by the water saturation track, as well as an in-gauge caliper reading.

The next unit is unit-4, which is a thin shaly sandstone rock that appears in all the wells. It's characterized by medium porosity and permeability and low water saturation. The low water saturation is an error caused by the high resistivity of the shale, and this is confirmed by the fact that the OWC is at 3120 M and the shallowest depth of unit-4 in all wells is 3127 m, with well AAM-5 as an exception. This confirms that the low water saturation is due to shale resistivity and not the presence of oil.

The last unit in the Nahr Umr Formation is unit-5. It's characterized by medium-high porosity and permeability and is water-filled, as indicated by the water saturation track.

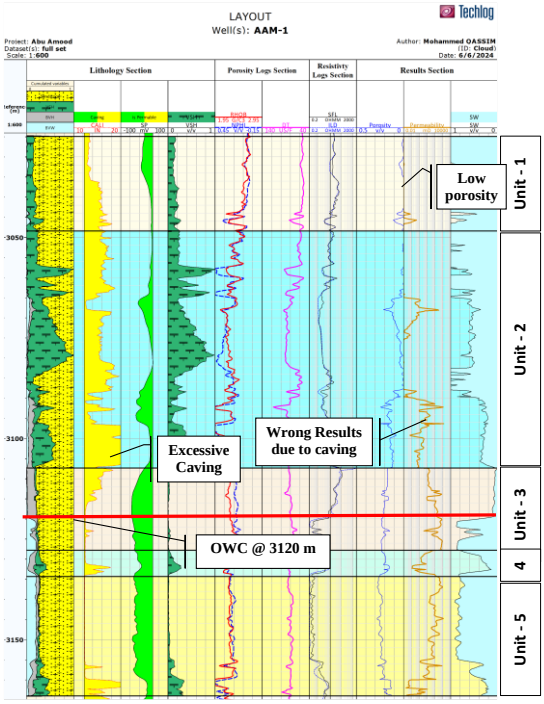


Fig. 6: AAM-1 conventional logs and interpretation results.

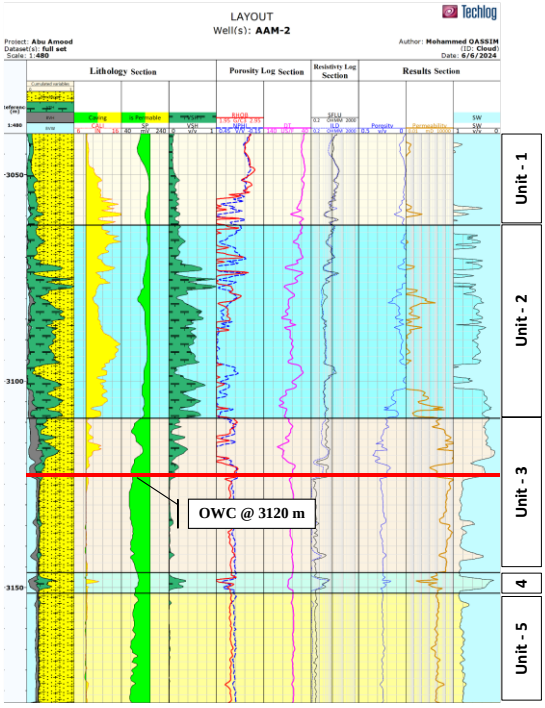


Fig. 7: AAM-2 conventional logs and interpretation results.

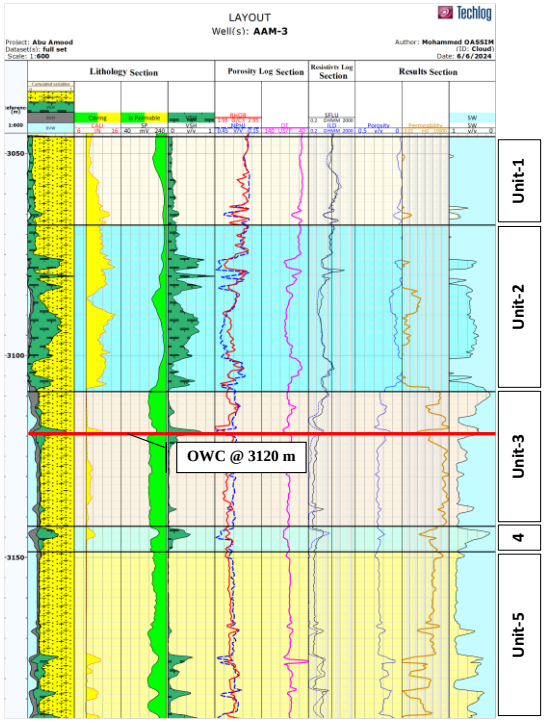


Fig. 8: AAM-3 conventional logs and interpretation results.

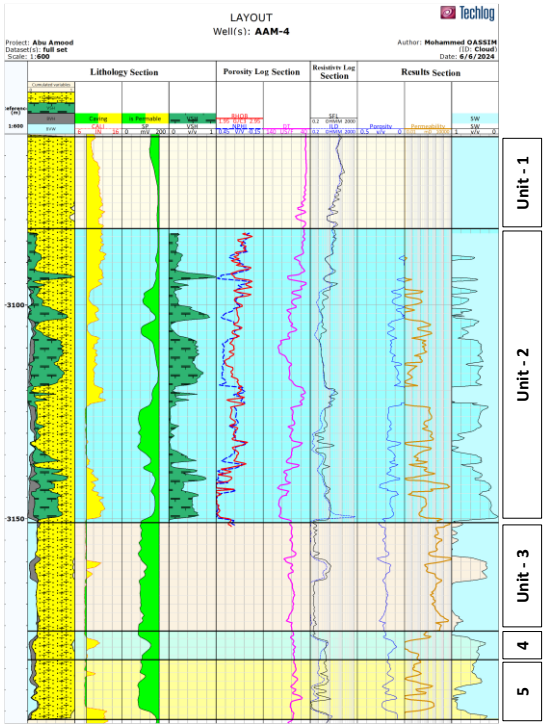


Fig. 9: AAM-4 conventional logs and interpretation results.

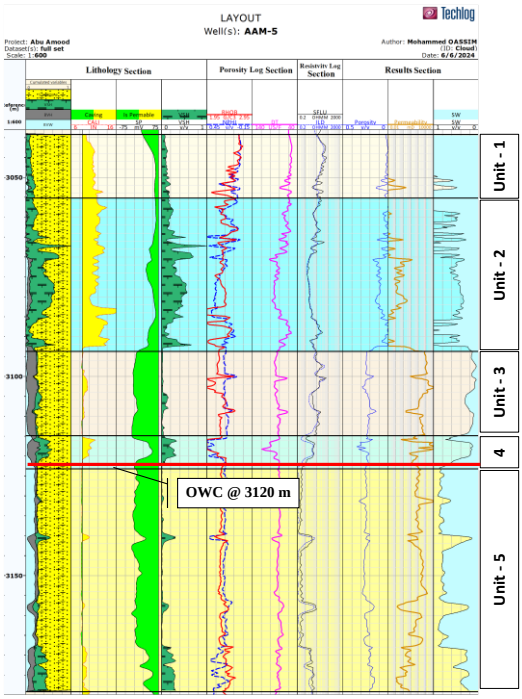


Fig. 10: AAM-5 conventional logs and interpretation results.

4. Conclusion

The Nahr Umr Formation in Abu-Amood Oil Field comprises five distinct units. Unit 3 (clean sandstone) emerged as the primary hydrocarbon-bearing zone due to its high porosity and permeability. The oil-water contact is established at 3120 m, aligning with log interpretations. Challenges include unreliable data in Unit-2 due to borehole caving and uncertainties in permeability estimation from limited core samples. This study successfully fills a knowledge gap by providing the first detailed evaluation of the Nahr Umr Formation, highlighting its potential as a viable reservoir. Future work should focus on core recovery improvements and advanced modeling to reduce uncertainties, particularly in shaly and unstable zones. These findings have paved the way for optimized resource extraction strategies in the Abu-Amood oil field.

5. Conflict of Interest

The authors declare that they have no conflict of interest.

6. Funding Statement

This research received no external funding.

7. References

Abdullah, M.D., Al-Yasseri, A. and Nasser, M., 2018. Thermal Maturity History and Petroleum Generation Modeling for selected Oil fields Southern Iraq. Iraqi Journal of Science, 59(4C), 2267–2278. https://ijs.uobaghdad.edu.iq/index.php/eijs/article/view/546

Al-Baldawi, B.A., 2021. Evaluation of Petrophysical Properties Using Well Logs of Yamama Formation in Abu Amood Oil Field, Southern Iraq. Iraqi Geological Journal, 54(1E), 67–77. https://doi.org/10.46717/igj.54.1E.6Ms-2021-05-27

Bassiouni, Z., 1994. Theory, Measurement, and Interpretation of Well Logs. Society of Petroleum Engineers. https://doi.org/10.2118/9781555630560

Hameed, R.H. and Al-Jawad, M., 2020. Determine the Method of Optimum Completion of Reservoirs Mauddud, Nahr Umr, Zubair and Ratawi) in Abu Amood Oilfield with a Proposed Design of Superficial Installation. Solid State Technology, 63.

Hussain, A., Nasser, M. and Hassan, G., 2021. Evaluation of Mishrif Reservoir in Abu Amood Oil Field, Southern Iraq. Iraqi Journal of Science, 62, 4758–4768. https://doi.org/10.24996/ijs.2021.62.12.14

Khorshid, S.Z. and Khaleel, A.I., 2017a. Designing of 3D Seismic Survey And Data Processing of Abu Amood Oil Field Southern of Iraq. International Journal of Advanced Engineering Research and Science, 4(10), 115–124. https://doi.org/10.22161/ijaers.4.10.20

Khorshid, S.Z. and Khaleel, A.I., 2017b. Structural and Stratigraphic Study of the Nahr Umr Formation (Lower Cretaceous) Using 3D Seismic Survey in Abu Amood Oil Field, Southern Iraq. IRAQI JOURNAL OF SCIENCE, 58(4A). https://doi.org/10.24996/ijs.2017.58.4A.15

Lazim, S., Hamd-Allah, S. and Jawad, A.H., 2018. Permeability Estimation for Carbonate Reservoir (Case Study/ South Iraqi Field). Iraqi Journal of Chemical and Petroleum Engineering, 19(3), 41–45. https://doi.org/10.31699/IJCPE.2018.3.5

Mahdi, Z. and Farman, G., 2023a. 3D Geological Model for Zubair Reservoir in Abu-Amood Oil Field. Iraqi Geological Journal, 56(1B), 40–50. https://doi.org/10.46717/igj.56.1B.4ms-2023-2-12

Mahdi, Z. and Farman, G., 2023b. Estimation of Petrophysical Properties for Zubair Reservoir in Abu-Amood Oil Field. Iraqi Geological Journal, 56(1B), 32–39. https://doi.org/10.46717/igj.56.1B.3ms-2023-2-11

Matinkia, M., Hashami, R., Mehrad, M., Hajsaeedi, M. R. and Velayati, A., 2023. Prediction of permeability from well logs using a new hybrid machine learning algorithm. Petroleum, 9(1), 108–123. https://doi.org/10.1016/j.petlm.2022.03.003

Nasser, M., Al-Jawed, S. and Hassan, M., 2021. Geological Modeling for Yamama Formation in Abu Amood Oil Field. Iraqi Journal of Science, 58(2C), 1051–1068. https://ijs.uobaghdad.edu.iq/index.php/eijs/article/view/5940

Odeh, H.S., 2021. Yamama platform and the effect on the configuration of reservoir units in the Abu Amood field. Journal of Petroleum Research and Studies, 8(2), 1–12. https://doi.org/10.52716/jprs.v8i2.248

Iraqi National Journal of Earth Science, Vol. 26, No.04, 2026 (130-137)

Iraqi National Journal of Earth Science

www.earth.uomosul.edu.iq

تقييم مكمن تكوين نهر عمر في حقل أبو عامود النفطي، جنوبي العراق

محمد قاسم عبد طالب [1*] ، **محمد صالح الجواد [2]**

m.murad1708@coeng.uobaghdad.edu.iq mjawad@coeng.uobaghdad.edu.iq

[1] قسم علوم هندسة النفط، كلية الهندسة، جامعة الفارابي، بغداد، العراق.

[2] قسم علوم هندسة النفط، كلية الهندسة، جامعة بغداد، بغداد، العراق.

*الباحث المراسل.

تاريخ الاستلام: 27 أيار 2025 تاريخ المراجعة: 01 أيلول 2025 تاريخ القبول: 30 كانون الأول 2025

تاريخ النشر الالكتروني: 01 تشرين الأول 2026

الملخص

تقدم هذه الدراسة أول تقييم شامل لتكوين نهر عمر في حقل أبو عمود النفطي جنوبي العراق لسد فجوة بحثية حرجة. باستخدام بيانات السجلات البئرية، قُسِّم التكوين إلى خمس وحدات صخرية. شملت المنهجية تصحيح أعماق السجلات، وحساب حجم الطين، وتقدير المسامية والنفاذية باستخدام طرق نيوترون–كثافة وقياس سرعة الموجات. جرى تحديد تشبع الماء بمعادلة أرشي (للمناطق النظيفة) وإندونيسيا (للمناطق الطينية). أظهرت النتائج أن الوحدة الثالثة (حجر رملي نقي) هي المستودع الرئيس بمسامية عالية ونفاذية مرتفعة، ووجود نفط فوق تماس الماء–النفط عند عمق 3120 متراً. بينما أظهرت الوحدتان الأولى والخامسة مسامية منخفضة وتشبعاً مائياً عالياً، وعانت الوحدة الثانية من نقص البيانات بسبب انهيار جدار البئر. تُبرز الدراسة إمكانات نهر عمر كمستودع هيدروكربوني وتحديات المناطق الطينية. توفر النتائج أساساً لاستكشافه مستقبلاً، مع التأكيد على تحسين استعادة العينات والنمذجة المتقدمة لتقليل الشكوك في التكوينات غير المتجانسة.

الكلمات المفتاحية:

أبو عامود، تقييم تكوين، نهر عمر.

DOI: 10.33899/injes.v26i4.56157 *©Authors, 2026, College of Science, University of Mosul.*

This is an open-access article under the CC BY 4.0 license (http://creativecommons.org/licenses/by/4.0/)

Iraqi National Journal of Earth Science, Vol. 26, No. 04, 2026 (138-150)

Iraqi National Journal of Earth Science

www.earth.uomosul.edu.iq

Assessment of Heavy Metal Pollution and Sources Identification in Urban Soil Using Pollution Indices and Statistical Analysis, Mosul, Iraq

Ruqaya B. Mohammed [1*], **Hazim J. Mahmood** [2]

ruqaya.23evp11@student.uomosul.edu.iq hazimjm@uomosul.edu.iq

[1] *Department of Environmental Science, College of Environmental Sciences, University of Mosul, Mosul, Iraq.*
[2] *Department of Environmental Technologies, College of Environmental Sciences, University of Mosul, Mosul, Iraq.*
** Correspondence author.*

Received: 24 May 2025 Received in revised form: 01 July 2025 Accepted: 03 August 2025
Available online: 01 October 2026

Abstract

This study aims to assess heavy metal pollution and identify its sources in the surface soil of Mosul's left side. Thirty-one composite soil samples were collected using a regular grid distributed over the study area with 2 × 2 km dimensions. Chemical analysis was conducted using the X-ray fluorescence (XRF) technique to determine the concentration of trace elements (V, Nb, Zr, Y, Th, Sn, Cr, Sb, As, Mn, Mo, Co, Cu, Zn, Ni, Pb) and major oxides (MgO, Al_2O_3, SiO_2, K_2O, TiO_2, Fe_2O_3). The calculations of soil pollution indices (contamination factor, degree of contamination, geo-accumulation index, Nemerow pollution index, enrichment factor) indicate that most study samples are contaminated with heavy metals. Principal component analysis shows the influence of geochemical processes such as chemical weathering and surface adsorption, as well as sedimentary processes like river deposition, in redistributing these elements in the environment. Meanwhile, it appears that the heavy metals (Cu, Zn, Pb, Sn, Sb, Mo) were affected by human activities in the city, particularly since these elements are clear indicators of pollution resulting from industrial waste such as batteries, metal coatings, and electronic waste, as well as the impact of military activities during the city's liberation from terrorist gangs. This is supported by the high concentrations of these elements in the industrial area. This study highlights the interaction of natural geological and geochemical factors with human factors in influencing the concentrations of heavy metals in the surface soil of Mosul City. The study also emphasizes the urgent need to take immediate measures to reduce soil pollution in the city, particularly after pollution indices in some areas have recorded high levels of contamination.

Keywords:

Heavy Metals, Urban Soil, Soil Pollution, Pollution Indices.

DOI: 10.33899/injes.v26i4.56158, *©Authors, 2026, College of Science, University of Mosul.*
This is an open-access article under the CC BY 4.0 license (http://creativecommons.org/licenses/by/4.0/).

==========

1. Introduction

Pollution is an environmental problem that generally affects life on planet Earth, endangering the lives of living organisms. Various environmental components have recently suffered increasing degradation coinciding with industrial growth and urban expansion. Soil is one of the most important environmental components experiencing increasing degradation, especially since soil often receives pollutants from all other environmental components, leading to their accumulation (Kharkan et al., 2019; Ranjani et al., 2021). Heavy metals also pose significant health risks to humans, especially since they can be transmitted through the food chain and thus accumulate in large quantities in the bodies of living organisms, even if they are present in the environment at low concentrations (Ibraheem et al., 2024). The sources of heavy metal entry into soil can be identified through two main sources: geological sources resulting from the natural concentration of these elements in soil, through weathering and erosion processes that occur on various types of rocks, minerals, non-metallic deposits, and ores. Anthropogenic sources include those caused by human activity such as industry, agriculture, transportation, urban waste, and occasional military acts. Uncontrolled heavy metal leakage into the land and rivers is a significant

environmental problem. They are hazardous and cannot be broken down into non-toxic forms, causing a global health issue (Al-Khafaji and Jaafar, 2023).

Assessing the level of heavy element pollution in urban soil can provide us with a thorough picture of the soil's condition as well as the magnitude of the potential health risk posed by exposure to these elements. Recently, certain pollution indices have been implemented, including the Geoaccumulation Factor (I_{geo}), the Enrichment Factor (EF), the Contamination Factor (CF), and the Improved Nemerow Index (I_N), which are effective tools for assessing and monitoring soil pollution levels. This has become essential in the field of urban management and planning and the development of sustainable policies to protect the urban environment from pollution (Kazem, 2017). In this context, there is an urgent need to study the surface soil of Mosul, the largest city in northern Iraq. This is especially true since the city has witnessed rapid events in recent years, including its exposure to intensive military operations during the liberation phase from terrorist groups that controlled the city between 2014 and 2017, followed by military operations and widespread destruction, and then rapid reconstruction and urban expansion since 2017. The city has received several environmental studies, including studies of soil pollution. However, these studies followed a selective sampling approach, focusing on collecting samples from industrial and commercial areas and roadsides, and did not delve deeply into identifying the sources of these elements (Al-Sheraefy et al., 2023; Bk et al., 2024a; Bk et al., 2024b; Ibraheem et al., 2024). Accordingly, the current study aims to fill this gap by conducting a comprehensive assessment of the level of soil pollution. The samples in this study were collected along a regular grid on the left side of the city, and statistical techniques were used to identify the most important sources of heavy metals in the soil and distinguish between natural sources and non-natural sources represented by human influence. This contributes to understanding the dynamics of urban soil pollution in the study area and enables appropriate decision-making and action.

2. Materials and Methods

A. Study area

Mosul is located in northern Iraq between longitudes 43°02′59.65" and 43°13′57.89" east, and latitudes 36°17′23.86" and 36°25′45.04" north. It is distinguished by its location on the banks of the Tigris River, which divides it into two parts: the western part, also known as the right side, and the eastern part, known as the left side. The study area is limited to the eastern part (left side) of the city (Fig. 1). The study area falls within an arid to semi-arid climate with hot summers and cold winters. Summer temperatures exceed 45°C, while winter temperatures drop below zero (Al-Ansari, 2021). Therefore, Iraq is affected by its location between the Arabian desert regions' dry subtropical climate and the Arabian Gulf's humid subtropical climate (Hameed and Khalaf, 2024). Geologically, the study area is covered by Miocene and Recent deposits. The oldest deposits are of the Fatha Formation (Middle Miocene), composed of mudstone, marl, limestone, gypsum, and anhydrite. The younger is the Injana Formation (Upper Miocene), composed of mudstone, siltstone, and sandstone, and covered by Quaternary deposits consisting of conglomerates, sand, clay, and gravel, followed by recent clastic deposits derived from the erosion of highlands along with river sediments (Al-Fahaam et al., 2023).

B. Field and laboratory work

Samples were collected on a regular grid measuring 2 x 2 km from 31 locations. Four samples were taken at each location and thoroughly combined to produce a composite sample for each site. Samples were collected at a depth of 0-15 cm. They were stored in plastic bags with coordinates and field notes.

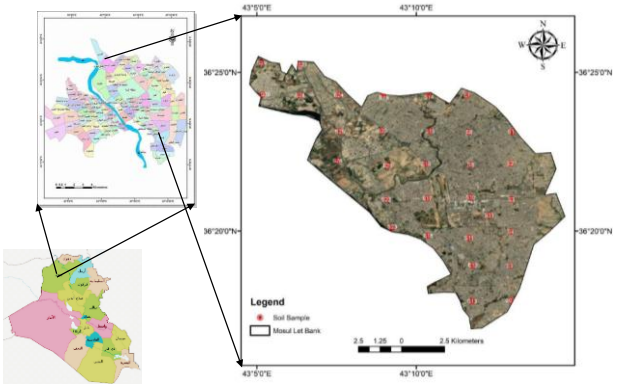


Fig. 1. Map of the study area showing the sampling locations.

Fig. 1: Map of the study area showing the sampling locations.

were recorded and transported to the laboratory. Then, the soil samples were prepared for laboratory analysis by air-drying. Once dried, the samples were crushed with a wooden hammer, ensuring not to turn the soil into a fine powder, and large stones were removed by hand. Next, the soil was sieved using a 2 mm sieve. Then, the sample was divided using a cone and square method, selecting a portion to be ground in a ceramic mortar, and subsequently sieved using a 200-mesh sieve to obtain a uniform powder suitable for chemical analysis. The element concentrations were determined using Spectro XEPOS X-Ray Fluorescence Spectroscopy (German, 2010) in the Iraqi-German Lab at the University of Baghdad. To achieve high analysis accuracy, the device performs an analysis of a standard reference sample. If the analysis matches the standard reference data, the device will move to a stage where the operator can enter samples into the device for analysis. However, if the analysis of the standard sample does not match, the device will not allow the entry of new samples and will instead move the operator to the maintenance steps.

C. Statistical analysis

The chemical data of the study samples are analyzed using SPSS version 20. Principal Component Analysis (PCA) is performed to determine potential causes or sources of heavy metal concentrations in soil. PCA is a popular statistical method for processing raw data to extract fewer and more usable variables for evaluating the main factors influencing element concentrations (Belkhiri et al., 2018; Dhannoun and Mahmood, 2019; Alaarajy et al., 2023).

D. Pollution indices

The following pollution indices are used to assess heavy metal soil contamination in the study area: Contamination Factor (CF), Contamination Degree (Cdeg), Geoaccumulation Index (I_{geo}), Improved Nemerow Index (I_N), and Enrichment Factor (EF).

1. Contamination factor (CF) and Contamination degree (Cdeg)

This factor is used to assess the extent of soil contamination with heavy metals and is calculated according to the following equation:

$$CF = \frac{(Cn)sample}{(Bn)background} \dots\dots\dots (1)$$

Where: *Cn* is the concentration of heavy metals in the soil of the study area, and *Bn* is the concentration of heavy metals in the Earth's crust according to (Kabata-Pendias, 2011).

Table 1: Classification of (CF) by Hakanson (1980).

Pollution factor	Pollution level classification
CF< 1	low pollution
$1 < CF \leq 3$	moderate pollution
$3 < CF \leq 6$	heavy pollution
CF> 6	very high pollution

The contamination degree (Cdeg) is used to determine the degree of soil pollution with heavy metals, which represents the sum of the contamination factors for the studied heavy metals (Hakanson, 1980), as in the following equation:

$$Cdeg = CF1 + CF2 + \dots\dots\dots + CFn \dots\dots\dots (2)$$

Where: *Cdeg* is the contamination degree, *CF* is the Contamination factor, and n is the number of heavy metals studied:

Table 2: Classification of (Cdeg) according to Hakanson (1980).

Pollution degree factor	Pollution level classification
$C_{deg} < 8$	low pollution
$8 \leq C_{deg} < 16$	moderate pollution
$16 \leq C_{deg} < 32$	heavy pollution
$C_{deg} \geq 32$	very high pollution

2. Geo-accumulation Index (Igeo)

The geo-accumulation Index (I_{geo}) is calculated to determine the extent of soil contamination with heavy metals. It was developed by Muller (1969) and is based on the following equation:

$$I_{geo} = log_2 \left[\frac{Cn}{1.5 * Bn}\right] \dots\dots\dots (3)$$

Where: *Cn* is the measured metal concentration, *Bn* is the concentration of heavy metal in the reference sample, and 1.5 is a constant value used to compensate for natural variations in the geochemical background.

Table 3: Classifications of (Igeo) according to Muller (1969).

Ground accumulation coefficient	soil quality
Igeo≤ 0	Uncontaminated
$0 < Igeo < 1$	Unpolluted to moderately polluted
$1 < Igeo < 2$	Moderately polluted
$2 < Igeo < 3$	Moderately to highly polluted
$3 < Igeo < 4$	highly polluted
$4 < Igeo < 5$	Highly to very highly polluted
Igeo≥ 5	Very highly polluted

3. Improved Nemerow Index (I_N)

It describes the state of soil pollution with heavy metals; it is calculated based on Guan et al. (2014) according to the following equation:

$$I_N = \sqrt[2]{\frac{(Igeo\ max)^2 + (Igeo\ average)^2}{2}} \ldots\ldots\ldots (4)$$

Where: $Igeo\ max$ is the maximum value of the Geoaccumulation index for the studied elements, and $Igeo\ average$ is the average concentration of the Geoaccumulation index for the elements.

Table 4: Classification of (I_N) according to Guan et al. (2014).

Nimro Laboratories	soil quality
$0 < I_N \leq 0.5$	Uncontaminated
$0.5 < I_N \leq 1$	Unpolluted to moderately polluted
$1 < I_N \leq 2$	somewhat polluted
$2 < I_N \leq 3$	Moderate to severe pollution
$3 < I_N \leq 4$	heavily polluted
$4 < I_N \leq 5$	heavily polluted
$I_N \geq 5$	highly polluted

4. Enrichment factor (EF)

This factor is used to assess the extent of element accumulation in the soil compared to the source rocks and aims to distinguish whether the sources of the element are of natural origin or human activities, and is calculated according to the following equation:

$$\mathbf{EF} = \frac{(Cn/Fe)samples}{(Bn/Fe)background} \ldots\ldots\ldots (5)$$

Where: (*Cn/Fe*) is the heavy metal concentration to iron concentration in the study sample, and (*Bn/Fe*) is the heavy metal concentration to iron concentration in the reference sample.

Iron is used as a reference element because it is a geochemically stable element, naturally abundant in soil, minimally influenced by anthropogenic factors, and often associated with heavy metals in soil (Sinex and Helz, 1981). If the EF value is <1, it indicates that the element comes from natural sources, while if EF>1, it suggests that there is enrichment of the element, which indicates that the element comes from human activities (Jiang et al., 2019).

Table 5: Classification of EF according to (Mmolawa et al., 2011; Barbieri et al., 2015).

Enrichment factor values	Enrichment ratio
$EF < 2$	Low enrichment
$2 < EF \leq 5$	Moderate or medium enrichment
$5 < EF \leq 20$	Great enrichment
$20 < EF \leq 40$	Very high enrichment
$EF > 40$	Very high enrichment

3. Results and Discussion

Table (6) includes the concentrations of the main oxides (Al_2O_3, Fe_2O_3, K_2O, SiO_2, MgO, TiO_2). Al_2O_3, Fe_2O_3, and MgO in the studied samples are usually the oxides most associated with clay minerals, while SiO_2 is a major component of sand and clay minerals. Potassium oxide is associated with minerals such as mica, while titanium oxide is associated with ilmenite minerals (Sandler et al., 2015). The trace element contents of (V, Nb, Zr, Y, Th, Sn, Cr, Sb, As, Mn, Mo, Co, Cu, Zn, Ni, Pb) are listed in Table (7).

These elements are characterized by their low natural concentrations in soil, but their importance often exceeds that of major elements from an environmental and geochemical perspective. Some elements, especially those known environmentally as heavy metals, have a significant environmental impact due to their toxicity and accumulation in the biosphere. Others, especially some rare elements (Y, Nb, Th), may be of great geochemical interest regarding element sources in soil (Kabata-Pendias, 2000).

The results indicate elevated concentrations of certain heavy elements in the study area, particularly the elements (Ni, Zn, Cu, Co, Mo, Mn, Cr) which exhibited concentrations surpassing the global average for soil. Additionally, it is observed that the concentrations in the industrial area samples are higher in comparison to the other samples for zinc and copper. This increase may be attributed to industrial waste (Alengebawy et al., 2021) resulting from the indiscriminate disposal of electronic devices and other sources (Kumar et al., 2019; Gebreyesus, 2014; Hasnine et al., 2017).

Table 6: Concentration of the major oxides %.

Sample No.	Fe_2O_3	TiO_2	K_2O	SiO_2	Al_2O_3	MgO
S1	5.19	0.80	1.20	34.36	7.91	3.42
S2	6.50	1.00	1.31	40.34	9.17	5.37
S3	6.12	0.89	1.30	36.84	8.31	5.18
S4	6.23	0.92	1.10	36.23	8.60	5.78
S5	6.62	0.87	1.10	35.97	8.87	4.61
S6	6.59	0.91	1.32	38.05	9.13	5.05
S7	5.64	0.81	0.89	30.64	7.47	3.96

S8	6.33	0.97	1.10	35.79	8.56	5.54
S9	6.86	1.25	1.00	35.50	8.33	4.77
S10	6.10	0.86	0.97	33.18	8.12	4.12
S11	6.77	0.93	1.18	39.22	9.53	5.19
S12	6.48	0.94	1.13	37.35	9.04	4.82
S13	7.18	0.80	1.22	39.34	9.69	5.09
S14	6.87	0.85	1.34	39.91	9.72	6.01
S15	6.57	0.97	1.03	35.47	8.50	4.93
S16	6.37	1.02	1.07	36.15	8.65	5.05
S17	6.93	0.90	1.14	37.37	9.30	4.74
S18	6.38	0.89	1.17	37.62	9.12	5.59
S19	6.60	0.87	1.09	36.23	8.92	4.61
S20	6.37	0.90	1.98	37.44	10.74	4.23
S21	5.83	0.88	1.75	38.00	9.24	4.07
S22	6.03	0.85	1.71	36.33	10.04	4.30
S23	5.23	0.72	1.48	39.77	7.88	3.45
S24	5.42	0.78	1.33	36.34	8.91	3.97
S25	5.13	0.78	1.43	42.52	7.87	4.43
S26	4.87	0.79	1.34	38.45	8.13	4.69
S27	5.35	0.84	1.39	37.14	8.69	4.22
S28	6.50	1.00	1.31	39.34	9.17	5.37
S29	5.82	0.80	1.67	38.58	9.71	4.02
S30	5.26	0.80	1.57	38.18	9.13	4.03
S31	4.93	0.76	0.93	30.46	6.50	2.82
Avg	6.07	0.88	1.27	36.86	8.76	4.59
Max	7.18	1.25	1.98	42.52	10.74	6.01
Min	4.87	0.69	0.89	30.46	6.50	2.82
Av . Crust	5.6	0.64	2.8	66.6	15.4	2.5

Av. Crust: Average Crust given by Rudnick and Gao (2003)

The elevated concentrations of the other elements could be a consequence of human activities such as waste burning and the operation of electrical generators, along with heavy traffic (Wuana and Okieimen, 2011; Arao et al., 2010). Natural processes also play a role in contributing to the high concentrations of some heavy elements via their spread through natural weathering processes (Bradl, 2005). The average concentration of the elements (Sb-Pb) did not exceed the global soil average across all samples in the study area, except for the industrial area sample, where it surpassed the global soil average. This may be linked to industrial activities, including industrial workshops, battery repair facilities, and battery sales (Ferretti et al., 1995; Ali et al., 2019; Hanif et al., 2025).

Table 7: The concentration of trace elements in ppm.

S. No.	Pb	Ni	Zn	Cu	Co	Mo	Mn	As	Sb	Cr	Sn	Th	Y	Zr	Nb	V
S1	24.0	140.8	143.0	50.8	ND	14.5	733.9	3.7	ND	219.6	0.3	7.0	19.2	156.9	7.5	50.4
S2	10.1	205.5	83.9	36.7	22.3	9.3	909.4	4.0	ND	395.3	ND	4.9	19.8	140.0	7.1	47.6
S3	11.0	199.6	84.1	36.0	14.3	17.5	898.5	3.6	ND	319.7	1.3	4.2	18.2	130.2	6.0	37.5
S4	10.2	197.1	77.3	35.1	12.1	12.4	842.8	4.1	ND	296.3	ND	4.4	18.3	125.9	6.7	61.6
S5	12.3	217.9	84.2	41.4	29.6	24.3	944.2	4.8	ND	269.2	ND	5.6	20.6	130.7	7.6	74.8
S6	11.3	218.8	84.5	41.2	19.2	17.0	925.6	4.6	ND	296.0	ND	5.3	20.6	131.7	7.3	66.9
S7	9.1	183.2	68.6	34.1	ND	24.7	804.0	3.9	ND	231.8	ND	4.7	17.9	105.3	4.9	33.6
S8	11.3	203.4	77.1	36.7	7.9	12.2	859.0	4.1	ND	352.0	ND	4.6	19.5	132.1	6.6	58.5
S9	10.1	196.8	79.7	31.9	19.5	23.8	889.2	4.1	ND	821.7	ND	3.8	21.2	195.3	7.4	76.2
S10	9.4	204.1	76.3	37.2	ND	12.9	919.4	4.5	ND	282.6	0.3	4.8	18.5	116.7	6.3	58.8
S11	11.0	243.8	86.3	44.7	22.9	46.8	904.0	5.0	ND	254.0	ND	5.0	20.6	117.3	7.1	60.8
S12	9.8	253.7	83.2	42.0	30.7	169.3	1013.2	5.2	ND	282.8	ND	4.6	19.8	116.4	7.2	60.2
S13	13.2	260.4	100.7	50.6	27.0	36.3	1079.0	5.5	ND	230.4	ND	5.8	21.1	113.9	6.8	61.1
S14	13.7	237.2	96.7	44.7	20.1	17.6	960.5	5.0	ND	230.7	0.3	5.4	19.9	122.1	6.9	69.5
S15	10.0	219.4	78.3	38.5	34.4	56.7	1024.8	5.5	ND	429.5	1.1	5.1	19.9	147.9	7.7	62.5
S16	9.7	198.4	73.4	34.2	12.3	34.5	865.2	4.3	ND	427.2	0.8	4.1	19.3	134.0	6.8	68.1
S17	10.0	221.8	86.5	44.7	28.5	17.8	907.8	5.7	ND	239.8	2.8	5.7	21.1	129.9	6.7	66.1
S18	11.4	211.3	83.6	40.2	17.5	13.9	917.9	4.4	ND	293.7	ND	4.8	19.6	128.4	6.4	59.4
S19	10.9	219.9	82.6	41.1	22.6	16.5	974.4	5.1	0.2	257.9	3.1	4.9	19.5	124.1	6.8	57.7
S20	14.8	166.9	104.9	40.3	15.7	25.6	893.1	4.4	ND	208.2	ND	7.6	23.9	168.1	8.7	60.5
S21	13.1	150.8	93.8	38.4	12.6	14.5	763.0	4.6	ND	233.0	ND	7.7	22.1	165.5	8.2	56.3
S22	13.4	169.3	92.6	35.0	18.7	11.6	791.6	4.2	ND	244.1	ND	6.3	21.1	149.9	8.6	54.6
S23	12.0	140.2	79.0	33.1	14.5	8.1	624.2	3.7	ND	174.2	ND	6.6	18.4	127.5	7.5	48.2
S24	11.6	143.6	77.9	34.7	14.6	18.0	664.4	4.8	ND	278.3	ND	6.8	19.9	147.3	8.0	57.1
S25	12.3	138.9	80.8	35.0	ND	12.6	665.4	3.9	ND	240.4	ND	5.8	19.1	150.8	8.0	54.6
S26	10.6	133.7	71.7	30.8	14.3	17.5	669.6	3.7	ND	272.9	ND	6.4	18.9	151.5	7.7	46.5

S27	11.4	138.6	78.7	39.1	13.1	7.9	695.0	4.4	ND	417.6	ND	6.6	21.1	176.6	7.3	40.9
S28	10.1	205.5	83.9	36.7	22.3	9.3	909.4	4.0	ND	395.3	ND	5.7	19.8	140.0	7.1	47.6
S29	12.3	158.8	93.1	36.4	15.0	18.9	755.7	4.4	ND	168.3	1.4	7.7	21.1	141.0	8.0	53.2
S30	11.4	140.7	79.1	33.2	14.5	24.6	689.4	4.1	ND	322.0	ND	5.1	19.9	157.0	7.5	56.0
S31	273.2	126.0	340.0	135.9	ND	13.9	665.5	3.8	3.7	292.2	13.2	7.7	17.8	175.8	6.9	40.3
Avg	19.9	188.7	93.1	41.3	16.4	24.2	843.8	4.4	0.3	302.5	0.8	5.6	19.9	139.7	7.2	55.8
Max	273.2	260.4	340.0	135.9	34.4	169.3	1079.0	5.7	3.7	821.7	13.2	7.7	23.9	195.3	8.7	76.2
Min	9.1	126.0	68.6	30.8	7.9	7.9	624.2	3.2	0.2	168.3	0.3	3.8	17.7	105.3	4.9	33.6
Av.Crust	15	20	70	55	10	1.5	900	1.8	0.2	100	2.5	7.2	33	165	20	135
K-P(2011)	27	29	70	38.5	11.3	1.1	488	6.83	0.67	59.5	2.5	9.2	23	267	12	129

Av. Crust: Average Crust (Kabata-Pendias, 2011)

K-P (2011): Kabata-Pendias (World-Soil Average)

ND= Not Detected

A. Sources of heavy metals

The chemical data of the soil samples are analyzed statistically using SPSS version 20, applying principal components analysis (PCA) to identify the potential factors or sources affecting heavy metal concentrations. Components with eigenvalues greater than one are selected (Fig. 2). The PCA results reveal five main components that influence the concentrations of trace elements in the surface soil of the study area. These components account for over 87% of the variance.

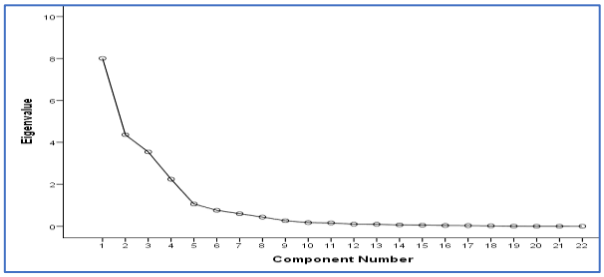


Fig. 2: Scree plot of the eigenvalues showing that the data have five major components with eigenvalues greater than 1.

Where the first component represents 28.52% of the variance, the second component represents 25%, the third 8.622%, the fourth 11.2%, and the fifth 5.99% of the total variance observed (Table 8).

The first component: The first component represents transition metals and iron oxides and comprises the elements Mn, Ni, Fe_2O_3, MgO, As, Co, and V. This reflects the influence of geochemical processes such as chemical weathering and surface adsorption, as well as the role of sedimentary processes, such as river sedimentation, in redistributing these elements into the environment. The close association between Fe_2O_3 and MgO reflects the presence of ferromagnesian minerals, such as pyroxene, amphibole, and biotite, which are major components of mafic igneous rocks (White, 2001) found in the upper Tigris River basin and abundant in river sediments in Mosul (Mahmood, 2021), indicating that these rocks contribute as a major source of these elements. Furthermore, the presence of Ni, Co, and V in this component suggests the potential presence of these elements within the crystal structure of ferromagnesian minerals, given their geochemical behavior similar to that of iron and magnesium. When these minerals are exposed to weathering processes, these elements are released into the environment, where they may remain in the form of secondary minerals, or these elements, in addition to arsenic, may undergo an adsorption process on the surfaces of iron and manganese oxides (White, 2001), which affects their geochemical availability and transfer to soil and groundwater.

The second component: The second component represents one of the main sources of surface soil pollution in Mosul City, reflecting industrial and military impacts on the environment. Heavy metals such as copper (Cu), zinc (Zn), lead (Pb), tin (Sn), and antimony (Sb) are clear indicators of pollution resulting from industrial waste such as batteries, metallic coatings, and electronic waste (Hou et al., 2025), in addition to the impact of military activities during the period of the city's liberation from terrorist gangs. This is supported by the fact that this component is not associated with the main oxides (Al_2O_3, SiO_2, MgO, Fe_2O_3, K_2O) (Table 8).

The third component is associated with the elements Y, Th, Nb, Al_2O_3, K_2O, and SiO_2. The association of this component with the oxides K_2O, Al_2O_3, and SiO_2 shows a strong association with potassium-rich clay minerals such as illite, indicating a natural source for these elements. The presence of some trace elements such as Y, Nb, and Th with Al_2O_3 and SiO_2 suggests that these elements may be associated with either clay minerals or secondary oxides formed as a result of chemical weathering processes, supporting the hypothesis of a natural source for this component.

From a geochemical perspective, this component reflects a natural geological source resulting from the long weathering of feldspar- and silicate-rich igneous rocks, which are found in the upper Tigris Basin areas (Westaway et al., 2009).

The fourth component: This component appears to indicate the presence of resistant minerals such as chromite ($FeCr_2O_4$), rutile (TiO_2), and zircon ($ZrSiO_4$), as the elements Cr, TiO_2 and Zr are observed to be present in this component. Geochemically, this indicates a natural geological source represented by mafic rocks rich in titanium and chromium (Fitzpatrick and Chittleborough, 2002), which were transported by the Tigris River after the source rocks were exposed to chemical and physical weathering. These resistant minerals are common in Tigris River sediments within the study area (Mahmood, 2021).

The fifth component: Related to molybdenum, it is a chemical pollutant associated with molybdenum (Mo). Elevated concentrations of this element indicate the effects of industrial and urban sources. Mo is primarily used to manufacture stainless steel and is also a component of industrial oils and greases. Elevated Mo concentrations may result from industrial discharges or recent metal waste (Geng et al., 2014). It may also be associated with agricultural activities, given its use in some chemical fertilizers. This component reflects the impact of human activities on the environment.

Table 8: Varimax-rotated principal component analysis of the soil samples

Variables	Component				
	1	2	3	4	5
Pb	-0.184	0.97	-0.077	0.007	-0.033
Ni	0.896	-0.172	-0.315	-0.024	0.152
Zn	-0.145	0.971	0.029	-0.03	-0.035
Cu	-0.009	0.986	-0.05	-0.07	0.007
Co	0.713	-0.098	0.183	0.048	0.445
Mo	0.305	-0.048	-0.084	-0.005	0.805
Mn	0.92	-0.087	-0.111	0.11	0.128
As	0.732	0.007	0.251	-0.095	0.413
Sb	-0.17	0.966	-0.1	0.016	-0.029
Cr	0.093	-0.031	-0.124	0.964	0.008
Sn	-0.124	0.937	-0.162	-0.049	0.006
Th	-0.389	0.384	0.686	-0.365	0.013
Y	0.348	0.115-	0.83	0.171	0.082
Zr	-0.421	0.309	0.544	0.623	-0.042
Nb	-0.143	-0.018	0.899	0.123	0.17
V	0.616	-0.134	0.278	0.346	0.159
Fe_2O_3	0.947	-0.144	0.005	0.196	-0.004
TiO_2	0.468	-0.138	-0.02	0.827	-0.026
K_2O	-0.172	-0.216	0.862	-0.209	-0.186
SiO2	0.286	-0.399	0.533	-0.088	-0.233
AL_2O_3	0.573	-0.339	0.66	-0.098	-0.067
MgO	0.731	-0.381	-0.123	0.188	-0.32
Eigen values	8.005	4.364	3.542	2.243	1.058
Variance %	36.385	19.835	16.099	10.193	4.81
Cumulative %	36.385	56.22	72.319	82.512	87.323

B. Pollution Assessment

1. Contamination Factor and Contamination Degree

Pollution factor calculations for the current study samples show significant variations in contamination values from one element to another, as well as clear variations between different locations. The highest rates are for molybdenum, antimony, and nickel, with contamination factor values above 9 for these elements, indicating very high contamination for each in general within the study area. Meanwhile, the contamination factor values for the remaining elements (Cu, Mn, Sn, As, Co, Cr, Pb) are less than or equal to 3, indicating moderate to low contamination (Table 9). The heavy elements can be ranked according to the contamination factor for the study area samples as shown in Fig. 3 as follows:

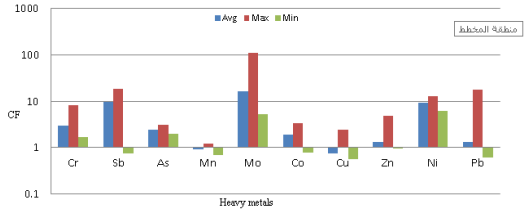


Fig. 3: Upper, lower and average limits of the contamination factor in the studied area

$$\boldsymbol{Mo > Ni > As > Co > Sb = pb = Zn > Cu = Mn}$$

The results of the contamination degree for the study samples range between (138.04-20.90) (Table 9 and Fig. 4), indicating that the study area falls within the highly to very highly polluted category (Hakanson, 1980). Twenty-three samples from the study area had a high degree of pollution, while samples (S31, S16, S13, S15, S12, S11, S9, and S5) in the industrial area, Al-Muthanna neighborhood, Al-Wahda neighborhood, Al-Bakr neighborhood, Jdeidat Al-Mufti, Al-Mithaq, Al-Salam and Al-Barid all fall within the very high pollution category. The reason for the increased pollution level in the industrial area is due to industrial waste, which leads to an increase in the concentration of heavy metals in the soil. As for the remaining sites, the reason for the increase may

be that these sites are commercial and have high traffic density, in addition to the recent military operations and the weapons remnants left behind, which play a major role in increasing the concentrations of heavy metals.

Table 9: Results of calculating the Contamination factor (CF) and the degree of contamination (Cdeg) for each element.

S. No.	Pb	Ni	Zn	Cu	Co	Mo	Mn	As	Sb	Cr	Cdeg
S1	1.597	7.041	2.043	0.924	NA	9.667	0.82	2.062	NA	2.20	26.35
S2	0.675	10.274	1.198	0.668	2.226	6.200	1.01	2.209	NA	3.95	28.41
S3	0.736	9.980	1.202	0.655	1.431	11.667	1.00	1.978	NA	3.20	31.84
S4	0.681	9.854	1.104	0.639	1.211	8.267	0.94	2.272	NA	2.96	27.93
S5	0.817	10.895	1.203	0.752	2.957	16.200	1.05	2.693	NA	2.69	39.26
S6	0.755	10.938	1.207	0.749	1.919	11.333	1.03	2.567	NA	2.96	33.46
S7	0.607	9.162	0.980	0.620	NA	16.467	0.89	2.167	NA	2.32	33.21
S8	0.755	10.168	1.102	0.668	0.786	8.133	0.95	2.272	NA	3.52	28.36
S9	0.675	9.838	1.139	0.580	1.950	15.867	0.99	2.293	NA	8.22	41.55
S10	0.625	10.204	1.090	0.677	NA	8.600	1.02	2.504	NA	2.83	27.55
S11	0.730	12.188	1.233	0.813	2.289	31.200	1.00	2.777	NA	2.54	54.77
S12	0.656	12.683	1.189	0.764	3.067	112.867	1.13	2.861	NA	2.83	138.04
S13	0.879	13.021	1.438	0.921	2.698	24.200	1.20	3.030	NA	2.30	49.69
S14	0.916	11.858	1.381	0.813	2.013	11.733	1.07	2.777	NA	2.31	34.87
S15	0.668	10.970	1.119	0.700	3.437	37.800	1.14	3.072	NA	4.29	63.20
S16	0.650	9.921	1.048	0.622	1.227	23.000	0.96	2.398	NA	4.27	44.10
S17	0.668	11.088	1.236	0.812	2.855	11.867	1.01	3.156	NA	2.40	35.09
S18	0.761	10.565	1.195	0.731	1.746	9.267	1.02	2.419	NA	2.94	30.64
S19	0.724	10.997	1.180	0.748	2.257	11.000	1.08	2.819	0.753	2.58	34.14
S20	0.984	8.345	1.499	0.732	1.573	17.067	0.99	2.419	NA	2.08	35.69
S21	0.873	7.540	1.339	0.699	1.258	9.667	0.85	2.567	NA	2.33	27.12
S22	0.891	8.463	1.323	0.636	1.872	7.733	0.88	2.314	NA	2.44	26.55
S23	0.798	7.009	1.128	0.601	1.447	5.400	0.69	2.083	NA	1.74	20.90
S24	0.774	7.178	1.112	0.630	1.463	12.000	0.74	2.693	NA	2.78	29.37
S25	0.823	6.942	1.155	0.636	NA	8.400	0.74	2.167	NA	2.40	23.27
S26	0.706	6.683	1.025	0.559	1.431	11.667	0.74	2.083	NA	2.73	27.63
S27	0.761	6.931	1.124	0.710	1.306	5.267	0.77	2.462	NA	4.18	23.51
S28	0.675	10.274	1.198	0.668	2.226	6.200	1.01	2.209	NA	3.95	28.41
S29	0.817	7.940	1.330	0.662	1.502	12.600	0.84	2.462	NA	1.68	29.84
S30	0.761	7.033	1.131	0.603	1.447	16.400	0.77	2.251	NA	3.22	33.61
S31	18.214	6.302	4.857	2.471	NA	9.267	0.74	2.104	18.442	2.92	65.32
Avg	1.324	9.437	1.329	0.752	1.907	16.165	0.94	2.435	9.598	3.02	37.86
Max	18.214	13.021	4.857	2.471	3.437	112.867	1.20	3.156	18.442	8.22	138.04
Min	0.607	6.302	0.980	0.559	0.786	5.267	0.69	1.767	0.753	1.68	20.90

NA= Not Available

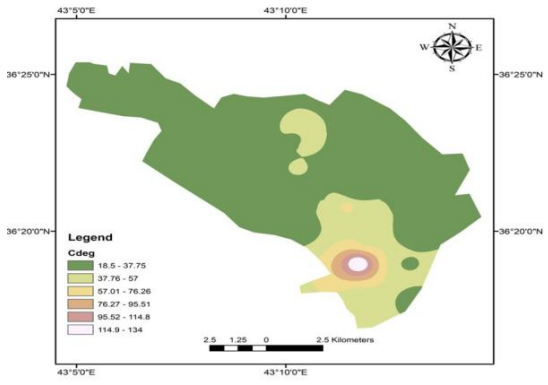


Fig. 4: Spatial distribution of pollution degree (Cdeg) in the surface soil of the study area

2. Geo-accumulation Index (I_{geo})

Calculating the geoaccumulation index (I_{geo}) for the current study samples (Table 10) revealed that the I_{geo} for all studied samples fall within the uncontaminated category for lead, zinc, copper, manganese, chromium, and antimony. Only the industrial area sample is severely contaminated with lead and antimony (Muller, 1969). While the nickel and molybdenum contamination levels in all study area samples range from moderate to severe, the arsenic and cobalt values fall within the moderately contaminated soil classification. Accordingly, the heavy metals can be ranked

according to the I_{geo} for the study area samples shown in Fig. 5 as follows:

Mo > Ni > Sb > Cr > As > Co > Zn > Mn > pb > Cu

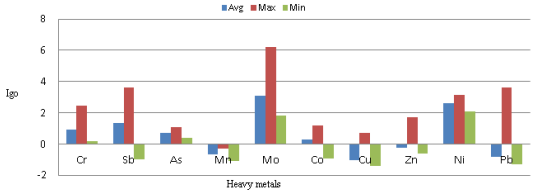


Fig. 5: Upper, lower and average limits of (I_{geo}) in the studied area

Table 10: Results of calculating the Geo-accumulation Index and the Improved Nemerow Index for each element.

S. No.	Pb	Ni	Zn	Cu	Co	Mo	Mn	As	Sb	Cr	I_N
S1	0.090	2.231	0.446	-0.699	NA	2.688	-0.879	0.459	NA	0.550	1.949
S2	-1.153	2.776	-0.324	-1.167	0.569	2.047	-0.570	0.558	NA	1.398	1.990
S3	-1.026	2.734	-0.320	-1.195	-0.068	2.959	-0.587	0.399	NA	1.092	2.116
S4	-1.140	2.716	-0.442	-1.231	-0.309	2.462	-0.680	0.599	NA	0.982	1.935
S5	-0.877	2.861	-0.319	-0.995	0.979	3.433	-0.516	0.844	NA	0.844	2.477
S6	-0.990	2.866	-0.313	-1.001	0.355	2.918	-0.544	0.775	NA	0.981	2.101
S7	-1.306	2.611	-0.614	-1.274	NA	3.457	-0.748	0.531	NA	0.628	2.462
S8	-0.990	2.761	-0.445	-1.167	-0.931	2.439	-0.652	0.599	NA	1.231	1.965
S9	-1.153	2.713	-0.398	-1.372	0.379	3.403	-0.602	0.612	NA	2.454	2.453
S10	-1.263	2.766	-0.460	-1.148	NA	2.519	-0.554	0.739	NA	0.914	1.980
S11	-1.038	3.022	-0.283	-0.883	0.610	4.379	-0.579	0.889	NA	0.760	3.143
S12	-1.193	3.080	-0.335	-0.973	1.032	6.234	-0.414	0.932	NA	0.915	4.468
S13	-0.771	3.118	-0.061	-0.704	0.847	4.012	-0.323	1.014	NA	0.619	2.902
S14	-0.712	2.983	-0.120	-0.883	0.425	2.968	-0.491	0.889	NA	0.621	2.156
S15	-1.166	2.870	-0.423	-1.099	1.196	4.655	-0.398	1.034	NA	1.518	3.354
S16	-1.207	2.725	-0.518	-1.271	-0.290	3.939	-0.642	0.677	NA	1.510	2.812
S17	-1.166	2.886	-0.279	-0.886	0.928	2.984	-0.572	1.073	NA	0.677	2.156
S18	-0.979	2.816	-0.328	-1.038	0.219	2.627	-0.557	0.690	NA	0.969	2.021
S19	-1.051	2.874	-0.346	-1.004	0.590	2.874	-0.470	0.910	-0.995	0.782	2.053
S20	-0.608	2.476	-0.001	-1.035	0.069	3.508	-0.596	0.690	NA	0.473	2.511
S21	-0.782	2.330	-0.163	-1.102	-0.253	2.688	-0.823	0.775	NA	0.635	1.918
S22	-0.751	2.496	-0.181	-1.237	0.319	2.366	-0.770	0.626	NA	0.702	1.787
S23	-0.910	2.224	-0.411	-1.319	-0.052	1.848	-1.113	0.474	NA	0.216	1.574
S24	-0.955	2.259	-0.432	-1.251	-0.036	3.000	-1.023	0.844	NA	0.891	2.137
S25	-0.866	2.210	-0.378	-1.237	NA	2.485	-1.021	0.531	NA	0.681	1.770
S26	-1.088	2.156	-0.549	-1.424	-0.068	2.959	-1.012	0.474	NA	0.864	2.100
S27	-0.979	2.208	-0.417	-1.079	-0.200	1.812	-0.958	0.715	NA	1.477	1.574
S28	-1.153	2.776	-0.324	-1.167	0.569	2.047	-0.570	0.558	NA	1.398	1.990
S29	-0.877	2.404	-0.173	-1.179	0.002	3.070	-0.837	0.715	NA	0.166	2.186
S30	-0.979	2.229	-0.408	-1.315	-0.052	3.451	-0.970	0.586	NA	1.102	2.457
S31	3.602	2.071	1.695	0.720	NA	2.627	-1.020	0.488	3.620	0.962	2.810
Avg	-0.180	2.653	-0.174	-0.997	0.129	3.430	-0.693	0.699	-0.130	0.936	2.300
Max	3.602	3.118	1.695	0.720	1.196	6.234	-0.323	1.073	3.620	2.454	4.468
Min	-1.306	2.071	-0.614	-1.424	-0.931	1.812	-1.113	0.237	-0.995	0.166	1.574

NA= Not Available

3. Improved Nemerow Index (IN)

The results of the Improved Nemerow Index (I_N) show that the values of the study samples range between (4.468-1.574) with an average of (2.440) (Table 10), meaning that this soil is moderately to severely polluted according to this index classification (Guan et al., 2014). It is shown that the sample S12 in Al-Wahda neighborhood falls within the classification of being highly polluted. As for the samples (S15 and S11) in Al-Barid and Al-Mithaq neighborhoods, it falls within the level of being severely polluted (Fig. 6).

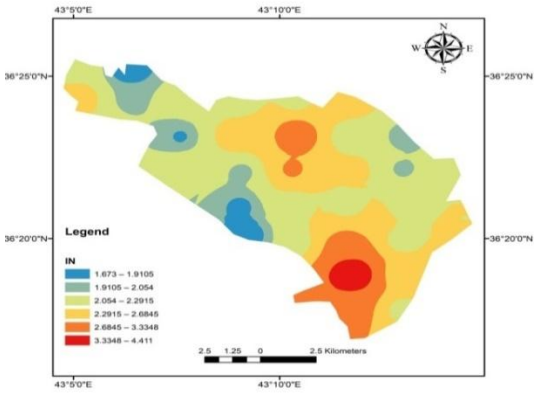


Fig. 6: Spatial distribution of (IN) in surface soil of study area

4. Enrichment factor

Table 11 shows that most of the heavy elements in the study samples, such as lead, zinc, copper, manganese, cobalt, arsenic, and chromium, are within the low to moderate enrichment level according to the classification of Mmolawa et al. (2011) and Barbieri et al. (2015). Nickel, molybdenum, and antimony are highly enriched. Sample S31 shows very high enrichment of lead and high enrichment of zinc, nickel, molybdenum, and antimony. Accordingly, the elements can be ranked according to the intensity of enrichment as shown in Fig. (7):

Mo>Ni>Sb>Cr>As>Co>pb>Zn>Mn>Cu

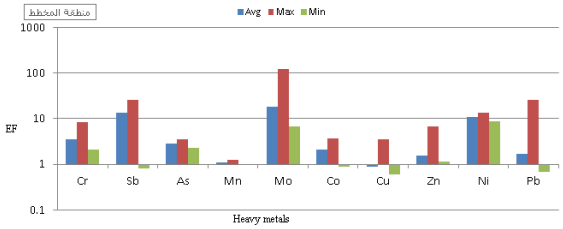


Fig. 7: Upper, lower and average limits of the enrichment factor in the studied area

Table 11: Results of calculating the Enrichment factor values for each element

Sample No.	Pb	Ni	Zn	Cu	Co	Mo	Mn	As	Sb	Cr
S1	2.15	9.49	2.75	1.25	NA	13.03	1.12	2.78	NA	3.02
S2	0.73	11.06	1.29	0.72	2.40	6.67	1.11	2.38	NA	4.35
S3	0.84	11.42	1.38	0.75	1.64	13.36	1.17	2.26	NA	3.73
S4	0.77	11.08	1.24	0.72	1.36	9.30	1.07	2.56	NA	3.40
S5	0.86	11.52	1.27	0.80	3.13	17.14	1.13	2.85	NA	2.91
S6	0.80	11.62	1.28	0.80	2.04	12.04	1.12	2.73	NA	3.21
S7	0.75	11.38	1.22	0.77	NA	20.44	1.13	2.69	NA	2.94
S8	0.83	11.24	1.22	0.74	0.87	8.99	1.08	2.51	NA	3.97
S9	0.69	10.04	1.16	0.59	1.99	16.19	1.03	2.34	NA	8.56
S10	0.72	11.71	1.25	0.78	NA	9.87	1.20	2.87	NA	3.31
S11	0.76	12.60	1.27	0.84	2.37	32.26	1.06	2.87	NA	2.68
S12	0.71	13.71	1.29	0.83	3.31	121.98	1.24	3.09	NA	3.12
S13	0.86	12.69	1.40	0.90	2.63	23.58	1.19	2.95	NA	2.29
S14	0.93	12.09	1.41	0.83	2.05	11.96	1.11	2.83	NA	2.40
S15	0.71	11.69	1.19	0.75	3.66	40.29	1.24	3.27	NA	4.67
S16	0.71	10.90	1.15	0.68	1.35	25.26	1.08	2.63	NA	4.79
S17	0.68	11.20	1.25	0.82	2.88	11.99	1.04	3.19	NA	2.47
S18	0.84	11.60	1.31	0.80	1.92	10.17	1.14	2.66	NA	3.29
S19	0.77	11.66	1.25	0.79	2.39	11.66	1.17	2.99	0.80	2.79
S20	1.08	9.18	1.65	0.80	1.73	18.77	1.11	2.66	NA	2.34
S21	1.05	9.05	1.61	0.84	1.51	11.60	1.04	3.08	NA	2.86
S22	1.04	9.83	1.54	0.74	2.17	8.98	1.04	2.69	NA	2.89
S23	1.07	9.39	1.51	0.81	1.94	7.23	0.95	2.79	NA	2.38
S24	1.00	9.27	1.44	0.81	1.89	15.50	0.97	3.48	NA	3.67
S25	1.12	9.47	1.58	0.87	NA	11.46	1.03	2.96	NA	3.35
S26	1.01	9.61	1.47	0.80	2.06	16.77	1.09	2.99	NA	4.01
S27	1.00	9.06	1.47	0.93	1.71	6.89	1.03	3.22	NA	5.58
S28	0.73	11.06	1.29	0.72	2.40	6.67	1.11	2.38	NA	4.35
S29	0.98	9.55	1.60	0.80	1.81	15.15	1.03	2.96	NA	2.07
S30	1.01	9.36	1.50	0.80	1.93	21.82	1.04	2.99	NA	4.38
S31	25.85	8.94	6.89	3.51	NA	13.15	1.07	2.99	26.17	4.24
Avg	1.53	10.88	1.53	0.87	1.89	18.63	1.10	2.81	1.58	3.55
Max	25.85	13.71	6.89	3.51	3.66	121.98	1.24	3.48	26.17	8.56
Min	0.68	8.94	1.15	0.59	0.87	6.67	0.95	2.26	0.80	2.07

NA= Not Available

4. Conclusion

The current study reveals that the surface soil in the left bank of Mosul City is contaminated with heavy metals. It appears that natural and human factors jointly influence the concentrations of heavy metals in the study area as follows:

The first factor includes the elements Mn, Ni, Fe_2O_3, MgO, As, Co, V, Y, Th, Nb, Al_2O_3, K_2O, SiO_2, TiO_2, Cr, and Zr, reflecting the influence of geochemical processes such as chemical weathering, adsorption on the surface of clay minerals, and the presence of weathering-resistant minerals. This also encompasses the role of sedimentary processes such as river sedimentation in concentrating and redistributing these elements in the environment. The second factor includes Cu, Zn, Pb, Sn, Sb, and Mo. These elements are clear indicators of pollution resulting from industrial waste, including batteries, metal coatings, electronic waste, and fuel combustion, as well as

waste from military operations. This is especially relevant since industrial and commercial areas, alongside locations that experienced intensive military operations, were among the most contaminated with heavy metals. Accordingly, the current study recommends taking urgent measures to reduce soil pollution in the city, including distancing industrial areas and vehicle repair workshops from residential communities. It also recommends investigating the health risks and effects of heavy metals in the surface soil of Mosul City.

5. Conflict of Interest

The authors declare that there are no conflicts of interest regarding the publication of this manuscript.

6. Funding Statement

This research received no external funding.

7. Author Contributions

First Researcher: Ruqaya Bader Mohammed
Sample collection, data analysis, and full preparation and writing of the research manuscript.
Second Researcher: Hazim Jumaa Mahmood
Proposing the research topic, conducting the statistical analysis, and reviewing the manuscript.

8. References

Alaarajy, G.G., Mahmood, H.J. and Abdulqader, O.N., 2023. Groundwater hydrochemistry and aquifer identification at Wana Area, Northwest of Mosul, Iraq. The Iraqi Geological Journal, 56 (2A), 85–101. https://doi.org/10.46717/igj.56.2A.7ms-2023-7-16

Al-Ansari, N., 2021. Topography and climate of Iraq. Journal of Earth Sciences and Geotechnical Engineering, 11(2), 1-13. https://doi.org/10.47260/jesge/1121

Alengebawy, A., Abdelkhalek, S.T., Qureshi, S.R. and Wang, M.Q., 2021. Heavy metals and pesticides toxicity in agricultural soil and plants: Ecological risks and human health implications. Toxics, 9 (3), 42. https://doi.org/10.3390/toxics9030042

Al-Fahaam, M.F., Mahmood, H.J. and Al-Sarraj, E.S., 2023. Spatial sampling of groundwater quality parameters on Mosul's Left Bank. The Iraqi Geological Journal, 56 (1D), 58–66. https://doi.org/10.46717/igj.56.1D.5ms-2023-4-14

Al-Khafaji, S.J. and Jaafar, S.W., 2023. Heavy metals pollution assessment in soil of Al-Zubair area, Southern Iraq. Iraqi National Journal of Earth Science, 23 (2), 91–104.

Ali, H., Khan, E. and Ilahi, I., 2019. Environmental chemistry and ecotoxicology of hazardous heavy metals: environmental persistence, toxicity, and bioaccumulation. Journal of Chemistry, 2019 (1), 6730305. https://doi.org/10.1155/2019/6730305

Al-Sheraefy, R.M., Al-Mallah, A.Y. and Hussien, A.K., 2023. Spatial distribution of heavy metals in the soil of different areas at Right Bank in Mosul City, Iraq: Part 1. The Iraqi Geological Journal, 56 (1C), 40–61. https://doi.org/10.46717/igj.56.1C.4ms-2023-3-15

Arao, T., Ishikawa, S., Murakami, M., Abe, K., Maejima, Y. and Makino, T., 2010. Heavy metal contamination of agricultural soil and countermeasures in Japan. Paddy and Water Environment, 8, 247–257. https://doi.org/10.1007/s10333-010-0205-7

Barbieri, M., Nigro, A. and Sappa, G., 2015. Soil contamination evaluation by Enrichment Factor (EF) and Geoaccumulation Index (Igeo). Senses Science, 2 (3), 94–97.

Belkhiri, L., Tiri, A. and Mouni, L., 2018. Assessment of heavy metals contamination in groundwater: a case study of the south of Setif area, East Algeria. Achievements and Challenges in Integrated River Basin Management. https://doi.org/10.5772/intechopen.75734

Bk, M.T., Al-Ahmadi, K.K. and Hamdon, A.N., 2024a. Spatio-temporal analysis of heavy metals concentration in the soil for selected sites in Mosul City. Iraqi National Journal of Earth Science, 24(1), pp.200–215. https://doi.org/10.33899/earth.2023.142140.1117

Bk, M.T., Al-Ahmadi, K.K. and Hamdon, A.N., 2024b. Evaluation of heavy metals in different soils from multiple areas within the city of Mosul. Journal of Rafidain Environment 2 (1), 14–27. (In Arabic)

Bradl, H.B., 2005. Sources and origins of heavy metals. In: Interface Science and Technology, Vol. 6, pp. 1–27. Elsevier. https://doi.org/10.1016/S1573-4285(05)80020-1

Dhannoun, H.Y. and Mahmood, H.J., 2019. The use of factor analysis in defining factors responsible for the variation of the concentrations of dissolved major ions in Tigris River water from Fishkabur to Baghdad. Iraqi National Journal of Earth Science, 19, 1–18. http://dx.doi.org/10.33899/earth.2019.170268

Fitzpatrick, R.W. and Chittleborough, D.J., 2002. Titanium and zirconium minerals. Soil Mineralogy with Environmental Applications, 7, 667–690.

Ferretti, M., Cenni, E., Bussotti, F. and Batistoni, P., 1995. Vehicle-induced lead and cadmium contamination of roadside soil and plants in Italy. Chemistry and Ecology, 11 (4), 213–228. https://doi.org/10.1080/02757549508039072

Gebreyesus, S.T., 2014. Heavy metals in contaminated soil: sources and washing through chemical extractants. American Scientific Research Journal of Engineering, Technology and Sciences (ASRJETS), 10, 54–60.

Geng, C., Gao, Y., Li, D., Jian, X., and Hu, Q., 2014. Contamination investigation and risk assessment of molybdenum on an industrial site in China. Journal of geochemical exploration, 144, 273-281. https://doi.org/10.1016/J.GEXPLO.2013.12.014

Guan, Y., Shao, C. and Ju, M., 2014. Heavy metal contamination assessment and partition for industrial and mining gathering areas. International Journal of Environmental Research and Public Health, 11, 7286–7303. https://doi.org/10.3390/ijerph110707286

Hakanson, L., 1980. An ecological risk index for aquatic pollution control: a sedimentological approach. Water Research, 14 (8), 975–1001. https://doi.org/10.1016/0043-1354(80)90143-8

Hameed, M.M. and KHALAF, S., 2024. Climate Changes and Societal Stability in Iraq: Proposed Measures. JOURNAL OF ECOHUMANISM Учредители: Transnational Press London, 4(1). https://doi.org/10.62754/joe.v4i1.6368

Hou, D., Jia, X., Wang, L., McGrath, S.P., Zhu, Y.G., Hu, Q. and Nriagu, J., 2025. Global soil pollution by toxic metals threatens agriculture and human health. Science, 388 (6744), 316–321. https://doi.org/10.1126/science.adr5214

Hanif, S., Ali, S., Chaudhry, A.H., Sial, N., Marium, A. and Mehmood, T., 2025. A review on soil metal contamination and its environmental implications. Nature Environment and Pollution Technology, 24 (1), 1–14. https://doi.org/10.46488/NEPT.2025.v24i01.D1684

Hasnine, M.T., Huda, M.E., Khatun, R., Saadat, A.H.M., Ahasan, M., Akter, S. and Ohiduzzaman, M., 2017. Heavy metal contamination in agricultural soil at DEPZA, Bangladesh. Environment and Ecology Research, 5 (7), 510–516. https://doi.org/10.13189/eer.2017.050707

Ibraheem, R.B., Al-Mallah, A.Y. and Al-Beyati, F., 2024. Untitled article. Iraqi National Journal of Earth Science, 24 (2), 72–87.

Jiang, F., Ren, B., Hursthouse, A., Deng, R. and Wang, Z., 2019. Distribution, source identification, and ecological-health risks of potentially toxic elements (PTEs) in soil of thallium mine area. Environmental Science and Pollution Research. https://doi.org/10.1007/s11356-019-04997-3

Kabata-Pendias, A., 2000. Trace elements in soils and plants. CRC Press. https://doi.org/10.1201/9781420039900

Kabata-Pendias, A., 2011. Trace elements in soils and plants, 4th ed. CRC Press, Taylor and Francis Group, Boca Raton, 534 p.

Kazem, M.A.K., 2017. Classification of some soils in Shatt al-Arab Region in Basra Governorate and evaluation of land suitability for agricultural purposes using remote sensing techniques. Unpublished Ph.D. Thesis, College of Agriculture, University of Basra, Iraq, 210 p.

Kharkan, J., Sayadi, M.H., Rezaei and M.R., 2019. Investigation of heavy metals accumulation in the soil and pine trees. Environmental Health Engineering and Management Journal, 6 (1), 17–25. https://doi.org/10.15171/EHEM.2019.03

Kumar, V., Singh, J., Kumar, P., 2019. Heavy metals accumulation in crop plants: sources, response mechanisms, stress tolerance and their effects. Contaminants in Agriculture and Environment: Health Risks and Remediation, 1, 38.

Mmolawa, K.B., Likuku, A.S. and Gaboutloeloe, G.K., 2011. Assessment of heavy metal pollution in soils along major roadside areas in Botswana. African Journal of Environmental Science and Technology, 5 (3), 186–196.

Muller, G., 1969. Index of geoaccumulation in sediment of Rhine River. GeoJournal, 2, 108–188.

Mahmood, H.J., 2021. The influential factors on the geochemistry of chemical elements in recent sediments of the Tigris River, Iraq. Research Journal of Chemistry and Environment, 25 (5), 151–159. http://dx.doi.org/10.5281/zenodo.5839283

Ranjani, M., Veerasingam, S., Venkatachalapathy, R., Mugilarasan, M., Bagaev, A., Mukhanov, V. and Vethamony, P., 2021. Assessment of potential ecological risk of microplastics in the coastal sediments of India: a meta-analysis. Marine Pollution Bulletin, 163, 111969. https://doi.org/10.1016/j.marpolbul.2021.111969

Rudnick, R.L. and Gao, S., 2003. Composition of the continental crust. In: Holland, H.D., Turekian, K.K. (Eds.), Treatise on Geochemistry, Vol. 3: The Crust. Elsevier-Pergamon, Oxford, pp. 1–64.

Sandler, A., Meunier, A. and Velde, B., 2015. Mineralogical and chemical variability of mountain red/brown Mediterranean soils. Geoderma, 239, 156–167. https://doi.org/10.1016/j.geoderma.2014.10.008

Sinex, S. and Helz, G., 1981. Regional geochemistry of trace elements in Chesapeake Bay sediments. Environmental Geology, 3 (6), 315–323. https://doi.org/10.1007/BF02473521

Westaway, R., Guillou, H., Seyrek, A., Demir, T., Bridgland, D., Scaillet, S. and Beck, A., 2009. Late Cenozoic surface uplift, basaltic volcanism, and incision by the River Tigris around Diyarbakır, SE Turkey. International Journal of Earth Sciences, 98, 601–625. https://doi.org/10.1007/s00531-007-0266-z

White, W.M., 2001. Geochemistry: An online textbook. Johns Hopkins University Press, 700p.

Wuana, R.A. and Okieimen, F.E., 2011. Heavy metals in contaminated soils: a review of sources, chemistry, risks and best available strategies for remediation. International Scholarly Research Notices, 2011 (1), 402647. https://doi.org/10.5402/2011/402647

Iraqi National Journal of Earth Science, Vol. 26, No. 04, 2026 (138-150)

Iraqi National Journal of Earth Science

www.earth.uomosul.edu.iq

تقييم التلوث بالمعادن الثقيلة وتحديد مصادرها في التربة الحضرية باستخدام مؤشرات التلوث والتحليل الإحصائي، الموصل، العراق

رقية بدر محمد [1*]، حازم جمعة محمود [2]

ruqaya.23evp11@student.uomosul.edu.iq hazimjm@uomosul.edu.iq

[1] قسم علوم البيئة، كلية علوم البيئة، جامعة الموصل، الموصل، العراق.

[2] قسم تقانات البيئة، كلية علوم البيئة، جامعة الموصل، الموصل، العراق.

**الباحث المراسل.*

تاريخ الاستلام: 24 أيار 2025 تاريخ المراجعة: 01 تموز 2025 تاريخ القبول: 03 آب 2025

تاريخ النشر الالكتروني: 01 تشرين الأول 2026

الملخص

تهدف الدراسة الحالية الى تقييم وتحديد مصادر تلوث التربة السطحية بالعناصر الثقيلة في الجانب الايسر من مدينة الموصل. تم جمع 31 عينة مركبة من التربة على شبكة منتظمة موزعة على منطقة الدراسة وبأبعاد 2×2 كم. أُجري التحليل الكيميائي باستخدام جهاز الاشعة السينية الوميضية (XRF) لتحديد تراكيز العناصر الاثرية (V، Nb، Zr، Y، Th، Sn، Cr، Sb، As، Mn، Mo، Co، Cu، Zn، Ni، Pb) والرئيسة (MgO، Al_2O_3، SiO_2، K_2O، TiO_2، Fe_2O_3). أظهرت نتائج حساب مؤشرات تلوث التربة (معامل التلوث ودرجة التلوث ومعامل التراكم الأرضي ومؤشر نيمرو للتلوث ومعامل الاغناء) ان اغلب عينات الدراسة ملوثة بالعناصر الثقيلة. يبين تحليل المركبات الاساسية، ان تأثير العمليات الجيوكيميائية مثل التجوية الكيميائية والامتزاز السطحي، بالإضافة إلى دور العمليات الرسوبية، مثل الترسيب النهري، في إعادة توزيع هذه العناصر في البيئة. في حين يبدو ان العناصر الثقيلة (Cu, Zn, Pb, Sn, Sb, Mo) قد تأثرت بالنشاطات البشرية في المدينة وخاصة ان هذه العناصر تُعتبر مؤشرات واضحة للتلوث الناتج عن النفايات الصناعية مثل البطاريات والطلاءات المعدنية والمخلفات الإلكترونية، إضافة إلى تأثير الأنشطة العسكرية خلال فترة تحرير المدينة من العصابات الارهابية. وما يؤيد ذلك ارتفاع تراكيز هذه العناصر بشكل ملحوظ في المنطقة الصناعية. بينت الدراسة مشاركة العوامل الطبيعية الجيولوجية والجيوكيميائية مع العوامل البشرية في التأثير على تراكيز العناصر الثقيلة في التربة السطحية لمدينة الموصل. كما اظهرت الدراسة الحاجة الملحة الى اتخاذ تدابير عاجلة للحد من تلوث التربة في المدينة، خاصة بعد ان سجلت مؤشرات التلوث في بعض المناطق مستويات عالية من التلوث.

الكلمات المفتاحية:

العناصر الثقيلة، التربة الحضرية، تلوث التربة، مؤشرات التلوث.

DOI: 10.33899/injes.v26i4.56158, ©Authors, 2026, College of Science, University of Mosul.

This is an open-access article under the CC BY 4.0 license (http://creativecommons.org/licenses/by/4.0/).

==========

Iraqi National Journal of Earth Science, Vol. 26, No. 04, 2026 (151-160)

Iraqi National Journal of Earth Science

www.earth.uomosul.edu.iq

An Assessment of Heavy Metal Pollution in Roadside Dust: A Case Study from Basrah Governorate, Southern Iraq

Iqbal O. Al-Taie [1*], **Hanan A. Darweesh** [1], **Yasmin I. Al Fraji** [1]

iqbal.ahmed@uobasrah.edu.iq hanan.darweesh@uobasrah.edu.iq yasmin.khalaf@uobasrah.edu.iq

[1] *Department of Geology, College of Science, University of Basrah, Basrah, Iraq.*

* *Correspondence author.*

Received: 09 May 2025 Received in revised form: 05 August 2025 Accepted: 02 October 2025

Available online: 01 October 2026

Abstract

This study assessed the extent and sources of heavy metal contamination in Roadside dust across Basrah Governorate, a major hub for petroleum production in southern Iraq. Samples were collected from six strategic industrial and urban locations. Concentrations of nickel (Ni), lead (Pb), cadmium (Cd), and chromium (Cr) were quantified, and pollution was evaluated using the geoaccumulation index (Igeo) and contamination factor (CF). Results indicate exceptionally high cadmium (Cd) contamination at the Al-Shuaiba industrial site (Igeo = 5.49; CF = 67.93), identifying it as a significant pollution hotspot. A distinct urban pollution pattern was also observed, with elevated lead (Pb) concentrations at the high-traffic Sa'ad Square site (Igeo = 2.22). Source apportionment via Pearson correlation supported these findings, revealing a strong, statistically significant positive correlation among Ni, Cd, and Cr ($p < 0.005$), suggesting a common industrial origin. Conversely, Pb showed no significant correlation with the other metals, corroborating its primary association with vehicular emissions. Notably, Ni contamination was minimal, and Cr levels remained consistently low, suggesting their lesser contribution to the overall pollution load in the studied area. In conclusion, this study identifies a dual-front environmental challenge in Basrah, necessitating the implementation of source-specific remediation and management strategies targeting both severe industrial cadmium emissions and widespread urban lead pollution.

Keywords:

Heavy metals, Roadside dust, soil contamination, pollution, geochemical index.

DOI: 10.33899/injes.v26i4.56161, *©Authors, 2026, College of Science, University of Mosul.*
This is an open-access article under the CC BY 4.0 license (http://creativecommons.org/licenses/by/4.0/).

==========

1. Introduction

Environmental pollution represents one of the most significant contemporary challenges, directly threatening key pillars of human well-being such as food security and public health (Food and Agriculture Organization, 2018). Its severity has markedly increased since the Industrial Revolution, becoming a central concern across vital sectors, including health, agriculture, and industry (Al-Sarrafi, 2009). In this context, soil serves as the fundamental substrate supporting agricultural and urban landscapes and is the primary medium for most human activities (Adhikari and Hartemink, 2016). Soil pollution often originates from mining, industrial activities, improper product use, and natural heavy metal concentrations intensified by mining and pesticide application (Al-Saad et al., 2007). Recent studies have continued to highlight these challenges across southern Iraq, emphasizing the need for ongoing regional environmental assessments (Al-Taie and Al-Khafaji, 2023).

A pollutant is defined as any foreign substance that causes harm to the environment or its living inhabitants (Siddiq et al., 2012). Pollution effectively occurs when the introduction of these substances disrupts an ecosystem's ability to maintain its dynamic equilibrium, thereby hindering the sustainability of life within it. Recent studies and a scientific review have confirmed that chemical pollution has surpassed safe planetary limits, threatening the stability of global ecosystems (Persson et al., 2022). Furthermore, the interactions between pollutants and the environment are complex; air pollutants, for instance, can contribute to the acidification of soil and water, thereby

degrading their quality and capacity to support life (Manisalidis et al., 2020).

More specifically, air pollution by fine particulate matter and dust is a serious environmental issue in urban areas. These particles are emitted from vehicle exhaust, industrial processes, and construction activities and may contain chemical compounds and heavy metals that pose a risk to human health upon inhalation (WHO, 2021). This challenge is exacerbated by rapid urban growth, the absence of environmental planning, and climatic factors such as drought and wind (EPA, 2022). Particles ranging from 2.5 to 10 micrometers in size are particularly dangerous, as they can penetrate the respiratory system and enter the bloodstream, worsening cardiovascular and respiratory diseases (European Environment Agency, 2023).

The intensity of a pollutant's impact depends on multiple factors, including its type, environmental concentration, and the duration of exposure (Castro-Gonzalez et al., 2017). This is particularly relevant to Basra, a major industrial and oil hub in southern Iraq, whose environment makes it susceptible to heavy metal accumulation in the soil and atmosphere (Jalal, 2020). Accordingly, this research aims to assess the concentrations of several heavy metals (chromium, nickel, lead, and cadmium) by analyzing roadside dust samples from selected areas of the Basra governorate. This makes the study of its geochemical environment an endeavor of both scientific and practical importance.

2. Research Area

Basrah, with an area of approximately 19,070 km2 (Central Statistical Organization, 2023), is situated between 46.7° E and 48.6° E longitude and 29.5° N and 31.3° N latitude (GADM, 2022). The area contains numerous oil fields, petrochemical facilities, fertilizer factories, and energy production facilities. The research region includes some Quaternary and recent sediments, primarily clay, silt, sand, and gravel (Al-Khafaji et al., 2010). The samples were collected from six stations: Al-Shuaiba, Al-Zubair, Al-Faw, Sa'ad Square, Al-Garma, and Al-Tanumah (Fig. 1).

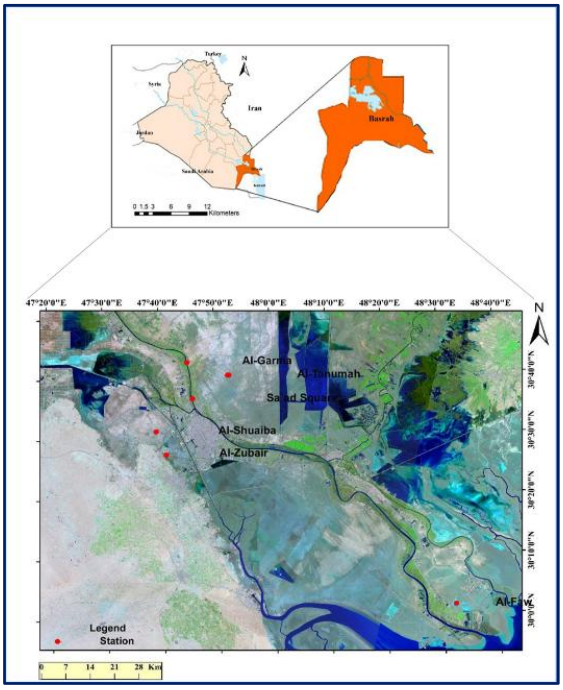


Fig. 1: Sample stations in the research area.

3. Procedures

A. Collecting and preparing samples

Roadside dust samples were collected in August 2021 from six sites across the Basrah Governorate: Al-Garma, Al-Tanumah, Sa'ad Square, Al-Shuaiba, Al-Zubair, and Al-Faw (Fig. 1). These locations were selected to represent a cross-section of local environments, including high-traffic roads, open areas, and mixed residential-commercial zones. At each site, approximately 250 g of surface dust was collected with a stainless-steel shovel and sealed in a labeled polyethylene bag. Before analysis, samples were processed in the lab by first manually removing visible debris (e.g., cigarette butts, glass, plastic). The cleaned samples were then air-dried to a constant weight at room temperature. Finally, each sample was thoroughly homogenized before being sieved with a ceramic mortar and pestle to obtain a fine, uniform powder for chemical analysis.

At Basrah City's Al-Wasal Science Center for Environmental Assessment, trace elements were analyzed using ICP-OES (iCAP™ PRO, Thermo Fisher Scientific, USA) with calibration performed using a multi-element standard solution (Carl Roth, Art. No. 2650.1, Lot 782085). Method detection limits (MDLs) were 0.5 ppm for Ni, 1.7 ppm for Pb, 0.1 ppm for Cd, and 0.4 ppm for Cr. Analytical accuracy was validated by analyzing certified

reference materials (CRMs), with recovery rates from 90% to 105%. Analytical precision was assessed by repeated measurements (triplicates) of selected samples. The relative standard deviation (RSD) was consistently below 5% for most measurements, though it was higher for concentrations approaching the method detection limit, which is typical for trace analysis.

B. Assessment of pollution levels

The contamination factor (CF) (Pecky, 2004) or pollution index (PI) (Faiz et al., 2009) was used to show the concentration level of heavy metals in the soil, and the geoaccumulation index (Igeo) (Muller, 1969) was utilized to evaluate the accumulation of elements in the soil. The following formulas are shown below:

$$CF = (Cn/Bn)$$

$$Igeo = \log_2 (Cn / 1.5Bn)$$

Where Cn represents the measured concentration of the studied metal in the roadside dust samples. Bn represents the geochemical background value of an element. For this study, the average elemental abundance in the Earth's crust, documented in the CRC Handbook of Chemistry and Physics (Lide, 2004), served as a proxy for natural background concentrations. The constant 1.5 is a correction factor that accounts for potential natural fluctuations in background values, thereby minimizing the misclassification of minor natural enrichments as anthropogenic contamination (Pan et al., 2017).

Tables 1 and 2, following Muller (1969) and Pekey et al. (2004), present the standard Igeo and CF values for heavy metals.

Table 1: Concentration factors (Pekey et al., 2004).

Category	Description
CF	Pollution Level
CFI < 1	Little
1 ≤ CFI < 3	Reasonable
3 ≤ CFI < 6	Great
CFI ≥ 6	Very Great

Table 2: Geoaccumulation index (Muller, 1969).

Category	Description
Igeo is equal to or less than 0	Almost uncontaminated
Igeo is between 0 and 1	Undirty to medium dirty
Igeo is between 1 and 2	Medium polluted
Igeo is between 2 and 3	Medium toward high dirty
Igeo is between 3 and 4	High polluted
Igeo is between 4 and 5	Highly toward exceedingly dirty
Igeo is equal to or more than 5	Exceedingly polluted

4. Results and Discussion

According to Kabata-Pendias and Pendias (1992), nickel is considered a human toxicant and often leads to respiratory diseases. Nickel concentrations at the Shuaiba station reached 247.03 ppm (Table 3); this severe level of contamination is directly related to the oil and gas exploitation sites there. As shown in Table 3 and Fig. 2, soil nickel levels ranged from 22.104 ppm (at Al-Faw station) to 247.03 ppm (at Al-Shuaiba station). Concentrations at three stations, Al-Shuaiba (247.03 ppm), Sa'ad Square (106.29 ppm), and Al-Zubair (91.55 ppm), exceeded 84 ppm, the normal concentration for uncontaminated soil (Kabata- Pendias, 2011). These levels were also higher at the Zubair station (91.55 ppm). Fayad et al. (2013) indicated that battery production, fuel combustion, and household cleaning products such as bleach and soap are significant contributors to nickel accumulation in urban soil. Table 3 and Fig. 2 show that lead concentrations ranged from approximately 10.16 ppm (at Al-Tanuma station) to 97.81 ppm (at Sa'ad Square station). This exceeds the natural limit for lead in soil (14 ppm). Vehicle emissions are a major source of lead in urban soils, as lead enters the environment through a variety of personal activities, including mining, smelting, and manufacturing (Li et al., 2009).

Montagne et al. (2007) demonstrated that lead-containing dust particles from roads, after short atmospheric residence times, contribute to lead accumulation on soil surfaces in the proximity to highways. Clausen et al. (2004) showed that cadmium levels in soil exceeded the global average of 0.15 ppm for uncontaminated soil. Table 3 and Fig. 2 show that cadmium ranges from 0.02 ppm (Al-Tanumah station) to 10.2 ppm (Al-Shuaiba station). These elevated levels, exceeding 0.5 ppm, may be attributed to human activity (CSO, 2014). Monitoring soil cadmium levels in the research area is essential, particularly where concentrations are high, given its accumulation in the human body and delayed toxicity from prolonged exposure (Certini et al., 2013). Due to human activities, including the use of solid waste and sewage, as well as industrial and agricultural processes, cadmium levels in the soil have risen above the natural limits of the element's concentration (Facchinelli et al., 2001). In addition, Giaccio et al. (2012) showed that cadmium is

utilized in electrical coatings, paints, and dyes in a variety of sectors.

Chromium concentrations ranged from 0.6 ppm at the Al-Tanumah station to 141.68 ppm at the Al-Shuaiba station (Table 3 and Fig. 2). The concentration at Al-Shuaiba exceeds the normal limit of 120 ppm (Kabata-Pendias, 2011), which indicates a significant localized source of contamination. In contrast, values at all other study sites were well below this limit (Table 3). Due to the strong binding of chromium (Cr^{3+}) to oxide surfaces, it is typically found in soils rich in metal oxides, especially iron oxides (such as goethite and hematite) and manganese oxides. Also, due to its similar size to iron (Fe^{3+}), it can replace iron atoms within the mineral's crystal structure, leading to its immobilization (Kabata-Pendias, 2011). The low chromium concentrations in the study area are mainly attributed to the naturally low geogenic background of chromium in the parent materials of Basrah, as well as the physicochemical properties of the street dust matrix, which is generally dominated by non-cohesive and coarse particles with limited capacity to retain heavy metals compared to clay-rich natural soils (Alloway, 2013). Sandy soils retain little Cr(III) due to low surface area and minimal cation exchange capacity; the region's clay minerals and their source composition further constrains overall chromium levels (Kabata-Pendias, 2011). These findings align with Al-Khafaji et al. (2010), who also reported low Cr levels in Basrah soils.

Table 3: The heavy metal concentrations (in ppm) within the soil at the study stations.

Station Name	Statistics	Ni	Pb	Cd	Cr
Al-Garma	1	63.11	22.6	0.24	30.97
	2	63.1	22.8	0.26	30.99
	3	63.13	22.4	0.22	30.95
	Mean	63.11	22.6	0.24	30.97
	SD	0.02	0.2	0.02	0.02
Al-Tanumah	1	28.17	10.16	0.020*	0.6
	2	28.15	10.2	0.023*	0.65
	3	28.19	10.12	0.017*	0.55
	Mean	28.17	10.16	0.02	0.6
	SD	0.02	0.04	0.003	0.05
Sa'ad Square	1	106.29	97.81	0.29	22.23
	2	106.3	97.85	0.27	22.24
	3	106.28	97.77	0.31	22.23
	Mean	106.29	97.81	0.29	22.23
	SD	0.01	0.04	0.02	0.01
Al-Shuaiba	1	247.03	59.42	10.19	141.68
	2	249	60.42	10.26	142.68
	3	245.06	58.4	10.14	140.68
	Mean	247.03	59.41	10.2	141.68
	SD	1.97	1.01	0.06	1
Al-Zubair	1	91.55	64.73	0.91	34.65
	2	92.55	65.73	0.92	35.65
	3	90.55	63.73	0.9	33.65
	Mean	91.55	64.73	0.91	34.65
	SD	1	1	0.01	1
Al-Faw	1	22.1	21.06	0.090*	2.59
	2	23.1	21.03	0.100*	2.61
	3	21.1	21.09	0.080*	2.57
	Mean	22.1	21.06	0.09	2.59
	SD	1	0.03	0.01	0.02
Method Detection Limit (MDL)		0.5	1.7	0.1	0.4

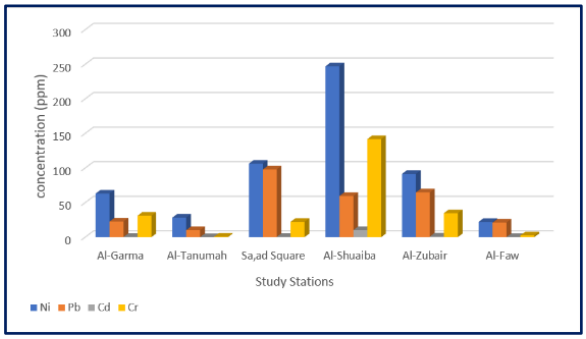


Fig. 2: Heavy metal content at the study stations.

It is acknowledged that several measurements of cadmium (Cd) at Al-Tanumah and Al-Faw stations registered below the formal method detection limit (MDL) of 0.1 ppm. These readings, however, were consistently above the instrument detection limit (IDL) of 0.001 ppm, representing quantifiable instrumental responses. They are reported herein to demonstrate the reproducibility of the analysis at these trace concentrations, with the understanding that they are associated with greater analytical uncertainty than levels above the MDL.

To investigate the potential origins of the heavy metals, a Pearson correlation analysis was performed (Table 4). While these findings should be interpreted with caution due to the limited sample size (n=6), the results revealed a strong, positive, and statistically significant relationship between Ni, Cr, and Cd, as seen in the Ni-Cr ($r = 0.968$, $p = 0.001$), Ni-Cd ($r = 0.933$, $p = 0.003$), and Cr-Cd ($r = 0.976$, $p < 0.001$) pairings. This tight grouping suggests a potential common origin from activities such as oil and gas processing or industrial waste (EPA, 2020; WHO, 2021). In contrast, lead (Pb) did not correlate significantly with any of the other metals ($p > 0.05$). The lack of correlation may indicate that lead pollution stems from a different

source and is primarily caused by traffic-related emissions from vehicles (WHO, 2021).

Table 4: Pearson Correlation Coefficients (r) for Heavy Metal Concentrations in roadside dust.

Heavy Metals	Statistic	Ni	Pb	Cd	Cr
Ni	Pearson Correlation	1	0.541	0.933**	0.968**
	p-value		0.134	0.003	0.001
Pb	Pearson Correlation	0.541	1	0.236	0.329
	p-value	0.134		0.326	0.262
Cd	Pearson Correlation	0.933**	0.236	1	0.976**
	p-value	0.003	0.326		< 0.001
Cr	Pearson Correlation	0.968**	0.329	0.976**	1
	p-value	0.001	0.262	< 0.001	

**. Correlation is significant at the 0.01 level (1-tailed). The critical value for r with df = 4 is 0.917.

Despite being a known environmental hazard due to its potential to bioaccumulate, chromium showed very little accumulation in the roadside dust of Basrah in our study. This was confirmed by the geoaccumulation index, which showed consistently low values at all sites. All six locations fell into the 'uncontaminated' class (Igeo ≤ 0. Even at its highest concentration at the Al-Shuaiba industrial site, the Igeo value was 0.32 (Table 5). This overall lack of significant accumulation strongly suggests that chromium has poor mobility in the soils of this region, a finding consistent with its tendency to become immobilized under the kinds of moderate redox conditions reported by Clausen et al. (2004).

Analysis of the Geoaccumulation Index (Igeo) revealed distinct spatial patterns of contamination across the study area, suggesting different pollution sources (Table 5, Fig. 3). The most alarming finding was the severe and highly localized contamination by cadmium (Cd) at the Al-Shuaiba industrial site. With an Igeo value of 5.49, this location is classified as heavily to extremely polluted, which strongly points to a specific industrial point source.

Lead (Pb) and, to a lesser extent, nickel (Ni), also showed notable contamination at specific sites. Lead pollution was most significant at Sa'ad Square, a high-traffic area, with an Igeo value of 2.22 ('moderately to heavily polluted'). Significant lead contamination was also found at Al-Zubair (Igeo = 1.62) and Al-Shuaiba (Igeo = 1.5).

In contrast, nickel (Ni) contamination was far less widespread than initially suggested, and was primarily confined to the Al-Shuaiba station, which had an Igeo value of 0.97 ('uncontaminated to moderately polluted'). All other stations showed no signs of nickel pollution, with negative Igeo values. Therefore, the primary heavy metal concerns identified by the Igeo analysis are the extreme cadmium enrichment at Al-Shuaiba and the significant lead pollution at traffic and industrial sites, making these the elements of greatest environmental concern in the study area.

Table 5: The geochemical accumulation index values (Igeo) at the study stations.

Station No.	Station Name	Geochemical accumulation index (Igeo)			
		Ni	Pb	Cd	Cr
1	Al-Garma	-1	0.11	0.09	-2.86
2	Al-Tanumah	-2.18	-1.05	-4.49	-8.55
3	Sa'ad Square	-0.25	2.22	0.35	-3.33
4	Al-Shuaiba	0.97	1.5	5.49	-0.32
5	Al-Zubair	-0.44	1.62	2.01	-3.1
6	Al-Faw	-2.52	0	-1.58	-6.34
	Range	-2.52-0.97	-1.05-2.22	-4.49-5.49	-0.32--8.55
	Average	-0.90	0.73	0.31	-4.08
Background value (Bn)		84	14	0.15	120

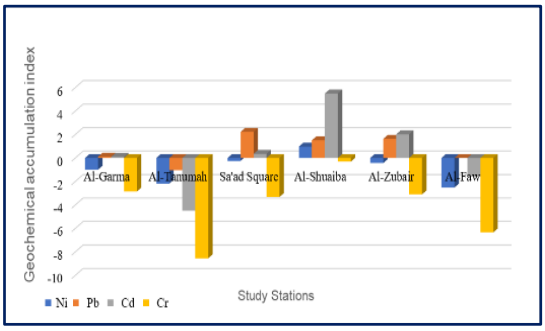


Fig. 3: The geochemical accumulation index (Igeo) distribution across the study stations.

The Contamination Factor (CF) analysis effectively distinguished between highly localized industrial pollution and more widespread urban pollution sources (Table 6, Fig. 4). Al-Shuaiba was confirmed as the primary industrial pollution source, with 'very high' contamination by cadmium (CF = 67.93). Significant cadmium contamination was observed in Al-Zubair, with a contamination factor of 6.06. The urban pollution signature was most evident at Sa'ad Square, which had the highest lead contamination level (CF = 6.98, 'very high contamination'), likely due to heavy traffic. Nickel contamination was generally low to moderate across most industrial and urban sites. In contrast, chromium levels were consistently low, with a CF value never exceeding 1.18, indicating minimal contamination from this element.

The overall enrichment hierarchy in the region, based on average CF values, was Cd (13.04) > Pb (3.28) > Ni (1.10) > Cr (0.32), highlighting the severe impact of industrial activities on cadmium levels in the environment. Chromium (Cr), with a CF consistently below 1 at most sites, was not associated with a significant pollution signature. This clear distinction between sources explains the overall enrichment hierarchy in the region (Cd > Pb > Ni > Cr) and highlights the critical impact of targeted industrial and vehicular emissions.

Table 6: Concentration factor (CF) values for the study stations.

Station No.	Station Name	Concentration Factor (CF)			
		Ni	Pb	Cd	Cr
1	Al-Garma	0.75	1.61	1.6	0.25
2	Al-Tanumah	0.33	0.72	0.13	0.005
3	Sa'ad Square	1.26	6.98	1.93	0.18
4	Al-Shuaiba	2.94	4.24	67.93	1.18
5	Al-Zubair	1.08	4.62	6.06	0.28
6	Al-Faw	0.26	1.50	0.6	0.02
Range		0.26-2.94	0.72-6.98	0.13-67.93	0.005-1.18
Average		1.10	3.28	13.04	0.32
Background value (Bn)		84	14	0.15	120

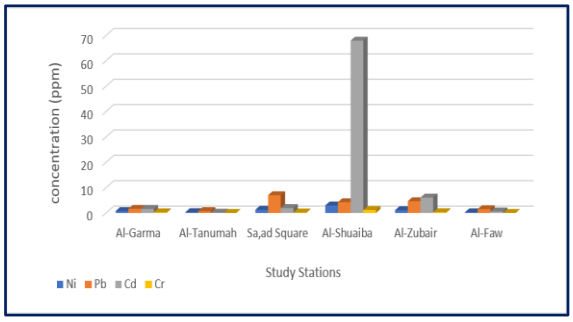


Fig. 4: Distribution of heavy metal concentration factors (CF) at the study stations.

To expand on the scientific context, the results of the current study were compared with average heavy metal concentrations reported from several local Iraqi studies and international studies, revealing significant differences that reflect variations in local environmental conditions and pollution sources (Table 7).

Table 7: A comparison of mean heavy metal concentrations (ppm) in roadside dust from the present study with other local and international studies.

References	Studied Area	Heavy metals (ppm)			
		Ni	Pb	Cd	Cr
Al-Khafaji and Jaafar (2023)	Iraq (Al-Zubair in Basrah)	23.21	19	0.32	34.5
Jalal (2020)	(Basrah) Iraq	374.3	64.96	0.17	980
Al-Sudani et al. (2021)	Iraq (Al-Anbar)	155.33	10.55	14.62	117.4
Al-Sarafi (2009)	Iraq (Al-Shuaiba in Basrah)	24.1	7.6	2.9	26.4
Zhao et al. (2020)	Southeast China (Xiamen, Fujian)	52	202	1.33	143
Tang et al. (2022)	Southeast China (Guangdong)	34.4	150	0.73	150
Al-Obaidy and Al-Mashhadi (2013)	Iraq (Baghdad)	86.76	87.06	0.29	23.09
Present Study	Iraq (Al-Basrah)	93.04	45.96	1.96	38.79

The average nickel (Ni) concentration was 93.04 ppm. This value was considerably higher than levels reported in other Basrah studies by Al-Khafaji and Jaafar (2023) and Al-Sarafi (2009), and comparable to the concentration found in Baghdad by Al-Obaidi and Al-Mashhadi (2013). However, it was significantly lower than the exceptionally high values recorded by Jalal (2020) in Basrah and Al-Sudani et al. (2021) in Al-Anbar. This suggests that the primary sources of pollution are likely anthropogenic, resulting from the oil industry and heavy traffic emissions.

The lead (Pb) concentration, at 45.96 ppm, was higher than in some local areas but still significantly lower than the levels recorded in major industrial cities by Tang et al. (2022), Zhao et al. (2020), Jalal (2020), or Al-Obaidi and Al-Mashhadi (2013). This indicates localized urban pollution, likely from vehicle emissions, such as tire wear and legacy leaded gasoline.

The cadmium concentration in the current study, 1.96 ppm, was notably higher than that in most other cited Iraqi studies, including Al-Khafaji and Jaafar (2023), Jalal (2020), and Al-Obaidi and Al-Mashhadi (2013). The value, however, was comparable to that reported by Al-Sarafi (2009) in Al-Shuaiba's industrial area and significantly lower than that found by Al-Sudani et al. (2021). This suggests contamination from a range of sources, including industrial sources such as electroplating and battery manufacturing.

The chromium (Cr) concentration was 38.79 ppm, which was relatively moderate. Unlike other metals, this value is consistent with regional background levels reported by Al-Khafaji and

Jaafar (2023). This suggests that chromium levels are more significantly influenced by widespread contamination and the characteristics of the region's soils, rather than by specific, high-intensity industrial sources such as tanneries or paint facilities.

Thus, heavy metal pollution in the study area can be classified as moderate to high. Overall, the contamination in the region indicates a complex, multi-source environmental problem caused by the combined effects of the oil industry, traffic, and agricultural practices, underscoring the need for targeted environmental management.

5. Conclusion

The study results show that heavy metal concentrations varied significantly across the different sites. The highest levels of nickel, cadmium, and chromium were consistently found at the Shuaiba Industrial Station, attributed to nearby oil fields, gas flaring, and oil spills. The highest lead concentration was also recorded at Sa'ad Square. Urban centers such as Sa'ad Square and Zubair were subsequently classified as highly polluted sites, where pollution is primarily associated with heavy vehicular traffic. In contrast, the Tanuma and Al-Faw stations showed minimal pollution due to their distance from these major sources. Pollution indices (CF and Igeo) confirmed these spatial patterns, showing that overall pollution levels varied significantly from low to very high in specific areas. Shuaiba stands out in these indices due to high to severe cadmium pollution levels from industrial and petroleum-related activities. Contrary to initial assessments, the geochemical accumulation index indicated that nickel accumulation was minimal. In contrast, heavy lead accumulation was primarily associated with the Sa'ad Square site, which has heavy traffic, while chromium showed minimal accumulation at all sites.

Furthermore, statistical analysis showed strong and significant correlation among nickel, cadmium, and chromium, while lead (Pb) showed no significant correlation with the other metals. However, these finding as preliminary due to the limited number of samples (n=6). With this caveat in mind, the correlation suggests that these elements may originate from shared sources, likely related to industrial and other human activities in the region, while lead contamination stems from a different source.

In conclusion, these results highlight the importance of monitoring these metals as environmental indicators. They also call for more detailed studies employing a larger sampling size to statistically validate these preliminary findings, accurately identify pollution sources, and develop effective strategies to mitigate the harmful impacts of both heavy industrial cadmium contamination and widespread urban lead contamination on the environment and public health.

6. Acknowledgements

The authors express their gratitude to the Department of Geology at the University of Basrah for their ongoing assistance. We are particularly grateful to the Al-Wasal Scientific Laboratory for Environmental Analysis in Basrah, southern Iraq, for their assistance in the laboratory analysis. We sincerely thank the editor and reviewers for their time and work in making the necessary revisions to the paper.

7. Conflict of Interest

The authors declare that none of their personal or financial conflicts could have influenced the work presented in this study.

8. Funding Statement

This research received no external funding.

9. Author contributions:

Iqbal O. Al-Taie: Conceptualization, Methodology, Validation, Investigation, Data curtain, writing – original draft, Visualization, Project administration.

Hanan A. Darweesh: Methodology, Visualization, Project administration, Writing, Review, and Editing.

Yasmin I. Al Fraji: Conceptualization, Methodology, Writing review, and Editing.

10. References

Adhikari, K. and Hartemink, A. E., 2016. Linking soils to ecosystem services - A global review. Geoderma, 262, 101-111. https://doi.org/10.1016/j.geoderma.2015.08.009

Alloway, B.J., 2013. Heavy metals in soils: trace metals and metalloids in soils and their bioavailability. Springer Science and Business Media.

Al-Khafaji, S.J., Al-Ali, S.H., and Al-Saad, H.A., 2010. Identification and upgrading of feldspar of some sand

deposits southern Iraq. Al-Basrah Research Journal. 36B, 12-35. https://www.iasj.net/iasj/article/261376

Al-Khafaji, S.J. and Jaafar, S.J., 2023. Heavy Metals Pollution Assessment in Soil of Al-Zubair Area, Southern Iraq. Iraqi National Journal of Earth Science, 23(2), 91-104. http://dx.doi.org/10.33899/earth.2023.139641.1072

Al-Obaidy, A.H. and Al-Mashhadi, A.M., 2013. Heavy Metal Contaminations in Urban Soil within Baghdad City, Iraq. Journal of Environmental Protection, 4, 72-82. http://dx.doi.org/10.4236/jep.2013.41008

Al-Saad, H.T., Abd, I.A., Al-Hello, M.A., and Zuhkair, M.K., 2007. Environmental assessment of trace metals pollution in sediment of Khor Al-Zubair, Iraq. Marina Mesopotamica, 22(1), 81-92.

Al-Sarafi, A.N., 2009. Environmental Effects of Industrial Pollutants in Maysan Governorate. Master's thesis, College of Arts, University of Basrah, 216 pages.

Al-Sudani, I.M., Al Lami, M.H., Abdul Hameed, M. Al Obaidy, J., Saja Al-Rubaye, M. J., 2021. Spatial Distribution of Some Heavy Metals in Urban Soil of Western Iraq. Annals of R.S.C.B. ISSN: 1583-6258, 25, 10550-10558.

Al-Taie, I.O. and Al-Kafaji, S.J. 2023. Pollution Assessment of Slabiat Soil Depression Southwestern Iraq. HIV Nursing, 23 (2), 432-440.

Castro-González, N., Calderón-Sánchez, F., Moreno-Rojas, R., Moreno-Ortega, A., Tamariz-Flores, J.V., 2017. Health risks in rural populations due to heavy metals found in agricultural soils irrigated with wastewater in the Alto Balsas subbasin in Tlaxcala and Puebla, Mexico. International Journal of Environmental Health Research, 27, 476-486. http://dx.doi.org/10.1080/09603123.2017.1386767

Central Statistical Organization, 2023. Geographic and administrative data of Basrah Governorate. Republic of Iraq, Ministry of Planning. Retrieved from https://cosit.gov.iq

Certini, G., Scalenghe, R. and Woods, W. I., 2013. The impact of warfare on the soil environment. Earth-Science Reviews, 127, 1-15. http://dx.doi.org/10.1016/j.earscirev.2013.08.009

Clausen, J., Robb, J., Curry, D. and Korte, N., 2004. A case study of contaminants on military ranges: Camp Edwards, Massachusetts, USA, Environmental Pollution, 129 (1), 13-21. http://dx.doi.org/10.1016/j.envpol.2003.10.002

CSO, 2014. Population Growth statistics: population estimates of Iraq by age group, region, and gender, Ministry of Planning. Central Statistical Organization. Republic of Iraq.

Environmental Protection Agency (EPA). 2020. Inventory of United States Greenhouse Gas Emissions and Sinks: 1990–2018. EPA. https://www.epa.gov/ghgemissions/inventory-us-greenhouse-gas-emissions-and-sinks-1990-2018

Environmental Protection Agency, 2022. Particulate Matter (PM) Pollution. https://www.epa.gov/pm-pollution

European Environment Agency, 2023. Air quality in Europe, a report. https://www.eea.europa.eu/air-quality

Facchinelli, A., Sacchi, E., and Mallen, L., 2001. Multivariate statistical and GIS-based approach to identify heavy metal sources in soils, Environmental pollution, 114 (3), 313-324. https://doi.org/10.1016/S0269-7491(00)00243-8

Faiz, Y., Tufail, M., and Javed, M.T., 2009. Geo-environmental assessment of soil and groundwater contamination in a coastal industrial area of Pakistan. Environmental Earth Sciences, 58(6), 1259-1273. https://doi.org/10.1007/s12665-008-0022-7

Fayad, N., Al-Noor, T.H., and Al-Noor, N.H., 2013. Analysis and assessment of essential toxic heavy metals, pH, and EC in Ishaqi River and adjacent soil. Advances in Physics Theories and Applications, 16, 25-37.

Food and Agriculture Organization of the United Nations., 2018. The State of Food Security and Nutrition in the World 2018: Building climate resilience for food security and nutrition. FAO. https://www.fao.org/3/I9553EN/i9553en.pdf

Giaccio, L., Cicchella, D., De Vivo, B., Lombardi, G., and De Rosa, M., 2012. Does heavy metals pollution affects semen quality in men? A case of study in the metropolitan area of Naples (Italy). Journal of Geochemical Exploration, 112, 218-225. https://doi.org/10.1016/j.gexplo.2011.08.009

GADM, 2022. Database of Global Administrative Areas. Retrieved from https://gadm.org/

Jalal, G. K., 2020. Urban Environmental Geochemistry of Basrah City, Southern Iraq. Master's thesis, College of Science, University of Basrah, 212.

Kabata-Pendias, A., and Pendias, H., 1992. Chapter 5: Trace elements in plants. In A. Kabata-Pendias and H. Pendias (Eds.), Trace elements in soils and plants. Boca Raton: CRC Press, 67-87.

Kapata-Pendias, A., 2010. Trace Elements in Soils and Plants. 4th ed., Boca Raton: CRC Press. 584p. ISBN 978-1-4200-9368-1 (hardback). https://doi.org/10.1201/b10158

Li, J., Lu, Y., Yin, W., Gan, H., Zhang, C., Deng, X., and Lian, J., 2009. Distribution of heavy metals in agricultural soils near a petrochemical complex in Guangzhou, China. Environmental monitoring and assessment, 153 (1), 365-375. https://doi.org/10.1007/s10661-008-0363-x

Manisalidis, I., Stavropoulou, E., Stavropoulos, A., and Bezirtzoglou, E., 2020. Environmental and health impacts of air pollution: A review. Frontiers in Public Health, 8, 14. https://doi.org/10.3389/fpubh.2020.00014

Montagne, D., Cornu, S., Bourennane, H., Baize, D., Ratié, C., and King, D., 2007. Effect of agricultural practices on trace-element distribution in soil. Communications in Soil Science and Plant Analysis, 38 (3-4), 473-491. https://doi.org/10.1080/00103620601174411

Muller, G., 1969. Index of geoaccumulation in sediments of the Rhine River. Geology Journal, 2, 109-118.

Pan, L., Hu, W., Wen, X., Liu, W., Li, D., and Wang, X., 2017. A review of heavy metal pollution in urban soils of China: Status, sources and consequences. Science of The Total Environment, 598, 436-444. https://doi.org/10.1016/j.scitotenv.2017.03.303

Pekey, H., Karakas, D., Aybert, S., Tohun, L. and Bakoglu, M., 2004. Ecological risk assessment using trace elements from surface sediment of Izmit Bay (Northeastern Marmara Sea). Turkey Marine Pollution Bulletin, 48, 946-953. https://doi.org/10.1016/j.marpolbul.2003.11.023

Persson, L., Almroth, B. C., Collins, C. D., Cornell, S., de Wit, C. A., Diamond, M. L., and Hauschild, M. Z., 2022. Outside the safe operating space of the planetary boundary for novel entities. Environmental Science and Technology, 56 (3), 1510-1521. https://doi.org/10.1021/acs.est.1c04158

Siddiq, M.A.M., Barua, P., and Ghani, M.H., 2012. Comparative study of physico-chemicalproperties of soil according to the age of aquaculture pond of Bangladesh. Mesopotamian. Journal of Marine Science, 27 (1), 29-38.

Tang, F.; Li, Z.; Zhao, Y.; Sun, J.; Sun, J.; Liu, Z.; Xiao, T.; Cui, J., 2022. Geochemical Contamination, Speciation, and Bioaccessibility of Trace Metals in Road Dust of a Megacity (Guangzhou) in Southern China: Implications for Human Health. International Journal of Environmental Research and Public Health19, 15942.

World Health Organization, 2021. Air pollution and health. https://www.who.int/airpollution

Zhao, L.; Yu, R.; Yan, Y.; Cheng, Y.; Hu, G.; Huang, H., 2020. Bioaccessibility and provenance of heavy metals in the park dust in a coastal city of southeast China. Applied Geochemistry, 123, 104798. https://doi.org/10.1016/j.apgeochem.2020.104798

Iraqi National Journal of Earth Science, Vol. 26, No. 04, 2026 (151-160)

Iraqi National Journal of Earth Science

www.earth.uomosul.edu.iq

تقييم تلوث الغبار بالعناصر الثقيلة من جوانب الطريق: دراسة حالة من محافظة البصرة، جنوبي العراق

اقبال عوفي[1*]، حنان عبدالقادر[1]، ياسمين ابراهيم[1]

iqbal.ahmed@uobasrah.edu.iq hanan.darweesh@uobasrah.edu.iq yasmin.khalaf@uobasrah.edu.iq

[1] قسم علم الأرض، كلية العلوم، جامعة البصرة، البصرة، العراق.

*الباحث المراسل.

تاريخ الاستلام: 09 أيار 2025 تاريخ المراجعة: 05 آب 2025 تاريخ القبول: 02 تشرين الأول 2025

تاريخ النشر الالكتروني: 01 تشرين الأول 2026

الملخص

أُجريت هذه الدراسة لتقييم مدى ومصادر تلوث المعادن الثقيلة في غبار الطرق في محافظة البصرة، وهي مركز رئيسي لإنتاج النفط في جنوب العراق. جُمعت العينات من ستة مواقع صناعية وحضرية استراتيجية. حُددت تراكيز النيكل (Ni) والرصاص (Pb) والكادميوم (Cd) والكروم (Cr)، وقُيّم التلوث باستخدام مؤشر التراكم الجيولوجي (Igeo) وعامل التلوث (CF). تشير نتائج الدراسة إلى تلوث مرتفع للغاية بالكادميوم (Cd) في موقع الشعيبة الصناعي (Igeo = 5.49؛ CF = 67.93)، مما يجعله نقطة تلوث رئيسية. كما لوحظ نمط تلوث حضري يتميز بارتفاع تركيزات الرصاص (Pb) في موقع ساحة سعد ذي الحركة المرورية الكثيفة (Igeo = 2.22). دعم تحليل توزيع المصادر عبر معامل ارتباط بيرسون هذه النتائج، كاشفًا عن ارتباط إيجابي قوي ذي دلالة إحصائية بين النيكل والكادميوم والكروم ($p < 0.005$)، مما يشير إلى الأصل الصناعي المشترك. في المقابل، لم يُظهر الرصاص أي ارتباطا ذي دلالة إحصائية مع المعادن الأخرى، مما يؤكد ارتباطه الأساسي بانبعاثات المركبات. والجدير بالذكر أن التلوث بالنيكل كان ضئيلًا، بينما ظلت مستويات الكروم منخفضة باستمرار، مما يشير إلى انخفاض مساهمتهما في إجمالي حمل التلوث في المنطقة المدروسة. وفي الختام، تُحدد هذه الدراسة تحديًا بيئيًا مزدوجًا في البصرة، مما يستلزم تطبيق استراتيجيات معالجة وإدارة خاصة بالمصدر تستهدف كلاً من انبعاثات الكادميوم الصناعية الشديدة وتلوث الرصاص الحضري واسع الانتشار..

الكلمات المفتاحية:

المعادن الثقيلة، غبار جوانب الطريق، تلوث التربة، التلوث، المعامل الجيوكيميائي.

DOI: 10.33899/injes.v26i4.56161, ©Authors, 2026, College of Science, University of Mosul.

This is an open-access article under the CC BY 4.0 license (http://creativecommons.org/licenses/by/4.0/).

Iraqi National Journal of Earth Science, Vol. 26 No. 04, 2026 (161-174)

Iraqi National Journal of Earth Science

www.earth.uomosul.edu.iq

Hydromorphometric Analysis of the Koya Basin in the Kurdistan Region of Iraq.

Ala Qader [1*] , **Shwan Seeyan [2]**

ala.qadir@su.edu.krd shwan.seeyan@su.edu.krd

[1] *Department of Earth Science and Petroleum, College of Science, University of Salahaddin, Erbil, Iraq.*

[2] *Department of Soil and Water, College of Agriculture, University of Salahaddin, Erbil, Iraq.*

* *Correspondence author.*

Received: 23 May 2025 Received in revised form: 29 July 2025 Accepted: 15 October 2025
Available online: 01 October 2026

Abstract

This study conducts a comprehensive hydromorphometric analysis of the Koya basin in the Kurdistan Region of Iraq, using ALOS PALSAR DEM data and GIS-based techniques to evaluate relief, linear, and areal parameters. The elongated basin (form factor = 0.21) features a sixth-order drainage network dominated by first-order streams, with high mean bifurcation ratios (Rb = 5.13) indicating structural control over drainage patterns. Moderate drainage density (1.95 km^{-1}) and infiltration number (4.31) reflect balanced dissection but elevated runoff potential, while rugged terrain (ruggedness number = 2.31) and significant relief (1,185 m) underscore topographic complexity. Comparative analysis reveals similarities to tectonically influenced basins in Erbil and Kirkuk, though Koya's hypsometric integral (0.47) and dissection index (0.81) suggest a mature yet dynamically evolving landscape. Slope and aspect analyses identify southwest-facing slopes as hotspots for erosion and reduced soil moisture retention. The findings highlight the interplay between geomorphology and hydrology, emphasizing that elongated basin geometry mitigates flood intensity, while high-drainage-density zones necessitate targeted management. This study provides the first district-scale hydromorphometric assessment of the Koya basin, offering critical insights for policymakers to optimize watershed management, prioritize flood mitigation in structurally active regions, and enhance groundwater recharge strategies in semi-arid environments

Keywords:

Hydromorphometry, Semi-Arid Region, Groundwater Recharge Management.

DOI: 10.33899/injes.v26i4.56166, ©Authors, 2026, College of Science, University of Mosul.
This is an open-access article under the CC BY 4.0 license (http://creativecommons.org/licenses/by/4.0/).

==========

1. Introduction

Hydro-morphometric studies are a significant aspect of hydrological and geomorphological investigations, providing insights into watershed characteristics, drainage systems, and their influence on water resource management (Horton, 1945). The integration of Remote Sensing and Geographic Information System (GIS) techniques has significantly enhanced the accuracy and effectiveness of hydro-morphometric analysis, making it feasible to analyze important morphometric parameters such as relief, linear, and areal parameters, which play an important role in watershed behavior, surface runoff potential, and erosion (Patel et al., 2013; Mohammed et al., 2026). The Koya basin, located in the Kurdistan Region of Iraq, is characterized as being topographically complex and having a plurality of drainage systems. Although various hydro-morphometric measurements have been conducted in Kurdistan provinces like Erbil and Kirkuk, very few scientific studies examine the entire Koya basin (Al-Saady et al., 2016). Earlier studies focus primarily on sub-watersheds or specific places in Koya rather than on a district-level study.

Most available studies are conducted on sub-watersheds or specific sites in Koya, not at the district level. Existing research has compared hydromorphometric parameters across different areas inside and outside Koya. For example, Ahmed et al. (2023) conducted research in the Erbil area using principal component analysis (PCA) to evaluate drainage density, basin shape,

and elevation trends. Likewise, Goran and Khattab (2023) analyzed the Hesh Karo River catchment using GIS, demonstrating strong hydrological relationships among stream length, stream order, and runoff potential. Al-Tamimi et al. (2022) investigated the Laylan sub-basin in Kirkuk Governorate and identified significant morphometric parameters, such as drainage density and stream frequency, to evaluate erosion processes.

Additionally, Ahmed and Jirjees (2022) carried out a flood hazard evaluation and research on water management practices in the Taqtaq watershed (Taqtaq sub-district, Koysinjaq district), which was beneficial. Fatah et al. (2020) conducted a comprehensive morphometric study of northeastern Erbil watersheds, highlighting the application of GIS-based methods in watershed management. Regardless of these beneficial attempts, no one has yet conducted a comprehensive hydro-morphometric study of the entire Koya basin. This research gap highlights the need for a district-scale morphometric study to provide a more detailed insight into Koya's hydrological and geomorphological characteristics.

Although there have been studies on some of the watersheds and sub-basins of Koya, no study has yet presented a full morphometric analysis at the district level. Either they concentrate on some limited sections of Koya, or they investigate watersheds in other regions of Kurdistan. This calls for a general review of the Koya basin's hydromorphometric parameters, including its relief, linear, and areal characteristics. By bridging this gap, the present study aims to provide fresh insight into the Koya basin's hydrological behavior and geomorphic dynamics.

The primary objective of this study is to conduct a hydromorphometric analysis of the Koya basin using ALOS PALSAR Digital Elevation Model (DEM) data and GIS-based techniques. The study is especially concerned with the analysis of relief, linear, and areal morphometric parameters; stream order extraction and classification to interpret drainage patterns; the establishment of the hydrological significance of the basin's topographic features; and the identification of possible applications to water resource management and flood hazard mitigation.

To attain these goals, the research aims to address the following research questions:

1. What are the dominant morphometric characteristics of the Koya basin in relation to relief, linear, and areal factors?
2. What is the resemblance of the hydromorphometric structure of the Koya basin to other studied watersheds in Kurdistan?
3. What are the morphometric implications for flood control and water resource management in the Koya basin?

This study aims to perform a comprehensive hydromorphometric analysis of the Koya Basin in the Kurdistan Region of Iraq, using ALOS PALSAR DEM data and GIS-based techniques, to assess its relief, linear, and areal parameters, interpret drainage patterns, and evaluate the basin's hydrological and geomorphological characteristics at the district level

GIS-based software is used to map the drainage network, delineate watersheds, and calculate key morphometric parameters. The methodology follows a systematic process that includes stream-order classification and calculation of hydromorphometric indices. The derived data are analyzed to prepare topographic and hydrological maps, facilitating an integrated interpretation of the drainage system of the Koya basin.

The outcome of this study will add to the body of knowledge in hydromorphometry by presenting the first-ever basin-level analysis of Koya. Unlike earlier studies that have addressed small watersheds, this study presents an integrated assessment of the entire basin, offering insightful information on drainage patterns, surface flow, and likely flood-prone zones.

The applications of this study include helping policymakers and conservation organizations with proper watershed management, delineating areas prone to flooding and suggesting mitigation measures, and aiding water conservation efforts by improving understanding of drainage patterns and their origin.

2. Study Area

Koya District is in the Kurdistan Region of Iraq, about 75 kilometers southeast of Erbil city. This area is located between the latitudes of 35° 49′ 35″ N and 36° 16′ 44″ N, and longitudes of 44° 15′ 18″ E and 44° 57′ 27″ E. The total study area is about 1911 square kilometers. The altitude over the study area ranges between 271 m and 1,455 m above sea level, which indicates a heterogeneous

topography affected by geological and structural factors, as shown in Figure 1. Koya District has a semi-arid climate with cold, wet winters and hot, dry summers. Between 2000 and 2023, the region was recorded to have an average annual temperature of 22.52 °C and an average yearly rainfall of 572. 84 mm. The region's geological structure showcases multiple lithological formations that intricately control both groundwater resources and surface water movement. The Pliocene deposits, as exemplified by the Bai Hassan and Muqdadiya formations, consist of conglomerates, gravels of mixed grain sizes, sand, and silt, withsilt, with some interbeds of clay, forming an intergranular aquifer. The Middle and Upper Miocene sediments represented by the Fatha and Injana formations consist of sandstone, marlstone, claystone, siltstone, and fine-grained clastics with gypsum and anhydrite beds, essentially constituting semi-impermeable strata with modest groundwater storage. The Paleocene and Eocene sediments represented by the Kolosh, Sinjar, Khurmala, Gercus, and Pila Spi formations contain well-karstified and bedded limestones, some crystalline and bituminous, constituting a karstic-fissured aquifer. However, the Kolosh and Gercus formations consist of impermeable clastic rocks with minimal potential for groundwater. The Cretaceous deposits, on the other hand, consisting of the Balambo, Qamchuga, Aqra-Bekhme, and Shiranish formations, contain extensive, layered well-karstified limestone, which is a highly effective karstic aquifer (Figure 2). Structurally, the Koya District is dominated by NW–SE-trending anticlines, i.e., the Bustana, Bani Bawi, and Safeen anticlines, which have been influenced by strike-slip faulting and extensive jointing in carbonate units, particularly the Pila Spi and Balambo units. The Bustana anticline has a steep southwestern side that dips at angles up to 55 degrees, while the northeastern side has a gentler slope, not going over 20 degrees (Haris et al., 2016). This area's complex structure, along with varying faulting and erosion, plays a big role in how surface water drains and how groundwater gets replenished (Ghafour et al., 2024).

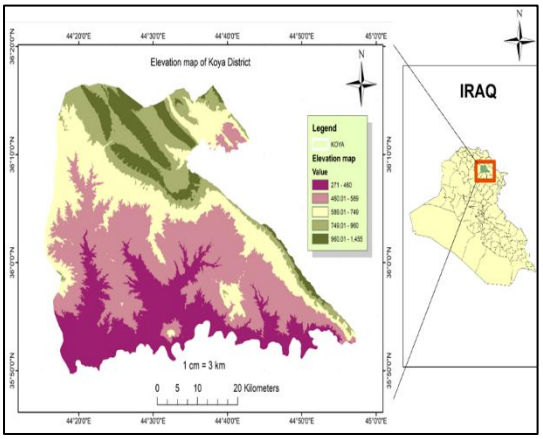


Fig. 1: Location Map of the study Area.

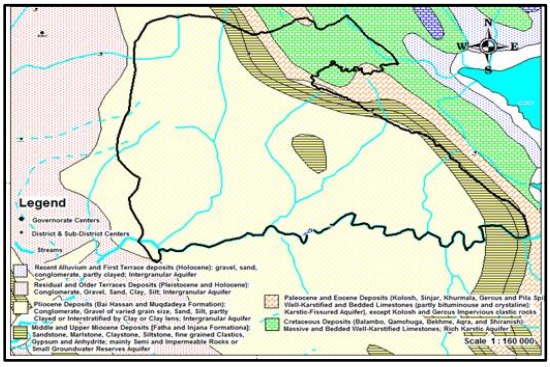


Fig. 2: Geological Map of the Study area showing formations and type of aquifers.

3. Methodology

In the present study, the Advanced Land Observing Satellite Digital Elevation Model (ALOS PALSAR DEM), with a resolution of 12.5 meters, was utilized and downloaded from the Alaska Satellite Facility. The process included processing the DEM to derive required terrain properties, including Hydromorphometric parameters. A topographic map was also created to supplement these analyses. Watersheds were delineated from the extracted drainage networks, which served as a basis for stream order classification. The morphometric parameters of the watersheds were then calculated to examine their physical and hydrological properties. The results were integrated to examine watershed dynamics and drainage patterns in the study area. The work steps are shown in the flowchart diagram below (Figure 3).

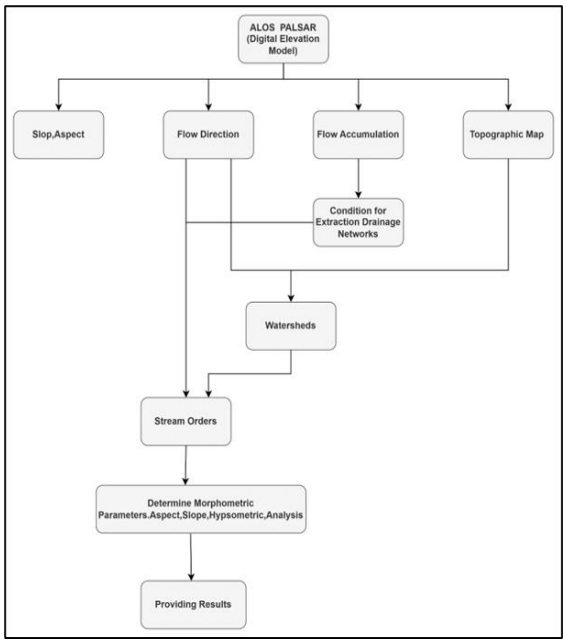


Fig. 3: The flow diagram shows the steps of the methods and data investigation.

The morphometric parameters have been divided into three types, including linear, areal, and relief aspects.

Linear Aspects of Morphometry

Linear aspects of morphometry help to evaluate the surface structure and drainage characteristics of a basin. These parameters are crucial for understanding the hydrologic behaviour and geomorphological development of a watershed (Strahler, 1957).

A. Basin Perimeter (P)

Basin perimeter is the total length of the outer boundary that encloses the drainage area. It is extracted using GIS tools during watershed delineation (Schumm, 1956).

B. Main Channel Length (Cl)

Main channel length is the distance measured along the longest stream from its source to the outlet. It is measured directly using the GIS line tool (Gregory and Wallingford, 1973)

C. Basin Width (Bw)

Basin width indicates the overall shape of the basin and is calculated by dividing the area by the basin length. It helps assess surface runoff and flood potential (Schumm, 1956).

Formula: $Bw = A / Lb$ (Schumm, 1956)

A = Basin area, Lb = Basin length

D. Lemniscate Factor (K)

The Lemniscate factor describes the shape of the basin, particularly its elongation. Lower values indicate an elongated basin shape (Chorley, 1957)

Formula: $K = (3.14 \times Lb^2) / (4 \times A)$ (Chorley, 1957)

K = Lemniscate factor Lb = Basin length A = Basin area

E. Basin Length (Lb)

Basin length is the longest dimension of a basin from the outlet to the farthest point. It can also be estimated using an empirical equation based on the basin area (Schumm, 1956).

Formula: $Lb = 1.312 \times A^{0.568}$ (Schumm, 1956)

Lb = Basin length; A = Basin area

F. Stream Order (Nu)

Stream order classifies stream segments based on a hierarchical system developed by Strahler. It reflects the complexity of the drainage network (Strahler, 1952).

Formula: Nu = Number of streams of a particular order u (Strahler, 1952)

G. Stream Length (Lu)

Stream length refers to the total length of all stream segments of a given order. It is extracted from GIS using the line features of stream orders (Horton, 1945).

Formula: Lu = Total length of streams of order u (km) (Horton, 1945)

H. Mean Stream Length (MLu)

Mean stream length is the average length of streams of a specific order and indicates the stages of basin development (Strahler, 1964). It is derived by dividing the total stream length (Lu) by the number of stream segments (Nu).

Formula: $MLu = Lu / Nu$ (Strahler, 1964).

MLu = Mean stream length, Lu = Total stream length of order, Nu = Number of streams of order

I. Stream Length Ratio (RLu)

The stream length ratio compares the length of streams in one order to the next lower order and helps in understanding the geomorphic

development of the basin (Horton, 1945). It is influenced by variations in slope and lithology.

Formula: RLu = Lu / Lu+1 (Horton, 1945)

RLu = Stream length ratio Lu = Stream length of order Lu+1 = Stream length of next higher order

J. Bifurcation Ratio (Rb)

Bifurcation ratio is the ratio of the number of streams in a given order to those in the next higher order (Strahler, 1957). It reflects the degree of branching and can indicate structural controls such as faults or joints.

Formula: Rb = Nu / Nu+1 (Strahler, 1957)

Rb = Bifurcation ratio; Nu = Number of streams of order; Nu+1 = Number of streams of next higher order

K. Mean Bifurcation Ratio

The mean bifurcation ratio is the average of all bifurcation ratios calculated between successive stream orders (Strahler, 1964). It helps assess the overall structural influence and the uniformity of the drainage pattern.

Formula: Mean of all Rb values (Strahler, 1964)

L. Rho Coefficient (ρ)

The rho coefficient is used to evaluate the relationship between stream length and bifurcation, and is useful in interpreting geological and drainage density characteristics (Strahler, 1964). It is calculated as the ratio of the stream length ratio to the bifurcation ratio.

Formula: ρ = RLu / Rb (Strahler, 1964)

ρ = Rho coefficient RLu = Stream length ratio Rb = Bifurcation ratio

Areal Aspect

Areal aspects refer to the parameters that describe the size, shape, and spatial distribution of a drainage basin, which directly influence surface runoff, infiltration, and hydrological response. These aspects help quantify how the basin area is utilized by drainage features and how efficiently it drains precipitation. Morphometric parameters under this category offer crucial insights into the basin's hydrological behavior and geomorphological development (Strahler, 1957).

A. Basin Area (A) (Km²)

The basin area (A) is the total land-surface area that contributes water to a drainage system, measured using GIS tools. It is fundamental for calculating most morphometric parameters and reflects the scale of hydrological processes within the watershed (Strahler, 1964).

B. Drainage Density (Dd)

Drainage density represents the total length of streams per unit area of the basin, indicating the closeness of channel spacing. High values suggest impermeable subsurface material or high relief (Horton, 1945).

Formula: Dd= Total Lu /A

Dd = Drainage density (km/km²)

Lu = Total length of streams (km)

A = Basin area (km²)

C. Stream Frequency (Fs)

Stream frequency refers to the number of streams per unit area. It reflects the texture of the drainage network and is influenced by lithology and slope (Horton, 1945).

Formula: Fs= Total Nu / A

Fs = Stream frequency (no./km²)

Nu = Total number of streams

A = Basin area (km²)

D. Drainage Texture (Dt)

Drainage texture is the relative spacing of drainage lines in a basin, calculated as the total number of streams per unit perimeter. A coarse texture suggests gentle terrain, while a fine texture suggests steep slopes (Smith, 1950)

Formula: Dt= Total Nu / P

Where:

Dt = Drainage texture

Nu = Total number of streams

P = Basin perimeter (km)

E. Drainage Intensity (Di)

Drainage intensity combines stream frequency and drainage density to reflect the potential for surface runoff. A high value indicates a well-developed drainage system (Faniran, 1968).

Formula: Di = Fs / Dd

Where:

Di = Drainage intensity

Fs = Stream frequency

Dd = Drainage density

F. Elongation Ratio (Re)

The elongation ratio is a shape parameter indicating how close the basin's shape is to a circle. Values near 1 suggest a circular basin, while lower values indicate elongation (Schumm, 1956)

Formula: $RE = 1.128\sqrt{A} / Lb$

Where:

Re = Elongation ratio

A = Basin area (km^2)

Lb = Basin length (km)

G. Circularity Ratio (Rc)

Circularity ratio expresses how circular the basin is and is useful in assessing erosion and maturity stage (Miller, 1953).

Formula: $RC= 4\pi A / P2$

Where:

Rc = Circularity ratio

A = Basin area (km^2)

P = Basin perimeter (km)

H. Form Factor (Rf)

Form factor describes the shape of the basin and its effect on flood peaks. Low values indicate elongated basins with lower peak flows (Horton, 1945).

Formula: $Ff = A / Lb^2$

Where:

Ff = Form factor

A= Basin area (km^2)

Lb = Basin length (km)

I. Infiltration Number (If)

The infiltration number represents the combined effect of drainage density and stream frequency on infiltration. Lower values indicate greater infiltration capacity (Faniran, 1968).

Formula: If = Fs * Dd

Where:

If = Infiltration number

Fs = Stream frequency

Dd = Drainage density

J. Length of Overland Flow (Lg)

This is the average length of water flow over the ground before entering a channel. It is inversely related to drainage density (Horton, 1945).

Formula: Lg = 1/2Dd

Where:

Lg = Length of overland flow (km)

Dd = Drainage density

K. Constant of Channel Maintenance (C)

This constant represents the required area to sustain one unit length of stream channel, inversely related to drainage density (Schumm, 1956).

Formula: C = 1/Dd

Where:

C = Channel maintenance constant

Dd = Drainage density

Relief Aspect

Relief aspects represent the vertical dimension of a drainage basin, which influences runoff velocity, erosion potential, and sediment transport. These parameters offer insight into the topographic variation, landscape maturity, and tectonic activity within the basin. Understanding relief aspects is essential in geomorphological and hydrological investigations (Strahler, 1957).

A. Maximum Height (H) (m)

This is the highest elevation point within the basin and serves as a reference for calculating relief.

Measured using: DEM analysis in GIS software.

B. Minimum Height (h) (m)

This is the lowest elevation point in the basin, typically located at the basin outlet.

Measured using: DEM and outlet point analysis.

C. Total Basin Relief (Rb)

It is the difference between the highest and lowest elevations within the basin, indicating the total vertical extent.

Formula: Rb=H-h

Where:

Rb = Total basin relief

H = Maximum elevation (m)

h = Minimum elevation (m)

D. Relief Ratio (Rh)

The relief ratio expresses the steepness or gradient of a basin by relating total relief to basin length. Higher values indicate steeper slopes (Schumm, 1956).

Formula: Rh= Rb/Lb

Where:
Rh = Relief ratio
Rb = Basin relief (m)
Lb = Basin length (km)

E. Relative Relief Ratio (Rr)

This parameter relates the maximum basin elevation to its perimeter, providing insight into terrain roughness (Melton, 1957)

Formula: $Rr = H / P$
Where:
Rr = Relative relief ratio
H = Maximum height (m)
P = Basin perimeter (km)

F. Absolute Relief (Ra)

Absolute relief refers to the maximum elevation from mean sea level in the basin and helps assess terrain roughness.

Measured using: GIS-derived DEM analysis.

G. Dissection Index (Di)

The dissection index estimates the degree of vertical dissection of the basin. Values close to 1 indicate deep dissection, while lower values reflect gentle terrain (Singh and Dubey, 1994).

Formula: $Di = Rb/Ra$
Where:
Di = Dissection index
Rb = Basin relief (m)
Ra = Absolute relief (m)

H. Ruggedness Number (Rn)

Ruggedness number combines basin relief and drainage density to express terrain ruggedness. It is a key indicator of erosion potential and surface roughness (Strahler, 1964)

Formula: $Rn = Dd * (Rb/1000)$
Where:
Rn = Ruggedness number
Dd = Drainage density (km/km²)
Rb = Basin relief (m)

I. Slope

It is a primary morphometric parameter that regulates the response of the land surface to runoff, erosion, and landform evolution. Commonly computed using Geographical Information Systems (GIS) tools with Digital Elevation Models (DEMs), it enables comprehensive analysis of slope gradients for watershed management and land use planning (Moore et al., 1991).

J. Hypsometric Integral (HI)

Is the ratio of watershed area to elevation, indicating the degree of basin development. A high HI denotes a young, dissected terrain, whereas a low HI implies an older, eroded basin. This parameter is useful for further exploring erosion rates, geomorphological evolution, and hydrological processes (Moore et al., 1991).

K. Aspect Analysis

Aspect analysis determines the direction a slope faces, which significantly influences hydrological processes by directing surface water flow, runoff, and erosion patterns (Moore et al., 1991). The orientation of slopes affects solar radiation exposure, impacting soil moisture, vegetation, and microclimates; for example, south-facing slopes in the northern hemisphere typically experience higher evaporation rates, while north-facing slopes retain more moisture (Wilson and Gallant, 2000) Categorizing aspects helps identify zones of water accumulation or efficient drainage, which is crucial for flood and erosion risk assessment and land-use planning (Moore et al., 1991) Incorporating aspect analysis into hydrological modeling improves prediction accuracy and supports sustainable watershed management by enhancing understanding of terrain-driven water dynamics (Wilson and Gallant, 2000).

4. Results

4.1. Linear

The Koya basin exhibits a sixth-order drainage basin, comprising 4,232 streams totaling 3,731 km, overwhelmingly dominated by first-order streams (Table 1). The stream order map visually represents this (Figure 4). The mean bifurcation ratio (Rb) is calculated at 5.13, stream length ratios range between 0.27 and 0.53, and the Rho coefficient (ρ) is measured at 0.44 (Table 1). According to Strahler (1964). A high bifurcation ratio implies that geological factors, such as rock structure and tectonic activity, play a dominant role in shaping drainage configuration. The stream length ratio demonstrates a systematic reduction in slope and flow energy with increasing stream order. As noted by Horton (1945), Rho indicates a

moderate level of drainage integration, supporting more sustainable water resource management.

Table 1: Summary of drainage basin linear aspect parameters in the study area.

Stream Orders (u)	Stream Numbers (Nu)	Stream Length (Lu) in (Km)	Mean Stream Length (MLu) in (Km)	Stream Length Ratio (RLu)	Bifurcation Ratio (Rb)	Mean Bifurcation Ratio	RHO Coefficient (ρ)
1st	3276	1948.24	0.59	0.50	4.37		0.11
2nd	750	974.85	1.30	0.53	4.49		0.12
3rd	167	516.47	3.09	0.36	5.39		0.07
4th	31	187.03	6.03	0.44	4.43	5.13	0.10
5th	7	82.09	11.73	0.27	7.00		0.04
6th	1	21.87	21.87	……..	……		
Total	4232	3731			7.00		0.44

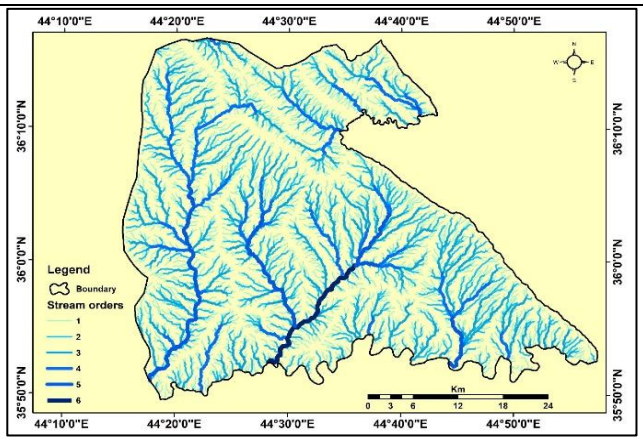


Fig. 4: Stream order distribution map of the study area.

The hierarchy of stream order reveals an inverse relationship, where both the number and total length of streams decrease with increasing stream order, as shown in (Figure.5) This pattern reflects a highly dissected terrain and indicates an early stage of geomorphic development, consistent with Horton's law of stream numbers.

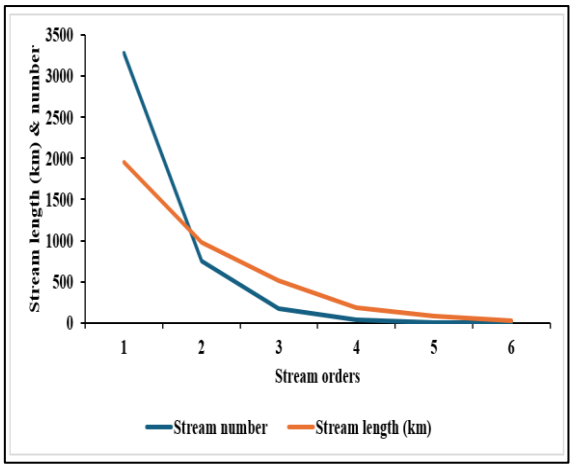


Fig. 5: Relationship between Stream length and Stream Number with Stream Order.

The linear morphometric measurements (Table 2) also substantiate these interpretations. The 277 km total basin perimeter reinforces an intricate and irregular drainage boundary, which may influence runoff direction and collection patterns. The 95.87 km length of the basin is the cause of an extended basin configuration that has a tendency to slow down peak discharge and reduce flood hazard.

The 65 km length of the main channel indicates how long water would spend flowing within the basin, determining the size and timing of flood peaks. These models are highlighted by a 3.78 Lemniscate Factor and basin width of 19.93 km, both pointing to the basin's stretched character. Together, these parameters provide the basis for both geomorphic maturity and tectonic control of the drainage system and offer solid groundwork for comparative analysis with other basins within the Kurdistan Region.

Table 2: Summary of drainage basin linear aspect parameters in the study area

No.	Parameters	Results
1	Basin perimeter (P) (Km)	277 km
2	Main channel length (Cl) km	65km
3	Basin Width (Bw)	19.93 km
4	Lemniscate Factor (K)	3.78
5	Basin Length (Lb) (Km)	95.87 km
6	Stream Orders (Nu)	See Table 1
7	Stream Length (Lu) (km)	See Table 1
8	Mean Stream Length (MLu) (Km)	See Table 1

9	Stream Length Ratio (RLu)	See Table 1
10	Bifurcation Ratio (Rb)	See Table 1
11	Mean Bifurcation Ratio	See Table 1
12	RHO Coefficient (ρ)	See Table 1

4.2. Areal

The areal morphometric parameters of the Koya basin define the spatial arrangement and hydrological sensitivity of the 1.911 km² basin area, a large catchment that yields significant surface runoff—crucial in determining flood characteristics and water control. The drainage density of 1.95 km^{-1} marks a moderately dissected terrain with evenly balanced infiltration and runoff, indicating neither highly permeable nor impermeable surface conditions. A stream frequency of 2.21 km^{-2} lends credence to this assumption, reflecting a moderate level of drainage activity and basin physiographic maturity. The high drainage texture value of 15.28 km^{-3} reflects rugged terrain or robust subsurface materials, which could increase runoff and exacerbate surface erosion during periods of heavy rainfall. The drainage intensity of 1.13 represents a proportional relationship between stream number and drainage density, implying a stable and cohesively functioning fluvial system. Both elongation ratio (0.51) and form factor (0.21) suggest an elongated basin shape, which is typical of lagged peak runoff and reduced flood intensity—attributes directly imputable to the third research objective of flood mitigation. Similarly, the low circularity ratio of 0.31 indicates an irregular, non-circular basin shape, which tends to spread runoff over longer periods and minimize flood concentration. The infiltration value of 4.31 indicates low potential infiltration and high runoff risk, which is vital in identifying risk zones and improving water resource planning. Overland flow length of 0.26 km, in combination with the channel maintenance constant of 0.51 km², also illustrates moderate surface roughness and levels of channel development and therefore provides essential information on landform evolution and surface water flows. This is as indicated in (Table.3).

Table 3: Summary of drainage basin areal aspect parameters in the study area.

No.	Morphometric Parameters	Result
1	Basin Area (A) (Km2)	1911 km2
2	Drainage Density (Dd)	1.95 km -1
3	Stream Frequency (Fs)	2.21 km-2
4	Drainage Texture (Dt)	15.28 km-3
5	Drainage intensity (Di)	1.13
6	Elongation ratio (Re)	0.51
7	Circularity ratio (Rc)	0.31
8	Form Factor (Rf)	0.21
9	Infiltration Number (If)	4.31
10	Length of Overland Flow (Lg)	0.26
11	Constant of channel maintenance (C)	0.51 km2

Drainage Density Map (Figure 6) illustrates the pattern of drainage density of the Koya Basin, classified into five classes from "Very Poor" to "High." High drainage density (red colors) indicates greater surface runoff and lower infiltration, which are generally found on steeper slopes or in less permeable bedrock. Very poor drainage density areas (green areas) indicate flatness or very permeable soil, which favors water infiltration and minimizes runoff.

In the lineament density map (Figure 7) of the Koya Basin, regions of high lineament density (red) occur predominantly in the northern basin. This indicates that there is high tectonic activity or structural change in the area. High fracture density tends to enhance secondary porosity and permeability, facilitating groundwater infiltration and storage. It could also provide conduits allowing contaminant flow. The central and southern areas have very low to low lineament densities (light blue and blue). That means the geologic conditions are comparatively stable with fewer fractures. Fewer fractures typically mean that there is less groundwater storage capacity and flow because of lower permeability.

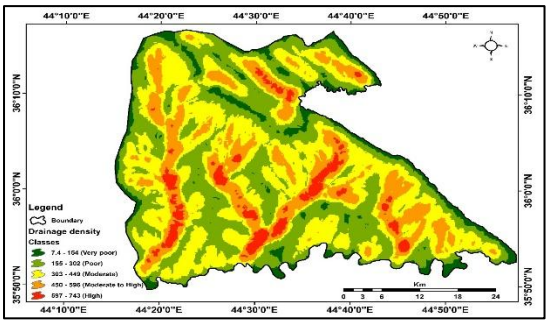


Fig. 6: Drainage density interpolation map for the study area.

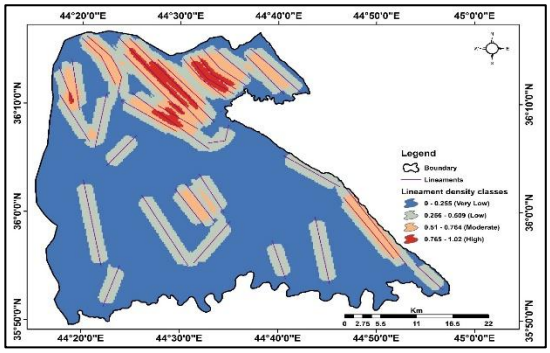


Fig. 7: Lineament density map for the study area.

The Drainage Density Map (Figure 6) spatially reinforces the numerical assessment, highlighting moderately dense drainage in elevated zones and validating the hydrological segmentation of the basin. In contrast, the Lineament Map (Figure 7) reveals the structural alignment of drainage channels, emphasizing tectonic influence and geological control, which directly aligns with the second research aim of comparing regional morphostructural characteristics. Together, these areal parameters and visual data synthesize a comprehensive understanding of the basin's form, function, and flood-related dynamics, addressing all three core research questions through both numerical and spatial perspectives.

4.3. Relief

The Koya basin exhibits a total basin relief of 1185 m, derived from a maximum elevation of 1455 m and a minimum of 270 m, as detailed in the (Table.4). This results in a relief ratio of 0.01 and a relative relief ratio of 0.01, indicating moderate overall steepness. The dissection index is 0.81, showing high levels of terrain dissection, while the ruggedness number is 2.31, reflecting moderately rugged terrain. These parameters collectively define the topographic framework for subsequent hydrologic and geomorphic processes, influencing drainage patterns and runoff dynamics.

Table 4: Summary of drainage basin relief aspect parameters in the study area.

No.	Morphometric Parameters	Result
1	Maximum height (H) (m)	1455 m
2	Minimum height (h) (m)	270 m
3	Total basin relief (Rb)	1185 m
4	Relief Ratio (Rh)	0.01
5	Relative Relief Ratio (Rr)	0.01
6	Absolute relief (Ra), m	1455 m
7	Dissection index (Di)	0.81
8	Ruggedness number (Rn)	2.31

The slope analysis, as illustrated in Fig. 8, reveals a dominance of gentle slopes (10–25°), with 1,123,765 count values, indicating that much of the district is characterized by moderately inclined terrain that promotes both runoff and infiltration. Steeper slopes (>40°) are less common, totaling 78,896 count values; these areas likely contribute to increased surface runoff and erosion potential. The distribution of slopes affects surface runoff and infiltration rates, thereby influencing streamflow dynamics and groundwater recharge.

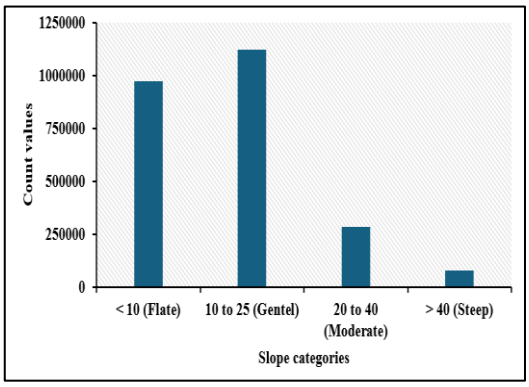


Fig. 8: Histogram showing the slope distribution for the study area.

Topographic slope distribution affects hydrological response, such as variability of streamflow and potential groundwater recharge, directly, as evidenced by work that links topography with the behavior of runoff and aquifer recharge. The distribution of topography can simply be observed on the map of slopes (Fig. 9), which classifies the slopes into five categories. On the map, the dominance of gentle slopes is indicated in green, dominating most of the study area. This prevalence of gentle slopes suggests a landscape of infiltration rather than rapid runoff, resulting in groundwater recharge and reduced flood risk in those green-dominated regions, whereas steeper slopes, colored orange and red, occur in the northern regions.

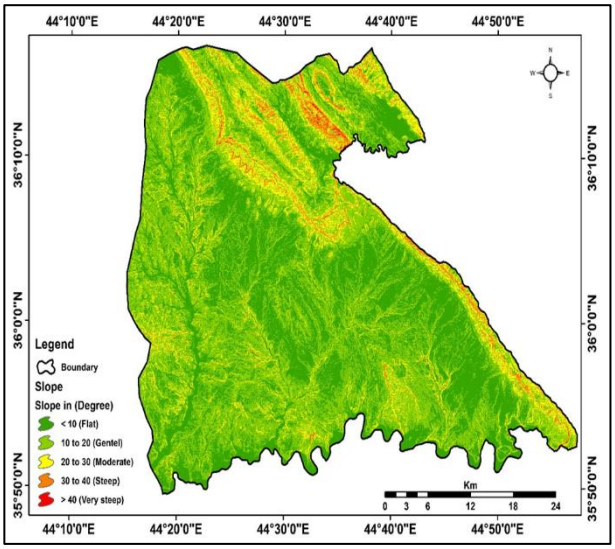


Fig. 9: Slope Map for the study area.

Aspect analysis, as in Fig. 10, indicates a prevalence of southwest-facing slopes (471,267 count values), potentially leading to increased evapotranspiration and reduced soil moisture on these slopes. This directional trend can influence microclimatic conditions, affecting vegetation patterns and, consequently, hydrological processes such as surface runoff and streamflow.

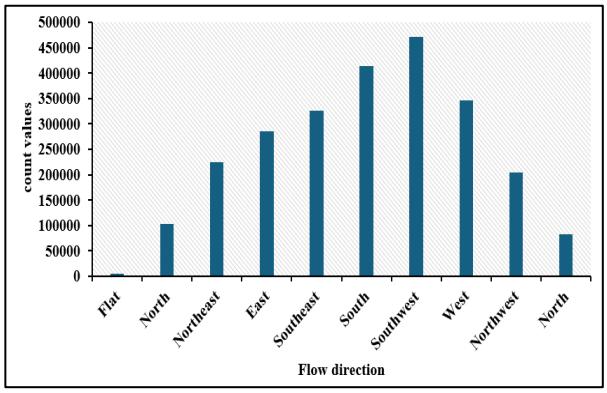


Fig. 10: Histogram showing the slope distribution (Aspect) for the study area.

This is visually supported by the flow direction (aspect) map (Fig.11), which clearly illustrates the spatial distribution and prevalence of southwest-facing slopes throughout the Koya basin. The map's color-coding, with a concentration of yellow indicating southwest-facing aspects, vividly highlights the area's most susceptible areas to direct sunlight. Furthermore, the flow-direction arrows converge along these southwest-facing slopes, suggesting a concentration of surface runoff and a potential for increased erosion in those specific locations.

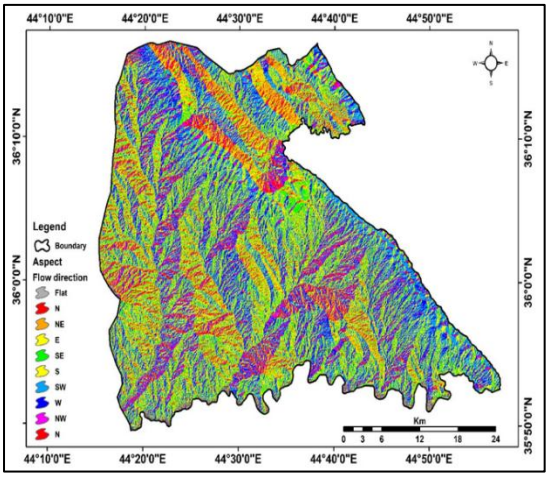


Fig. 11: Flow direction Map of the study area.

The hypsometric analysis shown in Table 5 provides an estimate of the hypsometric integral as 0.47 and hence shows the basin to be at a mature phase of development. The S-shaped hypsometric curve revealed in Fig. 12 represents an environment where the middle elevations have the largest contribution to the area of the basin. A shape of this type represents dynamic equilibrium between erosional and depositional activity, with moderate transport and sediment yield in the basin. This affects long-term water resources availability and control within the basin because a well-balanced sediment regime is vital to maintaining water quality and reservoir capacity.

Table 5: Summary of drainage basin areal aspects parameters in the study area

Value	Area (km^2)	Min	Max	Range	Mean	Mean-Min	H-integral	accumulation area (a)	a/A	h	h/H
1	172.58	270	388	118	349.48	79.48	0.67	1912.56	1.00	118.00	0.10
2	483.44	389	507	118	454.86	65.86	0.56	1739.98	0.91	236.00	0.20
3	570.42	508	625	117	563.83	55.83	0.48	1256.54	0.66	353.00	0.30
4	270.91	626	744	118	675.88	49.88	0.42	686.12	0.36	471.00	0.40
5	159.59	745	862	117	800.70	55.70	0.48	415.21	0.22	588.00	0.50
6	118.53	863	981	118	919.60	56.60	0.48	255.62	0.13	706.00	0.60
7	84.21	982	1099	117	1035.93	53.93	0.46	137.09	0.07	823.00	0.70
8	39.22	1100	1218	118	1147.02	47.02	0.40	52.88	0.03	941.00	0.80
9	10.92	1219	1336	117	1268.12	49.12	0.42	13.67	0.01	1058.0	0.90
10	2.75	1337	1455	118	1374.37	37.37	0.32	2.75	0.00	1176.0	1.00

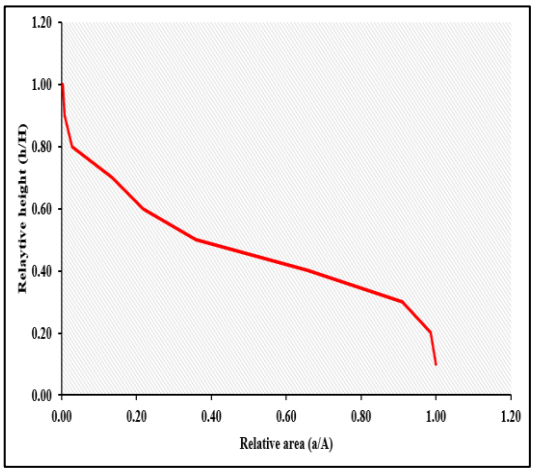


Fig. 12. Hypsometric Curve.

5. Conclusion and Discussion

The hydromorphometric analysis of the Koya basin reveals a landscape shaped by structural controls and climatic dynamics. The basin's elongated geometry (form factor = 0.21) and sixth-order drainage network, dominated by first-order streams, reflect a balance between erosional processes and tectonic influences, as evidenced by high bifurcation ratios (Rb = 5.13) and lineament density in the northern regions. Moderate drainage density (1.95 km^{-1}) and elevated infiltration numbers (If = 4.31) indicate susceptibility to rapid runoff, particularly on steep, southwest-facing slopes where erosion and evaporation are pronounced. A comparative assessment aligns Koya's hydromorphometry with tectonically active basins in Erbil and Kirkuk, yet its unique relief (1,185 m) and dissection index (0.81) distinguish it as a mature but dissected terrain.

These findings underscore the need for integrated water management strategies. Prioritizing afforestation in high-density drainage zones, constructing erosion-control structures in rugged northern areas, and promoting infiltration practices in permeable southern regions can mitigate flood risks and enhance groundwater sustainability. The study establishes a foundational framework for basin-scale hydro-morphometric analysis in semi-arid regions, bridging critical gaps in the existing literature. Future work should integrate hydrological modelling and field validation to refine flood hazard mapping and optimize resource allocation in Koya's complex terrain.

6. Acknowledgements

We would like to extend our heartfelt thanks to the Department of Earth Sciences and Petroleum at Salahaddin University, whose support and guidance were invaluable throughout the course of this research. This work would not have been possible without the valuable insights and encouragement provided by our colleagues and academic mentors

7. Conflict Of Interest

We declare that there is no conflict of interest regarding the conduct or publication of this research.

8. Funding Statement

This research received no external funding.

9. Author Contributions

Ala Qader: Conducted the research, processed and analyzed the ALOS PALSAR DEM data using GIS techniques, delineated the drainage basin and stream network, calculated the linear, areal, and relief morphometric parameters, prepared the maps, figures, and tables, interpreted the results, and prepared and wrote the manuscript.

Shwan Seeyan: Supervised the research, provided scientific guidance throughout the study, contributed to the interpretation and discussion of the results, and reviewed and revised the manuscript.

Both authors contributed to the final review and approval of the manuscript.

10. References

Ahmed, A., Al Maliki, A., Hashim, B., Alshamsi, D., Arman, H., and Gad, A., 2023. Flood susceptibility mapping utilizing the integration of geospatial and multivariate statistical analysis, Erbil area in Northern Iraq as a case study. Scientific Reports, 13(1), 11919.

Ahmed, H.A.K. and Jirjees, S.J., 2022. Morphometric Analysis of Taqtaq Watershed/Koysinjaq District, Iraqi-Kurdistan Region. Zanco Journal of Human Sciences, 26(2), pp. 206–220.

Al-Saady, Y.I., Al-Suhail, Q.A., Al-Tawash, B.S., and Othman, A.A., 2016. Drainage network

extraction and morphometric analysis using remote sensing and GIS mapping techniques (Lesser Zab River Basin, Iraq and Iran). Environmental Earth Sciences, 75(18). https://doi.org/10.1007/s12665-016-6038-y

Al-Tamimi, O.S., Abo-Khomra, N.K., and Othman, A.A., 2022. Delineate the hydrological boundaries situation using the morphometric analysis and geological features: A case study of Laylan sub-basin, Kirkuk/NE Iraq. IOP Conference Series: Earth and Environmental Science, 1120(1), 012013.

Chorley, R.J., 1957. Climate and Morphometry. The Journal of Geology, 65(6). https://doi.org/10.1086/626468

Faniran, A., 1968. The index of drainage intensity: a provisional new drainage factor. Aust J Sci, 31(9), pp. 326–330.

Fatah, K.K., Seeyan, S., and Jirjees, S., 2020. Morphometric analysis using geo-information techniques for different watersheds in northeastern part of Erbil City, Kurdistan Region, North Iraq. The Iraqi Geological Journal, 88–104.

Ghafour, B.D., Hamawandy, M.J., and Sissakian, V.K., 2024. Geotechnical Assessment of the Slopes of Hamamok Dam, NE of Koya, Kurdistan Region of Iraq. ARO-The Scientific Journal of Koya University, 12(1), pp. 181–190.

Goran, R.A. and Khattab, M.F.O., 2023. Hydro-Morphometric Characters of Watershed Heshkaro River in Duhok City, Kurdistan Region, Northern Iraq Using Geospatial Techniques. The Iraqi Geological Journal, pp. 194–206.

Gregory, K.J. and Wallingford, D.E., 1973. Drainage Basin Form and Process - A Geomorphological Approach, https://doi.org/10.1016/0043-1354(74)90155-9

Mohammed, A.H., Mohammed, A.A., Salih, S.A., and Salih, A.M., 2026. Hydro-morphometric and Hydrochemical Criteria to Select the Optimal Location for Small Dam in Um Al-Shibabit Valley, Al-Shirqat, Northern Iraq. In Iraqi National Journal of Earth Science. https://doi.org/10.33899/injes.v26i1.60179

Haris, A., Hamma, H., Abdwllah, D., Bibani, M., Muhealddin, H., Mustafa, H. K., Sissakian, H., Al, V., Sadiq, S., Muhmed, A., Govar, H., Haris, G., Mohammed, D., Majeed, M., Halmat, H., Muhealddin, H., Mustafa, H., Sissakian, V., and Al-Ansari, N., 2016. Mechanism of Haibat Sultan Mountain Landslide in Koya, North Iraq. Engineering, 8, pp. 535–544. https://doi.org/10.4236/eng.2016.88050

Horton, R.E., 1945. Erosional development of streams and their drainage basins: Hydrophysical approach to quantitative morphology. Bulletin of the Geological Society of America, 56(3). https://doi.org/10.1130/0016-7606(1945)56[275:EDOSAT]2.0.CO;2

Melton, A., 1957. An Analysis of the Relations Among Elements of Climate, Surface Properties, and Geomorphology. Technical Report (United States. Office of Naval Research), 11.

Miller, V.C., 1953. A quantitative geomorphic study of drainage basin characteristics in the Clinch Mountain area, Virginia and Tennessee. Department of Geology, Columbia University, New York.

Moore, I.D., Grayson, R.B., and Ladson, A.R., 1991. Digital terrain modelling: A review of hydrological, geomorphological, and biological applications. Hydrological Processes, 5(1). https://doi.org/10.1002/hyp.3360050103

Patel, D. P., Gajjar, C. A., and Srivastava, P. K., 2013. Prioritization of Malesari mini-watersheds through morphometric analysis: A remote sensing and GIS perspective. Environmental Earth Sciences, 69(8). https://doi.org/10.1007/s12665-012-2086-0

Schumm, S.A., 1956. Evolution of drainage systems and slopes in badlands at Perth Amboy, New Jersey. Bulletin of the Geological Society of America, 67(5). https://doi.org/10.1130/0016-7606(1956)67[597:EODSAS]2.0.CO;2

Smith, K.G., 1950. Standards for grading texture of erosional topography. American Journal of Science, 248(9). https://doi.org/10.2475/ajs.248.9.655

Strahler, A.N., 1952. Hypsometric (area-altitude) analysis of erosional topography. Bulletin of the Geological Society of America, 63(11). https://doi.org/10.1130/0016-7606(1952)63[1117:HAAOET]2.0.CO;2

Strahler, A.N., 1957. Quantitative analysis of watershed geomorphology. Eos, Transactions American Geophysical Union, 38(6). https://doi.org/10.1029/TR038i006p00913

Strahler, A.N., 1964. Quantitative Geomorphology of Drainage Basin and Channel Networks. Handbook of Applied Hydrology.

Wilson, J.P., and Gallant, J.C., 2000. Terrain Analysis: Principles and Applications. John Wiley and Sons.

Iraqi National Journal of Earth Science, Vol. 26 No. 04, 2026 (161-174)

Iraqi National Journal of Earth Science

www.earth.uomosul.edu.iq

التحليل الهيدرومورفومتري لحوض كويا في إقليم كردستان العراق

نالا قادر [1]* ، شوان سييان [2]

ala.qadir@su.edu.krd shwan.seeyan@su.edu.krd

[1] قسم علوم الأرض والنفط، كلية العلوم، جامعة صلاح الدين، أربيل، العراق.

[2] قسم علوم التربة والمياه، كلية الزراعة، جامعة صلاح الدين، أربيل، العراق.

**الباحث المراسل.*

تاريخ الاستلام: 23 أيار 2025 تاريخ المراجعة: 29 تموز 2025 تاريخ القبول: 15 تشرين الأول 2025

تاريخ النشر الالكتروني: 01 تشرين الأول 2026

الملخص

تجري هذه الدراسة تحليلا هيدرومورفومتريا شاملا لحوض كويه ، إقليم كردستان العراق باستخدام بيانات ALOS PALSAR DEM والتقنيات القائمة على نظم المعلومات الجغرافية لتقييم معلامات الارتفاع والخطية والمساحية. يتميز الحوض الممدود (عامل الشكل = 0.21) بشبكة تصريف من الدرجة السادسة تهيمن عليها جداول الرتبة الأولى ، مع نسبة تشعب عالية (متوسط Rb = 5.13) تشير إلى تحكم التركيبة في أنماط الصرف. تعكس كثافة الصرف المعتدلة (1.95 كم⁻¹) ورقم التسلل (4.31) معامل ارتشاح متوازنا ولكن إمكانات الجريان السطحي المرتفعة ، بينما تؤكد التضاريس الوعرة (درجة الوعورة = 2.31) والتضاريس الكبيرة (1،185 مترا) التعقيد الطبوغرافي. يكشف التحليل المقارن عن أوجه تشابه مع الأحواض المتأثرة تكتونيا في أربيل وكركوك، على الرغم من أن تكامل قياس الارتفاع في كويا (0.47) ومؤشر قياس درجة خشونة سطح الأرض (0.81) يشيران إلى مشهد ناضج ولكنه يتطور ديناميكيا. تحدد درجة ميل واتجاه الميل للاراضي والجوانب المنحدرات المواجهة للجنوب الغربي كنقاط ساخنة للتعرية وتقليل الاحتفاظ برطوبة التربة. تسلط النتائج الضوء على التفاعل بين الجيومورفولوجيا والهيدرولوجيا ، مع التأكيد على أن هندسة الحوض الممدود تخفف من شدة الفيضانات ، في حين أن المناطق ذات كثافة التصريف العالية تتطلب إدارة مستهدفة. تقدم هذه الدراسة أول تقييم هيدرومورفومتري على مستوى المنطقة لحوض كويه ، وتقدم رؤى مهمة لصانعي السياسات لتحسين إدارة الاحواض المائية ، وإعطاء الأولوية للتخفيف من حدة الفيضانات في المناطق النشطة تكتونيا ، وتعزيز استراتيجيات إعادة تغذية المياه الجوفية في البيئات شبه القاحلة.

الكلمات المفتاحية:

قياس الهيدرومورفوميات، المنطقة شبه القاحلة، تغذية المياه الجوفية، إدارة موارد المياه الجوفية.

DOI: 10.33899/injes.v26i4.56166, ©Authors, 2026, College of Science, University of Mosul.

This is an open-access article under the CC BY 4.0 license (http://creativecommons.org/licenses/by/4.0/)

Iraqi National Journal of Earth Science, Vol. 26, No. 04, 2026 (175-183)

Iraqi National Journal of Earth Science

www.earth.uomosul.edu.iq

Study of Radon Concentration in Well Water in the Districts of Kirkuk Governorate

Lana H. Mohammed [1], Alyaa H. Mohammed [2], Ebtihal G. Khidher [2*], Mohammed Ahmed Omar [3]

lanahedayet@uokirkuk.edu.iq alyaahussein@uokirkuk.edu.iq e.gh.abbosh@uokirkuk.edu.iq mohammedahmedomer@uokirkuk.edu.iq

[1] *Department of Physics, College of Education for Women, University of Kirkuk, Kirkuk, Iraq.*
[2] *Department of Physics, College of Education for Pure Science, University of Kirkuk, Kirkuk, Iraq.*
[3] *Health, Safety and Environment Authority, North Gas Company, Kirkuk, Iraq.*
** Correspondence author.*

Received: 13 May 2025 Received in revised form: 03 September 2025 Accepted: 02 November 2025
Available online: 01 October 2026

Abstract

This study evaluates the radon ^{222}Rn concentrations in well water from seven districts (Qara Hanjir, Yaychi, Taza, Laylan, Altun Kupri, Dibis and Hawija) of Kirkuk Governorate, Northern Iraq, using the RAD7–H_2O dosimeter. A total of 21 samples were collected (three from each district): Qara Hanjir, Yaychi, Taza, Laylan, Altun Kupri, Dibis, and Hawija. This study is motivated by the fact that radon in groundwater is a significant source of natural radiation exposure, with potential health effects such as lung and stomach cancer if concentrations exceed the international safety limits. The measured radon concentrations ranged from 7.93 Bq\l in Altun Kupri to 18.7 Bq\l in Dibis District. According to the United States Environmental Protection Agency (USEPA) guideline of 11 Bq. l^{-1}, only Taza and Altun Kupri were within the permissible limit, while the other districts exceeded it. The annual effective dose of inhalation ranged from 0.020 $mSv.y^{-1}$ in Altun Kupri to 0.047 $mSv.y^{-1}$ in Dibis, whereas the ingestion dose varied from 1.67 $mSv.y^{-1}$ in Altun Kupri to 3.92 $mSv.y^{-1}$ in Dibis. Compared with the international standards, inhalation doses remained well below the permissible limits, while ingestion doses in some districts (Dibis and Laylan) slightly exceeded the ICRP lower threshold (3 $mSv.y^{-1}$), just above the UNSCEAR global average (1.15 $mSv.y^{-1}$). The calculated excess lifetime cancer risk (ELCR) values are within acceptable ranges, indicating a limited long-term risk from inhalation exposure, but ingestion exposure requires continuous monitoring.

Keywords:

RAD7, Radon concentrations, Pollution; Groundwater.

DOI: 10.33899/injes.v26i4.56209, ©Authors, 2026, College of Science, University of Mosul.
This is an open-access article under the CC BY 4.0 license (http://creativecommons.org/licenses/by/4.0/).

==========

1. Introduction

Radioactive pollution is the most common and dangerous kind of pollution. This is a result of the nuclear industry's growth, the use of nuclear energy, the amount of radioactive waste produced by the industry, the use of nuclear energy to generate electricity, and the use of radioisotopes in industry, research, medicine, and agriculture. Radionuclides can arise in two ways: either organically and spontaneously as a result of natural radioactivity, or artificially through man-made intervention in the form of radioactive nuclides (Mdekil et al., 2024). Naturally radioactive elements in the earth's crust, energy streams entering the atmosphere, and the byproducts of radioactive decay are the main causes of natural radiation. Hawas et al. (2024) said that "These radionuclides can be present in both surface water and groundwater, as they originate from rocks and soils that contain naturally occurring radioactive materials". Sabbarese et al. (2021) declared that Radium, uranium, and radon isotopes are among the common radionuclides found in sources of drinking water. Another source is fission products resulting from human action.

Taher et al. (2024) explained that Radon is considered a colorless, odorless, tasteless, and radioactive noble gas, naturally formed as a byproduct of uranium decay, and it is the main source of more than 50% of the natural radiation humans are exposed to. The concentrations of radon in groundwater are determined by the level of radium in the rocks that make up the aquifers (Makolli et al., 2025), where dissolved radon is produced by the presence of natural uranium in the soil and rocks that interact with water (Caridi et al., 2016).

In Iraq, in recent years, wars have exacerbated radioactive contamination due to the use of depleted uranium and the looting of nuclear facilities, causing significant damage to public life, including water pollution. Therefore, water systems exposed to this type of contamination require careful monitoring to ensure that drinking water is free from any radioactive contamination (Shlioh and Saleh (2018); Abad Ibrahim et al. (2017); Ahmed et al. (2019); Abojassim (2020); Hawas et al. (2024b)).

Recent years have seen a growing focus on the study of natural radioactivity in water. In Dhi-Qar Marzaali et al.(2021) used the RAD7–H_2O dosimeter and reported radon concentrations between 0.032 and 0.78 $Bq.l^{-1}$, all within acceptable limits based on international standards. In Haditha City, radon concentrations in 22 water samples collected from three districts and the Euphrates River varied from 0.0091 to 0.031 $Bq.l^{-1}$, with corresponding annual effective doses of 0.033–0.113 $\mu Sv.y^{-1}$, also well below the WHO and USEPA standards (Al-Paruany et al., 2022). In Baghdad (Al-Bayaa region), another study measured radon in both tap and well water, with concentrations ranging from 2.30 to 5.60 Bq\land annual effective doses of 8.40–20.4 $\mu Sv.y^{-1}$, which were all below the WHO limits (Jameel, 2023). More recently, a study conducted in Baghdad by Abdulkhaleq et al. (2024) showed that radon levels in 15 bottled drinking water samples varied widely from 3.5 to 74 $Bq.m^{-3}$, as measured by the RAD7 technique. Collectively, these studies indicate that radon concentrations in Iraqi drinking water sources are generally within international safety limits, although local variations are evident depending on geological and hydrological conditions. The present study aims to determine the concentrations of radon (^{222}Rn) in well water from seven districts of Kirkuk Governorate using the RAD7–H_2O dosimeter. It further seeks to evaluate the annual effective doses from ingestion and inhalation of radon and to estimate the excess lifetime cancer risk (ELCR). The results are compared with international safety standards set by USEPA, ICRP, and UNSCEAR to assess the potential radiological health risks associated with groundwater consumption in the study area.

2. Study Area

Kirkuk is one of the major cities in Iraq due to its extensive oil fields and ancient geological formations rich in naturally occurring radioactive materials (NORM), such as uranium and thorium. These elements decay into 226Ra and 222Rn, which may be released into groundwater. Previous studies (e.g., Zaidan, 2010) have shown that formation water and oil-associated sludge can contain high concentrations of these radionuclides. Therefore, Kirkuk provides an ideal environment for monitoring and evaluating natural radiation associated with oil industry activities. In this study, water samples were collected from seven districts across the governorate. Qara Hanjir District, located northeast of Kirkuk, is one of the province's main agricultural regions. Yaychi District, situated to the southwest, is known for its cultivation of grains and vegetables. Taza District, positioned south of Kirkuk, is characterized by its fertile soil and diverse agricultural production. Laylan District, in the east, relies heavily on well water for irrigation, making it a significant agricultural area. Altun Kupri District, found in the northwest, is notable for growing various crops. Dibis District, located west of Kirkuk, is considered a vital agricultural zone. Lastly, Hawija District, in the southwest, is known for its extensive agricultural lands. The geographical distribution of these districts in relation to the administrative divisions of Kirkuk is illustrated in Fig. 1.

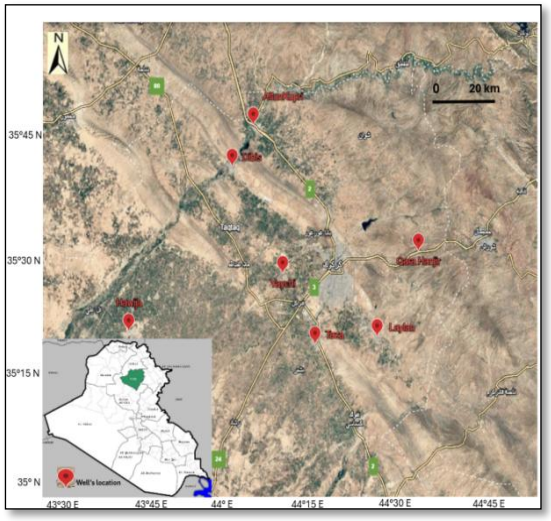


Fig. 1: The Map of Iraq and the locations of samples of well water from Kirkuk Governorate.

3. Methodology

In this research, we measured the concentration of radon gas in water using the RAD7 system. An electronic radon monitor (Rad7–H_2O, Durridge Co., USA) is what makes RAD7 a reliable method for radon detection (Salih, 2021; Hawas et al., 2024a). This device is specially made to determine with high precision the amount of radon gas present in water. It operates based on a solid-state ion-implanted silicon detector that converts alpha radiation into electrical signals. The key feature of the RAD7 system is its ability to electronically determine the energy of each alpha particle emitted by radon progeny (^{218}Po and ^{214}Po), thereby allowing accurate identification of the isotopes involved and quantification of radon concentration in the sample. Measurements are performed using the RAD-H_2O dosimeter, which is connected to the RAD7 unit. Prior to analysis, the system is dried by circulating air through a desiccant in a closed loop for 10 minutes until humidity drops below 6%. Once the system is ready, the measurement begins by transferring radon from the water sample into the air loop via a five-minute aeration process. This process ensures that approximately 94% of radon is extracted from the water, depending slightly on ambient temperature, and generally remains above 90% efficiency. The RAD7 system then performs four five-minute measurement cycles, during which radon decay products are detected and analyzed. The RAD7 is capable of distinguishing newly captured radon from residual radon left from prior analyses (Subberet and Ali, 2012). The system records output average radon concentration, standard deviation, time and date of measurement, procedure type, and number of cycles after each test.

Standard deviation (SD) is a measure of how dispersed data are around the mean. That is, it shows how far values vary from the mean. The use of Standard Deviation in analyzing radon concentration data measures the variability of radon concentrations in different areas; the standard deviation helps determine the stability or fluctuation of radon concentration in water. Kareem et al. (2020) state that if the standard deviation is low, this means that the radon concentration in all samples is similar, and therefore there is consistency in the data; but if the standard deviation is high, this indicates significant variations between samples, which may indicate the presence of variable sources of radon leakage into the water. We use the equation (1) from Abojassim (2020)

$$SD = \sqrt{\frac{\sum(X_i - \bar{X})^2}{N-1}} \qquad (1)$$

Where SD is the standard deviation, x_i , $\bar{x}$ and N are the count, average, and number of samples, respectively.

Radon is introduced into the human body via ingestion and inhalation, as it is released from water into the air. Radon in water contributes to radiation exposure in the stomach and lungs. For ingestion, the annual effective dose is calculated using the formula (2) (Kandari et al., 2016):

$$E_{ing}(\frac{mSv}{y}) = C_w \times C_{Rn} \times EDC \qquad (2)$$

whereE_{ing} is the effective dose from ingestion (Sv),$EDC$is the ingesting dose conversion factor of ^{222}Rn 3.5nSv/Bq (for adults); C_{Rn} is the radon concentration in Becquerels per liter, C_w is the water consumption (60 liters per year).

To calculate the annual effective dose resulting from inhaling radon gas from drinking water, we use the following equation (3): Duggal et al. (2013)

$$E_{inh} = C_{Rn} \times R_{aw} \times F \times O \times DC \qquad (3)$$

Where E_{inh} is Effective dose from inhaling radon in unit of Sv, $C_{Rn}$is the radon concentration in the water,R_{aw}= 10-4 l/m3 Radon transfer rate from water to air, F- is Equilibrium coefficient between radon and its radioactive decay products was equal to 0.4;O- is average time spent indoors = 7000 h/y;DCF- is Radon dose conversion factor = 9 nSv (Bqhm-3)$^{-1}$. Excess lifetime cancer risk (ELCR) is determined using the following equation (4) based on calculated values of annual effective dose (AED) (Aswood et al., 2022)

$$ELCR = AED\ (\frac{mSv}{y}) \times DL\ (y) \times RF\ (\frac{1}{Sv})\ (4)$$

Where DLis life expectancy (=70 y); is RF: risk factor (=0.055 Sv-1)

We have collected seven water samples (each with a volume of 450 ml) from different districts within Kirkuk Governorate, located in northern Iraq. From each selected well, three water samples were obtained using either hand pumps, tube wells, deep dug wells exceeding 50 meters, or domestic water taps connected to groundwater sources at similar depths, after allowing water to run for 10 minutes to ensure sample freshness. All samples were stored in filled, tightly sealed containers to minimize air gaps and prevent radon gas loss. Subsequently, the samples were analyzed using the RAD7 device to determine radon gas concentrations. The water sampling followed a purposive sampling approach, targeting wells located in districts surrounding Kirkuk Governorate. These areas were deliberately chosen due to their geological features, including the presence of sedimentary rocks and oil-bearing formations known to contain natural radionuclides such as uranium and thorium, which may lead to elevated levels of radon in groundwater. This strategy ensured a representative evaluation of radon distribution across the studied region.

The RAD-7 dosimeter consists of a semiconductor material (Diab,2019). It fundamentally comprises a periodic-fill cell. This cell is filled with air through a small opening.

A pump draws air into the cell once at each pre-selected interval for the decay of radon or ^{218}Po, allowing for counting, after which the cycle is repeated. The RAD-7 device operates on the basis of a solid-state detector. This device is a silicon ion-implanted Dosimeter that utilizes semiconductor material to convert radiation into an electrical signal. One advantage of solid-state Dosimeters for radon or its progeny is their ability to electronically discriminate the energy associated with incoming alpha radiation, as shown in Fig. 2.

In this context, specific radionuclides can be identified, such as ^{218}Po, which has an alpha energy of 6.00 MeV, and ^{214}Po, with an energy of 7.69 MeV. The RAD7 device (commonly used with the RAD H_2O accessory) measures radon in water samples over a range of concentrations from less than 10 pCi.l^{-1} up to greater than 400 pCi · L-1 (Abdulkhaleq et al., 2024). The equipment is both portable and battery-operated, facilitating rapid measurements. An accurate radon measurement in water can be obtained within one hour of sampling. The RAD H_2O provides results following a 30-minute analysis, demonstrating sensitivity that is comparable to or surpasses that of liquid scintillation methods. In a 5-minute aeration process, the available radon is eliminated from the water (Kareem et al., 2020).

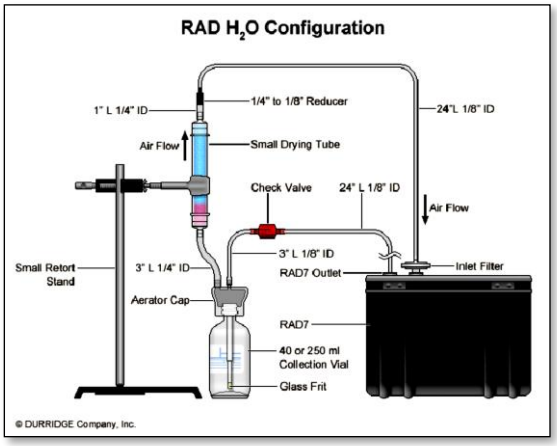


Fig. 2: RAD7 H_2O device and measurement system of radon gas in water.

4. Results and Discussion

A. Radon concentration

The findings about radon concentration in 21 groundwater samples obtained from 7 wells across the districts and sub-districts of Kirkuk Governorate, Iraq, are presented in Table 1. The radon concentration ranges from 7.93 Bq/L in Altun Kupri District to 18.70 Bq/L in Dibis District; see Fig. 3. The permissible maximum concentration level for ^{222}Rn in water is 11 Bq/L recommended by the US Environmental Protection Agency (USEPA) and Al-Hamadwi et al. (2012). In this study, all values found were higher than international standards except in Taza and Altun Kupri Districts. The fluctuations in radon concentration may be attributed to the geological structure of the region, the depth of the water source, and variations in climate (Duggal et al., 2013)

Table 1: The Radon concentrations and the locations of well water samples in some districts in Kirkuk

No	Location	Mean Concentration (Bq/l)	Standard Deviation	SD % of Mean
1	Qara Hanjir District	10.83	0.35	3.2
2	Yaychi District	13.03	0.32	2.4

3	Taza District	9.2	0.30	3.2
4	Laylan District	15.87	0.31	1.9
5	Altun Kupri District	7.93	0.15	1.8
6	Dibis District	18.7	0.40	2.1
7	Hawija District	12.13	0.25	2.0

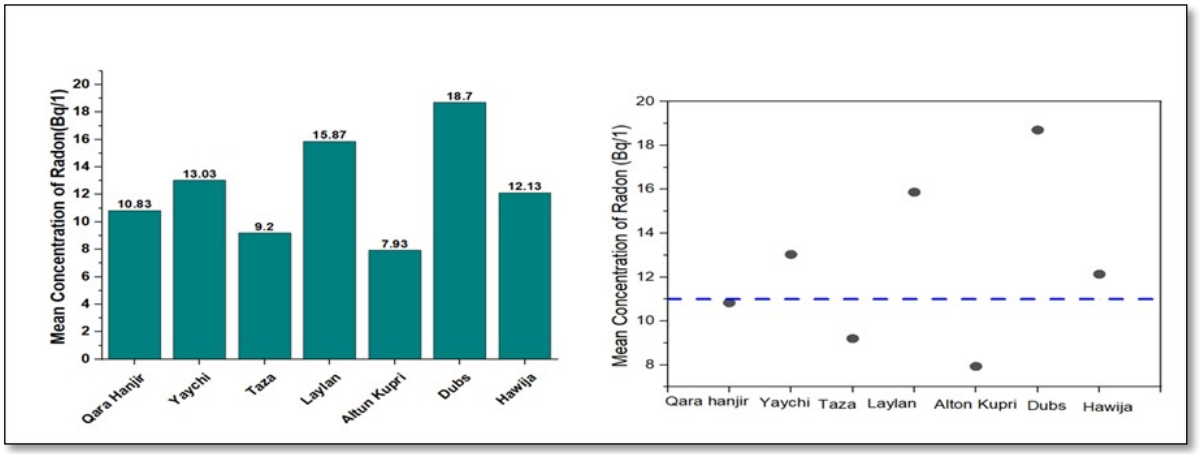


Fig. 3: Radon Concentration in the well water samples; the blue dashed line represents the maximum permissible concentration level for 222Rn in water by (USEPA).

Table 2 presents the variation in radon concentrations in different districts by calculating the standard deviation (Fig. 4). The results show that the standard deviation values, expressed as a percentage of the mean, are generally low, with a range of (1.8%–3.2%), suggesting good consistency among the measurements across the study area.

Table 2: The Standard Deviation and the locations of the well water samples.

No	Location	Coordinates (Lat, Long)	Elevation (m)	Radon Concentration Bq/l			MEAN
1	Qara Hanjir	35°29'35"N, 44°38'20"E	762.35	10.5	11.2	10.8	10.83
2	Yaychi	35°26'47"N, 44°13'50"E	260.19	12.8	13.4	12.9	13.03
3	Taza	35°17'58"N, 44°19'42"E	239.18	8.9	9.5	9.2	9.2
4	Laylan	35°18'53"N, 44°30'54"E	336.98	15.6	16.2	15.8	15.87
5	Altun Kupri	35°45'24"N, 44°08'31"E	257.48	7.8	8.1	7.9	7.93
6	Dibis	35°40'12"N, 44°04'40"E	248.78	18.3	19.1	18.7	18.7
7	Hawija	35°19'29"N, 43°46'00"E	191	11.9	12.4	12.1	12.13

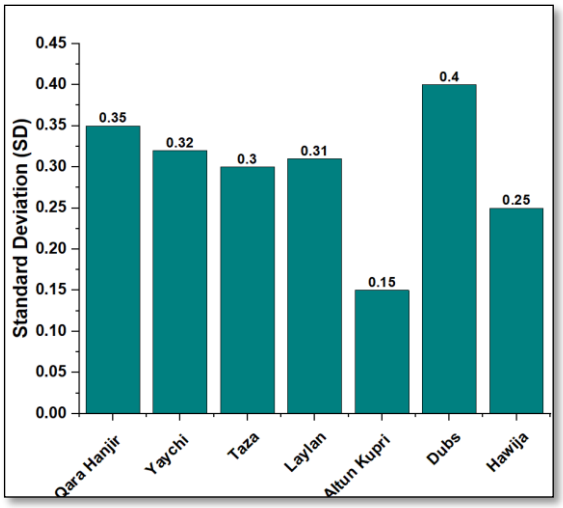


Fig. 4: Standard deviation and the locations of the well water samples.

B. The annual effective dose

The annual effective doses resulting from the ingestion and inhalation of radon in groundwater across different districts were assessed and compared to the international standards established by the International Commission on Radiological Protection (ICRP) and the United Nations Scientific

Committee on the Effects of Atomic Radiation (UNSCEAR). The ICRP recommends a yearly effective dose from natural radiation exposure between 3 and 10 mSv/year, whereas UNSCEAR estimates the global average annual effective dose from natural radionuclide intake to be around 1.15 mSv/year (Kandari et al., 2016)

The annual effective doses for inhalation and ingestion are presented in Table 3. The annual dose for ingestion ranges from 1.67 mSv/y in Altun Kupri District to 3.92 mSv/y in Dibis District. It was found that the Dibis and Laylan Districts slightly exceed the minimal ICRP action level threshold of 3 mSv/y,

while all districts exceed the UNSCEAR limits. The calculated inhalation doses were significantly below the thresholds established by ICRP and UNSCEAR, with values ranging from 0.020 to 0.047 mSv/y. (Figs. 5 and 6).

Table 3: mean Radon concentrations and Ingestion doses with Inhalation doses of the well water samples in the Kirkuk Governorate

No	Location	Mean Concentration (Bq/1)	Ingestion Dose (mSv/y)	Inhalation Dose (mSv/y)
1	Qara Hanjir	10.83	2.27	0.027
2	Yaychi	13.03	2.74	0.033
3	Taza	9.2	1.93	0.023
4	Laylan	15.87	3.33	0.040
5	Altun Kupri	7.93	1.67	0.020
6	Dibis	18.7	3.92	0.047
7	Hawija	12.13	2.55	0.030

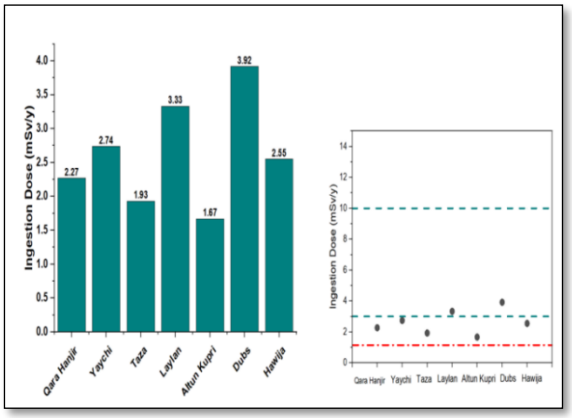


Fig. 5: Ingestion Doses of Radon gas in well water samples and the locations in some districts in Kirkuk Governorate; the green dashed line is the recommended effective dose by ICRP, and the red dashed line is for UNSCEAR.

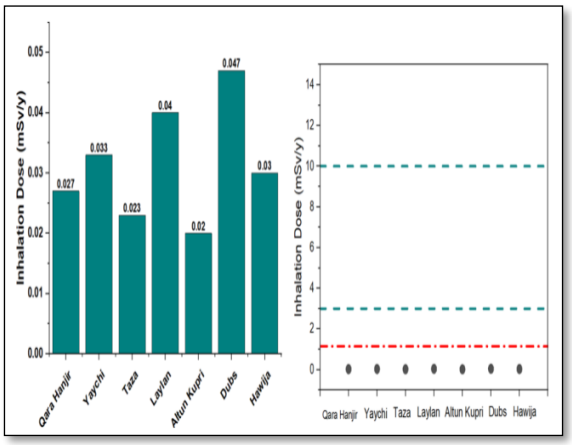


Fig. 6: Inhalation Doses of Radon gas in well water samples in the locations of the districts in Kirkuk Governorate; the green dashed line is the recommended effective dose by ICRP and the red dashed line is for UNSCEAR.

The data characteristics presented in Table (4) show how the radon gas (^{222}Rn) concentrations, annual effective inhalation dose, and excess lifetime cancer risk (ELCR) are identified across the studied districts to be very diverse. The excess lifetime cancer risk and the annual inhalation dose are found to be directly correlated based on Eq. (4). The ELCR results are within the safe range because the inhalation dose is less than the permissible limit (Cousins et al., 2010)

The presence of radon gas (^{222}Rn) in groundwater samples from the studied districts of Kirkuk can be primarily attributed to the region's geological structure. Kirkuk is known for its oil-bearing formations and sedimentary rocks, which often contain uranium (^{238}U) and thorium (^{232}Th), the parent isotopes of ^{226}Ra and ^{222}Rn. As these radionuclides undergo natural radioactive decay, radon gas is released and can migrate through fractures and pores into surrounding aquifers.

Moreover, studies have shown that radon concentrations in groundwater are positively correlated with the uranium content of local rocks and soils. According to the UNSCEAR (2000) report (Charles, 2001), the sedimentary formations, especially those rich in organic matter, phosphate, or clay, are more likely to contain uranium and therefore generate radon over time. This geological context explains the spatial variability of radon levels across the sampled areas.

Given that some districts in Kirkuk exceed the international safety limit for radon in drinking water (11 Bq/L as recommended by the USEPA), periodic monitoring of radon levels is essential. Regular assessment helps track variations caused by geological factors or industrial activities and supports health risk evaluations related to chronic radon exposure through ingestion or inhalation, ultimately contributing to public safety in at-risk regions.

Table 4: Results of annual effective dose and excess lifetime cancer risk

No.	Location	Mean Concentration (Bq/1)	Inhalation Dose (mSv/y)	Excess lifetime cancer risk (ELCR $\times 10^{-3}$)
1	Qara Hanjir District	10.83	0.027	0.105
2	Yaychi District	13.03	0.033	0.126
3	Taza District	9.2	0.023	0.089
4	Laylan District	15.87	0.040	0.153
5	Altun Kupri District	7.93	0.020	0.076
6	Dibis	18.7	0.047	0.181
7	Hawija	12.13	0.030	0.117

5. Conclusion

Radon concentration measurement results in 21 groundwater samples collected from seven wells in different regions of Kirkuk Governorate, Iraq, showed a radon concentration range from 7.93 Bq\lin theAltunKupri region to 18.70 Bq\linDibis region. Radon concentration in drinking water is not recommended to exceed 11 Bq/L (USEPA). Only the samples from Taza and Altun Kupri regions were within the USEPA's permissible limit, while the remaining measured values exceeded this level. The variability in radon concentration is attributed to the geological conditions, variation in depth for water sources, and climate variation across the study regions. Annual effective doses due to inhalation and ingestion of radon gas across regions of Kirkuk from groundwater are assessed and then compared with set international limits of ICRP and UNSCEAR. Ingestion doses in the Dibis and Laylan regions exceeded the ICRP recommended lower limit (3 $mSv.y^{-1}$), with all regions exceeding the UNSCEAR limit (1.15 $mSv.y^{-1}$). However, inhalation doses between the study regions are considerably lower and below the internationally recommended risk limits. The data demonstrated a direct relationship between radon gas concentration (^{222}Rn), annual effective dose from inhalation, and estimated lifetime cancer risk (ELCR) in the study regions is due to soil contamination in the region leading to an increase in radon levels contaminating the water. However, ELCR values for lung cancer are still safely within the acceptable range, as the annual inhalation doses are below the ICRP permissible limit (ICRP, 2011).

6. Acknowledgements

The authors expressed appreciation to the College of Science, University of Kirkuk, for allowing the use of the RAD7 dosimeter, which was essential for data collection

7. Conflict Of Interest

We declare that there is no conflict of interest regarding the conduct or publication of this research.

8. References

Abad Ibrahim, A., Hassan, I. and Moklofe, S. 2017. Radon Concentrations in Tap and Ground Water in Kirkuk Governorate Using Active Detecting Method RAD7. International Journal of Physics, 5(2), pp. 37–42. Available at: https://doi.org/10.12691/ijp-5-2-1

Abdulkhaleq, N.A., Dawood, S.K., Qader, K.M. and Taher, S.Y. 2024. Evaluation of radon concentrations in drinking water available in Baghdad Governorate markets, Iraq. E3S Web of Conferences, 583, 02010. https://doi.org/10.1051/e3sconf/202458302010

Abojassim, A.A. 2020. Comparative study between active and passive techniques for measuring radon concentrations in groundwater of Al-Najaf City, Iraq. Groundwater for Sustainable Development, 11. https://doi.org/10.1016/j.gsd.2020.100476

Ahmed, M.T., Najemalden, M.A., Abdulwhab, A.A. and Ahmed, R.T. 2019. Estimation of radon gas concentration in soil and drinking water supply samples of Kirkuk Governorate, Iraq. Journal of Garmian University, 6 (SCAPAS Conference), pp. 26–33. https://doi.org/10.24271/garmian.scpas4

Al-Hamadwi, A.A., Al-Bayati, A.A. and Al-Mashhadani, A.H. 2012. Radon and Thoron Concentration Measurement of Ground Water in Kufa City by Using RAD7 Detector. Journal of Kufa-Physics, 4(2). https://journal.uokufa.edu.iq/index.php/jkp/article/view/7547

Al-Paruany, K.B., Al-Hadiathy, A.-H.A., Abdul, E.H., Abass, A. and Abd, A. 2022. Assessment of radon gas concentration in tap water supply of Haditha Town/west Al-Anbar Governorate/Iraq. IOP Conference Series: Earth and Environmental Science, 1080(1), 012002. https://doi.org/10.1088/1755-1315/1080/1/012002

Aswood, M.S., Alhous, S.F. and Abdulridha, S.A. 2022. Lifetime cancer risk evaluation due to inhalation of radon gas in dwellings of Al-Diwaniyah Governorate, Iraq. Nature Environment and Pollution Technology, 21(1), pp. 331–337.

Caridi, F., Marguccio, S., Belvedere, A., D'Agostino, M., Marcianò, G., Sabatino, G. and Belmusto, G. 2016. Radon radioactivity in groundwater from the Calabria region,

south of Italy. Journal of Instrumentation, 11(05), P05012. https://doi.org/10.1088/1748-0221/11/05/P05012

Charles, M. 2001. UNSCEAR Report 2000: Sources and effects of ionizing radiation.

Cousins, C., Valentin, J. and Eckerman, K.F. 2010. ICRP Publication 115: Lung Cancer Risk from Radon and Progeny and Statement on Radon. Annals of the ICRP, 40(1), pp. 1–64. https://doi.org/10.1016/j.icrp.2011.08.011

Diab, H.M. 2019. Accuracy and precision of RAD7 and RAD H2O accessories radon detector in water measurement based on counting statistics for sniff and normal modes. Romanian Journal of Biophysics, 29(2).

Duggal, V., Mehra, R. and Rani, A. 2013. Determination of 222Rn level in groundwater using a RAD7 detector in the Bathinda district of Punjab, India. Radiation Protection Dosimetry, 156(2), pp. 239–245. https://doi.org/10.1093/rpd/nct054

Hawas, G.N., Ibrahim, A.A. and Al-Tamimi, O.S. 2024a. Evaluation of Radon Concentrations in The Soil of Kirkuk City. Iraqi National Journal of Earth Science, 24(1), pp. 122–135. https://doi.org/10.33899/earth.2023.140762.1092

Hawas, J.N., Ibrahim, A.A. and Al-Tamimi, O.S. 2024b. Radon concentrations in the groundwater of Kirkuk City, Iraq. Kirkuk Journal of Science, 19(2), pp. 17–26. https://doi.org/10.32894/kujss.2024.145296.1129

Jameel, A.N. 2023. Measurement of Radon Concentration in Drink and Well Water Samples for Selected Regions in Baghdad City. Ibn AL-Haitham Journal for Pure and Applied Sciences, 36(3), pp. 100–108.

Kandari, T., Aswal, S., Prasad, M., Bourai, A.A. and Ramola, R.C. 2016. Estimation of annual effective dose from radon concentration along Main Boundary Thrust (MBT) in Garhwal Himalaya. Journal of Radiation Research and Applied Sciences, 9(3), pp. 228–233. https://doi.org/10.1016/j.jrras.2015.10.005

Kareem, D.O., Ibrahim, A.A. and Ibrahiem, O.S. 2020. Heavy metal and radon gas concentration levels in Khasa River in Kirkuk City (NE Iraq) and the associated health effects. Arabian Journal of Geosciences, 13(19), p. 1023.

Makolli, S., Dizman, S., Hodolli, G., Kadiri, S. and Cadraku, H. 2025. Radiological Assessment of Soil and Rock Samples from Stubla Village, Kosovo. Journal of Radiation Protection and Research, 50(1), pp. 29–38. https://doi.org/10.14407/jrpr.2024.00241

Marzaali, A.A., Al-Shareefi, M.A. and Abojassim, A.A. 2021. Practical Study to Assess Radioactive Radon Gas in Groundwater Samples of Dhi-Qar Governorate. IOP Conference Series: Earth and Environmental Science. IOP Publishing Ltd. https://doi.org/10.1088/1755-1315/722/1/012022

Mdekil, A.S., Al-Mayah, W.T. and Al-Tmemy, W.B. 2024. Calculation the Excess Lifetime Lung Cancer Risk and Human Health Risk Assessment by Inhalation of Radon Gas in the Health Centers of Al–Hay City in Wasit, Iraq Using LR-115 Detector. Cross Current International Journal of Medical and Biosciences, 6(04), pp. 84–91. https://doi.org/10.36344/ccijmb.2024.v06i04.001

Sabbarese, C., Ambrosino, F., DOnofrio, A., Pugliese, M., La Verde, G., D'Avino, V. and Roca, V. 2021. The first radon potential map of the Campania region (southern Italy). Applied Geochemistry, 126, p. 104890. doi: 10.1016/j.apgeochem.2021.104890

Salih, N.F. 2021. Determine the contaminations of radon in the drinking water using NTDs (CR-39) and RAD7 detectors. Arabian Journal for Science and Engineering, 46(6), pp. 6061–6074.

Shlioh, N.H. and Saleh, N.A. 2018. Evaluation the radon concentration in groundwater and surface water in the selected samples for Al-Shomaly, Iraq. Biochemical and Cellular Archives, 18(1), pp. 843–846.

Subber, A.R.H. and Ali, M.A. 2012. Measurement of radon exhalation rate from core of some oil wells in Basra Governorate in the southern Iraq. Advances in Applied Science Research, 3(1), pp. 563–571.

Taher, S.Y., Aboud, K.H., Jassim, A.S. and Abojassim, A.A. 2024. Radon concentrations in water using RAD-7: Technical Review. International Journal of Geography, Geology and Environment, 6(1), pp. 356–360. https://doi.org/10.22271/27067483.2024.v6.i1e.240

Zaidan, J.A.R. 2010. Natural Occurring Radioactive Materials (NORM) in the oil and gas industry. Journal of Petroleum Research and Studies, 1(1), pp. 4–21.

Iraqi National Journal of Earth Science, Vol. 26, No. 04, 2026 (175-183)

Iraqi National Journal of Earth Science

www.earth.uomosul.edu.iq

دراسة تركيز غاز الرادون في مياه الآبار في أقضية مدينة كركوك

لانه هدايت محمد[1]، علياء حسين [2]، ابتهال غفران خضير[2]* ، محمد احمد عمر[3]

e.gh.abbosh@uokirkuk.edu.iq alyaahussein@uokirkuk.edu.iq lanahedayet@uokirkuk.edu.iq

mohammedahmedomer@uokirkuk.edu.iq

[1] قسم الفيزياء، كلية التربية للبنات، جامعة كركوك، كركوك، العراق.

[2] قسم الفيزياء، كلية التربية للعلوم الصرفة، جامعة كركوك، كركوك، العراق.

[3] قسم السلامة، هيئة الصحة والسلامة والبيئة، شركة غاز الشمال، كركوك، العراق.

**الباحث المراسل.*

تاريخ الاستلام: 13 أيار 2025 تاريخ المراجعة: 03 أيلول 2025 تاريخ القبول: 02 تشرين الثاني 2025

تاريخ النشر الالكتروني: 01 تشرين الأول 2026

الملخص

تهدف هذه الدراسة إلى تقييم تراكيز غاز الرادون 222 Rn في مياه الآبار ضمن سبعة أقضية تابعة لمحافظة كركوك (قرة هنجير، يايجي، تازة، ليلان، آلتون كوبري، الدبس، والحويجة)، شمالي العراق، باستخدام كاشف RAD7–H2O. تم جمع 21 عينة ماء (ثلاث عينات من كل قضاء). وقد استندت هذه الدراسة إلى حقيقة أن الرادون الموجود في المياه الجوفية يُعد أحد المصادر الرئيسة للتعرض الطبيعي للإشعاع، والذي قد يؤدي إلى آثار صحية خطيرة مثل سرطان الرئة والمعدة في حال تجاوز تركيزه الحدود المسموح بها دوليًا. تراوحت تراكيز الرادون المقاسة بين 7.93 بيكريل/لتر في قضاء آلتون كوبري و18.7 بيكريل/لتر في قضاء الدبس. ووفقًا لإرشادات وكالة حماية البيئة الأمريكية (USEPA) ، التي تحدد الحد الأقصى المسموح به بـ 11 بيكريل/لتر، فإن منطقتي تازة وآلتون كوبري فقط كانتا ضمن هذا الحد، بينما تجاوزت بقية الأقضية الحد المسموح به. تراوحت الجرعة الفعالة السنوية الناتجة عن الاستنشاق بين 0.020 مللي سيفرت/سنة في آلتون كوبري و0.047 مللي سيفرت/سنة في الدبس، في حين تراوحت جرعة الابتلاع بين 1.67 مللي سيفرت/سنة في آلتون كوبري و3.92 مللي سيفرت/سنة في الدبس. وبالمقارنة مع المعايير الدولية، فإن جرعات الاستنشاق كانت دون الحدود المسموح بها، بينما تجاوزت جرعات الابتلاع في بعض المناطق (الدبس وليلان) الحد الأدنى الذي حددته اللجنة الدولية للحماية من الإشعاع (ICRP) البالغ 3 مللي سيفرت/سنة، وكانت أيضًا أعلى من المتوسط العالمي الذي حددته لجنة الأمم المتحدة العلمية المعنية بآثار الإشعاع الذري (UNSCEAR) البالغ 1.15 مللي سيفرت/سنة. كانت قيم خطر الإصابة بالسرطان على مدى الحياة (ELCR) المحسوبة ضمن الحدود المقبولة، مما يشير إلى أن خطر التعرض طويل الأمد عبر الاستنشاق محدود، إلا أن التعرض عبر الابتلاع يتطلب مراقبة مستمرة.

الكلمات المفتاحية:

RAD7، تركيزات الرادون، التلوث، المياه الجوفية.

DOI: 10.33899/injes.v26i4.56209, *©Authors, 2026, College of Science, University of Mosul.*
This is an open-access article under the CC BY 4.0 license (http://creativecommons.org/licenses/by/4.0/).

Iraqi National Journal of Earth Science, Vol. 26, No. 04, 2026 (184-192)

Iraqi National Journal of Earth Science

www.earth.uomosul.edu.iq

Three-dimensional Slope Stability Evaluation Under Seismic Load: A Case Study in Balaroa, Central Sulawesi, Indonesia

Rahmat Yusup Borman [1*], **Busthan Azikin** [2], **Hendra Pachri** [3]

rahmatyusufborman@gmail.com bazikingeo@gmail.com hendrapachri@unhas.ac.id

[1] *Geological Engineering Department, Hasanuddin University, Gowa, Indonesia.*
** Correspondence author.*

Received: 03 February 2025 Received in revised form: 01 April 2025 Accepted: 23 June 2025
Available online: 01 October 2026

Abstract

The 2018 Mw 7.4 Palu earthquake was one of the largest natural disasters in Indonesia's history. This catastrophic event was followed by massive mass movements in the Balaroa area, leading to extensive damage to infrastructure and a huge loss of life. A three-dimensional slope stability analysis under seismic conditions emerged as one of the effective solutions for preventing and mitigating the impact of mass movement disasters triggered by earthquakes, particularly in large areas. The objective of this study is to evaluate the map results of the factor of safety (FoS) with the actual massive mass movement that occurred during the 2018 Mw 7.4 Palu earthquake. The research methodology is a three-dimensional stability analysis under non-seismic and seismic conditions with a seismic load coefficient (Kh) under the 2018 Mw 7.4 Palu earthquake using Plaxis 3D LE. The input variables used in this research are the study area 3D modelling, soil parameters, and the seismic load coefficient. The 3D slope stability analysis results show that the FoS map under non seismic condition with FoS values of 2.07 to 4.46, and the results under the 2018 Mw 7.4 Palu earthquake have FoS 0.66-0.90. This evaluation is based on the comparison between the analysis result with the actual massive mass movement under the 2018 Mw 7.4 Palu earthquake condition. This analysis results in an area relatively consistent with the actual mass movement in the study area. It can be interpreted that the massive landslide that occurred in the study area was significantly influenced by the Mw 7.4 Palu earthquake event on 28 September, 2018.

Keywords:

Slope stability, Factor of safety, Earthquake, Seismic load, Mass movement.

DOI: 10.33899/injes.v26i4.60921, *©Authors, 2026, College of Science, University of Mosul.*
This is an open-access article under the CC BY 4.0 license (http://creativecommons.org/licenses/by/4.0/).

==========

1. Introduction

Historically, landslides triggered by earthquakes have been among the most prevalent natural disasters, particularly in high-magnitude earthquakes. Notable examples include the 6.7 Mw Northridge earthquake in California in 1994 (Havenith et al., 2016), the 8.0 Mw Wenchuan earthquake in China in 2008 (Chen et al., 2020), and the 7.3 Mw Chi-Chi earthquake in Taiwan in 1999 (Havenith et al., 2016). In Indonesia, earthquake-induced landslides have also been recorded, including the 5.6 Mw Cianjur earthquake in 2022 (Supendi et al., 2022) and the 7.4 Mw Palu earthquake in 2018, which resulted in landslides in areas such as Petobo, Sibalaya, Jono Oge, and Balaroa (PusGen, 2019).

The 2018 Palu earthquake, with a magnitude of 7.4, is a significant example of a large-scale natural disaster occurring in the study area. According to data from the National Disaster Management Agency of Indonesia, this seismic event resulted in 2,113 confirmed fatalities, 1,309 individuals reported missing, and 4,162 injuries. Additionally, approximately 223,000 people were displaced, and the earthquake inflicted significant damage on the infrastructure, affecting 68,451 buildings (PusGen, 2018). The event also triggered extensive landslides and liquefaction in areas such as Balaroa and Petobo, which were key contributors to the high casualty rate and considerable destruction of infrastructure in the affected region.

Slope stability analysis under seismic loading is typically performed using two-

dimensional cross-sectional models. This approach limits the effectiveness of mitigation strategies for broader or regional areas and requires a substantial amount of time for analysis. However, Plaxis 3D Limit Equilibrium (LE), a software developed by Bentley Systems Team, facilitates three-dimensional slope stability evaluations on a regional scale by employing the method of columns, which extends the traditional method of slices used in 2D analysis (Bentley Systems Team, 2021). Consequently, three-dimensional slope stability analysis emerges as an optimal approach for mitigation, management, and spatial planning, especially in regions vulnerable to earthquake-induced landslides.

To effectively reduce the risk and impact of earthquake-triggered landslides in the future, it is crucial to implement early and optimal mitigation strategies. One promising approach is to conduct additional research focused on the early detection of landslide risks associated with earthquakes, which will help identify regions vulnerable to such disasters. This research includes performing three-dimensional slope stability analyses under seismic loading across an extensive spatial range.

This research, "Three-Dimensional Slope Stability Evaluation Under Seismic Loading in Alluvial Formations", uses a three-dimensional stability analysis approach to determine the distribution of the safety factor (SF) under earthquake influence. The analysis employs Plaxis 3D LE under non-seismic conditions and uses seismic coefficients from the 2018 earthquake.

2. Study Area

The geology of the Palu area consists of five formations: the Alluvium and Coastal Deposits, the Formation of the Celebes Molasse, the Formation of Granite and Granodiorite, the Metamorphic complex, and the Formation of Tinombo Ahlburg (Fig. 1) (Sukamto, 1973). The research area is regionally classified into Alluvium and Coastal Deposits formations, which are estimated to be of Holocene age. These formations comprise sand, silt, gravel, and cobbles of varying sizes, originating from river, delta, and shallow marine environments, and representing the region's youngest sediments. These materials comprise the Palu Valley's primary components (Sukamto, 1973).

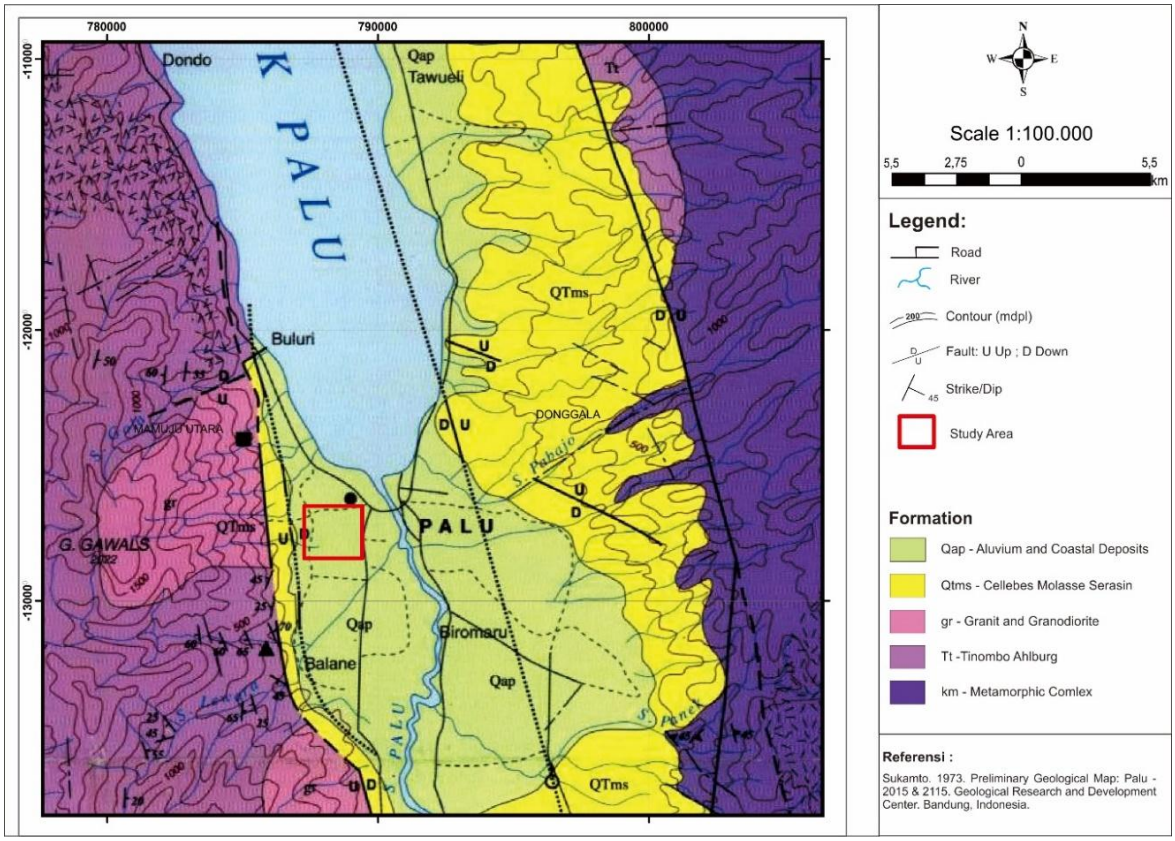


Fig. 1: Geological map of the study area (Sukamto, 1973).

The Palu-Koro Fault, an active fault, traverses the study area and extends over 300 km through Palu Bay, linking to the North Sulawesi subduction zone in the northern part of Sulawesi. This fault runs along the western boundary of the valley and research area with a dip ranging from 50 to 80 degrees toward the east (Socquet et al., 2006). Geomorphic features like streams and Quaternary alluvial fans provide evidence of left-lateral offset (Bellier et al., 2001). It is believed that the Palu-Koro Fault penetrates the thin lithosphere and is seismically locked at a depth of 12 km. GPS monitoring has revealed a high slip rate for the fault, with lateral displacement averaging around 39 mm per year, along with an extension rate of 11 to 14 mm per year (Socquet et al., 2006).

Seismicity in Sulawesi is primarily influenced by several geological features, including the subduction zone in northern Sulawesi, the Palu-Koro Fault, the Matano Fault, and the Molucca Sea Plate subduction zone to the east. The region's seismic activity is notably impacted by the Palu-Koro Fault, which runs directly through the area. Earthquakes generated here are typically shallow strike-slip events (≤40 km) that occur predominantly around the Palu-Koro Fault, exhibiting seismic magnitudes of ≥4 Mw (PusGen, 2017).

The 28 September 2018 Palu earthquake had a magnitude of 7.4, followed and triggered by a large scale of mass movement in the Balaroa area. This natural disaster caused extensive damage to infrastructure and led to a significant loss of life. Balaroa is a sub-district within Palu City, located in Central Sulawesi Province. The region impacted by the earthquake-triggered mass movement covers approximately 40 hectares and stretches about 980 meters in length (PusGen, 2019) (Fig. 2). The United States Geological Survey (USGS) indicated that the epicenter of the earthquake was situated roughly 72 km north of the study area, occurring at a depth of 10 km. Geodetic evidence points to fault displacement extending up to 150 km. Fig. (3) shows the main shock, along with several foreshocks and aftershocks, highlighting their respective magnitudes (PusGen, 2018).

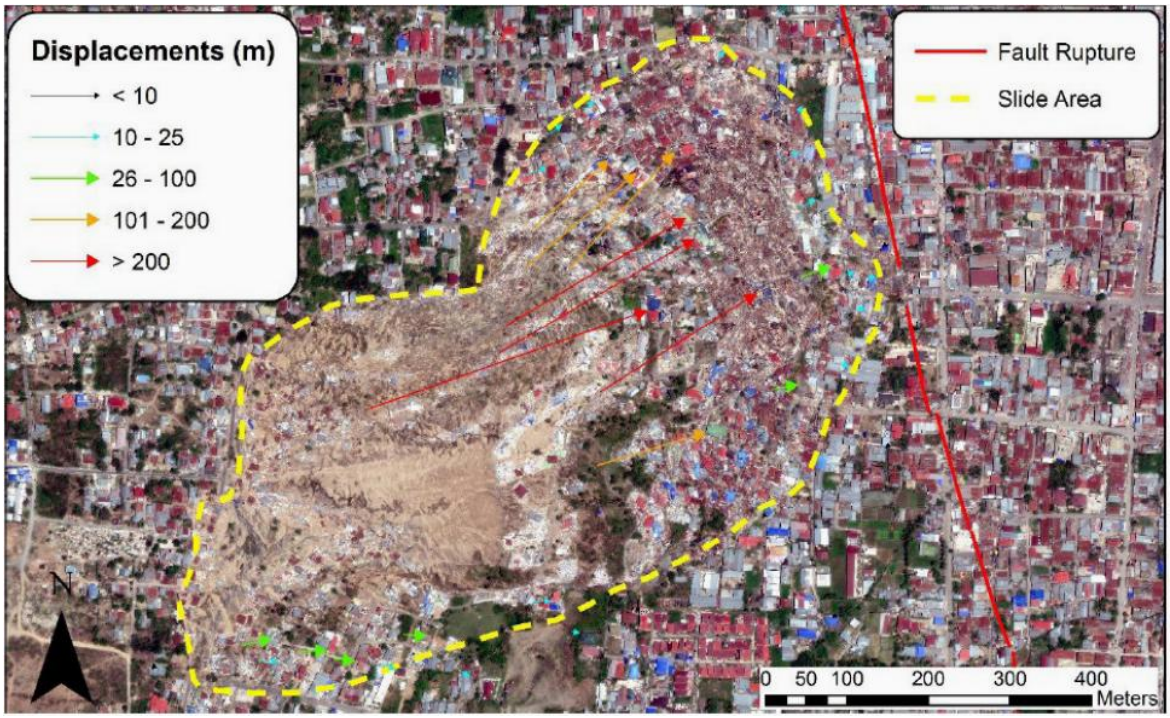


Fig. 2: Massive mass movement triggered by the 7.4 Mw Palu Earthquake on September 28, 2018 in the study area (Balaroa) (PusGen, 2019).

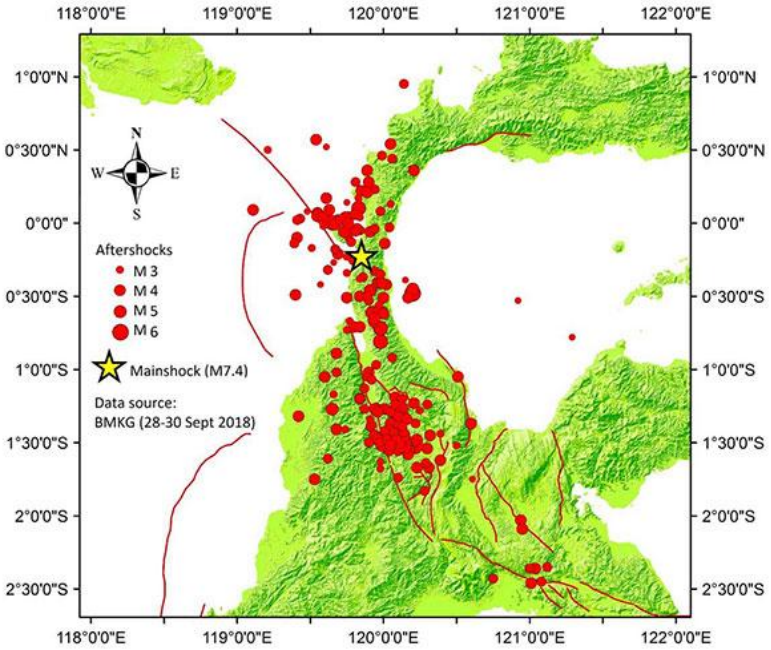


Fig. 3: Main shock and aftershock of the Palu Earthquake on September 28, 2018 (PusGen, 2018).

3. Materials and Methods

The slope stability analysis in this research involves simulations under two conditions: without the influence of an earthquake (non-seismic analysis) and under the seismic conditions of the 2018 Mw 7.4 Palu earthquake. The input parameter values used in this study are presented in Table 1.

Table 1: Study Data Parameters.

Type of data	Data Source	Description
Soil property parameters (unit weight, cohesion, internal friction angle)	Soil sample (primary data)	Soil input parameters in the three-dimensional slope stability analysis using Plaxis 3D LE
Groundwater table	JICA, 2019	Groundwater input parameters in the three-dimensional slope stability analysis using Plaxis 3D LE
N-standard penetration test (SPT) value	JICA, 2019	Input data to determine seismic coefficient
Peak ground acceleration (PGA) of the Palu earthquake on September 28, 2018.	Sahadewa et al., 2019	Input data to determine the seismic coefficient
Digital Elevation Model (DEM)	Website: *tanahair.go.id*	Surface input parameters in the three-dimensional slope stability analysis using Plaxis 3D LE

The calculation of seismic load values in this study employs the pseudo-static method, which involves determining the seismic load coefficient. The seismic load coefficient used in this study is based on the conditions of the 7.4 Mw Palu earthquake on September 28, 2018. The seismic data used for the coefficient calculation are obtained from ground motion recordings by seismographs during the 2018 Palu earthquake (Fig. 4).

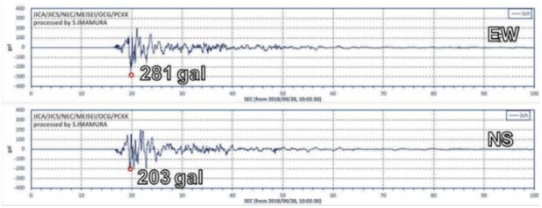


Fig. 4: Horizontal ground motion due to the 2018 Palu earthquake recorded by JICA-BMKG (Sahadewa et al., 2019).

This ground motion data allowed for the calculation of the Peak Ground Acceleration (PGA) used in the study, which is a maximum PGA of 281 gal. PGA is calculated by observing the specific site and considering the amplification factor, including the soil classification and the site

coefficient (F_{PGA}). The soil classification is determined based on the average value of N-SPT using the calculation procedure for calculation according to the Indonesian Standard (SNI 8560:2017, 2017). Based on JICA (2019), the soil classification of the study area has revealed a medium soil site (SD) class with an average N-SPT of 23.9. The soil classification was then used to determine the site coefficient (F_{PGA}), which was then processed to derive the seismic load coefficient (Kh) used in this study. The seismic coefficient (Kh) is expressed as (PUPR, 2004):

$$Kh = {PGA_M}/{g}$$

Where: Kh = seismic load coefficient representing the horizontal seismic load as a fraction of gravitational acceleration; PGA_M (modified peak ground acceleration) = adjusted peak ground acceleration considering the influence of site classification, expressed in gal (cm/s²); g = gravitational acceleration constant equals 980 cm/s².

The three-dimensional modelling of the study area is a preparatory stage before the stability analysis process. This stage involves creating a 3D surface model of the study area representing its condition before the 2018 Palu earthquake, as well as a 3D subsurface model based on the geological and geotechnical conditions of the study area.

The three-dimensional surface model in this study uses surface contour data of the Balaroa area based on National Digital Elevation Model (DEMNAS) data that shows the condition before the 7.4 Mw Palu earthquake disaster in September 2018, which is then exported into Plaxis Designer in the form of contours and converted into a mesh design (Fig. 5). The input soil parameters used in the analysis include soil unit weight (γ), cohesion (c), and internal friction angle (φ) (table 2), which were acquired through soil sampling in the study area and subsequently processed using laboratory soil mechanics testing.

Table 2: Input soil properties of the study area.

Material	γs (gr/cm³)	γd (gr/cm³)	c (kPa)	Φ⁰ (degree)
Sand	1.66	1.40	3.6	29

The slope stability analysis method used is the limit equilibrium method under static earthquake conditions. The slope stability analysis is performed using the Plaxis 3D LE software. Plaxis 3D LE is software developed by the Bentley Systems Team for analyzing slope stability using the method of columns, an extension or development of the 2D slope stability analysis (Bentley Systems Team, 2021). This is a three-dimensional analysis capable of assessing stability across a wide area. Using Plaxis 3D LE allows for modelling the combination of complex topographies with 3D parameter distribution, including subsurface properties, as well as incorporating additional parameters like seismic load coefficients. The calculation of the factor of safety (FoS) in this analysis method is performed using the formula shown in Equation 2 (Bentley Systems Team, 2021).

$$FoS = \frac{\sum(c'A+(N-uA)\tan\phi)\cos\alpha_x}{\sum N\cos\gamma_x+\sum Wkh\pm\sum D_x\pm P} \qquad (2)$$

Where: c'= Cohesion; N = force normal to the column surface; ϕ = Internal Friction Angle (°); P = resultant force from external water pressure; α = angle between the column and x-axis (°); u = Pore Water Pressure; Dx = total force acting horizontally on the column along the x-axis; γx = angle of the normal force acting at the base of the column; A = volume area of the column; kh = Seismic coefficient; W=weight.

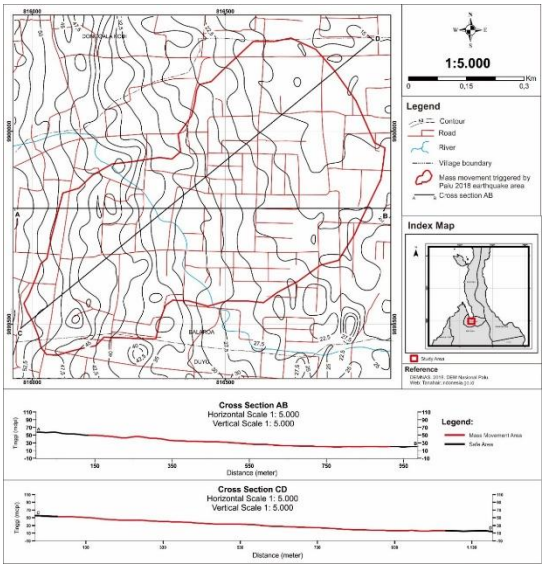


Fig. 5: Study area contour map and cross section.

The results of this analysis include the distribution of potential slip surfaces and the distribution of slope Factor of Safety (FoS) values for the study area in a 3D model. The analysis specifically focuses on the seismic conditions during the 2018 Palu earthquake.

4. Results and Discussion

The design of the three-dimensional model used in this study is based on the pre-7.4 Mw Palu earthquake condition on September 28, 2018. This condition also shows that the surface topography used was the condition before the mass movement triggered by the earthquake occurred in the study area. The subsurface model is based on the input data of the geological and geotechnical conditions of the study area.

The Three-dimensional slope stability analysis in this study is designed based on two simulation conditions: without seismic load (non-seismic analysis) and under the seismic conditions of the Palu earthquake on September 28, 2018. The slope stability analysis is performed using the Plaxis 3D LE software to calculate the factor of safety (FoS) value.

The base data for this modelling utilises DEMNAS data recorded in 2017, which is then exported into Plaxis Designer in the form of contours and converted into a mesh design. From this design, volume modelling is carried out, which serves as a reference for the 3D modelling used in the slope stability analysis (Fig. 6).

After the slope stability analysis results are obtained, validation is performed by comparing the factor of safety (FoS) from the map result of the 3D stability analysis with the minimum factor of safety (FoS<1) as a reference for assessing potential landslide hazards. This validation is carried out for both scenarios: without the influence of seismic load and with the influence of the 2018 Mw 7.4 Palu earthquake.

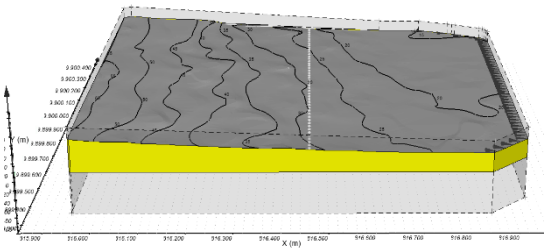


Fig. 6: 3D model design of the study area.

A. Three-dimensional Slope Stability Analysis Without Seismic Load (non-seismic Load)

This slope stability analysis simulation represents the original slope stability of the study area before the occurrence of the mass movement triggered by the 7.4 Palu earthquake in the study area. The results of the slope stability analysis under non-seismic conditions show that the distribution of factor of safety (FoS) values in the study area ranges from 2.07 to 4.46, as shown in Figs. 7 and 8.

Based on the factor of safety (FoS) map result of the slope stability analysis under non-seismic conditions with spatial distribution, the slip surface areas in the study location are distributed in several zones, primarily in the steeper slope western part of the study area. In contrast, in the gentler eastern part of the study area, no slip surfaces are identified.

According to the validation of the factor of safety (FoS), the slip surfaces formed in this study analysis have a factor of safety (FoS) greater than the minimum factor of safety (FoS) (i.e., FoS > 1). Therefore, it can be interpreted that under the simulated slope stability analysis without seismic influence (non-seismic), the whole study area is in a stable state.

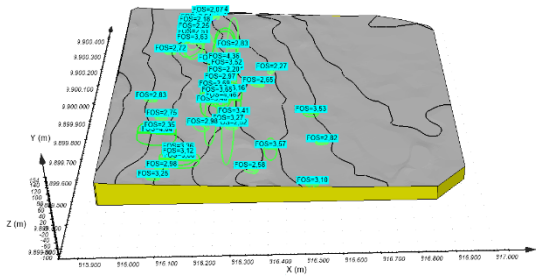


Fig. 7: 3D model of the slope stability analysis under the condition without seismic load showing a FoS range of 2.07 to 4.46.

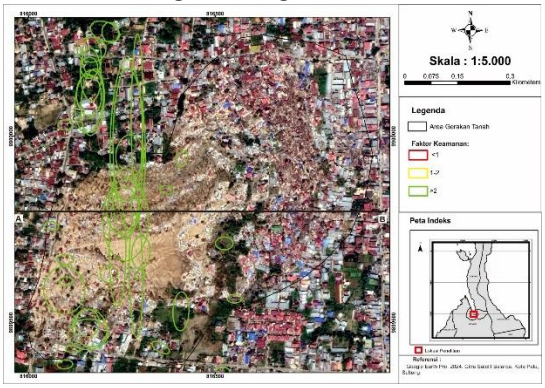


Fig. 8: Overlay map of the Balaroa landslide area and the results of slope stability analysis under non-seismic conditions with a Factor of Safety (FoS) ranging from 2.07 to 4.46.

B. Three-dimensional slope stability analysis under the 7.4 Palu Earthquake (seismic load)

The Three-dimensional slope stability analysis in this study is designed under seismic conditions. The seismic influence applied in this

actual landslide.

Table 3: Input seismic load coefficient data

Under Condition	Seismic load coefficient (Kh)
7.4 Palu Earthquake 2018	0.35

The results of the slope stability analysis show that the distribution map of the Factor of Safety (FoS) in the study area ranges from 0.66 to 0.90, as shown in Figs. 9 and 10. Based on these results, the spatial distribution of slip surfaces extends across almost the entire study area, particularly in regions with steeper slopes, where the Factor of Safety (FoS) is less than 1.

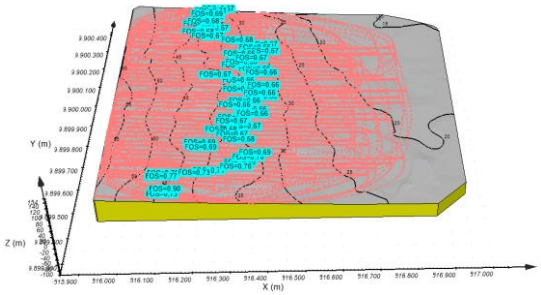


Fig. 9: 3D model of the slope stability analysis results for the Palu 2018 earthquake scenario with a Factor of Safety (FoS) ranging from 0.66 to 0.90.

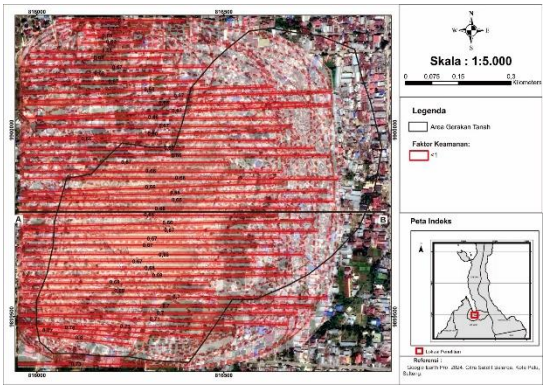


Fig. 10: Overlay map of the Balaroa landslide area and the results of slope stability analysis under the Palu 2018 earthquake scenario with a Factor of Safety (FoS) ranging from 0.66 to 0.90.

The map of the factor of safety result (FoS) in this analysis indicates that almost the whole study area was in an unstable state (FoS<1). Compared with the map of the factor of safety stability analysis is based on the seismic load coefficient values derived from seismographic records of the 2018 Palu earthquake event (Table 3). This simulation shows the current slope stability condition of the study area, which is indicated by the factor of safety (FoS) and compared with the

result (FoS) under non-seismic conditions, it can be interpreted that the seismic event was the main factor in decreasing the factor of safety (FoS). This seismic event caused an increase in soil shear stress beyond its shear strength. The imbalance caused the driving forces for soil movement to exceed the resisting forces. This condition triggered instability of the slope, causing a landslide to occur.

Based on the comparison of the spatial distribution of potential slip surface results from the slope stability analysis and the area coverage of the actual massive mass movement triggered by the 2018 Mw 7.4 Palu Earthquake, as shown in Fig. (10), it is identified that the result of the analysis area has the same coverage area as the mass movement that occurred in Balaroa after the earthquake. This area analysis result is relatively consistent with the actual mass movement in the study area. It can be interpreted that the massive landslide that occurred in the study area was significantly influenced by the Mw 7.4 Palu earthquake event on 28 September, 2018.

5. Conclusion

The three-dimensional slope stability analysis results under non-seismic conditions showed a distribution of FoS from 1.36 to 4.98. This condition shows that the FoS values are greater than the minimum standard of FoS (i.e., FoS >1). It can be interpreted that under the simulated slope stability analysis without seismic influence (non-seismic), the whole study area was in a stable state.

The three-dimensional slope stability analysis results under the 2018 Palu earthquake condition show that the map distribution of FoS in the study area ranges from 0.66 to 0.90, as shown in Figs. 9 and 10. According to these results, the spatial distribution of slip surfaces extends across almost the entire study area, particularly in regions with steeper slopes. Compared to the factor of safety (FoS) distribution under non-seismic conditions, it can be interpreted that the seismic event was the primary factor contributing to the

reduction in FoS. The earthquake induced an increase in soil shear stress, exceeding its shear strength. This imbalance caused the driving forces of soil movement to surpass the resisting forces, ultimately triggering slope instability and resulting in a landslide.

The evaluation of this study is based on the comparison between the three-dimensional slope stability analysis result with the actual massive mass movement coverage area that occurred in the study area during the 2018 Mw 7.4 Palu earthquake. The evaluation result shows that the analysis area has the same coverage area as the mass movement that occurred in Balaroa after the earthquake. This evaluation result is consistently the same as the actual mass movement in the study area. It can be concluded that the massive mass movement that occurred in the study area was significantly influenced by the Mw 7.4 Palu earthquake event on 28 September, 2018.

6. Acknowledgements

The authors are appreciative of the support from the Geological Engineering Department, University of Hasanuddin.

7. Conflict of Interest

The authors declare that they have no conflict of interest.

8. Funding Statement

This research received no external funding.

9. References

Bellier, O., Sebrier, M., Beaudouin, T., Villeneuve, M., Braucher, R., Bourles, D., Siame, L., Putranto, E. and Pratomo, I., 2001. High slip rate for a low seismicity along the Palu-Koro active fault in central Sulawesi (Indonesia). Terr. Nova. pp. 463-470. https://doi.org/10.1046/j.1365-3121.2001.00382.x.

Bentley Systems Team, 2021. Plaxis LE Slope Stability: 2D/3D Limit Equilibrium Slope Stability Analysis (Theory Manual). Delft.

Chen, Y., Liu, G., Li, N., Du, X., Wang, S. and Azzam, R., 2020. Stability evaluation of slope subjected to seismic effect combined with consequent rainfall. Engineering Geology. Vol. 266. https://doi.org/10.1016/j.enggeo.2019.105461.

Havenith, H., Torgoev, A., Braun, A., Schogel, R. and Micu, M., 2016. A New Classification of Earthquake-Induced Landslide Event Sizes Based on Seismotectonic, topographic, climatic, and geologic factors. Journal Geoenvironmental Disaster. https://doi.org/10.1186/s40677-016-0041-1.

JICA, 2019. Boring Survey for Basic Response for Central Sulawesi Earthquake (Phase 1) Under the JICA Survey For Disaster Information Collection in Indonesia. PT. Indra Karya, Jakarta.

SNI 8560:2017, 2017. Persyaratan Perancangan Geoteknik. National Standardization Agency of Indonesia, Jakarta.

PUPR (Ministry of Public Works and Housing), 2004. Stability Analysis of Embankment Dams Due to Seismic Loads. Ministry of Public Works, Jakarta.

PusGen (Pusat Studi Gempa Nasional), 2017. Indonesian Earthquake Source and Hazard Map 2017. Ministry of Public Works and Housing, Jakarta.

PusGen (Pusat Studi Gempa Nasional), 2018. Study of the Palu Earthquake in Central Sulawesi Province on September 28, 2018. Ministry of Public Works and Housing, Bandung.

PusGen (Pusat Studi Gempa Nasional), 2019. Preliminary Investigation of Landslides and Liquefaction: Geotechnical Extreme Events Reconnaissance (GEER) from the 28 September 2018 Palu Earthquake (Geotechnical Report on 2018 Palu-Donggala Earthquake). Ministry of Public Works and Housing, Jakarta.

Sahadewa, A., Irsyam, M., Hanifa, R., Mikhail, R., Pamumpuni, A., Nazir, R., Pramono, S., Sabaruddin, A., Faizal, L., Ridwan, M., Himawan, A., Simatupang, P., Akatas, I. M., Harninto, D. S., Djarwadi, D., Kartawiria, A., Djunaidy, M., Suhendra, I., Kawanda, A. and Widodo, Y., 2019. Overview of the 2018 Palu earthquake. Proceedings of the 7th International Conference on Earthquake Geotechnical Engineering. Pp. 857–869.

Socquet, A., Simons, W., Vigny, C., McCaffrey, R., Subarya, C., Sarsito, D., Ambrosius, B. and Spakman, W., 2006. Microblock rotations and fault coupling in SE Asia triple junction (Sulawesi, Indonesia) from GPS and earthquake slip vector data. Journal of Geophysical Research: Solid Earth, 111(B8). http://dx.doi.org/10.1029/2005JB003963.

Sukamto, R., 1973. Preliminary Geological Map: Palu – 2015 and 2115. Geological Research and Development Center. Bandung.

Supendi, P., Priyobudi, J., Jatnika, J., Sianipar, D., Ali, Y. H. and Heryandoko, N., 2022. Analysis of the Cianjur Earthquake (West Java) Mw 5.6 on November 21, 2022. Meteorology, Climatology, and Geophysics Agency (BMKG), Jakarta.

Iraqi National Journal of Earth Science, Vol. 26, No. 04, 2026 (184-192)

Iraqi National Journal of Earth Science

www.earth.uomosul.edu.iq

تقييم ثلاثي الأبعاد لأستقرار المنحدرات تحت تأثير الأحمال الزلزالية: دراسة حالة في بالاروا، وسط سولاويسي، أندونيسيا

رحمت يوسف بورمان [1*]، بوستان أزيكن [2]، ندرا بتشري [3]

rahmatyusufborman@gmail.com hendrapachri@unhas.ac.id bazikingeo@gmail.com

[1] قسم الهندسة الجيولوجية، جامعة حسن الدين، غوا، إندونيسيا.

**الباحث المراسل.*

تاريخ الاستلام: 03 شباط 2025 تاريخ المراجعة: 01 نيسان 2025 تاريخ القبول: 23 حزيران 2025

تاريخ النشر الالكتروني: 01 تشرين الأول 2026

الملخص

كان زلزال بالو (7.4 Mw) سنة 2018 أحد اكبر الكوارث الطبيعية في تاريخ أندونيسيا. أعقب هذا الحدث الكارثي تحركات جماعية هائلة في منطقة الاروا مما أدى إلى أضرار جسيمة في البنية التحتية وخسارة فادحة في الأرواح. ظهر تحليل استقرار المنحدر ثلاثي الأبعاد في ظل الظروف الزلزالية كأحد الحلول الفعالة للوقاية من آثار كوارث الحركة الجماعية الناجمة عن الزلازل وتخفيفها، وخاصة في المناطق الواسعة. كان الهدف من هذه الدراسة هو تقييم نتيجة خريطة عامل الأمان (FoS) مع الحركة الجماعية الهائلة الفعلية التي حدثت خلال زلزال بالو 2018 Mw 7.4. كانت منهجية البحث هي تحليل الاستقرار ثلاثي الأبعاد في ظل الظروف غير الزلزالية والزلزالية مع معامل الحمل الزلزالي (Kh) تحت زلزال بالو 2018 Mw 7,4، باستخدام Plaxis 3D LE. كانت متغيرات الإدخال المستخدمة في هذا البحث هي النمذجة ثلاثية الأبعاد لمنطقة الدراسة ومعلمات التربة ومعامل الحمل الزلزالي. تُظهر نتائج تحليل استقرار المنحدر ثلاثي الأبعاد أن خريطة FoS في ظل ظروف غير زلزالية، حيث تراوحت FoS بين 2.07 و4.46، ونتائج زلزال بالو الذي بلغت قوته 7.4 درجة على مقياس ريختر عام 2018، حيث تراوحت FoS بين 0.66 و0.90. يستند هذا التقييم إلى مقارنة نتائج التحليل بحركة الكتلة الهائلة الفعلية في ظل زلزال بالو الذي بلغت قوته 7.4 درجة على مقياس ريختر عام 2018. وتتوافق نتائج هذا التحليل نسبيًا مع حركة الكتلة الفعلية في منطقة الدراسة. ويمكن تفسير ذلك بأن الانهيار الأرضي الهائل الذي حدث في منطقة الدراسة قد تأثر بشكل كبير بزلزال بالو الذي بلغت قوته 7.4 درجة على مقياس ريختر في 28 ايلول 2018.

الكلمات المفتاحية:

استقرار المنحدرات، عامل الأمان، زلزال، حمل زلزالي، تحرك جماعي.

DOI: 10.33899/injes.v26i4.60921, ©Authors, 2026, College of Science, University of Mosul.

This is an open-access article under the CC BY 4.0 license (http://creativecommons.org/licenses/by/4.0/)

Iraqi National Journal of Earth Science, Vol. 26, No. 04, 2026 (193-205)

Iraqi National Journal of Earth Science

www.earth.uomosul.edu.iq

Reservoir Quality Assessment of Subsurface Sections Across Jurassic Period (Mus and Sargelu) Formations in Duhok Governorate, Kurdistan Region, Iraq

Parween Ramadhan Abid [1], **Rzger Abdulkarim Abdula** [2*]

parweenhajani@gmail.com rzger.abdulkarim@tiu.edu.iq

[1] *Department of Geosciences, College of Science, University of Duhok, Duhok, KRG, Iraq.*
[2] *Department of Petroleum and Mining Engineering, Faculty of Engineering, Tishk International University, Erbil, Iraq.*
** Correspondence author.*

Received: 03 February 2025 Received in revised form: 05 May 2025 Accepted: 15 July 2025
Available online: 01 October 2026

Abstract

This study investigates the reservoir characteristics of Jurassic subsurface formations, specifically the Mus and Sargelu formations in Duhok Governorate within the Kurdistan Region of Iraq. Through the interpretation of detailed well log data from the X Well, essential petrophysical properties such as porosity, permeability, water saturation, and lithology are assessed to pinpoint potential hydrocarbon-bearing zones. The Sargelu Formation, encountered between depths of 1345 and 1420 meters, is characterized by heterogeneous lithologies dominated by fractured limestones interbedded with shale layers. Notably, this interval reveals effective porosity values reaching up to 18%, enhanced permeability due to fracturing, and favorable water saturation, especially between 1385 and 1400 meters. In contrast, the Mus Formation, situated between 1875 and 1925 meters, comprises primarily limestone and dolomite, displaying variable porosity and resistivity patterns. Crossplot interpretations and Pickett plots indicate potential hydrocarbon presence despite limited direct evidence from gas indicators. Overall, both formations exhibit considerable but variable reservoir quality controlled by lithologic heterogeneity, degree of fracturing, porosity distribution, and shale content. The integrated petrophysical analysis provides a deeper understanding of Jurassic reservoir behavior in this relatively underexplored region of northern Iraq.

Keywords:

Petrophysical properties, Reservoir quality, Jurassic, Well log analysis, Porosity, Permeability.

DOI: 10.33899/injes.v26i4.60917, ©Authors, 2026, College of Science, University of Mosul.
This is an open-access article under the CC BY 4.0 license (http://creativecommons.org/licenses/by/4.0/).

==========

1. Introduction

The Jurassic succession in northern Iraq plays a critical role in the region's petroleum systems, particularly due to the presence of rich source rocks such as the Sargelu and Naokelekan formations (Abdula, 2015; Abdula, 2017a). These formations play a pivotal role in hydrocarbon generation, migration, and entrapment, and are therefore of strategic importance for petroleum exploration and development activities. The Mus Formation represents the only Lower Jurassic unit in Iraq deposited under normal marine conditions, contrasting with the sabkha and evaporitic environments of other Lower Jurassic formations (Bellen et al., 1959). The Mus Formation in Jabal Kand-1 Well is thermally mature, but has a low potential for generating hydrocarbons (Al-Habba, 1988; Abdula, 2017b). In contrast, the Mus Formations are the source of the condensate that is produced from the Samawa-1 Well in southern Iraq (Samarrai, 1988, in Sadooni, 1997). These Jurassic formations, containing Type IIS kerogen, are the main contributors to oil generation and expulsion from the Late Cretaceous to the Pliocene (Pitman et al., 2004). Supporting units such as the Gotnia Formation act as regional seals, while others like the Butmah Formation offer potential reservoir facies. Depositional environments shaped by transgressive-regressive cycles favored both organic-rich sedimentation and reservoir development (Pitman et al., 2004).

Petrophysical log analysis is a valuable and essential tool to describe reservoir properties (Asquith et al., 2004). The importance of petrophysical understanding of well logs is to distinguish the volumetric portions of the geologic unit constituents (solid, liquid, and gas states) by merging the data offered by different types of well logs (Ellis and Singer, 2007).

Agada et al. (2013) examined fractured systems in the Sargelu and Naokelekan formations, illustrating how fracture networks enhance reservoir permeability and fluid migration. Tectonostratigraphic contrasts were addressed by Al-Naqib and Al-Juboury (2014), who delineated petroleum and non-petroleum zones based on regional geological variation. The Lower and Middle Jurassic formations in Zab-1 Well have kerogen types II and II-S in the immature to early mature stage of thermal maturity of oil (Abdula, 2016).

Petrophysical characterization using well log data was applied by Zangana et al. (2020) to assess Early Jurassic reservoirs such as Butmah Formation, while Ali et al. (2022) further classified porosity types across multiple wells. Dohan et al. (2022) provided detailed petrographic insight into the Sargelu Formation, identifying its depositional environments and diagenetic features. Recent advancements include integrated petrophysical and geochemical approaches by Alrekabi and Al-Fatlawi (2024), Khudhair and Idan (2024), and Al-Dabagh and Asaad (2025), highlighting the growing emphasis on reservoir heterogeneity and rock-type distinction in oil fields such as Garraf and Shaikan. Despite these efforts, many Jurassic successions in northern Iraq remain underexplored or inconsistently evaluated, underlining the importance of this study in contributing a more detailed and localized understanding of reservoir quality and hydrocarbon distribution. Well consideration of reservoir depiction signifies the main key element for successful field development planning, and precise reservoir description is essential for effective and improved control of heterogeneity (Shedid, 2018). Recognition of reservoir quality is an important objective in the reservoir characterization process. The quality of a reservoir is defined by its hydrocarbon storage capacity, and storage capacity is a function of porosity, whereas deliverability is a function of permeability. Thus, both porosity and permeability are the main reservoir quality controlling factors (El Sharawy and Nabawy, 2019).

The aim of this study is to assess the reservoir quality of Mus and Sargelu Jurassic formations in the Duhok area, northern Iraq. This evaluation is achieved by analyzing well log data to determine key petrophysical parameters, identify productive reservoir intervals, understand the distribution of hydrocarbons, and evaluate the factors influencing reservoir heterogeneity and effectiveness. This study may be of strategic importance in regional hydrocarbon exploration and development.

2. Study Location

The present study focuses on the Jurassic stratigraphic succession within the Kurdistan Region of northern Iraq, specifically in the Duhok area. The investigation is based on subsurface data obtained from the X Well, which penetrates several Jurassic formations that are critical to the regional petroleum system. The selection of this area is justified by its geological complexity and its potential for hosting both source and reservoir rocks within a relatively well-preserved stratigraphic framework. The well location is illustrated on the location map (Figure 1), which incorporates elements adapted from Sissakian and Al-Khalidi (2012) and supplemented with satellite imagery obtained from Google Earth.

This well intersects key Jurassic stratigraphic units. The studied formations (Mus and Sargelu), as part of the Jurassic succession of Iraq are exhibit varied lithologies, predominantly comprising limestones, dolomites, and shales. Both formations hold significant reservoir potential, primarily influenced by factors such as natural fracturing and dolomitization, which enhance porosity and permeability characteristics within these carbonate units. A stratigraphic column illustrating the vertical distribution, lithological composition, and relative thicknesses of the Mus and Sargelu formations in the X Well is provided to support the subsurface interpretation (Fig. 2). Mackertich and Samarrai (2013) present a detailed well-specific stratigraphic column for the Kurdistan region, showcasing the Jurassic succession in the area, including the Sargelu and Mus formations along with their thickness variations.

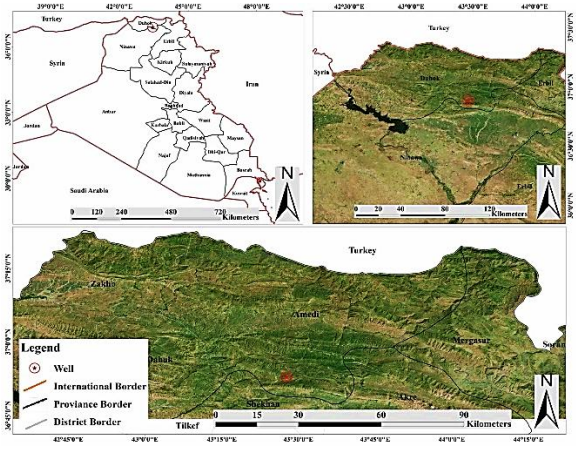


Fig. 1: Location map showing the studied area with locations of oil exploration wells. The upper part of the map is adapted from Sissakian and Al-Khalidi (2012), while the lower part is based on imagery from Google Earth.

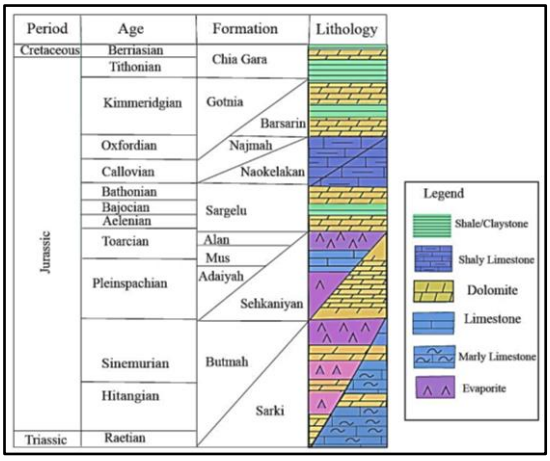


Fig. 2: Schematic stratigraphic column showing Jurassic succession in the Kurdistan Region of northern Iraq (Mackertich and Samarrai, 2013) based on data from X Well, and highlighting key formations, particularly Mus and Sargelu formations, along with associated lithologies such as limestone, dolomite, marl, shale, and evaporites. The column is not to scale and is intended only as a conceptual illustration of the stratigraphic relationships.

3. Geological Setting

Iraq lies in the transition between the Arabian Shield in the Southwest and the extremely distorted Taurus and Zagros Suture Zone in the North and Northeast. It is strongly affected by eustatic sea-level fluctuations. The development of the region has been influenced by the mobility of the Precambrian basement and by tectonism along the Neo-Tethyan margin (Jassim and Buday, 2006). Depending on the tectonic subdivision of Iraq, the study area is located in the Foothill Zone in northern Iraq.

The major tectonic event was begun after Triassic when the Gondwana splits, Indian Plate started to separate and, in the Late Jurassic isolated from Arabia (Grabowski Jr. and Norton, 1995). A new passive margin and new accommodation space were developed along the subsiding shelf at the plate's northeast edge as a consequence of rifting that occurred in the late Early Jurassic (Sharland et al., 2004). The Triassic was a time of general steadiness as represented by the deposition of evaporite and carbonate units, e.g., Butmah, Alan, Mus, and Adaiyah, or their equivalents, Sarki and Sehkaniyan formations. Due to Toarcian rifting, a new basin formed in the Middle Jurassic. It was characterized by the deposition of the Sargelu and its equivalents throughout the region (Sadooni, 1997). The variety in Najmah Formation thickness as described by Dunnington (1958) reflects the basin geometry from the Bathonian onwards. The Najmah oolites are developed along the western margin of a basin, which is represented to the east-northeast by the Naokelekan Formation in the Mountainous Zone (Sadooni, 1997).

4. Methodology

This study utilizes well log data to characterize reservoir properties, focusing on porosity, permeability, lithology, and hydrocarbon saturation. Data from the X well log were analyzed to interpret Jurassic formations, including the Mus and Sargelu formations. The methodology involves petrophysical interpretation utilizing gamma-ray (GR), neutron porosity (NPHI), bulk density (RHOB), resistivity (LLD & MSFL), and other log-derived parameters to evaluate reservoir quality. Cross plots and well log correlation techniques were employed to distinguish lithological variations, shale content, and hydrocarbon-bearing zones. The porosity-permeability relationships were assessed to determine reservoir effectiveness, while water saturation calculations aided in identifying hydrocarbon saturation potential. Additionally, stratigraphic correlations and formation thickness variations were analyzed to understand reservoir distribution and heterogeneity. The integration of petrophysical data with geological information provides a comprehensive interpretation of

reservoir characteristics, aiding in the identification of productive hydrocarbon zones.

5. Result

The X well log provides an in-depth profile of lithology, rock types, fossil content, and mineral content. The differentiation of the Mus and Sargelu formations in the studied well (X Well, Duhok area) is based on a combination of wireline log signatures, lithological characteristics, and regional stratigraphic context. Although petrographic thin sections were not initially included, future versions of this study will incorporate petrographic imagery from representative samples, highlighting features such as micritic vs. sparry textures, fossil fragments, dolomitization, shale content, and porosity types (e.g., vuggy, intercrystalline, moldic). These features are essential for confirming facies assignments and lithological boundaries, especially when differentiating closely spaced carbonate units with similar log signatures.

The Sargelu Formation, in turn, exhibits a distinct gamma-ray log character due to its high organic content and interbedded shale and limestone units. Sargelu Formation covers the depth interval between 1345 and 1420 meters (Figs. 3 and 4), and directly beneath it, the Alan Formation extends from 1420 m to 1875 m, primarily characterized by evaporites and anhydrites, acting as an effective seal between the Sargelu and Mus formations. The lower boundary of the Sargelu Formation is characterized by a shift from organic-rich, dark argillaceous, pyritic shales or micritic limestones with elevated gamma ray in the Sargelu Formation, with increased gamma ray, bitumen staining, and vuggy porosity into cleaner, more anhydritic dolomites (Alan Formation). The upper contact with the Naokelekan Formation is recognized by the appearance of argillaceous, pyritic shales and finely crystalline micritic limestones with elevated gamma-ray values—belonging to the Naokelekan Formation. These boundary interpretations are consistent with regional stratigraphy and supported by petrophysical parameters such as bulk density, neutron porosity, and resistivity trends.

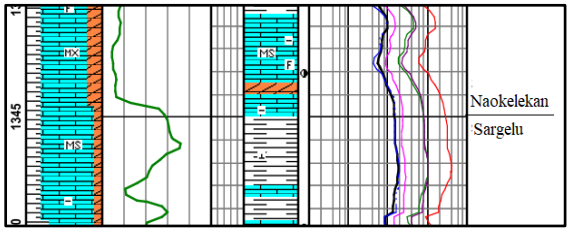


Fig. 3:Upper boundary of Sargelu with Naokelekan formations is situated at 1345 meters.

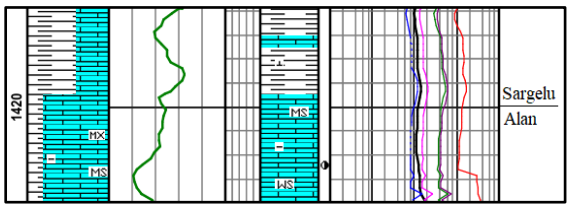


Fig. 4: Lower boundary of Sargelu with Alan formations is situated at 1420 meters.

The Mus Formation is covering the depth between 1875 and 1925 meters (Figs. 5 and 6), all of which critically influence reservoir characterization. The upper boundary of the Mus Formation is marked by a sharp increase in gamma-ray response and a distinct change from the overlying clean, evaporitic dolomite or anhydrite facies (interpreted as part of the Alan Formation) to downward tight, crystalline dolomite and anhydrite with very low porosity and high resistivity (Mus Formation), consistent with descriptions by Jassim et al. (2006), then the transition into dark-colored, organic-rich laminated limestones with bitumen staining, increased gamma-ray values, and signs of vuggy porosity—typical markers for the lower contact of Mus Formation with Adiyah Formation.

The thickness of the formations in this study also shows slight variation compared to their respective type sections. The Sargelu Formation in the studied well is approximately 75 meters thick, while the Mus Formation measures around 50 meters. These thicknesses differ slightly from standard regional averages due to structural setting, local depositional dynamics, and possibly erosional truncation or facies change. Such thickness variations are not uncommon in subsurface sections, particularly in tectonically active areas like the High Folded Zone of northern Iraq. The dominant lithology includes dolomitic limestones (DOLICLS), marlstones (MARLST), and shales (SH). For a detailed interpretation of the Jurassic formations in the X well log, let's break down each formation's key properties and

potential for hydrocarbons, focusing on their depth, lithology, reservoir properties, and overall hydrocarbon potential.

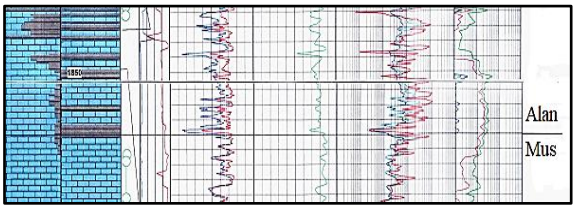


Fig. 5: Upper boundary of Mus with Alan formations is situated at 1875 meters.

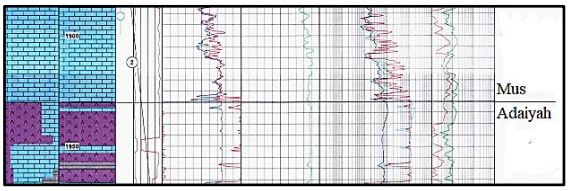


Fig. 6: Lower boundary of Mus with Adaiyah formations is situated at 1925 meters.

Mus Formation

Mus Formation is found at depths of approximately 1875-1925 meters. It is composed of limestone, dolomite, and some marl (Jassim et al., 2006) (Fig. 7). The crossplot in Fig. 8 of RHOMAA (bulk density) vs. DTMAA (acoustic transit time) for the Mus Formation reveals that the data points primarily cluster around a density of approximately 2.7 g/cm³ and a transit time of about 50 µs/ft, indicating that the formation is predominantly composed of limestone (calcite).

There is also a minor trend in the crossplot data toward dolomite, suggesting localized dolomitization within the Mus Formation. Additionally, scattered points trending toward quartz and anhydrite indicate the possible presence of these minerals in smaller quantities. The figure includes arrows marked as "gas direction" to denote data points with decreased bulk density and increased transit time, features typically associated with gas-filled porosity.

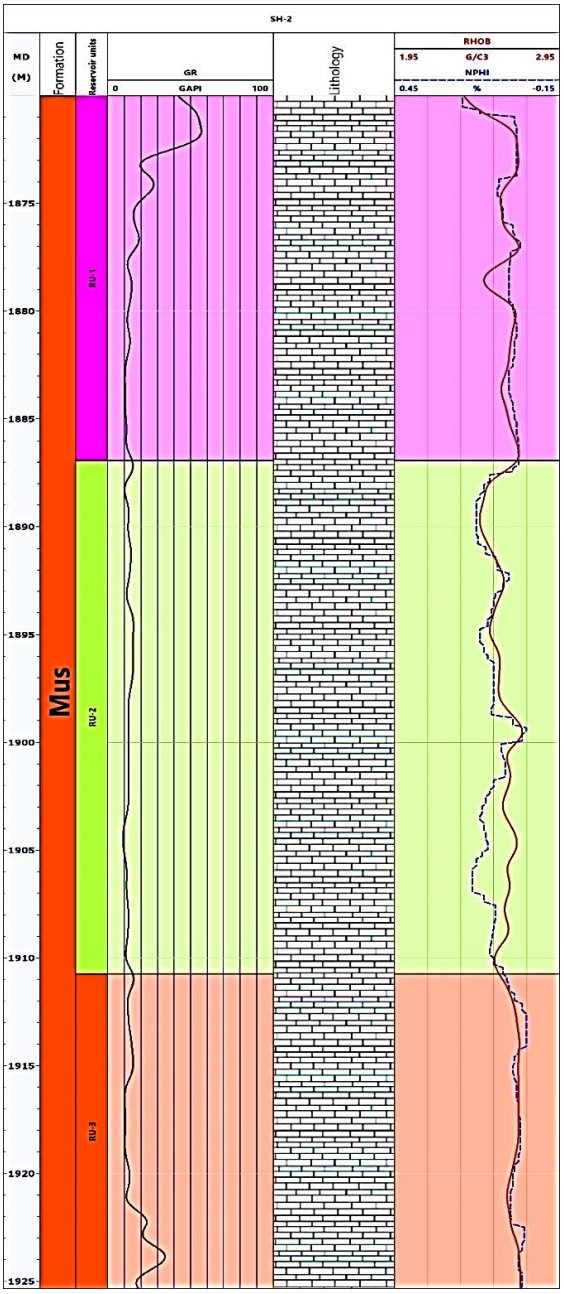


Fig. 7: Well log data of the Mus Formation showing gamma-ray (GR), neutron porosity (NPHI), bulk density (RHOB), lithology, and reservoir units RU-1, RU-2, and RU-3. The well log data used in this study were obtained from the Ministry of Natural Resources (MNR) of the Kurdistan Regional Government (KRG).

It is important to clarify that no direct evidence of gas (such as mud gas shows, formation testing, or pressure measurements) is available in this study; therefore, these indications should be considered as log-based anomalies rather than conclusive proof of gas accumulation. Furthermore, salt-related responses inferred from SNP (Sigma Neutron Porosity) and CNL (Compensated Neutron Log) signatures are visible

in the plot but do not correlate with the main data cluster of the Mus Formation. These signals are likely attributable to nearby salt-bearing units or lithological inclusions from adjacent formations. The Mus Formation demonstrates characteristics of a carbonate reservoir, with localized dolomitization and potential, though unconfirmed, indicators of gas presence.

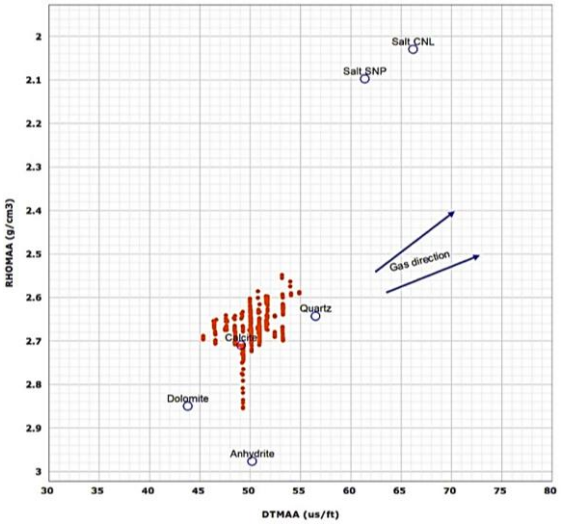


Fig. 8: Crossplot of RHOMAA (bulk density) versus DTMAA (acoustic transit time) for the Mus Formation, illustrating a predominantly limestone composition. Minor trends toward dolomite suggest localized dolomitization, while log-based anomalies may indicate potential zones of gas presence.

The V_{sh} curve shows a high volume of shale, which diminishes the RU-2 interval of the Mus Formation is the cleanest zone with the lowest V_{sh} values, indicating its potential as the primary reservoir target. In contrast, RU-1 and RU-3 have higher shale content, which could impact porosity and permeability negatively. Further analysis, such as porosity and saturation logs, would be necessary to confirm the reservoir quality of RU-2 (Fig. 9).

The Mus Formation has variable porosity and permeability, often ranging from 5-12% in the limestone layers. Dolomite intervals can have better porosity (10-15%) and permeability. The crossplot of effective porosity versus deep resistivity for the Mus Formation indicates a variation in fluid saturation and rock properties across the formation.

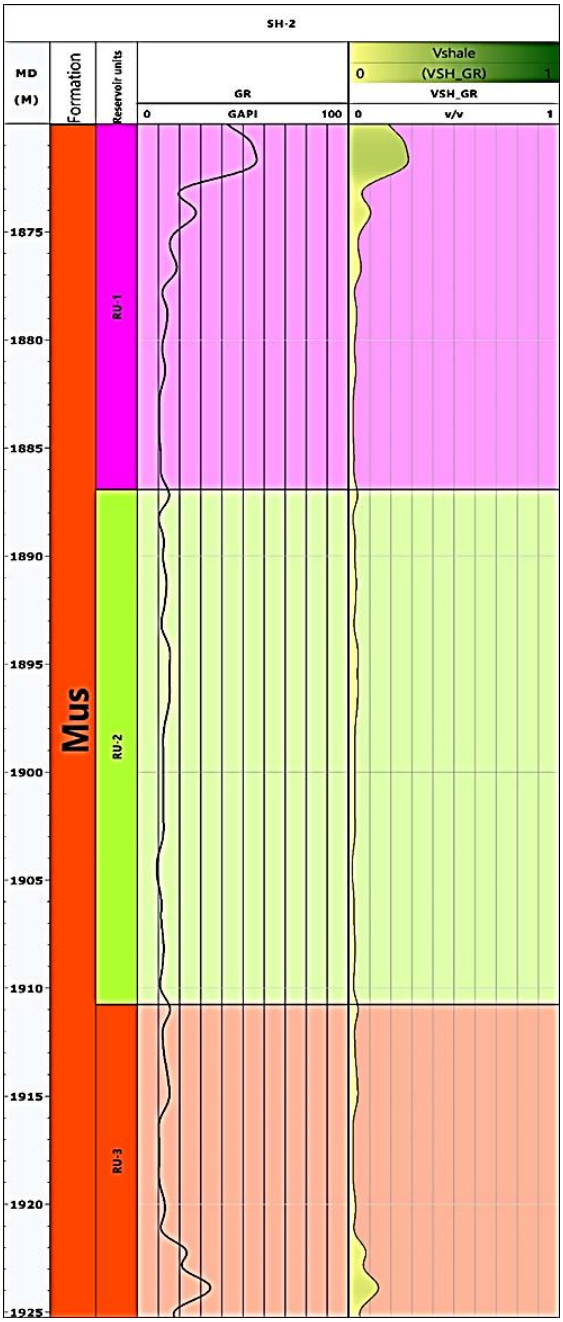


Fig. 9: Well log of the Mus Formation showing gamma-ray (GR) and shale volume (V_{sh}) distribution across reservoir units RU-1, RU-2, and RU-3.

Data points with high resistivity (>100 Ohm-m) and moderate to low porosity suggest potential hydrocarbon-bearing zones, as hydrocarbons impede electrical conductivity compared to water. Points with moderate resistivity (10–100 Ohm-m) and moderate porosity may indicate mixed fluid zones, with both hydrocarbons and water present in the pore spaces. In contrast, low resistivity values (<10 Ohm-m) correspond to water-saturated zones, where the higher electrical

conductivity is due to the presence of formation water. The porosity values range between 10% and 25%, consistent with carbonate reservoirs, and higher porosity zones indicate better reservoir quality with greater potential for fluid storage (Fig. 10). The clustering of data points at moderate to high resistivity with significant porosity highlights intervals of interest that may serve as hydrocarbon reservoirs. Further analysis, such as fluid saturation modeling and integration with other well logs, is required to validate these observations. This approach aids in the evaluation of water saturation and hydrocarbon potential of the reservoir.

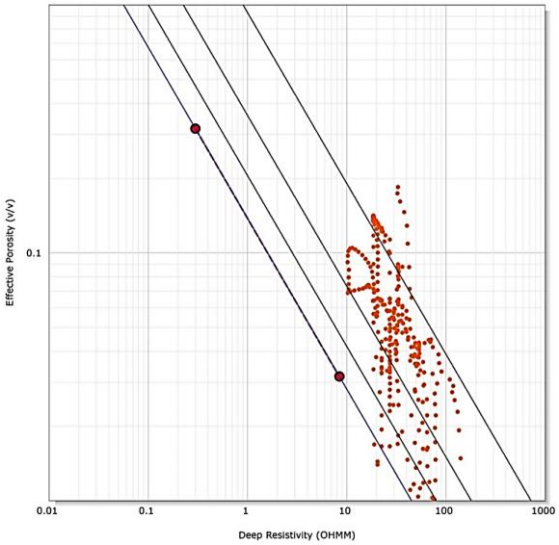


Fig. 10: Pickett plot displaying the relationship between deep resistivity and effective porosity.

Sargelu Formation

The petrophysical analysis of the Sargelu Formation, covering the depth interval between 1345 and 1420 meters (Fig. 11), reveals a complex and heterogeneous subsurface sequence that is predominantly composed of limestone interbedded with minor shale layers and dolomite (Abdula et al., 2015). Figure 11, which was generated using Techlog 2018 software, represents a well log section of the Sargelu Formation between the depths of 1345 and 1420 meters. It displays gamma-ray (GR) readings and the derived shale volume (V_{sh}_GR).

The GR curve, measured in GAPI units, indicates the natural radioactivity of the formation. Higher GR values (closer to 150 GAPI) correspond to shale-rich intervals, while lower GR values (closer to 0 GAPI) suggest cleaner lithologies, such as limestone or dolomite.

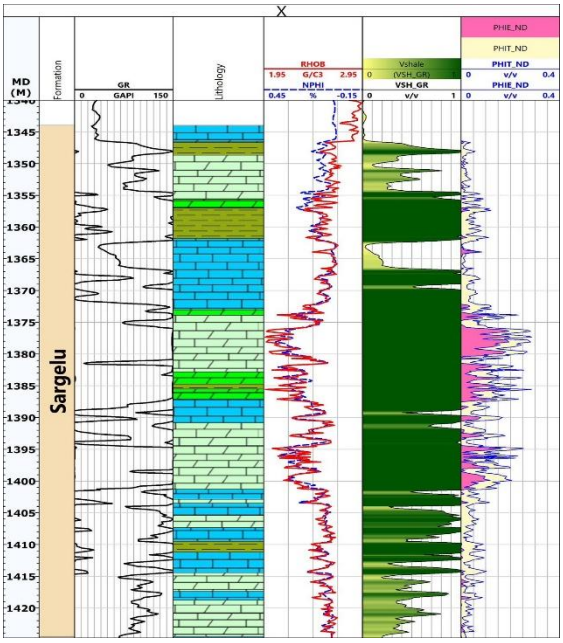


Fig. 11: Well log interpretation of the Sargelu Formation (1345–1420 m). Clean carbonate zones with low shale content and high porosity indicate good reservoir quality.

The V_{sh}_GR track, derived from the GR curve, quantifies the shale content, with a scale ranging from 0 (clean rock) to 1 (100% shale). Dark green areas in the V_{sh}_GR track indicate high shale content, while light green or white areas represent lower shale content. The alternating high and low GR values reflect lithological variability within the Sargelu Formation, which is characterized by interbedded shale and carbonates. Shale-rich intervals may act as barriers or seals for hydrocarbons, whereas the cleaner carbonate layers likely represent potential reservoirs, especially if enhanced by natural fractures. This interpretation aligns with the Sargelu Formation's role as both a source and reservoir rock in the Jurassic petroleum system. Figure 11 provides a detailed well log interpretation for the Sargelu Formation, focusing on effective porosity (PHIE) and other reservoir properties. The left track shows neutron (NPHI_D, in blue) and bulk density (RHOB, in red) curves, which are essential for lithological identification and porosity estimation. Deviations between these curves often indicate gas presence or changes in lithology. The middle track includes the gamma-ray (GR) curve and the derived shale volume (V_{sh}_GR), where green shading highlights shale content, and lighter areas

represent cleaner lithologies, such as carbonates. The right track displays total porosity (PHIT_ND, in blue) and effective porosity (PHIE_ND, in pink). Effective porosity (PHIE) represents the interconnected pore spaces available for fluid flow, excluding isolated pores or clay-bound water. In contrast, total porosity (PHIT) includes both interconnected and isolated pores (Fig. 11). The Sargelu Formation shows variable effective porosity, with higher values corresponding to cleaner carbonate intervals and lower values in shale-rich zones with higher GR and V_{sh}_GR readings. This variability emphasizes the potential of the Sargelu Formation as a hydrocarbon reservoir, where intervals with higher PHIE are more favorable for hydrocarbon storage and flow, particularly in fractured or carbonate-rich zones.

The analysis of well log data in this study reveals that the Sargelu Formation exhibits notable variability in porosity and fluid saturation in Fig. 12. Specifically, the SW_AR (water saturation in the uninvaded zone) and SXO_AR (water saturation in the flushed zone) curves indicate significant hydrocarbon presence within the depth interval of 1385 to 1400 meters. In this zone, low SW_AR values suggest that the pores are predominantly occupied by hydrocarbons, while higher SXO_AR values reflect partial displacement of hydrocarbons by drilling mud filtrate in the flushed zone. These interpretations are based directly on the petrophysical analysis conducted. On the other hand, the resistivity logs (LLD and MSFL) confirm the presence of hydrocarbons in these zones, with high deep resistivity values correlating with lower water saturation. The distribution of moved hydrocarbons (green) and residual oil (brown) further supports the interpretation that the Sargelu Formation has experienced hydrocarbon migration and entrapment. Figure 12 displays that the Sargelu Formation exhibits good reservoir potential, with intervals of effective porosity and hydrocarbon saturation. Limestone intervals exhibit porosities ranging from 8% to 12% and permeability between 5 and 30 millidarcies, providing excellent reservoir characteristics. Porosity greater than 5% is significant, while more than 25% is exceptional porosity (Selley, 1998).

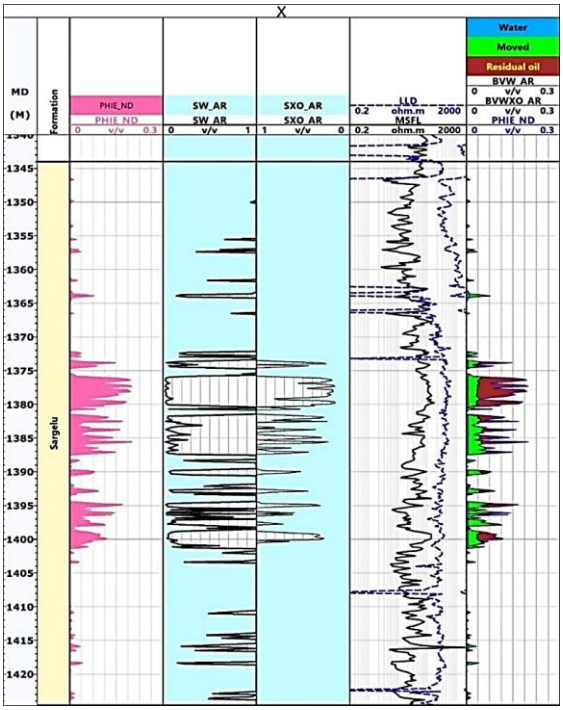


Fig. 12: Revised well log interpretation of the Sargelu Formation. The highlighted zone shows hydrocarbon presence characterized by low water saturation (SW_AR), higher flushed zone saturation (SXO_AR) indicating mud filtrate displacement, and high resistivity confirming hydrocarbon saturation.

The permeability-porosity crossplot indicates a logarithmic relationship between effective porosity (PHIE_ND) and permeability (K), where higher porosity generally results in increased permeability. The provided cutoff values—PHIE_ND = 0.03 v/v and SW = 0.24—help define productive reservoir intervals (Figures 13 and 14).

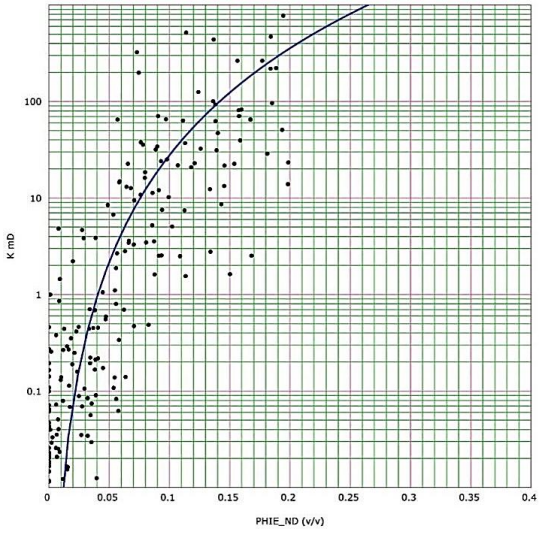


Fig. 13: Permeability vs. effective porosity (PHIE_ND) crossplot.

The cutoff values of PHIE_ND = 0.03 v/v and Sw = 0.24 were derived based on the data distribution and fitted trendlines observed in Figures 13 and 10, which represent crossplots of permeability vs. porosity and water saturation vs. porosity, respectively.

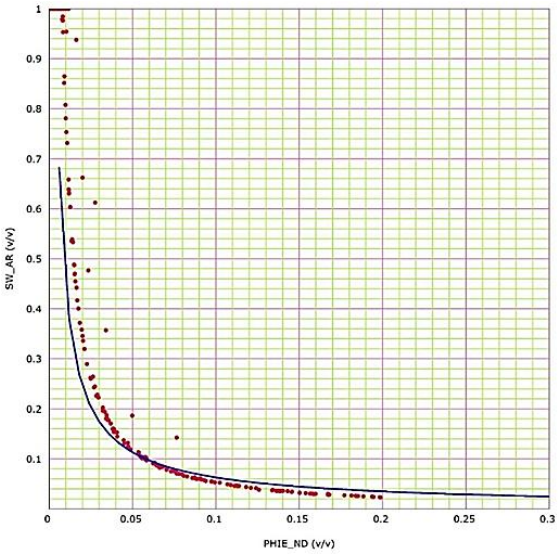


Fig. 14: Crossplot of effective porosity (PHIE_ND) versus water saturation (Sw) for the Sargelu Formation.

In Figure 13, the permeability (K) versus effective porosity (PHIE_ND) crossplot displays a strong positive correlation as porosity increases, permeability also increases, particularly beyond the 0.03 v/v threshold. Below this porosity value, permeability remains consistently low, often below 1 mD, indicating poor fluid flow capacity. However, once porosity exceeds 0.03 v/v, there is a marked increase in permeability, often surpassing 10 mD, which is indicative of effective reservoir intervals. This inflection point justifies using 0.03 v/v as the lower porosity cutoff for identifying productive zones.

Similarly, in Figure 14, which shows the relationship between water saturation (Sw_AR) and porosity, a clear inverse trend is observed: water saturation decreases as porosity increases. The majority of the data points fall below the Sw value of 0.24, particularly in the porosity range above 0.03 v/v. These low Sw values indicate reduced water content and higher hydrocarbon saturation, which are favorable for hydrocarbon production. The fitted curve reinforces this trend, further validating the Sw = 0.24 cutoff as an effective threshold for distinguishing between hydrocarbon-bearing and water-bearing zones. Both cutoff values are not arbitrarily chosen but are empirically supported by the clustering and trends seen in the data. The intersection of porosity above 0.03 v/v and Sw below 0.24 marks the transition into zones with both sufficient pore volume and favorable fluid saturation, which are key indicators of reservoir productivity.

In Figure 15, the provided well log from the Sargelu Formation covers a depth interval from approximately 1345 m to 1415 m, and includes gamma-ray (GR), density (RHOB), neutron porosity (NPHI), and permeability (K) measurements. The gamma-ray log indicates moderate to high natural radioactivity, reflecting a sequence dominated by alternating shale and carbonate lithologies.

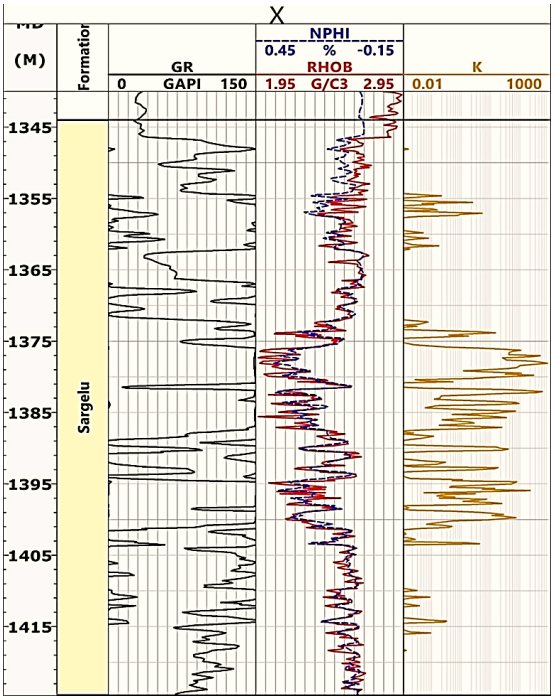


Fig. 15: Well log analysis of the Sargelu Formation showing gamma ray (GR), neutron porosity (NPHI), bulk density (RHOB), and permeability (K) curves.

The neutron and density porosity logs display variable separation, suggesting heterogeneous porosity typical of mixed carbonate-shale successions. Permeability is relatively low in the upper part of the interval, from 1345 m to about 1365 m, corresponding to tighter lithologies. Between 1365 m and 1385 m, permeability improves moderately, while the most significant and continuous permeability enhancement occurs between 1385 m and 1400 m. This zone likely represents cleaner carbonate beds or intervals affected by secondary porosity development such

as fracturing. Below 1400 m, permeability decreases markedly, indicating a transition to tighter, more shale-rich rocks. The Sargelu Formation in this section shows its best reservoir potential between 1385 m and 1400 m, while both the upper and lower sections are characterized by poorer reservoir quality.

Three RU zones refer to distinct reservoir units within the Sargelu Formation identified based on well log data. These zones are classified based on key reservoir characteristics, such as gamma ray values, porosity, bulk density (RHOB), and permeability.

RU-1: This is the first reservoir unit, characterized by moderate porosity and lower permeability compared to RU-2. While it may still contain hydrocarbons, its lower permeability suggests limited fluid flow capacity and potentially lower reservoir quality.

RU-2: This is considered the best reservoir unit, showing favorable characteristics such as lower gamma ray values, a strong RHOB-NPHI crossover (indicating good porosity), and higher permeability. These attributes suggest that RU-2 has significant hydrocarbon potential with good fluid flow capacity.

RU-3: This reservoir unit is similar to RU-1, with moderate to low porosity and permeability, but it may also exhibit some heterogeneity, which could affect its overall reservoir potential. Though it could contain hydrocarbons, the lower permeability and potential for variability make it less favorable than RU-2.

RU-2 appears to be the best reservoir zone due to lower gamma ray values, strong RHOB-NPHI crossover, and higher permeability (Fig. 16). RU-1 and RU-3 may contain hydrocarbons, but exhibit lower permeability and potential heterogeneity (Fig. 16).

Natural fracturing within the formation further enhances its capacity for hydrocarbon storage and flow. Renowned as one of the most significant Jurassic reservoirs in the region. The Sargelu Formation holds substantial hydrocarbon potential, particularly within its fractured limestone zones. Log-based indicators, including density-neutron crossovers, gamma ray lows, and sonic-density separation, further support the presence of fracture-enhanced porosity in the carbonate sections (Aqrawi et al., 2010). Structurally, the Sargelu Formation is situated within the High Folded Zone of the Zagros Fold-Thrust Belt, where compressional tectonics have created extensive fracture systems in Jurassic carbonates (Garfunkel, 2004; Al-Ameri and Zumberge, 2012). Numerous regional studies have also recognized the Sargelu Formation as a key petroleum system element, acting both as a source and a fractured reservoir unit in northern Iraq (Jassim and Al-Gailani, 2006; Aqrawi et al., 2010; Abdula, 2020).

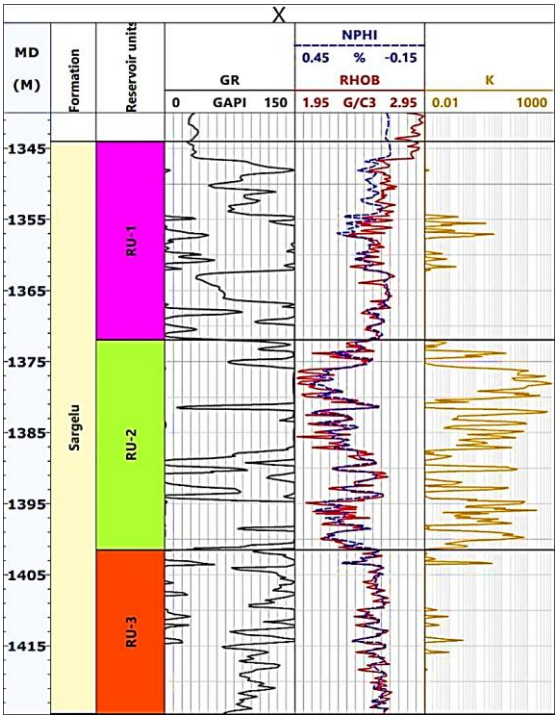


Fig. 16: Well log data of the Sargelu Formation with reservoir units RU-1, RU-2, and RU-3.

6. Conclusion

This study highlights the differing reservoir potentials of the Jurassic Sargelu and Mus formations in the Duhok region, as revealed through comprehensive petrophysical analysis. The Sargelu Formation stands out for its superior reservoir quality, particularly between 1385 and 1400 meters, where fractured limestones and interbedded shales exhibit high porosity, favorable water saturation, and enhanced permeability due to natural fracturing. Well log interpretations identify clean carbonate intervals within this depth range, which are likely to serve as productive hydrocarbon reservoirs. In contrast, the Mus Formation displays more lithological diversity, consisting mainly of limestone and dolomite, along with subordinate marl and shale. While some sections of the Mus Formation show moderate

porosity and resistivity values suggesting hydrocarbon potential, the increased shale content in other zones may hinder reservoir performance. Overall, the Sargelu Formation demonstrates more favorable reservoir characteristics than the Mus Formation, largely due to its cleaner lithology and greater fracture development. The integration of petrophysical data including porosity, resistivity, and lithological profiles offers valuable insights into reservoir heterogeneity and highlights promising zones for hydrocarbon exploration within the Jurassic stratigraphy of northern Iraq.

7. Acknowledgements

The corrections and suggestions provided by anonymous reviewers and editor staff of INJES are highly acknowledged. Their help has been incorporated into the improvement of the manuscript.

8. Conflict of Interest

The authors declare that they have no conflict of interest.

9. Funding Statement

This research received no external funding.

10. Author Contributions

Parween Ramadhan Abid performed analysis and conducted result interpretation and wrote the whole manuscript. Rzger Abdulkarim Abdula contributed to critically reviewing the manuscript and contributing ideas to improve the paper.

11. References

Abdula, R.A., 2015. Hydrocarbon potential of Sargelu Formation and oil-source correlation, Iraqi Kurdistan. Arabian Journal of Geosciences, 8(8), 845-5868. https://doi.org/10.1007/s12517-014-1651-0

Abdula, R.A., Balaky, S.M., Nourmohamadi, M.S., and Peroui, M., 2015. Microfacies analysis and depositional environment of the Sargelu Formation (Middle Jurassic) from Kurdistan Region, northern Iraq. Donnish Journal of Geology and Mining Research, 1(1), pp. 001-026.

Abdula, R.A., 2016. Organic geochemical assessment of Jurassic potential source rock from Zab-1 Well, Iraqi Kurdistan. Iraqi Bulletin of Geology and Mining, 12(3), pp. 53-64.

Abdula, R.A., 2017a. Source rock assessment of Naokelekan Formation in Iraqi Kurdistan. Journal of Zankoy Sulaimani, 19(1), pp. 103-124.

Abdula, R.A., 2017b. Petroleum system modeling of Jabal Kand Oil Field, Northern Iraq. ZANCO Journal of Pure and Applied Sciences, 29(2), pp. 88-95.

Abdula, R.A., 2020. Oil and gas generation history based on burial history reconstruction and thermal maturity modeling of petroleum systems in Kurdistan Region, Iraq. Journal of Petroleum Research and Studies (JPRS), 29(12), pp. E95-E120. https://doi.org/10.52716/jprs.v10i4.370

Agada, S., Chen, F., Geiger, S., Toigulova, G., Agar, S., Benson, G., Shekhar, R., Hehmeyer, O., Aour, F. and Mutti, M., 2013. Deciphering the fundamental controls of flow in carbonates using numerical well-testing, production optimisation, and 3D high-resolution outcrop analogues for fractured carbonate reservoirs. SPE Europe featured at EAGE Conference and Exhibition. SPE-164805-MS.

Al-Ameri, K. and Zumberge, J., 2012. Middle and Upper Jurassic hydrocarbon potential of the Zagros Fold Belt, North Iraq. Marin and Petroleum Geology 36: pp. 13-34.

Al-Dabagh, M.M. and Asaad, I.S., 2025. Investigation of petrophysical properties of Butmah Formation (Early Jurassic) using well logs of selected wells, northern Iraq.

Al-Habba, Y.K., 1988. Possible petroleum source rocks in the well Kand-1. Oil Exploration Company Archives, Baghdad, unpublished report, (In Arabic)

Ali, M.S., Al-Dabagh, M.M., and Asaad, I.S., 2022. Determination of porosity types impressive on Butmah Formation (Early Jurassic) in selected wells, Northern Iraq (case study). AIP Conference Proceedings, AIP Publishing.

Al-Naqib, S.Q. and Al-Juboury, A.I., 2014. A new look on the Jurassic formations of the western part of Iraq. Arabian Journal of Geosciences, 7, pp. 559–588.

Alrekabi, H.M. and Al-Fatlawi, O.F., 2024. Integrating rock typing and petrophysical evaluations to enhance reservoir characterization for Mishrif Formation in Garraf oil field. Iraqi Geological Journal, pp. 131–152. https://doi.org/10.46717/igj.57.1D.12ms-2024-4-22

Aqrawi, A.A.M., Goff, J.C., Horbury, A.D., and Sadooni, F.N., 2010. The petroleum geology of Iraq. Scientific Press, London.

Asquith, G.B., Krygowski, D., and Gibson, C.R., 2004. Basic well log analysis, American Association of Petroleum Geologists, Tulsa.

Bellen, R.V., Dunnington, H., Wetzel, R., and Morton, D., 1959. Lexique stratigraphique international. Asie, Iraq, 3, 324 P.

Dohan, A.H., Hassan, F.N., and Kadhim, L.S., 2022. Depositional environment of Middle Jurassic Sargelu Formation based on petrographical study in selected wells at Balad, Ajil, and Baiji oilfields, Central Iraq. Tikrit Journal of Pure Science, 27, pp. 31–42. https://doi.org/10.25130/tjps.v27i3.53

Dunnington, H.V., 1958. Generation, migration, accumulation, and dissipation of oil in northern Iraq: Middle East.

Ellis, D.V. and Singer, J.M., 2007. Well logging for earth scientists, Springer. https://link.springer.com/book/10.1007/978-1-4020-4602-5

El Sharawy, M.S. and Nabawy, B.S., 2019. Integration of electrofacies and hydraulic flow units to delineate reservoir quality in uncored reservoirs: A case study, Nubia Sandstone Reservoir, Gulf of Suez, Egypt. Natural Resources Research, 10(4), pp. 1587-1608. https://doi.org/10.1007/s1105 3-018-9447-7

Garfunkel, Z., 2004. Origin and structure of the Dead Sea basin: a review. In: C. Morley (ed.), Evolution and Dynamics of Sedimentary Basins in the Zagros and Makran Region. Geological Society, London, Special Publications, 372, pp. 1–23.

Grabowski, J.R., G.J. and Norton, I.O., 1995. Tectonic controls on the stratigraphic architecture and hydrocarbons systems of the Arabian Plate. Society of Exploration Geophysicists, Tulsa, OK (United States).

Jassim, S.Z. and Al-Gailani, M., 2006. Hydrocarbons, chapter 18, in Jassim, S.Z., and J.C. Goff, eds., Geology of Iraq, first edition: Brno, Czech Republic, Prague and Moravian Museum, pp. 326-354.

Jassim, S.Z., Buday, T., Cicha, I., and Prouza, V., 2006. Late Permian-Liassic Megasequence AP6. Chapter 9, in: Jassim and Goff, 2006 (Eds.), Geology of Iraq, Prague: Dolin; Brno: Moravian Museum, pp. 124-144.

Jassim, S.Z. and Buday, T., 2006. Units of the Stable Shelf, chapter 5. Geology of Iraq (1st ed.). Brno, Czech Republic, Prague and Moravian Museum, pp. 53-72.

Khudhair, M. H. and Idan, R. M., 2024. Geochemistry and reservoir properties of the Upper Jurassic formations in selected oilfields, Central Iraq. IOP Conference Series: Earth and Environmental Science. IOP Publishing, 012031.

Mackertich, D. and Samarrai, A., 2013. The History of Hydrocarbon Exploration in Iraqi Kurdistan: 1901 to 2012. Geol-Soc-Zagros-Conference-Presentation.

Pitman, J. K., Steinshouer, D., and Lewan, M. D., 2004. Petroleum generation and migration in the Mesopotamian Basin and Zagros Fold Belt of Iraq: Results from a basin-modeling study. GeoArabia, 9(4), pp. 41–92.

Sadooni, F. N., 1997. Stratigraphy and petroleum prospects of Upper Jurassic carbonates in Iraq. Petroleum Geoscience, 3, 233-243.

Selley, R.C., 1998. Elements of Petroleum Geology. 2nd edition, Academic Press, London, United Kingdom. 471 P.

Sharland, P.R., Casey, D.M., Davies, R.B., Simmons, M.D., and Sutcliffe, O. E., 2004. Arabian plate sequence stratigraphy–revisions to SP2. GeoArabia, 9, pp. 199-214. https://doi.org/10.2113/geoarabia0901199

Shedid, S.A., 2018. A new technique for identification of flow units of shaly sandstone reservoirs. Journal of Petroleum Exploration and Production Technology 8, pp. 495–504. https://doi.org/10.1007/s13202-017-0350-2

Sissakian, V.K. and Al-Khalidi, Z.B., 2012. The Lithological Map of Iraq. Iraqi Bull. Geol. Min., 8(3), pp. 1-13.

Zangana, H.A., Sherwani, G.H., Tawfeeq, Y.J., and Al-Ansari, N., 2020. Reservoir characterization of the Early Jurassic Butmah Formation using well log data in selected wells from Iraqi Kurdistan Region. Open Journal of Geology, 10, pp. 1173–1188.

Iraqi National Journal of Earth Science, Vol. 26, No. 04, 2026 (193-205)

Iraqi National Journal of Earth Science

www.earth.uomosul.edu.iq

تقييم جودة الخزن في تكوينات العصر الجوراسي (موس و سرگلو) في محافظة دهوك، إقليم كردستان، العراق

بروين رمضان عابد[1] **رزگار عبدالكريم عبدالله [2]***

parweenhajani@gmail.com rzger.abdulkarim@tiu.edu.iq

[1] قسم علوم الأرض، كلية العلوم، جامعة دهوك، دهوك، أقليم كوردستان، العراق.

[2] قسم هندسة النفط و المعادن، كلية الهندسة، جامعة تيشك الدولية، اربيل، أقليم كوردستان، العراق.

**الباحث المراسل.*

تاريخ الاستلام: 05 شباط 2025 تاريخ المراجعة: 05 أيار 2025 تاريخ القبول: 15 تموز 2025

تاريخ النشر الالكتروني: 01 تشرين الأول 2026

الملخص

تبحث هذه الدراسة في خصائص مكامن التكوينات تحت السطحية الجوراسية، وتحديدًا تكويني موس وسارگلو في محافظة دهوك، ضمن إقليم كردستان العراق. ومن خلال تحليل بيانات مجسات الآبار التفصيلية من بئر X ، تم تقييم الخصائص البتروفيزيائية الأساسية، مثل المسامية والنفاذية وتشبع الماء والخصائص الصخرية لتحديد المناطق المحتملة الحاملة للهيدروكربونات. يتميز تكوين سارگلو، الواقع بين أعماق 1345 و 1420 مترًا، بخصائص صخرية غير متجانسة تهيمن عليها أحجار جيرية متشققة متداخلة مع طبقات الصخر الطفل الصفحي. ويكشف هذا الفاصل عن قيم مسامية فعالة تصل إلى 18%، ونفاذية متزايدة نتيجة التشقق، وتشبع مائي مناسب، خاصةً بين 1385 و1400 متراً. في المقابل، يتكون تكوين موس، الواقع بين 1875 و1925 مترًا، بشكل أساسي من الحجر الجيري والدولوميت مع أنماط متفاوتة من المسامية والمقاومة. تشير تفسيرات المخططات المتقاطعة ومخططات بيكيت إلى احتمال وجود هيدروكربونات على الرغم من محدودية الأدلة المباشرة من مؤشرات الغاز. بشكل عام، يتميز كلا التكوينين بجودة خزن كبيرة، وإن كانت متفاوتة، تتحكم فيها التباينات الصخرية، ودرجة التشقق، وتوزيع المسامية، ومحتوى الصخر االطفل الصفحي. يوفر التحليل البتروفيزيائي المتكامل فهمًا أعمق لسلوك الخزانات الجوراسية في هذه المنطقة غير المستكشفة نسبيًا في شمالي العراق.

الكلمات المفتاحية:

خصائص البتروفيزيائي، جودة الخزانات ،الجوراسي، تفسير مجسات الأبار ، المسامية ،النفاذية .

DOI: 10.33899/injes.v26i4.60917, *©Authors, 2026, College of Science, University of Mosul.*

This is an open-access article under the CC BY 4.0 license (http://creativecommons.org/licenses/by/4.0/)

Iraqi National Journal of Earth Science, Vol. 26, No. 04, 2026 (206-218)

Iraqi National Journal of Earth Science

www.earth.uomosul.edu.iq

Analysis of the Morphometric Characteristics and Their Relationship with the River Network Properties of Valley Al-Amghar Basin, Southwestern Al-Muthanna Desert: An Applied Statistical Study

Hader M. A. Al-Kafari [1*] **Safaa A. Al-Asadi** [1]

gaky.gon1991@gmail.com safaa.al_asadi@uobasrah.edu.iq

[1] *Department of Geography, College of Education, University of Basrah, Basrah, Iraq.*
** Correspondence author.*

Received: 07 February 2025 Received in revised form: 17 April 2025 Accepted: 20 June 2025
Available online: 01 October 2026

Abstract

Valley Al-Amghar basin, located in the southwestern part of the Al-Muthanna desert, is characterized by its flat terrain and general topographic smoothness with minimal relief variations. The basin extends over a length of 85.32 km with a low topographic difference of 158 meters, resulting in a gentle slope averaging 1.85. This has significantly influenced sedimentary properties and the flow velocity within the basin. The basin contains 7,747 watercourses, reflecting the impact of topographic factors on the fluvial network's characteristics and including stream orders, lengths, and both numerical and linear drainage densities. The study focuses on the influence of low-gradient terrain on the development of the fluvial network, employing geomorphological indicators such as relative relief, ruggedness ratio, and hypsometric integral. Stream orders are classified using Strahler's method. Results indicate that larger sub-basins exhibit a greater number and length of streams, with a positive correlation between basin area and stream number, and an inverse relationship between hypsometric integral and topography. Stream density increases in areas with moderate slopes and softer lithology, while the hypsometric integral decreases as ruggedness increases.

Keywords:

Al-Amgher, Ruggedness Ratio, River Network, River Orders, Pearson.

DOI: 10.33899/injes.v26i4.60919, *©Authors, 2026, College of Science, University of Mosul.*
This is an open-access article under the CC BY 4.0 license (http://creativecommons.org/licenses/by/4.0/).

==========

1. Introduction

The study of the relationship between terrain characteristics and river network properties is a vital topic in morphometric studies and water resource management (Schumm and Sugden, 1984). Such studies contribute to understanding the behavior of river basins and their capacity to manage floods and optimize water resource utilization (Strahler, 1952). This research aims to analyze the relationship between the topography of the Al-Amghar Valley basin and the properties of its river network, emphasizing how topographic features influence surface runoff dynamics and the basin's ability to form efficient river networks (Horton, 1945). Topography plays a pivotal role in defining river network characteristics, including stream orders, channel lengths, and both numerical and linear densities. Variations in slopes highlight differences in relief, which are determined by rock types influencing surface runoff dynamics and water velocity within the basin. These variations significantly impact the sedimentary processes and erosion patterns (Summerfield, 2014 and 1991; Tarboton, 1997; Bishop, 2004). Topographic features also shape the river networks by influencing water distribution and flow. Areas with gentle slopes often exhibit higher network density due to slower runoff (Qin and Wang, 2022; Boothroyd, 2023; Rahaman et al., 2017). Analyzing this relationship aids in understanding the geomorphological processes and environmental planning by

revealing how topography shapes local hydrology, streamflow patterns, and water discharge (Arefin and Alam, 2020; Gajbhiye, 2014).

2. Materials and Methods

Study Area

The Valley Al-Amghar basin is located in the southwestern Badia of Al-Muthanna Governorate in Iraq. Geographically, the basin lies between latitudes 29°42'21"N and 28°56'37"N, and longitudes 45°09'60"E and 45°43'50"E. The basin spans an area of 1778.76 km², with 1504.55 km² (84.5% of its area) situated within the administrative boundaries of Al-Muthanna Governorate, while the remaining 274.21 km² (15.5%) extends into the Kingdom of Saudi Arabia (Fig. 1) (Jasib, 2011; Ministry of Water Resources, 2013; Directorate of Al-Muthanna Municipality, 2022).

A. Geology

The basin falls within the Salman Zone, which is part of a secondary fault network including the Euphrates Fault, stretching from the northeast to the southeast (Wajid, 2017). This zone is characterized by geological formations from the Tertiary and Quaternary periods (Al-Zurfi, 2021), as given in Table (1).

Table 1: Geological formations in the Al-Amghar basin.

Geological time	Geological Formation	Area (km^2)	Percentage (%)
Tertiary Deposits	Dibdibba Formation	1236.31	69.5
	Middle Dammam Formation	356.54	20.04
	Upper Dammam Formation	103.11	5.8
	Al-Zahra Formation	3.49	0.2
Quaternary Deposits	Depression-Fill Deposits	52.84	2.97
	Valley-filling Deposits	26.47	1.49
	Total	1778.76	100

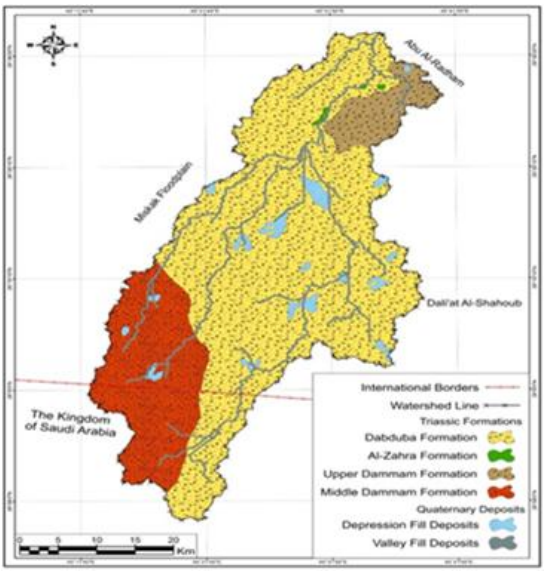


Fig. 1: Location and geology of valley Al-Amghar in Iraq.

B. Climate of the Al-Amghar basin

The climate of the Al-Amghar basin is characterized by long dry periods throughout the year. It is influenced by a variety of climatic variables, with temperature and precipitation being the most significant. Data from six surrounding meteorological stations (Basra, Nasiriyah, Samawah, Hafar Al-Batin, Rafha, and Al-Qaisumah) provide insights into these climatic conditions (Table 2).

The region experiences high temperatures in the summer ranging from 34.6°C to 39.1°C. In winter, the temperature drops to a range between 12.7°C and 14.2°C. The annual average temperature fluctuates between 24.4°C and 27°C.

Precipitation is almost nonexistent during the summer months. In winter, however, rainfall ranges from 45.9 mm to 79.4 mm with the total annual rainfall varying between 99 mm and 127.3 mm depending on the station.

Table 2: Climatic data (temperature and precipitation) of the study area (2000–2023).

Seasons			Stations					
			Samawah	Nasiriyah	Basrah	Rafha	Hafar Al-Batin	Qaisumah
Winter	Temperature	Average	13.9	14.2	14.2	12.7	13.6	14.2
	Rainfall	Total	46.2	55.8	79.4	45.9	54	58
Spring	Temperature	Average	26.6	26.3	26	24.2	25.9	26.5
	Rainfall	Total	32	32.1	22.3	30.1	29	30
Summer	Temperature	Average	38.3	39.1	38.4	34.6	35.9	36.9
	Rainfall	Total	0	0	0	0	0	0
Autumn	Temperature	Average	27.5	28.3	27.9	25.8	26.6	27.6
	Rainfall	Total	34.8	28.4	25.6	23	29	28
Annual Average		Temperature	26.6	27	26.6	24.4	25.6	26.3
Annual Total		Rainfall	113	116.3	127.3	99	112	116

3. Results Topographic Characteristics

The topographic features of the Al-Amghar basin represent the final form of the watershed, shaped by geomorphological factors such as weathering and erosion. Weathering processes break down rocks into smaller pieces, which are then transported by erosional forces (water and wind). These processes contribute to the change in the basin's topography, influenced by geological formations since the basin's inception to the present day (Maria and Lestiana, 2018). Topographic characteristics vary among different basins and attributed to many factors such as rock type, vegetation, soil, and climate. The topography tends to be more rugged in areas with geological weaknesses, especially during successive geological periods (Shekar and Mathew, 2023). To understand these features, it is essential to analyze the spatial characteristics of the basin (Table 3). The basin's size can impact water runoff and river network density, thereby influencing the development of topographic features. The basin's spatial dimensions, particularly its longitudinal dimensions, are key to understanding these features.

Table 3: Spatial Characteristics of the Al-Amghar and its sub-basins.

Basin	Area (km^2)	Percentage %	Basin Length (km)	Basin Width (km)
1	736.47	41.41	73.13	10.0
2	866.32	48.70	65.8	13.1
3	78.24	4.39	13.84	5.65
4	97.73	5.50	23.73	4.11
Average	444,69	25	44,12	8,21
Al-Amghar	1778.76	100	85.32	20.84

A. Relief Ratio

The slope steepness ratio is a measure of the average gradient of the basin and represents the topographic relief affecting water flow and sediment transport. This ratio helps in determining the density, frequency, and depth of the river network as well as the amount of sediment carried by the flow (Petticrew and Lobb, 2013). It is calculated using the following formula (Strahler, 1957).

Ruggedness Ratio=Difference between the highest and lowest points in the basin (m)/Basin length (km)

From Table (4), it is clear that the ruggedness ratio in the basin reached 1.85, and the average of the secondary basins is 2.75. There is variation in the relative ruggedness between the secondary basins with the third basin recording

the highest value of 3.68, while the second basin recorded the lowest value of 1.62. It is evident from the table that the third and fourth basins recorded the highest values of 3.68 and 3.66 respectively. This is due to the smaller size of these two basins compared to the others and the proximity of the contour lines, which leads to increased river erosion. On the other hand, the first and second basins recorded values of 2.05 and 1.62 respectively. This decrease is attributed to the larger size of these two basins and the wider spacing of the contour lines indicating lower slopes, which leads to a lower ruggedness ratio. The variation between the secondary basins is not large indicating similar environmental conditions and the dominance of low-resistant rocks to water and wind erosion processes. Overall, all the ruggedness ratio values are considered low compared to basins located in mountainous areas, where this ratio can exceed 100.

B. Relative Relief

Relative relief illustrates the relationship between the topographic range and the perimeter of the basin, representing the degree of ruggedness of the drainage basins. High values

indicate the inability of the rocks to resist erosion and their geological weakness, while low values indicate the high resistance of the rocks. It is calculated according to the following relationship (Melton, 1957).

$$\text{Relative Relief} = (\text{Basin Relief}) / (\text{Basin Perimeter in km}) * 10$$

Table (4) reveals that the mean relative relief of the Al-Amghar watershed is 5.39, while the mean of the sub-watersheds is 8.77. There is a significant variation among the sub-watersheds, with the fourth sub-watershed recording the highest value of 13.46, attributed to its small size and closely spaced contour lines. Conversely, the second sub-watershed recorded the lowest value of 4.81 due to its larger size, being the largest among the sub-watersheds. The higher values of relative relief result in increased surface runoff velocity and affect the characteristics of river flow consequently.

C. Ruggedness Value

It is a measure used to determine the extent of the impact of topography on the river network and the intensity of drainage within the basin. It illustrates the relationship between the topographic development of the basin and the branching of river channels. Alternatively, it is the process of measuring the relationship between the ruggedness of the basin and the length of the river drainage network. Strahler (1964) confirmed that a higher value of this indicator indicates an increase in drainage density due to the increase in the number of channels. The decrease in this value is due to the lower number of channels and the smaller size of the basin. It is calculated according to the following equation (Minár and Evans, 2008).

$$\text{Ruggedness Value} = (\text{Basin Relief}) * (\text{Drainage Density}) / 1000$$

From Table (4), it is also clear that the average ruggedness value in the study area is 0.27, and the average for the secondary basins is 1.37. There is a clear variation between the secondary basins, with the fourth basin recording the highest value of 2.68. This is due to the intensity of ruggedness and the presence of water erosion during rainfall, which transported sediments down the slopes from the upper reaches of the basin. Water erosion alters the shape of the basin and increases the branching of the drainage networks, leading to higher ruggedness in this basin. On the other hand, the second basin recorded the lowest value of 0.38, which is attributed to the less intense topography and the gentler slope in this basin.

D. Hypsometric Integration

It is an index that shows the relationship between the basin area and its topography, and the results of this index indicate the geomorphological stage reached by the basin. It is expressed by the following equation (Strahler, 1952).

$$\text{Hypsometric Integration} = (\text{Basin Area in km}^2) / (\text{Basin Relief in m})$$

From Table (4), it is clear that the average hypsometric integration for the study area is 11.25, and the average of the secondary basins is 3.91. As for the secondary basins, there is a clear variation, with the second basin recording the highest value of 8.09. This increase in value, along with the main basin, is due to the larger area of these basins, indicating an advanced stage in the erosion cycle, where the topography becomes more level. These basins are characterized by a flatter surface, unlike the fourth basin, which recorded the lowest value of 1.12. This is attributed to its smaller area and more rugged topography, indicating a less mature geomorphological stage with more prominent topographic features.

E. Geomorphic Number

It is a measure that shows the relationship between the topography (ruggedness) and the slope degree of the surface in the river basin. It depends on the drainage density and slope, reflecting the mutual influence between them in the formation of the basin's geomorphological surface. The geomorphic number is directly proportional to the slope, where a low geomorphic number indicates less sloping topography, while a high value indicates steep topography (Ahmed, 2016).

$$\text{Geomorphic Number} = \text{Ruggedness Value} / \text{Ruggedness Ratio}$$

It can be observed from Table (4) that the average geomorphic number for the study area is 0.14, indicating the presence of moderately

sloping topography in the region. Meanwhile, the secondary basins recorded a higher average of 0.43, suggesting steeper topography compared to the main basin. The second basin recorded the lowest geomorphic number of 0.23, which is due to the larger area of this basin, leading to more level topography. On the other hand, the fourth basin recorded the highest value of 1.11, indicating more rugged topography. Moreover, it is clear in Table (4) that the surface slope within the basin is relatively gentle due to the less varied topography

Table 4: Topographic characteristics of the secondary basins in the Al-Amghar basin.

Basin	Maximum Elevation in the Basin (m)	Minimum Elevation in the Basin (m)	Ruggedness Ratio (m/km)	Relative Relief	Ruggedness Value	Hypsometric Integral	Geometric Number
1	367	217	2.05	6.95	0.62	4.90	0.30
2	375	268	1.62	4.81	0.38	8.09	0.23
3	287	236	3.68	9.89	1.80	1.53	0.48
4	312	225	3.66	13.46	2.68	1.12	0.73
Average	335.25	236.5	2.75	8.77	1.37	3.91	0.43
Al-Amghar	375	217	1.85	5.39	0.27	11.25	0.14

Moreover, it is clear in Table (4) that the surface slope within the basin is relatively gentle due to the less varied topography between the basins, indicating a relative flattening of the terrain and a decrease in slope variation between the secondary basins.

4. Characteristics of Drainage Networks

Drainage networks are a true reflection of the natural conditions, including geological structure, climatic conditions, and tectonic factors. These factors, such as the type of rocks, tectonic uplift movements, rainfall, and the effect of temperature on weathering, determine the shape and design of drainage networks. Additionally, climate plays a crucial role in determining the density and temporal distribution of water, thus influencing the formation of drainage networks.

A. River Order

River order is defined as a classification system used to determine the rank of watercourses based on their connection to other streams. It starts from the streams that have no tributaries (first order) to the main rivers that receive flow from multiple tributaries (Miller and Wohl, 2020). The researcher relied on the Strahler (1952) method for calculating river orders, which is one of the simplest and most effective methods for determining river hierarchy (Fig. 2). Due to the simplicity of this method, it has been made easier to compare river basins with other studies. The variation in the number of river orders is due to the nature of the rocks that make up the basin. An increase in their number indicates that the rocks are resistant to channel widening. Conversely, in less resistant rocks, the number of streams decreases, but their width increases (Charlton, 2007).

Table (5) shows that the total number of river orders in the Al-Amghar basin is 7,747 watercourses. The number of streams varied according to the level of each order, with the first-order streams totalling 5,869, which represents 75.75% of the total watercourses in the basin. The second order recorded 1,454 streams, accounting for 18.76%, while the third order had 329 streams, or 4.24%. The fourth order had 77 streams, representing 0.99%. The fifth, sixth, and seventh orders recorded 14, 3, and 1 stream, respectively, accounting for 0.18%, 0.05%, and 0.03%. It can be observed from Table 5 that the number of streams decreases as their order increases. (Table .5) also compares the river orders among the different basins. It shows that the second basin is recorded as the highest in river orders with 3,618 streams, or 46.70% of the total watercourses. This is due to the large area of this basin, which is the largest secondary basin in terms of area (866.32 km²), representing 48.70% of the total basin area. This larger area results in greater water flow and, consequently, more streams. In contrast, the third basin records the lowest number of river orders with only 356 streams, accounting for 4.59% of the total river orders in the basin. This is also due to its smaller area, as it has the smallest area among the secondary basins, with 78.24 km², or 4.39% of the total area, leading to less water yield and fewer streams.

Table 5: Orders of drainage networks and total number of channels for the Al-Amghar basin

Basin	First Order	Second Order	Third Order	Fourth Order	Fifth Order	Sixth Order	Seventh Order	Total km	Percentage%
1	2519	638	145	30	6	2	1	3341	43,12
2	2743	677	151	40	6	1	0	3618	46,70
3	274	61	17	3	1	0	0	356	4,59
4	333	78	16	4	1	0	0	432	5,59
Al-Amghar	5869	1454	329	77	14	3	1	7747	100
Percentage%	75,75	18,76	4,24	0,99	0,18	0.05	0.03	100	-

B. Stream Lengths

The total length of the watercourses in the Al-Amghar basin is 5,509.1 km. The stream lengths vary between the different orders. The first order has the highest total length of 3,118.47 km, representing 56.60% of the total length of the basin. This increase in length is due to the higher number of first-order streams, which account for 5,869 streams, or 75.75% of the total number of streams in the study area. There is a direct correlation between the number of streams and their lengths in each order, where the total length increases with the number of streams, especially in lower river orders, which tend to have longer lengths due to higher stream density. The second order recorded a total length of 1,228.17 km, or 22.29%. The third order recorded 598 km, or 10.85%. The total length of the fourth order was 285.88 km, or 5.18%; the fifth order recorded 128.51 km, or 2.33%; the sixth order recorded 122.38 km, or 2.22%; and the seventh order recorded 28.16 km, or 0.53%. The variation in stream lengths is also attributed to geomorphological factors such as slope, rock permeability, and topographic conditions. Steep areas tend to have longer streamed due to increased surface runoff and faster water flow. Regarding the secondary basins, it can be observed from Table (6) that the second basin recorded the highest stream length of 2,725.1 km, or 49.46%. This is due to the fact that this basin is the largest in area and has the highest number of watercourses. Therefore, it is natural for the stream lengths to increase with the number of streams due to the large size of the basin compared to other secondary basins. On the other hand, the third basin recorded the lowest total length of 217.19 km, or 3.96%, due to the same factors mentioned above. The third basin is the smallest in area among the secondary basins in the study area.

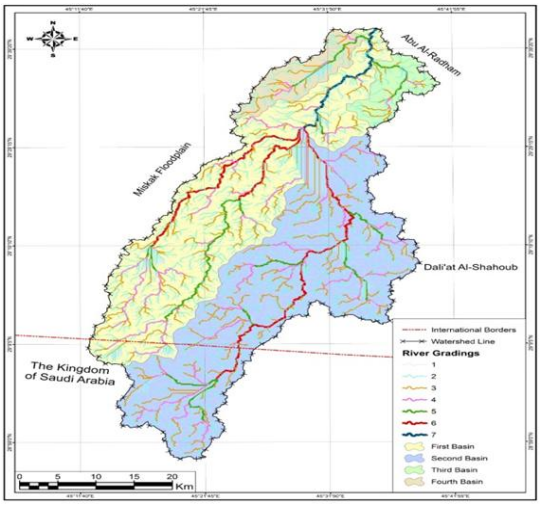


Fig. 2: River orders in the Al-Amghar basin.

C. Stream Length Rates

This function is derived by dividing the total length of watercourses in a given order by the number of streams in that order (Strahler, 1957) as follows:

Stream Length Rate for a given order = Total length of streams in that order / Number of streams in the same order

According to Table (7), the average length of the watercourses in the study area is found to be 0.71 km. Regarding river orders, the first order recorded the lowest average length, at 40.79 km. As for the secondary watersheds, the variation in watercourse lengths is minimal. The third watershed recorded the lowest average length at 0.61 km, due to the lower number and lengths of the watercourses in this watershed, which is smaller in area compared to the other secondary watersheds. In contrast, the second watershed recorded the highest average length, attributed to the increased number and length of watercourses due to the larger area of this watershed, which is the largest among the secondary watersheds in the study area.

Table 6: Total Lengths of River Orders in the Al-Amghar basin.

Basin	First Order	Second Order	Third Order	Fourth Order	Fifth Order	Sixth Order	Seventh Order	Total km	Percentage%
1	1248.52	542.21	219	127.92	47.19	57.4	28.16	2270.54	41,21
2	1585.93	564.37	314	142.48	53.12	64.99	0	2725.1	49,46
3	119.58	51.24	28	6.24	11.95	0	0	217.19	3,96
4	164.45	70.36	36	9.24	16.25	0	0	296	5,37
Al-Amghar	3118.47	1228.17	598	285.88	128.51	122.38	28.16	5509.1	100
Percentage%	56,60	22,29	10,85	5,18	2,33	2.22	0,53	100	

Table 7: Average lengths of watercourses in the Al-Amghar basin.

Basin	First Order	Second Order	Third Order	Fourth Order	Fifth Order	Sixth Order	Seventh Order	Total km
1	0,49	0,84	1,51	4,26	7,86	28,7	28,16	0,67
2	0,57	0,83	2,07	3,56	8,85	64,99	0	0,75
3	0,43	0,84	1,64	2,08	11,95	0	0	0,61
4	0,49	0,90	2,25	2,31	16,25	0	0	0,68
Al-Amghar	0,53	0,84	1,81	3,71	9,17	40,79	28,16	0,71

D. Drainage Density

Drainage density refers to the spread of the river network (streams and channels) and its tributaries within the area of the river basin. The spread of the network varies depending on the geological structure, soil type, vegetation cover, and slope. Drainage density indicates how fragmented the Earth's surface is by watercourses. Two types of drainage density can be distinguished:

Longitudinal Drainage Density: This refers to the ratio of the total length of the watercourses in the river basin to the total area of the basin. This relationship can be expressed mathematically by the following equation (Anderson and Anderson, 2010).

Longitudinal Drainage Density=Total length of watercourses, km/Area of the basin, km²

This criterion is directly proportional to water discharge. As observed in Table (8), the longitudinal drainage density in the study area is 3.09 km. Regarding the secondary watersheds, the variation is very minimal. The second watershed recorded the highest value at 3.14 km, which is attributed to the larger area of this watershed, leading to an increase in the number of river channels. On the other hand, the third watershed recorded the lowest value at 2.77 km. This slight variation between the secondary watersheds may be due to the harmony and consistency in the geological formations that make up each watershed.

Numerical Drainage Density: It refers to the number of watercourses present within a unit area of the river basin. This can be calculated using the following equation (Harrel and Dorris, 1968).

Numerical Drainage Density=Total number of watercourses of all orders/Area of the basin km²

From Table (8), it is clear that the numerical drainage density in the study basin area is 4.35 channels/ km². As for the secondary watersheds, the variation between them is very minimal. The third watershed recorded the highest value at 4.55 channels/km², which is due to the smaller size of the watershed, as there is an inverse relationship between numerical density and area. On the other hand, the second watershed recorded the lowest value at 4.17 channels/km², due to its larger area. It is observed from Table (8) that there is an inverse relationship between numerical and longitudinal density. The values of longitudinal density increase with the increase in the area of the basin. Thus, the highest value is recorded in the second watershed at 3.14, which is the largest secondary watershed. The lowest value is recorded in the third watershed, which is the smallest in area among the secondary watersheds. Conversely, there is an inverse relationship with numerical density, where the values increase as the area decreases and decrease as the area increases, in contrast to longitudinal density, which decreases with larger areas and increases with smaller areas. This confirms the findings in Table 8.

Table 8: Longitudinal and numerical drainage density, and basin texture of valley Al-Amghar basins.

Basin	Drainage Density (Length)	Drainage Density (Numerical)	Topographic Texture	Actual Length (km)	Ideal Length (km)
1	3.08	4.53	15.49	73.13	71.16

2	3.14	4.17	16.28	65.8	63.09
3	2.77	4.55	6.90	13.84	12.90
4	3.02	4.42	6.68	23.73	22.6
Al-Amghar	3.09	4.35	26.43	85.32	83.12

E. Basin Texture

Basin texture is an indicator that measures the degree of convergence and divergence between watercourses within a basin. Basin texture is influenced by a set of natural factors, the most important of which are the type of rocks, topography, climate, soil, as well as natural vegetation, regional tectonics, and the geomorphological stage the basin is undergoing. It can be calculated using the following equation (Kauffman, 1977)

Basin Texture = Number of Watersheds / Perimeter of the Basin

From Table (8), it is evident that the average basin texture for the study area is 26.43, indicating a fine basin texture. Basins are classified into three categories based on the value of basin texture: Category 1: Coarse texture (0-4); Category 2: Medium texture (4-10); Category 3: Fine texture (greater than 10) (Scheidegger, 1966). The average value of the secondary watersheds is 10.21, with noticeable variation among the secondary basins. The first watershed recorded the highest value at 15.49, while the fourth watershed recorded the lowest value at 6.68, indicating medium roughness. The high value of basin texture in the valley is attributed to the large number of river tributaries that characterize the watershed.

F. Bifurcation Ratio

This ratio is defined as the number of channels in a given river order divided by the number of channels in the next higher river order. Typically, the natural bifurcation ratio ranges between 3 and 5 undersimilar geological and climatic conditions within the basin. It is calculated using the following equation (Guha and McGregor, 2009).

Bifurcation Ratio = Number of channels in a given river order / Number of channels in the next higher river order

The bifurcation ratio is one of the most important morphometric variables that indicates the degree of water discharge and helps predict flood risks. Any increase in the bifurcation ratio signifies an increase in the process of water erosion caused by an increase in the amount of rainfall. As a result, the ability of water to transport sediment load increases. A higher bifurcation ratio through river channel systems contributes to the development of first-order channels into second-order channels, which -in turn- leads to the widening and deepening of watercourses and a retreat of the watershed divide (Kaufmann and Weber, 2011). Table (9) illustrates the bifurcation ratio in the study area, which is 4.31. Regarding the bifurcation ratio of the river orders, the fourth order recorded the highest value at 5.5, while the sixth order recorded the lowest value at 3. The remaining river orders varied between these two values. As for the secondary watersheds, the second watershed recorded the highest value at 4.32, while the first watershed recorded the lowest value at 3.86 (Table 9). All values in both the main basin and the secondary basins fall within the range of 3-5, which confirms the similarity of the geological and climatic conditions that constitute the basin.

Table 9: Bifurcation ratios in the Al-Amghar basin.

Basin	First Order	Second Order	Third Order	Fourth Order	Fifth Order	Sixth Order	Bifurcation Ratio
1	3.94	4.4	4.83	5	3	2	3,86
2	4.05	4.48	3.77	6.66	6	1	4,32
3	4.49	3.58	5.66	3	-	-	4,18
4	4.26	4.87	4	4	-	-	4,28
Al-Amghar	4.03	4.41	4.27	5.5	4.66	3	4,31

G. Pearson's Statistical correlation importance

This correlation between terrain characteristics and river network properties is of great importance in hydrological studies. Terrain directly influences the development of river networks through slope and gradient, which, in turn, determines how responsive the watersheds are to the development of river orders (Lane, 2002). This relationship helps in identifying the basin's ability to generate surface runoff within its

unique terrain environment. In this study, the researcher relied on statistical analysis using Pearson's correlation coefficient to measure the strength of the relationship between these variables and to determine their mutual effects. It is expected that the results will contribute to improving the understanding of surface runoff dynamics, thereby providing scientific applications in water resource management and flood prediction (Naghettini, 2017). The data for terrain characteristics and river network properties are obtained using the GIS 10.8 program relying on digital elevation models (DEM), in addition to field studies of the basin for accurate observation of these characteristics. Table (10) illustrates the correlation between terrain characteristics. It shows a strong positive relationship between the slope percentage and relative terrain, where watersheds with higher relative terrain tend to have a higher percentage of slope. This suggests that areas with steeper terrain may experience higher erosion rates, indicating a significant effect of slope on sediment transport and soil erosion processes. This also applies to the roughness value, which is a result of the relative terrain with a very strong positive correlation. The geometric number also follows this trend except for the hypsometric integral. Finally, the exception to this positive correlation is the hypsometric integral, which exhibits an inverse relationship with all terrain characteristics. This could be due to areas with higher hypsometric integral values being less prone to erosion, indicating that more stable, less steep terrains are less susceptible to surface erosion due to surface runoff (Strahler, 1964). As shown in the table, terrain characteristics are strongly positively correlated with each other, except for the hypsometric integral, which exhibits an inverse relationship. As for the correlation between river network properties. Table (10) shows that the number of river orders is strongly positively correlated with the length of river orders and longitudinal drainage density. This is because the number of river orders, which determines the length and longitudinal density, directly affects both properties. The numerical drainage density is also related to the basin's topographic texture with a very strong positive correlation. However, it is inversely related to numerical drainage density: as the numerical density increases, the topographic texture decreases, indicating the fragmentation of the basin and the degree of proximity and divergence between the watercourses (Ayyana and Muhammad, 1987). Finally, the bifurcation ratio is weakly positively correlated with all properties except for its inverse relationship with numerical drainage density. From the table, it can also be observed that the overall relationship between river network properties is of a varied positive correlation, except numerical drainage density.

Additionally, Table (10) shows that the slope ratio, relative terrain, roughness value, and geometric number share similar relationships with all river network properties, as they are inversely correlated except for numerical density and bifurcation ratio, which exhibit a positive relationship. This means that an increase in the number of river orders in a particular basin may reduce the erosion rate in that basin. This could be due to the distribution of surface runoff across multiple channels, thus reducing the erosive force (Mishra and Pandey, 2014). The inverse relationship between the slope ratio and river order lengths indicates that areas with higher terrain may not support the formation of long river orders. This reflects the impact of steep slopes, which limit the development of river channel lengths. In contrast, the hypsometric integral is positively correlated with all properties except for numerical density. This suggests that areas with a high hypsometric integral tend to have river networks with longer channel lengths. It reflects the influence of rugged terrain on the length of river channels and enhances the likelihood of complex surface runoff patterns in elevated areas, as well as increased surface water flow and soil erosion due to the terrain. Overall, the relationship between terrain characteristics and river network properties is generally inverse, meaning that as the terrain characteristics decrease, the river network properties increase

Table 10: Pearson correlation statistical relationship between terrain characteristics and river network properties of the Al-Amghar basin

	Ruggedness Ratio	Relative Relief	Ruggedness Value	Hypsometric Integral	Geometric Number	River Order	Order Lengths	Drainage Density (Length)	Drainage Density (Numerical)	Topographic Texture	Bifurcation Ratio
Ruggedness Ratio	1										
Relative Relief	0.929*	1									
Ruggedness Value	0.946	0.989**	1								
Hypsometric Integral	-0.881	-0.869	-0.881*	1							
Geometric Number	0.802	0.956*	0.951*	-0.783	1						
River Order	-0.809	-0.779	-0.825	0.964*	-0.731	1					
Order Lengths	-0.819	-0.789	-0.830	0.974**	-0.733	0.999**	1				
Drainage Density (Length(	-0.798	-0.525	-0.567	0.660	-0.285	0.616	0.627	1			
Drainage Density (Numerical)	0.600	0.506	0.433	-0.615	0.268	-0.421	-0.458	-0.675	1		
Topographic Texture	-0.840	-0.812	-0.856	0.971*	-0.761	0.998*	0.998*	0.632	-0.432	1	
Bifurcation Ratio	0.062	0.033	0.124	0.261	0.143	0.143	0.174	0.060	-0.661	0.113	1

*Correlation is significant at the 0.05 level; ** Correlation is significant at the 0.01 level; The pink color represents a very strong to strong positive (direct) correlation; The green color represents a very strong to strong negative (inverse) correlation.

5. Conclusions

The ruggedness ratio of 1.85 reflects the moderate nature of the terrain in the basin. The relationship between area and relative terrain indicates that this terrain value is higher in the third and fourth basins, which are the smallest in area. As for the roughness value, it increases as a result of the increased branching of the river network.

It is observed that the basin is in an advanced stage of the erosion cycle, as indicated by the hypsometric integral. The use of the Strahler (1964) method helped in analyzing the river network pattern in detail, highlighting the role of the terrain in determining the water drainage networks. High terrain values increase the surface runoff within the river network. The total number of river orders reached 7,747 streams with a total length of 5,509 km. The correlation relationship varies, with a strong positive correlation between relative terrain and ruggedness indicating the effect of slope on river network characteristics. An inverse relationship is found between relative terrain and roughness, meaning lower erosion rates. As for river network properties, a positive correlation was observed between the number of orders and their lengths, while an inverse relationship is found between both longitudinal and numerical density due to the area.

6. Conflict of Interest

The authors declare that they have no conflict of interest.

7. Funding Statement

This research received no external funding.

8. References

Ahmed, F. and Rao, K. S., 2016. Hypsometric analysis of the Tuirini drainage basin: A geographic information system approach. International Journal of Geomatics and Geosciences, 6(3), pp. 1685-1695.

Al-Zurfi, N.Q.M., 2021. Hydrological assessment for rainwater harvesting potential in Al-Muthanna desert (Valley Al-Ghadhari): An applied study. M.Sc. thesis, Faculty of Education for Humanities, University of Al-Muthanna, Al-Muthanna, Iraq.

Anderson, R.S. and Anderson, S.P., 2010. Geomorphology: the mechanics and chemistry of landscapes. Cambridge University Press.

Arefin, R. and Alam, J., 2020. Morphometric study for water resource management using principal component analysis in Dhaka City, Bangladesh: a RS and GIS

approach. Sustainable Water Resources Management, 6, pp. 1-20.

Ayyana, A. and Muhammad, F., 1987. Introduction to Statistical Analysis in Geography. University Knowledge House.

Bishop, M. and Shroder, J.F., 2004. Geographic Information Science and Mountain Geomorphology. Springer Science and Business Media.
Boothroyd, R.J., 2023. National-scale geodatabase of catchment characteristics in the Philippines for river management applications. PLOS One, 18(3), p.e0281933.
https:// doi.org/10.1371/journal.pone.0281933

Charlton, R., 2007. Fundamentals of Fluvial Geomorphology. Routledge.
https://doi.org/10.4324/9780203371084

Directorate of Al-Muthanna Municipality, Department of Planning and Follow-up, GIS Unit, 2022. Administrative Map of Al-Muthanna, Scale 1:250000.

Gajbhiye, S., Mishra, S.K. and Pandey, A., 2014. Hypsometric analysis of Shakkar River catchment through geographical information system. Journal of the Geological Society of India, 84, pp.192–196

Guha, S. and McGregor, A., 2009. Stream order and order statistics: Quantile estimation in random-order streams. SIAM Journal on Computing, 38(5), pp.2044–2059. https://doi.org/10.1137/07069328X

Harrel, R.C. and Dorris, T.C., 1968. Stream order, morphometry, physico-chemical conditions, and community structure of benthic macroinvertebrates in an intermittent stream system. American Midland Naturalist, pp. 220–251, https://doi.org/10.2307/2423611

Horton, R.E., 1945. Erosional development of streams and their drainage basins; hydrophysical approach to quantitative morphology. Geological Society of America Bulletin, 56(3), pp. 275–370. https://doi.org/10.1130/0016-7606(1945)56[275:EDOSAT]2.0.CO;2

Jasib, 2011. Landforms of dry valley basins in the Basiya area using GIS. Ph.D. Thesis, Faculty of Arts, University of Basra, Basra, Iraq.

Kauffman, E.G., 1977. Geological and biological overview: Western Interior Cretaceous basin. The Mountain Geologist.

Kingdom of Saudi Arabia, General Authority for Meteorology and Environmental Protection, 2023. Open Data Department, Office of Open Data, Information Request Management. www.en.climate-data.org. https://doi.org/10.1016/j.giq.2010.07.002

Lane, B., 2002. Statistical Methods in Hydrology. Iowa State Press, Iowa.

Melton, M.A., 1957. An analysis of the relations among elements of climate, surface properties, and geomorphology. Department of Geology, Columbia University, New York.

Minár, J. and Evans, I.S., 2008. Elementary forms for land surface segmentation: The theoretical basis of terrain analysis and geomorphological mapping. Geomorphology, 95(3–4), pp.236–259. https://doi.org/10.1016/j.geomorph.2007.06.003

Ministry of Industry and Minerals, General Directorate of Geological Survey and Mining, 1996. Geological Map of Iraq, Scale 1:1000000, Baghdad, Iraq.

Ministry of Transport and Communications, General Directorate of Meteorology and Seismology, Climate Department, 2023. Unpublished Data, Baghdad, Iraq.

Ministry of Water Resources, General Directorate of Survey, Department of Map Production, (2013). Administrative Map of Iraq, Scale 1:1000000, Baghdad, Iraq.

Naghettini, M., 2017. Fundamentals of Statistical Hydrology.

Qin, Z. and Wang, J., 2022. Multifractal correlation between terrain and river network structure in the Yellow River Basin, China. ISPRS International Journal of Geo-Information, 11(10), p.519. https://doi.org/10.3390/ijgi11100519

Rahaman, M.F., Jahan, C.S., Arefin, R. and Mazumder, Q.H., 2017. Morphometric analysis of major watersheds in Barind Tract, Bangladesh: A remote sensing and GIS-based approach for water resource management. Hydrology, 5(6), pp.86–95.

Scheidegger, A.E., 1966. Effect of map scale on stream orders. Hydrological Sciences Journal, 11(3), pp.56–61. https://doi.org/10.1080/02626666609493480

Shekar, P.R. and Mathew, A., 2023. Morphometric analysis of watersheds: A comprehensive review of data sources, quality, and geospatial techniques. Watershed Ecology and the Environment. https://doi.org/10.1016/j.wsee.2023.12.001

Strahler, A.N., 1952. Dynamic basis of geomorphology. Geological Society of America Bulletin, 63(9), pp. 923–938. https://doi.org/10.1130/0016-7606(1952)63[923:DBOG]2.0.CO;2

. https://doi.org/10.1130/0016-7606(1952)63[1117:HAAOET]2.0.CO;2

Strahler, A.N., 1957. Quantitative analysis of watershed geomorphology. Eos, Transactions American Geophysical Union, 38(6), pp. 913–920.

Strahler, A.N., 1964. Quantitative geomorphology of drainage basin and channel networks. Handbook of Applied Hydrology.

Sukristiyanti, S., Maria, R., and Lestiana, H., 2018. Watershed-based morphometric analysis: A review. IOP Conference Series: Earth and Environmental Science, 118(1), p.012028. DOI 10.1088/1755-1315/118/1/012028

Summerfield, M.A., 1991. Tectonic geomorphology. Progress in Physical Geography, 15(2), pp.193–205. https://doi.org/10.1177/030913339101500206

Summerfield, M.A., 2014. Global Geomorphology. Routledge.

Tarboton, D.G., 1997. A new method for the determination of flow directions and upslope areas in grid digital elevation models. Water Resources Research, 33(2), pp. 309–319. https://doi.org/10.1029/96WR03137

U.S. Landsat 8 Satellite, OLI Image, Bands (2-3-4), Acquisition Date (if known).

Wajid, Z.S.J., 2017. Hydrology and geomorphology of Valley Abu Gar Basin in Al-Muthanna Governorate. Ph.D. Thesis, Faculty of Arts, University of Kufa, Najaf, Iraq. https://www.en.climate-data.org/, https://www.weatheronline.co.uk/

Iraqi National Journal of Earth Science, Vol. 26, No. 04, 2026 (206-218)

Iraqi National Journal of Earth Science

www.earth.uomosul.edu.iq

تحليل الخصائص التضاريسية وعلاقتها بخصائص الشبكة النهرية لحوض وادي الامغر

جنوب غربي بادية المثنى: دراسة احصائية تطبيقية

حيدر مزهر عبدعون الكفاري [1*] ، **صفاء عبدالامير رشم الاسدي [1]**

gaky.gon1991@gmail.com safaa.al_asadi@uobasrah.edu.iq

[1] قسم علوم الجغرافية، كلية التربية للعلوم الانسانية، جامعة البصرة، البصرة، العراق.

*الباحث المراسل.

تاريخ الاستلام: 07 شباط 2025 تاريخ المراجعة: 17 نيسان 2025 تاريخ القبول: 20 حزيران 2025

تاريخ النشر الالكتروني: 01 تشرين الأول 2026

الملخص

يعد حوض وادي الأمغر أحد الاحواض التي تقع في الجنوب الغربي من بادية المثنى. حيث تتميز منطقة الدراسة وبادية المثنى بصورة عامة باستواء سطحها وانبساطها العام وقلة التضرس فيها ويعزى انخفاض الخصائص التضاريسية الى امتداد الحوض الذي يبلغ طوله 85.32 كم مع انخفاض الفارق التضاريسي الى 158 م. وقد أسهم ذلك في انخفاض معدل الانحدار الى 1.85 مما انعكس على الخصائص الرسوبية وسرعة المياه الجارية داخل الحوض. سجل الحوض وجود 7747 مجرىً مائياً مما يوضح مدى تاثير هذه العوامل التضاريسية على تشكيل خصائص الشبكة النهرية مثل عدد المراتب، اطوالها، والكثافة العددية والطولية، مع التركيز على تأثير التضاريس منخفضة الانحدار على تشكيل الشبكة النهرية. تم استخدام المؤشرات التضاريسية كالتضاريس النسبية ونسبة التضرس والتكامل الهبسومتري، مع تصنيف المراتب النهرية وفق طريقة "ستراهلر". أظهرت النتائج أن الأحواض الأكبر مساحة تتميز بعدد وأطوال أكبر من المجاري، مع علاقة طردية بين المساحة وعدد المجاري، وعلاقة عكسية بين التكامل الهبسومتري والتضاريس وزيادة كثافة المجاري في المناطق ذات الانحدار المعتدل والصخور الأقل صلابة. كما تبين أن التكامل الهبسومتري ينخفض مع زيادة التضرس.

الكلمات المفتاحية:

الامغر، نسبة التضرس، الشبكة النهرية، المراتب النهرية، بيرسون

DOI: 10.33899/injes.v26i4.60919, *©Authors, 2026, College of Science, University of Mosul.*

This is an open-access article under the CC BY 4.0 license (http://creativecommons.org/licenses/by/4.0/)

Iraqi National Journal of Earth Science, Vol. 26, No. 04, 2026 (219-234)

Iraqi National Journal of Earth Science

www.earth.uomosul.edu.iq

Comprehensive Review of Meteorological Drought in Iraq

Sura B. Idrees [1*], **Omar M.A. Mahmood Agha** [1]

Sura.basim1994@gmail.com O.agha@uomosul.edu.iq

[1] *Department of Dams and Water Resources Engineering, College of Engineering, University of Mosul, Mosul, Iraq.*
* *Correspondence author.*

Received: 22 February 2025 Received in revised form: 20 May 2025 Accepted: 14 September 2025
Available online: 01 October 2026

Abstract

Drought is a serious environmental phenomenon characterized by a severe and continuous decrease in rainfall rates and elevated temperatures, which leads to a reduction in soil moisture and serious climatic, environmental, and economic damage. It manifests in various forms, including meteorological, agricultural, and hydrological droughts, each linked to specific causes and effects. Monitoring and assessing drought depend on the use of suitable indicators, which vary in effectiveness depending on regional climatic and geographical conditions. Drought is a recurring problem in Iraq, which is located in arid and semi-arid regions. Continued drought leads to a scarcity of water resources. A review of previous studies shows the existence of research gaps, most notably the lack of comprehensive studies comparing different drought indicators to determine the most appropriate ones for the conditions of Iraq, especially the southern regions, which are characterized by scarcity of rain and high evaporation rates. Therefore, choosing the most appropriate indices is necessary for a more accurate understanding of the drought phenomenon and for developing appropriate strategies for water resource management and adaptation to this recurring event. This situation confirms the urgent need to conduct in-depth studies to address these gaps and provide practical solutions that enhance the sustainability of natural resources in the region.

Keywords:

Drought severity, Semi-arid, Drought index

DOI: 10.33899/injes.v26i4.60926, ©Authors, 2026, College of Science, University of Mosul.

This is an open-access article under the CC BY 4.0 license (http://creativecommons.org/licenses/by/4.0/).

==========

1. Introduction

Drought is a complex and prolonged climatic event that affects both the environment and human societies considerably. It is generally defined as a state of water deficiency caused by a sustained reduction in rainfall over an extended period (Lloyd-Hughes, 2014). The consequences of drought, such as reduced water availability and damaged ecosystems, often lead to severe economic losses, particularly in regions that rely on rain-fed agriculture and water-intensive industries (Al-Bazaz and Mahmood Agha, 2023).

Three major factors contribute significantly to the global aggravation and worsening of drought: population density, increased demand for water, and climate change. The continued increase in the global population places increased pressure on available water resources, exacerbating communities' vulnerability to drought. Increased demand for water — driven by urbanization, agriculture, and industry — further depletes water supplies and reduces resilience during droughts. Climate change alters rainfall patterns and increases the frequency and intensity of extreme weather events, including droughts. These interconnected factors highlight the urgent need to study climate change and its impact on drought (Dierauer and Zhu, 2020).

The American Meteorological Society divides drought into four types based on its stages: (1) meteorological drought, where rainfall is more than 25% below normal levels for a given area; (2) agricultural drought; (3) hydrological drought; and (4) socioeconomic drought (Subramanya, 2017).

Globally, droughts have been exacerbated by climate change, resulting in altered precipitation

patterns and increased evaporation rates. In many regions, such as Iraq, drought has become a recurring environmental issue affecting agricultural productivity, water supply, and economic stability (IPCC, 2013). Iraq's geographic location in an arid and semi-arid zone places it at a heightened risk for drought, particularly in its southern regions, where rainfall is scarce and evaporation is high. Despite the pressing need for drought management strategies, the country continues to experience recurrent droughts that have widespread implications for water resource management and climate adaptation. Several studies have examined drought conditions in Iraq, with a focus on different regions and drought indices. For example, Sulaiman and Younis (2021) assessed the temporal and spatial patterns of drought using the Standardized Precipitation Index (SPI) and the Chinese Z-index (CZI) in Nineveh Governorate. Their findings revealed a pronounced vulnerability to drought, especially during periods of low precipitation. Similarly, Al-Timimi et al. (2012) and Salman et al. (2018) highlighted the critical role of meteorological factors in drought occurrence across Iraq, particularly in the northern and central regions, where precipitation trends are highly variable.

In addition, Mahmood Agha et al. (2025) and Al-Juboori (2023) conducted predictive analyses of drought conditions using traditional and hybrid models. Their studies identified the most effective approaches for forecasting drought severity and duration, offering valuable insight into future drought preparedness—complementing earlier findings regarding spatial and temporal drought behavior in the region.

However, these studies have notable limitations. Most research has focused on specific regions of Iraq, with limited cross-regional comparisons and a lack of comprehensive analysis of the drought indices that are most suitable for Iraq's unique climatic conditions. For instance, while the SPI has been widely used, studies have suggested that other indices such as the CZI and deciles index (DI) might offer more localized insights into drought severity, particularly in Iraq's arid and semi-arid zones (Sulaiman and Younis, 2021; Gaznayee et al., 2022). Moreover, the temporal coverage of these studies is often limited, which may affect the reliability of drought predictions, especially in light of rapidly changing climate patterns.

International studies, such as those conducted in the USA (Myronidis et al., 2018) and in China (Li and Cai, 2024), provide valuable insights into drought monitoring techniques and indices. However, they often overlook regional variances in drought dynamics, which are crucial for understanding and addressing the unique challenges posed by drought in Iraq. While these studies have contributed to the development of global drought monitoring frameworks, their direct applicability to Iraq is limited due to differences in climate, geography, and socioeconomic conditions.

This review aims to fill the gap in the existing literature by critically evaluating the most relevant drought indices for Iraq with a particular focus on meteorological drought. It will assess the strengths and limitations of various indices, including SPI, CZI, and DI, and their effectiveness in capturing the nuances of drought in Iraq's diverse climatic regions. The findings from this review will provide important insights for policymakers, aiding in the development of more effective and region-specific drought management strategies. Additionally, this review will contribute to the academic discourse on drought monitoring by providing a detailed comparison of indices in the context of Iraq's specific environmental conditions.

The need for effective drought monitoring is especially urgent in Iraq, given its vulnerability to climate change and the intensifying demands on its water resources. Recent climate models indicate that Iraq will experience more frequent and severe droughts in the coming decades, further exacerbating existing water scarcity issues. The agricultural sector, which is highly dependent on rainfall, is particularly at risk; drought leads to reduced crop yields, loss of livestock, and economic instability for rural communities. As such, the development of accurate drought indices tailored to Iraq's specific needs is not only a scientific necessity but also an essential tool for decision-makers. By providing a deeper understanding of drought conditions, this review can help inform better land management, water conservation, and agricultural practices, which are critical for the country's long-term resilience.

In addition to its academic value, this review aims to bridge the gap between research and practice by offering practical solutions to the

drought challenges facing Iraq. It will highlight the most suitable indices for monitoring drought in various regions of Iraq, helping stakeholders, from local farmers to national policymakers, better predict, mitigate, and adapt to drought conditions. Given the escalating water crisis and the rising frequency of drought events in Iraq, the application of the findings from this review is vital to enhance drought preparedness and response strategies. Ultimately, this work will contribute to Iraq's ability to effectively manage its water resources in an increasingly volatile climate.

Table 1: Previous Studies on Drought in Different Regions.

Region	Authors
USA	Myronidis et al., 2018
China	Li and Cai, 2024; Javed et al., 2021
Syria and Jordan	Al-Qinna et al., 2011; Abd-Elhamid et al., 2024
Iran	Morid et al., 2006; Mahmoudi et al., 2019; Sadeghpour and Yavari, 2009
Turkey	Katipoglu, Acar, and Şengül, 2020A; Ozkaya and Zerberg, 2019; Öz et al., 2024; Şener and Davraz, 2024
Iraq	Sulaiman and Younis, 2021; Al-Timimi et al., 2012; Mahmood Agha and Şarlak, 2016; Salman et al., 2018; Yaseen and Awchi, 2024; Kazanchie al., 2024; Yenigun and Ibrahim, 2019; Mahmood Agha and Al-Aqeeli, 2021; Mahmood Agha, 2021; Gaznayee et al., 2022; Yahya et al., 2022; H. Al-Bazaz and A., 2023; Jameel et al., 2023; Hasan et al., 2023; H. J. Al-Bazaz and Mahmood Agha, 2024; Governorate, 1965,Mahmood Agha ,2025; Al-Juboori,2023.

2. Study area

Iraq is located in the subtropical latitudes in the Northern Hemisphere, between longitudes (38.45°–48.45°) east of the Greenwich meridian and latitudes (29.5°–37.5°) north of the equator. It is classified within the northern temperate region. The climate of Iraq is divided into two groups: The first is the central and southern regions, characterised by a continental and subtropical climate, which tends to be dry and moderately arid. The second group is the northern region, which is a mountainous area influenced by the Mediterranean climate (Salman et al., 2020). The average annual rainfall is 154 mm across the region, but it is distributed asymmetrically. Rainfall decreases to less than 100 mm in the southern regions, while it exceeds 1200 mm in the northeast of the country (Brouwer and Heibloem, 1986). These numbers are not fixed, as they vary from year to year and from season to season. In terms of temperatures, during winter, minimum temperatures range from negative values on the slopes of frozen mountains in the northern region to 4 °C–5 °C in the south. In summer, minimum temperatures in the northern regions range from 27 °C to 31 °C, while maximum temperatures may reach 41°C–45 °C. The high temperatures in summer part of Iraq to the risks of drought and the resulting natural disasters (Salman et al., 2017).combination of low rainfall in winter and exposes a large.

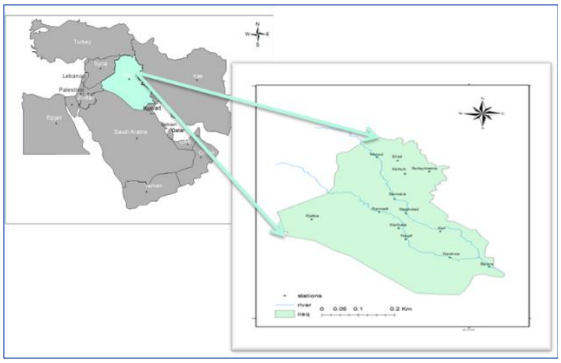


Fig.1: Iraq location in the Middle East.

3. Drought index definitions and categories

Drought indices are essential tools for identifying droughts, assessing their severity and monitoring their evolution over time. Common indices are based on meteorological and hydrological variables. Drought indices are determined by drought triggers, which serve as threshold values for these indices. These triggers distinguish different drought categories and determine when response actions should be initiated or terminated. Drought categories are often classified into severity levels such as mild, moderate, severe, and very severe. Given the complex nature of drought and its dependence on multiple factors such as water supply and demand, hydrological and political boundaries, and antecedent conditions, the indices used should be sensitive to spatial and temporal context. This diversity of definitions has led to the development of more than 150 definitions of drought (Wilhite and Glantz, 1985), which is reflected in the wide variety of indices used to monitor and analyze the phenomenon. Recently, many drought indices have been developed based on the basis of rainfall, temperature, and soil moisture datasets (Mishra and Singh, 2011).

A. Input variables

Different variables are used to predict drought, and these depend on the specific type of drought being predicted or detected. Input variables differ on the basis of the type of drought index applied in the analyses. For example, some drought indices would consider precipitation and temperature values only, while others would utilize a group of climate variables such as precipitation only. Once the relevant variables are identified, the indicators that can be used for drought detection can be determined. In the case of meteorological drought, rainfall is the key factor, and its deficits are commonly used to detect and analyze drought severity

The aim of this study is to investigate meteorological drought with a particular focus on its analysis using various indices.

When choosing to adopt a particular indicator over another, the purpose of determining the type of drought is taken into account, that is, whether it is for prediction or evaluation. Available data also need to be considered, such as precipitation, temperature, soil moisture, and satellite images, in addition to the geographical area, where the characteristics of drought differ from one region to another (Yihdego et al., 2019). Some studies are intended to study agricultural drought, identify areas exposed to drought, and manage the agricultural plan in proportion to the type and degree of the affected drought. Others are conducted to support water resource management and decision-making with regard to whether water should be stored or released from reservoirs. Studies can also be conducted for civil planning and assessing the risks of drought for a specific area and examining the risks related to and resulting from this phenomenon, and its negative effects on various civil areas to activate emergency plans when necessary (Li et al., 2024).

Most previous research discussed in this paper utilized actual meteorological data recorded by the Iraqi Meteorological and Seismological Organization, the accredited and official source of Iraqi weather and climate data. These data hold accurate details about temperature, precipitation, atmospheric pressure, and relative humidity, which are vital parameters for assessing meteorological drought conditions. These data have been utilized intensively in previous research to identify climate trends in Iraq and study the development of drought over different periods of time. However, some studies have coverage problems with respect to data for particular areas or discontinuity in data from year to year, which could influence the accuracy of the analysis in certain cases. Most studies conduct tests on the data before its use to ascertain the quality and reliability of the climatic and hydrological data(Mohammed and Scholz, 2023). Testing the data for quality is crucial prior to any study related to climate or water resources. If the data are non-homogeneous, then the stations with unreliable data can be excluded (Mahmood Agha et al., 2017).

B. Drought Indices

1. Deciles Index (DI)

The DI is a method that divides a long-term series of precipitation data into 10 categories or ‘deciles’ to better assess precipitation anomalies in comparison to normal levels. The values are arranged from lowest to highest, with the first decile representing the lowest 10% of precipitation and the 10th decile representing the highest 10%. The middle values, such as the fifth decile, correspond to normal precipitation conditions. The cases are then classified on the basis of their level of dryness or humidity as outlined in Table 2 to allow for easier comparison with other methods (Tadić et al., 2015).

Table 2: Decile index limits.

	DI	Percentage	Classification
1	Deciles 1-2	Lowest 20%	Much below normal
2	Deciles 3-4	Next lowest 20%	Below normal
3	Deciles 5-6	20% Middle	Near normal
4	Deciles 7-8	Next highest 20%	Above normal
5	Deciles 9-10	Highest 20%	Much above normal

Calculation method

i. Rainfall record data are arranged in ascending order for each time period.

ii. Divide the data into 10 equal groups and calculate percentages using the relationship:

$$\boldsymbol{D_k = \left(\frac{k \times (N+1)}{10}\right)} \ldots\ldots\ldots (1)$$

Where: $\boldsymbol{D_k}$ is the percentage.

iii. Rainfall bands that correspond to each percentile are identified.

One disadvantage of the decile system is that, within the Australian Drought Monitoring System, it requires a long series of climate records because

it facilitates accurate calculations (Nagarajan, 2009).

2. Standardized Precipitation Index (SPI)

The SPI measures actual rainfall compared with a probability distribution, making it an effective tool for assessing drought across time and different regions. The SPI is calculated on the basis of long-term data and transformed to a normal distribution with mean zero and one standard deviation, where positive values indicate above-average precipitation and negative values indicate lower precipitation. The SPI is increasingly used to assess drought severity in many countries and is sometimes superior to the Palmer Drought Severity Index (PDSI) in some studies (Naresh Kumar et al., 2009).

The SPI is calculated by calculating the gamma probability function for a specific time series of rainfall, where each month is calculated separately, and the gamma distribution is defined by the following formula:

$$g(x) = \frac{1}{\beta^{\alpha}\Gamma(\alpha)} x^{\alpha-1} e^{-x/\beta} \quad for\ x > 0 \ldots (2)$$

$$\Gamma(\alpha) = \int_0^{\infty} y^{\alpha-1} e^{-y} dy \ldots\ldots (3)$$

Where: $\Gamma(\alpha)$: gamma function; (x): the rain value at which the distribution is to be evaluated; α: the shape parameter of the distribution and has a value greater than one; β: the scale parameter of the distribution and has a value greater than one

$$\alpha = \frac{1}{4A}\left(1 + \sqrt{1 + \frac{4A}{3}}\right) \ldots\ldots\ldots (4)$$

$$\beta = \frac{\overline{x}}{\alpha} \ldots\ldots\ldots (5)$$

$$A = ln(x) - \frac{\sum ln(x)}{n_e} \ldots\ldots\ldots (6)$$

Where: n_e: The number of rain coordinates recorded in the rain record.

Substituting the values of α and β, the gamma distribution function becomes as follows:

$$G(x) = \int_0^x g(x)dx = \frac{1}{\beta^{\alpha}\Gamma(\alpha)} \int_0^x x^{\alpha-1} e^{-x/\beta} dx \quad \ldots\ldots (7)$$

We assume that the value of $s = x/\beta$ produces a gamma distribution function as follows:

$$G(x) = \frac{1}{\Gamma(\alpha)} \int_0^x s^{\alpha-1} e^{-s} ds \ldots\ldots (8)$$

Since the values of the gamma function are not defined at zero values and rain records contain zero values, the following function is derived to calculate the cumulative probability of the gamma distribution:

$$H(x) = q + (1+q)G(x) \ldots\ldots (9)$$

Where: q: the probability of zero values and it is calculated by dividing the number of zero rain data in the data series (m) by the number of rain coordinates in the rain record (n) ($q=m/n$), and used to deduce the values of the Standard Rainfall Index (*SPI*) (Iwata et al., 2012).

The cumulative probability values of the gamma distribution are transformed into a normal distribution as a random variable using the following equations:

$$SPI = -\left(s - \frac{2.515517 + 0.802853s + 0.010328s^2}{1 + 1.432788s + 0.189269s^2 + 0.001308s^3}\right)$$

For 0 < H(x) ≤ 0.5 ……..(10)

$$SPI = -\left(s - \frac{2.515517 + 0.802853s + 0.010328s^2}{1 + 1.432788s + 0.189269s^2 + 0.001308s^3}\right)$$

For 0 < H(x) < 1 ……..(11)

Where:

$$s = \sqrt{ln\left(\frac{1}{(H(x))^2}\right)} \quad for\ 0 < H(x) \le 0.5 \ldots\ldots\ldots (12)$$

$$s = \sqrt{\ln\left(\frac{1}{(1 - H(x))^2}\right)} \quad for\ 0.5 < H(x) < 1 \ldots\ldots (13)$$

It is classified as shown in Table 3 (Asadi Zarch et al., 2015)

Table 3: SPI, CZI, MCZI, ZSI, and RDI index limits.

SPI, CZI, MCZI, RDI, and ZSI	Classification
2 or more	Extremely wet
1.5-1.99	Very wet
1.49-1	Moderately wet
-0.99 to 0.99	Near normal
-1 to -1.49	Moderately dry
-1.5 to -1.99	Severely dry
and less than-2	Extremely dry

disadvantage of the SPI is that drought is evaluated based on total rainfall only, neglecting other parameters such as humidity, radiation, and soil conditions (Labudová et al., 2015). In addition, the SPI schedule takes into account only rainfall and cannot explain the role of global warming in changes in drought (Tayfur, 2021)

3. Z-Score index (ZSI)

ZSI is an analogue of CZI, but with fewer requirements than the latter in terms of inputs, and is presented in the following format:

$$ZSI = \frac{P - \overline{P}}{SD} \times 100 \ldots\ldots\ldots (14)$$

Where: $\overline{P}$: Average monthly rainfall (mm);

P: Rainfall in a particular month (mm); *SD*: Standard deviation for any measurement period.

The equation is called standardization or normalization. The Z score indicates the number of standard deviations the rainfall value is above or below the mean. This index is not the same as the SPI because it does not require adjusting the data to fit a gamma or Pearson type III distribution (Katipoglu et al., 2020). Drought is classified based on the ZSI results as shown in Table 3 (Mahmoudi et al., 2019).

4. China Z-index

The National Climate Center of China developed the CZI as an improvement to the SPI (Wu et al., 2001). The CZI is a composite climatic drought index based on climatological precipitation data and the Pearson type III distribution.

The following is the basic equation for *CZI*:

$$CZI = \frac{6}{c_S}\left(\frac{c_S}{2}\emptyset + 1\right)^{1/3} - \frac{6}{c_S} + \frac{c_S}{6} \ldots\ldots (15)$$

Where: *cs*: deviation coefficient; $\emptyset$: uniform variable.

The cs and $\emptyset$ equations are calculated as follows:

$$c_S = \frac{\sum_{i=1}^{n}(pi-p)^3}{ns^3} \ldots\ldots (16)$$

$$\emptyset = \frac{pi-p}{s} \ldots\ldots (17)$$

Where: *s* is the average sample variance; *n* is the total number of months.

Table 3 determines the drought state.

5. Modified China Z-Index (MCZI)

The modified CZI (MCZI) is a tool used to evaluate the level of drought in a specific area. This indicator is based on measurements of rainfall, temperature, and humidity, and aims to determine the extent of dryness or humidity in each environment. The MCZI calculates deviations from normal climatic conditions, which helps identify drought periods and estimate their impact on agriculture and water resources. These data are used in planning and resource management, especially in areas affected by climate change. The MCZI is calculated in the same way as the CZI except that instead of the mean, the median is used in calculating this indicator (Sulaiman and Younis, 2021).

6. Percent of normal precipitation index (PNPI)

The percent of normal precipitation index was first developed by Ndlovu and Demlie (2020). This indicator measures the ratio of actual precipitation to the normal rate and is expressed as a percentage. The % normal index is effectively used to raise awareness about drought conditions at local and seasonal levels, and is expressed in the following formula:

$$PNI = \frac{P_i}{P} \times 10 \ldots\ldots (18)$$

Where: *PNI*: Percentage of Natural Precipitation Index; *Pi*: Actual rainfall; *P*: Rainfall rate. Table 4 is used to classify drought (Asrari et al., 2011).

Table 4: PNPI index limits.

PNPI	Classification
More than 120	Humid
80 to 120	Normal
70 to 80	Light drought
55 to 70	Moderately drought
40 to 55	Severely drought

7. Bhalme and Mooley Drought Index (BMDI)

This index was invented by Bhalme and Mooley in 1980. It calculates the percentage deviation of monthly or annual rainfall compared to its normal mean. This index is similar to the Palmer index, as it considers the influence of precipitation from the previous month in its calculations, making it a redundant index (Eslamian et al., 2017).

Calculation method:

i- Calculating the average ($\bar{x}$) and standard deviation (s) of the monthly precipitation data during the study period.

ii- Calculating the monthly humidity index (MI), the percentage deviation of monthly rainfall from its long-term average.

iii- Determining the minimum values of monthly humidity during the study period and finding their cumulative value.

iv-Fitting linear regression on the highest value of monthly cumulative humidity using the least squares technique.

The classification is done according to Dunkel (2015) Table 5.

Table 5: BMDI Index limits.

BMDI	Classification
-0.99 to 0.99	Near to normal
-1 to -1.99	Weak drought
-2 to -2.99	Moderate drought Severe
Less than or equal to -3	Severe drought

8. Reconnaissance Drought Index (RDI)

The Reconnaissance Drought Index (RDI) is used to detect drought on the basis of potential evaporation and transpiration (PET) values and

rainfall data, where the maximum and minimum temperature values are used to calculate PET. These are referred to as the initial values of the RDI (Oksal and Beden, 2024), and the calculation is done using the equations:

$$a_k^{(i)} = \frac{\sum_{j=1}^{k} P_{ij}}{\sum_{j=1}^{k} PET_{ij}} \quad \ldots\ldots\ldots(19)$$

Where: *Pij* and *PETij* are *i* by hydrological year respectively; *j*: of the year are the rainfall and PET values for the month; *n* is the total number of years of available data.

The second natural RDI is calculated every year using equation (19), where the arithmetic average of the values calculated for n years is known.

$$RDI_n^{(i)} = \frac{a_k^i}{\bar{a}_k} - 1 \quad \ldots\ldots\ldots\ldots\ldots(20)$$

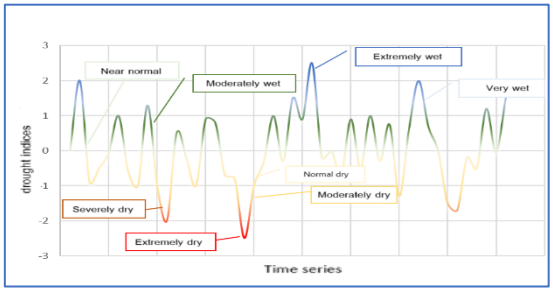


Fig. 2: Drought classification scheme.

In calculating the standard RDI, an equation similar to the index equation (SPI) is used.

$$RDI_{st(k)}^{(i)} = \frac{y_k^i - \bar{y}_k}{\bar{\sigma}_k} \quad \ldots\ldots\ldots\ldots\ldots\ldots (21)$$

Where : $\bar{y}_k$ and $\bar{\sigma}_k$ express the average and standard deviation, respectively.

This index is classified based on Table 3.

9. Percent of Normal by Mean

The percent of normal by mean (PN) index is an effective and simple tool for drought assessment and is preferred for its ease of calculation and ability to accurately describe drought conditions. The statistical construction of this index has been criticized for inconsistency in two aspects (Morid et al., 2006). Firstly, because no statistical transformation is used for the log rainfall distribution, the difference between the mean value and the median value can undermine its accuracy. Secondly, as a result of the different distribution of seasons and regions, this indicator cannot be used to compare drought across seasons and regions. Therefore, this method lacks the required robustness, according to the index using the following equation:

$$PN(\%) = \frac{P-X}{X} \times 100 \quad \ldots\ldots\ldots\ldots(22)$$

Where:

P: the amount of observed rainfall (mm)

X: the average rainfall for a given period (mm).

The results are classified as shown in Table 6.

Table 6: PN index limits.

PN	Classification
More than 110	wet
80 to 110	normal
55 to 80	Moderately dry
40 to 50	Very dry
Less than 40	Extremely dry

10. Drought theory

All drought indices allow the identification of dry and wet periods within a specific time scale for any location where rainfall and temperature data are recorded. Positive values indicate an increase in the amount of rain compared with the general average, which means wet years, while negative values indicate a decrease in the amount of rain compared with the general average, which indicates dry years (Majid Kalyana and Awchi, 2015). Fig. 2 shows the classification of drought based on dependence on drought indicators according to the classification by Tsakiris et al. (2007).

Yevjevich (1969) proposed the theory of continuous events or the theory of runs, which is considered an important tool for studying and analyzing drought statistical properties. This theory depends on the principle of continuity of observed values -for example, positive values- so that the previous or next value is of a different type,

for example, negative values (Al-Mohseen, 2009). The periods and occurrences of drought are typically derived from historical records by using non-parametric methods. However, such methods are often limited in scope and may lack sufficient reliability for accurately characterizing drought behavior. A more consistent and comprehensive approach is required to overcome these limitations. Therefore, this theory has been adopted to provide a more systematic representation of drought characteristics.

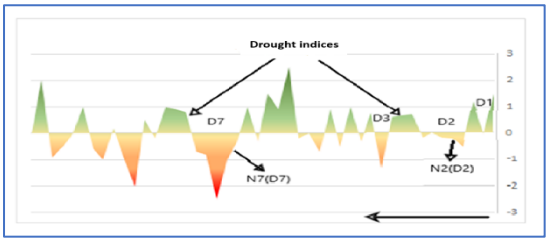


Fig. 3: Drought Indices: Duration, Intensity and Frequency Calculations.

Many indices can be inferred from drought, periods and duration of its occurrence, and by relying on clear inputs such as the total rain and monthly temperatures only. From these indices, the value of dehydration sustainability (drought duration Di) shown in Fig. 2 can be inferred. Drought values can be calculated by using Equation (22). In addition to calculating the drought intensity by calculating the amount of rain deficiency from normal rates and using Equation (23) (Awchi et al, 2017), the percentage of dry frequency can be calculated (relative frequencies) by dividing the number of years of dehydration by the number of overall years (Mahmood Agha et al., 2017).

$$M_j = \sum_{i=1}^{t} |\bar{x} - x_i| \ldots\ldots\ldots\ldots (23)$$

Where:

M_j: Total drought value (mm); $\bar{x}$: Rain rate for the data series; X_i: Rain value at time *i*; *t*: Number of periods of rain deficit during the dry period.

$$I_j = \frac{M_j}{D_j} \ldots\ldots\ldots\ldots (24)$$

Where: D_j : Drought Sustainability (Year); I_j: Drought Intensity (mm/year).

4. Previous studies

Given the complexity of drought as a phenomenon and the diversity of its wide-ranging impacts across various sectors, numerous studies have aimed to develop indices for assessing drought characteristics and comparing its patterns across different environmental settings. However, variations in climatic and hydrological characteristics from one region to another make it challenging to adopt a single, universally applicable index. Accordingly, this review seeks to provide a comprehensive overview of the relevant research efforts. It begins by examining studies that focus on the comparison of drought indicators, followed by a review of global studies, regional research with an emphasis on the Middle East, and studies that specifically address drought conditions in Iraq.

A. Comparing the indicators of climate drought

Many studies have compared drought indicators in different regions of the world. For example, in Iran, the performance of seven indicators (DI, PN, SPI, CZI, MCZI, EDI) was monitored for 32 years. The results showed that the SPI and CZI indicators operate symmetrically but are slow in responding to determine the beginning of drought. Moreover, the DI responds greatly to precipitation events but for only one year, with a contrast in time and space. SPI and EDI are able to determine the beginning of drought and in temporal and spatial contrast consistently, thus being recommended for studying the drought properties in the region (Morid et al., 2006). Similarly, another study conducted in Iran used six indicators of meteorological drought (PN, SPI, CZI, MCZI, Z-Score, and the drought index of Idu Marton) in six climatic zones to assess the spatial and temporal dynamics of drought. The results showed that the Z-Score, CZI, and MCZI indices are effective alternatives to SPI, especially when long-term time series are limited, or when the use of SPI is complicated, with their effectiveness depending on the duration of drought and climatic conditions (Shahabfar and Eitzinger, 2013). Several studies have been conducted to assess drought indicators and their effectiveness across various regions. For example, in Oregon, USA, drought indicators were evaluated using rainfall, temperature, and evaporation data from 88 climate stations. The Pearson's correlation coefficient between the indices showed that the Z3 aridity index exhibited the strongest correlation ($r > 0.65$) with streamflow variables (Myronidis et al., 2018). In Iran, drought indicators such as SPI, PN, ZSI, Di, CZI, EDI and MCZI were compared across 41 stations for the 1985–2013 period. The results indicated that ZSI, SPI and CZI showed similar characteristics in terms of assessing drought conditions, whereas Di and PN exhibited different behaviors. Moreover, the MCZI index was less effective in drought monitoring, with SPI and EDI emerging as the most reliable indicators in that region (Mahmoudi et al., 2019). In Turkey, a study of the Euphrates basin's drought from 1966–2017 compared various indices, including SPI, ZSI, RAI, SPEI, and RDI, and found that the indices based on the SPI, Z-score index (ZSI), and others such as RDI and SPEI exhibited similar patterns. However, RDI and SPEI, which depend more on temperature data, are more effective than SPI and ZSI in detecting drought conditions, especially when considering the role of evaporation and water consumption (Katipoglu et al., 2020). The phenomenon of drought in the Mekera Basin in northern Algeria was studied using eight rain

indices (SPI, RDI, RAI, ZSI, CZI, MCZI, PNI, DI), where the results showed strong correlations between most indices (r>0.68) with the superiority of DI and Z-Score in monitoring drought events, which support the importance of integrating indices to improve the spatial and temporal assessment of drought (Elhoussaoui et al., 2021).

These studies evidently show that while different drought indices can provide valuable insights, their effectiveness varies depending on regional conditions and the specific characteristics of the area under study. The comparison of multiple drought indices highlights the importance of selecting the most suitable indicators for each region. Furthermore, it underscores the need for further research to refine these indicators for more accurate drought monitoring and prediction, especially in areas with complex climatic conditions.

In Iraq, Sulaiman and Younis (2021) evaluated the performance of three drought indices (SPI, DI and CZI) based on observational data from meteorological stations in the Nineveh region (Mosul, Tel Afar and Sinjar) for the period 1981–2018. The results revealed that the DI demonstrated the highest correlation coefficient, indicating its superior suitability for drought assessment in the region due to its ability to capture local variations in precipitation and moisture levels. Also, a study was conducted in Salah al-Din Governorate in Iraq for the period (1990-2021) to estimate the climatic drought indicators (SPI, RDI, PNI, RAI, ZSI, and Papa) and study their relationship to desertification and land degradation using rainfall, temperature, humidity, and evapotranspiration data. The results showed that severe droughts occurred during 1990-1993 and 1998-2000, and the drought continued during 2020-2021 compared to wet years between 2015-2018. It also showed that there are strong correlations between SPI and the rest of the indicators (r>0.97, R^2 reaches 0.99 with RDI), which indicate a high agreement between these indicators in the assessment of drought in the region (Khalaf and Hummadi, 2023). In comparison, research in China analyzed indicators such as geophysical and hydrological indices (GEVI, HI, K, PA) and found that SPI, SPEI, and the PDSI provided the most reliable drought assessments across different time scales, particularly when considering rainfall and temperature variability (Li and Cai, 2024).

While these findings provide useful insights into drought monitoring, this research highlights a critical gap in understanding the best indices for Iraq, especially considering the region's unique climatic conditions. This review aims to address this gap by evaluating the suitability of different drought indices, such as SPI, DI and CZI, for Iraq. In conclusion, while indices such as SPI and CZI are useful in other regions, Iraq's complex climate necessitates further exploration to select the most accurate and region-specific drought indicators. The results of this review will contribute to better-informed decisions regarding drought preparedness and water resource management in Iraq, and it will offer essential guidance for policymakers seeking effective drought mitigation strategies in the face of climate change.

B. Studies related to meteorological drought in the Middle East

Over the years, drought has been considered a clear problem that threatens the world in general and the Middle East in particular. Hence, researchers in the Middle East have been studying drought characteristics. In Jordan, a study of drought characteristics was presented using the SPI in addition to the NDVI, revealing the repetition of drought in uneven periods and showing that the intensity increased over time (Al-Qinna et al., 2011). A study in Sistan and Baluchistan Province in Iran, which was obtained using the Markov series, showed that drought might exceed 70% in the central regions of the country (Sadeghpour and Yavari, 2009). Drought in Syria was evaluated using remote sensing data and the SPI. Findings showed that severe drought events were recorded in 1990, 2014, and 2016, with 2016 having the highest severity of drought (Abd-Elhamid et al., 2024). In Turkey, a comprehensive study was conducted on the basis of data from 219 stations distributed in the region using SPI, SPEI, and RDI. The results of the study confirmed that the region has been subjected to moderate drought (Öz et al., 2024). Another study was conducted in Turkey using data from three stations over 57 years from 1965 to 2022 on the basis of SPI, RAI, CZI, and ZSI. The RAI gave the highest value to drought (−4.5) and proved the existence of an increased link between indices over a one-year time scale and the occurrence of drought (Şener and Davraz, 2024).

A study in East Asia showed that the responses of soil moisture and hydrological drought to meteorological drought differ spatially and temporally, showing a weak correlation between soil moisture and meteorological drought in the north of the region in the short term (1-6 months) versus stronger correlations in the south in the long term (9-24 months). Hydrological droughts have also shown a strong and persistent correlation with atmospheric droughts across all durations, with delays of up to 8-10 months in the north compared to rapid responses in the South (Mtupili et al., 2025).

A review of the literature on drought in many regions of the world, in general, and in the Middle East region in particular, with the exception of Iraq, showed that the regions in general had been exposed to droughts in different return periods. Each study specialized in different indicators, obtained results for a specific region, and recommended the use of appropriate evidence according to the hydrological conditions to which the region is exposed and the nature of its rain distribution.

C. Studies on climate drought in Iraq

Iraq is one of the areas that is most affected by drought. The effects of drought, along with the increasing problems of water shortage, have given rise to the urgent need to study drought and its effects, and to analyze the consequences of this catastrophic phenomenon. From this point of view, many researchers have written about drought and applied analysis methods using several indices.

A study was presented to detect drought in Iraq using GIS and remote sensing based on the SPI and the anomaly of the Normalized Difference Vegetation Index (NDVI). The final drought maps showed that 14.4%, 61.6%, 23.2%, and 0.8% of the study area were classified as slight, moderate, severe, and very severe drought, respectively. The results also indicated that the northwestern region of Iraq is more prone to drought (Al-Timimi et al., 2012). Drought has also been studied throughout Iraq to detect temporal and spatial changes using RDI, showing that the year 2008 was the worst year of drought over all parts of Iraq (Mahmood Agha and Şarlak, 2016). Man Kendall studied drought in Iran, finding a decrease in the annual number of rainy days and confirming the increase in drought period (Salman et al., 2018). In addition, the state of drought throughout Iraq was discussed through the SPI and the theory of flow to analyze the characteristics of atmospheric drought, its quantity, severity, and rain deficit. The northern region was the most prone to drought, and the Iraq region was subjected to varying periods of drought that affected 45% of the study area (Yaseen and Awchi, 2024). In Iraq, research has been conducted to evaluate the performance of the CZI, MCZI, and SPI on a time scale of 1, 3, 6, 9, and 12 months, relying on rain data for the 1980–2021 period for five meteorological stations. The results showed an interconnection and high similarity between the results of the indices with the increase in time ranges. The SPI is more sensitive to detecting the beginning of drought and has more severe characteristics than other indices, while the MCZI identifies moisture earlier than the other two can. Moreover, SPI and CZI have been observed to be good indicators for describing drought in the Iraq region (Kazanchi et al. 2024).

We conclude from the above findings that the Iraq region has generally been exposed to periods of severe drought, which sometimes reached critical levels. Moreover, northern Iraq is the most affected by high drought levels. Specialized studies have been conducted to analyze drought in northern Iraq in particular. One study analyzed drought properties in terms of its duration and intensity using the SPI for different time scales (1, 3, 6, 9, 12 months). The results showed that the year 2008 was the driest year during the study period (Yenigun and Ibrahim, 2019). Also, the effect of the Arctic Oscillation Index (AOI) on drought indicators in northern Iraq was studied using the SPEI for 3, 6, and 12 months. The SPEI and the AOI showed a higher correlation in the 12-month time scale than in the 3- and 6-month time scales for all regions (Mahmood Agha and Al-Aqeeli, 2021). Scientists have also studied droughts by using the CZI for a one-month time scale in Nineveh Governorate for Mosul, Sinjar, and Tal Afar stations. All stations experienced dry periods during the month of March (Mahmood Agha, 2021). Recently, a study on drought and forecasting in the Kurdistan Region of Iraq used the RDI for the 1973–2020 period to detect the beginning and end of drought, as well as to predict future drought by using two types of artificial neural networks. The findings show that the driest years were 1998–1999 for the Amadi, Erbil, and Sulaymaniyah stations and 2007–2008 for the rest of the nine stations (Gaznayee et al., 2022).

In this study, we aim to analyze climatic drought in Iraq by using multiple drought indices, building on previous research that explored the effectiveness of various drought indices in the region. Numerous studies have evaluated the performance of drought indices in different regions of Iraq, but these have been limited to a few commonly used indices, focusing on various aspects such as rainfall, effective runoff, and temperature variability. For example, one study developed a multivariate drought index that combines rainfall and effective flow data for northeastern Iraq. Another study focused on climate change impacts in northern Iraq (Erbil, Dohuk, Sulaymaniyah, Mosul and Kirkuk) using the SPI for the 1980–2020 period. The study concluded that all regions experienced drought, as indicated by values below (−1), indicating deficits in soil moisture, groundwater, and water bodies (Jameel et al., 2023).

Further research in northern Iraq utilized rainfall variables and effective flow to model a drought index through the coupling method. The Frank function was the best choice for modelling the cumulative distribution function, and the proposed binary index showed a strong match with SPI and SRI, demonstrating its applicability (Hasan et al., 2023). In Nineveh Governorate, drought was assessed using SPI and CZI, revealing a clear decrease in rainfall levels and a noticeable increase in temperatures, with the Tel Abta station experiencing the highest frequency of drought events(Al-Bazaz and Mahmood Agha, 2024). A separate analysis in Sulaymaniyah, northern Iraq, assessed drought using SPI, SPEI, and RDI for different time intervals (3, 6, 9, and 12 months). The Darbandikhan station had the highest drought frequency, with significant drought observed at the Sulaymaniyah and Dokan stations (Governorate, 1965; Haveen M. Rasheed, 2024). A study based on rainfall data (1980-2021) for five stations in Iraq indicated the evaluation of the SPI and ZSI indicators on time scales of 1-12 months, where it was found that the correlation between them is weak in short periods and increases in long periods (9-12 months), especially in the northern regions. SPI showed a higher ability for early detection of drought with sharper and longer periods, while ZSI was more suitable for moisture analysis over the 12 months (Kazanchi and Awchi, 2025).

In addition, many recent studies have addressed the topic of hydrological drought forecasting using various indicators and traditional or hybrid models, focusing on analyzing the characteristics of drought in terms of intensity, duration, and frequency. For example, Mahmood Agha et al. (2025) presented a study that examined the drought characteristics of the upper Zab River using the standard discharge index (SSI) on the 6- and 12-month scales, and applied traditional forecasting models such as the ARIMA model and two exponential smoothing models, where the ARIMA model proved its efficiency in representing the temporal behavior of drought with high accuracy amounting to 92.4% (R2) at the 6-month scale. In another study, Al-Juboori (2023) developed a hybrid model using KNN and K-means techniques to predict drought based on the SDI index, and the model achieved a performance 85% higher than the traditional model.

Although these studies focused on hydrological drought, the similarity in the methodology of analysis and forecasting is directly relevant to the topic of climatic drought, since the same models and indicators can be used to analyze the characteristics of meteorological drought with higher accuracy. The adoption of advanced statistical methods such as ARIMA can contribute to the construction of an effective forecasting system that enhances the capacity of Hydro-planning and Climate Adaptation in dry and semi-dry environments.

While previous studies explored drought indices in Iraq, a comprehensive and integrated approach to evaluate meteorological drought across different regions, incorporating multiple drought indices, is still needed. This study aims to fill this gap by analyzing meteorological drought in Iraq using a combination of established indices, which will provide a more comprehensive understanding of drought patterns and their implications.

This review found that the studies that included northern Iraq were extensive and were conducted using many indices such as SPI, SPEI, CZI, and MCZI. Overall, the results show that the region suffers from drought and that the northern region is the most exposed part to drought on varying time scales.

5. Conclusions and Recommendations

A review of the previous literature related to the Middle East, especially Iraq, shows that the

region suffers from successive droughts ranging from light to very severe. Together, these studies demonstrate the occurrence of drought, but most lack data for northern Iraq.

This gap is the absence of a comprehensive study that can determine the most appropriate and most accurate indices for drought measurement, taking into account the conditions of the region, especially the distribution of rain and other climatic factors that affect it. Although most studies indicated that the length of the time chain used for drought analysis is equal to or more than 30 years, the validity of the use of indicators based on shorter time chains is worth investigating. This approach is of particular importance in dry and semi-dry areas such as northern Iraq, where rains are rare and evaporation rates are high, thereby making these areas more vulnerable to repeating droughts. Moreover, the literature still lacks a comprehensive analysis that compares different indicators to determine their suitability for the conditions of northern Iraq. Clear recommendations on the selection of the most appropriate index are also lacking, which can provide an accurate and comprehensive picture of the drought phenomenon in this region. Some studies, such as that of Sulaiman and Younis (2021), suggest that the DI is effective in northern Iraq. These findings are geographically limited. Therefore, this review underscores the need for a comprehensive nationwide study to identify the most suitable drought index for Iraq as a whole. Bridging this research gap is an important step towards a better understanding of this phenomenon and effective adaptation measures.

Table 7: Summary of studies conducted in Iraq.

Meteorological drought indices	Reference
SPI, NDVI	Al-Timimi 2012
RDI	Mahmood Agha and Şarlak 2016
MK	Salman et al. 2018
SPI	Yenigun and Ibrahim 2019
SPI, CZI, Deciles	Sulaiman and Younis 2021
SPEI	Mahmood Agha and Al-Aqeeli 2021
CZI	Mahmood Agha 2021
RDI	Gaznayee et al. 2022
SPI	Jameel et al. 2023
SPI, RDI, PNI, RAI, ZSI, Papa	Khalaf and Hummadi, 2023
SPI, SPEI, RDI	Haveen M.Rasheed 2024
SPI	Yaseen and Awchi 2024
CZI, MCZI, SPI	Kazanchi And Taymoor Awchi 2024
ZSI, SPI	Kazanchi And Taymoor Awchi 2025

6. Conflict of Interest

The authors declare that they have no conflict of interest.

7. Funding Statement

This research received no external funding.

8. Author Contributions

Sura Basim Idrees Al-Kalo: Conceived and prepared the manuscript; conducted the literature search and collected the relevant references; wrote and organized the manuscript; and prepared the manuscript for submission.

Omar Miqdad Abdul-Ghani Agha: Proposed the research topic and contributed to defining the research methodology; reviewed and evaluated the results; critically reviewed the discussion section; and provided scientific guidance, comments, and suggestions throughout the preparation and revision of the manuscript.

Both authors reviewed and approved the final version of the manuscript.

9. References

Abd-Elhamid, H.F., Zeleňáková, M., Soľáková, T., Saleh, O.K. and El-Dakak, A.M., 2024. Monitoring flood and drought risks in arid and semi-arid regions using remote sensing data and standardized precipitation index: A case study of Syria. Journal of Flood Risk Management, 17(1), e12961. https://doi.org/10.1111/jfr3.12961

Al-Bazaz, H. and Mahmood Agha, O.M.A.M., 2023. A Study of the Homogeneity of Climatic Data for Rain, Temperature and Humidity for Nineveh Governorate. Al-Rafidain Engineering Journal (AREJ), 28(2), pp. 173–185. https://doi.org/10.33899/rengj.2023.137763.1225

Al-Bazaz, H. J. and Mahmood Agha, O.M.A., 2024. Climate change and the behaviour of meteorological drought and its impact on wheat yield. Engineering and Applied Science Research, 51(2), pp. 248–258. https://doi.org/10.14456/easr.2024.24

Al-Juboori, A.M., 2023. Prediction of Hydrological Drought in Semi-arid Regions Using a Novel Hybrid Model. Water Resources Management, 37(9), pp. 3657–3669.https://doi.org/10.1007/S11269-023-03520-1/METRICS

Al-Qinna, M.I., Hammouri, N.A., Obeidat, M.M. and Ahmad, F.Y., 2011. Drought analysis in Jordan under current and future climates. Climatic Change, 106(3), pp. 421–440. https://doi.org/10.1007/S10584-010-9954-Y/METRICS

Al-Mohseen, K.A., 2010. Frequency Analysis of Hydrologic Drought (Case Study). Al-Rafidain

Engineering Journal, 18(6), https://doi.org/10.33899/rengj.2010.35187

Al-Timimi, Y.K., George, L.E. and Al-Jiboori, M.H., 2012. Drought Risk Assessment In Iraq Using Remote Sensing And GIS Techniques. Iraqi Journal of Science, 53(4), pp. 1078–1082.

Asadi Zarch, M.A., Sivakumar, B. and Sharma, A., 2015. Droughts in a warming climate: A global assessment of Standardized precipitation index (SPI) and Reconnaissance drought index (RDI). Journal of Hydrology, 526(July), pp. 183–195. https://doi.org/10.1016/j.jhydrol.2014.09.071

Asrari, E., Masoudi, M. and Afrough, E., 2011. Analyzing Spatial and Temporal Pattern of Humid, Normal and Drought Years Using Percent of Normal Precipitation Index (PnPI) in Fars Province, Iran. Journal of Applied Sciences in Environmental Sanitation, 6(3), pp. 299–308.

Awchi, T.A. and Kalyana, M.M., 2017. Meteorological drought analysis in northern Iraq using SPI and GIS. Sustainable Water Resources Management, 3(4), pp. 451–463. https://doi.org/10.1007/S40899-017-0111-X

Brouwer, C. and Heibloem, M., 1986. Irrigation Water Needs: Irrigation Water Management. Training Manual No. 3, http://www.fao.org/3/u3160e/u3160e04.htm#2.1.1

Dierauer, J.R. and Zhu, C., 2020. Drought in the Twenty-First Century in a Water-Rich Region: Modeling Study of the Wabash River Watershed, USA. Water 2020, Vol. 12, 181 P., https://doi.org/10.3390/W12010181

Dunkel, Z., 2015. Categorisation of Drought Indices Used in Agricultural Meteorology. November.

Elhoussaoui, A., Zaagane, M. and Benaabidate, L., 2021. Comparison of various drought indices for assessing drought status of the Northern Mekerra watershed, Northwest of Algeria. Arabian Journal of Geos, 14(10). https://doi.org/10.1007/S12517-021-07269-Y

Eslamian, S., Ostad-Ali-Askari, K., Singh, V.P., Dalezios, N.R., Ghane, M., Yihdego, Y., and Matouq, M., 2017. A Review of Drought Indices. International Journal of Constructive Research in Civil Engineering (IJCRCE), 3, pp. 48–66. https://doi.org/10.20431/2454-8693.0304005

Gaznayee, H.A.A., Al-Quraishi, A.M.F., Mahdi, K., Messina, J.P., Zaki, S.H., Razvanchy, H.A.S., Hakzi, K., Huebner, L., Ababakr, S.H., Riksen, M., and Ritsema, C., 2022. Drought Severity and Frequency Analysis Aided by Spectral and Meteorological Indices in the Kurdistan Region of Iraq. Water 2022, Vol. 14, 3024 P., 14(19), 3024. https://doi.org/10.3390/W14193024

Governorate, S., 1965. Journal of Engineering Physics. International Journal of Heat and Mass Transfer, 8(7), 1052. https://doi.org/10.1016/0017-9310(65)90089-x

Hasan, I.F., Kamal, N.H.M., Awchi, T.A. and Abdullah, R., 2023. Drought Assessment Using Two-Variate Modelling. IOP Conference Series: Earth and Environmental Science, 1222(1). https://doi.org/10.1088/1755-1315/1222/1/012022

IPCC, 2013. Climate Change 2013: The Physical Science Basis. Contribution of Working Group I to the Fifth Assessment Report of the Intergovernmental Panel on Climate Change. Cambridge: Cambridge University Press.

Iwata, T., Nishiyama, N., Nagano, K., Izumi, N., Tsukioka, T., Chung, K., Hanada, S., Inoue, K., Kaji, M. and Suehiro, S., 2012. Preoperative serum value of sialyl Lewis X predicts pathological nodal extension and survival in patients with surgically treated small cell lung cancer. Journal of Surgical Oncology, 105(8), pp. 818–824. https://doi.org/10.1002/jso.23002

Jameel, M., Hameed, S., Shemal, K., Al-Ansari, N. and Abed, S.A., 2023. Spatial and Temporal Assessment of Drought in the Northern Prone of Iraq Using Standardized Precipitation Index. Engineering. https://doi.org/10.4236/eng.2023.1510047

Katipoglu, O.M., Acar, R. and Şengül, S., 2020. Comparison of meteorological indices for drought monitoring and evaluating: A case study from the Euphrates Basin, Turkey. Journal of Water and Climate Change, 11(1S), pp. 29–43. https://doi.org/10.2166/wcc.2020.171

Kazanchi, S.R. and Awchi, T.A., 2024. Meteorological Drought Analysis Using Multiple Indices for Selected Stations in Iraq. Tikrit Journal of Engineering Sciences, 31(2), pp. 91-105. https://doi.org/10.25130/tjes.31.2.9

Kazanchi, S.R. and Awchi, T.A., 2025. Evaluation of SPI and ZSI, Meteorological Drought Indices on Different Time Scales in Iraq. AIP Conference Proceedings, 3211(1). https://doi.org/10.1063/5.0257186/3346170

Khalaf, A.A. and Hummadi, A.H., 2023. Time Series Analysis of Drought Indices for Monitoring Desertification and Land Degradation. Iraqi National Journal of Earth Science, 23(2), pp. 189–202. https://doi.org/10.33899/earth.2023.139660.1068

Li, L. and Cai, H., 2024. A comparative study of various drought indices at different timescales and over different record lengths in the arid area of northwest China. Environmental Science and Pollution Research, 31(17), pp. 25096–25113. https://doi.org/10.1007/S11356-024-32803-2

Li, H., Guo, J., Yan, D., Wang, H. and Jiang, X., 2024. Hydrological Drought Risk Assessment and Its Spatial Transmission Based on the Three-Dimensional Copula Function in the Yellow River Basin. https://doi.org/10.3390/w16131873

Labudová, L.Í.V.I.A., Turňa, M.A.R.O.Š. and Nejedlík, P.A.V.O.L., 2015, September. Drought monitoring in Slovakia. In Towards Climatic Services. International scientific conference.

Mahmood Agha, O.M. A., Ahmed, K.A., and Naser, A.I., 2025. Hydrological drought characteristics prediction using traditional models for the Great Zab River in Iraq. Theoretical and Applied Climatology, 156(5), pp. 1–15. https://doi.org/10.1007/S00704-025-05515-X

Mahmood Agha, O.M.A., and Al-Aqeeli, Y.H., 2021. Analysis of the Standardized Precipitation Evapotranspiration Index over Iraq and its relationship with the Arctic Oscillation Index. Hydrological Sciences Journal, 66(2), pp. 278–288. https://doi.org/10.1080/02626667.2020.1854765

Mahmood Agha, O.A. M. and Şarlak, N., 2017. Analysis of Meteorological Drought in Iraq Using the Reconnaissance Drought Index (RDI). International Journal of Advanced Research, 5(3), pp. 473–479. http://dx.doi.org/10.21474/IJAR01/3535

Mahmood Agha, O.M.A.M., 2021. Investigating the Meteorological Drought Using CZI in Nineveh Governorate, Iraq. Tikrit Journal of Engineering Sciences, 28(4), pp. 14–24. https://doi.org/10.25130/tjes.28.4.02

Mahmood Agha, O.M.A. M., Bağçacı, S.Ç., and Şarlak, N., 2017. Homogeneity Analysis of Precipitation Series in North Iraq. IOSR Journal of Applied Geology and Geophysics, 05(03), pp. 57–63. https://doi.org/10.9790/0990-0503025763

Mahmood Agha, O.M.A.M., and Şarlak, N., 2016. Spatial and temporal patterns of climate variables in Iraq. Arabian Journal of Geosciences, 9(4). https://doi.org/10.1007/s12517-016-2324-y

Mahmoudi, P., Rigi, A. and Miri Kamak, M., 2019. A comparative study of precipitation-based drought indices with the aim of selecting the best index for drought monitoring in Iran. Theoretical and Applied Climatology, 137(3–4), pp. 3123–3138. https://doi.org/10.1007/s00704-019-02778-z

Majid Kalyana, M. and A. Awchi, T., 2015. Investigating the Meteorological Drought in Northern Iraq Using Deciles Method. Al-Rafidain Engineering Journal (AREJ), 23(3), pp. 12–21. https://doi.org/10.33899/rengj.2015.101539

Mishra, A.K. and Singh, V.P., 2011. Drought modeling - A review. Journal of Hydrology, 403(1–2), pp. 157–175. https://doi.org/10.1016/j.jhydrol.2011.03.049

Mohammed, R. and Scholz, M., 2023. Quality Control and Homogeneity Analysis of Precipitation Time Series in the Climatic Region of Iraq. Atmosphere, 14(2), pp. 1–12. https://doi.org/10.3390/atmos14020197

Morid, S., Smakhtin, V. and Moghaddasi, M., 2006. Comparison of seven meteorological indices for drought monitoring in Iran. International Journal of Climatology, 26(7), pp. 971–985. https://doi.org/10.1002/joc.1264

Mtupili, M., Wang, R., Gu, L. and Yin, J., 2025. Delayed Response of Soil Moisture and Hydrological Droughts to Meteorological Drought Over East Asia. International Journal of Climatology, 45(9), e8883. https://doi.org/10.1002/JOC.8883

Myronidis, D., Fotakis, D., Ioannou, K. and Sgouropoulou, K., 2018. Comparison of ten notable meteorological drought indices on tracking the effect of drought on streamflow. Hydrological Sciences Journal, 63(15–16), pp. 2005–2019. https://doi.org/10.1080/02626667.2018.1554285

Nagarajan, R., 2009. Drought Indices. Drought Assessment, pp. 160–204. https://doi.org/10.1007/978-90-481-2500-5_5

Naresh Kumar, M., Murthy, C.S., Sesha Sai, M.V.R. and Roy, P.S., 2009. On the use of Standardized Precipitation Index (SPI) for drought intensity assessment. Meteorological Applications, 16(3), pp. 381–389. https://doi.org/10.1002/MET.136

Ndlovu, M.S. and Demlie, M., 2020. Assessment of meteorological drought and wet conditions using two drought indices across KwaZulu-Natal Province, South Africa. Atmosphere, 11(6), 623 P. http://dx.doi.org/10.3390/atmos11060623

Oksal, N.G.S. and Beden, N., 2024. Drought analysis based on SPI and RDI drought indices in the Burdur Basin. Turkish Journal of Engineering, 8(1), pp. 127–138. https://doi.org/10.31127/tuje.1326875

Öz, F.Y., Özelkan, E. and Tatlı, H., 2024. Comparative analysis of SPI, SPEI, and RDI ındices for assessing spatio-temporal variation of drought in Türkiye. In Earth Science Informatics. Springer Berlin Heidelberg. https://doi.org/10.1007/s12145-024-01401-8

Salman, S.A., Shahid, S., Afan, H.A., Shiru, M.S., Al-Ansari, N. and Yaseen, Z.M., 2020. Changes in climatic water availability and crop water demand for Iraq region. Sustainability (Switzerland), 12(8), pp. 14–27. https://doi.org/10.3390/SU12083437

Salman, S.A., Shahid, S., Ismail, T., Chung, E.S. and Al-Abadi, A.M., 2017. Long-term trends in daily temperature extremes in Iraq. Atmospheric Research, 198, pp. 97–107. https://doi.org/10.1016/J.ATMOSRES.2017.08.011

Salman, S.A., Shahid, S., Ismail, T., Rahman, N. bin A., Wang, X. and Chung, E.S., 2018. Unidirectional trends in daily rainfall extremes of Iraq. ThApC, 134(3–4), 1165–1177. https://doi.org/10.1007/S00704-017-2336-X

Şener, E. and Davraz, A., 2024. Comparison of drought indices in the analysis of temporal and spatial changes of climatic drought events: a case study in the Egirdir Lake basin (Isparta/Turkey). In Natural Hazards (Vol. 120, Issue 14). Springer Netherlands. https://doi.org/10.1007/s11069-024-06711-0

Shahabfar, A. and Eitzinger, J., 2013. Spatio-temporal analysis of droughts in semi-arid regions by using meteorological drought indices. Atmosphere, 4(2), pp. 94–112. https://doi.org/10.3390/atmos4020094

Subramanya, K., 2017.Engineering Hydrology. book https://idr.l3.nitk.ac.in/jspui/handle/123456789/14285

Sulaiman, Z.A. and Younis, A.M., 2021. Comparison of different drought indices in Nineveh. 1–5. Proceedings of Academica Sera International Conference, Istanbul, Turkey, 20th – 21st April, 2021

Tadić, L., Dadić, T. and Bosak, M., 2015. Usporedba različitih metoda za ocjenu suše na područjukontinentalne Hrvatske. Gradjevinar, 67(1), pp. 11–22. https://doi.org/10.14256/JCE.1088.2014

Tayfur, G., 2021. Discrepancy precipitation index for monitoring meteorological drought. Journal of Hydrology, 597, 126174. https://doi.org/10.1016/J.JHYDROL.2021.126174

Tsakiris, G., Pangalou, D. and Vangelis, H., 2007. Regional drought assessment based on the Reconnaissance Drought Index (RDI). Water Resources Management, 21(5), pp. 821–833. https://doi.org/10.1007/S11269-006-9105-4

Wilhite, D.A. and Glantz, M.H., 1985. Glantz,1987. Understanding the Drought Phenomenon: The Role of Definitions, 10(3), pp. 111–120. http://digitalcommons.unl.edu/droughtfacpub%0AWilhite

Wu, H., Hayes, M.J., Weiss, A. and Hu, Q., 2001. An evolution of the standardized precipitation index, the China-Z index and the statistical Z-score. International Journal of Climatology, 21(6), pp. 745–758. https://doi.org/10.1002/joc.658

Yahya, B.M., Seker, D.Z. and Ahmed, K.A., 2022. Drought Monitoring Based on Predicted SPI Using Fuzzy Controller System. Iraqi National Journal of Earth Science, 22(2), pp. 140–152. https://doi.org/10.33899/earth.2022.176633

Yaseen M. Ismael and Taymoor A. Awchi, 2024. IOP Conf. Ser.: Earth Environ. Sci. 1374012063 https://doi.org/10.1088/1755-1315/1374/1/012063

Yenigun, K. and Ibrahim, W.A., 2019. Investigation of drought in the northern Iraq region. Meteorological Applications, 26(3), pp. 490–499. https://doi.org/10.1002/MET.1778

Yevjevich, V., 1969. An objective approach to definitions and investigations of continental hydrologic droughts. Journal of Hydrology, 7(3), 353. https://doi.org/10.1016/0022-1694(69)90110-3

Yihdego, Y., Vaheddoost, B. and Al-Weshah, R.A., 2019. Drought indices and indicators revisited. Arabian Journal of Geosciences, 12(3), pp. 1–12. https://doi.org/10.1007/S12517-019-4237-Z

Iraqi National Journal of Earth Science, Vol. 26, No. 04, 2026 (219-234)

Iraqi National Journal of Earth Science

www.earth.uomosul.edu.iq

مراجعة شاملة للجفاف المناخي في العراق

سرى باسم ادريس[1*]، عمر مقداد عبد الغني[1]

Sura.basim1994@gmail.com O.agha@uomosul.edu.iq

[1] قسم هندسة السدود والموارد المائية، كلية الهندسة، جامعة الموصل، موصل، العراق.

*الباحث المراسل.

تاريخ الاستلام: 22 شباط 2025 تاريخ المراجعة: 20 أيار 2025 تاريخ القبول: 14 أيلول 2025

تاريخ النشر الالكتروني: 01 تشرين الأول 2026

الملخص:

الجفاف هو ظاهرة بيئية خطيرة تتميز بانخفاض حاد ومستمر في معدلات هطول الأمطار وارتفاع درجات الحرارة، مما يؤدي إلى انخفاض رطوبة التربة وحدوث أضرار مناخية وبيئية واقتصادية جسيمة. ويتجلى الجفاف بأشكال متعددة، تشمل الجفاف المناخي والزراعي والهيدرولوجي، حيث يرتبط كل نوع بأسباب وآثار محددة. تعتمد مراقبة الجفاف وتقييمه على استخدام مؤشرات مناسبة تختلف في فعاليتها تبعاً للظروف المناخية والجغرافية لكل منطقة. ويُعد الجفاف مشكلة متكررة في العراق، الذي يقع ضمن المناطق الجافة وشبه الجافة، حيث يؤدي استمرار الجفاف المناخي إلى ندرة الموارد المائية. وقد أظهرت مراجعة الدراسات السابقة وجود فجوات بحثية، أبرزها غياب الدراسات الشاملة التي تقارن بين مؤشرات الجفاف المختلفة لتحديد الأنسب منها لظروف العراق، لا سيما المناطق الجنوبية التي تتميز بندرة الأمطار وارتفاع معدلات التبخر. لذا فإن اختيار المؤشرات الأكثر ملاءمة يُعد خطوة ضرورية لفهم أدق لظاهرة الجفاف ووضع استراتيجيات مناسبة لإدارة الموارد المائية والتكيف مع هذا الحدث المتكرر. وتؤكد هذه الحالة على الحاجة المُلِحّة لإجراء دراسات معمقة لمعالجة هذه الفجوات وتقديم حلول عملية تعزز استدامة الموارد الطبيعية في المنطقة.

الكلمات المفتاحية:

شدة الجفاف، شبه جاف، دليل الجفاف

DOI: 10.33899/injes.v26i4.60926, *©Authors, 2026, College of Science, University of Mosul.*

This is an open-access article under the CC BY 4.0 license (http://creativecommons.org/licenses/by/4.0/).

Iraqi National Journal of Earth Science, Vol. 26, No. 04, 2026 (235-243)

Iraqi National Journal of Earth Science

www.earth.uomosul.edu.iq

Late Middle Miocene (Serravallian) of the Fat'ha Formation, Northern Iraq: Palynofloral Evidence

Ahmed S. Qulmani [1*], **Maha A. Al-Hasson** [1]

ahmed.24scp5@student.uomosul.edu.iq drmahamustafa@uomosul.edu.iq

[1] *Department of Geology and Petroleum, College of Science, University of Mosul, Mosul, Iraq.*
* *Correspondence author.*

Received: 23 February 2025 Received in revised form: 29 April 2025 Accepted: 07 July 2025
Available online: 01 October 2026

Abstract

This study represents the first palynological investigation conducted on the Middle Miocene Fat'ha Formation in Northern Iraq. Twelve samples were collected from an outcrop section of the Fat'ha Formation in Zawita, Northern Iraq. These samples yielded well-preserved and well-diversified palynomorph assemblages. Three species of spores related to three genera and nine pollen species related to nine genera were investigated and identified, as follows (Spirosyncolpites bruni, Pinuspollenites Subgenus Strobus sp, Abies sp.1, Arecipites pflugii, Monocolpopollenites tranquillus, Tubulifloridites sp, Quercus sp.2, Trivestibulopollenites betuloides, Carya sp, Polypodiaceoisporites fossulatus, Baculatisporites primarius, Camarozonosporites rarus). Analysis of palynomorph species assemblages from the Fat'ha Formation at the Zawita section shows no significant variations throughout the entire section, suggesting a single palynomorph assemblage biozone. This biozone was correlated with its equivalent in neighbouring Turkey, Iranian realms, and other sections around the world. The stratigraphic distribution of the identified species confirms, for the first time, that the Fat'ha Formation was assigned to the late Middle Miocene (Serravallian).

Keywords:

Serravallian age, Fat'ha Formation, Palynomorphs.

DOI: 10.33899/injes.v26i4.60927, *©Authors, 2026, College of Science, University of Mosul.*
This is an open-access article under the CC BY 4.0 license (http://creativecommons.org/licenses/by/4.0/).

==========

1. Introduction

Gachsaran Formation, formerly known as the Lower Fars series (Gill and Ala, 1972; Kashfi, 1980; Tucker and Shawket, 1980; Mahdi, 1983; Aqrawi, 1993; Tucker, 1999; Bahroudi and Koyi, 2004; Seyrafian and Mojikhalifeh, 2005; Habibi and Ruban, 2017; Sakhavati et al., 2020; Tavakolian et al., 2022) was first described from its type locality, the Fars Province NW Iran, by Busk and Mayo (1918) and van Bellen et al., (1959). Jassim et al. (1984) described the equivalent of the Lower Fars series and were the first to propose the name Fat'ha Formation and define its type section in the Fat'ha Gorge, 10 km north of Beji town in Iraq. The formation consists of anhydrites, gypsum, salt interbedded with limestones and marls (Al-Juboury and McCann, 2008; Al-Jaberi and Salim, 2022). The formation is widely distributed across Iraq, mainly in the Foothill Zone and Mesopotamian Basin, but it is absent in some areas (Aqrawi,1993). The formation continues into the Jazira area of Syria, along the Turkish-Syrian border (Weber, 1963), Iran, Kuwait, and Saudi Arabia (Powers et al.,1967). The formation was originally subdivided into an informal unit in Bellen et al. (1959) and Ditmar et al. (1971). Later, Jassim and Buday (2006) and Al Juboury and McCann (2008) subdivided the Fat'ha Formation into two members from the base to the top: 1) the Lower Member consists of organo-detrital limestone and anhydrite (or gypsum), green dolomitic marl, and thin limestone and cyclically interbedded gypsum; and 2) the Upper Member consists of red and green mudstone and gypsum, a few recrystallized shelly limestone beds and thin oolitic limestone beds, with calcarenite beds at the top. The formation thickness varies greatly, reaching a maximum of 900m. In the Kirkuk Basin, it reaches 600 m, whereas in the Sinjar Basin, it thins out markedly

near the AboJir high. The sedimentary facies of the Fatha Formation differ from one place to another, depending on its location in the sedimentary basin (Al-Taiiy and Al-Badrani, 2025). The fossils are very rare and mainly include foraminifera (Miliolids), with ostracods also common, assigned to the middle Miocene of the Fat'ha Formation in southern Iraq (Shareef et al., 2023). However, recent biostratigraphic studies based on nannofossils suggest an early Miocene – Aquitanian age for the Fat'ha Formation in northern Iraq (Kharajiany, 2023. The depositional environments are interpreted as restricted hypersaline to continental and open marine settings (Bellen et al., 1959; Al Juboury and McCann, 2008). Palynology is a useful tool in evolutionary, ecological and biostratigraphic studies (Germeraad et al., 1968; Muller, 1981; Traverse, 2007; Jaramillo et al., 2010) because the palynomorphs, including pollen, spores and dinoflagellates, are among the most abundant fossil groups found in sedimentary rocks (Pardo-trujillo et al., 2003; Traverse, 2007; Jaramillo et al., 2010; Rodríguez-Forero et al., 2012). These microfossils span a wide temporal range, from millions of years ago to the present, and occur in all types of environments (e.g., freshwater lacustrine deposits and deep-marine sediments), reflecting both forest- and grass-dominated ecosystems of the past (Boucot, 1999; Traverse, 2007). Many previous studies focus on the Fat'ha Formation because of its widespread distribution and provides a regional seal to numerous oil reservoirs. In addition, the formation yields economically important deposits of sulfur found in evaporite beds in Iraq (Al-Sawaf, 1977; Jassim et al., 1997; Jassim et al., 1999).

Several studies have been conducted on the Fat'ha Formation (Middle Miocene), focusing on various aspects including ostracod palaeoecology, foraminiferal biostratigraphy, and sedimentology. Kharruffa (2008) studied the distribution of ostracods within the formation. Al-Hadithi and Aziz (2019), Khalaf and Kharofa (2020 Ostracods within the same formation. Al-Shareefi et al. (2022) nanobiostratigraphy and ostracod paleoecology of the Fat'ha. Additionally, Aziz and Kasim (2023) studied ostracods from the Takia area in the Darbandi Bazian Anticline. Shareef et al. (2023) studied ostracoda and foraminifera of the Fat'ha Formation across. Furthermore, Abdulla (1994 studied the Fat'ha Formation from a selected well. Al-Taiiy and Al-Badrani (2025) studied the lithofacies and Age Determination of the Fatha Formation in Mushak. Mohammed and Al-Shareefi (2021) studied some records of ostracods from the Middle Miocene.

This work aims to determine the age of the studied section and to constrain the age of the Fat'ha Formation by using the palynomorphs for the first time. The results are then compared with other local and regional age-equivalent pollen and spore assemblages and corresponding zonal schemes to solve the problem of the unconstrained age of the studied formation. This study also aims to update the stratigraphic framework of the Fat'ha Formation by providing a detailed field description of the studied section, including its facies characteristics.

2. Geological Setting

The studied section is located in the Dohuk area, Zawita Valley, where the Fat'ha Formation is exposed in the Bekhair Anticline (Fig. 1A), with coordinates (43°09'05.8"E) and (36°55'28.2"N) within the High Folded Zone in northern Iraq (Jassim and Buday, 2006) (Fig. 1B).

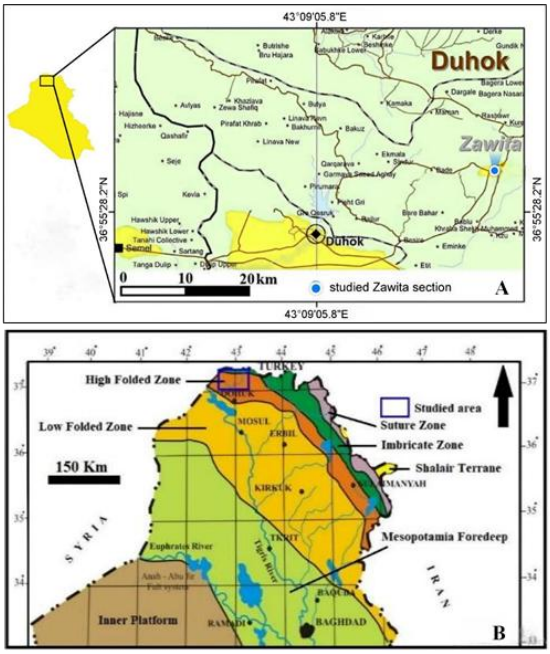


Fig. 1: Location map of the studied section and area. A: Satellite image from Google map© showing the study section in the Bekhair anticline, Northern Iraq. B: Structural map of N Iraq (Jassim and Buday, 2006; modified).

The Fat'ha Formation is part of the AP11 Megasequences, which span the latest Eocene to the Recent and include the middle Miocene sequence (Bellen et al., 1959; Sissakian et al.,

2016; Ameen, 2022). This formation was formerly assigned to the Lower Fars Series (Gill and Ala, 1972), whose equivalent in Iran is the Gachsaran Formation. The Middle Miocene sequence was deposited during a period of marine transgression and significant subsidence within a large, extensive basin that overlapped the margins of an older Oligocene–Early Miocene basin (Fig.2). The AP11 megasequence is associated with the collision of Neo-Tethyan terranes along the northern and eastern margins of the Arabian Plate, as well as with the initiation of rifting in the Gulf of Aden and Red Sea along its southern and western boundaries. The development of these rift systems was accompanied by thermal doming, extensive flood basalt volcanism, and crustal extension. The Gulf of Aden began opening during the Oligocene, followed by the onset of Red Sea rifting in the Early Miocene (Makris and Henke, 1992). The northward and northeastward movement of the Arabian Plate, coupled with the closure of the Neo-Tethys Ocean, resulted in folding and thrusting of the Neo-Tethyan terranes along the plate's northeastern edge (Jassim and Goff, 2006).

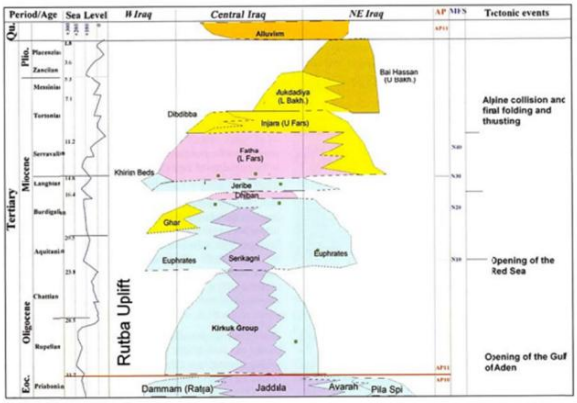


Fig. 2: Stratigraphic chart of AP11 megasequence (Jassim and Goff, 2006).

Stratigraphic Description of the studied Section

The Fat'ha Formation is composed of alternating sequences of green and red claystone and limestone. The base of the Fat'ha Formation overlies a 1.4-meter-thick layer of light brown, hard, well-bedded limestone enriched with iron oxides. This interval corresponds to an unconformity that typically underlies the top of the Pila Spi Formation. The Fat'ha Formation begins with a conglomerate layer, 60 centimeters thick (Fig. 3), followed by a brecciated limestone, 2 meters thick, and fossiliferous siltstone, 90 cm thick. Next, a 1 m-thick green soft marl, followed by marly limestone, 2m thick, and then 2 m-thick red claystone. These successions are overlain by a yellow soft marl layer, 50 cm thick. Next, a 2 m-thick dark blue soft marl layer, overlain by a 4 m-thick yellow limestone layer. This interval is followed by a hard, light brown marl limestone layer, 5 meters thick, succeeded by a well-bedded, light brown limestone layer, 60 cm thick. Above this, a boudin-bearing soft marl limestone, 1 m thick, is followed by a yellow marlstone, 70 cm thick, and then 2.5m thick red claystone. Then, a 40 cm-thick layer of green siltstone rich in fossils (Gastropods), which is overlain by a 60 cm-thick layer of fossiliferous limestone. Then, a 70 cm-thick interval of gray marly limestone, followed by a 5 m-thick marl interbedded with mudstone. This interval is succeeded by a 1-meter-thick layer of hard brown marl limestone, followed by a 3-meter dark gray marl. The sequence ends with a 1-meter-thick sandstone belonging to the Injana Formation. (Fig. 4). The total thickness of the formation is approximately 22 meters (Fig. 5).

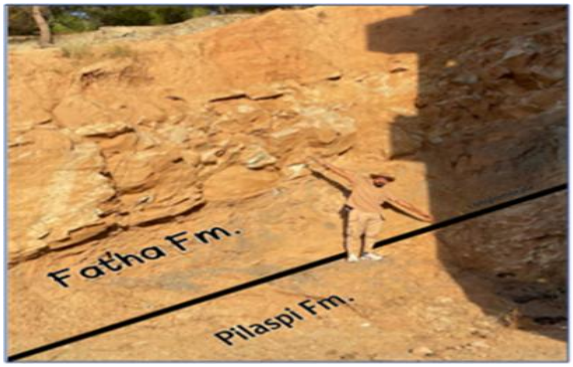


Fig. 3: Field photos show the lower contact between Pila Spi and Fat'ha Formation.



Fig. 4: Field photos show the upper contact between the Fat'ha and Injana formations.

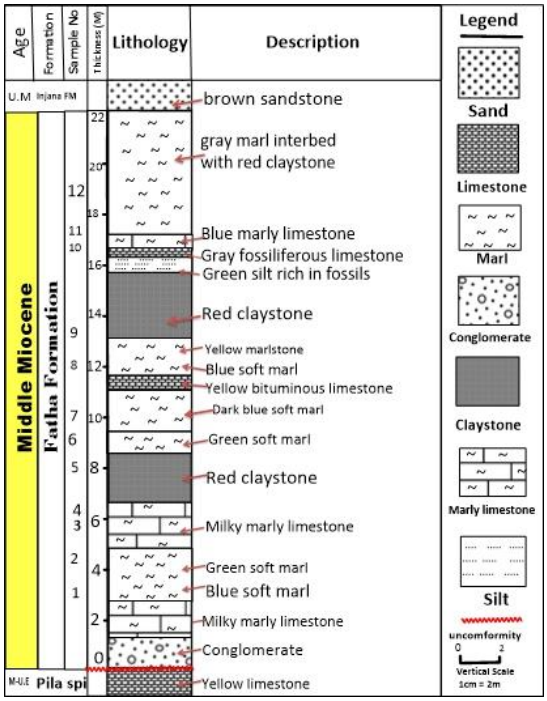


Fig. 5: Stratigraphic column of the Fat'ha Formation in the studied section.

3. Methodology

A total of twelve outcrop samples were collected from the studied section. These samples were processed in the laboratory following the preparation method developed by Barss and Williams (1973), with modifications introduced by Al-Ameiri (1986). The procedure was conducted with careful attention to preserve palynomorph grains for palynological analysis. The preparation process involved treating the samples with hydrochloric acid (HCl) to remove carbonates, followed by hydrofluoric acid (HF) to dissolve silicates. The remaining residues were sieved, thoroughly cleaned, and mounted on slides for microscopic examination. Microscopic observations were performed at a private laboratory in Ankara (Hasan Can laboratory) using an Olympus CX22 microscope, according to standard palynological techniques. The accompanying image illustrates the laboratory setup and the hands-on procedures involved in the sample preparation.

Identification of Spores and Pollen Grains in the Studied Section

Twelve samples from the studied section were analyzed to investigate spores and pollen grains. A total of twelve species were identified, as summarized in Fig. 6. These species were carefully selected based on their significance and preservation in each sample.

The percentage compositions of pollen and spores are defined as follows:

- **Osmundaceae, Pteridaceae, and dinocyst assemblage (at the base of the formation).**

(Gymnosperm: 10%; Angiosperms:18%; Fern: 25%)

- **Juglandaceae, Fagaceae, and Asteraceae assemblage (in the middle of the formation).**

(Gymnosperm: 8%; Angiosperms:30%; Fern: 18%)

- **Pinaceae, Fabaceae and dinocyst assemblage (at the top of the formation).**

(Gymnosperm: 23%; Angiosperms:22%; Fern: 17%)

Anteturma	Turma	Subturma	Species
VARIGERMINANTES	SACCITES	DISACCITES	*Pinuspollenites* Subgenus *Strobus* sp.
			Abies sp.1
			Arecipites pflugii
	PLICATES	MONOCOLPATES	*Monocolpopollenites tranquillus*
		STEPHANOCOLPITES	*Spirosyncolpites bruni*
		TRICOLPORATES	*Tubulifloridites* sp.
		TRIPTYCHES	*Quercus* sp. 2
	POROSES	TRIPORINES	*Trivestibulopollenites betuloides*
			Carya sp.
PROXIMEGERMINANTES	TRILETES	ACAVATITRILETES	*Polypodiaceoisporites ?fossulatus*
		AZONOTRILETES	*Baculatisporites*
			Camarozonosporites rarus

Fig. 6: The taxonomic classification of the species studied used here according to Burger (1994) and Smith and Buttworth (1967), modified from Traverse (1988).

4. Results

The analyzed samples contained well-preserved pollen grains and spores, making them suitable for a comprehensive appraisal of the palynology of the Fat'ha Formation (Plate 1). A

total of 12 species are identified, belonging to twelve genera within the studied section

A single palynomorph assemblage biozone (F1) is recognized:

***Carya* sp. – *Quercus* sp., Assemblage Biozone (F1).**

This biozone is characterized by the absence of an Oligocene –Miocene sporomorph assemblage including *Engelhardia*, Arecaceae, and *Castanea*, *Castanopsis* (Bozukov et al. 2009; Akkiraz et al., 2012). Additionally, no Early Miocene sporomorph assemblage, including Myricaceae, Castanea, Engelhardia, Sapotaceae and Quercus, is found within this biozone (Akgün et al. 2007).

This biozone is also characterized by the occurrence of middle Miocene age index species, including *Carya sp.*, *Fagus* sp., *Quercus* sp. and *Pinus* spp. (Bouchal et al.,2018).

We point out the absence of *Cedrus* spp. in the studied section, which is considered an index species for early middle Miocene (Langhian) age, as noted by Bouchal et al. (2019).

We have noted, in addition, the occurrences of late middle Miocene (Serravallian) sporomorphs in a mixed assemblage including Juglandaceae, *Carya*, *Fagus*, and Asteraceae (Akgün et al.,2007).

Age estimates: Serravallian (Late Middle Miocene) age

Assemblage: Juglandaceae, *Carya*, *Fagus*, Asteraceae, *Quercus* sp. and *Pinus* spp., *Carya* sp.

5. Discussion

We point out, through the analysis of the samples of the studied section, the absence of genera such as *Engelhardia*, Arecaceae and *Castanea*-*Castanopsis* that were documented at the Oligocene –Miocene transition (Bozukov et al. 2009; Akkiraz et al., 2012).

According to Akgün et al. (2007), the Early–Middle Miocene age is characterized by the dominance of Myricaceae, Castanea, *Engelhardia*, Sapotaceae and *Quercus*. This assemblage was absent in the studied section except for *Quercus* sp., suggesting that the studied interval is younger than the Early- Middle Miocene age.

The dominant occurrences of *Fagus* sp., the occurrences of *Quercus* sp. and *Pinus* spp. index species indicate an age of Middle Miocene (Bouchal et al. 2019). These occurrences were observed in the studied section; therefore, our sporomorph assemblage is designated as Middle Miocene age.

According to Javadi and Abassi (2024), the taxa *Inuspollenites* subgenus *Strobus* and *Pinuspollenites* Subgenus *Pinus* sp. are assigned to the Middle Miocene age, which is in agreement with current biostratigraphic constraints of the studied assemblage.

Yavuz-Işık (2007) suggested that *Quercus* spp. is abundantly recorded within the middle Miocene strata. The aforementioned taxa have indeed been recorded in the studied section.

The mixed occurrences of Juglandaceae, Carya, Fagus, and Asteraceae in this study point to a late middle Miocene (Serravallian) age. These findings are consistent with palynomorph data from the Turkish realm, as reported by Akgün et al. (2007), who highlighted that the Serravallian is mainly characterized by mixed forest taxa, including Juglandaceae, *Carya*, Carpinus, Pterocarya, Alnus, Asteraceae, and Fagus. Furthermore, the absence of *Cedrus* spp. in the studied section supports a Serravallian (Late Middle Miocene) age, as noted by Bouchal et al. (2019). The accepted age for the investigated plant-bearing successions recovered from the Fat'ha Formation studied section is late Middle Miocene (Serravallian), in particular spanning from the top of early Middle Miocene (Langhian) into the late Middle Miocene (Serravallian) age.

6. Conclusion

The palynological content of the Fat'ha Formation, exposed at the Zawita section, near Dohuk City, Northern Iraq, has been studied to constrain its age. The formation yields a diverse palynofloral assemblage, with twelve species identified: three fern species (representing three genera) and nine pollen species (representing nine genera). This study shows that pollen grains are reliable microfossils for age diagnostics of the Middle Miocene (Serravallian), particularly indicating the limited nature of continental environments in comparison to macrofossils. The key findings concern the index genus *Quercus* that occurs in the Middle Miocene. Additionally, we also note the mixed occurrences of a late Middle Miocene (Serravallian) sporomorph assemblage (including Juglandaceae, *Carya*, *Fagus*, and Asteraceae), which closely resembles the early

Middle Miocene palynoflora assemblage previously documented in the Turkish realm. This study confirms, for the first time in Iraq, that the Fat'ha Formation can be dated to the Late Middle Miocene (Serravallian).

7. Acknowledgements

The author would like to express sincere gratitude to the staff of Hassan Jan Private Laboratory (Ankara, Turkey) for their assistance in sample preparation and laboratory analysis. Appreciation is also extended to colleagues and supervisors for their valuable support and scientific guidance.

8. Conflict Of Interest

The author declares no conflict of interest regarding the publication of this paper.

9. Funding Statement

This research received no external funding.

10. Author Contributions

Maha A. Al-Hasson: Conceptualized the study, provided writing guidance, and supervised the project.

Ahmed S. Qulmani: Conceived the study, collected samples, analyzed data, and was responsible for manuscript writing, data visualization (tables and figures), and final editing.

11. References

Abdulla. R., 1994. Sedimentology of Fat'ha Formation from selected well in northern Meshraq area. (In Arabic).

Akgün F, Kayseri MS, Akkiraz M.S., 2007. Palaeoclimatic evolution and vegetational changes during the Late Oligocene–Miocene period in western and central Anatolia (Turkey). Palaeogeography, Palaeoclimatology, Palaeoecology 253: pp. 56-90.

Akkiraz.M., Akgün.F., Utescher.T., Wilde.V., 2012. Paleo-flora and Climate of Lignite-bearing Lower−Middle Miocene Sediments in the Seyitömer and Tunçbilek Sub-basins, Kütahya Province, Northwest Turkey (Turkish J. Earth Sci.), Vol. 21, pp. 213–235. DOI: https://10.3906/yer-1007-45

Al-Ameri TK, Al-Najar, T.K., Batten, DJ. 2001. Palynostratigraphy and palynofacies indications of depositional environments and source potential for hydrocarbons: the mid-Cretaceous Nahr Umr and lower Mauddud formations, Iraq. Cretac Res 22:735–742. (In Arabic).

Al-Hadithi, Z., and Aziz, N. 2019. Paleoecology and Statistical Study of Ostracoda, Fat'ha Formation (Middle Miocene) from Bazian Anticline, Al-Sulaymaniyah Area, Kurdistan Region, Iraq. Iraqi National Journal of Earth Science, 19(2), 119-0. (In Arabic). DOI: https://10.33899/earth.2019.170284

Al-Jaberi, M.H., and Salim, L. N., 2022. Depositional Properties of the Middle Miocene Fat'ha Formation in K Oilfield, Southern Iraq. The Iraqi Geological Journal, 139-152. (In Arabic). DOI: 10.46717/igj.55.2B.12Ms-2022-08-28. DOI: https://10.46717/igj.55.2B.12Ms-2022-08-28

Al-Juboury, A.I., and McCann, T., 2008. The Middle Miocene Fat'ha (Lower Fars) Formation, Iraq. GeoArabia, 13(3), 141-174. DOI: https://10.2113/geoarabia1303141

Al-Sawaf, F.D.S. 1977. Sulfate reduction and sulfur deposition in the Lower Fars Formation, Northern Iraq. Economic Geology, Vol. 72, pp. 608-618.

Al-Shareefi, I., Al-Badrani, O. and Kharofa, L., 2022. Nannobiostratigraphy and Ostracoda Paleoecology of Fat'ha Formation, Bashiqa Anticline, Northeastern Iraq. Iraqi Journal of Science, Vol. 63, No.4, p. 1574 – 1590. DOI: https://10.24996/ijs.2022.63.4.18

Al-Taiiy A., Al-Badrani O., 2025. Lithofacies and Age Determination Study of Fatha Formation in Mushak, Salah Al-Din Government, Northern Iraq. Iraqi National Journal of Earth Science. DOI: https://10.33899/earth.2024.147524.1242

Ameen, F. A., 2022. Sequence stratigraphy of the Oligocene and Miocene successions from selected wells in Garmian district, Kurdistan region/Iraq. In Recent Research on Geomorphology, Sedimentology, Marine Geosciences and Geochemistry: Proceedings of the 2nd Springer Conference of the Arabian Journal of Geosciences (CAJG-2), Tunisia 2019, pp. 209-212. Springer International Publishing.

Aqrawi, A. A. M.,1993. Miocene evaporitic sequence of the southern Mesopotamian Basin. Marine and Petroleum Geology, 10(2), pp. 172-179.

Aziz, N., and Kasim, Z., 2023. Some New Ostracod Species of Genera Schneiderella, Sulcostocythere, and Neomonoceratina, from the Fat'ha Formation (Middle Miocene) in the Takia Area, Darbandi Bazian Anticline, Sulaimaniyah Area, Kurdistan Region, Northeastern of Iraq. Iraqi Bulletin of Geology and Mining, 19(1), pp. 49-59. https://doi.org/10.59150/ibgm1901a04

Bahroudi, A., and Koyi, H. A. 2004. Tectono-sedimentary framework of the Gachsaran Formation in the Zagros foreland basin. Marine and Petroleum Geology, 21(10), pp. 1295-1310.

Barss, M. S. and Williams, G. L., 1973. Palynology and nano-fossil processing techniques. Geological Survey of Canada Paper, 25 P.

Bellen, R.C., Van Dunnington, H.V., Wetzel, R., Morton, D.M. 1959. Lexique Stratigraphique, International. Asie, Iraq, 3c (10a), 333 P.

Bouchal, J.M., 2019. The middle Miocene palynofloras of the Salihpaşalar lignite mine (Yatağan Basin,

southwest Anatolia): environmental characterization and comparison with palynofloras from adjacent basins. Palaeobiodiversity and Palaeoenvironments, 99: 591-636. DOI: https://10.1007/s12549-018-0345-0

Bouchal, J.M., Zetter, R., Denk, T. 2016. Pollen and spores of the uppermost Eocene Florissant Formation, Colorado: a combined light and scanning electron microscopy study. Grana, 55(3): 1-67. https://doi.org/10.1080/00173134.2015.1108362

Boucot, A. J., 1999. Southern African Phanerozoic marine invertebrates: Biogeography, paleoecology, climatology and comments on adjacent regions. Journal of African Earth Sciences, 28(1), pp. 129-143.

Bozukov, V., Utescher, T., and Ivanov, D., 2009. Late Eocene to early Miocene climate and vegetation of Bulgaria. Review of Palaeobotany and Palynology, 153(3-4), 360-374. DOI: https://10.1016/j.revpalbo.2008.10.05

Burger, D., 1994. Guide to genera file of fossil spores and pollen of Jansonius and Hills (1976). Australian Geological Survey Organisation record 1994/46. 36 p.

Busk, H.G. and MAYO, H.T., 1918. Some notes on the geology of the Persian oil fields: Journal Institute Petroleum Technology, v. 5, p. 5–26.

Ditmar, V., 1971. Geological conditions and hydrocarbon prospects of the Republic of Iraq (Northern and Central parts), North Oil Company, Iraq.

Germeraad, J.H. et al. 1968. Palynology of Tertiary sediments from tropical areas. Review of Palaeobotany and Palynology Vol. 6 # 3 P. pp. 189- 348

Gill, W. D., and Ala, M.A., 1972. Sedimentology of Gachsaran Formation (Lower Fars Series), southwest Iran. AAPG Bulletin, 56(10): pp. 1965-1974.

Goff, J.C., R.W. Jones and A.D. Horbury 1995. Cenozoic basin evolution of the northern part of the Arabian. Plate and its control on hydrocarbon habitat. In M.I. Al-Husseini (Ed.), Middle East Petroleum Geosciences Conference, GEO'94. Gulf PetroLink, Bahrain, Vol. 1, pp. 402-412.

Habibi, T., and Ruban, D. A., 2017. Outstanding diversity of heritage features in large geological bodies: The Gachsaran Formation in southwest Iran. Journal of African Earth Sciences, 133, 1-6. DOI: https://10.1016/j.jafrearsci.2017.05.010

Jaramillo, C.A., and Dilcher, D. L., 2001. Middle Paleogene palynology of Central Colombia, South America: A study of pollen and spores from tropical latitudes, Palaeontographica Abteilung B 258 4-6, 87-213

Jaramillo, C., 2010. The late Miocene paleogeography of the Amazon Basin and the evolution of the Amazon River system. Earth Sci. Rev. 99 (3–4), 99–124. DOI: 10.1016/j.earscirev.2010.02.005

Jassim, S. Z., Jibril, A. S., and Numan, N. M., 1997. Gypsum karstification in the middle Miocene Fat'ha Formation, Mosul area, northern Iraq. Geomorphology, 18(2), 137-149.

Jassim, S.Z. and Goff, J.C., 2006. Geology of Iraq. Dolin, Prague and Moravian Museum, Czech Republic, 395 p.

Jassim, S. Z., Karim, S. A., Basi, M. Al-Mubark, M.A., and Munir, J., 1984. Final report on the regional geological survey of Iraq. Vol. 3. Stratigraphy. Internal report. Geological Survey of Iraq.

Jassim, S.Z. and Buday, T., 2006. Latest Eocene-Recent Megasequence AP11. In S.Z. Jassim and J.C. Goff (Eds.), Geology of Iraq. Chapter 14, p. 169-184. Dolin and Moravian Museum, Czech Republic.

Javadi, F. and Abbassi, N., 2024. Miocene miospores in the Upper Red Formation, Zanjan, northwestern Iran. Geopersia, 14(1): pp. 199-212. DOI: https://10.22059/GEOPE.2024.365656.648730

Kashfi, M. S., 1980. Stratigraphy and environmental sedimentology of Lower Fars Group (Miocene), south-southwest Iran. AAPG Bulletin, 64(12), pp. 2095-2107.

Khalaf, S.K., Kharofa, L.H., 2020. Paleontological study of Ostracoda in the Fat'ha Formation (Middle Miocene) Hammam Al-Alil area, northern Iraq. Iraqi Bulletin of Geology and Mining. (In Arabic)

Kharajiany, S. O. A. 2023. Calcareous-nannofossil biostratigraphy of the Miocene Fat'ha Formation at the Miryas section, Qaradagh Mountain Series, Sulaimaniyah, Kurdistan Region, Iraq. Australian Journal of Earth Sciences, 70(8), 1172-1183. DOI: https://10.1080/08120099.2023.2232436

Kharruffa, L.H., 2008. Systematic Study and Stratigraphical Distribution of Ostracoda in Fat'ha Formation (Middle Miocene) from selected locations; Northern Iraq, College of Science, University of Mosul. (In Arabic)

Mahdi, A. H. I., 1983. Stratigraphical and palaeoenvironmental studies in the Lower Fars Formation (Miocene) of northern Iraq. University of London, Bedford College (United Kingdom).

Makris, J., and Henke, C., 1992. Crustal structure of the Arabian Peninsula derived from seismic refraction data.

Muller, J., 1981. Fossil pollen records of extant angiosperms. Botan. Rev. 47 (1), 1–142. Nesbitt, H.W., Young, G.M., 1982. Early Proterozoic climates and plate motions inferred from major element chemistry of lutites. Nature 299 (5885), 715–717.

Mohammed and Al-Shareef, 2021. Some records Ostracod species of genus Paijenborchellina from the Middle Miocene Fat'ha Formation, Eastern Butmah Anticline, Northwestern Mosul City, Iraq, Iraqi National Journal of Earth Science. (In Arabic) DOI: https://10.33899/earth.2021.170377

Pflug H. 1953. Zur Entstehung und Entwicklung des Angiospermenpollens in der Erdgeschichte. Palaeontographica B 96: 60-171.

Powers, R.W., Ramírez, L.F., Redmond, C.D., and Elberg, E.L. Jr. 1967. Geology of the Arabian Peninsula: Sedimentary Geology of Saudi Arabia. U.S. Geological Survey Professional Paper 560-D, 147 P.

Rodríguez-Forero, G., F.E. Oboh-Ikuenobe, C. Jaramillo-Muñoz, M.J. Rueda-Serrano, And E. Cadena-Rueda. 2012. Palynology of the Eocene Esmeraldas Formation, Middle Magdalena Valley Basin, Colombia. Palynology 36: 96–111. DOI: https://10.1080/01916122.2012.650548

Sakhavati, B., Yousefirad, M., Majidifard, M. R., Solgi, A., and Maleki, Z., 2020. Age of the Gachsaran Formation and equivalent formations in the Middle East based on foraminifera. Micropaleontology, 66(5), 441-465. DOI: https://10.47894/mpal.66.5.06

Seyrafian, A., and Mojikhalifeh, A., 2005. Biostratigraphy of the late Paleogene- early Neogene succession, north-central border of Persian Gulf, Iran. Carbonates and Evaporites, 20(1), pp. 91-97.

Shareef, N. F., Mahdi, M. M., and Mohamed, A. H., 2023. Combined Ostracoda and Foraminiferal Biozonation with Environment of Fat'ha Formation (Middle Miocene) in Different Oilfields, Southern Iraq. The Iraqi Geological Journal, 188-211. DOI: 10.46717/igj.56.1D.15ms-2023-4-24

Sissakian, V. K., Karim, S. A., Al-Kubaisyi, K. N., Al-Ansari, N., and Knutsson, S., 2016. The Miocene sequence in Iraq: a review and discussion on the stratigraphy, paleogeography and economic potential. Journal of Earth Sciences and Geotechnical Engineering, 6(3), 271-317.

Smith, V. H. and Butterworth, M.A., 1967. Miospores in the Coal seams of the Carboniferous of Great Britain. Spec. Pap. Palaeont.1, Palaeont. Assoc., London, P. 1-324.

Tavakolian, I., Yassaghi, A., and Najafi, M., 2022. Structural style in the south Dezful Embayment, SW Iran: Combined influence of the Zagros frontal fault system and the detachment in the Miocene Gachsaran Formation. Journal of Petroleum Geology, 45(3), pp. 303-323. DOI: https://10.1111/jpg.12821

Traverse, A., 1988: Paleopalynology. Unwin, London. 600 P.

Traverse, A., 2007. Paleopalynology (Vol. 28). Springer Science and Business Media.

Tucker, M. E., 1999. Sabkha cycles, stacking patterns and controls: Gachsaran (Lower Fars/Fatha) Formation, Miocene, Mesopotamian Basin, Iraq. Neues Jahrbuch für Geologie und Paläontologie-Abhandlungen., 214(1).

Tucker, M. E., and Shawket, M. G., 1980. The Miocene Gachsaran formation (formerly lower Fars) of the Mesopotamian basin, Iraq: Sabkha cycles and depositional controls.

Weber, F., 1963. Geologie des Irak: Beiträge zur regionalen Geologie der Erde. Borntraeger, Berlin, p. 327

Yavuz–Işik, N. 2007. Pollen analysis of coal-bearing Miocene sedimentary rocks from the Seyitömer Basin (Kütahya), Western Anatolia. Geobios 40, 701–708. DOI: https://10.1016/j.geobios.2006.11.006

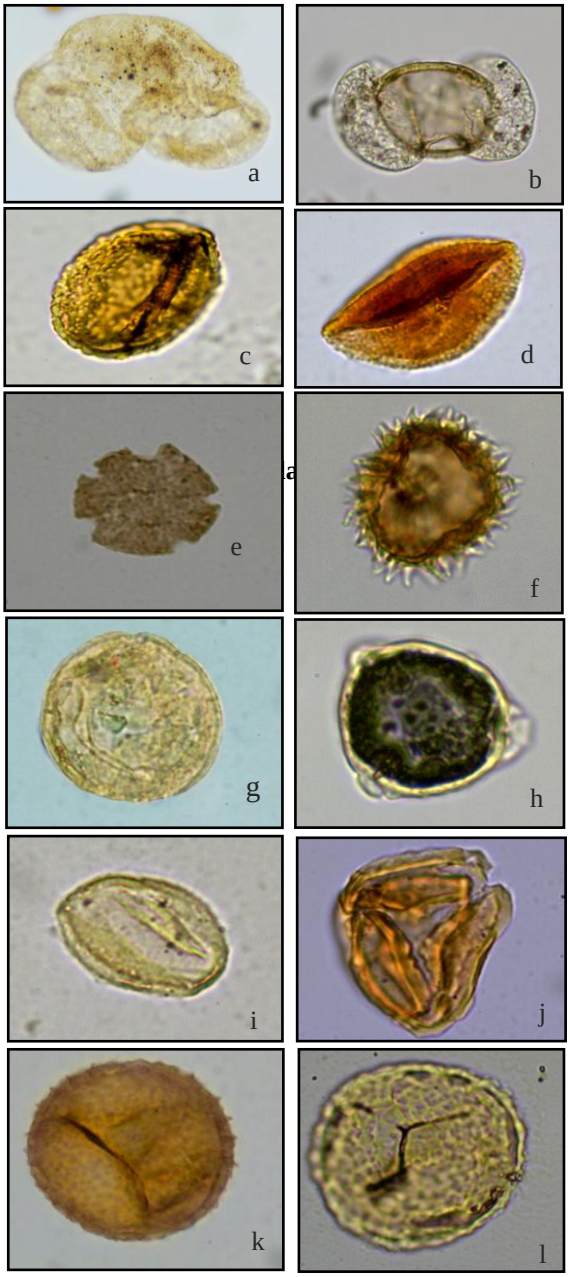


Plate 1: a. Pinuspollenites Subgenus Strobus sp. (118 µm), b. Abies sp.1 (125 µm), c. Arecipites pflugii (28 µm), d. Monocolpopollenites tranquillus (30 µm), e. Spirosyncolpites bruni (29 µm), f. Tubulifloridites sp. (50 µm), g. Quercus sp. (28 µm), h. Trivestibulopollenites betuloides (32 µm), i. Carya sp. (27 µm) j. Polypodiaceoisporites? fossulatus (45 µm), k. Baculatisporites primarius (42µm), l. Camarozonosporites (Hamulatisporis) rarus (50µm).

Iraqi National Journal of Earth Science, Vol. 26, No. 04, 2026 (235-243)

Iraqi National Journal of Earth Science

www.earth.uomosul.edu.iq

المايوسين الأوسط المتأخر (سيرفاليان) لتكوين الفتحة، شمالي العراق: الأدلة البالينوفلورية

احمد قولماني [1*] ، **مهى الحسون [1]**

ahmed.24scp5@student.uomosul.edu.iq drmahamustafa@uomosul.edu.iq

[1] قسم علوم الأرض والنفط، كلية العلوم، جامعة الموصل، الموصل، العراق.

*الباحث المراسل.

تاريخ الاستلام: 23 شباط 2025 تاريخ المراجعة: 29 نيسان 2025 تاريخ القبول: 07 تموز 2025

تاريخ النشر الالكتروني: 01 تشرين الأول 2026

الملخص

تُعدُّ هذه الدراسة أول تحقيق بالينولوجي يُجرى على تكوين الفتحة من عصر الميوسين الأوسط في شمال العراق. تم جمع اثنتي عشرة عيّنة من مقطع سطحي لتكوين الفتحة في منطقة زاويتا، شمال العراق. وقد أظهرت هذه العينات تجمّعات بالينومورفية محفوظة بشكل جيد ومتنوعة، اذ تم تحديد ودراسة ثلاث أنواع من الأبواغ تعود إلى ثلاثة أجناس وتسعة أنواع من حبوب اللقاح تعود إلى تسعة أجناس، وهي كما يلي:

Spirosyncolpites bruni, Pinuspollenites Subgenus Strobus sp., Abies sp.1, Arecipites pflugii, Monocolpopollenites tranquillus, Tubulifloridites sp., Quercus sp.2, Trivestibulopollenites betuloides, Carya sp., Polypodiaceoisporites fossulatus, Baculatisporites primarius, Camarozonosporites rarus.

بينت تحاليل تجمّعات الأنواع البالينومورفية المستخلصة من تكوين الفتحة في مقطع زاويتا عدم تواجد فاختلافات كبيرة في محتواها، مما يشير إلى أنها تمثل تجمعا بالينومورفيا لنطاق حيوي واحد. وقد تمّت مضاهاة هذا النطاق مع ما يُعادله في تركيا وإيران المجاورتين، وكذلك مع مقاطع أخرى حول العالم. وتُؤكد التوزيعات الطباقية للأنواع المُحددة، ولأول مرة، أن تكوين الفتحة يعود إلى أواخر الميوسين الأوسط (سيرفاليان).

الكلمات المفتاحية:

عمر سيرافاليان ، تكوين الفتحة، بالينومورفات.

DOI: 10.33899/injes.v26i4.60927, ©Authors, 2026, College of Science, University of Mosul.

This is an open-access article under the CC BY 4.0 license (http://creativecommons.org/licenses/by/4.0/)

Iraqi National Journal of Earth Science, Vol. 26, No. 04, 2026 (244-256)

Iraqi National Journal of Earth Science

www.earth.uomosul.edu.iq

Utilizing Shear Wave Velocity Techniques for Identifying Engineering Challenges in 6th October City, Egypt

Diaa Hamed [1*]

dzeinalabedein@kau.edu.sa

[1] *Department of Geology, Faculty of Science, Al-Azhar University, Naser City, Cairo 11884, Egypt.*
** Correspondence author.*

Received: 18 April 2025 Received in revised form: 20 May 2025 Accepted: 19 June 2025
Available online: 01 October 2026

Abstract

In Egypt, geophysical surveys are now more critical, especially following the significant impact of the October 1992 earthquake on structures in Greater Cairo. Engineering site investigations aim to determine the depth and lithological composition of the bedrock, groundwater depth, and lateral lithological variations, and to identify faults or fissures. To meet these objectives, shallow seismic refraction surveys were conducted in a selected area within 6th October City, Egypt, to assess subsurface characteristics before commencing construction activities. The first step was taken to identify the underlying geological structure by acquiring fifteen seismic refraction profiles over the research region. The primary wave velocity distribution analysis identified the existence of three separate geoseismic strata characterized by velocity ranges of (685 to 835 m/s), (680 to 1030 m/s), and (1340 to 1525 m/s). The sediment layers exhibit shear wave velocities ranging from 356 to 440 m/s, 360 to 536 m/s, and 690 to 790 m/s, respectively. These findings indicate that the first layer has low velocity values, which reflect a sediment composition consisting of sandy gravel. On the other hand, the second layer consists of coarse gravelly sand, while the third layer consists of clayey limestone. The sediment layers were analyzed using a basic equation to derive geophysical characteristics, which include the velocity of the shear wave, the density of the rock, and material indices (including material index, Poisson's ratio, N-value, and stress ratio). According to these data, the sediment layers beneath the surface in this area have a moderate to high level of competence.

Keywords:

Geotechnical, Poisson's ratio, Shear wave.

DOI: 10.33899/injes.v26i4.60961, ©Authors, 2026, College of Science, University of Mosul.
This is an open-access article under the CC BY 4.0 license (http://creativecommons.org/licenses/by/4.0/).

==========

1. Introduction

Shallow geophysical techniques such as seismic refraction methods are highly sought after for detecting subsurface structures and lithologic layers at shallow depths (less than 100 ft). Utilizing shallow geophysical methods offers precise and affordable solutions for engineering, environmental, and archaeological surveys. They enhance the interpretive abilities of geophysicists and augment the capabilities of engineers and geologists by leveraging basic geophysical principles. Seismic refraction techniques have significantly contributed to numerous engineering endeavors, including constructing hydroelectric power plants, subways, roads, and tunnels over the past three decades.

Seismic methods have become essential for calculating elastic moduli, which help estimate elastic deformation in civil engineering projects (Harden and Drnevich, 1972; David and Taylor Smith, 1979; Stumpel et al., 1984; Ghanem et al., 2021; Mohsain and Al-Khalidy, 2022).

The interpretation of the moduli called dynamic elastic obtained from foundation rock's velocity measurements during earthquakes and machine cyclic loading indicates extra stresses that may surpass the rock materials' ultimate bearing capability (Bowles, 1984). Relying exclusively on soil competence ratings is insufficient for determining foundation placements, particularly in earthquake-prone areas.

For engineers, soil is the material that covers bedrock after it has weathered and is often used as the foundation for construction projects. Soil

geotechnical properties depend on the elasticity of the underlying source rocks, which can be measured using traditional geophysical methods (Dutta, 1984; Abed Elrahman et al., 1991 and 1992; Al-Juraisy and Al-Saigh, 2010; Al-Nuaiemy et al., 2018).

Understanding soil stiffness, usually measured by shear wave velocity (Vs), is crucial for predicting soil behavior during earthquakes. Additionally, evaluating site amplification depends on soil stiffness (Borcherdt, 1994). Determining shear wave velocity in each subsurface layer allows us to estimate ground shaking at a given location (Hunter et al., 2002). This study will use this technique for accurate predictions. Located 32 km south of Cairo and within 20 km of the Great Pyramids of Giza (Fig. 1), 6th October City has been the subject of intensive investigation by numerous scientists for engineering and environmental purposes (e.g., Abd Elrahman et al., 1991 and others).

The study area's surface geology (Fig. 2) reveals that the Gebel Qatrany Formation, consisting of strata of reddish claystone, burrowed siltstone, and continental and coastal marine deposits, is present throughout. In the region, the sediment composition generally comprises lithic pieces, gravel, sand, silt, and clay, with the exception of some regions where the topsoil has a distinct composition.

This study aims to ascertain the shear wave velocity in each soil horizon for engineering and geotechnical purposes. In order to examine the challenges faced on the engineering site and provide an accurate representation of the underground layers and velocities in the study area, we conducted a shallow seismic refraction investigation. This study utilizes geotechnical data collected from subsurface investigations to evaluate the response of the site. The dataset obtained by Mohamed in 1991, 2003, and 2009 consists of measurements of various parameters such as thickness, density, damping factors, P-wave and S-wave velocities, and others, obtained by geotechnical boreholes and seismic surveys. This approach combines P-wave velocity data obtained from seismic refraction surveys with S-wave velocity data obtained from the multi-channel approach of Surface Waves (MASW) surveys.

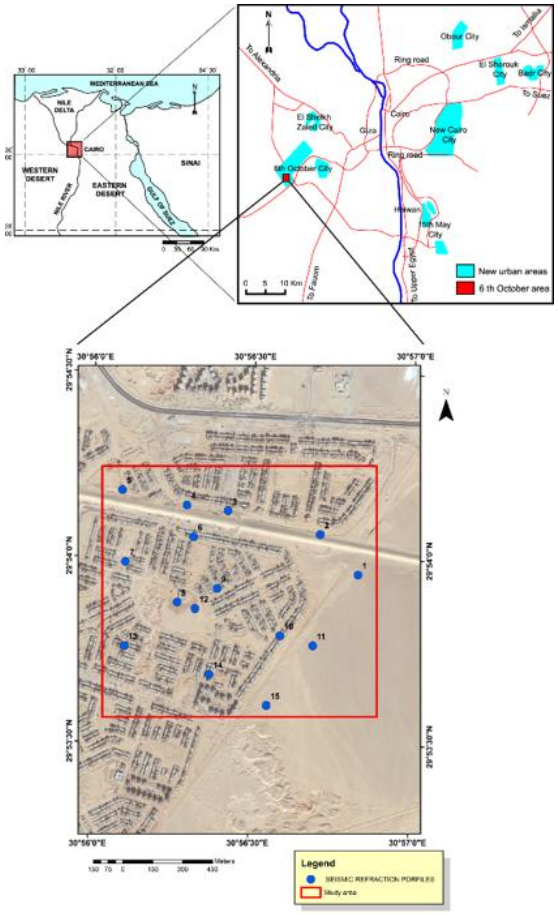


Fig. 1: Location map of the study area showing seismic refraction spreads in 6th of October City.

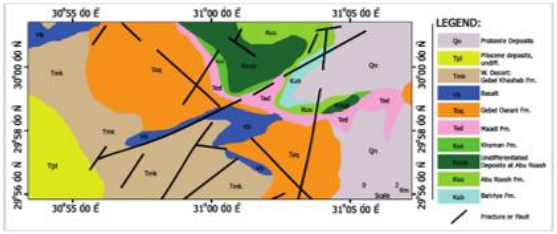


Fig. 2: Regional geologic map (modified after Conoco Coral, 1987).

2. Materials and Methods

A comprehensive geophysical investigation was carried out using both seismic refraction and Multi-Channel Analysis of Surface Waves (MASW) techniques to assess subsurface conditions in the selected area within 6th October City, Egypt.

Fifteen seismic refraction profiles were acquired across the study area using a linear array of 40 Hz vertical-component geophones spaced at 2-meter intervals, with a total spread length of approximately 94 meters. Seismic energy was generated using controlled hammer impacts at

multiple shot points located at both ends, midpoints, and along the profile line at 5-meter intervals. Data acquisition was performed using a Strata View seismograph (Geometrics Inc., USA), equipped with 48 channels for signal amplification and recording.

In addition to P-wave data obtained from seismic refraction, S-wave velocities were determined using the MASW method, which involves analyzing the dispersion characteristics of surface waves (Rayleigh waves). This method allows for reliable estimation of shear wave velocity profiles down to depths exceeding 30 meters.

The MASW data were collected using the same geophone array configuration as the refraction survey. Surface waves were generated using a sledgehammer and metal plate source, and the resulting wavefield was recorded by the multichannel seismograph. The recorded data were then processed using standard MASW procedures to generate phase velocity dispersion curves, which were subsequently inverted to obtain 1D shear wave velocity profiles for each survey line.

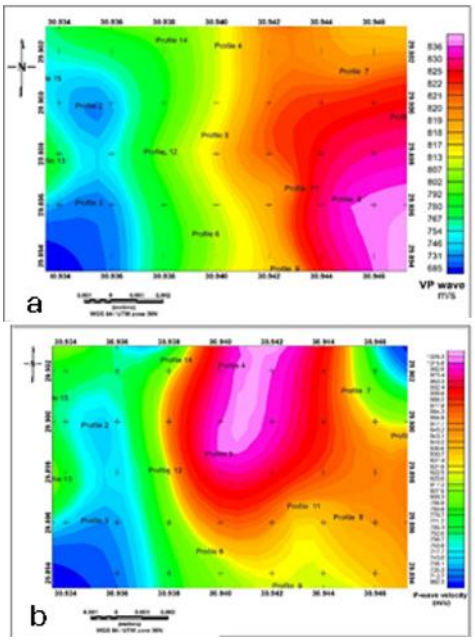
All field data processing and inversion steps were conducted by the author using specialized software tools. The final S-wave velocity models were integrated with P-wave velocity results to derive key elastic parameters, including Poisson's ratio, Young's modulus, rigidity modulus, and bulk modulus. These parameters were used to evaluate the geotechnical competence of the subsurface layers and their suitability for foundation engineering applications.

The shear wave velocity (Vs) values reported in this study were derived from field measurements using the MASW technique and subsequent data processing conducted by the author. The methodology followed standard procedures for surface wave analysis, including dispersion curve extraction and inversion modeling to produce reliable Vs profiles for each seismic line.

3. Seismic velocities

One important premise of the seismic refraction method is the rate of propagation, or seismic wave velocities, in a given medium. We have calculated the reciprocal slope of selected segments on the time-distance curve to find the seismic wave velocities for each sediment layer. A total of 31 seismic sites across the study region will have their P-wave and SH-wave seismic velocities assessed for the three layers of underlying sediment. Fig. 3 illustrates the lateral variation of P-wave velocities across the study area for (a) the first layer (685–835 m/s), (b) the second layer (680–1030 m/s), and (c) the third layer (1340–1525 m/s), indicating lithological differences among the geoseismic layers. Fig. 4 displays the observed SH-wave velocity distribution for (a) the first layer (356–440 m/s), (b) the second layer (360–536 m/s), and (c) the third layer (690–790 m/s). The increasing velocities with depth reflect enhanced material stiffness and competence in deeper subsurface layers over the surface layers.

The primary wave velocity analysis in the studied region indicates the presence of three separate geo-seismic strata with velocities ranging from 685 to 835 m/s, 680 to 1030 m/s, and 1340 to 1525 m/s. Similarly, the distribution of shear wave velocity reveals the presence of three distinct geo-seismic strata with velocities ranging from 356 to 440 m/s, 360 to 536 m/s, and 690 to 790 m/s, respectively. The first layer has low velocity values, indicating the presence of sand with a composition that includes gravel. In contrast, the second layer consists of course, gravelly sand. The second layer is notable for its clearly differentiated top and lower sections. The velocity measurements of the third layer suggest that it has a texture characterized by the presence of clay and limestone.



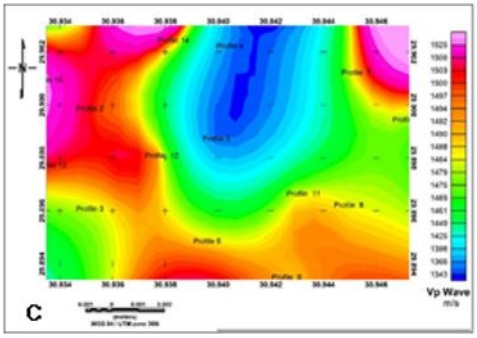


Fig. 3: Spatial distribution maps of P-wave velocities for (a) the first layer (685–835 m/s), (b) the second layer (680–1030 m/s), and (c) the third layer (1340–1525 m/s).

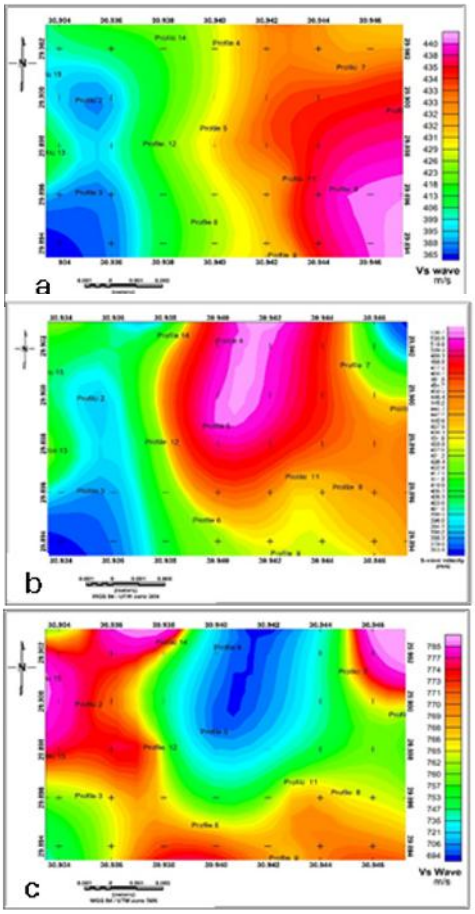


Fig. 4: Distribution of shear wave (SH-wave) velocities for (a) the first layer (356–440 m/s), (b) the second layer (360–536 m/s), and (c) the third layer (690–790 m/s).

4. Geotechnical characteristics of the foundation material

At the surveyed sites, measuring the P-wave and SH-wave velocities across the subsurface sediment layers is a critical tool for calculating their geotechnical properties, such as elastic moduli, competence scales, and bearing capacities. Understanding these geotechnical properties is critical for determining the bedrock's competence in engineering and environmental work in the study area.

4.1 Elastic moduli

4.1.1. Poisson's Ratio (σ):

Fig. 5 displays the Poisson's ratio values distribution. The maps illustrate that the values in the first layer vary between 0.3016 and 0.3079. The lowest Poisson's ratio value is in the southwest, while the southeast exhibits larger values. Similarly, the second layer has a minimum value of 0.3015 in the southwest and higher values of 0.3129 in the northern region. Poisson's ratio values in the third layer exhibit lower values (0.3175) in the northern region and higher values (0.3200) in the northeastern region of the study area.

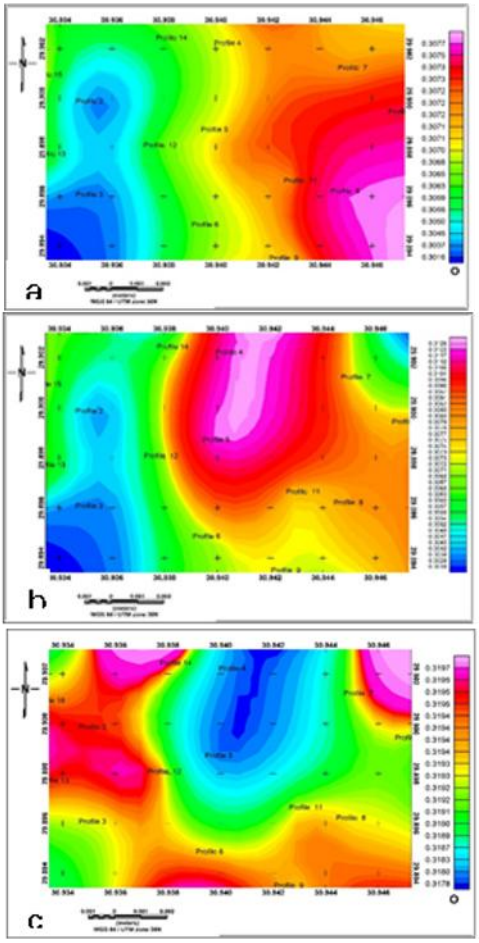


Fig. 5: (a) First, (b) Second, and (c) Third-layer Poisson's Ratio (σ).

4.1.2. Kinetic Rigidity Modulus (μ):

Fig. 6 depicts the measured values of the kinetic rigidity modulus for the sediment layers in the research region. The results in the first layer range from 174 dyn/cm² to 392 dyn/cm², showing the presence of soil components that vary from

quite low to competent. The minimum values represent the southwestern and western corners, progressively rising towards the southeastern portion of the region.

Conversely, the (μ) values for the second layer (Fig. 6.b) vary between 120 dyn/cm² and 896 dyn/cm², with the lowest values seen in the northeast and southwest corners. The (μ) of the second layer exhibits a progressive rise as one moves towards the northern region of the area. The overall results indicate materials that range from low to competent quality. In addition, the observed values of the kinetic stiffness modulus for the third sediment layer vary from 2470 dyn/cm² to 3972 dyn/cm². The results exhibit a minimal magnitude in the northern region and progressively escalate towards the northeastern and northwestern sections, suggesting the presence of less proficient and less stiff materials in that stratum.

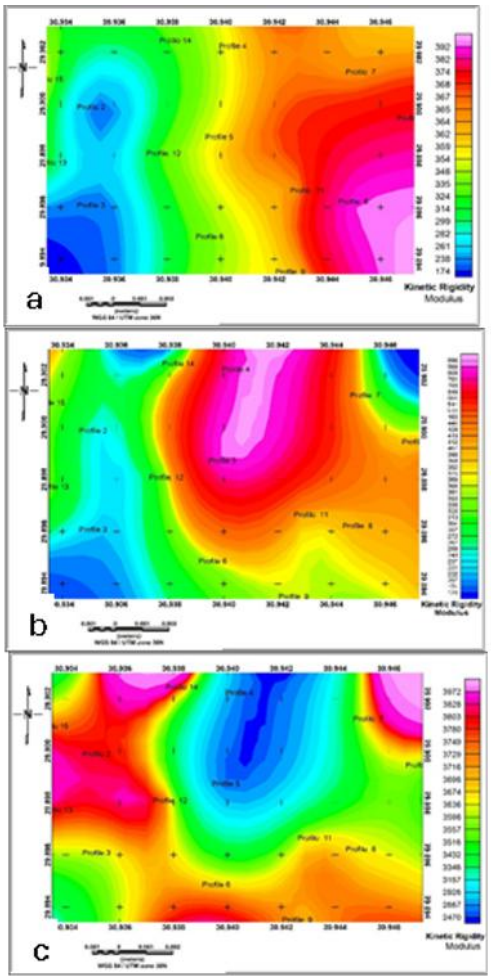


Fig. 6: (a) First, (b) Second, and (c) Third layer Kinetic Rigidity Modulus (μ).

4.1.3. Kinetic Young's Modulus (E):

Fig. 7 depicts the spread of Young's modulus values. The first layer has a range of values spanning from 452.5 to 1025.5 dyn/cm², with lower values observed in the southern and western regions, gradually increasing towards the eastern region. Conversely, the values for the second layer vary between 309 and 2352 dyn/cm², with the lowest values seen in the northeast and southwest regions and gradually increasing towards the north and central parts. In addition, the (E) values for the third layer vary between 6509 and 9684 dyn/cm², with lower values seen in the northern and central regions and increasing towards the northeastern and western corners.

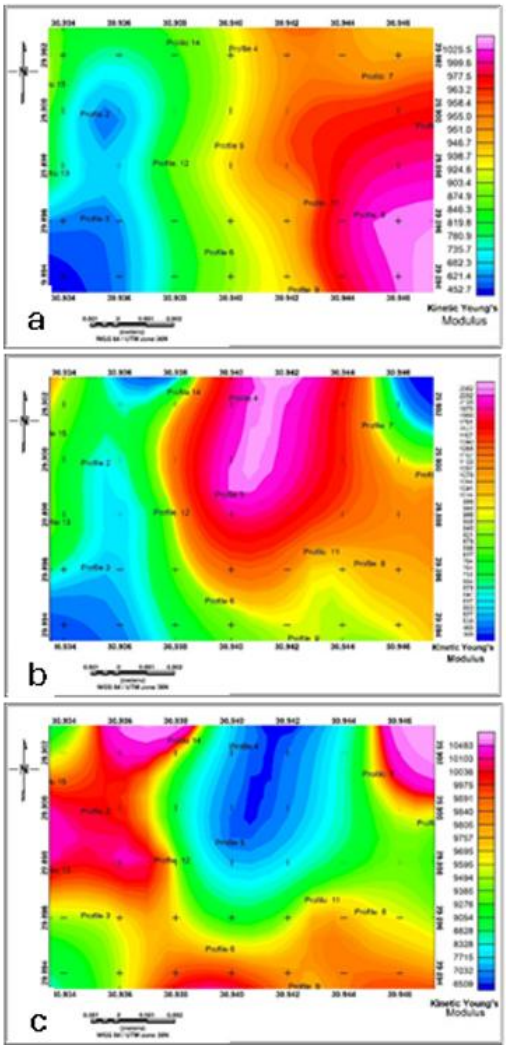


Fig. 7: (a) First, (b) Second, and (c) Third layer Kinetic Young's Modulus (E).

4.1.4. Kinetic Bulk Modulus (K):

Fig. 8 displays the bulk modulus values recorded in the region. The first layer records values ranging from 378.5 dyn/cm² to 888 dyn/cm², primarily in the southwestern and western parts, with the southeastern corner recording the highest values. In contrast, the values recorded in the second layer range from 235

dyn/cm2 to 2096 dyn/cm2, with lower values scattered across various sites, especially in the northeastern and southwestern parts. In comparison, higher values are more common in the central and northern parts of the region. The values recorded in the third layer range from 6509 dyn/cm2 to 10483 dyn/cm2, with lower values located in the northern part and the higher values scattered across various sites, especially in the northeastern and northwestern parts.

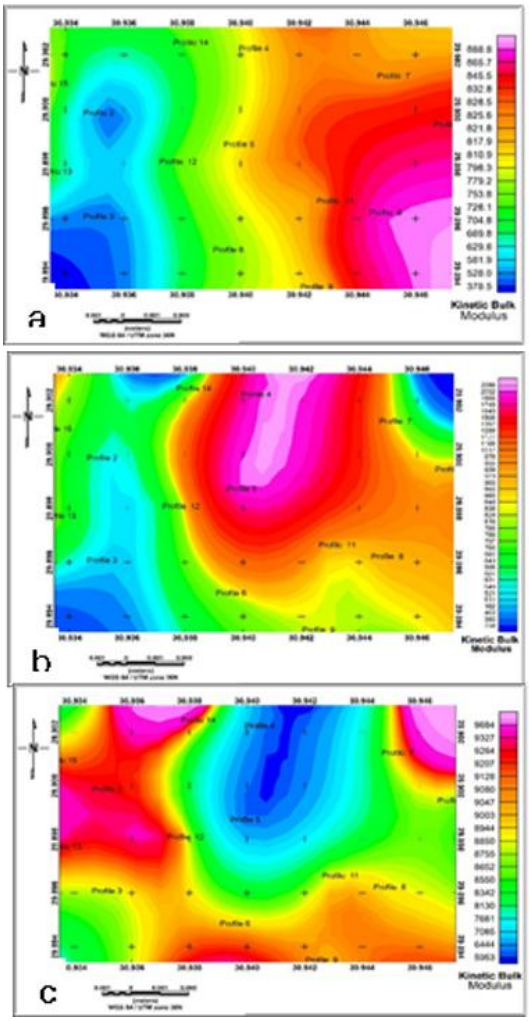


Fig. 8: Kinetic Bulk Modulus (K) for (a) first, (b) second, and (c) third layer.

4.2. Standard penetration test (SPT) [n-value]:

The SPT is a geotechnical method used to assess the resistance of sediment layers to penetration. Table 1 presents a categorization of N-values, which are determined by geophysical assessments of different soil types using the methodologies used by Imai and Yoshimura (1975) and Stumpel et al. (1984). Fig. 9 presents the recorded N-values for the sediment layers under investigation. The N-values of the first layer vary between 60 and 105.5. On the other hand, the N-values for the second layer range from 50 to 190. The lowest values are seen in the southwest and northeast, suggesting the presence of hard and compact soil. The data indicate a steady rise in the center and northern areas. The N-values of the third layer vary between 401 and 569, suggesting the presence of a hard and very dense layer.

Table 1: Classification of N-values with types of soil (After Bowles, 1984).

Cohesionless soil				
N-values	0-10	11-30	31-50	> 50
State	Loose	Medium	Dense	Very Dense
Cohesive soil				
N-Value	< 4	4-6	6-15	16-25	> 25
State	Very Soft	Soft	Medium	Stiff	Hard

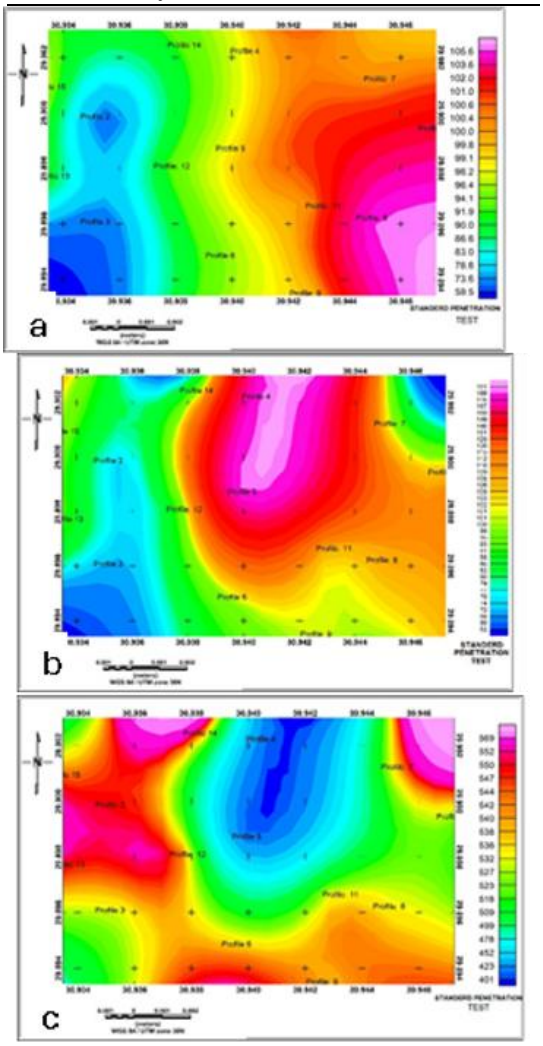


Fig. 9: N-values for the (a) first, (b) second, and (c) third layer.

4.3. Material competence scales:

4.3.1 The Material Index (*v*):

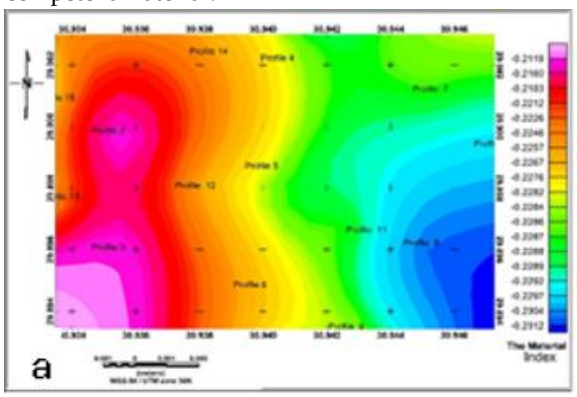
According to Abd Elrahman (1989), material index values range between (+1) and (-1), as shown in Table 2, which illustrates the

classification of the material index according to the foundation.

Table 2: Classification of the material index for foundation purposes (After Abd Elrahman 1989).

Category I -1 < ν < -0.5	Category II -0.5 < ν < 0	Category III 0 < ν < 0.5	Category IV ν > 0.5
Soft recent river, stream deposits, wind blows sand, clay, and volcanic ashes	Partly consolidated. Highly porous alluvial deposits, highly fractured limestone, basalt, and cavernous carbonate deposits.	Non-porous hard indurated rocks	Very hard indurated sedimentary rocks
Non-competent to less competent	Fairly to moderately competent	Competent	Very high competent

Fig. 10 presents the material index values for the research area. The first layer values vary from -0.312 to -0.2119. The lower values in the southeastern sections indicate the presence of less capable material, while the higher values in the western and southwestern parts indicate the presence of material that is of good to fairly capable quality. In the central portion of the region, the data indicate a range of materials with varying degrees of competence, from reasonably competent to less competent. The numbers in the second stratum span from -0.2503 to -0.2072. The southwestern and western areas have the most elevated values, whilst the northern portion of the study zone has the most diminished values. The third layer values vary from -0.2797 to -0.2713, indicating the presence of fairly to moderately competent material.



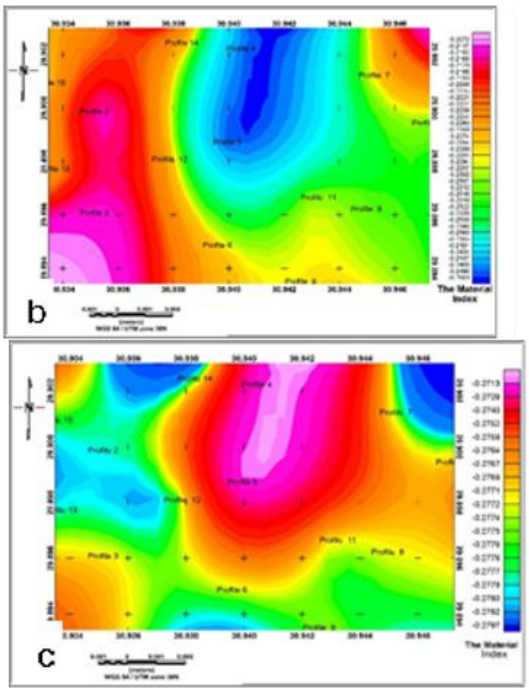
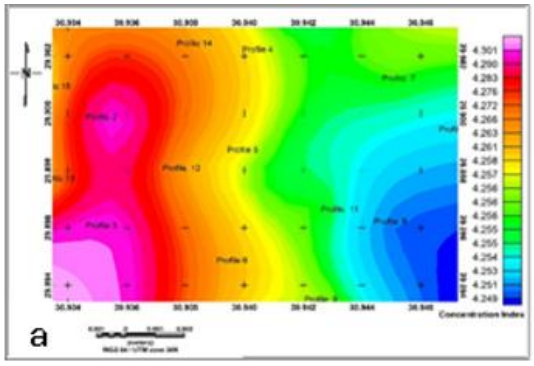


Fig. 10: (a) First, (b) Second, and (c) Third layer Material Index (ν).

4.3.2. Concentration Index (Ci):

In civil engineering, soil compaction assesses competence via the concentration index (Ci). Fig. 11 displays concentration index values recorded in the study. Initially, values range from 4.249 to 4.301 in the first layer, lower in the east and southeast, denoting materials of modest quality. Conversely, higher values in the west and southwest suggest moderately highly competent materials. Similarly, the values of the second layer vary from 4.20 to 4.30, with lower concentrations in central and northern areas extending towards the west and southwest, indicating moderately competent materials. The third layer shows values from 4.1257 to 4.1463, with the highest values in the central and northern regions and the lowest in the northeast and west.



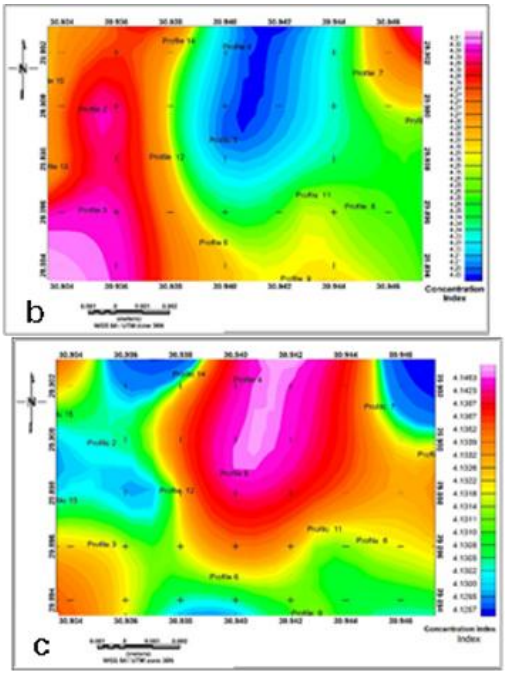
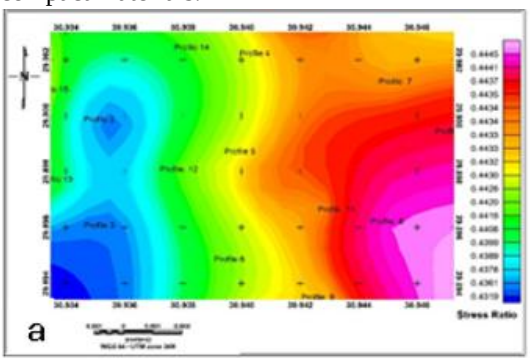


Fig. 11: (a) First, (b) Second, and (c) Third layer Concentration Index (Ci).

4.3.3 Stress Ratio (Si):

The seismic wave velocity through sediment materials correlates directly with the difference in pressure between the sediment layers and the fluids that occupy the intergranular pore spaces of these sediments (Buckingham, 2005) .

In Fig. 12, the Si values vary from 0.4319 to 0.4445 in the first layer, with lower values more common in the southwest. This suggests reasonably to moderately compact materials. Conversely, higher Si values are in the northeast and southeast regions, indicating relatively less compact to moderately compact materials. The Si values in the second layer vary from 0.4322 to 0.4547, with lower values primarily in the southwest and gradually increasing toward the north and central areas, indicating moderately compact materials.



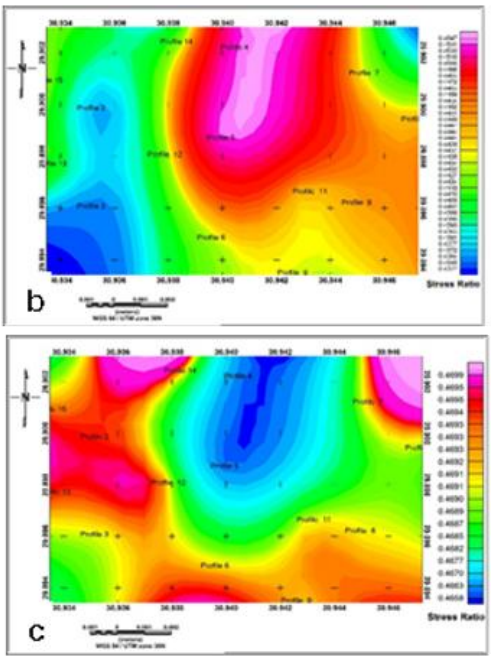


Fig. 12: (a) First, (b) Second, and (c) Third layer Stress Ratio (Si).

4.3.4. Density Gradient (Di):

From an engineering perspective, the density gradient value (Di) of materials is closely linked to their material competence and the compression velocity (Vp). As discussed by Cordier (1985), "Compaction" refers to sediments transitioning from their original loose state to a denser state due to overburden weight or tectonic movements.

Fig. 13 displays the range of density gradient values in the first layer, which exhibits minor fluctuations, ranging from 0.00000226 to 0.00000315. In this layer, the eastern and southeastern regions of the study region show lower density gradient values, suggesting the presence of fairly competent material. In contrast, the western and southwestern regions display elevated values, indicating the presence of materials with modest competence.

The Di values in the second layer vary between $0.15*10^{-5}$ and $0.34*10^{-5}$. The northern and central regions display the lowest scores, indicating a modest degree of proficiency. In contrast, the western and southwestern regions display values that suggest the presence of exceptionally capable materials. In the third layer, the Di values vary from $0.64*10^{-5}$ to $0.\ 85*10^{-5}$. The center and northern areas have the highest values, while the western and northeastern regions display the lowest values.

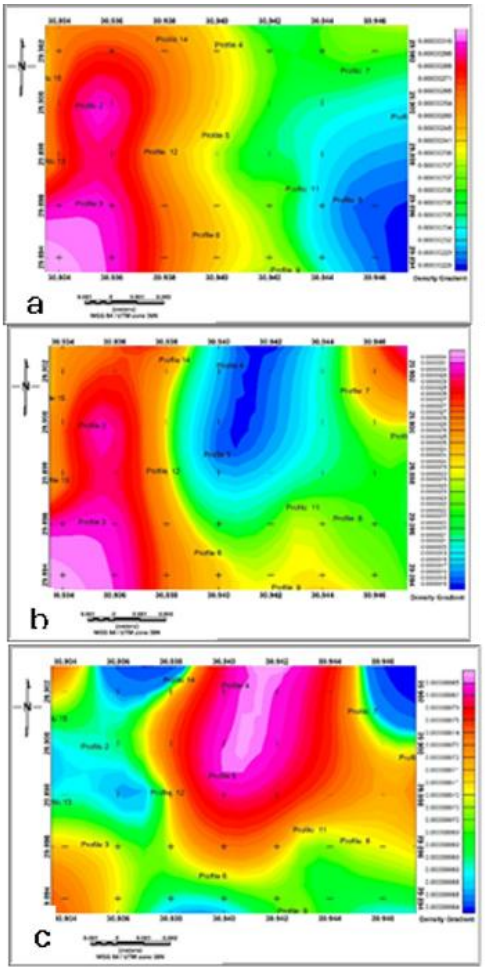


Fig. 13: Density Gradient (Di) for first layer (a), second layer (b), and third layer (c).

5. Foundation materials bearing capacity

5.1. Ultimate Bearing Capacity (Qult):

The soil's ability to withstand the weight of the foundation without collapsing is referred to as it carrying capacity (Lukić et al., 2017). The Qult of soil refers to the highest pressure it can withstand before it fails, as stated by Damane (2019). The shear strength coefficient defines the maximum load-bearing capacity (Qult).

The Qult values depicted in Fig. 14 range from 1784 to 3169 kPa and are generally considered to be quite low. The first layer showed comparatively lower results in the southern and western regions of the research area. Conversely, the southern and eastern corners of the research area have elevated values of first layer bearing capacity, indicating that these regions are more prone to include materials with less ultimate bearing capacity. Conversely, the second layer exhibits a range of ultimate bearing capacity values ranging from 1590 to 5725 kPa. The western, southwestern, and northeastern parts have notably low values, suggesting the existence of materials with inadequate ultimate bearing capability. In contrast, the central and northern areas have the highest values of ultimate bearing capacity for this layer, suggesting the presence of materials with relatively high ultimate bearing capacity. The values in the third stratum range from 12035 to 17060 kPa. The western and northeastern regions of the research area demonstrate the highest values, whilst the center and northern regions display the lowest values.

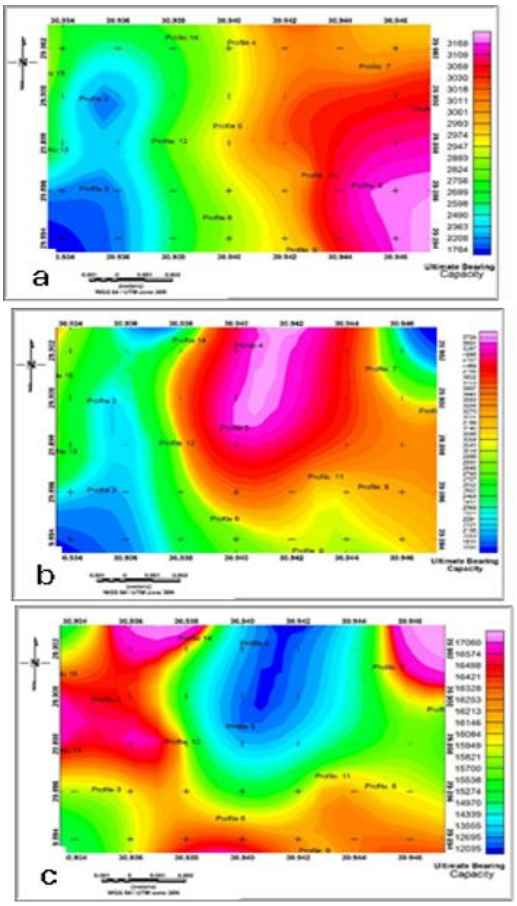
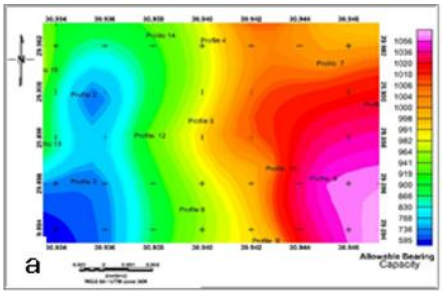


Fig. 14: (a) First, (b) Second, and (c) Third layer Ultimate Bearing Capacity (Qult).

5.2. Allowable Bearing Capacity (Qa):

The Qa refers to the highest level of stress that may be exerted on the soil to maintain its stability and prevent shear failure and excessive settlement (Bowles, 1988). Fig. 15 is a figure that shows the permissible range of bearing capacity values (Qa). Upon a more detailed analysis of the figure, it becomes evident that the Qa values for the first layer vary between 595 kPa and 1056 kPa. The southern and western regions demonstrate lower levels, whilst the eastern and southeastern regions display the greatest values. The Qa values for the

second layer vary between 530 kPa and 1909 kPa. The southern and western regions have a higher concentration of materials with a low permitted bearing capacity, whereas the values steadily increase as you move towards the center and northern sections of the region. For the third layer, the acceptable range of bearing capacity values is from 4012 kPa to 5690 kPa. The western and northeastern regions have the highest values, while the center and northern regions have the lowest values.



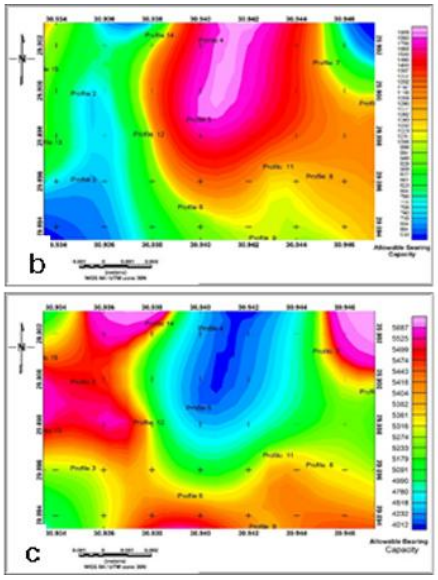


Fig. 15: (a) First, (b) Second, and (c) Third layer Allowable Bearing Capacity (Qa).

Table 3: Presents a thorough overview of the estimated elastic moduli, material competency, and foundation material-bearing capability.

Mechanical Properties		Surface layer		Second Layer		Third Layer	
		From	To	From	To	From	To
Elastic moduli	Poisson's ratio	0.3016	0.3077	0.301	0.3126	0.3178	0.3525
	Kinetic rigidity modulus	174	390	120	896	2470	3972
	Kinetic Young's modulus	452.5	1025.5	309	2352	6509	10483
	Kinetic bulk modulus	378.5	888	235	2096	5953	9684
	N-value	60	105.5	50	190	401	569
Material competence	Material index	-0.312	- 0.2119	-0.2503	-0.2072	-0.2797	-0.2713
	Concentration index	4.249	4.301	4.20	4.30	4.1257	4.1463
	Stress ratio	0.4319	0.4445	0.4322	0.4547	0.4658	0.4699
	Density gradient	0.00000226	0.00000315	0.0000015	0.0000034	0.0000064	0.0000085
Foundation material bearing capacity	Ultimate bearing capacity	1784	3169	1590	5725	12035	17060
	Allowable bearing capacity	595	1056	530	1909	4012	5690

6. Results

The subsurface investigation of the selected area in 6th October City, Egypt, using shallow seismic refraction and MASW techniques revealed the presence of three distinct geoseismic layers.

Layer 1 (sandy gravel): P-wave velocities range from 685 to 835 m/s, and S-wave velocities vary between 356 and 440 m/s. This layer is approximately 7 meters thick and exhibits low material competence. N-values range from 60 to 105.5, indicating medium to dense cohesionless soil.

Layer 2 (coarse gravelly sand): Characterized by P-wave velocities ranging from 680 to 1030 m/s and S-wave velocities from 360 to 536 m/s, with a thickness of about 11 meters. N-values here range from 50 to 190, reflecting increasing competence compared to the upper layer.

Layer 3 (clayey limestone): Shows the highest seismic velocities, with P-waves ranging from 1340 to 1525 m/s and S-waves from 690 to 790 m/s. N-values exceed 400, reaching up to 569, indicating very high competence.

Elastic moduli were calculated for all layers as follows:

Poisson's ratio: Ranges from 0.3016–0.3079 (Layer 1), 0.3015–0.3129 (Layer 2), and 0.3175–0.3200 (Layer 3).

Kinetic Rigidity Modulus (μ): Increases with depth, ranging from 174 dyn/cm² to 3972 dyn/cm².

Young's Modulus (E): Varies from 452.5 dyn/cm² in layer 1 to 9684 dyn/cm² in layer 3.

•Bulk Modulus (K): Also increases with depth, showing values from 378.5 dyn/cm² to 9684 dyn/cm².

Foundation bearing capacities were estimated as follows:

Ultimate Bearing Capacity (Qult): Layer 1 ranges from 1784 to 3169 kPa, layer 2 from 1590 to 5725 kPa, and layer 3 from 12035 to 17060 kPa.

Allowable Bearing Capacity (Qa): Values increase with depth, from 595 to 1056 kPa in layer 1, 530 to 1909 kPa in layer 2, and 4012 to 5690 kPa in layer 3.

7. Discussion

The variation in seismic wave velocities and geotechnical parameters across the three identified layers provides valuable insights into the engineering characteristics of the subsurface materials in 6th October City. Layer 1, composed of sandy gravel, exhibits relatively low P- and S-wave velocities, indicating limited load-bearing capacity and potential settlement risks under heavy structures. The moderate N-values suggest that this layer may require ground improvement techniques before construction. Layer 2, consisting of coarse gravelly sand, shows improved mechanical properties, making it suitable for light to medium infrastructure. However, its heterogeneous nature may lead to differential settlement if not properly evaluated. Layer 3, characterized by high P- and S-wave velocities and N-values exceeding 400, demonstrates excellent mechanical behavior and is interpreted as compact clayey limestone. This layer represents the most competent foundation stratum, ideal for supporting large-scale and critical infrastructure such as high-rise buildings and bridges.

The observed increase in elastic moduli (rigidity, Young's, and bulk) with depth further supports the progressive enhancement in material stiffness and strength. Poisson's ratio values also show an upward trend, suggesting increased compressibility in deeper layers, which should be considered in dynamic loading conditions such as earthquakes. These findings align with previous studies conducted in similar geological settings, including Sadat City (Abd Elrahman et al., 1992) and Mosul Dam (Al-Juraisy and Al-Saigh, 2010), where higher shear wave velocities correlated with greater foundation stability.

The integration of seismic refraction and MASW methods proved effective in delineating subsurface stratigraphy and estimating key geotechnical parameters without invasive drilling. However, future work should include borehole verification and laboratory testing to refine these interpretations and enhance reliability for engineering design.

8. Conclusions

This study successfully applied seismic refraction and MASW techniques to assess subsurface conditions in 6th October City, Egypt. Three distinct geoseismic layers were identified based on variations in P- and S-wave velocities, elastic moduli, and geotechnical indices.

•Layer 1 (sandy gravel) is unsuitable for direct foundation support due to its low competence and requires treatment or deep foundations.

•Layer 2 (gravelly sand) offers moderate bearing capacity and is appropriate for light to medium structures.

•Layer 3 (clayey limestone) presents the highest mechanical strength and is recommended as the optimal foundation layer for heavy infrastructure.

The results indicate a clear correlation between seismic velocities and material competence, confirming the effectiveness of geophysical methods in preliminary site investigations. The allowable and ultimate bearing capacities increase significantly with depth, particularly in Layer 3, which exhibits Qa values exceeding 4000 kPa.

These findings provide essential guidance for civil engineers and planners in selecting suitable foundation depths and designing safe and economical infrastructure projects in the study area. Future research should incorporate direct borehole data and dynamic site response modeling to further validate these results.

9. Conflict of Interest

The authors declare that they have no conflict of interest.

10. Funding Statement

Research received no external funding.

11. References

Abd Elrahman, M.M. 1989. Evaluation of kinetic moduli of surface materials and their application to engineering geological maps in the Ma'Barrisabah area (Dhamar province), Northern Yemen. Egypt. J. Geol., 33(1-2), pp. 228-252.

Abd Elrahman, M., Setto, I., and Elwerr, 1991. Seismic refraction interpretations in the distinctive district of 6th October City. EGS. Proc. of the 9th Ann. Meet. 3, pp. 229-242.

Abd Elrahman, M., Setto, I., and Elwerr, 1992. Inferring mechanical properties of foundation materials in the 2nd industrial zone, Sadat City, from geophysical measurements. EGS. Proc. of the 10th Ann. Meet. 10, pp. 50-62.

Abd Elrahman, M.M. 1991. Assessment of rock material competence by seismic measurements with an emphasis on soil competence scales and their applications in some urban areas in Yemen. EGS. Proc. of the 9th Ann. Meet. 9, pp. 205-230.

Al-Juraisy B.A. and Al-Saigh, N.H., 2010, The Investigation of Subsurface Channels in the Western Part of Mosul Dam by Seismic Refraction, Iraqi National Journal of Earth Science (INJES), Volume 10, Issue 1, June 2010, Page 81-90, 10.33899/earth.2010.5563

Al-Nuaiemy A., Al-Juraisy, B., and Al-Mafrajim M., 2018, The Use of the Seismic Refraction Tomography Survey Method and the Multi-Channel Analysis Technique of Surface Waves in the Geotechnical Assessment of the Al-Amal Apartments Site in Kirkuk, Northern Iraq, Ali, Iraqi National Journal of Earth Science (INJES), Vol. 18, Issue 2, December 2018, pp. 89-104, http://10.33899/earth.2018.159260

Borcherdt, R.D., 1994. Estimates of site-dependent response spectra for design (methodology and justification). Earthquake spectra, 10(4), pp. 617-653.

Bowles, J.E., 1984. Physical and geotechnical properties of soils. New York, McGraw-Hill Book Company, 2nd Edition, 578 P.

Bowles, J.E., 1988. Foundation Analysis and Design, 4th Edition, McGraw-Hill Book Company, New York.

Coral, C., 1987. Geological map of Egypt. By Egypt. Gen. Pet. Corporation and CONOCO. Coral, Cairo, Scale 1:500000. NH 36 NW, Cairo sheet.

Cordier, J.P., 1985. Velocities in Refraction Seismology. Radial Publisher Company, Holland, 276 P.

Damane, M. 2019. An investigation into the volume change characteristics of loess-like soil in Mount Moorosi Village in Lesotho, Engineering and the Built Environment, Department of Civil Engineering. http://hdl.handle.net/11427/31497

David and Taylor Smith 1979. Applications of Vp and Vs in Lithology. Geophysics; Cambridge University Press, New York, 860 P.

Dutta, N.P 1984. Seismic refraction method to study the foundation rock of a dam. Geophysical Prospecting, 32, pp. 1103-1110.

Ghanem, F. K., Al Amoush, H., and Al-Tarazi, E. 2021. Geotechnical engineering evaluation of superficial deposits utilizing seismic methods at Al al-Bayt University, Jordan. The Iraqi Geological Journal, pp. 11–28.

Harden and Dranevich, 1972. Elastic Moduli Estimation for Civil Engineering; Cambridge University Press, pp. 12-29.

Buckingham, M.J., 2005. Compressional and shear wave properties of marine sediments: Comparisons between theory and data. The Journal of the Acoustical Society of America, 117(1), pp.137-152.

Hunter, J.A., Benjumea, B., Harris, J.B., Miller, R.D., Pullan, S.E., Burns, R.A., Good, R.L., 2002. Surface and downhole shear wave seismic methods for thick soil site investigations. Soil Dynamics and Earthquake Engineering 22, pp. 931–941. DOI: https://10.1016/S0267-7261(02)00117-3

Imai, T. and Yoshimura, M., 1975. The relation of mechanical properties of soils to P and S-wave velocities for soil ground in Japan, OYO Corp., Urawa Res. Inst. Paper RP-447.

Lukić Kristić, I., Szavits-Nossan, V., Miščević, P. 2017. Direct method for determination of shallow foundation settlements, GRAĐEVINAR, 69 (6), pp. 467-477. https://doi.org/10.14256/JCE.1926.2016.

Mohamed, A.M.E., 2003. Estimating earthquake ground motions in the Northwestern part of the Gulf of Suez. Egypt. Ph.D. Thesis, Fac. Sc., Ain Shams Uni. pp. 93–138.

Mohamed, A.M.E., 2009. Estimating the near-surface amplification factor to minimize earthquake damage: a case study in west Wadi Hagoul area, Gulf of Suez. Egypt. J. Geophys. Prospect.57, pp. 1073–1089. http://dx.doi.org/10.1111/j.13652478.2009.00796.x.

Mohamed, A.M.E., Deif, A., El-Hadidy, S., Sheriff, R.E. 1991. Encyclopedic dictionary of exploration geophysics, 3rd Edition. Society of Exploration Geophysicists.

Mohsain, A.F., and Al-Khalidy, A.A.L. 2022. Geotechnical Assessment of Dar Al Salam Complex in Hilla City, Babylon Using the Seismic Refraction. The Iraqi Geological Journal, pp. 95–101.

Sjogren, B., Ofsthus, A., and Sandberg, J. 1979. Seismic classification of rock mass qualities. Geophysical Prospecting, 27, pp. 409-422.

Stumpel, M., Kahler, S., Meissner, R., and Nikereit, B. 1984. The use of seismic shear waves and compressional waves for lithological problems of shallow sediments. Geophysical Prospecting, 32, pp. 662-675.

Iraqi National Journal of Earth Science, Vol. 26, No. 04, 2026 (244-256)

Iraqi National Journal of Earth Science

www.earth.uomosul.edu.iq

استخدام تقنيات سرعة موجة القص لتحديد التحديات الهندسية في مدينة السادس من أكتوبر، مصر

ضياء حامد [1]*

dzeinalabedein@kau.edu.sa

[1] قسم علوم الأرض، كلية العلوم، جامعة الأزهر، القاهرة، مصر.

* الباحث المراسل.

تاريخ الاستلام: 18 نيسان 2025 تاريخ المراجعة: 20 أيار 2025 تاريخ القبول: 19 حزيران 2025

تاريخ النشر الالكتروني: 01 تشرين الأول 2026

الملخص:

في مصر، باتت المسوحات الجيوفيزيائية أكثر أهمية، لا سيما بعد الأثر الكبير الذي خلفه زلزال أكتوبر 1992 على المنشآت في القاهرة الكبرى. تهدف الدراسات الهندسية للمواقع إلى تحديد عمق وتكوين الصخور الأساسية، وعمق المياه الجوفية، والتغيرات الجانبية في التركيب الصخري، وتحديد الصدوع أو الشقوق. ولتحقيق هذه الأهداف، أُجريت مسوحات انكسار زلزالي سطحية في منطقة مختارة داخل مدينة السادس من أكتوبر بمصر، لتقييم خصائص باطن الأرض قبل البدء بأعمال البناء. تمثلت الخطوة الأولى في تحديد البنية الجيولوجية الأساسية من خلال الحصول على خمسة عشر مقطعًا انكساريًا زلزاليًا فوق منطقة الدراسة. وكشف تحليل توزيع سرعة الموجة الأولية عن وجود ثلاث طبقات جيولوجية زلزالية منفصلة، تتميز بنطاقات سرعة تتراوح بين (685 إلى 835 م/ث)، و(680 إلى 1030 م/ث)، و(1340 إلى 1525 م/ث). تُظهر طبقات الرواسب سرعات موجات قص تتراوح بين 356 و440 م/ث، و360 و536 م/ث، و690 و790 م/ث على التوالي. تشير هذه النتائج إلى أن الطبقة الأولى تتميز بقيم سرعة منخفضة، مما يعكس تركيبًا رسوبيًا يتكون من حصى رملي. في المقابل، تتكون الطبقة الثانية من رمال حصوية خشنة، بينما تتكون الطبقة الثالثة من حجر جيري طيني. تم تحليل طبقات الرواسب باستخدام معادلة أساسية لاستخلاص الخصائص الجيوفيزيائية، والتي تشمل سرعة موجة القص، وكثافة الصخور، ومؤشرات المواد (بما في ذلك مؤشر المادة، ونسبة بواسون، وقيمة N، ونسبة الإجهاد). وفقًا لهذه البيانات، تتمتع طبقات الرواسب تحت سطح الأرض في هذه المنطقة بمستوى صلابة يتراوح بين المتوسط والعالي.

الكلمات المفتاحية:

الهندسة الجيوتقنية، نسبة بواسون، موجة القص

DOI: 10.33899/injes.v26i4.60961, ©Authors, 2026, College of Science, University of Mosul.

This is an open-access article under the CC BY 4.0 license (http://creativecommons.org/licenses/by/4.0/).

Iraqi National Journal of Earth Science, Vol. 26, No. 04, 2026 (257-262)

Iraqi National Journal of Earth Science

www.earth.uomosul.edu.iq

Measurement of Magnetic Intensity Using Three Different Sensor Levels and Three Vertical Gradient Determinations to Detect Subsurface Engineering Utilities.

Ahmad S. Al-Banna [1*], Hayder H. Majeed [2], Fitian R. Al- Rawi [1], Tariq Safa Aldin [1]

geobanna1955@yahoo.com haidargeo38@gmail.com drfitian@yahoo.com triqsaaldan@yahoo.com

[1] *Department of Geology, College of Science, University of Baghdad, Baghdad, Iraq.*
[2] *Directorate General of Education, Diyala, Ministry of Education.*
* *Correspondence author.*

Received: 31 July 2025 Received in revised form: 01 September 2025 Accepted: 16 November 2025
Available online: 01 October 2026

Abstract

Total Magnetic Intensity (TMI) is measured in southern Baghdad at a site located at the University of Baghdad. These measurements are used to investigate the best sensor levels and the suitable vertical gradients to detect subsurface engineering utilities. The measurement is achieved along three E-W parallel profiles. The length of each profile is 28 meters. The spacing distance between stations for the western half (0-14 meters) of the profile is two meters, while it is one meter for the eastern half (14-28 m). The magnetic measurements were carried out using three sensor levels, these are (2.44 m, 1.83 m, and 1.22 m, to determine the best height suitable for investigating shallow subsurface buried objects. Three vertical magnetic gradient values are determined for each station from the three-level magnetic measurements. This study concludes that the sensor height (1.22m) is better than the others in detecting the shallow sources. The three vertical magnetic gradient profiles coincide in detecting the subsurface sources. The vertical gradient results are better than the relatively high sensor-level measurements. The vertical gradient also seems not to be affected by the spacing distance between stations, as the total magnetic intensity measurements.

Keywords:

Magnetic, Vertical gradient, Sensor height, Engineering utilities, Baghdad.

DOI: 10.33899/injes.v26i4.60971, ©Authors, 2026, College of Science, University of Mosul.

This is an open-access article under the CC BY 4.0 license (http://creativecommons.org/licenses/by/4.0/).

==========

1. Introduction

Since the beginning of geophysical prospecting, the magnetic method has been applied. At first time, it was used in mining prospecting, especially in searching for Iron ores; then it was used in petroleum exploration (Nettleton, 1971). The theory of the magnetic method is described in many references (e.g., Grant and West, 1965; Kaufman et al., 2008; Hinze et al., 2013). The percentage of ferromagnetic minerals, mainly magnetite, within the rocks is the main effective factor in the magnetic method (Dobrin and Saviet, 1988). With the development of aeromagnetic survey at twentieth century, the magnetic method became widely used to

explore the basement rock depth, igneous intrusions, faults, shallow and deep geological features, including mineralization zones (Nettleton, 1971; Sharma, 2012; Hinze et al., 2013; Al-Banna and Al-Khishef, 2019; Al-Hadithi and Al-Banna, 2022; Abdelrady et al., 2023).

The magnetic method application in shallow surveys includes waste sites, underground storage tanks, drums, buried pipes, archaeology, and groundwater investigation (Breiner, 1973; Tyagi et al., 1983; Emerson et al., 1992; Marco et al., 2002; Burger et al., 2006; Schmidt, 2007;

Canbay et al., 2010; Morsy and Rashed, 2013; Moskowitz et al., 2015; Oni et al., 2020; Alao et al., 2024).

The shallow underground engineering utility includes pipelines, cables, wires, and subsurface concrete engineering utilities. The underground utilities investigation is important to detect the exact location before excavation for additional construction (Lanka et al., 2001). Resistivity, ground-penetrating radar, gravity, and magnetic methods were applied to detect

subsurface utilities (Al-Saady et al., 2022; Al-Mahemmdi et al., 2023).

This study attempts to assess the ability of the three determined vertical magnetic gradients to detect subsurface engineering utilities at a small site at the University of Baghdad. It also attempts to find out the best height of the magnetic sensor to explore shallow engineering targets.

2. Materials and methods

A. Location and description of the studied site

The study site is located on a pedestrian walkway in front of the Geology Department at the University of Baghdad (Jadiriyah). The coordinates of the base station are latitude (33° 16′ 16″ N) and longitude (44° 22′ 46″ E) (Fig. 1).

The studied site represents a long, horizontal, and flat concrete pedestrian walkway with a width of 4.3 meters. This concrete walkway covers alluvial sediments, which are part of the sediments of the Tigris River basin. The walkway trends in an east-west direction. Beneath the study site, there are many subsurface engineering utilities, including electrical cables, pipes, and a concrete irrigation canal, which is open to the surface outside the walkway (Fig. 2). The depth of the considered objects is within the upper 2.0 meters from the earth surface.

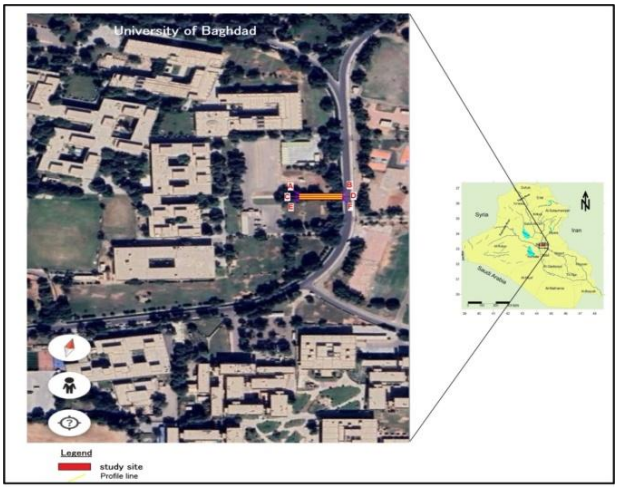


Fig .1: Location of the study site

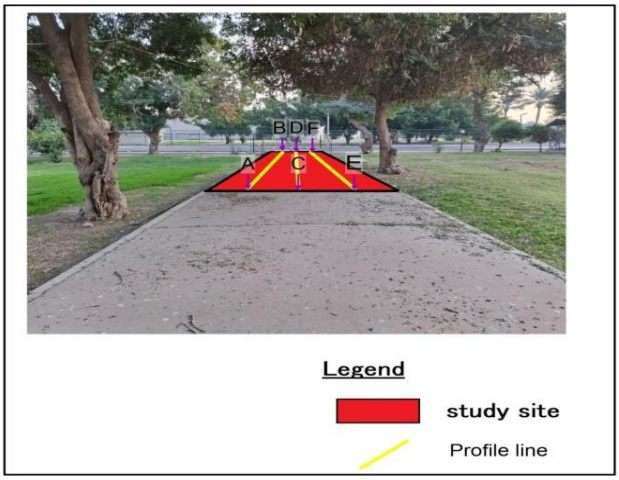


Fig. 2: Engineering utilities including electrical cables, pipes, and concrete irrigation canal under study area; the considered profiles are in yellow color.

B. Data acquisition

Three parallel profiles are established at the end of the pedestrian walkway, on its eastern side near the ring road in Baghdad University campus. The total magnetic intensity measurement is achieved using a portable proton magnetometer G-816 with an accuracy of 1 nT (Breiner, 1973) (Fig. 3). The length of each profile is 28 meters. CD profile passes through the center of the walkway, dividing it into northern and southern parts. Profile AB is one meter apart from the central profile, one meter toward the north. Profile EF is one meter from the central profile toward the south. Each profile includes twenty-two measurement stations. The spacing distance at the western side of the profiles (0-14 meters) is two meters, while at the eastern side (14- 28 meters), the profile spacing is one meter (Fig. 4). Station number eleven in profile CD (central profile) is considered as basestation.

The magnetic measurement is carried out by starting from the base station, then measuring many stations and reoccupying the base station again at an interval of 5 minutes. The magnetic measurements are achieved with three levels: 2.44 m, 1.83 m, and 1.22 meters for each station. The accuracy of measurement is determined using control stations, which is found to be ±7 nT.



Fig. 3: The proton magnetometer used in the study area

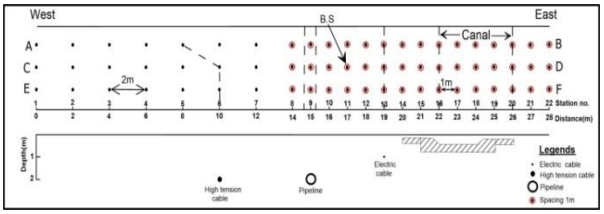


Fig. 4: Sketch of stations' locations in the study site and subsurface engineering utilities.

C. Corrections and magnetic anomaly determination

The correction used in this study is the diurnal correction only. This correction is determined using a drift curve depending on repeating measurements at the base station every 5 minutes. The maximum variation in the magnetic values at the base station in each loop survey did not exceed 25 nT.

The normal magnetic variation correction is neglected due to the short distance of 28 meters profile relative to the global magnetic variation. The elevation correction is also neglected because the variation in elevation between the lowest and highest stations did not exceed 0.10 meters.

After data correction, the magnetic anomaly is measured by subtracting the total magnetic intensity of the base station from the value of each station for all profiles with the three sensor heights. The vertical magnetic gradient is obtained by dividing the difference between magnetic values from every two levels by the vertical distance between sensor levels. The procedures can be simplified by the following equations:

Vertical Magnetic Gradient (VMG) = ΔMagnetic values/ Δ Sensor's level

So, we get three vertical gradients from the three sensor level differences:

VMG1 (nT/m) = Magnetic value (1.22)- Magnetic value (1.83)/ 0.61

VMG2 (nT/m) = Magnetic value (1.22)- Magnetic value (2.44)/1.22

VMG3 (nT/m) = Magnetic value (1.83)- Magnetic value (2.44)/ 0.61

3. Results and Discussion

The magnetic anomaly determined at the three levels (2.44m, 1.83m and 1.22 meters) of profile AB is shown in Figure (5), while the vertical magnetic gradients (VMG1, VMG2, and VMG3) of profile AB are presented in Figure (6). The same procedure is applied to the other profiles. The magnetic anomalies along profile CD for the three considered elevations and the vertical magnetic gradients (VMG1, VMG2, and VMG3) are presented in Figures (7 and 8), respectively. The final results of the magnetic anomalies and the vertical magnetic gradients (VMG1, VMG2, and VMG3) for the three sensor heights of profile EF are shown in Figs. 9 and 10, respectively.

Figs. 4, 6, and 8 show that the low sensor height level is the best level for detecting the shallow sources. At the same time, the vertical magnetic gradients between the three considered levels coincide mostly in locating the subsurface objects (Figs. 6, 8 and 10). The vertical magnetic gradient with a relatively high distance (1.22 meters) is less effective than the low distance (0.61 meters). The variations in spacing distance between the stations along the profiles show the same result in the vertical gradient measurement technique.

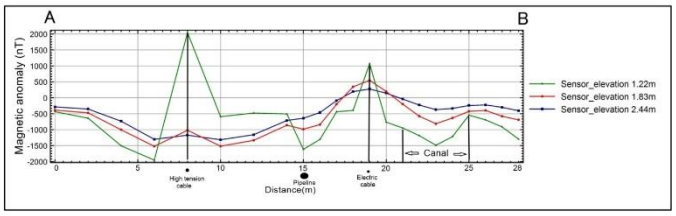


Fig.5: Magnetic profile (AB) using sensor heights (2.44 m, 1.83 m, and 1.22 m), and the detected subsurface sources in the study site

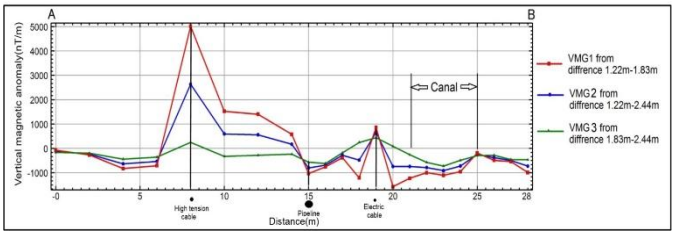


Fig. 6: Three vertical magnetic gradients along profile (AB), and subsurface sources in the study site

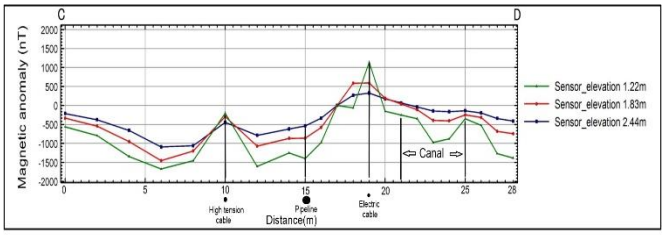


Fig. 7: Magnetic profile (CD) using sensor heights of 2.44 m, 1.83 m, and 1.22 m, and subsurface sources in the study site.

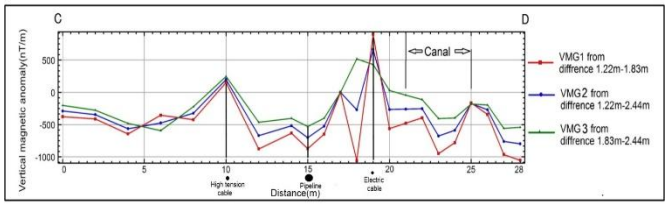


Fig.8: Three vertical magnetic gradients along profile (CD), and subsurface sources in the study site.

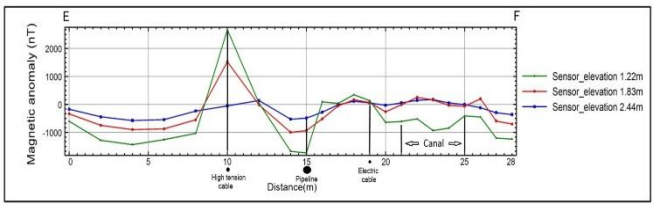


Fig. 9: Magnetic profile (EF) using sensor heights (2.44 m, 1.83 m, and 1.22 m), and the detected subsurface sources in the study site.

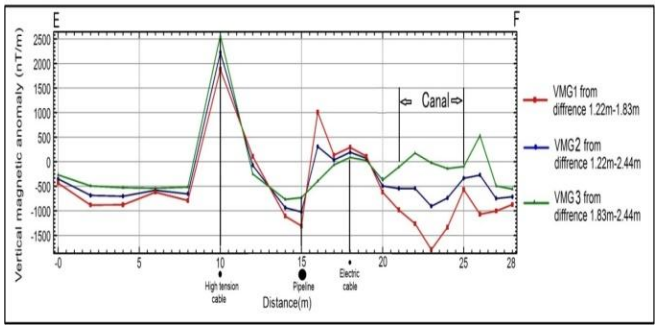


Fig. 10: Three vertical magnetic gradients along profile (EF), and subsurface sources in the study site.

4. Conclusions

The magnetic anomaly with three sensor heights along three parallel profiles is measured to detect shallow engineering sources in the study area. The vertical magnetic gradient is determined between the three considered sensor levels. It is concluded from the results of this study that the lowest sensor level is more suitable than the relatively high sensor levels in detecting shallow subsurface objects. The vertical gradient shows better results than the total magnetic intensity measurements. The determined vertical gradient between low sensor levels is better than at relatively high distances. The vertical gradient seems not to be affected by the spacing distance between measurement stations, as the total magnetic intensity measurements.

5. Acknowledgments

The authors are grateful to Dr. Jassim M. Thabit for his assistance in the magnetic field measurements.

6. Conflict of Interest

The authors declare that there are no conflicts of interest regarding the publication of this manuscript.

7. Funding Statement

Research received no external funding.

8. References

Abdelrady, M., Moneim M. A., Alarifi S. S., Abdelrady A., Othman A., Mohammed M. A. A. and Mohamed A. 2023. Geophysical investigation for the identification of subsurface features including mineralization zones, Journal of King Saud University-Science, 35: 1-11, DOI: org/10.1016/j.jksus.2023.102809.

Alao, J.O., Lawal, K.M., Dewu, B.B. and Raimi, J., 2024. The study of magnetic anomalies due to shallow underground targets and the environmental applications, Results in Earth Science, 2: 1-9. DOI: org/10.1016/j.rines.2024.100016.

Al-Banna, A. S. and Al-Khishef, Dh. S., 2019. Evaluation of the tectonic boundaries in Tikrit- Kirkuk area using potential data, north - central Iraq. Iraqi Journal of Science, 60 (3): 528-535. DOI:10.24996/IJS.2019.60.3.12.

Al-Hadithi, S.J. and Al-Banna, A.S. 2022. Using source parameter imaging technique to the aeromagnetic data to estimate the basement depth of Tharthar Lake area and surrounding area in central Iraq, Iraqi Geological Journal, 55(1F): 151-159. DOI: 10.46717/igj.55.1F.12Ms-2022-06-27.

Al-Saady, H. A., Karim, H. H., and Al-Menshed, F. H. 2022. Subsurface investigation of void using ground penetration radar in Basimayah Site southern Baghdad, central Iraq. Iraqi Geological Journal, 55(1D):35-46. DOI: https://10.46717/igj.55.1D.3Ms-2022-04-19.

Breiner, S., 1973. Application manual for portable magnetometers, GeoMetrics. Sunnyvale, California, 58 P.

Burger, H.R., Sheehen, A.F., and Jones, C.H. 2006. Exploration using magnetic method, in Introduction to Applied Geophysics, exploring the shallow subsurface, New York. W.W. Norton and Co., 389 P.

Canbay M.M., Aydin A. and Kurtulis C., 2010. Magnetic susceptibility and heavy- metal contamination in topsoil along the Izmil Gulf coastal area and IZAYTAS (Turkey), Journal of Applied Geophysics, 70:46-57. DOI: 10.1016/j.jappgeo.2009.11.002.

Dobrin M. B. and Saviet C. H., 1988. Introduction to geophysical prospecting, 4th Edition, McGraw-Hill, 867 P.

Emerson D.W., Reid J.E., Clark M.S., Hallet M.S.C. and Manning P.B., 1992. The geophysical responses of buried

drums- field tests in Weathered Hawkesbury Sandstone, Sydney Basin, NSW, Exploration Geophysics, 23: pp. 589-617.

Grant F.S. and West G.F., 1965. Interpretation theory in applied geophysics, McGraw- Hill Inc., 584 P.

Hinze W.J., Frese R.R. and Saad A.H., 2013, Gravity and magnetic exploration, principles, practices and applications, Cambridge University Press, 512 P.

Kaufman A.A., Kleinberg R.L. and Hansen R., 2008. Principles of the magnetic method in geophysics. Methods in Geochemistry and Geophysics 42, Elsevier Science, 1st Edition, 320 P.

Lanka M., Butler A., and Sterling R., 2001. Use of approximate reasoning technique for locating underground utilities. Tunneling and Underground Space Technology, ScienceDirect 16(1): 13-31. DOI: https://org/10.1016/S0886-7798 (01)00058-x.

Marco M., Cafarella L., Di Mauro D., and Zirizzotti A., 2002. Ground magnetometric survey and integrated geophysical methods for soil buried waste detection: A case study, Annals of Geophysics, 45(3/4): 563-573. DOI: https://10.4401/ag-3519.

Morsy M. and Rashed M., 2013. Integrated magnetic, gravity, and GPR Survey to locate the probable source of hydrocarbon contamination in Sharm El-Sheikh area, south Sinai, Egypt, Journal of Applied Geophysics, 88: 131-138. DOI: 10.1016/j.jappgeo.2012.11.003

Moskowitz B.M., Jackson M. and Chandler V., 2015. Geophysical properties of the near surface earth: Magnetic properties, in Schubert, G. Treatise on Geophysics, 2nd Edition: Elsevier, 11:139-174.

Nettleton, L.L., 1971. Elementary gravity and magnetics for geologists and seismologists, SEG, Monograph series. 132p.

Oni, A.G., Eniola, P.J., Olorunfemi M.O., Okunubi, M.O., and Osotuyi, G.A., 2020. The magnetic method as a tool in groundwater investigation in a basement complex terrain: Modomo Southwest Nigeria, as a case study, Applied Water Science, 10(8): 1-18. DOI: 10.1007/s13201-020-01279-z.

Schmidt A., 2007. Archaeology, magnetic methods. In D. Gubbins and E. Herrero-Bervera (eds.), Encyclopedia of Geomagnetism and Paleomagnetism: 23-31. Encyclopedia of Earth Science Series, Heidelberg, New York: Springer. DOI: https://10.007/978-1-4020-4423-6_9.

Sharma, P.V., 2012. Magnetic surveying, environmental and engineering geophysics, Cambridge, Cambridge University Press, pp. 65-111, https://10.1017/CBO9781139171168.

Tyagi S.A.E., Lord J., and Koerner R.M., 1983. Use of a proton precession magnetometer to detect buried drums in sandy soil, Journal of Hazardous Materials, 8: pp. 11-23.

Iraqi National Journal of Earth Science, Vol. 26, No. 04, 2026 (257-262)

Iraqi National Journal of Earth Science

www.earth.uomosul.edu.iq

قياس الشدة المغناطيسية باستخدام ثلاثة مستويات مختلفة للمتحسس وحساب ثلاثة مستويات للانحدار العمودي للكشف عن المرافق الهندسية تحت سطح الأرض.

أحمد شهاب البناء [1*]، حيدر حميد مجيد [2]، فتيان رشيد الراوي [1]، طارق صفاء الدين [1]

geobanna1955@yahoo.com haidargeo38@gmail.com drfitian@yahoo.com triqsaaldan@yahoo.com

[1] قسم علوم الأرض، كلية العلوم، جامعة بغداد، بغداد، العراق.

[2] المديرية العامة للتربية ديالى، وزارة التربية والتعليم.

** الباحث المراسل.*

تاريخ الاستلام: 31 تموز 2025 تاريخ المراجعة: 01 أيلول 2025 تاريخ القبول: 16 تشرين الثاني 2025

تاريخ النشر الالكتروني: 01 تشرين الأول 2026

الملخص

تم قياس شدة المغناطيسية الكلية (TMI) في جنوبي بغداد في موقع داخل جامعة بغداد. استخدمت هذه القياسات للتحقق من أفضل ارتفاع للمجس، ومسافات الانحدار العمودي المناسبة للكشف عن المرافق الهندسية تحت سطح الأرض. تم إجراء القياس على طول ثلاثة مقاطع متوازية من الشرق إلى الغرب. يبلغ طول كل مقطع 28 متراً. تبلغ المسافة الفاصلة بين محطات القياس في الجانب الغربي (0–14 متراً) مترين، بينما تبلغ متراً واحداً في الجانب الشرقي (14–28 متر). أجريت القياسات المغناطيسية باستخدام ثلاثة مستويات للمجس، وهي (2.44 م، 1.83 م، 1.22 م)، لحساب الارتفاع المناسب لكشف الأهداف المدفونة تحت سطح الأرض. تم حساب قيم الانحدار العمودي للمغناطيسية لكل محطة، من قياسات الارتفاعات الثلاثة. خلصت هذه الدراسة إلى أن ارتفاع المجس (1.22 م) هو الأفضل من غيره في اكتشاف المصادر الضحلة. تتطابق مقاطع الانحدار المغناطيسي العمودي الثلاثة في اكتشاف المصادر تحت السطحية. اظهر الانحدار العمودي نتيجة أفضل من قياسات مستويات المجس المرتفعة نسبيًا. ويبدو أيضًا أن مسوحات الانحدار العمودي لا تتأثر بمسافة التباعد بين المحطات مثل ما هي في قياسات الشدة المغناطيسية الكلية.

الكلمات المفتاحية:

المغناطيسية، الانحدار العمودي، ارتفاع المجس، المرافق الهندسية، بغداد.

DOI: 10.33899/injes.v26i4.60971, ©Authors, 2026, College of Science, University of Mosul.

This is an open-access article under the CC BY 4.0 license (http://creativecommons.org/licenses/by/4.0/).

==========

Iraqi National Journal of Earth Science, Vol. 26, No. 04, 2026 (263-282)

Iraqi National Journal of Earth Science

www.earth.uomosul.edu.iq

Groundwater Overdraft and Climate-Driven Land Subsidence in the Sulaimani-Sharazoor Basin, Iraq: Insights from InSAR Techniques

Shahrayar Tawfeeq San [1*], **Dara Hama Amin** [2]

Shahrayar.san3017@gmail.com dara.amin@univsul.edu.iq

[1] *Directorate of Irrigation, Ministry of Agriculture and Water Resources, Kurdistan Region, Sulaimanyah, Iraq.*

[2] *Department of Earth Science and Petroleum, College of Science, University of Sulaimani, Sulaimanyah, Iraq.*

** Correspondence author.*

Received: 14 August 2025 Received in revised form: 13 September 2025 Accepted: 12 October 2025

Available online: 01 October 2026

Abstract

The lack of extensive quantitative monitoring hinders the assessment of global groundwater depletion and its impacts. This study integrates satellite data to evaluate surface subsidence in the central part of the Sulaimani-Sharazoor Basin from 2017 to 2024, linking groundwater extraction, climatic factors, and land use changes to surface displacement. Sentinel-1 SAR data, comprising 91 pairs of single-look complex (SLC) images, were processed using the European Space Agency Sentinel Application Platform (ESA SNAP) toolbox and Differential Interferometric Synthetic Aperture Radar (DInSAR) to quantify subsidence. Results reveal significant subsidence in unconsolidated aquifers, driven by groundwater extraction, drought, and extensive well drilling. Vertical displacement might have peaked at -27 cm in 2021 and -26 cm in 2017, coinciding with periods of decreased annual precipitation and limited surface drainage. Surface displacements may have decreased by -6 cm in 2018 and -3 cm in 2019, respectively, indicating heightened rainfall and recharge rates. Urban areas experienced infrastructure damage, while agricultural areas and water bodies contributed to irregular displacement patterns. The study highlights groundwater extraction as a major driver of subsidence, exacerbated by climatic variability and land use changes. The statistical examination of the variable data revealed that all essential parameters remained within acceptable bounds, thereby bolstering the study's validity. These findings underscore the need for sustainable groundwater management and enhanced monitoring to mitigate subsidence risks in the area and similar regions.

Keywords:

Groundwater extraction, Drought, Surface displacement, Well-based validation, Semi-arid region.

DOI: 10.33899/injes.v26i4.60975, ©Authors, 2026, College of Science, University of Mosul.

This is an open-access article under the CC BY 4.0 license (http://creativecommons.org/licenses/by/4.0/)

1. Introduction

Groundwater is a vital component of global water resources and serves as the primary source of freshwater worldwide. It plays a critical role in sustaining ecological systems and ensuring food security, particularly in arid and semi-arid regions (Arriana Brand et al., 2011; Aeschbach-Hertig and Gleeson, 2012; Famiglietti, 2014; Majumdar et al., 2020; Mohammed et al., 2022). Approximately 50% of the global population relies on groundwater for drinking water, while 43% depends on it for agricultural irrigation (UNWWAP, 2015). However, the over-extraction of groundwater has led to significant environmental challenges, including the irreversible compaction of subsurface sediments, which accounts for nearly 60% of land subsidence globally (National Research Council, 1991). In regions heavily dependent on groundwater for irrigation, extraction rates often exceed natural replenishment rates, resulting in substantial declines in water storage and groundwater levels. This overexploitation has led to widespread groundwater degradation, with severe consequences for ecosystems and human activities. For instance, Poland (1984) identified 17 major subsidence areas in the United States caused by groundwater depletion, with subsidence rates ranging from 0.3 to 9.0 meters per year.

Differential subsidence and the flexure of surface sediments, often caused by groundwater extraction, can lead to surface deformation. This deformation poses significant risks to infrastructure, including buildings, pipelines, roads, and other subsurface structures, due to the development of tensional or compressional stresses (Vasco, 2019; Land Subsidence Task Committee, 2022). Remote sensing has emerged as a powerful tool for detecting, mapping, and monitoring Earth's resources and natural hazards across spatial and temporal scales (Dubovyk, 2017).

The integration of remote sensing with Geographic Information Systems (GIS) enables the creation of extensive databases for research, often without the need for field verification (Khan et al., 2020; Alkaradaghi et al., 2022). Among these techniques, Interferometric Synthetic Aperture Radar (InSAR) has become a key methodology for measuring land-surface deformation with high spatial precision.

The European Space Agency's (ESA) Copernicus program provides continuous and open access to Synthetic Aperture Radar (SAR) data from the Sentinel-1 mission, which consists of two identical satellites (Torres et al., 2017). Recent Sentinel-1 and ESA SNAP-based studies in neighboring regions highlight the severity of land subsidence linked to groundwater depletion, providing critical context for the current work. In Turkey, Yeşilmaden et al. (2021) demonstrated groundwater over-extraction in the Konya Basin using Sentinel-1 data, revealing subsidence rates exceeding 50 mm/year in agricultural zones. Similarly, Ghorbani et al. (2022) quantified subsidence in Iran's Ardabil Plain, correlating deformation hotspots with overexploited aquifers, while Elhag et al. (2025) identified urban infrastructure risks from InSAR-derived displacement patterns in Makkah City, Saudi Arabia. These studies underscore the regional applicability of InSAR for groundwater management but also reveal a critical gap. No comparable work exists for Iraq, despite shared hydrogeological stressors (e.g., aridification, unregulated drilling, and groundwater overdraft). Our study fills this void as the first to assess groundwater-induced subsidence in Iraq using Sentinel-1 and SNAP, advancing the theoretical framework of Terzaghi (1925) and Ohenhen and Shirzaei (2022), who attributed irreversible compaction to clay-layer susceptibility. The Kurdistan Region of Iraq faces a pressing challenge of increasing groundwater demand, driven by rapid population growth and urban expansion (Hamamin, 2024; Khalil et.al., 2024). This study focuses on the impact of surface displacement in rural and urban areas within the Sulaimani-Sharazoor Basin from 2017 to 2024.

The SSB, designated as a hydrogeological hotspot, provides an ideal setting for investigating groundwater dynamics and their environmental interactions. Notably, the basin is dominated by intergranular unconfined aquifers, which provide an optimal medium for conducting studies on groundwater-related surface deformation. Current assessment methods here rely on outdated techniques and lack modern geospatial tools, a critical limitation in a region with weak institutional water management frameworks. Therefore, this study aims to be the first to assess groundwater-induced subsidence in Iraq using Sentinel-1 data and SNAP software. The primary objectives are to: (1) quantify the rate and spatial extent of land surface displacement in the SSB from 2017 to 2024; (2) establish a novel correlation between InSAR-derived displacements, hydrologic data (surface runoff, spring records), and field surveys to validate the impact of compounded climatic and human factors on groundwater depletion and associated infrastructure damage; and (3) provide empirical evidence to support policy reform and prioritize regulatory interventions, offering a transferable monitoring model for data-scarce regions.

2. Location of study area

The Sharazoor Sub-Basin (SSB)is the central part of the Sulaimani-Sharazoor Basin and encompasses an area of 638.8 km² in the southeastern part of the Sulaymaniyah Governorate, Kurdistan Region, Iraq. It is delineated by geographical coordinates ranging from 35°12′54″ N to 35°28′29″ N in latitude and from 45°29′0.4″ E to 45°50′16″ E in longitude. The region's altitudes vary from 471 to 1403 meters above mean sea level. The basin's principal urban centers comprise Arbat, Zarain, and Halabjae-taza, in addition to villages and camps such as Kani Panka, Greza, and Barikae-kon. The SSB

encompasses Darbandikhan Lake to the east and southeast, while the Baranan hills are situated to the south and southwest, with Arbat marking its western boundary (Fig.1).

The study area is considered one of Iraq's most agriculturally and industrially prosperous areas, with a population of around 180,000, comprising 110,000 urban inhabitants and 30,000 rural inhabitants. The demographic divide is characterized by densely populated urban regions with sophisticated infrastructure, in contrast to rural communities dependent on subsistence agriculture and conventional water sources (Osman, 2021).

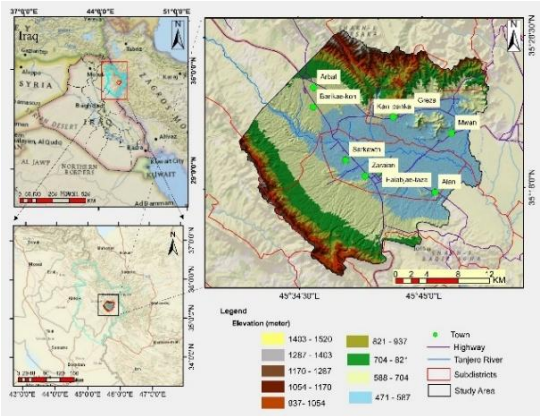


Fig. 1: Location map of the study area (Google Earth, 2022).

3. Tectonic and Geological settings

The Arabian Plate, particularly Iraq, characterized by its three primary tectonic zones, was significantly impacted by the Nabta Orogeny (680–640 million years ago) (Stern and Johnson, 2010; Jassim and Goff, 2006). The Arabian and Eurasian tectonic plates merge in Kurdistan. Collisions during the Laramide orogeny resulted in the formation of SSB tectonics. The upper folded zone features dextral strike-slip faults in the vicinity of Halabja-Said Sadiq. The High Folded Zone (HFZ) features steep gorges and carbonate fold structures that originated during the Late Cenozoic Zagros orogeny (Sissakian et al., 2014). The uplifts of the Cretaceous, Paleocene, and Oligocene periods formed Eocene molasse basins (Jassim and Goff, 2006), whilst the southwest anticlines feature significant thrust faults. The limestone-rich Baranan Mountain escarpment delineates the southern boundary of the research area (Numan and Al-Azzawi, 1993). Numerous stratigraphic units are observable and truncated in the study area. The oldest rocks, the Valanginian–Turonian Balambo Formation, are visible at the crests of anticlines, whilst the younger units, the Kometan and Shiranish formations, are found in the limbs and troughs of synclines. Central to the word Derbendikhan Lake are the Quaternary deposits. Quaternary sediments exhibit a thickness of 5–150 meters and consist of clay, silt, sand, and gravel. Erosion transported sediments and particles of diverse sizes around higher mountains to occupy depressions and valleys. Rock fragments are transported by seasonal stream floods subsequent to significant rainfall (Ali, 2007). The substantial Upper Cretaceous–Paleogene flysch sequence of the early Zagros Foreland Basin, known as the Tanjero Formation, is situated under the Quaternary deposits in the research region (Sharbazheri and Muhammed, 2009). Fig. 2 illustrates this. The Oligocene Kolosh Formation comprises marlstone. Slippage on Kolosh marlstone leads to Sinjar carbonate outcrops, and the southern area is marked by the Gercus and Pila Spi formations and the Baranan Mountain anticline(Karim and Ali, 2004).

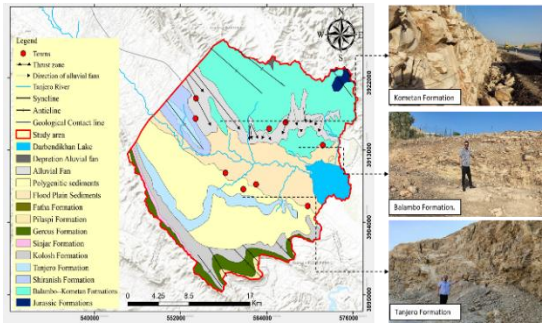


Fig. 2: Geological map of the study area (modified from Sissakian and Fouad, 2015).

4. Hydrology and Hydrogeological setting

The SSB is acknowledged as an essential hydrological plain distinguished by intricate terrain, featuring steep gorges and narrow valleys (Sissakian, 2014). Precipitation in SSB predominantly occurs from October to May, averaging 650–700 mm per year, while evapotranspiration measures 690 mm. Primary water sources comprise direct precipitation and the Tanjero River, which feeds into the Darbandikhan Reservoir. Hydrogeologically, multiple formations contribute to groundwater snowmelt, and three principal tributaries are notable resources,

including the karstic Sinjar Formation and the high-yield karstic fissure aquifer of the Balambo and Kometan formations. The Shiranish Formation acts as an aquiclude for deeper aquifers, whereas the Tanjero Formation comprises layers that establish semi-confined conditions. Groundwater in the SSB is utilized for both domestic and irrigation purposes via a network of wells. Pumping tests performed in the sub-basin reveal aquifer transmissivity values between 5 and 409 m^2/day, hydraulic conductivity ranging from 0.2 to 4.9 m/day, well discharge rates from 52 to 1,642 m^3/day, and static water levels at depths of 3 to 59 meters beneath the ground surface. Unconfined aquifers are the predominant type in the region (Ali, 2007; Stevanovic and Iurkiewicz, 2004; Al-Basrawi and Al-Jiburi, 2014; Hamamin and Nadiri, 2018). Groundwater extractions display notable spatial variability, with discharge rates categorized into three classifications utilizing GIS natural breaks (Fig. 3).

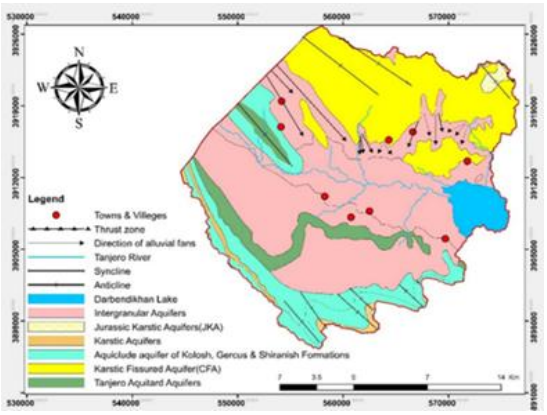


Fig. 3: Existence of aquifers within the SSB.

The groundwater output from 358 wells was categorized into five classifications based on groundwater withdrawals, highlighting significant geographical disparities in supply throughout the SSB utilizing GIS natural breaks (Fig. 3). The discharge rates vary widely, with elevated values (70-298 l/sec) mainly found along mainstream channels, indicating strong groundwater-surface water interactions. Intermediate rates (23–69 l/sec) form transitional buffers around high-discharge areas, while the lowest rates (<23 l/sec) are observed farther from primary streams, particularly affecting the Tanjero and Shiranish formations and indicating diminished aquifer recharge.

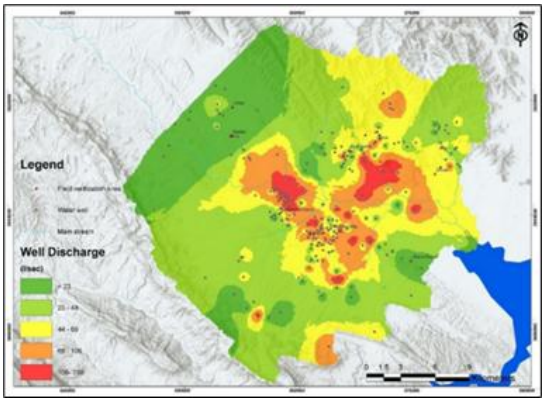


Fig.4: Spatial distribution of average well discharge (liter\sec). Data sourced from well profiles provided by the Sulaimani Groundwater Directorate (2025).

5. Methodology

A. DInSAR

This study integrates six primary datasets to analyze surface displacement and hydrological dynamics in the SSB, which include:

1. ESA Data and InSAR processing parameters for Sentinel-1 in the SSB.
2. DINSAR techniques face three inherent constraints.
3. Field validation protocols. The European Space Agency (ESA) Copernicus program provides open access to Synthetic Aperture Radar (SAR) data from the Sentinel-1 mission, which operates in exclusive instrument acquisition modes: https://browser.dataspace.copernicus.eu/.

The mission includes two identical satellites. This study uses Sentinel-1 C-band data from the S1A satellite platform, available since 2014, with a descending orbit repeating every 12 days. It employs the Interferometric Wide (IW) mode, yielding dual-polarization data processed through the ESA SNAP 9.0 toolbox to measure land displacement from 2017 to 2024 using 232 Level-1 SLC images, each with a spatial resolution of 32 m. The Terrain Observation and Progressive Scan (TOPS) technique was incorporated to mitigate noise and scalloping effects (De Zan and Guarnieri, 2006) (Fig. 5). Image pairs were selected based on three criteria: (1) temporal baseline (12 days) to minimize decorrelation, (2) perpendicular baseline (76-150 m) to reduce

geometric distortions, and (3) seasonal matching (dry-to-dry/wet-to-wet periods) to isolate groundwater-induced deformation from precipitation effects. The co-registration of SAR images was followed by the generation of interferograms, which incorporated flat-earth phase (5 degrees with over 500 estimation points), topographic influences utilizing the SRTM DEM, atmospheric conditions, and deformation signals. The Goldstein phase filter (α = 0.64-128, window size 32×32 pixels) was employed to enhance phase quality; however, its efficacy was constrained in low-coherence regions (threshold $\gamma > 0.2$). Phase unwrapping addressed elevation ambiguities by transforming wrapped phases into absolute displacements, subsequently converting these into line-of-sight surface deformation (in meters) via the Phase to Displacement operator. The analysis omitted 50 of 236 Sentinel-1 acquisitions, representing 21%, due to persistent incoherence ($\gamma < 0.3$), primarily during peak vegetation growth (May-September 2020-2022) and significant precipitation events (November 2019, March 2021). The areas of Barikae-kon, Halabjae-taza, Zarayan, and Arbat towns experienced a loss exceeding 40% of their data; however, the winter months (December-February) maintained over 85% of usable coverage. DInSAR techniques are subject to three intrinsic limitations: (1) atmospheric delays result in a vertical uncertainty of ±1.1 cm, especially during humid summer months; (2) alterations in

vegetation within irrigated croplands lead to seasonal coherence loss ($\Delta\gamma > 0.3$ between planting and harvest cycles), requiring InSAR augmentation; and (3) pronounced topography (>15° slopes) at basin peripheries causes layover distortions, impacting certain image footprints. While short temporal baselines (<12 days) diminished phase unwrapping inaccuracies, the 32m pixel resolution constrained the identification of small-scale features.

To address these factors, we employed multi-track validation (descending orbits) and eliminated pixels with low confidence (coherence <0.3 or atmospheric SNR <2). In order to assure accurate results, displacement values were obtained from the nearest high-coherence pixels ($\gamma > 0.4$) within a 10-meter radius of each well's GPS-verified coordinates, considering Sentinel-1's intrinsic resolution constraints (~5 × 20 m). This methodology adheres to recognized groundwater-InSAR research (Chaussard et al., 2014) and incorporates geolocation uncertainties intrinsic to SAR geometry. For wells containing multiple valid pixels within the buffer zone, we utilized averaged displacements, while omitting other wells affected by nearby structures that induced layover or shadow effects.

The geocoding utilized a DEM with a resolution of 12.5m to correct geometric distortions, with the final outputs exported as KMZ files for visualization in Google Earth (Braun and Veci, 2020). Spatial analysis was performed in ArcMap 10.8, incorporating geological, hydrological, and land-use maps alongside DEM-derived raster computations (Mogaji and Lim, 2017) (Fig. 5).

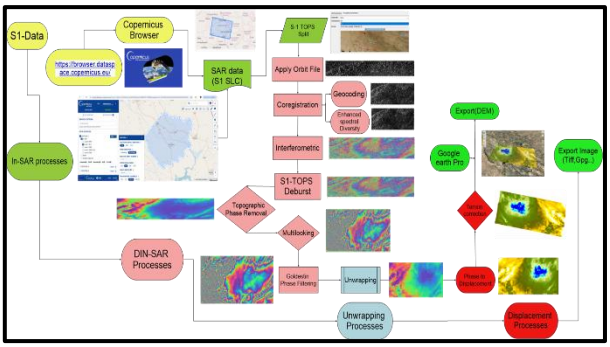


Fig. 5: Workflow for dataspace in Copernicus web side, InSAR images from Sentinel-1, DInSAR processing, displacement processing and export image displacement, using the ESA SNAP toolbox.

Table 1: Sentinel-1A SAR data specifications used in the study.

Parameter	Specification
Satellite platform	Sentinel-1A
Processing level	Level-1 Single Look Complex (SLC)
Acquisition mode	Interferometric Wide Swath (IW)
Orbit direction	Descending
Relative orbit no.	1–175
Repeat cycle	12 days
Polarization	VV, VH (dual-pol)
Swath	IW1
Bursts per image	5–7
Spatial resolution	32 m (range) × 32 m (azimuth)
Temporal coverage	March 2017 – December 2024
Total acquisitions downloaded	232 SLC images
Distorted SLC	50
SLC Used	182 images SLC
DInSAR	91 images
Processing tool	ESA SNAP 9.0

B. Hydrological data integration

1. Thickness of Recent Deposit (RD)

A map illustrating the thickness of recent deposits (RD) was produced utilising GIS software, integrating data from more than 128 wells and monitoring boreholes. The alluvial

deposits display a thickness variation of 0 to 140 meters, with maximum thickness recorded in the plain region, especially within the central depression and the Tanjero stream corridor, where depths attain 100 meters. The thickness progressively escalates towards the peripheries of Darbandikhan Lake, varying from 45 to 140 meters, whereas the northwestern and southern

areas are distinguished by superficial deposits with thicknesses between 0 and 50 meters (Fig. 6). The variations in thickness are affected by local geological and topographical factors, such as sediment sources from erosion, tectonic activity, and climatic changes (Syvitski, 2003).

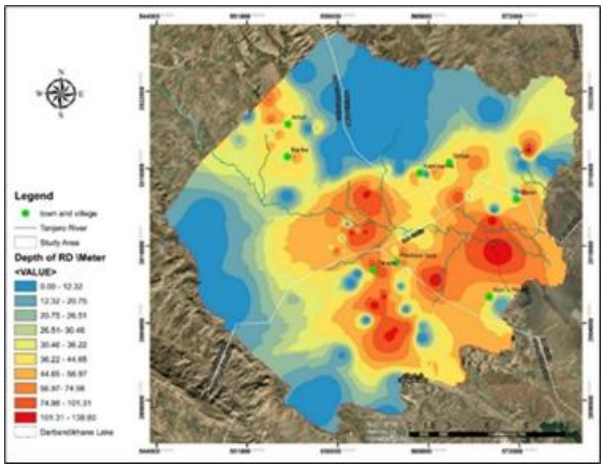


Fig. 6: Isopach map of the depth distribution of RS.

2. Monitoring well data

Piezometric data are crucial for the preparation and analysis of maps depicting variations in groundwater levels (Rafiei et al., 2022). This study utilized data from nearly 100 production wells, along with monthly groundwater level time-series data from five monitoring wells in the unconfined aquifer of the SSB. The monitoring well data, spanning from 2017 to 2024, were collected and managed by the Groundwater Directorate of Sulaymaniyah.

The historical groundwater level data were initially categorized by year, and trends in water level fluctuations for each well were examined. The average fluctuations in groundwater levels throughout the study area were assessed.

The Inverse Distance Weighting (IDW) interpolation method was utilized to interpolate groundwater level data and produce flow net maps (Fig. 7). The groundwater map demonstrates flow dynamics and potential within the study area, revealing pronounced hydraulic gradients particularly near Gazetteer Village and the Arbat district. Groundwater predominantly flows from elevated regions, such as Baranan Dagh mountain, to lower areas including Zarayan town, Mwan village, and Halabjae-taza district, affected by human activities near wells. Primary recharge sources encompass rivers, springs, and lakes, which maintain groundwater levels in locations such as the Tanjero stream and Darbandikhan lake, whereas areas like Greza and Kharaba villages demonstrate diminished potential and increased deformation risks.

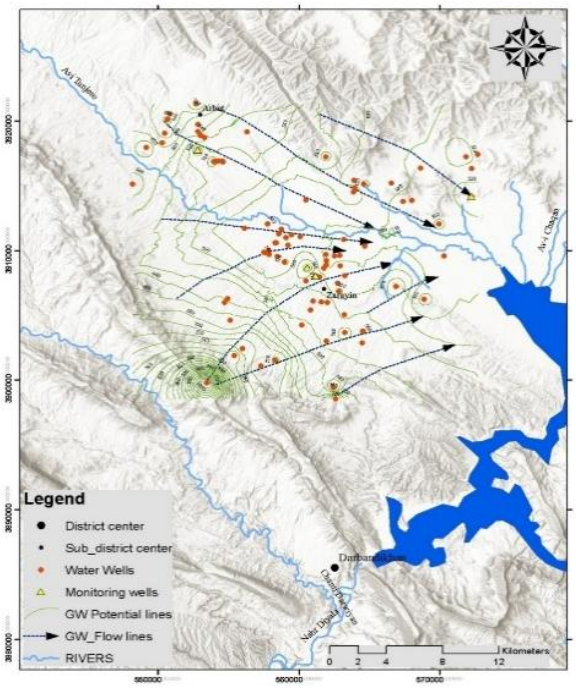


Fig.7: Spatial distribution of groundwater levels and flow directions.

3. Surface water discharge measurements

The discharge data for the Tanjero River and prominent springs within the SSB were acquired from the Department of Watershed Management,

Irrigation Directorate of Sulaimani (IDS, 2025). The surface runoff data derived from karst springs spanning the years 2017 to 2024 offer valuable insights into the characteristics of aquifers and the unique attributes of karst rock-fissure massifs (Table2). The analysis of annual hydrograph curves and methodical evaluations of the flow discharge from Kanipanka springs serve as essential instruments for comprehending water levels and groundwater depletion from 2017 to 2024. The dataset comprises discharge measurements in m³/sec for the Tanjero River and the Kanipanka springs (Upper Qalijo Channel, Lower Qalijo Channel, and Mwan stream) spanning from 2017 to 2024. The measurements are encapsulated in Table 2.

Table 2: Annual average inflow rate of Tanjero stream and Kanipanka springs from 2017-2024 (as acquired from the IDS, 2025).

Year	Tanjero stream (m³/sec)	Kani Panka (m³/sec)
2017	13.1	0.45
2018	25.1	0.6
2019	55.2	1.9
2020	9.5	0.65
2021	7.3	0.1
2022	6.1	0.15
2023	9.2	0.35
2024	24.9	0.55
Avg.	18.8	0.59

According to IDS (2025), the surface runoff data derived from karst springs spanning the years 2017 to 2024 offer valuable insights into the characteristics of aquifers and the unique attributes of karst rock-fissure massifs (Table4.2). The analysis of annual hydrograph curves and methodical evaluations of the flow discharge from Kanipanka springs serve as essential instruments for comprehending water levels and groundwater depletion from 2017 to 2024 (Fig. 8).

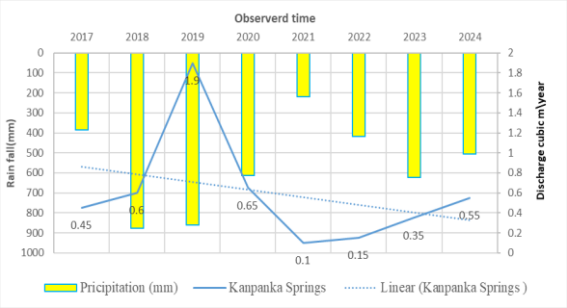


Fig. 8: The comparison between total rainfall (mm) and annual discharge of the Kanipanka springs (Kanipanka channels, Qalinjo and Mawan). (IDS, 2025).

6. Results

This study investigates the interaction between water-bearing units and evaluates land subsidence in the SSB using processed radar imagery. Additionally, monitoring well data were analyzed to assess groundwater level changes, and the relationship between these changes, surface runoff, and land subsidence was examined.

6.1. InSAR Verification

A reduction in groundwater levels markedly affects the effective stress in aquifers, resulting in consolidation, compaction, and subsequent land subsidence, as outlined by Valizadeh et al. (2005). Terzaghi (1925) elucidates that diminished pore-fluid pressure resulting from decreased groundwater levels leads to the compaction of the aquifer framework, whereas elevated pressures bolster its structural integrity, facilitating elastic rebound. Seasonal variations in groundwater generally produce slight, reversible deformations, considered normal within aquifer systems, as noted by Phillips and Galloway (2008). A detailed spatial analysis reveals a distinct hydro-mechanical relationship within the study area: steep groundwater potential gradients between 650 and 1000 m are associated with notable subsidence zones in regions like Arbat and Gazeteer Village, highlighting that considerable groundwater extraction intensifies land subsidence (Fig. 7). The study examines groundwater level (GWL) fluctuations to improve model accuracy and understanding of local aquifer dynamics. Piezometric data from 100 production wells and four monitoring wells in the unconfined aquifer are used to compare model predictions with local trends and remote sensing data. GWL data from 2017 to 2024 show short-term and long-term changes. Data collection issues, especially the COVID-19 pandemic, affected measurement consistency. The GWL was unstable from 2017 to 2020, but it improved in 2019. The dropping significantly since 2021, indicating groundwater overextraction. Improvements from 2023 to 2024 may indicate management or precipitation changes affecting aquifer replenishment (Fig. 9).

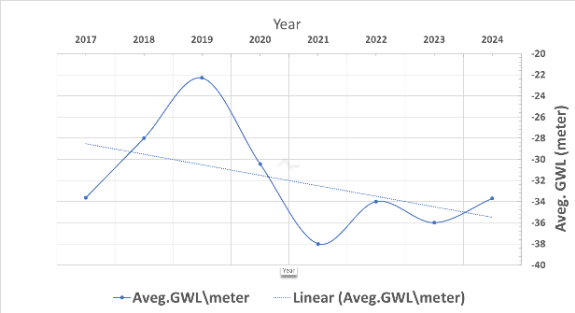


Fig. 9: Annual groundwater level trend in the SSB (2017-2024).

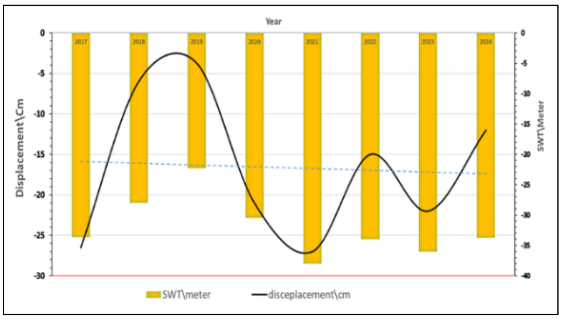


Fig. 10: The correlation between SWL and surface displacement.

The correlation between the groundwater level curve and deformation patterns suggests that flow disruptions near densely clustered wells, particularly around Zaraian, Barikae-kon, and Nasir Camp, align with subsidence hotspots, thereby reinforcing this hydro-mechanical connection. The slight shift of -3.7 cm during 2018-2019 indicates diminished groundwater extraction, recovery of pore pressure, and heightened annual precipitation relative to the norm. During the drought period and extensive well drilling and extraction from 2020 to 2021, which continued into 2024, the SWL reached its maximum depletion, accompanied by significant surface displacement in certain areas of the study (Fig.10).

The hydrogeological structure of unconfined aquifers demonstrates that declining water tables reduce pore pressure, leading to compaction. The isopach map visually corroborates this trend (Fig. 6; Fig. 4), demonstrating more pronounced water-level declines in unconfined aquifers compared to confined systems. Moreover, the basin's stratified aquifers demonstrate differing levels of susceptibility, especially the Shiranish and Tanjero formations. The marlstone and marly limestone, varying in thickness from 20 to 35 meters across both formations, may constitute 68% of the overall compaction resulting from delayed drainage. Karim and Surdashy (2006) assert that the Tanjero Formation comprises a significant sequence of bluish to white marl, which closely resembles the lithology of the Shiranish Formation in the area of interest. The karstified regions of the Balambo limestone exhibit a swift reaction of the water table with negligible compaction, leading to a differential subsidence of 0.5-1.2 cm annually along lithologic boundaries.

The correlation between precipitation, aquifer dynamics, and land subsidence becomes more evident during droughts, particularly in years characterized by low precipitation, such as 2016-2017 and 2020-2021(Fig.11).

The recorded displacement of -26 cm in 2020-2021 corresponds with the year's insufficient rainfall of only 220 mm, signifying aquifer overexploitation and the compaction of unconsolidated clays and silts, a phenomenon corroborated by Galloway et al. (1999). In contrast, periods of increased precipitation, specifically 2017-2018 and 2018-2019, led to diminished subsidence levels owing to improved groundwater recharge, temporarily stabilizing the unsaturated aquifer system in the SSB. The minimal displacement of -3.7 cm documented between 2018 and 2019 illustrates diminished groundwater extraction and an increase in pore pressure recovery. These findings are comparable to observations in other regions, such as California's San Joaquin Valley, where extended drought conditions prompted heightened groundwater extraction and considerable subsidence, as recorded by Smith et al. (2017). The data obtained from the SSB supports this correlation, indicating significant subsidence during periods of low precipitation, as demonstrated by the -0.27 m displacement recorded in 2020-2021 with merely 200 mm of rainfall.

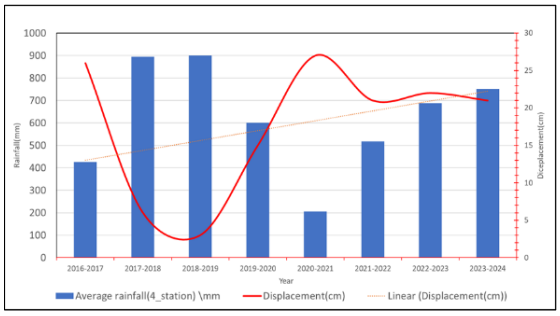


Fig. 11: The relationship between annual precipitation and surface movement.

6.2 Land subsidence and surface water discharge

This study investigates the influence of surface water resources on groundwater recharge and their resultant effects on subsurface compaction and land subsidence, specifically focusing on the Tanjero River and Kani Panka springs from 2017 to 2024. The analysis reveals a substantial correlation between surface water discharge and land subsidence, demonstrating that enhanced surface water availability can rejuvenate unconfined aquifers and alleviate subsidence (Fig.12). Data reveal that the total inflow from the Tanjero River rose from 13.1 m³/sec in 2017 to 24.9 m³/sec by 2024. Simultaneously, the discharge from Kani Panka Spring increased from 0.45 m³/sec to 0.55 m³/sec. These alterations corresponded with differing degrees of surface displacement throughout the examined years. In 2018, a significant increase in Tanjero River discharge to 25.1 m³/sec was associated with a decrease in subsidence to -0.06 m. A peak discharge of 55.2 m³/sec in 2019 led to negligible subsidence of -0.037 m, indicating that substantial surface water influx can beneficially affect groundwater levels.

Since 2020, there have been variations in discharge rates and surface displacement. In 2020, a decrease in inflow to 9.5 m³/sec caused subsidence of -0.21 m, and in 2021, additional reductions in discharge resulted in a notable subsidence of -0.27 m. The inverse relationships highlight the aquifer system's sensitivity to changes in surface water availability.

In 2024, the IDS data indicated a significant rise in total surface water availability. The findings suggest that increasing surface water discharge can effectively stabilize groundwater systems, mitigating subsidence by enhancing aquifer replenishment. Conversely, reduced discharge rates lead to intensified subsidence resulting from decreased groundwater replenishment and increased subsurface compaction.

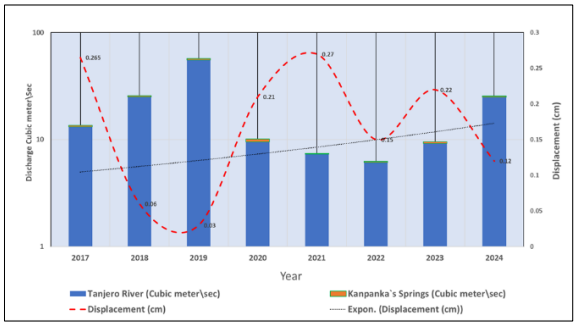


Fig. 12: Correlation between average runoff (m³/sec) and surface displacement.

6.3 Subsidence patterns and temporal trends

The data analyzed were produced by exporting pair-level-1 SLC images from C-SAR, Sentinel-1, into the ESA SNAP 9 software and subsequently converting them to TIFF format for raster analysis in ArcGIS following the completion of the DInSAR application. This study exclusively examines the risks associated with land subsidence due to the continuous depletion of groundwater resources, disregarding any positive (uplift) indicators. From 2017 to 2024, notable fluctuations in annual surface displacement were documented, closely correlating with climatic trends and groundwater extraction levels. The research utilizes DInSAR processing in conjunction with GIS raster computations to assess negative subsidence data, particularly focusing on values ranging from maximum subsidence to zero (Fig.13).

The examination of surface displacement during the specified period indicates significant alterations. In 2017, a significant increase in subsidence was observed, with a maximum displacement of -26 cm recorded. In 2018, a decrease to a minimum of -6.0 cm was observed. The minimum subsidence recorded during the study period was -3.0 cm in 2019, coinciding with significant precipitation and aquifer replenishment. The most substantial subsidence transpired in 2021, recognized as the driest year on record, with a measurement of -27.0 cm. In 2022, recorded displacement was -15.0 cm, whereas in

2023, subsidence reached a maximum of -22.0 cm. The ultimate documented displacement in 2024 was -12.0 cm.

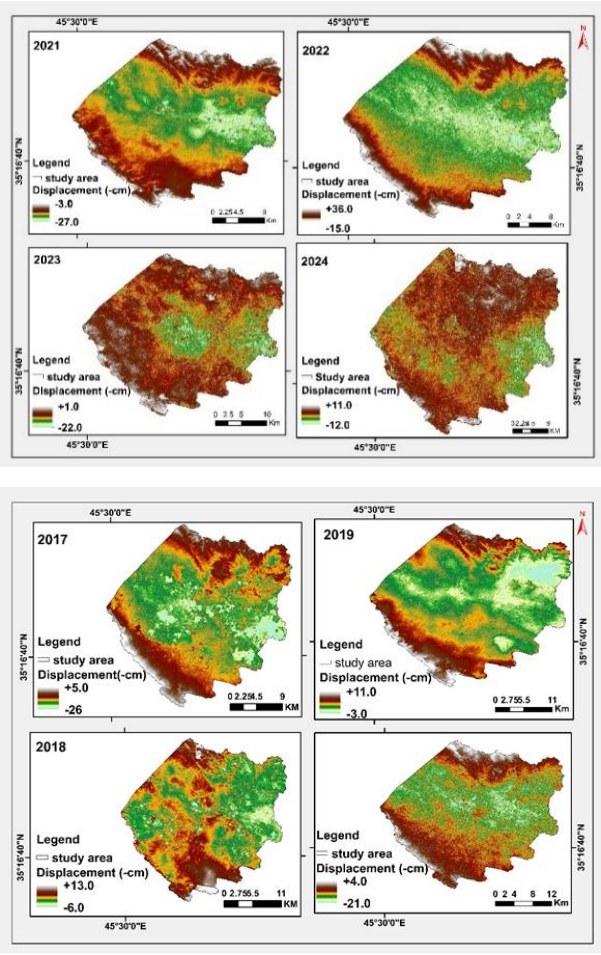


Fig. 13: Cumulative annual vertical subsidence maps for 2017–2024 in the SSB by m.y-1.

The average annual surface displacement over the eight-year study period is determined to be -10.5 cm per year (Fig.14), signifying a gradual subsidence of the land surface in the basin, particularly in its central and western areas.

The study identifies several towns and villages as pivotal sites undergoing substantial land subsidence. The areas adjacent to Arbat, Barikae-kon, Sarkawtn, Zarain, and Halabjae-taza exhibit the most significant negative displacement values. The geological context indicates that these hotspots are primarily located within the basin's unconsolidated deposits, marked by clay-rich layers that demonstrate increased vulnerability to contraction. Conversely, stable zones like Mwan and Alan exhibit diminished displacement values in comparison to the central hotspots, signifying relative stability in these areas.

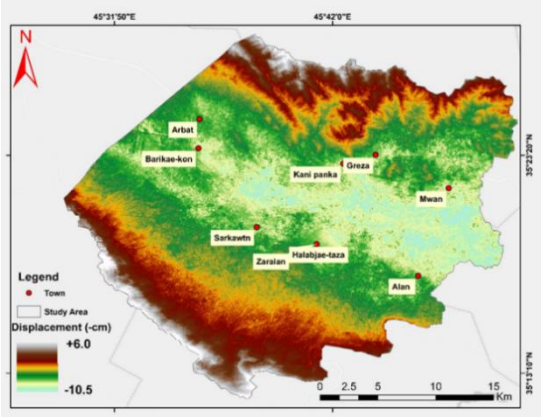


Fig. 14: Average annual cumulative subsidence (m.yrs-1.) in the SSB from 2017 to 2024.

7. Discussion

7.1. Driver Analysis

The primary contributors to subsidence in the SSB basin appear to be groundwater overextraction and the prevalence of numerous clay layers within recent sediment; however, six supplementary factors warrant consideration as well.

1. Seasonal, topographic, and climatic factors significantly affect tropospheric water vapor, leading to 10 cm inaccuracies in deformation caused by 20% variations in relative humidity (Zebker et al., 1997; Qiu et al., 2023).

2. DInSAR is an accurate technique for monitoring ground displacement to the centimeter or millimeter level; nevertheless, atmospheric variations can compromise the reliability and precision of the results, complicating DInSAR processing.

3. The neotectonics map indicated vertical uplift movements in the HFZ ranging from 0.0022 to 0.0086 m/100 years; however, the precise amount of vertical displacement was not specified (Sissakian et al., 2020). According to Zebari et al. (2023) and Othman et al. (2018), the uplift rate in the Zagros Mountains is reported to be between 0.7 and 1.3 mm/year and 0.33 to 1.67 mm/year, respectively. The magnitude 7.3 quake in November 2017 during the Zagros Mountain development in the Sarpel Zahab vicinity demonstrated this occurrence in

the SSB, leading to considerable instantaneous modifications to the landscape near Darbandikhan Lake.

4. Urban expansion and subsidence assessed in the vicinity of Arbat, Sarkawtn Camp, and Halabjae-taza.

5. Clay shrinkage-swelling cycles, seasonal moisture variations, and flood length affect erosion and sediment deposition (Fernandez et al., 2025). Comparable amounts of disruption were noted, with soil moisture varying by as much as 10 degrees Celsius, approximately equivalent to 1 mm for a C-band wave, a specific microwave frequency utilized in radar and satellite communications (Beale, 2019).

6. Unexplained alterations may signify natural phenomena, including intricate subterranean conditions, unregulated human operations from industries, multiple storage facilities, and illicit well drilling.

7.2. Groundwater discharge and land subsidence correlation

Spatial examination of well discharge rates (varying from <23 to 300 l/sec) indicates a direct correlation with the extent of land subsidence in the research region. Regions characterized by comparatively low discharge rates (<44 l/sec), especially in the western and southwestern sectors of the examined territory, demonstrate negligible subsidence (<10 cm.yr-1), highlighting the stabilizing influence of natural replenishment and a reduced number of active production wells in contrast to the central region. Conversely, regions exhibiting moderate-to-high discharge (>70 l/sec) at the center and along primary streams correspond with elevated subsidence rates (>20 cm.yr-1), signifying aquifer overexploitation and ensuing compaction, as illustrated in deformation rate maps (Fig. 9), particularly in the years 2020, 2021, and 2023. Seasonal reductions in groundwater during droughts probably intensified this trend, demonstrated by a 3.0 cm/yr rise in subsidence in low-discharge wells, as illustrated in Fig. 7, aligning with global models of clay-layer compression (Galloway and Burbey,2011).

These results support focused replenishment efforts in areas with diminished discharge to alleviate subsidence hazards.

7.3. Urbanization-Enhanced Subsidence

The analysis indicates that urban expansion has intensified groundwater-related subsidence through two primary mechanisms:

1. Direct loading effects: The density of buildings in Halabjae-taza town and Barikae-kon village in the western and central parts of the area has clearly risen.

2. Hydrologic disruption: The area of impervious surfaces increased by approximately 20 km², resulting in a reduction of natural recharge by about 10%, particularly in Arbat town and Sarkawtn Camp during the period from 2012 to 2024.

3. Fig. 15 demonstrates the expansion of the urban area from 2012 to 2024, highlighting the sudden establishment of three camps in 2014 behind Arbat town and Sarkawtn Camp, which resulted in an increased demand for groundwater through the drilling of over 17 wells.

Additionally, as indicated in Table3, the urban area experienced a 30% increase from 2017 to 2024, suggesting that the growth could exceed this range if assessed from 2012.

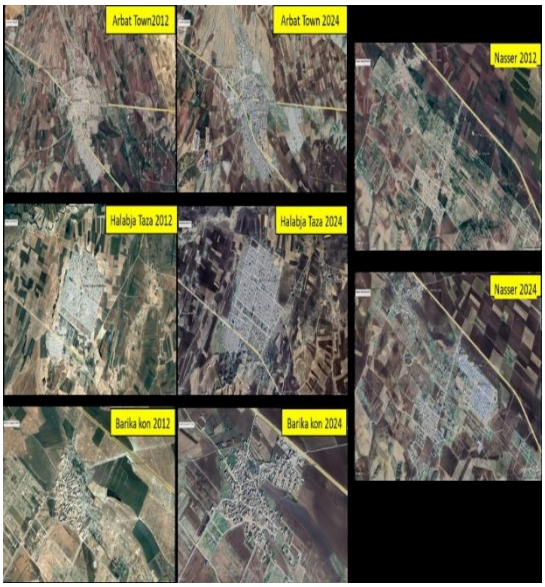


Fig. 15: The expansion of urban infrastructure (roads and buildings) in selected locations within the SSB from 2012 to 2024in the SSB (Google Earth Pro).

Table 3: Subsidence attribution in the SSB.

Process	Key Evidence	Spatial Pattern
Groundwater extraction	Well density vs. subsidence R^2=0.74	Concentric around pumping wells, discharge, and SWL
Tropospheric noises	Terrain elevation, Local weather, convection, and wind	Elevation and weather parameters
Tectonics	InSAR fault-parallel trends	Linear along anticline
Horizontal deformation (Flooding, Farming, Channeling)	Field work	Seasonal deformation
Natural compaction and clay shrinkage-swelling	Deformation in undeveloped areas	Fluvial corridors
Urban loading	Building permits vs. subsidence	Radial near cities
Undocumented anthropogenic factors	Complex industrial factories, and illegal drilling wells, Land Use	

8. Validation

Due to the absence of precise leveling or GPS station data during the study period, Earth observation-based validation of DInSAR processing results was not feasible. Additionally, the lack of sufficient SAR data for the SSB necessitated the use of a comparative validation approach. For this purpose, DInSAR processing results were validated against groundwater level data from 4 monitoring wells and 2 surface water discharge measurements. Subsidence values at the monitoring well locations were extracted from the displacement maps and compared with the observed data. The study ultimately finds a commendable quantitative correlation between subsidence estimates obtained from InSAR data and those from monitoring wells, thereby validating the visual trends observed in displacement maps. Slight variations between datasets may be ascribed to the differing temporal acquisition periods of the imagery. Field surveys were executed to corroborate the findings by collecting additional evidence of subsidence in the SSB area.

8.1. Statistical comparison between variables

The Study performed an exhaustive statistical evaluation juxtaposing in-situ measurements with DInSAR-derived displacements, employing a hierarchical methodology that involved the examination of Pearson correlation coefficients (r) and coefficients of determination (R^2) from ordinary least squares regression. The results indicate substantial hydrological connections with surface movements throughout the SSB, particularly illustrated in Fig. 16.

In panel (a), a robust association was identified between total precipitation and displacement, with a Pearson coefficient of r = 0.87 and R^2 = 0.75. This suggests that around 75.7% of the variation in displacement can be accounted for by rainfall patterns, demonstrating a nearly linear correlation (slope = 0.62 cm/mm rainfall). The association highlights the synergistic impacts of immediate precipitation and postponed groundwater replenishment in the fractured aquifers of the area. The low p-values corroborate the statistical significance of these results. The one-tailed p-value is 0.000108, while the two-tailed p-value is 0.000217, both considerably below the standard cutoff of 0.05, indicating merely a 0.02% probability that these findings are attributable to random variation.

Panel (b) examines the correlation between static water levels (SWL), resulting in r = 0.74 and R^2 = 0.55. The results demonstrate that 55.0% of the variability in SWL can be attributed to aquifer compaction affected by urban development and agricultural groundwater withdrawal methods. The examination distinctly indicates a nonlinear pattern at SWL depths exceeding 15 m, implying stress-dependent compressibility in clay interbeds, in alignment with poroelastic theory. The notable p-value of 0.0002 further substantiates the strength of these results.

Panel (c) displays information for Kanipanka Springs, indicating an R^2 of 0.65 and an r value of 0.81, albeit with increased variability attributed to localized karst conduit flow impacting water retention. The correlation exhibits considerable significance with a p-value of 0.00199. Furthermore, panel (d) assesses the influence of Tanjero River runoff, assigning 64.0% of the variance in displacement to its effects (r = 0.80),

with a notably robust correlation noted during the spring snowmelt phase. The coefficient derived from this analysis is likewise noteworthy, registering below 0.01.

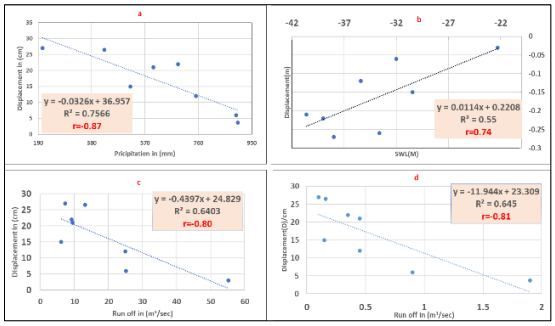


Fig. 16: Hydrological influences on surface displacement in the SSB: Correlations of InSAR-derived displacement with (a) Rainfall, (b) Static Water Level, (c) Kanipanka Springs discharge. and (d) Tanjero River runoff.

8.2. Field survey

The SSB exhibits distinct subsidence patterns tied to its aquifer characteristics and anthropogenic activities. In some areas of the basin, subsidence was accompanied by infrastructure cracks, especially in Barikae-kon village (Fig.17, FV-01,02), while in others, it occurred as uniform and homogeneous settlement. Specific areas within the basin exhibited significant deformation, including alteration of Tanjero River`s meandering, irrigation channels, pools, and soil cracks (Fig. 17, V-03, 04). These features generated anomalous signals in SLC images, which were used to assess displacement over the study period. In northwestern settlements (Arbat town, Barikae-kon village), damage to infrastructure, including cracked mosque foundations, fractured school walls, and ruptured pipelines, stems from excessive groundwater extraction via shallow wells (20-50 m depth) tapping unconfined aquifers of the floodplain sediments and aquiclude beds within the Shiranish Formation, respectively (Table 4, FV-03,04). The areas exhibiting the greatest distortion correspond to the rampant drilling of wells, both legal and illegal, in residential neighborhoods. The eastern regions adjacent to Darbandikhan Lake and the Tanjero River exhibit distinct processes: riverbank erosion and sediment deposition occur due to seasonal flooding (Fig.18, FV05-06), while areas near the Darbandikhan reservoir experience subsidence resulting from poroelastic loading during variations in water levels (Fig.19). An empirical study indicates that thin (10–45 meters) unconfined aquifers in alluvial sediments are the first to collapse under pumping stress. After the 2021 drought, most wells in Sarkawtn Camp and Barikae-kon Village were desiccated, although denser strata (70-140 m) exhibit more pronounced deformation, especially in Halabjae-taza and Mowan Village.

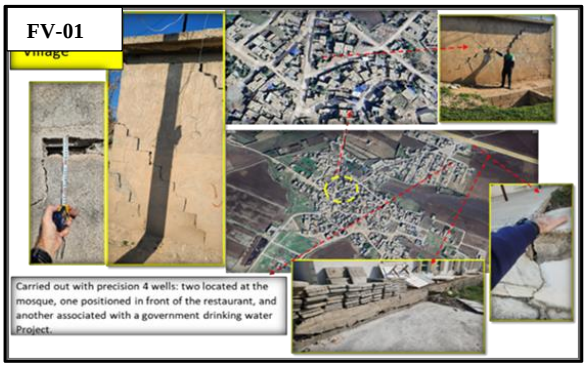






Fig. 17: Infrastructure deformation in Barika Kon town due to excessive well drilling, and subsidence effects in Kazhaw village (irrigation channels), Arbat, Halabjai Taza, and Nasser Camp (schools, mosques, and residential buildings).

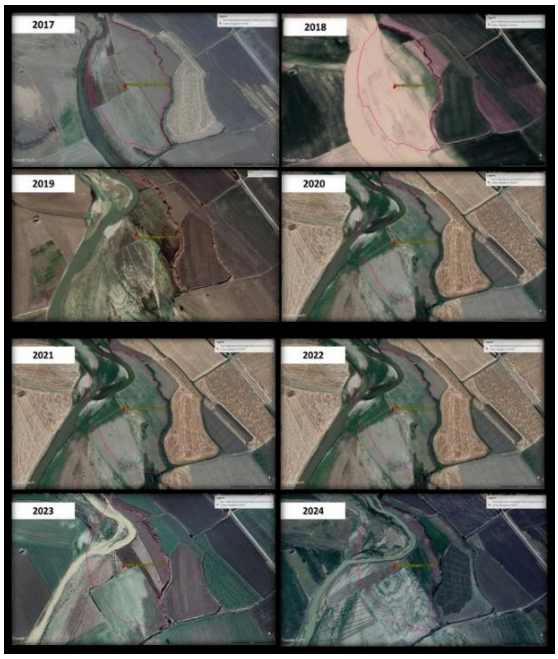


Fig. 18: Comparison of surface displacement in the SSB between 2021 (during drought conditions) and 2024 (following lake level recovery), derived from Sentinel-1 data.

Table 4: Field validation sites with quantified subsidence

Site ID	Location Name	Easting (X)	Northing (Y)	Elevation (m)	Deformation Type	Field Evidence	Coherence (γ)	Measurement Method
FV-01	Barika-Kon	554,006	3,916,912	615	Well tilt + cracks	9.8 cm tilt	0.32	Field Survey
FV-02	Irrigation Channel	572,705	3,909,821	487	Infrastructure damage	Pipe rupture	0.35	Field Survey
FV-03	Shallow Well	572,911	3,909,809	468	Well casing subsidence	7cm offset	0.29	Field Survey
FV-04	Swamp Area	571,571	3,910,451	490	Ground fissures	10m fissure	0.38	GPS survey
FV-05	Tanjero River	572,333	3,909,635	487	Channel migration	Bank collapse	0.41	Google Earth pro, Field Survey
FV-06	Polygon (2017-2024)	574,418	3,908,501	481	Composite	Vertical erosion by shifting of Tanjero River	<0.3	Google Earth pro

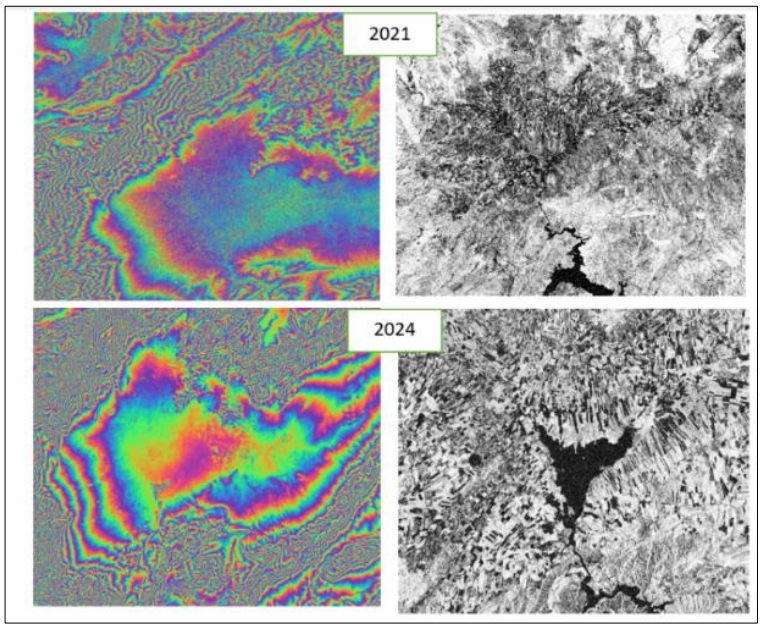


Fig. 19: FV-06, Signal decorrelation and phase distortion in Sentinel-1 DInSAR processing caused by fluvial geomorphological changes along the Tanjero channel shifts (1.1 km² study reach, 2017-2024) based on observed (Google Earth Pro, 2025).

8.3. Land use and recent sediment thickness

The validation of land use changes from 2017 to 2024 highlights the significant impact of human activities, including urban expansion and industrial development, on water resources. The proportion of wet years increased from 66.26% in 2017 to 69.30% in 2024, driven by consistent precipitation and improved irrigation practices.

By 2024, vegetation cover expanded across agricultural, urban, and aquatic environments, resulting in a 94% reduction in barren land (from 6.07 km² to 0.36 km²) due to enhanced land use and soil moisture retention (Lucas-Borja et al., 2020). Specifically, urban areas grew from 3.8% in 2017 to 5.03% in 2024, while cropland usage increased by 3.5% over the same period (Fig.20).

Surface water bodies reached their lowest extent in 2017 and 2021, as evidenced by Sentinel-2 imagery. In 2019, surface water coverage peaked at 0.25%, coinciding with minimal surface displacement (-3.5 cm).

In 2024, surface water coverage was 0.07%, with rainfall variability contributing to annual increases in water stress, as indicated by data on urban areas, croplands, and barren land (Table 5).

Table 5: Data collection of Land use/Land cover derived from Sentinel-2, 2025.

Year	2017	2019	2021	2024	(17-24) %
Land use			100%		
Water	0.048	0.25	0.028	0.07	46%
Tree	0.005	0.042	0.016	0.00	200%
Crop	66.26	69	63.68	69.30	4.6%
Urban	3.885	4.4	4.79	5.03	30%
Barren ground	0.956	0.039	0.042	0.06	-94%
Range land	28.84	26.3	31.44	25.55	-11.40

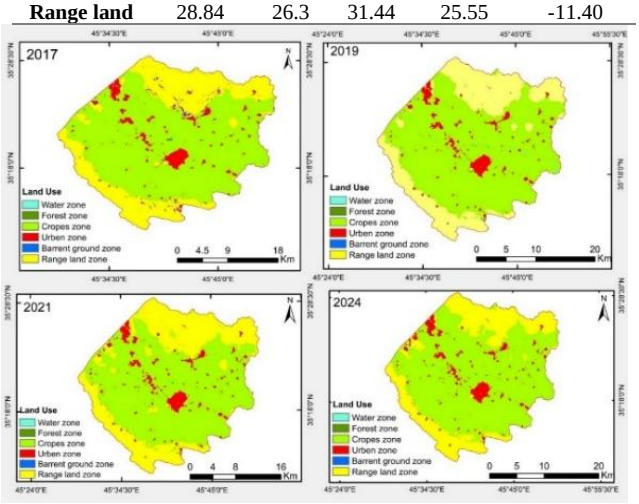


Fig. 20: Variations in land use and land cover in the SSB from 2017 to 2024, obtained from Sentinel-2 imagery (2025).

9. Limitation

The study acknowledges several technical constraints that influence interpretation of the subsidence patterns, including:

1. The radar coherence issues result in significant seasonal variation in temporal sampling and utility of DInSAR images over the SSB. As a result of heightened precipitation and soil moisture, coherence levels fell below 0.4 during the winter and rainy periods. These conditions alter surface dielectric properties and may lead to temporal decorrelation between image acquisitions (Zebker and Villasenor, 1992; Danklmayer et al., 2009).

2. Seasonal agricultural practices in autumn and spring lead to alterations in surface roughness and influence plant growth, resulting in volume dispersion and a decline in phase stability (Moran et al. 977). Local meteorological and hydrological variables contribute to a reduced coherence in summer acquisitions.

3. Tropospheric interference in the Whole Sharazoor plain is influenced by rising water levels in the Darbandikhan lake, which increase ambient vapor pressure and alter tropospheric conditions. This leads to atmospheric phase delays (APDs) that complicate the identification of ground deformation signals (Hanssen, 2001; Doin et al., 2009). The unique conditions produce intermittent data gaps, particularly during humid periods, which impede analytical coherence thresholds. Notably, maximum effects are recorded in the southern and eastern mountainous margins of the basin. While atmospheric corrections and spatiotemporal filtering have been employed to address these issues, residual uncertainties persist in steep topographic areas.

4. Field validation efforts, while extensive, faced inherent accuracy limitations, including positional uncertainty from total station measurements and well depth estimation errors.

5. The groundwater level interpolation, while generally robust, showed edge effects within 500 m of basin boundaries where well density decreased, resulting in local root mean square error (RMSE) values up to 3.4 m. Additionally, the impact of water storage fluctuations in the Darbandikhan Lake on land stability remains underexplored.

6. The quantity of high-resolution images during the dry season exceeds that of the rainy season; for instance, in 2017, 2021, and 2023, the count of accurate and uninterrupted images surpassed that of prior years. Drought affects the spatial resolution and coherence of DInSAR data, since it exacerbates decorrelation and diminishes soil moisture levels. Conversely, rainy seasons enhance vegetation, soil moisture, and ambient noise, resulting in expedited decorrelation and signal deterioration. This underscores the significance of accounting for environmental factors in InSAR data creation (Ferretti et al., 2005). The convergence of multiple validation methods (InSAR and ground surveys) provides confidence that these limitations do not alter the fundamental conclusions regarding dominant subsidence drivers in the SSB basin. Future studies should address these gaps to develop sustainable groundwater management strategies and mitigate subsidence risks in the SSB. Future studies should focus on integrating additional remote sensing data and expanding monitoring networks to improve the accuracy of subsidence predictions and support informed decision-making for water resource management in the region.

10. Conclusion

The study investigates the significant impact of groundwater extraction and climatic change on land subsidence within the SSB from 2017 to 2024, utilizing Sentinel-1 SAR data in conjunction with DInSAR algorithms to analyze spatiotemporal ground surface deformation. The findings establish a direct correlation between decreasing annual seasonal rainfall, total saturated SWLs, surface runoff, and vertical displacement. Groundwater over-extraction emerges as the principal cause of notable subsidence patterns, exacerbated by the unique lithology of the basin, which includes compressible clay and silt layers prone to irreversible compaction. The study emphasizes the necessity of employing InSAR and remote sensing technologies for effective subsidence monitoring and mitigation strategies to counteract environmental degradation. Local drought conditions have intensified the reliance on groundwater, while variable snowmelt has disrupted natural recharge dynamics, destabilizing pore pressure equilibrium.

Additionally, rapid urban development has increased surface loading and contributed to the subsidence crisis. Pilot measures in collaboration with the KRG aim to address these issues by prioritizing infrastructure inspections, choosing

suitable artificial recharge sites, and advising on water-efficient agricultural practices.

Results demonstrate a 15–20% reduction in displacement rates post-regulatory interventions at high-risk wells. This framework provides a basis for sustainable water management in data-scarce regions, and future studies may integrate real-time piezometric data to further refine assessments of groundwater dynamics and subsidence rates.

11. Acknowledgments

The authors extend their sincere gratitude to the University of Sulaimani for its unwavering support and collaboration throughout this research. Special thanks are due to Dr. Sayantan Majumdar from the Desert Research Institute, USA, and Dr. Hedayat K. Xan from Soran University, Iraq, for their invaluable guidance, insightful suggestions, and support, which greatly contributed to the successful completion of this study. We also acknowledge the assistance of Mr. Ari Ismail from the Irrigation Directorate of Sulaymaniyah, as well as Dr. Peshawa Mahmood and Mr. Sarmand from the Groundwater Directorate of Sulaymaniyah, for providing essential data and facilities that were instrumental in accomplishing this work.

12. Conflict of Interest

The authors declare that there are no conflicts of interest regarding the publication of this manuscript.

13. Funding Statement

Research received no external funding.

14. References

Aeschbach-Hertig, W. and Gleeson, T., 2012. Regional strategies for the accelerating global problem of groundwater depletion. Nat Geosci 5: pp. 853–861. https://doi.org/10.1038/ngeo1617.

Al-Basrawi, N.H. and Al-Jiburi, H.K., 2014. Hydrogeology of the high folded zone. Iraqi Bulletin of Geology and Mining, 6, pp.163-183.

Ali, S.S., 2005. Effect of slide masses on groundwater occurrence in some areas of Sharazoor plain/NE Iraq. In Water Resources and Environmental Problems in Karst–Proceedings of the International Association of Hydrogeologists. International Conference, Karst CVIJIĆ. https://www.academia.edu/download/78823826/slide_20and_20groundwater.pdf.

Ali, S.S., 2007. Geology and Hydrogeology of Sharazoor-Piramagroon Basin.

Alkaradaghi, K., Hamamin, D., Karim, H., Al-Ansari, N., Ali, S. S., Laue, J., and Ali, T., 2022. Geospatial Technique Integrated with MCDM Models for Selecting Potential Sites for Harvesting Rainwater in the Semi-arid Region. Water, Air, and Soil Pollution, 233(8). https://doi.org/10.1007/s11270-022-05796-2.

Al-Mubarak, M., and Amin, R.M., 1983. Report on the regional geological mapping of the eastern part of the Western Desert and western part of the Southern Desert. GEOSURV, int. rep., (1380).

Arriana Brand, L., Stromberg, J.C., Goodrich, D.C., Dixon, M.D., Lansey, K., Kang, D., Brookshire, D.S. and Cerasale, D.J., 2011. Projecting avian response to linked changes in groundwater and riparian floodplain vegetation along a dryland river: a scenario analysis. Ecohydrology, 4(1), pp. 130-142. https://doi.org/10.1002/eco.143.

Beale, J., Snapir, B., Waine, T., Evans, J., and Corstanje, R. (2019). The significance of soil properties to the estimation of soil moisture from C-band synthetic aperture radar. Hydrology and Earth System Sciences Discussions, 2019, 1-32. https://doi.org/10.5194/hess.2019-294

Bety, A.K.S., 2013. Urban geomorphology of Sulaimani City, using remote sensing and GIS techniques, Kurdistan Region, Iraq. Unpublished PhD Thesis, Faculty of Science and Science Education, University of Sulaimani, 125 P.

Buday, T. and Jassim, S.Z., 1987. The Regional Geology of Iraq: Tectonism, Magmatism, and Metamorphism. I.I. (Eds.). Baghdad, 445 P.

Braun, A., Veci, L., 2021. Sentinel-1 Toolbox TOPS Interferometry Tutorial. Tutorial, 25 P. https://pdf4pro.com/amp/view/sentinel-1-toolbox-tops-interferometry-tutorial 7363e6.html.

Chaussard, E., Bürgmann, R., Shirzaei, M., Fielding, E. J., and Baker, B., 2014. Predictability of hydraulic head changes and characterization of aquifer-system and fault properties from InSAR-derived ground deformation. Journal of Geophysical Research: Solid Earth, 119(8), pp. 6572-6590. https://doi.org/10.1002/2014JB011266.

De Zan, F. and Guarnieri, A.M., 2006. TOPSAR: Terrain observation by progressive scans. IEEE Transactions on Geoscience and Remote Sensing, 44(9), pp. 2352-2360. https://doi.org/10.1109/TGRS.2006.873853.

Dubovyk, O., 2017. The role of Remote Sensing in land degradation assessments: opportunities and challenges. European Journal of Remote Sensing, 50(1), pp. 601-613. https://doi.org/10.1080/22797254.2017.1378926.

Elhag, M., Chaabani, A., and Zhang, L., 2025. Assessment of surface deformation patterns using InSAR data: Implications for human impacts in Makkah City, Saudi Arabia. Kuwait Journal of Science, 52(3), 100419. https://doi.org/10.1016/j.kjs.2025.100419.

Famiglietti, J.S., 2014. The global groundwater crisis. Nature Climate Change, 4(11), pp. 945-948. https://doi.org/10.1038/nclimate2425.

Ferretti, A., Prati, C., Rocca, F., Casagli, N., Farina, P., and Young, B., 2005. Permanent Scatterers technology: a powerful state of the art tool for historic and future monitoring of landslides and other terrain instability phenomena. In Proceedings of the International Conference on Landslide Risk Management, Vancouver, BC, Canada (Vol. 31).

Fernandez, J.E., Kim, S., Jang, E., and Kang, W., 2025. Assessment of Floodplain Sediment Deposition Using Synthetic Aperture Radar-Based Surface Deformation Analysis. Water, 17(21), p.3137.https://doi.org/10.3390/w17213137

Galloway, D.L., Jones, D.R., and Ingebritsen, S.E. (Eds.). (1999). Land subsidence in the United States (Vol. 1182). Geological Survey

Galloway, D.L., Burbey, T.J., 2011. Regional land subsidence accompanying groundwater extraction. Hydrogeology Journal, 19(8), pp. 1459-1486. https://doi.org/10.1007/s10040-011-0775-5.

Ghorbani, Z., Khosravi, A., Maghsoudi, Y., Mojtahedi, F. F., Javadnia, E., and Nazari, A., 2022. Use of InSAR data for measuring land subsidence induced by groundwater withdrawal and climate change in Ardabil Plain, Iran. Scientific Reports, 12(1), 13998. https://doi.org/10.1038/s41598-022-17438-y.

Hamamin, D.F., 2024. Integration of multi-geostatistical approaches for deciphering groundwater potential zones in complex water-bearing mediums. Groundwater for Sustainable Development, 26, 101208. https://doi.org/https://doi.org/10.1016/j.gsd.2024.101208.

Hamamin, D.F., and Nadiri, A.A., 2018. Supervised committee fuzzy logic model to assess groundwater intrinsic vulnerability in multiple aquifer systems. Arabian Journal of Geosciences, 11(8). https://doi.org/10.1007/s12517-018-3517-3.

Herrera-García, G., Ezquerro, P., Tomás, R., Béjar-Pizarro, M., López-Vinielles, J., Rossi, M., and Ye, S., 2021. Mapping the global threat of land subsidence. Science, 371(6524), pp. 34-36. https://doi.org/10.1126/science.abb8549.

Jassim, S.Z. and Goff, J.C., eds., 2006. Geology of Iraq. DOLIN, SRO, distributed by Geological Society of London.

Khan, M.J. and Hasan, S.A., 2020. GIS-based screening model of coastal city Karachi for plantation of biofuel source. Scientific Reports, 10(1), p.4666. https://doi.org/10.1038/s41598-020-61052-9.

Khalil, A., Abdullah, O.A.I. and Kareem, A.T., 2024. GIS Application for Creating Potential Flood Map Using AHP: A Case Study in Chaq-Chaq Valley, Sulaymaniyah City, Kurdistan Region, Iraq. The Iraqi Geological Journal, pp. 254-263. https://doi.org/10.46717/igj.57.2C.17ms-2024-9-25.

Land Subsidence Task Committee, 2022. Investigation of land subsidence due to fluid withdrawal. Reston, VA: American Society of Civil Engineers.https://doi.org/10.1061/9780784415702.in.

Majumdar, S., Smith, R., Butler Jr., J.J. and Lakshmi, V., 2020. Groundwater withdrawal prediction using integrated multitemporal remote sensing data sets and machine learning. Water Resources Research, 56(11), p. e2020WR028059.https://doi.org/10.1029/2020WR028059.

Mogaji, K.A. and Lim, H.S., 2017. Application of a GIS-/remote sensing-based approach for predicting groundwater potential zones using a multi-criteria data mining methodology. Environmental Monitoring and Assessment, 189, pp. 1-26. https://doi.org/10.1007/s10661-017-5990-7.

Mohammed, S. A., Attarnejad, R., and Hamamin, D. F., 2022. Aquifer feature estimation in Basara basin using a groundwater modeling system for smart agriculture. Computers and Electrical Engineering, 103.https://doi.org/10.1016/j.compeleceng.2022.108354.

National Research Council, 1991. Mitigating losses from land subsidence in the United States.

Numan, N., and Azzawi, N., 1993. Structural and geotectonic interpretation of vergence directions of anticlines in the foreland folds of Iraq.

Ohenhen, L.O. and Shirzaei, M., 2022. Land subsidence hazard and building collapse risk in the coastal city of Lagos, West Africa. Earth's Future, 10(12), e2022EF003219. https://doi.org/10.1029/2022EF003219.

Osman, M., 2021. Kurdistan Region of Iraq population analysis report. Kurdistan Region Statistics Office in Kurdistan Regional Government. https://krso.awrosoft.krd/content/upload/1/root/kurdistan-population-analysis-report-6-english-final-corrected-29052022.pdf.

Phillips, S.P. and Galloway, D., 2008. Groundwater: pumping and land subsidence. In Encyclopedia of Water Science (pp. 466-470). Taylor and Francis Publishing. https://doi.org/10.1201/NOE0849396274.

Poland, J., 1984. Guidebook to studies of land subsidence due to ground-water withdrawal, UNESCO: United Nations Educational, Scientific and Cultural Organization. France. https://coilink.org/20.500.12592/12jm9cp.

Qiu, L., Chen, P., Yao, Y., Chen, H., Tang, F., and Xiong, M. (2023). An interferometric synthetic aperture radar tropospheric delay correction method based on a global navigation satellite system and a backpropagation neural network: More suitable for areas with obvious terrain changes. Sensors, 23(24), 9760. https://doi.org/10.3390/s23249760

Rafiei, F., Gharechelou, S., Golian, S., and Johnson, B. A., 2022. Aquifer and Land Subsidence Interaction Assessment Using Sentinel-1 Data and DInSAR Technique. ISPRS International Journal of Geo-Information, 11(9). https://doi.org/10.3390/ijgi11090495.

Sharbazheri, K., Ghafor, I. and Muhammed, Q., 2009. Biostratigraphy of the cretaceous/tertiary boundary in the Sirwan Valley (Sulaimani Region, Kurdistan, NE Iraq). Geologica Carpathica, 60(5), 381 P. https://doi: 10.2478/v10096-009-0028-x.

Smith, R.G., Knight, R., Chen, J., Reeves, J.A., Zebker, H.A., Farr, T. and Liu, Z., 2017. Estimating the permanent loss of groundwater storage in the southern San Joaquin Valley, California. Water Resources Research, 53(3), pp. 2133-2148. https://doi.org/10.1002/2016WR019861

Sissakian, V.K., Al-Ansari, N. and Abdullah, L.H., 2020. Neotectonic activity using geomorphological features in the Iraqi Kurdistan region. Geotechnical and Geological Engineering, 38(5), pp. 4889-4904. https://doi.org/10.17656/jzs.10477.

Sissakian, V.K., Al-Ansari, N. and Abdullah, L.H., 2020. Neotectonic activity using geomorphological features in the Iraqi Kurdistan region. Geotechnical and Geological Engineering, 38(5), pp. 4889-4904. https://doi.org/10.17656/jzs.10477

Sissakian, V.K. and Fouad, S.F., 2015. Geological map of Iraq, scale 1: 1000 000, 2012. Iraqi Bulletin of Geology and Mining, 11(1), pp.9-16. Southern Desert and the eastern part of the Western Desert. GEOSURV, Int. Rep. No. 1380. https://ibgm-iq.org/ibgm/index.php/ibgm/article/view/263/258.

Sissakian, V., Al-Ansari, N. and Knutsson, S., 2014. Origin of Some Transversal Linear Features of NE-SW Trend in Iraq, and Their Geological Characters. Natural Science, 6, pp. 996-1011. https://doi.org/10.4236/ns.2014.612091.

Stern, R.J. and Johnson, P., 2010. Continental lithosphere of the Arabian Plate: a geologic, petrologic, and geophysical synthesis. Earth-Science Reviews, 101(1-2), pp. 29-67. https://doi.org/10.1016/j.earscirev.2010.01.002

Stevanovic, Z. and Markovic, M., 2004. Hydrogeology of Northern Iraq, General Hydrogeology and Aquifer Systems, Vol. 2. Food and Agriculture Organization of the United Nations, Rome. 246 P. https://ibgm-iq.org/ibgm/index.php/ibgm/article/view/369/363.

Stevanović, Z., Iurkiewicz, A. and Maran, A., 2009. New insights into karst and caves of Northwestern Zagros (Northern Iraq). Acta Carstologica, 38(1).

Syvitski, J.P., 2003. Sediment fluxes and rates of sedimentation. Encyclopedia of Sediments and Sedimentary Rocks. Kluwer Academic Publishers, Dordrecht, Netherlands, pp. 600-606. https://doi.org/10.1007/978-1-4020-3609-5_180.

Terzaghi, K., 1925. Principles of soil mechanics: III. Determination of permeability of clay. Engineering News Record, 95(21), pp. 832-836. Their remedial works. Dissertation, Power and Water Industrial University, Tehran, Iran.

Torres, R., Navas-Traver, I., Bibby, D., Lokas, S., Snoeij, P., Rommen, B., Geudtner, D., 2017. Sentinel-1 SAR system and mission. In 2017 IEEE Radar Conference (RadarConf) (pp. 1582-1585). IEEE.

UNWWAP, W., 2015. The United Nations world water development report 2015: water for a sustainable world. UN World Water Assessment Program.

Valizadeh, R., Yaghobi Kikleh, B. and Mosivand, H., 2005. An interpretation to Hamadan central plain sinkholes. In: Proceedings of the conference on hazards of sinkholes in karst terrains, Kermanshah, Iran (In Farsi).

Vasco, D.W., Farr, T.G., Jeanne, P., Doughty, C. and Nico, P., 2019. Satellite-based monitoring of groundwater depletion in California's Central Valley. Scientific Reports, 9(1), 16053 P. https://doi.org/10.1038/s41598-019-52371-7.

Yeşilmaden, H.M., İnan, Ç.A. and Kurtuluş, B., 2021. Land subsidence assessment under excessive groundwater pumping using ESA Sentinel-1 satellite data: a case study of Konya Basin, Turkey. Environ Earth Sci 80: 409. https://doi.org/10.1007/s12665-021-09718-z**.**

Zebker, H.A., Rosen, P.A. and Hensley, S., 1997. Atmospheric effects in interferometric synthetic aperture radar surface deformation and topographic maps. Journal of Geophysical Research: Solid Earth, 102(B4), pp. 7547-7563. https://doi.org/10.1029/96JB03804.

Zebari, M., Preusser, F., Grützner, C., Navabpour, P., and Ustaszewski, K. (2021). Late Pleistocene-Holocene Slip Rates in the Northwestern Zagros Mountains (Kurdistan Region of Iraq) Derived from Luminescence Dating of River Terraces and Structural Modeling. Tectonics, 40(8), e2020TC006565. https://doi.org/10.1029/2020TC006565.

Iraqi National Journal of Earth Science, Vol. 26, No. 04, 2026 (263-282)

Iraqi National Journal of Earth Science

www.earth.uomosul.edu.iq

الاستنزاف المفرط للمياه الجوفية وتأثير المناخ على هبوط الأرض في حوض السليمانية– شارزور، العراق: تحليل بواسطة تقنية InSAR

شهريار توفيق سان احمد [1*] ، دارا فايق حمه امين [2]

Shahrayar.san3017@gmail.com dara.amin@univsul.edu.iq

[1] مديرية الري، وزارة الزراعة والموارد المائية، إقليم كردستان، السليمانية، العراق.

[2] قسم علوم الأرض والنفط، كليةعلوم، جامعة السليمانية، السليمانية، العراق.

* الباحث المراسل.

تاريخ الاستلام: 14 آب 2025 تاريخ المراجعة: 13 آب 2025 تاريخ القبول: 12 تشرين الأول 2025

تاريخ النشر الالكتروني: 01 تشرين الأول 2026

الملخص

يعد نقص الرصد الكمي عائقا امام تقييم استنزاف المياه الجوفية وتبعاتها على المستوى العالمي. تدمج هذه الدراسة بيانات الأقمار الصناعية لتقييم هبوط سطح الأرض في حوض السليمانية– شهرزورل (SSB) للفترة من 2017 إلى 2024، بربط تصريف المياه الجوفية والعوامل المناخية وتغيرات استخدام الأراضي بانزياح السطح. تمت معالجة بيانات Sentinel-1 SAR ، المكونة من 232 صورة رادارية (SLC) باستخدام ESA SNAP وأسلوب التداخل التفاضلي للرادار (DInSAR) لقياس الهبوط. أظهرت النتائج هبوطاً ملحوظا في الطبقات الحاملة للمياه الجوفية الغير متماسكة تحت تأثير الاستخراج الجائر للمياه الجوفية ودورات الجفاف وعمليات الحفر المكثف للآبار. بلغ هبوط الأراضي ذروته عند −27 سم في 2021 و −26.5 سم في 2017، متزامناً مع انخفاض حاد في هطول الأمطار والتصريف السطحي. في المقابل، انخفض الانزياح إلى −6 سم في 2018 و −3 سم في 2019بعد هطول أمطار أكثر من المتوسط وزيادة تغذية المياه الجوفية. تعرضت المناطق الحضرية لأضرار في البنى التحتية، بينما ساهمت الأراضي الزراعية والمسطحات المائية في أنماط غير منتظمة للانزياح. تؤكد نتائج هذه الدراسة على أن الاستخراج الجائر للمياه الجوفية هو الفاعل الرئيسي للهبوط، تفاقم الحال تحت تأثير التغيرات المناخية واستخدام الأراضي. "تبرز هذه النتائج على ضرورة اعتماد سياسات مستدامة لإدارة المياه الجوفية في المناطق المعرضة للهبوط

الكلمات المفتاحية:

استخراج المياه الجوفية، الجفاف، انزياح السطح، بيئة شبه جافة، معايرة باستخدام بيانات الآبار.

DOI: 10.33899/injes.v26i4.60975, *©Authors, 2026, College of Science, University of Mosul.*

This is an open-access article under the CC BY 4.0 license (http://creativecommons.org/licenses/by/4.0/)

Iraqi National Journal of Earth Science, Vol. 26 No.04, 2026 (283-292)

Iraqi National Journal of Earth Science

www.earth.uomosul.edu.iq

Assessing the Drinking Water Quality Index in Arid Areas: An Analysis of the El Hadjeb Region in Biskra, Southeastern Algeria.

Warda Chaib[1*], Farida Bettiche [1], Nora Salemkour [1], Asma Rezeg [1], Halima Mancer [1], Khadidja Bouzid [1], Nora Bouchahm [1]

wardalita1@yahoo.fr farida.bettiche@gmail.com salemkour_bio@yahoo.fr rezegasma@gmail.com mancerhalima@yahoo.fr khadidja_07@hotmail.com bouchahm_nora@yahoo.fr

[1] *Scientific and Technical Research Center for Arid Areas (CRSTRA), Biskra, Algeria.*
** Correspondence author.*

Received: 05 August 2025 Received in revised form: 20 September 2025 Accepted: 09 October 2025
Available online: 01 October 2026

Abstract

Investigating the hydrogeochemical processes and regional variations in groundwater quality within the Lower Eocene aquifer of the El Hadjeb region in southeastern Algeria is the aim of this study. The groundwater samples are tested for electrical conductivity (EC), pH, temperature (T), total dissolved solids (TDS), and major ionic elements like Na^+, K^+, Ca^{2+}, Mg^{2+}, CO_3^{2-}, HCO_3^-, Cl^-, and SO_4^{2-}. In semi-arid and arid regions, the aquifer is a very important source of water. The findings indicate that sodium chloride (Na-Cl) is the predominant hydrochemical facies of the groundwater with evaporite mineral undersaturation and a small amount of dolomite precipitation. The modal Gibbs diagrams suggest that the main geochemical regulators are evaporation and rock-water interactions. The samples examined had Water Quality Index (WQI) values between 87.26 and 153. 33.33% of the samples fall into the "good" category and 66.66% into the "poor" category. High WQI values, which indicate declining water quality, are associated with increases in SO_4^{2-}, K^+, Na^+, Ca^{2+}, Mg^{2+}, HCO_3^-, Cl^-, and TDS. These results demonstrate how important effective groundwater management is to maintaining the sustainability of this fragile aquifer.

Keywords:

Groundwater, Lower Eocene aquifer, Water Quality Index (WQI), El Hadjeb.

DOI: 10.33899/injes.v26i4.61113, ©Authors, 2026, College of Science, University of Mosul.

This is an open-access article under the CC BY 4.0 license (http://creativecommons.org/licenses/by/4.0/) .

==========

1. Introduction

Having access to safe, potable water is very important for keeping people healthy, and it is still a big subject of interest (Kada and Demdoum, 2020). Groundwater represents the leading source of both drinking water and irrigation worldwide (Aragaw and Gnanachandrasamy, 2021; Li et al., 2021). In dry and semi-arid climates, access to freshwater plays a pivotal role in supporting regional development. Uncontrolled extraction of groundwater could lead to severe repercussions in the future, impacting both the aquifer and crop sustainability (e.g., depletion of deep-water resources). Algerian Saharan groundwater, an important supply for drinking, industrial, and agricultural water, is the second most significant source (Lezzaik et al., 2018). El Hadjeb region, located in Biskra in the northeastern Algerian Sahara, experiences a hot and arid climate, low rainfall, and high temperatures with rapid evaporation rates. Within this region, there are considerable water reserves in the subsurface, comprising overlapping aquifers ranging from the uppermost free surface water aquifer to the deepest Albian aquifer. Notably, the groundwater resources within these aquifers meet the water demands of "El Hadjeb," catering to both the shallower terminal aquifer and the deeper confined continental intercalaire. The Lower Eocene formation, which is the main focus of this investigation, emerges as the most promising water reservoir in the study area due to its cracked

limestone composition. Water quality is closely linked to the physical and chemical variables that define its composition in a specific environment. Geological formations and human activities play a key role in determining these water quality parameters (Subramani et al., 2005). Groundwater is the dominant water provision for almost all uses in arid and semi-arid regions (Al-Shaibani, 2008). Numerous studies have demonstrated that anthropogenic activities exert a considerable influence on groundwater quality in arid and semi-arid areas across the globe (He et al., 2020; Li et al., 2019). To effectively manage and evaluate these water resources, it is important to have a deep understanding of the hydrogeological and hydrogeochemical properties of these aquifers (Umar et al., 2001). The main processes affecting the hydrochemical quality of groundwater are sorption, desorption, ion exchange, and mineral dissolution and precipitation within the groundwater flow (Apodaca et al., 2002). Several investigations have examined groundwater geochemistry. In the Tongchuan area of China, Li et al. (2018) used geochemical data to trace key hydrochemical mechanisms and evaluated how geological structures have an effect on the chemistry of groundwater. In Tunisia, Houatmia et al. (2016) employed various water quality parameters for hydrochemical characterization and assessment of water geochemistry in aquifer systems. Previous Algerian studies, such as Ziani et al. (2017), utilized graphical tools to study the geochemical processes that happen in the shallow aquifer of Djacer spring in Quaternary alluvial formations. In their study of the El Guettar Oasis aquifer system, Mokadem et al. (2015) combined hydrogeological, hydrochemical, and isotopic data to find the principal processes and controlling factors influencing groundwater composition and flow dynamics in southwestern Tunisia.

The goal of this study is to make important contributions to science by looking at the hydrochemical properties of the aquifer system, identifying the main factors and mechanisms governing its chemical composition, applying water quality indices to determine if groundwater is safe for people to drink, and improving understanding of the geochemical transformations responsible for mineral accumulation within the Lower Eocene aquifer in the investigated region.

2. Geology and hydrogeology

The area of study is located about 14 kilometres southwest of Biskra's centre in southeast Algeria. It is situated between Tolga and El Outaya to the north, Oumache and M'lili to the south, Biskra to the east and Bouchagroune to the west; its area spans 208.75 km². This area is known for its extremely dry climate, with an average of 137.16 mm of precipitation per year, most of which falls between October and January. Temperatures average 34.64 °C annually, ranging from 7.10 °C during the colder months to peaks of around 41.28 °C in summer. Estimated annual evapotranspiration reaches approximately 1175.13 mm. Geographically, the Ziban area reflects contrasting structural features between the northern Atlas formations and the southern Saharan zones. From a geological perspective, Biskra serves as a transitional zone, where structural and sedimentary characteristics intersect. Mountainous terrain dominates the northern sector, while the southern part corresponds to a subsiding basin within the northern fringe of the Sahara. Hydrogeologically, the Biskra region hosts four principal aquifer systems: 1. The Quaternary aquifer, 2. The integrated Lower Eocene–Senonian limestone aquifer, 3. The sand aquifer of the Mio-Pliocene, 4. Sandstone aquifer of the Continental Intercalaire.

The most widely used groundwater source in the area is the limestone aquifer, which was created by the Lower Eocene and Senonian. This is the subject of the current study.

This aquifer is particularly accessible in the western part of the study zone, where its depth is relatively shallow—reaching up to 200 meters—compared to depths exceeding 400 meters further east. Groundwater extraction yields vary, with flow rates ranging from 10 liters per second via pumping to 30 liters per second through artesian discharge.

The upper boundary of this aquifer comprises clayey-sandy deposits from the Mio-Pliocene in the northern areas, and Eocene marls with gypsum layers in the south. The main reservoir consists predominantly of fractured white limestone from the Lower Eocene, along with dolomitic marl-limestone formations from the Upper Senonian. The base of the aquifer is underlain by carbonate rocks assigned to the Lower Senonian. In the study zone, the aquifer depth ranges between 120 and 350 meters.

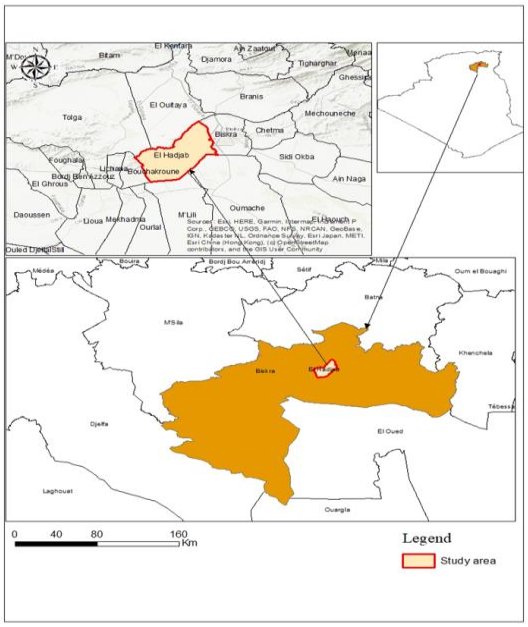


Fig. 1: Study area location.

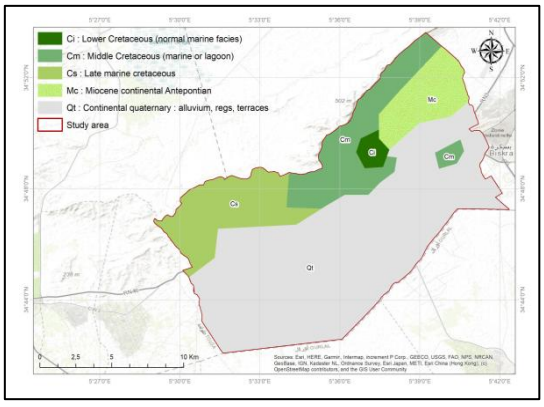


Fig. 2: Geological map of the research region based on the geological map of Algeria and modified using the GIS system.

3. Materials and methods

A. Sampling and Physicochemical Characterization

From wells located in the Lower Eocene aquifer, nine different water samples were taken (Table 1). The groundwater in the El Hadjeb region was tested in May 2017 during a field work carried out to investigate the Lower Eocene aquifer. All analyses were conducted at the Laboratory of the Scientific and Technical Research Centre for Arid Regions (CRSTRA), Biskra. Analytical precision was ±0.01 for pH, ±2% for EC, and ±5% for the major cations and anions. Temperature, pH, and electrical conductivity are important physicochemical parameters. To ensure consistent and accurate data collection during sampling, field measurements of these parameters were made using a WTW multiparameter probe (Weilheim, Germany) in situ. Samples of water were analyzed to determine the presence of main and trace dissolved elements. The amounts of calcium (Ca2+), magnesium (Mg2+), chloride (CI-), and bicarbonate (HCO3-) were measured using a titration technique. The concentration of sulfate ions (SO_4^{2-}) was measured using a UV- visible spectrophotometer. Potassium (K^+) and sodium (Na^+) were detected using flame photometry at the same laboratory. Mineral saturation indices for a range of common minerals that could be present in the investigated sites were calculated at the measured discharge temperatures. Analysis was performed using PHREEQC version 2.7 software following the procedures outlined by Parkhurst and Appelo (1999) and interfaced with Diagrams version 6.59. The Piper diagram is then generated using the AqQA RockWare version 1.5 demo software package.

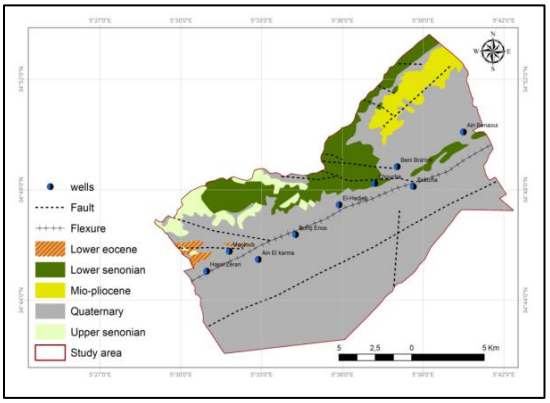


Fig. 3: Map of the study area's hydrogeology and the distribution of wells located in agricultural areas.

Table 1: Geographic coordinates and details of the sampled wells in the El Hadjeb region

Well ID	Longitude (E)	Latitude (N)	Depth (m)
El-Hadjeb	5°35' 52,80"	34°47'27,6"	160
Beni Brahim	5°38' 2,4"	34°48'50,4"	130
Ain Benaoui	5°40' 30"	34°50'6"	150
Bordj Enos	5°34' 15,6"	34°46'22,8"	96
Choucha	5°37' 12"	34°48'14,4"	104
Magloub	5°31' 48"	34°45'46,8"	---
Hassi Zerari	5°30' 57,6"	34°45'3,6"	210
Ain El Karma	5°32' 52,80"	34°45'28,8"	250
Zaatcha	5°38' 38,4"	34°48'7,2"	260

B. Water Quality Evaluation

B.1. Assessment of Groundwater Quality for Drinking purposes

The Water Quality Index (WQI) method examines various factors to determine the safety of water for multiple purposes, including supporting aquatic life, irrigating crops, enhancing landscape aesthetics, offering recreational and aesthetic benefits, and ensuring potability (Bouslah et al., 2017). WQI is a rating that reflects the combined impact of various water suitability parameters (Ramakrishnaiah et al., 2009). This process consists of generating a single index value that encapsulates the combined influence of various water quality parameters on the suitability of water for human consumption (Chung et al., 2015; Tiwari and Mishra, 1985). The original WQI was developed by Brown et al. (1970), and its calculation requires several consecutive steps.

B.2. Calculation of quality rating (qn)

The quality score (q_n) assigned to the nth parameter is calculated by using the ratio of its measured concentration in the water sample to the corresponding permissible limit set by the WHO (2011), and multiplying the result by 100 (Table 2).

$$q_n = 100\left[{}^{(V_n - V_{i0})}\!/_{(S_n - V_{i0})}\right] \quad (1)$$

Where: q_n denotes the quality score attributed to the nth parameter; V_n corresponds to the observed concentration (mg/L) of the respective chemical constituent in the sample of water; S_n refers to the maximum allowable concentration of that parameter as defined by regulatory standards; V_{i0} indicates the theoretical or ideal concentration of the parameter in uncontaminated water.

All ideal (V_{i0}) values are assumed to be zero (0) for drinking water in all parameters except pH, where it is 7.0, and dissolved oxygen = 16.6 $mg.dm^{-3}$ (Tripathy and Sahu, 2005).

B.3. Unit Weight Calculation (Wn)

The unit weight (Wn) for the nth parameter is determined by applying the following formula:

$$W_n = {}^{K}\!/_{S_n} \quad (2)$$

Where: W_n refers to the unit weight assigned to the nth water quality parameter, S_n represents the guideline or permissible concentration for the corresponding parameter, and K is the proportionality constant

B.4. WQI Calculation

The Water Quality Index (WQI) is computed utilizing the equation:

$$WQI = {}^{\sum q_n w_n}\!/_{\sum w_n} \quad (3)$$

See Table (3) for more details.

Table 2: WHO guideline values and corresponding relative weights used in water quality index calculation.

Water quality parameter	World Health Organization (WHO, 2011)	1/Sn	K	Relative weight Wn
pH	6.5–8.5	0,117	2,634	0,31
CE (µS/cm)	300a	0,00333		0,00878
TDS (mg/L)	600	0,00166		0,00439
TH (mg/L)	500	0,02		0,005268
Cl- (mg/L)	250	0,004		0,010536
SO_4^{2-} (mg/L)	250	0,004		0,010536
HCO^{3-} (mg/L)	120	0,0083		0,02195
Ca^{+2} (mg/L)	75b	0,0133		0,03512
Mg^{+2} (mg/L)	50b	0,02		0,05268
Na^{+} (mg/L)	200	0,005		0,01317
K^{+}(mg/L)	12	0,083		0,2195
NO_3 (mg/L)	10	0,1		0,2634
	a WHO (2006) b WHO (2004)			

Table 3: WQI classification system for groundwater quality (Ramakrishnalah et al. 2009; Ketata et al., 2011).

Classification of drinking water quality.		
WQI range	Class	Type of water
<50	I	Excellent water
50–100	II	Good water
100–200	III	Poor water
200–300	IV	Very Poor water
>300	V	Water unsuitable for drinking

4. Results and discussion

A. Water Chemistry

The chemical analyses of groundwater samples collected from the study area are presented in Table 4. Groundwater samples extracted from the Lower Eocene aquifer show pH values varying between 6.00 and 7.72. Electrical conductivity (EC) values in the Lower Eocene

aquifer vary from 2920 to 7010 µS/cm with an average of approximately 4307 µS/cm. The electrical conductivity values demonstrate that most drillings surpass the recommended quality of water standards based on the World Health Organization Standards (WHO, 2002). Electrical conductivity indicates the concentration of total dissolved solids and major ions in the water body (Deshpande and Aher, 2012). The large changes in

EC values are due to the long-term interaction of groundwater with rock and the effects of humans on the environment (Nazzal et al., 2014). Furthermore, the total dissolved solids (TDS) range from 2055 to 4590 mg/L with a mean value of 3087.44 mg/L. The main sources of total dissolved ions (TDS) in water are anions like carbonate, bicarbonate, chloride, and sulfate, as well as cations like calcium and magnesium (Houatmia et al., 2016). The calcium and magnesium concentrations range from 228 to 480 mg/L and 60 to 216 mg/L, respectively, with average values of 348.89 and 160.80 mg/L. Deposits of gypsum and carbonate break down to produce calcium and magnesium. Magnesium, in conjunction with calcium, is obtained from magnesium-rich carbonate formations such as dolomite. Magnesium is commonly found in evaporite rocks like carnallite ($KMgCl_3 \cdot 6(H_2O)$) and biotite. Potassium levels range from 11.30 to 22.82 mg/L, associated with the alteration of potassic clays. Potassium concentrations are higher in aquifers with thin clayey layers. Sodium concentrations range between 203.78 and 1246.14 mg/L, primarily attributed to evaporitic deposits and base exchange processes. The main source of chloride is the dissolution of natural ions dissolving, such as sylvite (KCl) and halite. Chloride levels range from 426 to 1420 mg/L. At levels between 425.86 and 1126.02 mg/L, sulphate ions (SO_4^{2-}) are linked to the production of evaporites, leaching, and the oxidation and dissolution of gypsum rocks.

Bicarbonate levels range from 200.08 to 275.72 mg/L because carbon dissolves in aquifers and carbonate weathering happens. Higher levels of Ca2+ and Mg^{2+} that come from calcite and dolomite buffering activities control the Total Hardness (TH) of groundwater.

Fig. 4 illustrates the total hardness (TH) of groundwater in the Lower Eocene aquifer. The values range from 122 to 203 °F. These results indicate that all examined wells exhibited "very hard water", a condition primarily influenced by the decomposition of carbonate and evaporite minerals.

Table 4: Statistical hydrogeochemical parameters

Wells	pH	TDS (mg/L)	EC (µS/cm)	TH (°F)	Ca (mg/L)	Mg (mg/L)	Na (mg/L)	K (mg/L)	Cl (mg/L)	SO_4 (mg/L)	HCO_3 (mg/L)	NO_3 (mg/L)
El-Hadjeb	6,99	3283	4620	122	260	136,80	772,80	18,81	1065	772,33	251,32	4,73
Beni Brahim	6,95	3323	5470	130	228	175,20	844,10	14,31	1278	555,79	222,04	5,14
Ain Benaoui	7,24	3624	5550	125	244	153,60	874,46	17,81	1420	664,06	244,00	5,25
Bordj Enos	7,2	2476	3640	145	480	60,00	518,88	16,31	745,5	425,86	224,48	3,98
Choucha	7,72	4590	7010	186	392	211,20	1246,14	18,81	1349	1126,02	241,56	2,86
Magloub	7,17	2055	2920	147	360	136,80	203,78	22,82	426	700,15	200,08	3,42
Hassi Zerari	7,02	2322	3090	180	360	216,00	213,90	11,80	426	880,60	207,40	2,67
Ain El karma	6,768	2622	3470	203	452	216,00	224,02	11,30	426	1046,62	241,56	1,54
Zaatcha	6	3492	3000	150	364	141,60	884,81	15,31	1313,5	490,83	275,72	4,80
Max	7.72	4590	7010	203	480	216	1246.14	22.82	1420	1126.02	275.72	5.25
Min	6	2055	2920	122	228	60	203.78	11.30	426	425.86	200.08	1.54
Mean	7.0	3087.44	4307.7	154.2	348.89	160.80	642.54	16.36	938.78	740.25	234.24	3.82

TDS: Total dissolved solids, EC: Electrical conductivity, TH: Hydrotimetric title, Min: Minimum, Max: Maximum

Sawyer and McCarty (1967) said that the overall hardness of the lower Eocene aquifer investigated at a temperature between 122 and 203°F, which suggests the water is exceptionally hard.

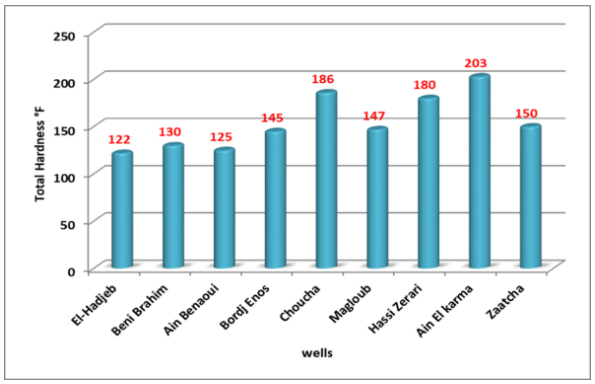


Fig. 4: Total Hardness (TH) of lower Eocene aquifer for the study area, May 2017.

B. Types of Water

The hydrochemical facies reveal the flow patterns of subterranean water and the influence of chemical processes within the geological environment (Bencer et al., 2016). Determined through the conversion of concentrations into meq/l and the classification of ions, these facies provide insights into flow and transport mechanisms in groundwater systems, offering valuable paleoenvironmental data (Hem, 1985; Glynn and Plummer, 2005; Ophori and Toth, 1989). The Piper diagram (Fig. 5) illustrates that the majority of water samples in the lower Eocene aquifer exhibit a Na-Cl water type.

C. Saturation Index (SI)

The minerals that make up rocks interact with groundwater in two ways: Secondary minerals form when the conditions are either thermodynamically stable or too full, while primary minerals dissolve and release ionic species into solution (Houatmia et al., 2016). Saturation indices (SI) are assessed using the geochemical modeling software PHREEQ C for the groundwater concerning mineral phases (Fig. 6). In this study, carbonate minerals exhibit varying degrees of saturation: dolomite often remains saturated, with an index ranging from +0.02 to +0.48, followed by calcite ranging from -0.08 to +0.28, and aragonite ranging from -0.22 to +0.14. In contrast, evaporite minerals show lower saturation indices than carbonate minerals. Gypsum shows saturation indices between -0.88 and -0.36, anhydrite ranges from -1.1 to -0.58, and halite is largely undersaturated (between -5.73 and -4.49). Groundwater is undersaturated with respect to evaporite minerals (halite, gypsum, and anhydrite), while carbonate minerals tend to precipitate mainly in the form of dolomite.

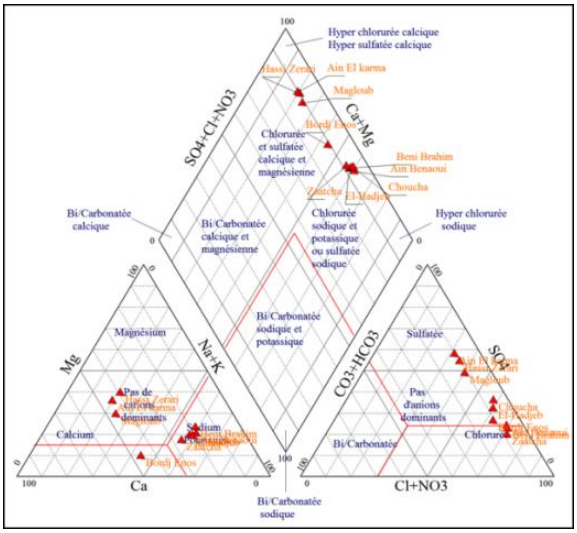


Fig.5: Piper diagram for groundwater samples from the study area, May 2017.

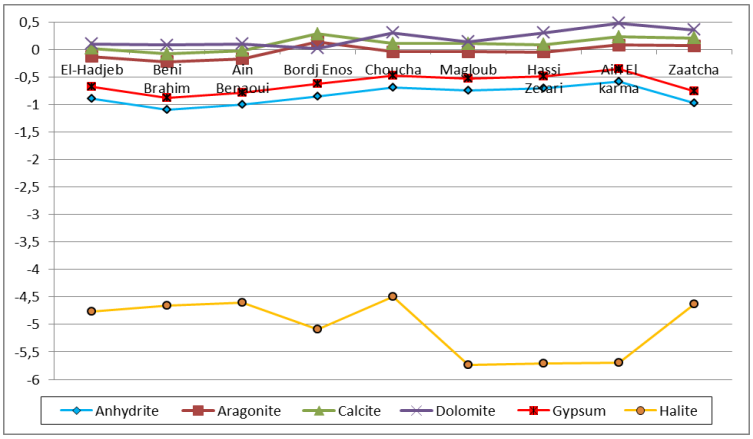


Fig.6: Mineral saturation indices for the Lower Eocene of the study area, May 2017.

D. Groundwater Geochemistry Regulation Mechanisms

Plotting Total Dissolved Solids (TDS) against the weight ratios of Na/(Na+Ca) and Cl/(Cl+HCO_3) according to Gibbs (1970) can provide information about the main natural processes affecting water chemistry, including fractional crystallization, weathering of rocks, and atmospheric precipitation and evaporation. Most of the samples of groundwater are found in the evaporation-influenced zone, as shown in Figure (7), suggesting that water irrigation return is a significant factor in the evaporation process.

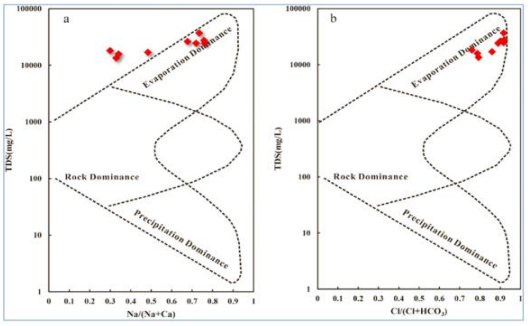


Fig.7: Gibbs plots explaining groundwater geochemical processes in the research area, May 2017.

E. Evaluation of the Potable Water Quality Index

According to the categorization by Ramakrishnaiah et al. (2009) and Ketata et al. (2011) as reported in Table (3), 33.33% of the samples are classified as belonging to the good water category (50-100), while 66.66% fall within the poor water category (100-200). The higher

levels of SO_4, K, Na, Ca, Mg, HCO_3, Cl, and TDS are linked to higher WQI values, which demonstrate that the groundwater in the studied area is of not good quality (Table 5).

Table 5: Water quality index calculation for drinking purposes.

Samples/parameters	El-Hadjeb	Beni Brahim	Ain Benaoui	Bordj Enos	Choucha	Magloub	Hassi Zerari	Ain El karma	Zaatcha
CE µs/cm	14,16	16,76	17	11,15	21,48	8,95	9,47	10,63	9,19
Ph	-0,22	-1,08	5,19	4,33	15,57	3,68	0,43	-5,02	-21,63
SO_4	3,41	2,45	2,93	1,88	4,97	3,09	3,89	4,62	2,17
NO_3	13,04	14,18	14,48	10,97	7,88	9,43	7,37	4,25	13,25
K	36,03	27,39	34,11	31,23	36,03	43,7	22,6	21,64	29,31
Na	5,33	5,82	6,03	3,58	8,59	1,4	1,47	1,54	6,1
Ca	12,75	11,18	11,96	23,53	19,22	17,65	17,65	22,16	17,84
Mg	15,09	19,32	16,94	6,62	23,3	15,09	23,82	23,82	15,62
HCO_3	4,81	4,25	4,67	4,3	4,63	3,83	3,97	4,63	5,28
Cl	4,70	5,64	6,27	3,29	5,95	1,88	1,88	1,88	5,8
TDS (mg/L)	2,51	2,55	2,78	1,9	3,52	1,57	1,78	2,01	2,67
TH (mg/L)	1,35	1,43	1,38	1,6	2,05	1,62	1,99	2,24	1,65
Overall WQI	112,95	109,9	123,74	104,37	153,17	111,89	96,32	94,41	87,26

5. Conclusion

To evaluate drinking water quality and identify hydrogeochemical processes, an investigation into the Lower Eocene aquifer in the El Hadjeb region was conducted. The groundwater from drinking wells is very hard, according to the total hardness (TH) analysis. Hydrochemical analysis indicated a Na-Cl water type, influenced by the study area's geology. The saturation index showed groundwater to be undersaturated with evaporite minerals like halite, gypsum, and anhydrite, with carbonate minerals primarily precipitating as dolomite. The Gibbs plot suggested that groundwater falls within the evaporation zone, likely due to irrigation return water causing evaporation. Overall, the calculated WQI values indicate that groundwater quality is generally unsuitable for drinking without treatment in the designated area.

6. Acknowledgments

The authors express gratitude for the support of the General Directorate for Scientific Research and Technological Development (DGRSDT) and the anonymous reviewers, whose perceptive comments greatly improved the quality of this work.

7. Conflict of Interest

The authors declare that they have no conflict of interest.

8. Funding Statement

Research received no external funding.

9. Author Contributions

Warda Chaib: Contributed to the conceptualization, methodology, data collection and analysis, interpretation, preparation of figures and tables, manuscript writing and revision, and overall coordination of the study.

Farida Bettiche: Contributed to the development of the methodology.

Nora Salemkour: Contributed to field data collection and sampling.

Asma Rezeg: Contributed to data analysis and interpretation.

Halima Mancer: Contributed to field data collection and sampling.

Khadidja Bouzid: Contributed to laboratory analyses.

Nora Bouchahm: Contributed to manuscript revision.

10. References

Al-Shaibani, A.M., 2008. Hydrogeology and hydrochemistry of a shallow alluvial aquifer, western Saudi Arabia. Hydrogeology Journal, 16, pp. 155–165.

Apodaca, L.E., Bails, J. B., and Smith, C. M., 2002. Water quality in shallow alluvial aquifers, upper Colorado River Basin, Colorado, 1997 1. JAWRA Journal of the American Water Resources Association, 38(1), pp. 133–149.

Aragaw, T.T. and Gnanachandrasamy, G., 2021. Evaluation of groundwater quality for drinking and irrigation purposes using GIS-based water quality index in urban area of Abaya-Chemo sub-basin of Great Rift Valley, Ethiopia. Applied Water Science, 11(9), 148.

Bencer, S., Boudoukha, A. and Mouni, L., 2016. Multivariate statistical analysis of the groundwater of Ain Djacer area (Eastern Algeria). Arabian Journal of Geosciences, 9, pp. 1–10.

Bouslah, S., Djemili, L. and Houichi, L., 2017. Water quality index assessment of Koudiat Medouar

Reservoir, northeast Algeria using weighted arithmetic index method. Journal of Water and Land Development, 35(1), 221.

Brown, R.M., McClelland, N.I., Deininger, R.A. and Tozer, R. G., 1970. A water quality index – do we dare. Water and Sewage Works, 117(10).

Chung, S., Venkatramanan, S., Kim, T., Kim, D. and Ramkumar, T., 2015. Influence of hydrogeochemical processes and assessment of suitability for groundwater uses in Busan City, Korea. Environment, Development and Sustainability, 17, 423–441.

Gibbs, R.J., 1970. Mechanisms controlling world water chemistry. Science, 170(3962), pp. 1088–1090.

Glynn, P.D. and Plummer, L. N., 2005. Geochemistry and the understanding of groundwater systems. Hydrogeology Journal, 13, 263–287.

He, X., Li, P., Ji, Y., Wang, Y., Su, Z. and Elumalai, V., 2020. Groundwater arsenic and fluoride and associated arsenicosis and fluorosis in China: occurrence, distribution and management. Exposure and Health, 12(3), 355–368.

Hem, J. D., 1985. Study and interpretation of the chemical characteristics of natural water (Vol. 2254). Department of the Interior, US Geological Survey.

Houatmia, F., Azouzi, R., Charef, A. and Bédir, M., 2016. Assessment of groundwater quality for irrigation and drinking purposes and identification of hydrogeochemical mechanisms evolution in Northeastern Tunisia. Environmental Earth Sciences, 75(9), 746.

Kada, H. and Demdoum, A., 2020. Assessment of the Hauterivian groundwater quality in zinc mining area for drinking and irrigation uses: Case of Chaabet el Hamra, Algeria. Journal of Water and Land Development, 46, pp. 131–139.

Ketata, M., Gueddari, M. and Bouhlila, R., 2011. Use of geographical information system and water quality index to assess groundwater quality in El Khairat deep aquifer (Enfidha, Tunisian Shelf). Iranica Journal of Energy and Environment, 2(2), pp. 133–144.

Lezzaik, K., Milewski, A. and Mullen, J., 2018. The groundwater risk index: Development and application in the Middle East and North Africa region. Science of the Total Environment, 628, pp. 1149–1164.

Li, P., He, X. and Guo, W., 2019. Spatial groundwater quality and potential health risks due to nitrate ingestion through drinking water: a case study in Yan'an City on the Loess Plateau of northwest China. Human and Ecological Risk Assessment: An International Journal, 25(1–2), pp. 11–31.

Li, X.Y., Wu, H., Qian, H. and Gao, Y., 2018. Groundwater chemistry regulated by hydrochemical processes and geological structures: a case study in Tongchuan, China.

Li, Y., Li, P., Cui, X. and He, S., 2021. Groundwater quality, health risk, and major influencing factors in the lower Beiluo River watershed of northwest China. Human and Ecological Risk Assessment: An International Journal, 27(7), pp. 1987–2013.

Mokadem, N., Hamed, Y., Hfaid, M. and Dhia, H. B., 2015. Hydrogeochemical and isotope evidence of groundwater evolution in El Guettar Oasis area, Southwest Tunisia. Carbonates and Evaporites, 30, pp. 417–437.

Nazzal, Y., Ahmed, I., Al-Arifi, N. S., Ghrefat, H., Zaidi, F. K., El-Waheidi, M. M. and Zumlot, T., 2014. A pragmatic approach to study the groundwater quality suitability for domestic and agricultural usage, Saq aquifer, northwest of Saudi Arabia. Environmental Monitoring and Assessment, 186(8), pp. 4655–4667. https://doi.org/10.1007/s10661-014-3728-3

Ophori, D. and Toth, J., 1989. Patterns of groundwater chemistry, Ross Creek Basin, Alberta, Canada. Groundwater, 27(1), pp. 20–26.

Ramakrishnaiah, C., Sadashivaiah, C. and Ranganna, G., 2009. Assessment of water quality index for the groundwater in Tumkur Taluk, Karnataka State, India. E-Journal of Chemistry, 6(2), pp. 523–530.

Sawyer, C. and McCarty, D., 1967. Chemistry of sanitary engineers. McGraw-Hill, New York, 518 P.

Subramani, T., Elango, L. and Damodarasamy, S., 2005. Groundwater quality and its suitability for drinking and agricultural use in Chithar River Basin, Tamil Nadu, India. Environmental Geology, 47, pp. 1099–1110.

Tiwari, T. and Mishra, M., 1985. A preliminary assignment of water quality index of major Indian rivers. Indian Journal of Environmental Protection, 5(4), pp. 276–279.

Tripathy, J. and Sahu, K., 2005. Seasonal hydrochemistry of groundwater in the Barrier Spit system of the Chilika Lagoon, India. Journal of Environmental Hydrology, 13.

Umar, A., Umar, R. and Ahmad, M., 2001. Hydrogeological and hydrochemical framework of regional aquifer system in Kali-Ganga sub-basin, India. Environmental Geology, 40(4), pp. 602–611.

WHO (World Health Organization), 2002. Guidelines for drinking-water quality (2nd ed., Addendum). Geneva, Switzerland: World Health Organization.

WHO (World Health Organization), 2004. Guidelines for drinking-water quality (3rd ed., Vol. 1: Recommendations). Geneva, Switzerland: World Health Organization.

WHO (World Health Organization), 2006. Guidelines for drinking-water quality (3rd ed., First Addendum to Volume 1: Recommendations). Geneva, Switzerland: World Health Organization.

WHO (World Health Organization), 2011. Guidelines for drinking-water quality (4th ed.). Geneva, Switzerland: World Health Organization.

Ziani, D., Abderrahmane, B., Boumazbeur, A. and Benaabidate, L., 2017. Water quality assessment for drinking and irrigation using major ions chemistry in the Semiarid Region: case of Djacer Spring, Algeria. Asian Journal of Earth Sciences, 10(1), pp. 9–21.

Iraqi National Journal of Earth Science, Vol. 26 No.04, 2026 (283-292)

Iraqi National Journal of Earth Science

www.earth.uomosul.edu.iq

تقييم مؤشر جودة مياه الشرب في المناطق الجافة: تحليل منطقة الحاجب بولاية بسكرة، جنوب شرقي الجزائر

وردة شايب[1*] ، فريدة بتيش[1] ، نورة سالم كور[1] ، أسماء رزاق[1] ،

حليمة منصر[1] ، خديجة بوزيد [1] ، نورة بوشحم [1]

rezegasma@gmail.com salemkour_bio@yahoo.fr farida.bettiche@gmail.com wardalita1@yahoo.fr

bouchahm_nora@yahoo.fr khadidja_07@hotmail.com mancerhalima@yahoo.fr

[1] مركز البحث العلمي و التقني للمناطق القاحلة ، بسكرة ، الجزائر.

** الباحث المراسل.*

تاريخ الاستلام: 05 آب 2025 تاريخ المراجعة: 20 أيلول 2025 تاريخ القبول: 09 تشرين الأول 2025

تاريخ النشر الالكتروني: 01 تشرين الأول 2026

الملخص

تهدف هذه الدراسة إلى تحليل العمليات الهيدروجيوكيميائية والتباينات الإقليمية في جودة المياه الجوفية ضمن طبقة الأيوسين السفلى في منطقة الحاجب الواقعة جنوب شرقي الجزائر. ولتحقيق هذا الهدف، تم إجراء تحاليل مختبرية شملت قياس التوصيلية الكهربائية (EC) ، ودرجة الحموضة (pH) ، ودرجة الحرارة(T) ، والمواد الصلبة الذائبة الكلية (TDS) ، إلى جانب تحديد تراكيز الأيونات الرئيسة، وهي: الصوديوم (Na^+) ، البوتاسيوم (K^+) ، الكالسيوم(Ca^{2+}) ، المغنيسيوم (Mg^{2+}) ، البيكربونات (HCO_3^-) ، الكلوريد (Cl^-) ، والكبريتات (SO_4^{2-}) . تُعد هذه الطبقة الجوفية مصدرًا مائيًا بالغ الأهمية في المناطق شبه الجافة والجافة، وقد أظهرت النتائج أن السحنة الهيدروكيميائية السائدة للمياه الجوفية هي كلوريد الصوديوم (Na-Cl)، معادن المتبخرات كانت تحت الاشباع وجزء صغير من معدن الدولومايت كان في حالة ترسيب، وظهور محدود لترسيب معدن الدولومايت. كما أوضحت مخططات جيبس أن العمليات الجيوكيميائية الرئيسة المتحكمة في جودة المياه هي التبخر وتفاعلات المياه مع الصخور. من خلال حساب مؤشر جودة المياه (WQI) ، وُجد أن القيم تراوحت ما بين 87.26 و153، حيث تنتمي 33.33٪ من العينات إلى فئة "جيدة"، بينما تقع 66.66٪ منها ضمن فئة "رديئة". وتشير القيم المرتفعة للمؤشر إلى تدهور جودة المياه، ويرتبط ذلك بارتفاع تراكيز SO_4^{2-} ، K^+، Na^+، Ca^{2+}، Mg^{2+}، HCO_3^-، Cl^-، و TDS. تؤكد هذه النتائج على أهمية تطبيق سياسات فعالة لإدارة الخزانات الجوفية الهشة من أجل ضمان استدامة هذا المورد الحيوي في ظل الظروف المناخية القاسية التي تميّز المنطقة.

الكلمات المفتاحية:

المياه الجوفية، طبقة الأيوسين السفلى، مؤشر جودة المياه، الحاجب .

DOI: 10.33899/injes.v26i4.61113, ©Authors, 2026, College of Science, University of Mosul.

This is an open-access article under the CC BY 4.0 license (http://creativecommons.org/licenses/by/4.0/)

Iraqi National Journal of Earth Science, Vol.,26 No.04, 2026 (293-308)

Iraqi National Journal of Earth Science

www.earth.uomosul.edu.iq

Microfacies Analysis and Depositional Environment of the Ibrahim, Azkand and Anah Formations in Selected Oil Fields of Northern Iraq.

Abdulla Ahmed Abid [1*], Faris Nejres Hassan Al Jubory [1], Saad Ahmed Mahmood [2]

abdulla.ahmed.a@st.tu.edu.iq faris77@tu.edu.iq saadhamdani71@gmail.com

[1] *Department of Applied Geology, College of Science, Tikrit University, Tikrit, Iraq.*

[2] *Department of Geology, North Oil Company, Kirkuk, Iraq.*

* *Correspondence author.*

Received: 06 July 2025 Received in revised form: 29 August 2025 Accepted: 24 September 2025
Available online: 01 October 2026

Abstract

This study focuses on the analysis of the Ibrahim, Azkand, and Anah formations within three major oil fields (X, Y, and Z) located in the Low Folded Zone of Iraq. Integrated microfacies and stratigraphic interpretations reveal a regressive depositional succession spanning the late Oligocene to early Miocene. The lower and middle intervals of the Ibrahim Formation are characterized by microfacies SMF-3, deposited in the deeper sector of Zone FZ-3, interpreted as a toe-of-slope environment under low-energy, distal slope conditions. The upper part of the Ibrahim Formation is dominated by microfacies SMF-4, reflecting a distinct shallowing into a shallower platform setting within the same zone (FZ-3) and marking the onset of a marine regression. The overlying Azkand Formation records continued platform progradation, with its lower section represented by microfacies SMF-5, indicative of an upper slope environment (Zone FZ-4), and its upper part is defined by microfacies SMF-7, characteristic of a high-energy reefal system (Zone FZ-5). The Anah Formation begins with microfacies SMF-8 in its lower part, deposited in an open marine platform interior (Zone FZ-7), and evolves upward into microfacies SMF-18 in the middle and upper sections, representing a restricted platform interior (Zone FZ-8). Gamma-ray logs, which show a decreasing radioactivity trend and confirm a shallowing-upward trend of the depositional environment, corroborate this regressive succession. The depocenter lies near field Z, while field Y occupies a basinal position. The paleo-shoreline extended northwest–southeast across Iraq, aligned through fields X and Z, delineating a rimmed carbonate platform with implications for reservoir characterization and exploration.

Keywords:

Depositional Environment, Microfacies, Oligocene, Kirkuk group, Iraq.

DOI: 10.33899/injes.v26i4.61124, ©Authors, 2026, College of Science, University of Mosul.

This is an open-access article under the CC BY 4.0 license (http://creativecommons.org/licenses/by/4.0/).

==========

1. Introduction

The Ibrahim, Azkand, and Anah formations are distinguished by their substantial oil production capabilities across several fields, establishing them as critical hydrocarbon reservoirs with outstanding petrophysical features (Jassim and Goff, 2006). Although the studied formations have been the subject of numerous investigations, most previous studies have been localized and focused on individual units or isolated outcrops. This study offers a unique regional synthesis by integrating microfacies and well-log data from the Anah, Azkand, and Ibrahim formations across multiple oil fields, demonstrating their deposition within a single and laterally continuous basin during the same geological interval. Unlike previous localized studies confined to individual formations or single fields, this cross-field, multi-formation approach reveals consistent basin-scale facies trends and paleoenvironmental patterns essential for reliable reservoir prediction. The Anah and Azkand formations, in particular, exhibit strong reservoir properties (porosity, permeability, and lithological uniformity), yet their lateral continuity and spatial quality distribution across fields remain poorly documented. By systematically correlating these units across the basin and linking facies to

depositional settings, this research provides a predictive sedimentological framework to target undrilled prospects and optimize field development, directly enhancing exploration efficiency and reducing drilling uncertainty.

The Ibrahim, Azkand, and Anah formations are deposited during the late Oligocene age as a third depositional cycle (Bellen et al., 1959) or second cycle according to Jassim and Goff (2006), while others consider them to be deposits of early Miocene age (Ighwan and Al-Rahman, 2009). Ditmar (1971) revised the three-fold classification of the Oligocene sedimentary cycle, redefining it into two distinct subcycles, as cited by Al-Shareeda et al. (2025). The Oligocene sequence in Iraq consists of nine formations called the Kirkuk Group, which is divided into the early, middle, and late Oligocene complex reefal system (back-reef, reef, and fore-reef). The late Oligocene includes the Anah, Azkand, and Ibrahim formations (Al-Hashimi and Amer, 1986).

Numerous research studies have addressed the depositional environments of the Ibrahim, Azkand, and Anah formations across Iraq. Karim et al. (2012) studied Oligocene carbonate succession exposed southeast of Derbandikhan and northeast of Kalar within the Sharwaldir anticline. The succession includes the Baba and Anah formations and a transitional zone between them, with depositional environments interpreted as fore-reef (lower), reef-crest (middle), and back-reef (upper). Lawa and Ghafur (2015) documented a progressive facies transition within the Oligocene Kirkuk Group in the Kurdistan Foreland Basin from inner ramp to outer ramp and finally to deep and planktonic-rich basinal deposits reflecting a deepening-upward depositional trend. Ghafor and Ahmad (2019) interpreted the Anah Formation in the Sangaw area (Sulaimaniyah) as deposited in a middle to inner carbonate ramp setting (40–80 m depth) under tropical and oligotrophic conditions. Abdulrahman and Awadh (2021) identified a deep shelf to lower slope environment for the Ibrahim Formation in Zurbatiya with evidence of significant meteoric and burial diagenesis. Mahdi et al. (2022) recognized six microfacies in the Khabaz Field reflecting a transition from back-reef to slope environments within the Azkand and Anah formations. Ghafor et al. (2023) confirmed a shallow euphotic and subtropical ramp setting for the Anah Formation in the Darzila section. Mohammed and Aljibouri (2023) assigned these formations in the Anah area to distinct reef, fore-reef, and back-reef paleoenvironments. Abood and Al-Zaidy (2024) documented six facies' associations in the Fallujah and Melh-Tharthar oilfields, indicating a prograding carbonate platform system. Most recently, Majeed et al. (2025) distinguished the Anah, Azkand, Ibrahim, and Palani formations in the Khabaz and Kirkuk fields through detailed microfacies analysis, refining their environmental and stratigraphic correlations.

2. Location

The study area is located in the southern and southeastern parts of the Kirkuk oil field, covering wells X1 and X2 in Field X, Y in Field Y, and Z in Field Z. The study area includes three important oilfields (X, Y, and Z). They are sited in northeastern Iraq within the Unstable Shelf in the low Folded Zone (Fouad, 2010). Field X is a subsurface and asymmetrical anticline located approximately 12 km southwest of Kirkuk City, extending in a northwest–southeast direction. The structure measures about 10 km in length and 5 km in width. Field Y is one of the major producing fields in northern Iraq. It consists of a long, elongated, and asymmetrical anticline trending northwest–southeast and situated to the east of Kirkuk. The field extends for nearly 30 km in length and 4.5 km in width. Field Z lies approximately 35 km southeast of Kirkuk and runs parallel to Field Y and is located about 14 km away from it. It is characterized by an asymmetrical longitudinal fold with a length of about 33 km and a width of 4 km (Fig. 1). The aims of the study are to characterize the microfacies types and to interpret their depositional environments using petrographic analysis and established microfacies models. Moreover, to describe vertical contacts between each formation and its immediate overlying and underlying units to determine whether they are conformable or unconformable. As well as to trace lateral lithological variations across wells and fields to assess spatial facies continuity or abrupt transitions, and to investigate potential controls on observed thickness differences across the study area. Also, to investigate and assess the roles of tectonic activity and to relate it to environmental and paleogeographic setting. Lastly, to reconstruct the paleo-shoreline position to predict the distribution

of potential reservoir facies such as grain-dominated and reefal carbonates.

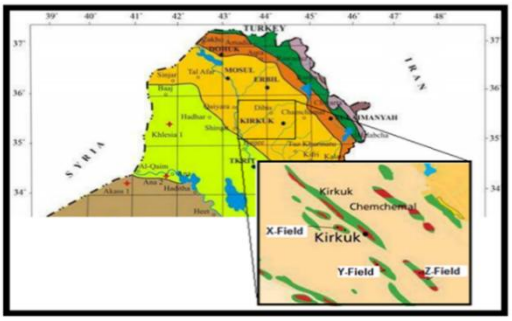


Fig. 1: Location map of the study area (modified from Fouad, 2010)

3. Geological Setting

The Anah, Azkand and Ibrahim formations, along with the Kirkuk Group, are assigned to the Oligocene depositional sequence (Bellen et al., 1959). The paleogeography and depositional history of the Oligocene follow quite closely the pattern set in Middle–Upper Eocene time. The northeastern margin of the depositional area lay much to the southwest of the position of the corresponding boundary of the Middle–Upper Eocene stages. Upper Oligocene sediments were deposited after regression and have a much smaller areal distribution than those of the Lower and Middle Oligocene (Dunnington, 2005). The Oligocene sediments in Iraq have a relatively restricted area of distribution and are reduced in thickness too. The underlying and overlying contact formations of the Oligocene are separated by a break and unconformity. A characteristic feature of the Oligocene is the absence of the molasse sediments in the foredeep (Buday, 1980). This sequence has commenced at the end of the Eocene, coinciding with tectonic adjustments that narrowed the main intraplate basin. These adjustments were driven by the westward tilting of the Arabian Plate and the uplift of the High Folded Zone during this period. The western shoreline migrated eastward toward the present-day Euphrates River, while the eastern shoreline retreated to the southwestern margin of the Butmah–Chemchemal Subzone within the Foothill Zone. The Neo-Tethys Ocean had become a narrow seaway, characterized by mixed siliciclastic and carbonate deposition. The Oligocene basin extended across several structural zones, including the Mesopotamian Zone, Makhul–Hemrin Subzone, Jazira Subzone, and the northern margin of the Rutba Subzone. Notably, areas such as the Salman Zone and parts of the Euphrates and Zubair subzones underwent uplift during this period. As shown in Fig. 2, the basin was relatively narrow, with thick fringing reefs developing along both the western and eastern margins. In contrast, the central part of the basin was dominated by thin marly deposits (Jassim and Goff, 2006).

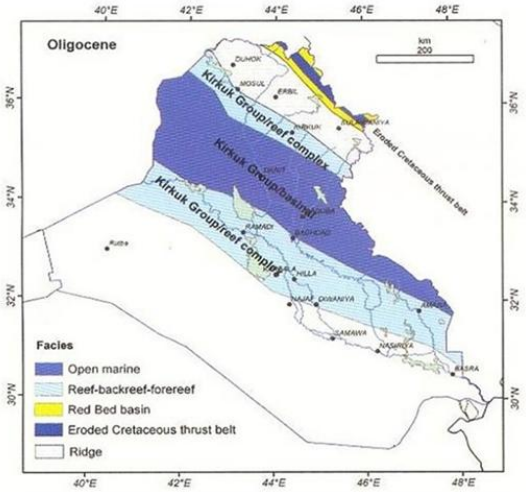


Fig. 2: Oligocene paleogeography (Jassim and Goff, 2006).

4. Methodology

Data (geological studies, logs, cores, cuttings, final well reports, and well file reports) are gathered for the four oil wells that have the most thin sections: two from the X oilfield and one from each of Y and Z.

Using a petrographic microscope, the lithology of the Ibrahim, Azkand, and Anah formations in wells X1 and X2 from field X, well Y from field Y, and well Z from field Z is determined using rock cutting samples accessible at the Geology Department, North Oil Company.

More than 250 thin sections of core and cuttings are used in petrographic analysis from the chosen wells. The description is achieved in the Geological Department Laboratory of Iraqi North Oil Company using a transmitted light microscope. The petrographic and textural properties are based on Dunham's (1962) classification.

The both Software's, Petrel 16 and Golden Grapher 16, are utilized in order to draw column stratigraphy, well correlation, and a paleo-depositional environment model for the studied formations.

Finally, a comparison between well log readings and microfacies analysis is conducted to enhance the accuracy of facies analysis in identifying the depositional environments.

5. Results and Discussion

The transition into the Early Miocene was marked by the Savian tectonic movement, which significantly affected the Zagros suture zone. This event is distinguished by the uplift of the Balambo–Tanjero trough (Abdulrahman and Awadh, 2021). The Oligocene stratigraphy is subdivided into nine formations grouped into three sequences interpreted as Early, Middle and Late Oligocene based on relative stratigraphic position rather than fossil evidence. These sequences exhibit lateral facies transitions from basinal to reef and back-reef environments (Bellen et al., 1959). Anah, Azkand and Ibrahim formations age back to the Late Oligocene to Early Miocene epochs as confirmed by Abid (1997); Ghafor and Ahmad (2019) and Abdulrahman and Awadh (2021) through detailed stratigraphic and lithological analysis.

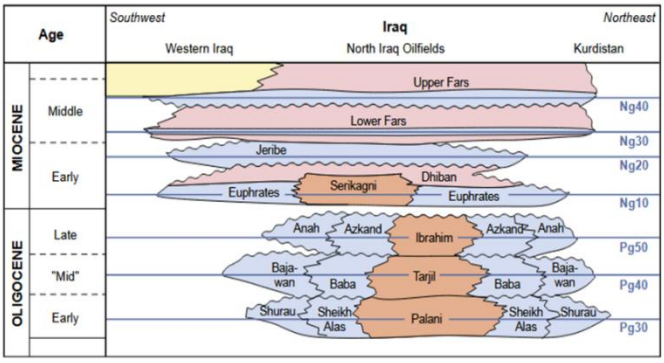


Fig. 3: Sequence stratigraphy of the mid-Miocene to Oligocene of Iraq after Sharland et al. (2004).

5.1. Lithostratigraphy

The Ibrahim Formation was initially characterized by Bellen et al. (1959) in the Ibrahim-1 well. It primarily consists of clayey limestone with glauconite and pyrite, and its lower and upper boundaries are unconformable with the Jaddala and Fatha formations respectively. In the present study, it appears that the Ibrahim Formation comprises partially dolomitized and recrystallized limestone interbedded with light brown marly limestone bands particularly in its lower parts.

According to NOC (2013) and based on the study result, the formation's thickness varied significantly across the study fields: approximately 50 meters in Field X, about 20 meters in Field Y, and 213 meters in Field Z. In both Fields X and Z, the upper boundary of the Ibrahim Formation is conformable with the Azkand Formation, whereas its lower contact is unconformable with the Tarjil Formation, but in Field Y, the lower boundary of the formation is unconformable with the underlying Tarjil Formation, while its upper boundary is conformable with the overlying basal anhydrite layer (NOC, 1988).

The type locality of the Azkand Formation is situated approximately 5 km northeast of Azkand village on the southern dome of the Qarah Chauq structure. It was first described by Bellen (1956, cited in Bellen et al., 1959) as dolomitic limestone with high porosity and interpreted to have been deposited in a fore-reef environment.

Based on the cutting description, gamma ray, sonic and FD-CNL logs with final well reports, it appears that the Formation consists of porous and oil-saturated dolomitic rocks with a coarse-grained, brown-colored texture and substantial porosity. These rocks interfinger with white and fractured limestone units. It is characterized by the presence of coral reef fragments in its middle sections and anhydrite nodules in its lower parts. The thickness of the formation is approximately 70 meters in Field X and up to 120 meters in Field Z, whereas the formation was not encountered in Field Y. In Fields X and Z, the formation is conformably bounded by the underlying Ibrahim Formation and the overlying Anah Formation.

The type locality of Anah Formation is located 15 km east of Nahiya, along the western bank of the Euphrates River. It was initially described by Bellen (1956, referenced in Bellen et al., 1959) as grey and coralline limestone interpreted to have been deposited in a back-reef setting. In its type section, the lower boundary is conformable with the underlying Azkand Formation, while the upper contact is marked by an unconformity with the overlying Euphrates Formation (Al-Sayyab and Al-Hamdani, 1990). The Anah Formation is described as consisting of massive and recrystallized limestone. Specifically, it comprises white and fine-crystalline porcelain limestone interbedded with dolomitic limestone rocks exhibiting a fine to medium texture. The formation's thickness reaches 10 meters in well Z1 and ranges between 16 and 19 meters in the wells of Field X. The Anah Formation is absent in Field

Y. In Field X, the base of the formation is in conformable contact with the underlying Azkand Formation, whereas the upper boundary is marked by a distinct unconformity beneath the Jeribe Formation. In Field Z, the Azkand Formation conforms to the Anah Formation lower limit, but they do not conform at the top boundary with the Euphrates Formation.

5.2. Microfacies Analyses

Microfacies analysis of carbonate rocks is implemented for understanding basin evolution and stratigraphic correlations (Scholle and Ulmer-Scholle, 2003). It is a detailed description and interpretation serve to infer depositional environments and interpret sedimentary depositional processes and diagenetic histories (Flügel and Munnecke, 2010; Tucker, 2011). Microfacies analysis involves the determination of microscopic lithofacies, which are defined previously by distinct assemblages of constituents (grains, textural attributes, and diagenetic alterations) identified through thin-section examination. The classification system of Dunham (1962), with its modifications by Embry and Klovan (1971) was applied in order to determine the depositional environments (physical, chemical and biological conditions under which sediments were deposited like shallow marine, reef, fluvial) for each formation within the study area. The identified facies (distinct rock units characterized by specific textures, compositions, and fossil content determined through petrographic analysis) are utilized and compared with the established standard facies models (Wilson, 1975; and Flügel, 2010).

5.2.1 Microfacies Analysis of Ibrahim Formation

1- Planktonic Foraminiferal Wackestone Microfacies (Ib1).

These facies are identified in the lower and middle parts of the Ibrahim Formation in the X and Z fields, whereas it constitutes the entire section of the formation in the Y field. The skeletal grains in these facies account 10-40% of its components and include the following planktonic foraminiferal genera: Globigerina, Globigerinoides, and Globorotalia. Additionally, the facies contain a minor proportion of benthic foraminifera such as Lepidocyclina, Amphistegina, Textularia sp., and Rotalia, along with scattered echinoderm fragments. The matrix varies between microcrystalline (micrite) in some intervals and fine sparry cement in others and some non-carbonate particles such as pyrite and rare glauconite. These facies have undergone diagenetic alterations, including dissolution, which has resulted in locally developed moldic porosity, as well as neomorphism that transformed some grains into a xenotopic fabric in certain areas. The intergranular pores are predominantly filled by drusy calcite cement, which also precipitated within some of the chambers of the planktonic foraminifera; fracture porosity filled with calcite is observed, particularly in sections from the Y field. The presence of benthic foraminifera reflects a warm temperate environment with water temperatures ranging between 14–26 °C (Murray, cited in. Rahman, 2007). This facies corresponds to the standard facies SMF-3 fora, and it falls within the deeper parts of the FZ-3 biofacies zone according to Wilson (1975) and Flügel (2010), indicating a Deep shelf - toe-of-slope depositional environment (Plate A: 1, 3, 4, 5, 6, 7, 8, 9).

2- Microbreccia, Bio-Lithoclastic Packstone Microfacies (Ib2).

This facies represents the upper part of the Ibrahim Formation in the X and Z fields, characterized by a color range from brown to grayish. The skeletal grains constitute 40–60% of the total components in these facies, and it is composed of relatively small planktonic foraminifera, including various genera such as Globigerina, Globigerinoides, and Globorotalia. These taxa are commonly associated with open marine, mid- to outer-shelf environments (Perch-Nielsen et al., 1985). In addition, the facies contain fine-grained breccias, debrites, and lithoclast grains with bioclasts including fragments of red algae, echinoderms, Amphistegina and Rotalia.

Lepidocyclina indicate a mixed biogenic input derived from both shallow-water and deeper marine environments. The matrix is primarily composed of micrite and fine sparite with minor amounts of quartz and silt-sized siliciclastic grains, suggesting limited terrigenous influence within the carbonate depositional system. These facies have undergone significant diagenetic modifications, particularly dolomitization, which is evident from the presence of fine-crystalline dolomite and micro-sucrose textures. Some dolomite rhombs

appear subhedral to euhedral. Additionally, dissolution processes have resulted in vuggy porosity, partially filled by anhydrite or calcite cements of localized post-depositional origin. Locally developed pyrite and minor glauconite are also present, indicating episodes of reducing conditions during early diagenesis. According to Schlager (2005), turbidites or debris-flow deposits are typically found in the toe-of-slope setting, representing reworked mixtures of shallow-water bioclasts and deeper marine benthic and planktonic sediments. Based on the above observations, this facies closely resembles the standard facies MFS-4, which belongs to facies zone FZ-3 as defined by Wilson (1975) and Fluügel (2010), commonly associated with the Deep shelf - toe-of-slope environment in a carbonate platform system (Plate A: 10, 11, 12).

5.2.2 Microfacies Analysis of Azkand Formation.

1- Larger foraminifera lime Packstone microfacies (Az1)

These facies are observed in the lower part of the Azkand Formation in the X and Z fields. Skeletal grains constitute approximately 50% of the facies components and are represented by large foraminiferal genera such as Lepidocyclina, Amphistegina, Operculina, and Miogypsinoides. In addition, red algae, echinoderm fragments and mollusks are identified. The matrix consists of fine spar and sparry calcite with the presence of pyrite grains within the matrix. The facies have been affected by diagenetic processes such as dolomitization, moldic porosity development, and micritization. Several types of porosity are recognized, including moldic porosity, intraparticle porosity, and vuggy porosity. The presence of large benthic foraminifera such as Miogypsina sp., coralline algae, other bioclasts, and skeletal echinoderms suggests a moderate- to high-energy depositional environment located on the upper part of a carbonate platform slope, at water depths less than 50 meters, under moderate salinity conditions (Geel, 2000), in these facies corresponding to the standard Wilson (1975) and Flügel (2010) SMF-5 facies in the FZ-4 slope environment. This interpretation is also consistent with the findings of Reijmer (2021) (Plate B: 9, 10, 11, 12).

2- Lime coral bindston-framestone lithofacies (Az2).

This microfacies represents the upper part of the Azkand Formation in the X and Z fields, which consists mainly of the massive coral genus Colpophyllia along with various algal species, and it includes some benthic foraminifera such as Rotalia and Amphistegina along with some mollusks and echinoderm fragments. The rock debris includes Corallina bioclasts. These facies have been affected by dolomitization, recrystallization, and chemical compaction (pressure solution). Porosity of various types has been observed, in addition to the presence of cement. The faunal diversity and presence of algae indicate a shallow and warm marine environment according to Reading (2009). Moreover, the occurrence of the genera Amphistigina and Operculina (Plate B: 2,5) suggests a reef environment of moderate to low energy conditions (Boudaugher-Fadel, 2018). Furthermore, this interpretation aligns with the findings of Pomar et al. (1996).

Accordingly, and based on the classifications of Wilson (1975) and Flügel (2010), this faunal assemblage corresponds to the standard microfacies SMF-7 within the Reef biofacies zone FZ-5 (Plate B: 1, 6, 7).

5.2.3 Microfacies Analysis of Anah Formation:

1- Fossiliferous Lime Wackestone microfacies (An1)

This facies occurs in the lower part of the Anah Formation within both the X and Z fields. It is characterized by a gray color and medium hardness. Skeletal grains constitute 10-40% of the total components in these facies. Fossils identified within these facies include Austrolina, Archaias, Purgo, Miogypsinoids, and Peneroplis. In addition, red and green algal fragments, mollusk shells, and coral pieces are also present. The facies have undergone several diagenetic processes, including dolomitization, dissolution, and recrystallization. Moldic porosity is observed, indicating post-depositional leaching of skeletal components. According to Pomar et al. (1996) and Youssef et al. (2021), this facies represents an outer lagoon environment. Furthermore, it closely resembles the standard microfacies SMF-8; the presence of calcareous algae supports the attribution to the FZ-

7 zone representing an open marine interior platform environment as defined by Wilson (1975) and supported by Flügel (2010) (Plate A:13, 15 and Plate B: 3, 8, 14).

2- Benthic foraminifera lime Grainstone - Packstone microfacies (An2)

These facies occur in the middle and upper parts of the Anah Formation within the X Field, in the Z Field area. They interfinger with other facies constituting the formation throughout the section where the formation is exposed. The dominant skeletal components are benthic foraminifera, particularly Miliolid, Peneroplis, and Dendritina (Plate B: 13). The matrix consists of micrite and fine-crystalline spar. These facies have been affected by various diagenetic processes such as dolomitization, recrystallization, and cementation. Porosity is moderate and mainly intergranular in nature. According to Beavington-Penney and Racey (2004), Peneroplis are commonly found in shallow marine environments less than 30 meters deep. Additionally, Geel (2000) indicated that low diversity among miliolids and other benthic foraminifera suggests a very shallow, restricted, and possibly hypersaline environment, as cited in Al-Jwaini (2015) based on Pomar's classification (Pomar et al., 1996), which divides the back-reef lagoon into an inner zone close to the shore and an outer zone farther from the coast but closer to the reef tract environment. Furthermore, following Wilson (1975) and Flügel (2010), this facies closely resembles the standard microfacies SMF-18. The presence of abundant miliolids and foraminifera exhibiting tolerance to high-salinity conditions suggests deposition in a restricted and hypersaline environment. This interpretation aligns with the microfacies criteria of Flügel (2010) and supports the assignment of this facies to the FZ-8 zone, which represents a restricted platform interior setting (Plate A: 2, 14 and Plate B: 15).

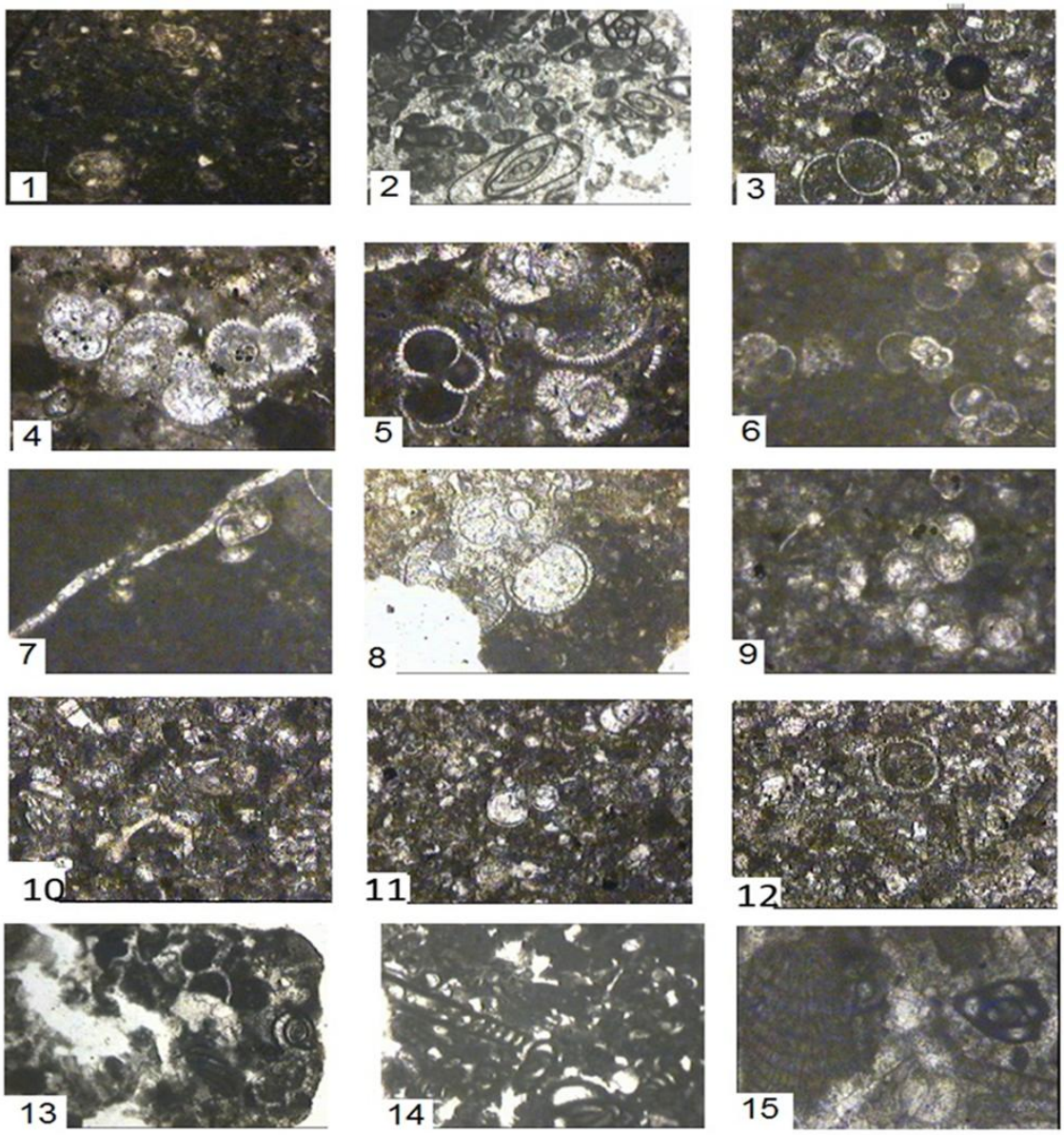


Plate A. 1: Planktonic Foraminiferal Wackstone Microfacies (Ib1), X2, 2346 m 2-*Miliolid* in Benthonic foraminifera lime Grainstone-Packstone microfacies (An2), X1, 2141m 3- Planktonic Foraminiferal Wackstone Microfacies (Ib1), X1, 2260 4- Planktonic Foraminiferal Wackstone Microfacies (Ib1), Y, 1966 m 5- *Globigerinidae Trilobites* in Planktonic Foraminiferal Wackstone Microfacies (Ib1), Y, 1966 m 6- *Globigerinid* in Planktonic Foraminiferal Wackstone Microfacies (Ib1), Y, 1983 m 7-Fracture in Planktonic Foraminiferal Wackstone Microfacies (Ib1), Y, 1983 m 8- *Globigerinoides subquadratus* in Planktonic Foraminiferal Wackstone Microfacies (Ib1), Z, 1884 m 9- Catapsydrax *dissimilis* in Planktonic Foraminiferal Wackstone Microfacies (Ib1), Z, 1887 m 10 Microbreccia, Bio-Lithoclastic Packstone Microfacies (Ib2), X1, 2240 m 11- Microbreccia, Bio-Lithoclastic Packstone Microfacies (Ib2), Z, 1780 m 12- Microbreccia, Bio-Lithoclastic Packstone Microfacies (Ib2), Z, 1776 m 13- Fossiliferous Lime Wackstone (An1), X2, 2220m 14- *Peneroplis sp.* in Benthonic foraminifera lime Grainstone-Packstone microfacies (An2), X2, 2212m 15- Red algae in - Fossiliferous Lime Wackstone (An1), X2, 2224 m. "All images were captured under a polarizing microscope at a magnification of 40x.

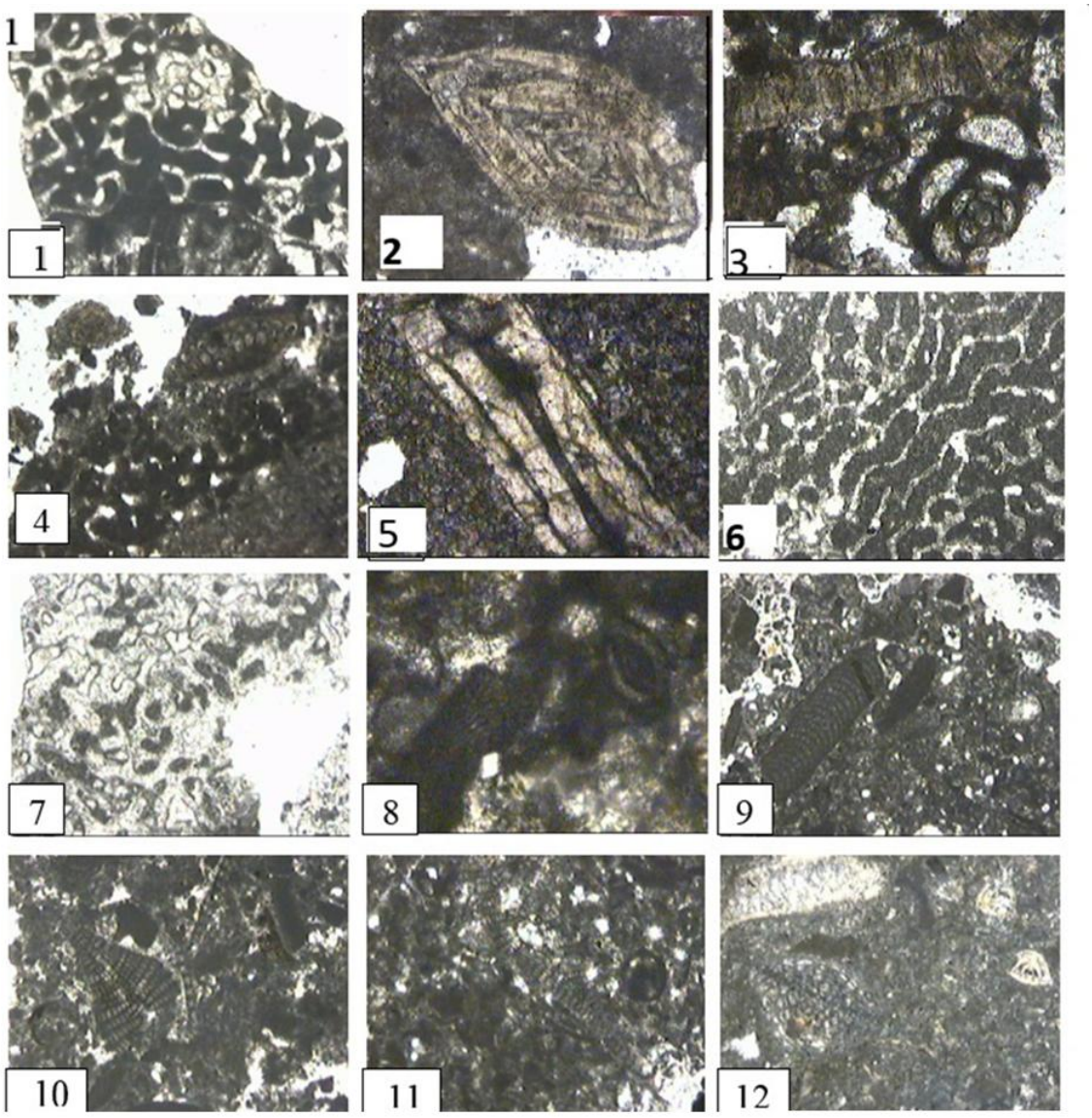


Plate B. 1: Lime coral bindston-framestone Lithofacies (Az2), X2, 2232m 2- Amphistegina, X1, 2175m 3- Austrolina, in Fossiliferous Lime Wackstone microfacies(An1), X1, 2141m 4-Miogysinoide X2, 2246m 5-Operculina, Z, 1668m 6- Lime coral bindston-framestone Lithofacies (Az2), X1,2178m 7- Lime coral bindston-framestone Lithofacies (Az2), Z1, 1638m 8- Fossiliferous Lime Wackstone (An1), X1, 2150m 9—Red algae in Larger foraminifera lime Packstone microfacies (Az1), Z, 1724m 10—Lepidocyclina in Larger foraminifera lime Packstone microfacies (Az1), X2, 2288m 11- - Lepidocyclina in Larger foraminifera lime Packstone microfacies (Az1), Z, 1728m 12- Lepidocyclina in Larger foraminifera lime Packstone microfacies (Az1), Z, 1746m 13- Dendritina, X2, 2212m 14- Fossiliferous Lime Wackstone (An1), Z, 1631m 15- - Benthonic foraminifera lime Grainstone-Packstone microfacies (An2), X1, 2136m."All images were captured under a polarizing microscope at a magnification of 40.

6. Paleoenvironment

The depositional environments of the Ibrahim, Azkand and Anah formations are interpreted through an integrated approach involving lithostratigraphic correlation, detailed facies analysis and the synthesis of electric log data from the examined wells (Fig. 4,5,6 and 7). The lower and middle parts of the Ibrahim Formation were deposited in the deeper parts of zone FZ-3, representing a deep shelf to toe-of-slope depositional environment, whereas the upper part of the formation was deposited in the shallower parts of the same environment or zone (FZ-3). These vertical facies transition is consistent with the depositional model reported by Abdulrahman and Awadh (2021) for the same formation. Similarly, the lower section of the Azkand Formation was deposited within zone FZ-4, which

is interpreted as an upper-slope environment that evolved gradually upward into a reefal setting (FZ-5) before end of the formation. This conclusion is compatible with the models proposed by Mahdi et al. (2022) and Abood and Al-Zaidy (2024). The lower part of the Anah Formation was deposited within zone FZ-7, interpreted as a platform interior with normal marine conditions within an open marine platform, while the middle and upper sections of the formation were deposited in a restricted platform interior environment assigned to zone FZ-8. Also, this depositional pattern is coordinated with the facies models proposed by Ghafor and Ahmad (2019); Mahdi et al. (2022) and Abood and Al-Zaidy (2024), supporting a vertical transition from open to restricted marine conditions during the formation accumulation.

On the other side, a deep depositional environment is evidenced by the existence of clay-rich intervals (marl), which is confirmed by the discernible relative rise in gamma ray log values at the beginning of the Ibrahim Formation, followed by a slow shallowing upward, which is demonstrated by the consecutive decrease in both the amount of clay (marl) and gamma ray log values at the Azkand and Anah formations in all of the wells under study. A regressive depositional history is supported by the vertical variation trend in the lithology and log response.

The Ibrahim Formation is interpreted to have been deposited in a deep shelf-to-toe-of-slope environment representing a relatively deep and low-energy sector of the basin, followed by the Azkand Formation accumulated within upper slope to reef-margin settings. This is indicative of a shallower and higher-energy zone near the platform break. Finally, the Anah Formation reflects deposition in shallower inner-platform settings trending toward coastal depositional systems.

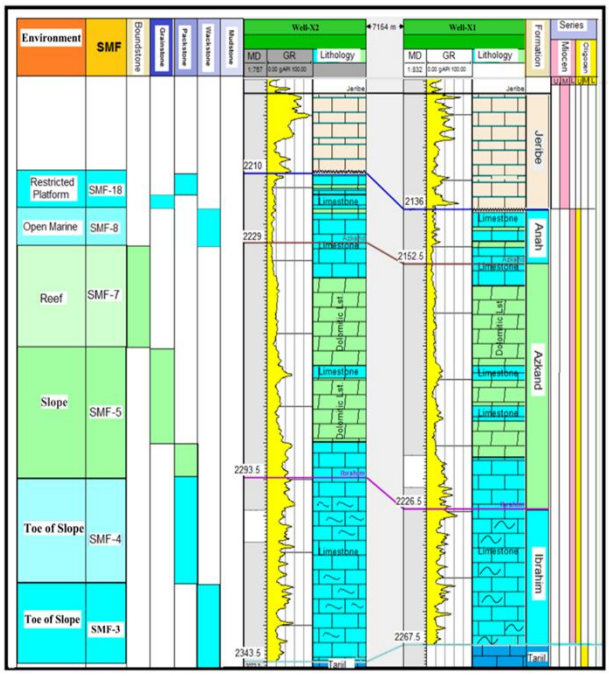


Fig. 4: Lithological column section showing microfacies and environment of studied succession in wells x1 and x2.

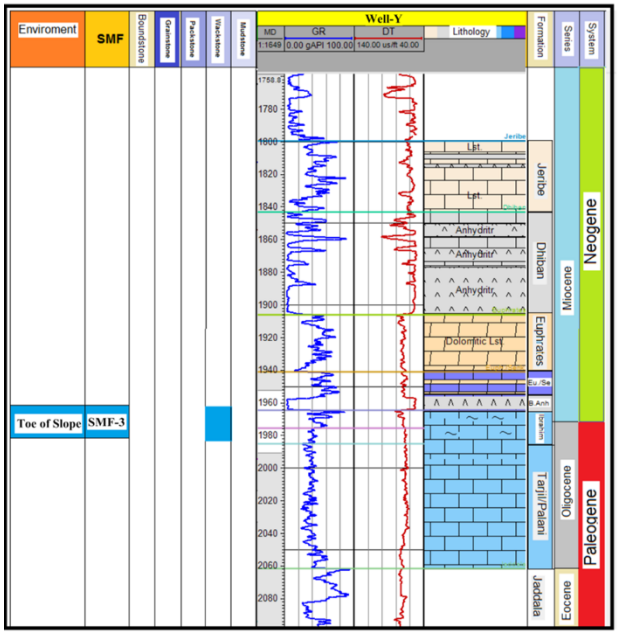


Fig. 5: Lithological column section showing microfiches and environment of studied succession in well Y.

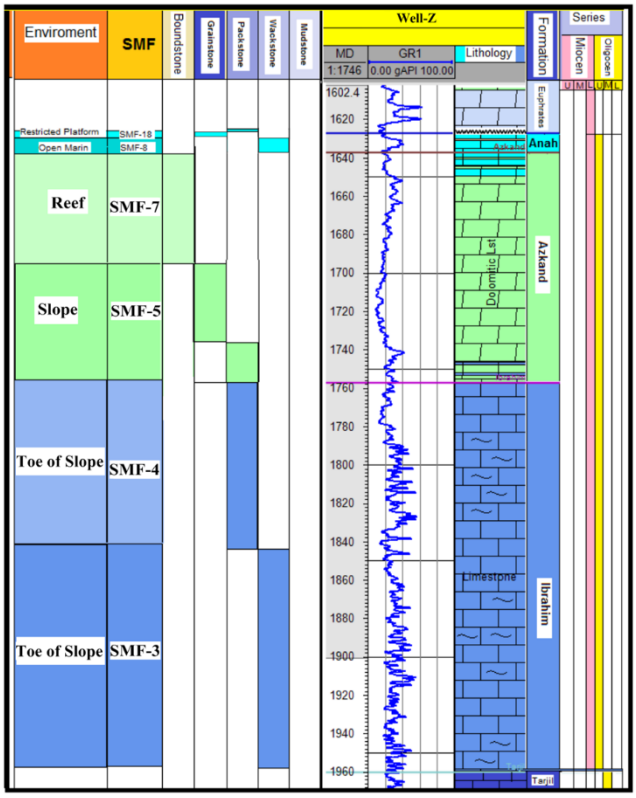


Fig. 6: Lithological column section showing microfiches and environment of the studied succession in well Z.

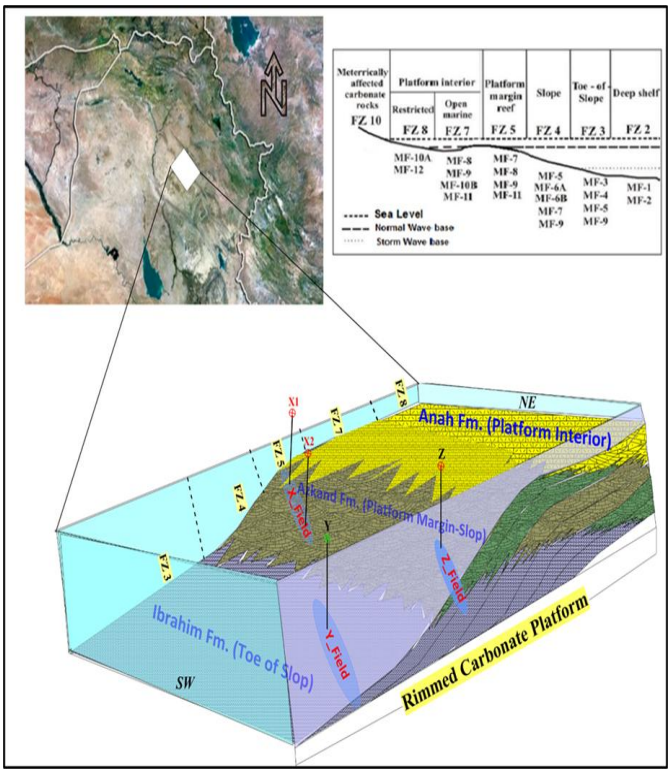


Fig.8: Rimmed carbonate platform model that describes the depositional setting of the Anah, Azkand, and Ibrahim Formations. According to Wilson (1975) and Flügel (2010).

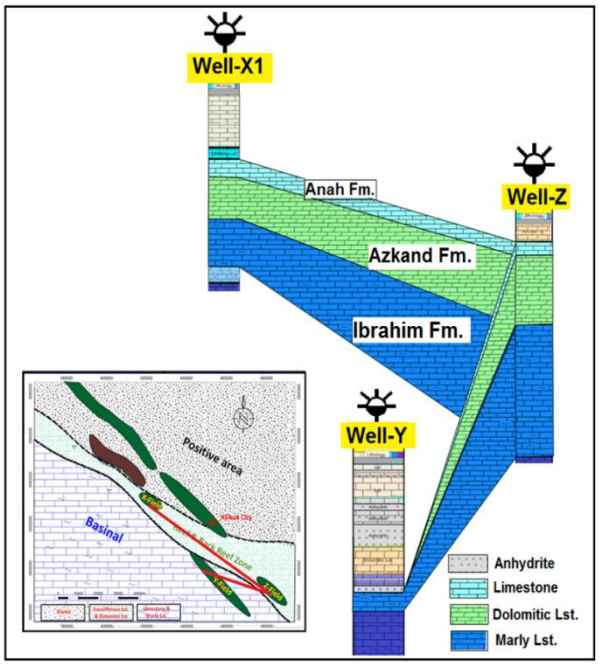


Fig.7: Lithology fence diagrams between X1, Y, and Z Wells in the study area.

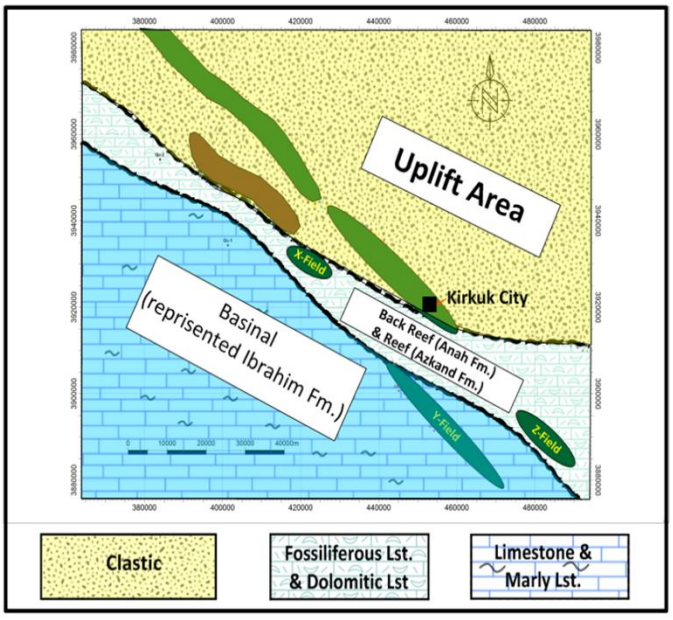


Fig. 9: Late Oligocene-Early Miocene paleo shoreline and the boundaries of the shallow and basinal facies in the study area (modified from Al-Eisa, 1992).

As shown in Fig. 8, which summarizes the reconstructed formations. According to Wilson (1975) and Flügel (2010). The Ibrahim Formation represents the distal margin of a rimmed carbonate platform. It was deposited in a deep-water and low-energy environment beyond the influence of normal wave action, where sediments were transported downslope via gravity-driven processes such as slumping and turbidity currents originating from the adjacent platform margin. This unit marks the outermost expression of the carbonate system, accumulating fine-grained carbonate debris and hemipelagic material in a setting characterized by limited bioturbation and episodic sedimentation. Overlying and laterally adjacent to the Ibrahim Formation, the Azkand Formation occurs exclusively within the platform margin reef and the upper part. It records deposition in a high-energy and shallow marine environment dominated by wave action, storm events, and reef growth. This zone represents the primary site of carbonate production, where framework-building organisms and skeletal debris accumulated rapidly, forming a prominent reef barrier that separated the platform interior from deeper waters. The Azkand Formation thus constitutes the structural and sedimentological keel of the platform system. Inland from the margin, the Anah Formation was deposited across the platform interior. It has been formed under low- to moderate-energy conditions in shallow and protected waters, where fine-grained carbonate sediments have accumulated with minimal reworking. This area experienced variable circulation ranging from semi-restricted lagoonal settings to more open marine conditions, supporting diverse benthic communities and promoting the development of mud-dominated deposits. Thus, the three formations were deposited contemporaneously along a lateral transect from the deep-water toe-of-slope (Ibrahim Formation) through the reef-rimmed margin (Azkand Formation) to the shallow platform interior (Anah Formation), reflecting a systematic environmental gradient controlled by water depth, hydrodynamic energy and proximity to the platform edge. This configuration illustrates a classic rimmed carbonate platform architecture, where lateral facies transitions record the interplay between carbonate production, wave energy and gravity-driven sediment transport during a single depositional phase. This finding is consistent with the conclusions given by Mahdi et al. (2022). The model represents a discrete depositional episode within a rimmed carbonate platform system, which was subsequently followed by phases of marine regression. These regressions triggered the progradation of Azkand Formation sediments over those of the Ibrahim Formation, while simultaneously, Anah Formation sediments were deposited overlying the Azkand Formation. This vertical stacking pattern is clearly documented in the stratigraphic logs of the studied wells, reflecting a regressive and shallowing-upward succession, wherein platform-derived facies progressively overstepped deeper-water slope and toe-of-slope deposits in response to falling relative sea level.

Based on a comparison of the thicknesses of the studied formations Anah, Azkand and Ibrahim (Table 1), it is observed that well Z, located in Field Z, lies within the central part of the sedimentary basin. This finding aligns with the study of Abid (1997), which indicated that the Oligocene basin comprises three main sedimentary centers aligned along a northwest–southeast axis. The first center lies north of Mosul, the second corresponds to the Kirkuk Basin, where well Z represents its depositional core, while the third is the Amara Basin.

Table 1: Studied formations' thicknesses.

Well Name	Anah	Azkand	Ibrahim
X1	16 m	74 m	41 m
X2	19 m	64 m	50 m
Y1	0 m	0 m	20 m
Z1	10 m	120 m	213 m

The Anah Formation was deposited in a restricted back-reef setting, where the absence of a well-defined lagoonal facies suggests a limited hydrodynamic circulation. This overall retrogradation pattern, as evidenced by the landward shift in facies belts and the observed regressive trend across the three formations, is likely consistent with sustained tectonic uplift within the basin, which led to a decrease in accommodation space driven by regional uplift. Based on this interpretation, a paleoenvironmental depositional model for the basin is consistent with the findings reported by North Oil Company (1992) in their studies of X field (NOC, 1992). Variations in formation thickness indicate that the depocenter was located near Field Z, where the

cumulative thickness reaches approximately 350 m compared to about 130 m in Field X. This observation is consistent with the findings of Jassim and Goff (2006). Field Y is interpreted to lie within a deep basinal setting. Based on this thickness distribution and depositional architecture, the paleo-shoreline is inferred to have run roughly parallel to the line connecting Fields X and Z, trending northwest–southeast relative to Iraq, and positioned slightly north of Field Y (Fig. 8). The 80 km distance between Fields X and Z includes a 40 km segment that lacks distinct surface expressions of subsurface structures.

Despite the absence of clear surface features, this area is considered prospective for hydrocarbon exploration due to its favorable paleogeographic position within the evolving carbonate platform system.

7. Conclusion

The Ibrahim, Azkand and Anah formations were deposited within a rimmed carbonate platform depositional system during the late Oligocene to early Miocene in the Low Folded Zone of Iraq. Detailed microfacies analysis of the carbonate successions in the X, Y, and Z oil fields identified six principal microfacies types reflecting a spectrum of depositional environments along the platform margin.

- The lower and middle parts of the Ibrahim Formation are characterized by microfacies SMF-3 and SMF-4 deposited in a toe-of-slope setting within zone FZ-3. The upper part of the formation shows a shallowing-upward trend consistent with a transition to a shallower platform environment within the same zone.
- The Azkand Formation exhibits microfacies SMF-5 in its lower section indicative of an upper slope environment (FZ-4), while its upper part is dominated by SMF-7 representing a reef setting within zone FZ-5.
- The Anah Formation with microfacies SMF-8 is interpreted as an open marine and platform interior environment (FZ-7), whereas SMF-18 in the middle and upper sections reflects a restricted platform interior setting (FZ-8).
- The vertical succession of microfacies supported by gamma ray log trends demonstrates a regressive and upward-shoaling pattern across all studied wells. The paleo-shoreline is inferred to have extended in a northwest–southeast direction passing through fields X and Z and lying slightly north of field Y.
- The significant thickening of the formations near field Z, reaching up to approximately 350 meters compared to ~130 meters in field X, indicates that the depocenter of the basin was located in the vicinity of field Z.

8. Acknowledgements

The authors would like to express their sincere gratitude to the Geology Department of Northern Oil Company for providing the facilities that helped in completing this work.

9. Conflict of Interest

The authors declare that they have no conflict of interest.

10. Funding Statement

Research received no external funding.

11. Author Contributions

Abdulla Ahmed Abid: Conceptualization; Writing – original draft; Investigation; Formal analysis; Visualization; Data curation. Developed the overall concept and design of the manuscript, prepared the research paper, participated in sample collection with the other authors, analyzed the data, and prepared the figures and tables.

Faris Nejres Hassan Al Jubory: Conceptualization; Supervision; Project administration; Writing – review and editing. Contributed to the development of the research ideas and writing approach, supervised the research and data-collection process, and conducted a comprehensive critical review and revision of the manuscript.

Saad Ahmed Mahmood: Investigation; Formal analysis. Contributed to sample collection and analysis of the resulting data.

Note: The contribution categories are aligned with the CRediT (Contributor Roles Taxonomy) framework, where applicable.

12. References

Abdulrahman, A. and Awadh, S.M., 2021. Depositional environment of the Ibrahim Formation and determining the Oligocene-Early Miocene boundary in Eastern Iraq,

The Iraqi Geological Journal, Vol. 54, No. 2E, pp. 85–97. https://doi.org/10.46717/igj.54.1F.8ms-2021-06-28

Abid, A., 1997. Biostratigraphy and Microfacies of the Late Oligocene–Middle Miocene formations, Center and North Iraq, Unpublished Ph.D. Thesis, University of Baghdad, 240 P. (In Arabic)

Abood, M.S. and Al-Zaidy, A.A., 2024. Depositional Environment and Stratigraphic Sequence of the Oligocene Succession in Fallujah and Melh-Tharthar Oilfields, Central Iraq, The Iraqi Geological Journal, Vol. 57, No. 1C, pp. 168–183. https://doi.org/10.46717/igj.57.2F.11ms-2024-12-21

Al-Eisa, M.E.S., 1992. Coral reef of Late Oligocene - Early - Miocene Kirkuk and surrounding areas.: Iraqi Geol. Jour., Vol. 25, No.2, pp.17-32.

Al-Hashimi, H. and Amer, R., 1986. Restudy of the Ibrahim Formation in the type section, Ibrahim Well No. 1, Mosul area, N. Iraq, Journal of the Geological Society of Iraq, Vol. 19, No. 3, pp. 93–100.

Al-Jwaini, Y.S.K., 2015. Sequence stratigraphy and reservoir characterization of the late Paleogene–early Neogene succession in Kirkuk area, Unpublished M.Sc. Thesis, University of Baghdad, Iraq, 142 P. (In Arabic)

Al-Sayyab, A.S. and Al-Hamdani, A.T., 1990. Biostratigraphy of the Anah and Euphrates Formations at Wadi Banat Al-Hassan (W. Iraq), Bulletin of the Iraqi Natural History Museum, Vol. 8, No. 3, pp. 61–83.

Al-Shareeda, W.M., Al-Abbasi, M.W., Al-Hamidi, R.I., and Malak, Z.A., 2025. Paleoenvironment and Petrophysical Properties of Bajwan Formation at Kirkuk Oil Field, Northeastern Iraq, Unpublished Report.

Beavington-Penney, S. J. and Racey, A., 2004. Ecology of extant nummulitids and other larger benthic foraminifera: applications in paleoenvironmental analysis, Earth-Science Reviews, Vol. 67, No. 3–4, pp. 219–265.

Bellen, R. V., Dunnington, H., Wetzel, R., and Morton, D., 1959. Lexique stratigraphique international: Asie, fascicule 10a, Iraq, Centre National de la Recherche Scientifique, Paris, Vol. III, 333 pages.

Boudaugher-Fadel, M.K., 2018. Evolution and geological significance of larger benthic foraminifera, UCL Press, 450 P.

Buday, T., 1980. The Regional Geology of Iraq, Volume I: Stratigraphy and Paleogeography. Directorate General of Geological Survey and Mineral Investigation, Baghdad, Iraq. 445 P.

Ditmar, V., 1971. Geological Conditions and Hydrocarbon Prospects of the Republic of Iraq (Northern and Central Parts), 120 P. (Unpublished)

Dunham, R.J., 1962. Classification of carbonate rocks according to depositional texture, in Ham, W. E. (Ed.), Classification of Carbonate Rocks, AAPG Memoir, Vol. 1, pp. 108–121.

Dunnington, H.V., 2005. Stratigraphic Lexicon of Iraq. Ministry of Oil, State Organization for Oil Projects, Baghdad, Iraq. 404 P.

Embry, A.F. and Klovan, J.E., 1971. A late Devonian reef tract on northeastern Banks Island, NWT, Bulletin of Canadian Petroleum Geology, Vol. 19, No. 4, pp. 730–781.

Flügel, E., 2010. Microfacies of Carbonate Rocks, Springer, Analysis, Interpretation and Application, 2nd Edition, 984 P. https://doi.org/10.1007/978-3-642-03796-2

Fouad, S.F., 2010. Tectonic and structural evolution of the Mesopotamia Foredeep, Iraq, Iraqi Bulletin of Geology and Mining, Vol. 6, No. 2, pp. 41–53.

Geel, T., 2000. Recognition of stratigraphic sequences in carbonate platform and slope deposits: empirical models based on microfacies analysis of Paleogene deposits in southeastern Spain, Palaeogeography, Palaeoclimatology, Palaeoecology, Vol. 155, No. 3–4, pp. 211–238.

Ghafor, I., Ahmad, P., and Khafaf, A.A., 2023. Biostratigraphy and paleoecology of the Anah Formation in Kurdistan Region, Iraq, Iraqi Bulletin of Geology and Mining, Vol. 19, No. 1, pp. 17–28. https://doi.org/10.59150/ibgm1901a02

Ghafor, I.M. and Ahmad, P.M., 2019. Biostratigraphy and paleoecology of the Anah Formation (Upper Oligocene) in the Sangaw area, Sulaimania Governorate, Kurdistan Region, NE Iraq, Iraqi Bulletin of Geology and Mining, Vol. 15, No. 2, pp. 1–15.

Karim K.H., Khanaqa, P.A., Ismail K.M. and Sissakian, V.K., 2012. Facies analysis of the Oligocene succession in Sharwaldir anticline, NE of the Kalar Town, NE Iraq. Iraqi Bull. Geol. Min., Vol. 8, No. 2, pp. 1-19.

Ighwan, T.A.R. and Al-Rahman, N.A.R.A., 2009. Stratigraphic Succession for (Aquitanian–Lower Early Langhian) Stage in Well Kor Mor / 3 at Kirkuk Area, Iraqi National Journal of Earth Science, Vol. 9, No. 1, pp. 1–14. https://doi.org/10.33899/earth.2009.40566

Jassim, S.Z. and Goff, J.C., 2006. Geology of Iraq, Dolin, s.r.o., distributed by Geological Society of London, 341 P.

Lawa, F.A. and Ghafur, A., 2015. Sequence stratigraphy and biostratigraphy of the prolific late Eocene, Oligocene and early Miocene carbonates from Zagros fold-thrust belt in Kurdistan region. Arabian Journal of Geosciences, Vol.8, No.10, pp. 8143 – 8174.

Mahdi, H.A.A.R., Al-Kubaisi, M.S. and Al-Jawad, S. N., 2022. Microfacies Analysis and Diagenetic Assessment of the Late Oligocene–Early Miocene Succession in Khabaz Oilfield, Northern Iraq, The Iraqi Geological Journal, Vol. 55, No. 2C, pp. 85–104. https://doi.org/10.46717/igj.55.1D.6Ms-2022-04-22

Majeed, H., Alawsi, M.D. and Al-Zaidy, A.A., 2025. Depositional Settings and Diagenetic Features of the Oligocene Sequence in the Kirkuk and Khabaz Oilfields, Northern Part of Iraq, The Iraqi Geological Journal, Vol. 58, No. 1C, pp. 57–74. https://doi.org/10.46717/igj.58.1A.5ms-2025-1-15

Mohammed, A.A. and Aljibouri, A.S., 2023. Microfacies Analysis and Depositional Environment of Upper Oligocene–Lower Miocene Succession in Wadi

Al-Khazgah of Anbar Governorate, Western Iraq, The Iraqi Geological Journal, Vol. 56, No. 2B, pp. 127–137. https://doi.org/10.46717/igj.56.2D.10ms-2023-10-16

NOC, 1988. Geological Study for Tertiary Reservoir in Jambur Oil Field, Unpublished Report.

NOC, 1992. Geological Study of Tertiary Reservoirs in Khabaz Field, Unpublished Report.

NOC, 2013. Geological and Petrophysical Study for Tertiary Reservoirs in Khabaz Field, Unpublished Report.

Perch-Nielsen, K., Saunders, J.B. and Bolli, H.M., 1985. Plankton Stratigraphy, Cambridge University Press, 925 P.

Pomar, L., Ward, W.C. and Green, D.G., 1996. Upper Miocene reef complex of the Llucmajor area, Mallorca, Spain, Field Trip Guidebook, SEPM, 85 P. (Unpublished)

Rahman, N.A.R.A., 2007. Sedimentological and Petrophysical Properties study of Stratigraphic Succession for (Aquitanian–Lower Early Langhian) Stage in Well Kor Mor / 3 at Kirkuk Area, Unpublished M.Sc. Thesis, University of Baghdad, 135 P. (In Arabic)

Reading, H.G., 2009. Sedimentary Environments: Processes, Facies and Stratigraphy, John Wiley and Sons, 552 P.

Reijmer, J.J., 2021. Marine carbonate factories: review and update, Sedimentology, Vol. 68, No. 5, pp. 1729–1796. https://doi.org/10.1111/sed.12878

Schlager, W., 2005. Carbonate Sedimentology and Sequence Stratigraphy, SEPM Concepts in Sedimentology and Paleontology, No. 8, 210 P.

Scholle, P.A. and Ulmer-Scholle, D.S., 2003. A Color Guide to the Petrography of Carbonate Rocks: Grains, Textures, Porosity, Diagenesis, AAPG Memoir, No. 77, 474 P.

Sharland, P.R., Casey, D.M., Davies, R.B., Simmons, M.D. and Sutcliffe, O.E., 2004. Arabian plate sequence stratigraphy – Revisions to SP2. Iraqi Bulletin of Geology and Mining style, GeoArabia, vol. 9, no. 1, pp. 199–214.

Tucker, M. E., 2011. Sedimentary Rocks in the Field: A Practical Guide, 4th Edition, John Wiley and Sons, 288 pages.

Wilson, J.L., 1975. The stratigraphy of carbonate deposits, in Carbonate Facies in Geologic History, Springer, pp. 20–55. https://doi.org/10.1007/978-1-4612-6383-8_2

Youssef, M., El-Sorogy, A., Al-Kahtany, K. and Saleh, M., 2021. Benthic foraminifera as bio-indicators of coastal marine environmental contamination in the Red Sea–Gulf of Aqaba, Saudi Arabia, Bulletin of Environmental Contamination and Toxicology, Vol. 106, No. 6, pp. 1033–1043. https://doi.org/10.1007/s00128-021-03192-w

Iraqi National Journal of Earth Science, Vol.,26 No.04, 2026 (293-308)

Iraqi National Journal of Earth Science

www.earth.uomosul.edu.iq

تحليل السحنات الدقيقة والبيئات الرسوبية لتكوينات إبراهيم وازقند وعنه في حقول نفطية مختارة من شمالي العراق

عبدالله احمد عبد [1*] ، فارس نجرس حسن الجبوري [1] ، سعد احمد محمود [2]

saadhamdani71@gmail.com faris77@tu.edu.iq abdulla.ahmed.a@st.tu.edu.iq

[1] قسم علوم الأرض التطبيقية، كلية العلوم، جامعة تكريت، تكريت، العراق.

[2] قسم علوم الأرض، شركة نفط الشمال، كركوك، العراق.

* الباحث المراسل.

تاريخ الاستلام: 06 تموز 2025 تاريخ المراجعة: 29 آب 2025 تاريخ القبول: 24 أيلول 2025

تاريخ النشر الالكتروني: 01 تشرين الأول 2026

الملخص

تركز هذه الدراسة على تحليل تكويناتإبراهيم وازقند وعنه في الحقول النفطية X وY وZ بمنطقة الطيات الواطئة في العراق. كشف التحليل التكاملي للسحنات الدقيقة والتتابع الطباقي عن تتابع ترسيبي تراجعي من الأوليغوسين المتأخر إلى الميوسين المبكر. يتميز الجزءان السفلي والأوسط من تكوين إبراهيم بالسحنة SMF-3، التي ترسبت في بيئة سفح المنحدر (FZ-3)، وتعكس ظروفًا منخفضة الطاقة. أما الجزء العلوي، فتهيمن عليه السحنة SMF-4، مما يدل على تضحل نحو منصة أقل عمقًا، مُعلنًا بداية التراجع البحري. يُظهر تكوين ازقند استمرار تقدم المنصة الكربوناتية؛ حيث يتمثل جزؤه السفلي بالسحنة SMF-5 (أعلى المنحدر، FZ-4)، في حين يُميّز الجزء العلوي السحنة SMF-7 (بيئة شعاب عالية الطاقة، FZ-5). أما تكوين عنه، فيبدأ بالسحنة SMF-8 (المنصة المفتوحة، FZ-7)، ثم يتطور عموديًا إلى السحنة SMF-18 (المنصة المقيدة، FZ-8). يدعم هذا التتابع التراجعي تسجيلات أشعة جاما التي تُظهر انخفاضًا تدريجيًا في النشاط الإشعاعي مؤكدة اتجاه التضحل التصاعدي. يقع مركز الحوض قرب حقل Z، بينما يحتل حقل Y موقعًا حوضيًا. ويمتد خط الساحل القديم باتجاه شمال غرب–جنوب شرق عبر العراق مرورًا بحقلي X وZ ومشكّلًا منصة كربوناتية ذات حواف (rimmed carbonate platform)، وهو ما له دلالات مهمة في توصيف المكامن النفطية والتوجهات الاستكشافية.

الكلمات المفتاحية:

بيئة الترسيب، السحنات الدقيقة، اوليغوسين، مجموعة كركوك، العراق.

DOI: 10.33899/injes.v26i4.61124, *©Authors, 2026, College of Science, University of Mosul.*

This is an open-access article under the CC BY 4.0 license (http://creativecommons.org/licenses/by/4.0/)

Iraqi National Journal of Earth Science, Vol. 26, No. 04, 2026 (309-322)

Iraqi National Journal of Earth Science

www.earth.uomosul.edu.iq

Sewage Sludge and Sediment Analyses as Indicators of Regional Heavy-Metal Pollution: A Case Study in El-Harrach, Algeria

Amina Bousseliou [1*], Issam Boudraa [2], Smaine Chellat [1], Brahim Kebabi [3]

amina.bousseliou@doc.umc.edu.dz issam.boudraa@umc.edu.dz smaine.chellat@umc.edu.dz brahim.kebabi@umc.edu.dz

[1] Laboratory of geology and environment, Department of Geological Sciences, Faculty of Earth Sciences, University of Constantine 1, Constantine, Algeria

[2] Laboratory of Advanced Materials Technology, National Polytechnic School, University of Constantine 3, Constantine, Algeria

[3] Laboratory of Pollution and Water Treatment, Department of Chemistry, University of Constantine 1, Constantine, Algeria.

** Correspondence author.*

Received: 13 July 2025 Received in revised form: 09 September 2025 Accepted: 24 October 2025
Available online: 01 October 2026

Abstract

This study examines pollution in the El-Harrach region in northern Algeria by analyzing concentrations of heavy metals and trace elements in sewage sludge and sediments. Three locations were sampled: upstream, within the Baraki wastewater treatment plant (WWTP), and downstream. To identify the major mineralogical components and pollutant composition, chemical analyses were performed using advanced methods, including X-ray diffraction (XRD), X-ray fluorescence (XRF), Inductively Coupled Plasma Mass Spectrometry (ICP-MS), Atomic Emission Spectroscopy (ICP-AES), and total organic carbon (TOC) analysis. Sediments were heavily enriched in heavy metals, particularly at the WWTP. This location yielded concentrations of 2200 ppm copper (Cu), 1160 ppm chromium (Cr), 1590 ppm zinc (Zn), and 320 ppm nickel (Ni). In the downstream areas, lead (Pb) and arsenic (As) were present at 330 ppm and 60 ppm, respectively. The upstream samples showed lower levels, with 410 ppm Cu, 680 ppm Cr, and 100 ppm Ni. Pollution level indicators, including the contamination factor (CF) and enrichment factor (EF), indicated extreme signs of pollution, primarily due to Cu, Zn, Cr, and As, resulting from the influence of industrial effluent and WWTPs. These findings indicate the need for continued environmental monitoring and implementation of effective remediation programs to mitigate these environmental and public health risks in the region.

Keywords:

Heavy metals, Contamination, Oued El-Harrach, Industrial discharges, Environmental pollution.

DOI: 10.33899/injes.v26i4.61125, ©Authors, 2026, College of Science, University of Mosul.
This is an open-access article under the CC BY 4.0 license (http://creativecommons.org/licenses/by/4.0/).

==========

1. Introduction

Heavy metals are toxic metallic elements with a density above 5 g/cm³ (Fergusson and Prucha, 1990; Zhao et al., 1998; Chen et al., 2015) and are generally represented by having an atomic number above 20 in the periodic table. These elements, such as copper (Cu), lead (Pb), chromium (Cr), zinc (Zn), nickel (Ni), and arsenic (As), exist in trace quantities under natural environmental conditions (Yildiz and Özkul, 2024). However, they are irreversible environmental pollutants caused by natural processes as well as a host of human activities. Uncontrolled heavy metal leakage into the land and rivers is a significant environmental problem. They are hazardous and cannot be broken down into non-toxic forms, causing a global health issue (Al-Khafaji and Jaafar, 2023).

Heavy metals are also found in association with fine-grained sediments and sludge, especially in organic-rich substrates (Robbe, 1981; Marchand et al., 2006; Banfalvi, 2011; Blais et al., 2005;

Atroune, 2012; Power and Chapman, 2018). Sediments serve as a container for metals present in the environment (Ouattara et al., 2021; Takahashi et al., 2023). The study of sediments thus makes it possible to understand the environmental changes that have taken place in river basins and offer valuable information on the accumulation of heavy metals (Leppänen and Kukkonen, 2004), thus reflecting the natural (geogenic) and human consequences (Konan et al., 2021), because soil pollution by trace metal elements has become an environmental problem of concern globally, raising concerns about its impacts on human health, biodiversity and the sustainability of terrestrial ecosystems (Masindi and Muedi, 2018). In the south of the Mediterranean, in France, the Marseille wastewater treatment plant is one of the largest in Europe (Ricou, 2023). Barcelona has implemented advanced wastewater treatment technologies in Spain, integrating biological and chemical processes to recycle water and reduce ecological impact (Silva, 2021). Italy, on the other hand, allows for efficient reuse of treated water for agricultural irrigation (Garrido-Cardenas et al., 2019). These countries are showing sustainable and innovative solutions to improve water quality and protect marine ecosystems.

In Algeria, the population and industry are concentrated in the north of Algeria and overlook the Mediterranean Sea, which has become a direct or indirect discharge (exoreic basin) for the wadis loaded with wastewater and untreated industrial liquid discharges. These wadis flow towards the north because of the slope of the Atlas chain, and they bring with them the ETMs that are often present there. Studies have already been conducted on sludge from wastewater treatment plants and ETMs in inland areas (Boudraa, 2020). On the other hand, in coastal and overpopulated areas such as the Wilaya of Algiers, the first study established that, given the volume of different wastes discharged without treatment, the Oued El Harrach, an open sewer, evacuates various pollutants. In addition, the Odors it emits disturb the living environment of the residents of the city of El Harrach (Atrounearound, 2012), caused by several factors such as high population density and intensive industrial activity, which increase the emissions of these elements into the atmosphere and surrounding waters (Mahia, 2015).

Although the Baraki wastewater treatment plant (WWTP) receives a large share of effluent from the urban and industrial networks of the wilaya of Algiers (Ferradj and Idouhar, 2016), it still does not remove all contaminants, including trace elements, and the effluent still does not comply with discharge standards for the natural environment (Louati, 2015). But it does not remove all types of contaminants, including trace elements. The objective of this study is to assess the status, the risk of pollution, and the potential sources of pollution in elements Fe, Pb, Cr, Ni, Cu, Zn, As, and Ga in the El-Harrach region of northern Algeria through the analysis of sediments upstream and downstream and the sewage sludge derived from the wastewater treatment plant.

2. Description of the Study Area

The watershed of Oued El-Harrach maritime is located in the Mitidja Oriental plain, with an area of 835.8 km², a perimeter of 142 km, and an altitude between 20 and 1629 m (Ammari, 2012; Bouchelouche et al., 2019). This watershed occupies nineteen communes in the central area of the Wilaya of Algiers, with a population of 1,200,000 inhabitants and a wastewater discharge of 107,569.67 m^3. The industrialization in this watershed is concentrated along the Oued El-Harrach and consists of three major industrial zones: the Oued Smar zone, the El Harrach zone, and the Ford zone of Constantine (Haouchine, 2010). The area studied is part of the sub-watershed from Beni Talha, south of Algiers, to Al-Sablât in the north via the Baraki wastewater treatment plant (Figure 1).

At the climatic level, this sloping basin is part of the Mediterranean region, with hot, humid winters and cool, dry summers. The average annual temperature is about 18 °C, with a maximum temperature of 30 °C during the summer, while the average annual precipitation is between 600 and 800 mm (Hamitouche et al., 2024). The average annual evaporation is estimated at 865 mm (Hadji and Belhocine, 2021).

The region of El Harrach and Algiers has a rich and varied geology, mainly shaped by tectonic and sedimentary events. El Harrach, located east of Algiers, is in the Italian zone of Algeria and is known for its complex structures resulting from the convergence between the African and Eurasian plates (Ficheur, 1901). This region is characterized by geological formations dating from the Mesozoic

and Cenozoic periods, including a series of flysch, marl, and limestone formations. The watershed of the Oued El-Harrah dominates the Mitidja plain. This area is largely made up of red sandy silt formations of superficial Plio-Quaternary age, about ten meters thick, resting on Tertiary and Cretaceous carbonate formations. To the west, the watershed is bounded by Cretaceous metamorphic and flysch basement (Zouakh and Bouhadad, 2013).

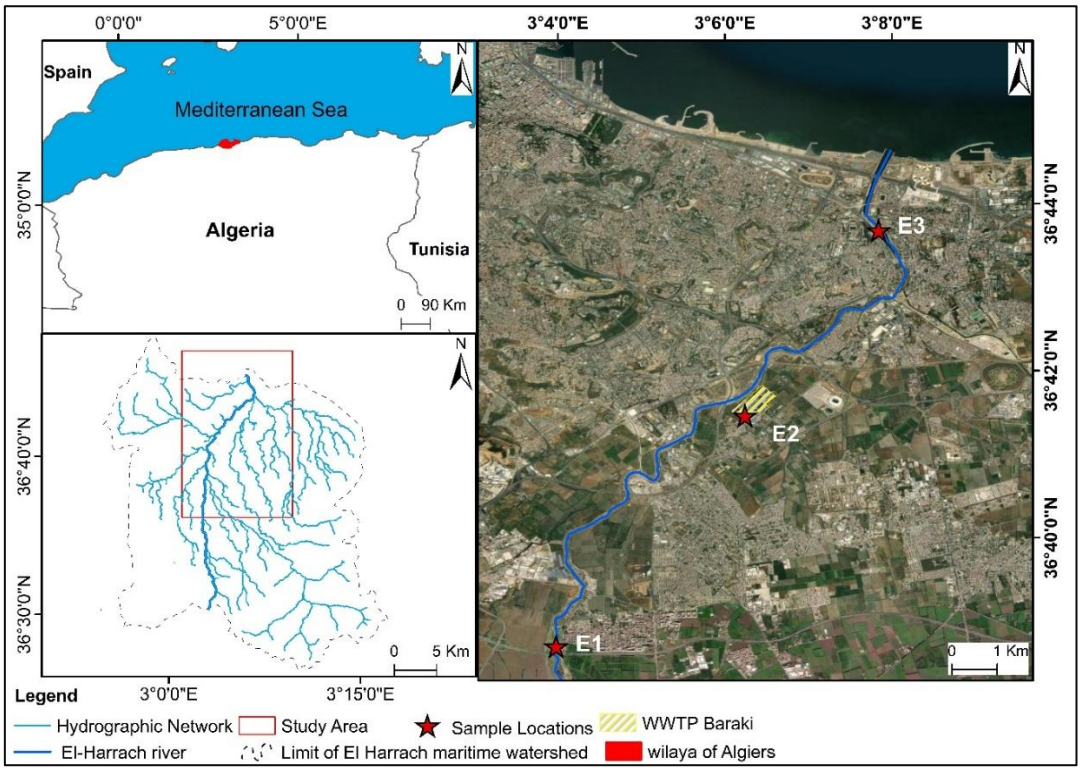


Fig. 1: Location and geographical location of the study area. (E1: Upstream, E2: Center, E3: Downstream.)

3. Materials and Methods

A. Sampling

After conducting exploration in the southern marine catchment area of Wadi El-Harrach and to accurately represent the study area, samples were taken from three sites in Wadi El-Harrach at a distance of 14 km and a depth of 20 cm from the fine sediments (silt) at the upstream E1 and downstream E3; other samples were taken in the middle of the E2 wastewater treatment plant (liquid sludge of Oued El Harrach) (Baraki wastewater treatment plant), each weighing 1.5 kg. The locations of these samples were determined by the Global Positioning System (GPS) and reported in the analytical maps. The liquid sludge was collected using a hand shovel, packed into sterile plastic boxes, numbered, transported in a cooler, and then stored in a laboratory refrigerator.

B. Geochemical analysis

Analysis by ICP-AES and ICP-MS

Three (3) representative samples were sent for geochemical analysis (major elements, trace elements, and rare earths) to the ALS Minerals laboratory in Seville, Spain. The method used for major elements, trace elements, and rare earth elements is an ultra-trace level method using Inductively Coupled Plasma Spectroscopy—Atomic Emission (ICP-AES) called "ME-MS61r". A prepared sample (0.25 g) is digested with perchloric, nitric, hydrofluoric, and hydrochloric acids. The residue is diluted with hydrochloric acid and analyzed by inductively coupled plasma atomic emission spectrometry.

X-ray diffraction (XRD) analysis

A 1 g sample of raw material was crushed to a particle size of 150 micrometers and then analyzed using an X-ray diffractometer (XRD)

"Olympus BTX-716 Benchtop XRD" equipped with a Cu-Kα anticathode (λ = 1.540598A°).

The analysis was conducted at the Sahara Geology Laboratory of the University of Ouargla. The X-ray spectra of all samples were recorded in the range of 2θ = 5° to 55°, with a step size of 5° at a scanning speed of 2°/min. The obtained data were compared with the model registered in the PDF2 database using PANalytical X'Pert HighScore Plus software.

X-ray fluorescence (XRF) analysis

The samples underwent pre-treatment at the chemistry laboratory of the University of Constantine 1. The liquid sludge was air-dried for 48 hours at room temperature. After complete drying, the samples were finely ground using a Retsch PM 100 mill for 45 minutes at 320 rpm, resulting in a powder with a particle size less than 100 nm. Subsequently, 10 grams of the powdered sample from each set were compressed into a 30 mm diameter pellet using a Retsch PP 25 manual pelletizer at a pressure of 10 tons. This was done to facilitate X-ray fluorescence (XRF) analysis using a Panalytical Epsilon 3 spectrophotometer available in the Pollution and Water Treatment Laboratory, Department of Chemistry, University of Constantine 1.

For accurate analysis, XRF data of all samples were recorded under different excitation conditions of DDP and current: 5.00 kV and 1000 µA, 30.00 kV and 300 µA, 12.00 kV and 519 µA, 20.00 kV and 450 µA, respectively. X-ray fluorescence (XRF) is particularly effective for detecting heavy metals in solid matrices, while inductively coupled plasma atomic emission spectroscopy (ICP-AES) allows for a broader analysis of elements, including transition metals, with increased sensitivity in complex sample matrices

Total organic carbon (TOC) analysis

To determine the total organic carbon concentration of the soluble matter in the samples, 10 g of crushed slurry is mixed with 100 ml of distilled water. After stirring the mixture for an hour, it is filtered through filter paper. Then, 10 ml of the solution from the last step is mixed with 90 ml of distilled water. The new solution is then tested with an Analytik Jena Multi N/C 3100 apparatus available at the Polytechnic Laboratory of Constantine University 3.

Assessment and monitoring of contamination

To assess the level of trace-element contamination in sediments (pollution indices), it is necessary to determine parameters such as the enrichment factor, contamination factor, geo-accumulation index, degree of contamination, and sediment pollution index. This information is essential for implementing appropriate measures to mitigate the negative impacts of pollution and preserve ecosystem biodiversity. The calculations were performed according to the protocols of Buzea et al. (2007), Kowalska et al. (2018), Al-Janabi et al. (2019), and Okereafor et al. (2020) to assess the environmental impact of pollution (Table 1). These parameters allow quantification of heavy-metal and other trace-element concentrations in sediments and comparison with reference values from Wedepohl (1995).

Table 1: Pollution indices and covariates utilized in this study.

Indices	Definition	Formulas	Classification
Contamination Factor (CF) (Hakanson, 1980)	The Contamination Factor (CF): considers the relative level of pollution in the soil.	$CF=C_N/C_B$ C_N: concentration of the element in the sample C_B: concentration of the background element	FC < 1: Low contamination 1 ≤ FC < 3 Moderate contamination 3 ≤ FC < 6 Considerable contaminations FC ≥ 6: Very high contamination
Enrichment Factor (EF) (Zoller, 1974) Classification Birch and Olmos (2008)	The enrichment factor (EF) is defined as a quantitative measurement used to assess the increase in the concentration of an element in the soil.	$FE=(C_N/C_{Fe})_E/(C_N/C_{Fe})_B$ $(C_N/C_{Fe})_E$: the ratio of the concentration of a C_N element and the concentration of iron C_{Fe} in the sediment $(C_N/C_Fe)_B$: the ratio of the concentration of a C_N element and the concentration of C_{Fe} iron in the background.	EF ≤ 1 No Enrichment 1 < FE ≤ 3 Minor Enrichment 3 < FE ≤ 5 Moderate Enrichment 5 < FE ≤ 10 Moderately severe enrichment 10 < FE ≤ 25 Severe Enrichment 25 < FE ≤ 50 Very severe enrichment 50 ≤ FE Extremely high enrichment
		$I\,geo=\log_2(C_N/1.5\times C_B)$	0 < I Geo < 1 Not contaminated

Geo-accumulation Index (I Geo) (Müller, 1969) Classification (Förstner, 1969)	Geo accumulation index (Igeo): is the presence of metals in the soil compared to the natural bottom level as a reference.	C_N: concentration of the element in the sample C_B: background element concentration 1.5: background exaggeration factor	1 < I Geo < 2: Not contaminated too moderately contaminated 2 < I Geo < 3 Moderately contaminated 3 < I Geo < 4 Moderately to severely contaminated 4 < I Geo < 5 Severely to extremely contaminated 5 < I Geo Extremely contaminated.
Degree of Contamination (DC) (Hakanson, 1980)	Degree of contamination (DC): is defined as the level relative to the level of pollution by trace elements in the soil.	$DC = \sum FC$	CD<8 Low 8≤CD<16 moderate 16≤CD<32 considerable 32≤CD Very high
Sediment Pollution Index (SPI) (Singh et al,2002).	Sediment pollution index (SPI): described as a parameter used to assess the degree of contamination of sediments by toxic substances,	$IPS = \sum (EF_m \times W_m) / \sum W_m$ W_m: toxicity weight or weighting factor for metal m. A weight of 1: Cr and Zn, 2: Cu and Ni, 5: Pb. FE_m: enrichment factor for metal m	0 ≤ IPS < 2 Sound sediment. 2 ≤ SPI < 5 Slightly polluted sediment. 5 ≤ SPI < 10 Moderately polluted sediment. 10 ≤ SPI < 20 Heavily polluted sediment. SPI ≥ 20 Hazardous sediments.

4. Results and discussion

A. Geochemical composition of the sludge

A. Analysis of the X-ray diffraction spectra (Figure 2) of sludge from three study sites (E1, E2, and E3) indicates a mineralogical composition dominated by quartz (SiO_2), alumina (Al_2O_3), and calcite ($CaCO_3$), as well as several clay and metal-bearing phases. These minerals were identified based on their characteristic peaks using the corresponding ASTM PDF sheets (00-001-0649, 01-072-1937, and 00-004-0878). Quartz, present in all samples, shows peaks at 20.72°, 26.65°, and 49.87° for the E1 sample; at 20.84°, 26.58°, and 50.01° for E2; and 20.76°, 26.49°, and 49.85° for E3, indicating a significant detrital input linked to the erosion of surface formations. The presence of calcite ($CaCO_3$) is identified by its peaks at 29.44°, 35.97°, 47.33°, and 48.49° for E1, at 29.33°, 35.93°, 47.44°, and 48.43° for E2, and at 29.22°, 35.97°, 47.27° and 48.23° for E3, resulting from the leaching of Cretaceous carbonate rocks. The alumina oxide (Al2O3) peaks at 13.79°, 32.25° and 34.88° for E1; at 13.82°, 32.30°, and 34.83° for E2; and at 13.74°, 32.51°, and 34.79° for E3. These are attributed to the geological alteration of aluminium-rich minerals and the dissolution of rocks containing aluminous phases. The presence of albite and clay minerals such as kaolinite, illite, and vermiculite reflects advanced alteration processes and marked pedogenetic dynamics (Kabata-Pendias, 2010).

Beyond this classic mineralogical composition, metal-bearing phases such as chalcopyrite (CuFeS2) and sinnerite (Cu6As4S9) were also identified. As part of the study of anthropogenic inputs, particularly industrial ones, the analysis of arsenosulvanite (Cu_3 (As, V) S_4), renierite, helvite, and litharge (PbO) provides a clear indicator of these inputs. These phases, which are not common in an ordinary sedimentary context, are often associated with trace metals such as Cu, Zn, Ni, Cr, Mn, and As, which can be used to trace their origins and propose the technique of their treatment (Fakhru et al., 2009; Boudraa et al., 2017). Their presence is typically linked to metallurgical or chemical discharges (Sundaray et al., 2010). Clay minerals and oxides (Fe, Mn, Al) play an essential role as geochemical traps. They act by adsorption or coprecipitation. This contributes to the partial immobilization of these elements in the sedimentary matrix (Förstner and Wittmann, 1981).

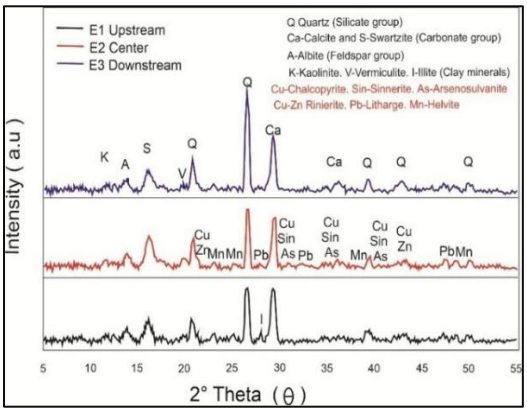


Fig. 2 X-ray diffractometry spectra of the sludge analyzed.

Semi-quantitative analysis of samples E1, E2 and E3, carried out by inductively coupled plasma mass spectrometry (ICP-MS) and inductively coupled plasma spectroscopy -Atomic Emission (ICP-AES), reveals a mineral composition dominated by silicon, aluminium, calcium and iron oxides. The respective contents vary between 18.8–42.5% for SiO_2, 6.03–11.85% for Al_2O_3, 11–16% for CaO, and 3.21–5.79% for Fe_2O_3 (Table 2). The presence of SiO2 and Al2O3 shows a composition of aluminosilicate resulting from the alteration and transport of detrital components of recent sandy-silty formations that cover the watershed studied. The dominance of these minerals, SiO_2, Al_2O_3, and Fe_2O_3, is reported by the work of Foroughi et al. (2018) and Kouassi et al. (2022).

Compared to the results of the sludge study in Zambia by Phiri et al. (2021), who reported quartz contents ranging from 10.5% to 19.1% in sludge effluents and solid deposits, the higher SiO_2 concentrations observed in this study (18.8% to 42.5%) indicate a significantly greater siliceous enrichment in the Oued El Harrach samples. This elevated quartz content suggests a more pronounced presence of siliceous minerals, likely reflecting differences in geological sources or environmental conditions between the studied locations. These findings underscore the importance of local geochemical and sedimentological factors in determining mineral composition in sediment samples.

Also, the high levels of total organic carbon (TOC) show that a lot of organic matter has built up from both natural sources (like algae growth and plant debris) and human-made sources, especially because treated or poorly treated domestic and industrial waste is still being released. The dual origin of organic matter is regularly seen in river systems that are influenced by urban and industrial activities (Vuillemin and Le Réveillé, 2001). The organic matter present can play a decisive role in the mobility or retention of trace metals, particularly through complexation, adsorption, or chelate formation, thus influencing the geochemical dynamics of pollutants in sediments.

Table 2: Chemical composition of sludge (% by weight).

Elements	E1	E2	E3
SiO_2	34	18.8	42.5
AL_2O_3	11.85	6.03	8.48
Fe_2O_3	4.87	3.21	5.79
CaO	16	11.05	16.6
MgO	1.15	1.11	1.06
Na_2O	0.69	0.38	0.65
K_2O	1.31	0.88	1.16
Cr_2O_3	0.018	0.022	0.028
TiO_2	0.59	0.38	0.4
MnO	0.04	0.03	0.05
P_2O_5	0.63	0.2	0.23
SrO	0.04	0.03	0.16
BaO	0.04	0.07	3.04
LOI	26.8	53.8	18.4
total	98.028	95.992	98.548
TOC	8.42	9.9	10.62

B. The concentration of target elements in the sludge

This analysis is crucial to understand their composition and assess their environmental impact. The results of the (ICP-MS) and (ICP-AES) analyses (Table 3) of the sludge show remarkably high concentrations of industrial elements (trace elements and primary elements), such as aluminium (Al), calcium (Ca), phosphorus (P), potassium (K), sodium (Na), magnesium (Mg), strontium (Sr), and chromium (Cr), in the three types of sludge, showing notably high concentrations of calcium and aluminium. Calcium levels reached 381250 ppm and aluminium levels 106050 ppm, far exceeding the background reference values of 29450 ppm for Ca and 77440 ppm for Al, indicating strong enrichment. Comparable studies on sewage sludge, such as Suanon (2017) in China, reported maximum values of 44800 ppm for Al and 20000 ppm for Ca, confirming the consistent accumulation of these elements in sludge over time. These elevated concentrations are likely due to mineral contributions from industrial effluents and urban discharges (Westerhoff et al., 2015; Yaseen and Scholz, 2018). Additionally, the significant concentration of vanadium (V) in the upstream sample (123 ppm in E1) may reflect specific industrial inputs or geogenic sources mobilized by anthropogenic activity.

The precious elements detected in the three samples analyzed (Table 3) generally exhibited negligible concentrations in the upstream and downstream. However, the distribution of the element ruthenium (Ru) exhibited a clear pattern of enrichment, where the downstream area showed the maximum value (1.66 ppm in E3), much higher than the background value of the Upper Continental Crust of approximately 1×10^{-4} ppm and also higher than the highest value of 0.110 ppm thus far recorded in sewage sludge by Suanon

(2017). This clear indication of enrichment points to spatial variation in the concentration of precious elements that cannot be explained by anything other than industrial effluents, as well as urban technological activity, producing the downstream load.

The rare earth elements (REE) identified in the sludge samples exhibit concentrations generally similar to or slightly lower than those of the background (Wedepohl, 1995), with certain enrichments around stations. Concentrations in the upstream sample (E1) vary between 0.14 mg/kg for lutetium (Lu) and 47.3 mg/kg for cerium (Ce), while the downstream values (E3) reach 36.9 mg/kg for Ce and 29.1 mg/kg for yttrium (Y). Relative to background, elements like lanthanum (La), yttrium (Y), and gadolinium (Gd) show an enrichment factor of more than 1, reflecting an accumulation in excess of natural geochemical background levels. Conversely, heavy rare earth elements like the elements ytterbium (Yb), thulium (Tm), and lutetium (Lu) exhibit minimal depression. The distribution pattern is indicative of both the natural lithogenic inputs as well as an anthropogenic component. The enrichment in La, Y, and Gd, especially at the downstream station, points towards the introduction of REE-bearing particles resulting from industrial and urban activity, among them the activity of metallurgy, battery manufacturing, as well as electronic waste. These results agree with the findings presented by Pourret and Hursthouse (2019), who explained the occurrence of REEs in watery environments as resulting from the remobilization of small fractions of particles, leaching of enriched soils, as well as industrial effluents.

Table 3: Concentrations (in ppm) of elements detected in the sludge studied.

Elements	E1	E2	E3
Industrial elements			
AL	106050	70180	84670
Ba	352	605	>10000
Ca	349870	381250	347370
P	4170	24420	950
K	34210	33110	26750
Na	5480	2980	4560
Mg	10520	13600	9450
W	1.8	1	1.4
Sr	421	338	1445
Sn	5.2	8.6	14.8
Cr	128	152	204
Ga	18.6	8.9	12.6
V	123	57	82
Rb	66	36.7	56.9
Nb	12.25	6.37	7.6
Hf	2.61	2.57	2.78
Precious elements			
Ru	1.03	0.59	1.66
Rare earth elements			
Ce	47.3	30.1	36.9
Nd	19.6	14.2	18.5
La	37.2	18	35.5
Y	19.3	27.7	29.1
Sm	3.92	2.96	3.71
Yb	1.56	0.87	1.26
Dy	2.78	2.01	2.93
Er	1.92	1.02	1.66
Ho	0.53	0.39	0.6
Tb	0.5	0.35	0.44
Tm	0.22	0.13	0.2
Lu	0.14	0.17	0.16
Pr	5.62	3.37	4.26
Gd	3.59	2.36	3.87

The relative amounts of different elements encountered in the analyzed samples (Fig. 3) show that the upstream sample (E1) is notably enriched with the elements Al, Ba, Ca, and K. In contrast, the downstream sample (E3) has the highest accumulation of elements, which suggests that elements from upstream springs and sludge in the center of the treatment plant accumulate downstream; this confirms that some elements are natural. They are the result of the alteration of the different rocks (leaching) of the mountains, and others are anthropogenic, agricultural, and industrial (Pourret and Hursthouse, 2019; Latosińska et al., 2021; Witkowska et al., 2021; Abbasi et al., 2024). Chemical and nutrient residues in treated wastewater show that the treatment process does not entirely remove these elements, which explains their presence in WWTP sludge (Suanon et al., 2017; Leppänen et al., 2024).

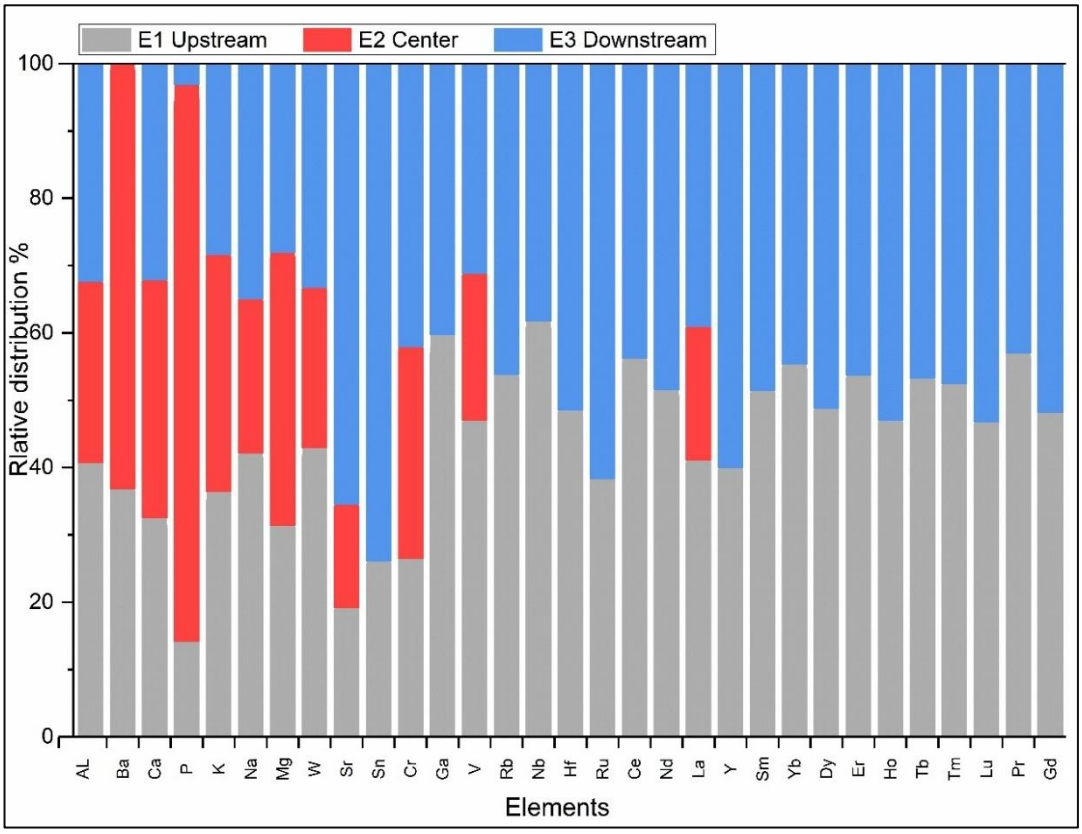


Fig. 3: Spatial variations in the relative distribution percentages of the target elements.

C. Pollution indices

Contamination factor (CF)

The analyzed sediments have a considerable number of metals. So, it is necessary to classify and quantify these metals to have an idea of their contamination rates and to investigate their origins. The results of the analyses (Figure 4a) show strong contamination ranging from 12 to 28 in all sediments by the metals Zn, Cr, Cu, and As; an extreme value of 153 for Cu in the WWTP sludge; and Ni is also present in the WWTP sediments with a value of 17.2. At the same time, Pb reaches a value of 19.41 downstream of Oued El Harrach. These values exceed the reference thresholds established by Hakanson (1980) (CF ≥ 6). The high values of CF are due to two main reasons: the first is the treatment press machine at the stations that concentrates metals in the sludge, and the second reason is due to the discharges of industrial activity near Oued El Harrach (De Fátima Braga Barbosa et al., 2019; Murillo et al., 2021), which gives rise to different types of industry such as battery production. Considerable contamination (3 ≤ FC < 6) has been observed for the elements Ti and Pb in samples taken upstream and at the WWTP, with values between 3.5 and 4.5. For Ni, values of 5.38 and 4.30 were recorded, respectively, in the upstream and downstream sediments. Meanwhile, Ga has a value of 3.57 in the upstream sediments, and Mn reached 3.52 in the WWTP sediments. Moderate contamination is also observed for Mn in upstream and downstream sediments, with values of 2.37 and 2.08, respectively. For Ga, values of 2.14 and 1.42 were recorded, respectively, in the WWTP and downstream sediments, while Ti has a value of 2.93 in the downstream sediments. In contrast, Fe has low contamination and is considered a mineral is observed with a value of 2.46. Moderate contamination (1 < Igeo < 2) of upstream Ni is observed, with a value of 1.07. In contrast, the geo-accumulation indices of Fe, Ti, Mn, and Ga in samples upstream and in the center of the treatment plant show no to moderately contaminated (0 < Igeo < 1). This suggests that the sediment is not contaminated with the elements mentioned.

Enrichment factor (EF)

The calculated enrichment factors reveal extremely *severe enrichment* (EF≥50) in metals according to the classification of *Birch and Olmos*

*(*2008). Cu values are 5.15 upstream and 283.94 at the WWTP, while Zn and Cr reach 56.43 and 61.17, respectively, in the WWTP sediments. Downstream, As has a value of 67.08 (Figure 4b). *A very severe enrichment* (25 <FE ≤ 50) has been observed in Zn and Cr in the sediments upstream and downstream, with values between 27.47 and 48.75. Cu and Pb show values of 39.09 and 43.4, respectively, in downstream sediments, while As shows values of 40.56 and 46.14 in upstream and WWTP samples. Ni has a value of 31.75 in the sludge from the water treatment plant. *Severe enrichment* (10 <FE ≤ 25) is observed for Ni downstream, with a value of 10.9. *Moderately severe enrichment* (5 < FE ≤ 10) was observed for Ti in all samples, as well as for upstream Pb and at the WWTP, with values of 7.15 and 6.51. Ga has a value of 7.24 upstream, while Mn is observed at the WWTP, and Ni is recorded downstream of the El Harrach wadi. *Moderate enrichment* (3 < FE ≤ 5) for upstream and downstream Mn, as well as for Ga, is poorly enriched compared to the geochemical background values generated by Wedepohl (1995) in the WWTP and downstream.

Geo-accumulation index (I Geo)

Calculations of the geo-accumulation index for each metal at the different sampling points according to the classification of Müller (1969). *Extreme contamination* (5 < I Geo) was observed for Cu upstream and at the wastewater treatment plant (WWTP) with values of 5.75 and 30.87, respectively, as well as for As in the WWTP and downstream with values of 5.07 and 6.02, and for Zn and Cr in the WWTP sludge (Figure 4c). *Contamination ranging from severe to extreme (*4 < I Geo < 5) for Zn upstream and downstream, with values of 4.82 and 4.24, and for As upstream with a value of 5.01. *Severe contamination* (3 < I Geo < 4) of upstream Cr with a value of 3.89, Ni in WWTP mud with a value of 3.45, and downstream Cu and Pb with values of 3.50 and 3.89, respectively. *Moderate to severe contamination* (2 < I Geo < 3) for downstream Cr of anthropogenic origin (Hernandez et al., 2003; Fatmi et al., 2023).

Degree of contamination (DC) and sediment pollution index (SPI)

The degree of contamination and the sediment pollution index provide information on the contamination of the sediments analyzed. Based on the calculation of the degree of contamination and the sediment pollution index (Anbalagan, 2023), sediments are classified according to their level of metal contamination. According to the classification of Hakanson (1980), the results of the sediment contamination degree are very high 32 ≤ DC with values of 111.53 and 111.85 upstream and at the WWTP (Figure 4d), and an extreme value downstream of 273.59. The IPS sediment pollution index, according to Singh et al. (2002), classifies all sediments in a 20 ≤ IPS hazardous zone with values of 23.82, 71.05, and 35.39. Upstream of the WWTP and downstream of Wadi El Harrach.

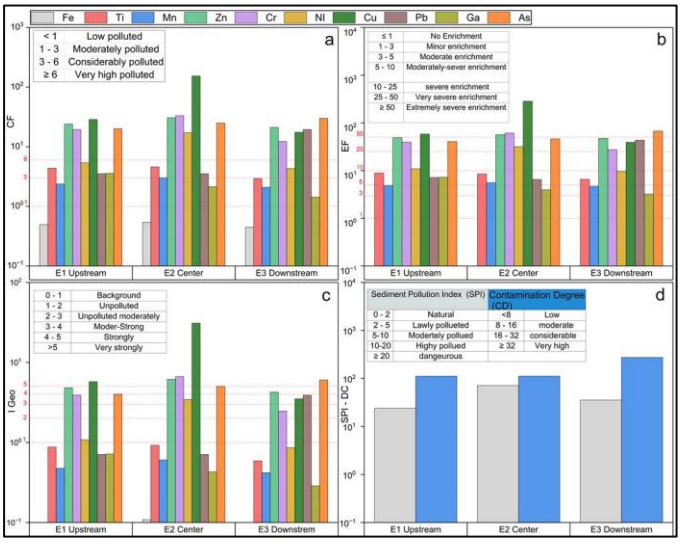


Fig. 4: a.Variations in the contamination factor in sediments; 4b: Enrichment factor (EF) values calculated for sediments according to the classification of Birch and Olmos (2008); 4c: Calculated geo-accumulation index values for trace elements in sediments; 4d: Calculated contamination degree and Sediment Pollution Index values for sediments.

5. Conclusion

This study provides compelling evidence of significant contamination in the El-Harrach region of northern Algeria, where industrial activities and high-density urban settlements contribute to substantial pollution loads. Geochemical and mineralogical analyses of sediments reveal the presence of essential minerals such as quartz, albite, calcite, and clay minerals (vermiculite, kaolinite, and illite), alongside secondary mineral phases incorporating heavy metals, including chalcopyrite, sinnerite, arsenosulvanite, renierite, helvite, and litharge. The presence of elevated levels of industrial provenance elements (Al, Ca, P, K, Na, Mg, Sr, Cr) and rare earth elements in WWTP sludge and river sediments is above the natural geochemical background levels and therefore indicates a strong anthropogenic impact. Various pollution indices (CF, I Geo, EF, CD, SPI) also indicate strong enrichment and severe contamination by Cu, Zn, Cr, and As, indicating that these sediments belong to the hazardous group. The inefficiency of the WWTP in managing heavy metal loads, particularly during periods of high rainfall and flooding, presents an urgent need for enhanced mitigation measures. Research points to the need for introducing advanced technologies in wastewater treatment processes. Stricter controls on industrial emissions and regular checks on sediment quality could make a real difference too. Collaboration among the Ministry of Environment, industry players, and research institutions seems crucial here. It would allow for ongoing evaluations and better handling of heavy metal pollution overall. Such joint actions might gradually reduce the pollution now affecting the Oued El Harrach basin. In the end, they could safeguard water quality and the broader environmental health for years to come

6. Acknowledgements

We sincerely thank the Sahara Geology Laboratory of the University of Ouargla, which provided us with a remarkable framework for analyzing the samples.

7. Conflict Of Interest

The author, BOUSSELIOU Amina, declares that there are no conflicts of interest regarding the publication of this paper titled "Sewage Sludge and Sediment Analyses as Indicators of Regional Heavy-Metal Pollution: A Case Study in El-Harrach, Algeria" submitted to the Iraqi National Journal of Earth Science (INJES). The research was conducted without any commercial or financial relationships that could be construed as a potential conflict of interest.

This statement ensures transparency regarding any potential conflicts and aligns with typical journal requirements for conflict-of-interest disclosures.

8. Funding Statement

Research received no external funding.

9. Author Contributions

(1) Amina. Bousseliou, as the first corresponding author, conducted comprehensive geological fieldwork and was responsible for collecting sediment samples from the El-Harrach River, as well as sludge samples from the wastewater treatment plant. She also performed extensive laboratory analyses. She processed and interpreted the analytical data and made a substantial contribution to the scientific interpretation of the results. She prepared the initial draft of the manuscript and incorporated subsequent revisions based on valuable feedback from the co-authors.

(2) Issam Boudraa contributed to the preparation and organization of data, literature research, and revision and editing of the manuscript.

(3) Smaine. Chellat contributed to the scientific review, proofreading, and final checking of the manuscript.

(4) Brahim. Kebabi supervised the laboratory analyses using X-ray fluorescence (XRF) and contributed to data processing and the determination of geochemical background values, which were used as a reference for comparing and interpreting element concentrations in the samples.

10. References

Abbasi, A., Mirekhtiary, F., Zakaly, H.M.H., 2024. Heavy metal levels of outdoor dust from the Eastern Mediterranean Sea region and assessment of ecological and health risk, Environmental Science and Pollution Research, Vol. 31, pp. 56295–56307. https://doi.org/10.1007/s11356-024-34794-6

Al- khafaji, S.J., Jaafar, S.W., 2023. Heavy Metals Pollution Assessment in Soil of Al-Zubair Area, Southern Iraq, Iraqi National Journal of Earth Science, Vol. 23, No. 2, pp. 91-104, https://doi:10.9719/eeg.2023.56.1.75

Al-Janabi, Z., Zaki, S., AlHassany, J., Al-Obaidy, A.H., Awad, E., Maktoof, A., 2019. Geochemical evaluation of heavy metals (Cd, Cr, Fe, and Mn) in sediment of Shatt Al-Basrah, Iraq, Engineering and Technology Journal, Vol. 37, pp. 237–241. https://doi.org/10.30684/etj.37.2c.6

Ammari, A., 2012. Vulnerability of dams to siltation (case of the Algiers coastal watershed), PhD Thesis, University Mohamed Khider, Biskra, Algérie, 268 P.

Anbalagan, S., Krishnakumar, S., Kasilingam, K., Singh, S.H., Pradhap, D., Saravanan, P., Neelavannan, K., Magesh, N., Selvakumar, S., 2024. Evaluation of potential trace element contamination and ecological risks of beach sediments, Andaman and Nicobar Archipelago, India, Total Environment Advances, Vol. 9, Article 200091. https://doi.org/10.1016/j.teadva.2023.200091

Atroune, F., 2012. Distribution of heavy metals in surface sediments carried by Oued El Harrach into the Bay of Algiers and its immediate environment, PhD. Thesis, Houari Boumediene University of Science and Technology (USTHB), Alger, Algérie, 293 P.

Banfalvi, G., 2011. Cellular Effects of Heavy Metals, Springer, Dordrecht, 348 P. https://doi.org/10.1007/978-94-007-0428-2

Birch, G.F., Olmos, M.A., 2008. Sediment-bound heavy metals as indicators of human influence and biological risk in coastal water bodies, ICES Journal of Marine Science, Vol. 65, No. 8, pp. 1407–1413. https://doi.org/10.1093/icesjms/fsn139

Blais, J.F., Dufresne, S., Mercier, G., 2005. État du développement technologique en matière d'enlèvement des métaux des effluents industriels, Revue des Sciences de l'Eau, Vol. 12, No. 4, pp. 687–711. https://doi.org/10.7202/705373ar

Bouchelouche, D., Hamil, S., Arab, S., Saal, I., Hafiane, M., Arab, A., 2019. Impact of pollution on the quality of water of Oued El Harrach (Algeria), In: Advances in Science, Technology and Innovation, Springer, Cham, pp. 141–144. https://doi.org/10.1007/978-3-030-01572-5_35

Boudraa, I., 2020. Study and characterization of sludge from several wastewater treatment plants in eastern Algeria, PhD Thesis, Université Frères Mentouri Constantine 1, Algérie, 312 P.

Boudraa, I., Bougherara, H., Cheurfi, W., 2017. Characterization of the sludge of Batna (Algeria) wastewater treatment plant for its valorization, Journal of New Technology and Materials, Vol. 7, No. 1, pp. 64–68. https://doi.org/10.12816/0044037

Buzea, C., Pacheco, I.I., Robbie, K., 2007. Nanomaterials and nanoparticles: sources and toxicity, Biointerphases, Vol. 2, No. 4, pp. MR17–MR71. https://doi.org/10.1116/1.2815690

Chen, H., Teng, Y., Lu, S., Wang, Y., Wang, J., 2015. Contamination features and health risks of soil heavy metals in China, Science of the Total Environment, Vol. 512–513, pp. 143–153. https://doi.org/10.1016/j.scitotenv.2015.01.025

De Fátima Braga Barbosa, A., Da Silva, C.M., De Oliveira Costa Júnior, C.E., 2019. Analysis of environmental management company acting on the State of Pernambuco, Brazil, International Journal of Advanced Engineering Research and Science, Vol. 6, No. 5, pp. 401–411. https://doi.org/10.22161/ijaers.6.5.54

Fakhru'l-Razi, A., Pendashteh, A., Abdullah, L.C., Biak, D.R.A., Madaeni, S.S., Abidin, Z.Z., 2009. Review of technologies for oil and gas-produced water treatment, Journal of Hazardous Materials, Vol. 170, No. 2–3, pp. 530–551. https://doi.org/10.1016/j.jhazmat.2009.05.044

Fatmi, B., Hazzab, A., Ghenaim, A., Rahmani, A., 2023. Anthropogenic pollution and ecological risk in urban sediments: assessing heavy metal and organic contamination in the Saida Watershed, North-Western Algeria, Water, Air, and Soil Pollution, Vol. 234, No. 11. https://doi.org/10.1007/s11270-023-06701-1

Fergusson, J.E., Prucha, F.P., 1990. The heavy elements: chemistry, environmental impact, and health effects, International Journal of Conservation Science, Vol. 614, p. 1.

Ferradj, A., Idouhar, M., 2016. Determination of anionic surfactants in a wastewater treatment plant in Algiers City, Desalination and Water Treatment, Vol. 57, No. 53, pp. 25677–25685. https://doi.org/10.1080/19443994.2016.1157038

Ficheur, M., 1901. Geological map of Algiers 1:50 000.

Foroughi, M., Chavoshi, S., Bagheri, M., Yetilmezsoy, K., Taghi Samadi, M., 2018. Alum-based sludge (AbS) recycling for turbidity removal in drinking water treatment: an insight into statistical, technical, and health-related standpoints, Journal of Material Cycles and Waste Management. https://doi.org/10.1007/s10163-018-0746-1

Förstner, U., Heling, D., et al., 1990. Sediment criteria development—contributions from environmental geochemistry to water quality management. In: Sediments and Environmental Geochemistry, Springer, Berlin, Heidelberg, New York, pp. 311–333.

Förstner, U., Wittmann, G.T.W., 1981. Metal Pollution in the Aquatic Environment, Springer-Verlag, Berlin Heidelberg, 486 P. https://doi.org/10.1007/978-3-642-69385-4

Garrido-Cárdenas, J.A., Esteban-García, B., Agüera, A., Sánchez-Pérez, J.A., Manzano-Agugliaro, F., 2019. Wastewater treatment by advanced oxidation processes and their worldwide research trends, International Journal of Environmental Research and Public Health, Vol. 17, No. 1, Article 170. https://doi.org/10.3390/ijerph17010170

Hadji, H. and Belhocine, C., 2021. Development of tools for calculating evaporation from water bodies (dams and hillside reservoirs) in the absence of data, Master's thesis, Kasdi Merbah University Ouargla, Algeria, 38 P.

Hakanson, L., 1980. An ecological risk index for aquatic pollution control: a sedimentological approach, Water Research, Vol. 14, pp. 975–1001. https://doi.org/10.1016/0043-1354(80)90143-8

Haouchine, N., 2010. Assessment of the hydrobiological quality of the Oued El Harrach river network (Blida and Algiers provinces), Magister Thesis, Houari Boumediene University of Science and Technology (USTHB), Algiers, 143 P.

Hernandez, L., Probst, A., Probst, J.L., Ulrich, E., 2003. Heavy metal distribution in some French forest soils: evidence for atmospheric contamination, Science of the Total Environment, Vol. 312, No. 1–3, pp. 195–219. https://doi.org/10.1016/s0048-9697(03)00223-7

Kabata-Pendias, A., 2010. Trace Elements in Soils and Plants (4th ed.), CRC Press, Boca Raton, 548 P. https://doi.org/10.1201/b10158

Konan, K.S., Kouamé, K.B., Konan, F.K., Boussou, K.C., Kouakou, K.L., 2021. Pollution of water for domestic use by metallic trace elements from anthropogenic activities: case of the sub-watershed of the Sassandra River upstream of the Buyo Dam, Proceedings of the International Association of Hydrological Sciences, Vol. 384, pp. 85–92. https://doi.org/10.5194/piahs-384-85-2021

Kouassi, N.L.B., Doubi, B.I.H.G., Diabate, D., Blonde, L.D., Albert, T., 2022. Recycling of alum sludge for Rhodamine B removal from industrial effluents, Chemistry Africa, Vol. 6, No. 1, pp. 485–498. https://doi.org/10.1007/s42250-022-00473-7

Kowalska, J.B., Mazurek, R., Gąsiorek, M., Zaleski, T., 2018. Pollution indices as useful tools for the comprehensive evaluation of the degree of soil contamination—a review, Environmental Geochemistry and Health, Vol. 40, No. 6, pp. 2395–2420. https://doi.org/10.1007/s10653-018-0106-z

Latosińska, J., Miłek, D., Komór, A., Kowalik, R., 2021. Selective collection of municipal waste in a residential district with multi-family buildings—Case study from Poland, Resources, Vol. 10, No. 8, Article 83. https://doi.org/10.3390/resources10080083

Leppänen, M.T., Kukkonen, J.V.K., 2004. Toxicokinetics of sediment-associated polybrominated diphenylethers (flame retardants) in benthic invertebrates (Lumbriculus variegatus, Oligochaeta), Environmental Toxicology and Chemistry, Vol. 23, No. 1, pp. 166–172. https://doi.org/10.1897/03-68

Louati, B., 2020. Étude d'impact des effluents industriels dans le bassin versant d'Oued Seybouse, Doctoral Thésis, Université d'Annaba, Annaba, Algérie, 281 P.

Mahia, M., 2015. Study on the industrial depollution of the Oued El Harrach watershed, Magister thesis, University of Annaba, Annaba, Algeria, 196 P.

Marchand, C., Lallier-Vergès, E., Baltzer, F., Albéric, P., Cossa, D., Baillif, P., 2006. Heavy metals are distributed in mangrove sediments along the mobile coastline of French Guiana, Marine Chemistry, Vol. 98, No. 1, pp. 1–17. https://doi.org/10.1016/j.marchem.2005.06.007

Masindi, V., Muedi, K.L., 2018. Environmental contamination by heavy metals. In: Tech eBooks. https://doi.org/10.5772/intechopen.76082

Müller, G., 1969. Index of geo-accumulation in sediments of the Rhine River, GeoJournal, Vol. 2, pp. 108–118.

Murillo-Tovar, M., Saldarriaga-Noreña, H., Saeid, A., Hato, M., Kwena, D., Gobeng, R., Monama, K., Ramohlola, A., Maity, M., Makhafola, T., Maponya, L., Katata-Seru, T., Somo, B., Mueller, E., Salinas, J., Hernández, E., Cerecedo, M., Reyes, V., Rodriguez, E., Mavumengwana, V., 2021. Trace metals in the environment—new approaches and recent advances, In: IntechOpeneBooks.https://doi.org/10.5772/intechopen.83504

Okereafor, U., Makhatha, M., Mekuto, L., Uche-Okereafor, N., Sebola, T., Mavumengwana, V., 2020. Toxic metal implications on agricultural soils, plants, animals, aquatic life and human health, International Journal of Environmental Research and Public Health, Vol. 17, No. 7, Article 2204. https://doi.org/10.3390/ijerph17072204

Ouattara, A.A., Sangare, N., Kouassi, N.L.B., Traore, K., 2021. Evaluation of trace metal contamination in the sediments of the N'zi River, Côte d'Ivoire, International Journal of Biological and Chemical Sciences, Vol. 15, pp. 2199–2208. https://doi.org/10.4314/ijbcs.v15i5.38

Phiri, C., Shimazui, D., Otake, T., Kikuchi, R., Chintu, I., Chirwa, M., Kalaba, L., Nyambe, I., Sato, T., 2021. Geochemical behaviour of heavy metals in sludge effluents and solid deposits on the Zambian Copperbelt: Implication for effluent treatment and sludge reuse, Science of The Total Environment, Vol. 769, 144342, https://doi.org/10.1016/j.scitotenv.2020.144342.

Pourret, O., Hursthouse, A., 2019. It's time to replace the term "heavy metals" with "potentially toxic elements" when reporting environmental research, International Journal of Environmental Research and Public Health, Vol. 16, No. 22, Article 4446. https://doi.org/10.3390/ijerph16224446

Power, E.A., Chapman, P.M., 2018. Assessing sediment quality, In: CRC Press eBooks, pp. 1–18. https://doi.org/10.1201/9781351076555

Ricou, C., 2023. How innovative solutions help Veolia to drive ecological transformation with its stakeholders, Field Actions Science Reports. Available online: http://journals.openedition.org/factsreports/7249

Robbe, D., 1981. Metal pollution in the natural environment: methodological guide for its study using sediments – Bibliographic report, Research report LPC No. 104, Laboratoire Central des Ponts et Chaussées, 88 P.

Silva, A.L.P., Prata, J.C., Duarte, A.C., Barcelò, D., Rocha-Santos, T., 2021. An urgent call to think globally and act locally on landfill disposable plastics under and after COVID-19 pandemic: pollution prevention and technological (bio)remediation solutions, Chemical Engineering Journal, Vol. 426, https://doi.org/10.1016/j.cej.2021.131201.

Singh, M., Müller, G., Singh, I.B., 2002. Heavy metals in freshly deposited stream sediments of rivers associated with urbanization of the Ganga Plain, India,

Water, Air, and Soil Pollution, Vol. 141, pp. 35–54. https://doi.org/10.1023/A:1021339917643

Suanon, F., Sun, Q., Yang, X., Chi, Q., Mulla, S.I., Mama, D., Yu, C.P., 2017. Assessment of the occurrence, spatiotemporal variations and geo-accumulation of fifty-two inorganic elements in sewage sludge: a sludge management revisit, Scientific Reports, Vol. 7, Article 5698. https://doi.org/10.1038/s41598-017-05879-9

Sundaray, S.K., Nayak, B.B., Lin, S., Bhatta, D., 2011. Geochemical speciation and risk assessment of heavy metals in the river estuarine sediments—a case study: Mahanadi basin, India, Journal of Hazardous Materials, Vol. 186, No. 2–3, pp. 1837–1846. https://doi.org/10.1016/j.jhazmat.2010.12.081

Takahashi, Y., Ojiro, R., Yamashita, R., Shimizu, S., Maeda, N., Zou, X., Tang, Q., Ozawa, S., Woo, G.H.,

Westerhoff, P., Lee, S., Yang, Y., Gordon, G.W., Hristovski, K., Halden, R.U., Pierre, H., 2015. Characterization, recovery opportunities, and valuation of metals in municipal sludges from US wastewater treatment plants nationwide, Environmental Science and Technology, Vol. 49, No. 16, pp. 9479–9488. https://doi.org/10.1021/es505329q

Witkowska, D., Słowik, J., Chilicka, K., 2021. Heavy metals and human health: possible exposure pathways and the competition for protein binding sites, Molecules, Vol. 26, No. 19, Article 6060. https://doi.org/10.3390/molecules26196060

Yaseen, D.A., Scholz, M., 2018. Textile dye wastewater characteristics and constituents of synthetic effluents: a critical review, International Journal of Environmental Science and Technology, Vol. 16, pp. 1193–1226. https://doi.org/10.1007/s13762-018-2130-z

Yildiz, U., Ozkul, C., 2024. Heavy metals contamination and ecological risks in agricultural soils of Uşak, western Türkiye: a geostatistical and multivariate analysis, Environmental Geochemistry and Health, Vol. 46, No. 2, Article 58. https://doi.org/10.1007/s10653-024-01856-0

Zhao, F.J., Shen, Z., McGrath, S.P., 1998. Solubility of zinc and interactions between zinc and phosphorus in the hyperaccumulator Thlaspi caerulescens, Plant, Cell and Environment, Vol. 21, No. 1, pp. 108–114.

Zoller, W.H., Gladney, E.S., Duce, R.A., 1974. Atmospheric concentrations and sources of trace metals at the South Pole, Science, Vol. 183, No. 4121, pp. 198–200. https://doi.org/10.1126/science.183.4121.198

Zouakh, D., Bouhadad, R., 2013. Study of the biological quality of Oued El Harrach and its tributaries, Journal of Agronomic Research, Vol. 6, No. 11, pp. 5–16. https://asjp.cerist.dz/en/article/72837.

Yoshida, T., Shibutani, M., 2023. Suppression of neurogranin expression by disruption of epigenetic DNA methylation in hippocampal mature granule cells after developmental exposure to neurotoxicants in rats, Toxicology Letters, Vol. 390, pp. 33–45. https://doi.org/10.1016/j.toxlet.2023.10.016

Vuillemin, M.H., Le Réveillé, G., 2001. Biodegradable organic carbon in treated wastewater from treatment plants in the Seine basin, Sciences Eaux and Territoires, pp. 3–12.

Wedepohl, K.H., 1995. The composition of the continental crust, Geochimica et Cosmochimica Acta, Vol. 59, pp. 1217–1232. https://doi.org/10.1016/0016-7037(95)00038-2

Iraqi National Journal of Earth Science, Vol. 26, No. 04, 2026 (309-322)

Iraqi National Journal of Earth Science

www.earth.uomosul.edu.iq

تحليل حمأة الصرف الصحي والرواسب كمؤشر للتلوث الإقليمي بالعناصر النزرة المعدنية: دراسة حالة لوادي الحراش، الجزائر

امينة بوالسليو [1]* ، عصام بودراع [2] ، سماعين شلاط [1] ،

إبراهيم كبابي [3]

amina.bousseliou@doc.umc.edu.dz issam.boudraa@umc.edu.dz smaine.chellat@umc.edu.dz

brahim.kebabi@umc.edu.dz

[1] مختبر الجيولوجيا و البيئة ، قسم علوم الجيولوجيا ، كلية علوم الأرض، جامعة قسنطينة 1، قسنطينة، الجزائر.

[2] مختبر تكنولوجيا المواد المتقدمة، المدرسة الوطنية المتعددة التقنيات، جامعة قسنطينة 3، قسنطينة، الجزائر.

[3] مختبر التلوث و معالجة المياه ، قسم الكيمياء، جامعة قسنطينة 1، قسنطينة، الجزائر.

** الباحث المراسل.*

تاريخ الاستلام: 13 تموز 2025 تاريخ المراجعة: 09 أيلول 2025 تاريخ القبول: 24 تشرين الأول 2025

تاريخ النشر الالكتروني: 01 تشرين الأول 2026

الملخص

تهدف هذه الدراسة إلى تقييم مستوى التلوث في منطقة وادي الحراش (شمال الجزائر) من خلال تحليل تراكيز العناصر النزرة المعدنية والمعادن الثقيلة في حمأة مياه الصرف الصحي والرواسب. شملت الدراسة ثلاث محطات أخذ عينات هي: المنبع، وداخل محطة تطهير المياه المستعملة ببرّاكي(WWTP) ، والمصب. ولتحديد التركيب المعدني والمكونات الكيميائية والملوثات، أُجريت تحاليل باستخدام تقنيات متقدمة شملت حيود الأشعة السينية(XRD) ، وفلورة الأشعة السينية (XRF)، ومطيافية البلازما المقترنة حثيًا مع مطياف الكتلة(ICP-MS) ، ومطيافية الانبعاث الذري بالبلازما المقترنة حثيًا(ICP-AES) ، بالإضافة إلى تحليل الكربون العضوي الكلي(TOC). أظهرت النتائج أن الرواسب، ولا سيما في محطة التطهير، تحتوي على تراكيز مرتفعة من المعادن الثقيلة، حيث بلغت تراكيز النحاس 2200 (Cu) جزءًا في المليون، والكروم 1160 (Cr) جزءًا في المليون، والزنك 1590 (Zn) جزءًا في المليون، والنيكل 320 (Ni) جزءًا في المليون. أما في منطقة المصب، فقد سُجلت تراكيز مرتفعة من الرصاص (Pb) بلغت 330 جزءًا في المليون، والزرنيخ 60 (As) جزءًا في المليون. في المقابل، أظهرت عينات المنبع مستويات أقل من التلوث، حيث بلغت تراكيز النحاس 410 أجزاء في المليون، والكروم 680 جزءًا في المليون، والنيكل 100 جزء في المليون. كما بينت مؤشرات تقييم التلوث، بما في ذلك معامل التلوث (CF) ومعامل الإثراء (EF) ، وجود مستويات مرتفعة جدًا من التلوث، خاصة بعناصر النحاس والزنك والكروم والزرنيخ، وهو ما يُعزى أساسًا إلى تصريف المخلفات الصناعية وتأثير محطة تطهير المياه المستعملة. وتؤكد هذه النتائج ضرورة الاستمرار في برامج الرصد البيئي، إلى جانب تنفيذ استراتيجيات فعالة للحد من التلوث وإعادة تأهيل البيئة، بهدف تقليل المخاطر البيئية والصحية التي تهدد منطقة وادي الحراش.

الكلمات المفتاحية:

المعادن الثقيلة، التلوث، وادي الحراش، التصريفات الصناعية، التلوث البيئي.

DOI: 10.33899/injes.v26i4.61125, *©Authors, 2026, College of Science, University of Mosul.*
This is an open-access article under the CC BY 4.0 license (http://creativecommons.org/licenses/by/4.0/)

Iraqi National Journal of Earth Science, Vol. 26, No. 04, 2026(323-337)

Iraqi National Journal of Earth Science

www.earth.uomosul.edu.iq

Model for Hazard Mapping and Disaster Management of Land Degradation Using Geospatial Techniques in Iraq: A Review

Mohammed H. Azeez [1*], Hisham M. Jawad Al Sharaa [2], Abdul Razzak T. Ziboon [3]

mohammed.aziz@stu.edu.iq Hisham.M.AlSharaa@uotechnology.edu.iq dr.abdulrazzak@esraa.edu.iq

[1] *Department of Surveying, Shatrah Technical Institute (STI), Southern Technical University (STU), Shatrah, Iraq.*
[2] *Department of Geomatics, College of Civil Engineering, University of Technology, Baghdad, Iraq.*
[3] *Department of Building and Construction Technology, College of Engineering, Al-Esraa University, Baghdad, Iraq.*
** Correspondence author.*

Received: 06 August 2025 Received in revised form: 21 September 2025 Accepted: 26 October 2025
Available online: 01 October 2026

Abstract

In this review article, we examined the previous literature on mapping and modeling degradation risk in the spatiotemporal context of Iraq, which is located in the Near East and North Africa (NENA) region, and is particularly vulnerable to land degradation and is losing thousands of hectares of land. Land degradation has been a significant focus of academic research globally and remains a major issue in the 21st Century. The review process was meticulously designed and conducted over the past decade (from 2015 to 2025) utilizing relevant keywords. We searched several databases, including Elsevier, Springer, IEEE, MDPI, Taylor and Francis, and Wiley. Our search yielded 54 relevant research articles. We conclude that there is a research gap that needs to be addressed, represented by the development of a model that considers the spatiotemporal aspects of land degradation in line with the definitions found in global literature. Additionally, the Dhi Qar and Ninewa Governorates have not received much attention from researchers, making them largely unexplored areas in this context. We also observed that the most widely used remote sensing data in the literature came from the Landsat satellite series.

Keywords:

Land degradation, Geospatial Modeling, Spatiotemporal, Iraq.

DOI: 10.33899/injes.v26i4.61126, ©Authors, 2026, College of Science, University of Mosul.
This is an open-access article under the CC BY 4.0 license (http://creativecommons.org/licenses/by/4.0/).

==========

1. Introduction

Land degradation is a significant global issue that affects various regions worldwide. Africa's yield loss from soil erosion ranges from 2 to 40% with a mean of 8.2%. South Asia loses 36 million tons of cereal equivalent annually, which is worth US$5,400 million due to water erosion and US$1,800 million due to wind erosion (Bridges, 2019). Land degradation in the Near East and North Africa (NENA), including Iraq, impacts around 410 million people, and approximately 86% of the region's land is affected by land degradation and desertification (Azeez et al., 2025; Ziadat et al., 2021). It is a complex problem influenced by numerous factors. It takes many forms, classified into five components: Soil Degradation, Vegetation Degradation, Water Degradation, Climate Degradation, and Losses Due to urban and industrial development (Dwivedi, 2018). This phenomenon has emerged as one of the most pressing environmental challenges faced by humanity today, making it essential to understand the global patterns associated with this land crisis (Prăvălie, 2021). Several definitions of land degradation exist, all of which emphasize the decline in land productivity. This decline is characterized by a reduction in the chemical, physical, and biological activities of the land, ultimately leading to a decrease in its economic value. These changes occur in place over a period of time (Li et al., 2021).

From a geospatial perspective, land degradation refers to changes in an input value at a specific spatial unit (such as a pixel) over a specific time period. The input value can be represented by

various indices such as the vegetation index, land use and land cover changes (LULC), or the drought index. Land degradation modelling has become increasingly complex as its factors are interdependent and interrelated; for example, drought is influenced by rainfall, temperature, and human water consumption. In addition, land degradation has a temporal dimension that influences its dynamics. Land degradation poses multiple risks and can occur through different pathways. There are seventeen recognized land degradation pathways including drought, biological invasions, coastal erosion, water-borne soil erosion, wind-borne soil erosion, land contamination, land subsidence, landslides, permafrost thaw, salinization, soil acidification, soil biodiversity loss, soil compaction, soil organic carbon loss, soil clogging, vegetation loss, and waterlogging (Prăvălie, 2021). Each of these pathways presents a distinct hazard encompassing a range of land degradation risks.

2. Objective and aim of study

The objective of this research review is to identify the latest studies in the field of hazard mapping and geospatial modeling of land degradation. The study has several goals: (i) To examine the role of remote sensing in modeling land degradation; (ii) To review literature that explores land degradation from a spatiotemporal perspective; (iii) To analyze existing research on land degradation modeling; (iv) To classify previous literature according to the regions of Iraq.

3. Concepts of land degradation

Understanding land degradation requires a clear grasp of what "land" means. Land can be defined as a specific area of the Earth's surface, which includes all aspects of the biosphere, both above and below this surface. This encompasses the near-surface climate, soil, terrain features, surface water bodies (lakes, rivers, marshes and swamps), sedimentary layers close to the surface and associated groundwater supplies. It includes plant and animal populations, patterns of human settlement and the physical effects of historical and current human activities (Pablo Muñoz et al., 2019). While there are more straightforward definitions of land such as "a terrestrial system that includes natural resources (soil, near-surface air, vegetation and other biota and water), ecological processes, topography, as well as human settlements and infrastructure within that system (Henry et al., 2018), the former definition provides a more comprehensive perspective on the concept of land.

All global definitions of land degradation cited in the literature refer to a decline in land productivity (Table 1). Land degradation is not static but rather dynamic, changing with the appropriate conditions for increasing degradation (such as drought) or land restoration (such as the restoration of vegetation cover) (Hermans and McLeman, 2021; King-Okumu et al., 2021).

The concept of dynamic land degradation can be understood as a movement through three-dimensional space (Fig.1a). In this representation, the x and y dimensions (For example, longitude and latitude, or north and east on a Universal Transverse Mercator, UTM) indicate the location of a spatial unit, which can be as small as a single pixel or as large as a specific area, whereas the third dimension represents time. Each value within a spatial unit at a specific time can change in a positive or negative direction. For instance, the Normalized Difference Vegetation Index (NDVI) is a straightforward metric for assessing land degradation (Dhaidan et al., 2021; Ziboon et al., 2022; Feng et al., 2022). Over a time series (such as ten years), a shift in the NDVI value from positive (indicating the presence of photosynthetic vegetation) to negative (signifying land devoid of vegetation cover) serves as evidence of land degradation. Conversely, an increase in the NDVI value indicates land restoration (Fig.1b). Land degradation occurs over a cumulative time series and reflects a continuous decline in the land's yield, as outlined in the definitions provided in Table (1).

The complexity of modeling land degradation arises from its intricate nature. There is typically a multi-faceted and interconnected spatial relationship among the various elements contributing to land degradation in a specific area (Prăvălie, 2021).

For example, the decline in vegetation cover can result from several factors: drought (climate degradation), overgrazing (human-caused degradation), and soil salinization (chemical degradation). Identifying the primary cause of land degradation is challenging. Is it drought that leads to decreased vegetation cover, which in turn exposes the soil to solar radiation, increasing land surface temperatures (LST), elevating evaporation

rates, and ultimately causing salinization? (Zheng et al., 2022) Or is it overgrazing those results in reduced vegetation?

Table 1: Global definitions of land degradation.

No	Definition	reference
1	A consistent decrease in the bio-productivity of terrestrial ecosystems over time is commonly referred to as land degradation.	Li et al.(Li et al., 2021)
2	Land degradation is a widespread, systemic occurrence that manifests in various forms across all regions of the terrestrial environment.	Scholes et al.(Pandit et al., 2018)
3	Land degradation entails a decline in the physical, chemical, or biological condition of land, potentially limiting its productive capacity.	Grainger (Grainger, 2015)
4	A long-term decline in ecosystem function and productivity	Lorenz et al. (Lorenz et al., 2019)
5	Land degradation arises from insufficient management of natural resources, such as soils, water, and vegetation.	Sutton et al.(Sutton et al., 2016)
6	The temporary or permanent loss of land's potential for production as a result of inadequate land management.	Zika and Erb (Zika and Erb, 2009)
7	The reduction in biological productivity and the decrease in the complexity of terrestrial ecosystems are collectively referred to as land degradation.	Stavi and Lal(Stavi and Lal, 2015)
8	Land degradation refers to the decline or loss of biological or economic productivity in arid regions.	D'Odorico et al. (D'Odorico et al., 2013)
9	The long-term loss of ecosystem function and productivity brought on by disturbances from which land cannot recover on its own is known as land degradation.	Bai et al.(Bai et al., 2008)
10	Land degradation is the decline in ecosystem functions and productivity over time, leading to a decrease in the economic value of land-derived services and products, caused by natural changes or human activities	Turner et al (Turner et al., 2016)

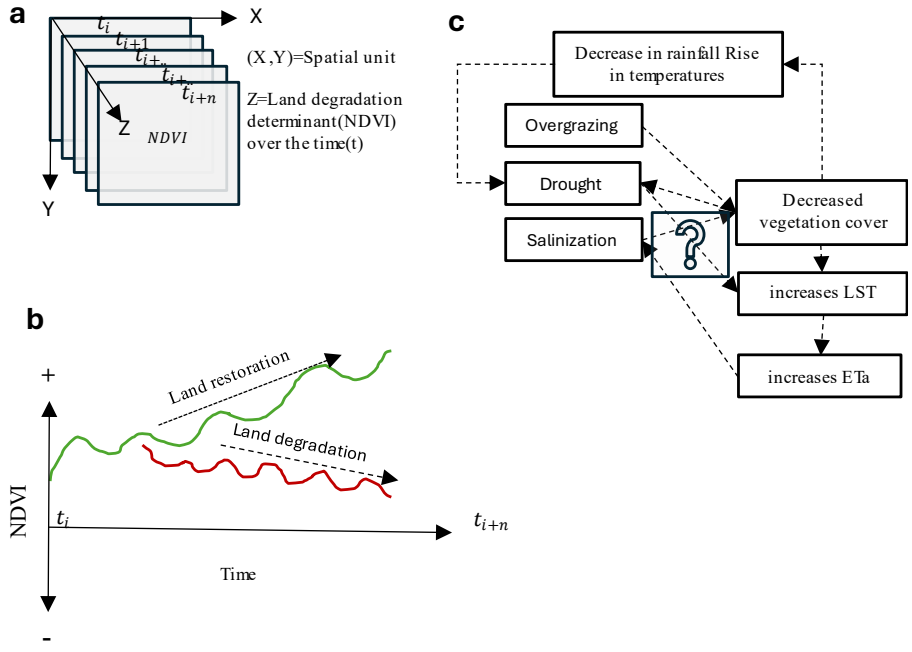


Fig.1: Concept of land degradation: a- Three-dimensional representation of land degradation; b- Representation of land degradation and land restoration in the time dimension based on the NDVI value; c- The relationship between the factors leading to land degradation.

Alternatively, could the salinity of the soil itself be a primary factor? (Al-Helaly et al., 2022) (Fig. 1c). Understanding the relationships among these degradation factors and their sequences is complex and requires a thorough analysis of the risks associated with land degradation. This analysis is essential for restoring the land and developing an effective reclamation plan.

In summary, land degradation is a complex issue that spans both spatial and temporal dimensions. To properly investigate this phenomenon, researchers must consider the extent

of the factors driving land degradation in spatial and temporal aspects.

4. Materials and Methods

The first step in our research methodology is to derive appropriate keywords. We have selected the keywords "hazards", "land degradation", "geospatial", "Time series", and "spatial-temporal". In some literature, the term "geospatial" refers specifically to Geographic Information Systems (GIS).In contrast, the abbreviation "GIS" is used more generally. Additionally, we have identified the most influential factors or pathways that lead to land degradation. Among the seventeen degradation pathways, Prăvălie (2021) identified five main factors leading to land degradation. These factors are drought, soil erosion, salinity, loss of organic carbon, and loss of vegetation cover.

The next step in our research methodology is to design the research process. We have conducted the research using the Google Scholar search engine and identified reputable sources of references and previous literature including Elsevier, Springer, IEEE, MDPI, Taylor and Francis and Wiley. The time frame for our research spans the previous ten years from 2015 to 2025 (Fig. 2). The restricted search terms we used are "Iraq" AND "degradation" AND "hazards" AND "geospatial" OR "GIS" AND "Time series" AND "spatial-temporal". The literature search results must contain the term "land degradation". Each result also needs to include at least one of the following terms: "Landsat," OR "Sentinel," OR "MODIS," which refer to the data sources used by researchers in the literature. Additionally, we employed terms related to the five main pathways leading to land degradation as further keywords.

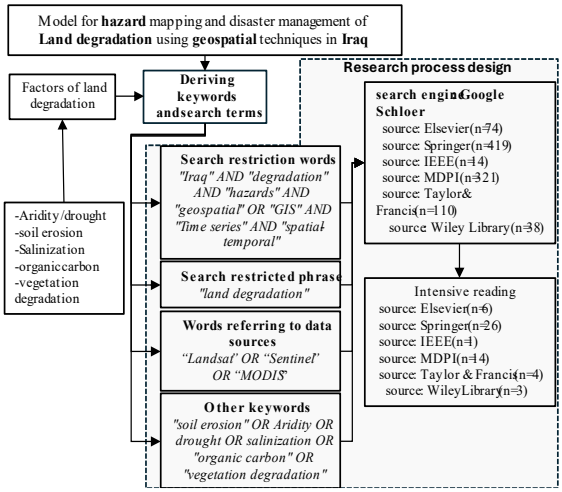


Fig. 2: Research methodology

5. Results

We initially obtained 976 articles categorized as follows: 419 from Springer, 321 from MDPI, 110 from Taylor and Francis, 74 from Elsevier, 38 from Wiley and 14 from IEEE. The keywords and phrases used in our search are not limited to their appearance in the abstracts or titles of the research articles. After a thorough reading, we found that the number of articles directly related to our chosen keywords decreased to 54. These are distributed as follows: 26 from Springer, 14 from MDPI, 4 from Taylor and Francis, 6 from Elsevier, 3 from Wiley, and 1 from IEEE.

A. The role of remote sensing as a data source

The Landsat satellite series is the most frequently utilized satellite data in the literature. The results indicate that thirty-three articles have employed data from the Landsat satellite series (Table 2). These data are used directly or to derive various indices. In several studies, researchers utilized Landsat data obtained from the Multispectral Scanner (MSS), Thematic Mapper (TM), Operational Land Imager (OLI) and Thermal Infrared Sensor (TIRS) to extract information on LULC, LST, NDVI, Normalized Difference Water Index (NDWI) and Normalized Difference Built-Up Index (NDBI) (Jasim et al., 2016; Ajaj et al., 2017; Hamad et al., 2017;Al-Abadi and Al-Ali, 2018; Hamad et al., 2018; Hameed et al., 2018; Hamad et al., 2019;Shihab and Al-hameedawi, 2020;Mustafa and Szydłowski, 2020; Kadhim et al., 2021; Khwarahm et al., 2021 ; Al-Quraishi et al., 2021;

Aldabbagh et al., 2022; Othman et al., 2022; Al-Hameedi et al., 2022; Gaznayee et al., 2022 b; Gaznayee et al., 2022 a; Tao et al., 2022; Rostam Hamadamin and Omer, 2023; Younus and Mohammed, 2024; Abdi et al., 2024; Kadhum et al., 2024; Al-Taei et al., 2024 ; Alzamili et al., 2025). Sahar et al. utilized the Natural Differential Sandy Land Index (NDSLI), which is derived from data collected by the MSS, TM, OLI, and TIR sensors on board Landsat satellites 5, 7, and 8, to extract and map sandy land areas (Sahar et al., 2021). Similarly, Al-Hedny and Alshujairy employed data from the MSS, TM, OLI, and TIR sensors on Landsat satellites 5 and 8 to calculate various indices, including the soil-adjusted vegetation index (SAVI), normalized difference built-up index (NDBI), structure index (UI), dry structure index (DBI), and dry bare soil index (DBSI); these indices are used to evaluate the extent of LU/LC changes resulting from uncontrolled urban expansion (Al-Hedny and Alshujairy, 2022).

In addition to data from the MSS, TM, OLI, and TIRS, Hason et al. (2020) and Khwarahm et al. (2021) utilized the Return Beam Vidicon (RBV) sensor on Landsat 1-4 to extract LULC information (Hason et al., 2020; Khwarahm et al., 2021). Kadhim et al. also derived the NDVI from the same sensors (Kadhim et al., 2021). Al-Hedny and Mhaimeed, and Othman et al. utilized MODIS-derived NDVI data with a spatial resolution of 250 meters (Al-Hedny and Mhaimeed, 2020; Othman et al., 2023). Abbas used the Multispectral Imager (MSI) aboard Sentinel-2 to derive salinization indices, which include the normalized difference salinity index (NDSI), salinity indices (SI1, SI2, SI3, SI4, SI5, and SI6), the brightness index (BI), and the vegetated soil salinity index (VSSI) (Abbas, 2023). At the same time, Ali et al. (2023) and M Amen et al. (2023) also employed the MSI on Sentinel-2 to extract LULC information.

The Sentinel-1 and Sentinel-2 satellites as well as MODIS, have been the least utilized in the literature. The C-SAR instrument on the Sentinel-1 satellite provided a digital elevation model (DEM), which Shihab and Al-hameedawi utilized in their research (Shihab and Al-hameedawi, 2020). In contrast, many other researchers have employed DEM data from the Shuttle Radar Topography Mission (SRTM) in their studies (Mustafa and Szydłowski, 2020; Othman et al., 2022; M Amen et al., 2023; Ali et al., 2023; Othman et al., 2023). Additionally, Al-Hameedi et al. have used DEM data from the Advanced Spaceborne Thermal Emission and Reflection Radiometer (ASTER) in their study (Al-Hameedi et al., 2022).

Climate data has also been important in land degradation research. Many studies have utilized remote sensing technology to collect climate data, including temperature, humidity, rainfall and wind. The Tropical Rainfall Measuring Mission (TRMM) has been utilized in previous literature as a source of climate data, including rainfall (Shihab and Al-hameedawi, 2020; Othman et al., 2022; Othman et al., 2023), as well as CHIRPS, which has been used less frequently in previous studies (Abdullah and Mustafa, 2025) .

B. Spatial-temporal dimension

Much of the previous literature has focused on researchers collecting data for specific years, as there is no established time series for data collection. Few studies have investigated regular or irregular time series to examine land degradation or its factors. For instance, Jasim et al. extracted LU/LC change information from irregular time series data with different periods in 2001, 2007, and 2013 (Jasim et al., 2016).

Ajaj et al. collected data over two-time frames: short-term (1990-2002 and 2002-2014) and long-term (1990-2014). During each period, they selected only two scenes from the study area in western Iraq (Ajaj et al., 2017). Hamad et al. collected data across two different periods: the first, in 1998, and the second, in 2015. In their study, there was no time series of data (Hamad et al., 2017). Hameed et al. used a long series of rainfall data from the GLDAS-2 database to analyze the Standardized Precipitation Evapotranspiration Index (SPEI) (Hameed et al., 2018).

Table 2: Data, data sources, temporal extension, and models used to represent spatiotemporal extension in the literature.

Reference	Satellite	Data /Indexes	Temporal dimension	Spatiotemporal
(Jasim et al., 2016)	Landsat 5,7,8	LULC	Irregular time series	MLC
	ASTER	DEM	Single scene	

(Ajaj et al., 2017)	Landsat 5,7,8	LULC	Irregular time series	MLC
(Hamad et al., 2017)	Landsat 5,7,8	NDVI	Irregular time series	Non
	SRTM	DEM	Single scene	
(Al-Abadi and Al-Ali, 2018)	Landsat 8	LULC	Single scene	Non
	SRTM	DEM	Single scene	
(Hamad et al., 2018)	Landsat 7,8	LULC	Irregular time series	Non
(Hamad et al., 2019)	Landsat8	NDVI	Single scene	Non
	MODIS	VHI, VDI	Regular time series	
(Al-Quraishi et al., 2020)	Landsat 7	NDVI, NDWI, LST	Single scene	Non
(Al-Hedny and Mhaimeed, 2020)	MODIS	NDVI	Regular time series	Non
(Mustafa, 2020)	ASTER	DEM	Single scene	MLC
	Landsat 8	LULC	Single scene	
(Shihab and Al-Hameedawi, 2020)	Landsat 8	LULC, STL	Single scene	Non
	TRMM	Rainfall, wind speed	Single scene	
	Sentinel-1	DEM, aspect, slope	Single scene	
(Mustafa and Szydłowski, 2020)	Landsat 5,7,8	LULC	Regular time series	Non
	SRTM	DEM	Single scene	
(Hason et al., 2020)	Landsat 1-8	LULC	Regular time series	Non
(Sahar et al., 2021)	Landsat 5,7,8	NDSLI	Irregular time series	Non
(Kadhim et al., 2021)	Landsat 1-8	NDVI	Irregular time series	Non
(Khwarahm et al., 2021)	Landsat 1-8	LULC	Irregular time series	CA–Markov
(Muneer et al., 2021)	Landsat 8	Row data	Single scene	Non
(Al-Quraishi et al., 2021)	Landsat 5,7,8	NDVI NDWI	Regular time series	Non
(Karimi Hazhir and Mustafa, 2022)	Landsat 8	LULC	Single scene	Non
(Aldabbagh et al., 2022)	Landsat 5,7,8	NDVI LULC	Irregular time series	Non
(Al-Hedny and Alshujairy, 2022)	Landsat 5,8	SAVI, NDBI, UI, DBI, DBSI	Irregular time series	
(Othman et al., 2022)	SRTM	DEM	Single scene	Non
	TRMM	Rainfall	Single scene	
	Landsat 8	LULC	Single scene	
	TRMM	Rainfall	Single scene	
(Al-Hameedi et al., 2022)	Landsat5,8	LULC, LST	Irregular time series	Non
	ASTER	DEM	Single scene	
(Gaznayee et al., 2022 b)	Landsat 5,7 8	NDVI LST	Regular time series	Non
(Gaznayee et al., 2022 a)	Landsat 5,7 8	NDWI	Regular time series	Non
(Mzuri et al., 2022)	Landsat 8	DEM LULC	Single scene	Non
(Amen et al., 2023)	SRTM	DEM	Single scene	Non
	Sentinel-2A	LULC	Single scene	
(Ali et al., 2023)	SRTM	DEM	Single scene	Non
	Sentinel-2A	LULC	Single scene	
(Othman et al., 2023)	SRTM	DEM	Single scene	Non
	MODIS	NDVI	Irregular time series	
	TRMM	Rainfall	Regular time series	

`	satellite	Data type	Temporal dimension	spatiotemporal
(Tao et al., 2022)	Landsat 5,8	LULC	Regular time series	Non
(Abbas, 2023)	Sentinel-2	NDSI, SI1, SI2, SI3, SI4, SI5, SI6, and BIVSSI	Single scene	Non
(Rostam Hamadamin and Omer, 2023)	Landsat 5,8	NDVI	Irregular time series	Non
(Younus and Mohammed, 2024)	Landsat 8	NDVI, VCI, NDWI	Single scene	Non
(Abdi et al., 2024)	Landsat 8	LULC, NDVI	Single scene	Non
(Kadhum et al., 2024)	Landsat 5,8	LST, NDVI	Regular time series	Non
(Al-Taei et al., 2024)	Landsat 7,8	LULC	Single scene	Non
(Waeli et al., 2024)	Landsat5,9	Row Data	Irregular time series	Non

(Al-Sulttani et al., 2025)	Landsat 8	Row Data	Single scene	Non
(Abdullah and Mustafa, 2025)	Sentinel-2	(LULC)	Single scene	ML
	CHIRPS	Rainfall, Temperature	Irregular time series	
(Alzamili et al., 2025)	Landsat 8	NDVI, NDBI, LST	Single scene	Non

Mustafa and Szydlowski studied LULC change in both temporal and spatial contexts (Mustafa and Szydłowski, 2020). In their research, they selected specific years across a time series that spanned from 1989 to 2019, recording their observations approximately every ten years. Tao et al. adopted similar approaches (Tao et al., 2022). In contrast, Hassan et al. utilized a long time series of Landsat satellite data to monitor land cover change in the Iraqi Marshlands, with their data collection spanning roughly 48 years (Hason et al., 2020). Their method involved selecting a scene for each year. Other researchers adopted similar approaches (Al-Quraishi et al., 2021; Gaznayee et al., 2022 b; Gaznayee et al., 2022 a; Kadhum et al., 2024). In addition, some researchers have recorded their observations using irregular time series data in their studies (Sahar et al., 2021; Kadhim et al., 2021; Khwarahm et al., 2021; Aldabbagh et al., 2022; Al-Hedny and Alshujairy, 2022; Othman et al., 2023; Waeli et al., 2024; Abdullah and Mustafa, 2025) (Table 2).

Most researchers in the literature present their results using thematic layers to illustrate the spatial dimensions of the factors of land degradation. Even those who use time series data present their results with separate thematic layers for each year. Very few studies have used models to visualize changes in both the temporal and spatial dimensions. For example, Khwarazm et al. and Al-Al-Hameedi et al. applied a Cellular Automata (CA)-Markov chain (CA–Markov) approach to investigate LULC and visualized these changes in both the spatial and temporal dimensions (Khwarahm et al., 2021; Al-Hameedi et al., 2022). Additionally, Abdullah and Mustafa employed machine learning (ML) models to identify changes in LULC as indicators of forest degradation (Abdullah and Mustafa, 2025). They visualized these changes in both spatial and temporal dimensions.

C. Land degradation modeling

Three articles focused directly on modeling land degradation. Mzuri et al. presented a study assessing land degradation in Duhok Governorate using the Analytic Hierarchy Process (AHP) (Mzuri et al., 2022). The inputs for their model included topographical information, rainfall, vegetation cover and LULC. Hamad and Surucu examined the sensitivity of the Harrir study area to land degradation using a modified Mediterranean Desertification and Land Use (MEDALUS) method (Hamad and Surucu, 2024). Their MEDALUS method incorporated inputs such as management quality, soil quality, climatic quality, and vegetation quality. Abdi et al. assessed land degradation in the Shaqlawa area employing various machine learning (ML) algorithms (Abdi et al., 2024). Their model inputs included land topography, soil type, LULC, weather information, and vegetation cover. A common aspect among these three studies is that they did not consider the temporal dimension of their model inputs. The data collected in each of these studies were not in a time series. Ajaj et al. investigated the detection of LCLU change using the maximum likelihood classifier (MLC) method in the western Iraq study area (Ajaj et al., 2017). Jasim et al. employed a combined model of Fuzzy AHP and MLC to investigate the impact of human and climatic factors on the development of land degradation phenomena in the study area of Anbar (Jasim et al., 2016). Hanson et al. collected data from a long-time series to study the impact of drought on the Iraqi marshes. In their study, drought was identified as a contributing factor to land degradation (Hason et al., 2020). However, the primary focus was not on land degradation itself. They employed the MLC method for supervised image classification, utilizing data collected from the Landsat satellite series, which dates back to 1972. This data collection method involved an irregular time series.

Gaznayee et al. examined the impacts of drought on vegetation cover and LST in the Kurdistan region (Gaznayee, 2022 b). They applied the Mann-Kendall test to identify monotonic trends and used Sen's Slope estimator to determine a non-parametric linear trend within their dataset. Their data consisted of time series for LST and NDVI. The Mann-Kendall and Sen's Slope tests focus on evaluating monotonic trends and the magnitude of the slope in a temporal dimension. To address spatial dimension issues,

the researchers utilized the Pearson correlation coefficient (PCC) to compare data for two consecutive years, such as 1999 and 2000. Using the same methodology and study area, Gaznayee et al. presented a study on the severity and frequency of drought (Gaznayee et al., 2022 a). However, they relied on different data sources and indices. Kadhum et al. took a similar approach to explore the correlation between human activities and severe climate fluctuations in Basra (Kadhum et al., 2024). They used the PCC to analyze the relationship between LST and NDVI. Almamalachy et al. utilized the Spearman correlation coefficient (SCC) to compare data derived from MODIS for two consecutive years to the monitoring of agricultural drought and changes in vegetation cover in Iraq (Almamalachy et al., 2020). The study of changes in vegetation cover, as mentioned in previous literature, is considered an indicator of land degradation, as researchers have implicitly or explicitly referred to this issue. Khalaf and Hummadi utilized six meteorological drought indices to assess the drought conditions affecting the Al-Botamaa area in Salah Al-Din Province. They gathered data on rainfall, temperature, evapotranspiration, and precipitation from the Prediction of Worldwide Energy Resources (POWER) database. Their findings were presented in a temporal dimension (Khalaf and Hummadi, 2023).

Numerous studies have investigated vegetation changes in Iraq using various methodologies and in different regions. For instance, Sayl et al. applied a weighted linear combination in the Wasit study area (Sayl et al., 2021). Sahar et al. utilized the K-Means method for supervised image classification in the Muthanna study area (Sahar et al., 2021). At the same time, Younus and Mohammed also employed the K-Means method for supervised image classification in the Diyala River basin (Younus and Mohammed, 2024). Additionally, Tao et al. employed a different approach, utilizing the MLC method for supervised image classification in conjunction with the CA–Markov approach in the regions of Baghdad, Basra, and Erbil (Tao et al., 2022). Khwarahm et al. used the same approach to investigate losses to Urban/industrial development as indicators of land degradation in the Duhok study area (Khwarahm et al., 2021). Moreover, Al-Hedny and Alshujairy explored urban and industrial development losses using the K-Means method for image classification in the Babylon study area (Al-Hedny and Alshujairy, 2022), and Mustafa and Szydłowski focused on similar losses in Erbil, also using supervised K-Means classification (Mustafa and Szydłowski, 2020).

Other studies have focused on the impact of urban and industrial development on vegetation cover loss, often considering it alongside various other factors. For instance, Kadhim et al. conducted research in the Basra area using the Coupled Human and Natural Systems (CHANS) model. Their analysis highlighted the relationship between human activities related to urban development and the resulting loss of vegetation cover. Additionally, a study by Karimi Hazhir and Mustafa in the Zakho area utilized a Multi-Criteria Decision Analysis (MCDA) model. This study expanded the parameters to include human impact, loss of vegetation cover, urban development, and soil erosion.

Several studies have focused on soil erosion as a significant factor in land degradation, employing various models. The most notable among these is the Revised Universal Soil Loss Equation (RUSLE), which has been applied in rugged areas of Iraq including the Khabur River basin (Othman et al., 2022), the Darbandikhan Lake basin (Othman et al., 2023), Ali al-Gharbi (Ali et al., 2023), and Dohuk Governorate (Mehri et al., 2024).

Al-Bawi et al. used the AHP-Technique for Order of Preference by Similarity to Ideal Solution (TOPSIS) model to investigate soil erosion and gully formation resulting from flash floods in Maysan Governorate (Al-Bawi et al., 2021). Meanwhile, Al-Sulttani et al. applied a range of machine learning algorithms to study soil erosion caused by wind and the formation of aeolian sand in the Najaf-Samawah area (Al-Sulttani et al., 2025). Awadh conducted an analytical study of wind-induced soil erosion across Iraq utilizing weather observations and a simple linear regression model (Awadh, 2023).

Additionally, three studies in our results addressed chemical soil degradation. Hamad et al. conducted a study to evaluate the release of heavy metals into soil in Haljurd-Sakran National Park. In their study, they employed the Inverse Distance Weighting (IDW) method to spatially represent areas with chemical degradation resulting from demining (Hamad et al., 2019). Bokde et al. utilized machine learning algorithms to investigate

soil salinization in Baghdad, Karbala, Diwaniya and Al Amarah (Bokde et al., 2021). Abbas employed polynomial regression to study soil salinization in the Wasit Governorate (Abbas, 2023).

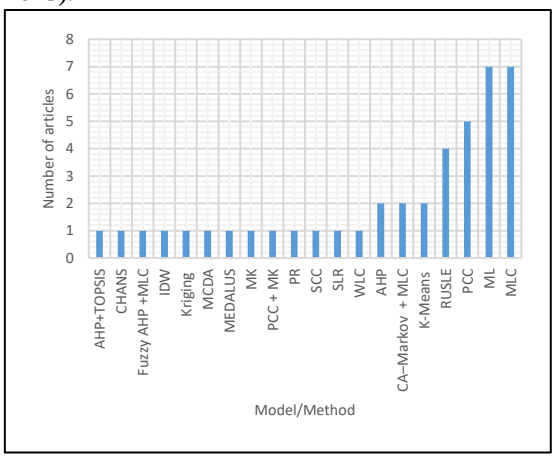


Fig. 3: A histogram of the most commonly used models or methods for modeling the causative factors of land degradation in previous literature.

In summary, our review of the literature reveals that ML and MLC methods are the most commonly used for studying land degradation and its contributing factors (Fig. 3). A total of 14 articles were identified that employed these models, with seven specifically utilizing ML techniques. The RUSLE model was referenced in four articles. Both the AHP model and the K-Means method were utilized in two articles each. Other models and methods were mentioned in only one article apiece. Notably, some researchers combined two models in their studies; for instance, the CA–Markov approach and the MLC were used in two research articles, while the Fuzzy AHP was integrated with the MLC method in one article. One article uses TOPSIS, which is part of the AHP model.

D. Land degradation categories

Based on our findings, we categorized the existing literature into five main categories: Chemical Degradation, Climate Deterioration, Losses Due to Urban and Industrial Development, Soil Degradation, and Vegetation Degradation. Each of these main categories contains several sub-categories. For instance, under Chemical Degradation, we identified sub-categories such as soil alkalinity and salinization (Fig. 4a).

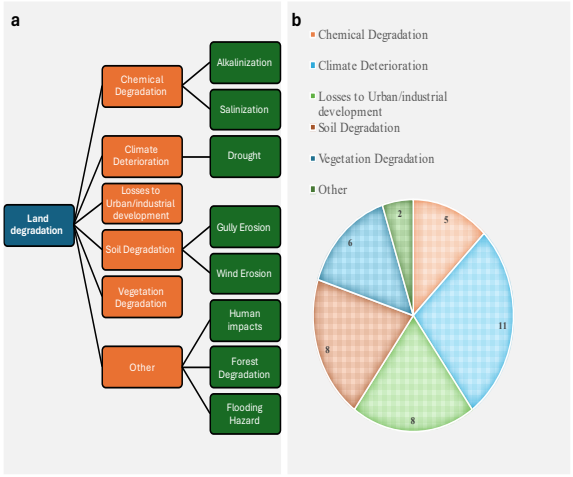


Fig. 4: Land degradation categories in previous literature.

A significant portion of existing research has focused on degradation associated with climate change with a particular emphasis on drought (Ajaj et al., 2017; Şarlak and Mahmood Agha, 2018; Hason et al., 2020; Al-Quraishi et al., 2020; Al-Hedny and Mhaimeed, 2020; Almamalachy et al., 2020; Hason et al., 2020; Al-Quraishi et al., 2021; Gaznayee et al., 2022 a; Khalaf and Hummadi, 2023; Kadhum et al., 2024). Eight articles highlighted urban development as a contributing factor to degradation (Jasim et al., 2016; Hamad et al., 2018; Mustafa, 2020; Khwarahm et al., 2021; Al-Hameedi et al., 2022; Al-Hedny and Alshujairy, 2022; Al-Hameedi et al., 2022; Naser and Al-Tuwayyij, 2023). At the same time, another six addressed vegetation loss as a factor contributing to land degradation (Hamad et al., 2017; Sayl et al., 2021; Sahar et al., 2021; Aldabbagh et al., 2022; Tao et al., 2022; Younus and Mohammed, 2024). Additionally, eight articles examined soil degradation including issues like wind erosion and the formation of gullies (Al-Abadi and Al-Ali, 2018; Al-Bawi et al., 2021; Othman et al., 2022; Othman et al., 2023); Ali et al., 2023; Mehri et al., 2024; Al-Sulttani et al., 2025; Awadh, 2023) . Five articles highlighted the chemical degradation of soils including salinization and alkalinization (Hamad et al., 2019; Bokde et al., 2021; Abbas, 2023; Sharaa et al., 2020; Jamil et al., 2023). Other articles classified degradation under additional factors such as forest degradation and human impact on vegetation cover (Kadhim et al., 2021; Abdullah and Mustafa, 2025) (Fig. 4b).

E. Previous literature on land degradation by region in Iraq

In Duhok and Al-Muthanna Governorates, extensive studies have been conducted on land degradation and its primary causes compared to other regions. Six research articles on land degradation have been published in the study areas of Duhok and Al-Muthanna Governorates (Fig. 5). Baghdad and Erbil Governorates followed, with four research articles each. In Sulaymaniyah, only two research papers were published. The remaining Iraqi regions have published only one research paper each, except for Dhi Qar and Ninewa. Notably, Dhi Qar and Ninewa did not have any research papers published on land degradation or its primary factors.

6. Discussion

In this literature review, we have found three studies that explicitly address the issue of land degradation. A common feature among these articles is their use of LCLU as indicators for measuring land degradation (Mzuri et al., 2022; Hamad and Surucu, 2024; Abdi et al., 2024). However, it should be noted that the data in these three studies cover only one year and lack a temporal dimension. Time-series data are essential for effectively studying land degradation.

Only six studies have examined land use and land cover (LULC) changes in the spatiotemporal dimension. Three of them employed a maximum likelihood classifier and post-classification methodology (Jasim et al., 2016; Ajaj et al., 2017; Mustafa, 2020), two utilized integrated Markov cumulative analysis models (Khwarahm et al., 2021; Al-Hameedi et al., 2022), and one employed machine learning (Abdullah and Mustafa, 2025). Significant weaknesses in this literature relate to data collection methodologies lacking continuous time series. The researchers selected specific periods but did not provide a clear justification for their choices.

Researchers have relied heavily on the products of the Landsat satellite series, as evidenced in the literature. The Landsat series has been operational since 1972, offering high temporal resolution for data collection. Improvements made to the Landsat series, particularly with Landsat 8, have led many researchers to adopt this data for monitoring and characterizing both natural and human-induced changes in land use and land cover on a global scale (Loveland and Irons, 2016). Landsat 8 data have several advantages, including higher radiometric and geometric resolution, improved acquisition processes, and wider spectral bands. In comparison to MODIS, which has a spatial resolution of 250 m, Landsat boasts a spatial resolution of 30m. Additionally, in terms of its operational history, Landsat predates Sentinel-1, which was launched in 2014.

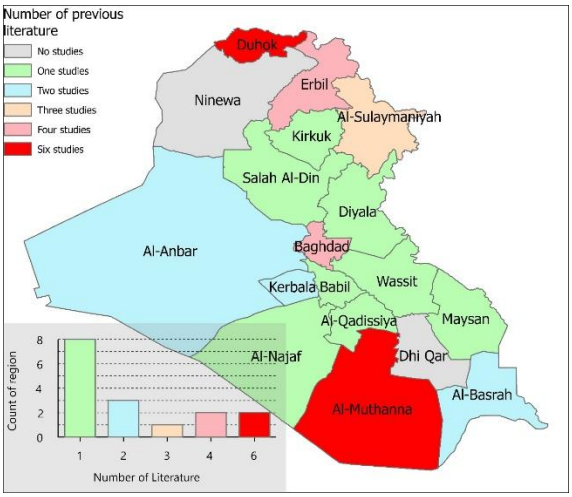


Fig. 5: Map (Not to scale) of the regions in Iraq where land degradation or the factors leading to it were studied.

7. Conclusion

Land degradation is a multidimensional phenomenon occurring in three dimensions: spatial (x, y) and time. Three studies have explicitly focused on land degradation modeling. However, this article does not consider the temporal dimension of land degradation according to international definitions. Most previous research examining the factors of land degradation has relied on data from the Landsat satellite series. The use of ML models has shown promise in modeling the factors of land degradation, and most of the studies found in our literature examined climate degradation, particularly drought, as a significant factor in the formation of the land degradation phenomenon in Iraq. It is worth noting that Dhi Qar and Ninewa Governorates have not received much attention from researchers regarding land degradation and its underlying causes. This review of the available literature highlights a significant research gap: the lack of studies that address land degradation from both a temporal and spatial perspective. This research gap opens new horizons for research in spatiotemporal modeling,

especially in geographic information systems, to model phenomena with a spatial and temporal dimension. Furthermore, we did not find any specific strategies in the literature for collecting data across consecutive time series. This makes data mining research crucial for developing databases that address historical data for Iraq including LULC, climate data, pollution and environmental data, hydrological data, etc., as these types of data are essential for studying land degradation.

8. Conflict Of Interest

The authors declare that there are no conflicts of interest regarding the publication of this manuscript.

9. Funding Statement

Research received no external funding.

10. References

Abbas, J.A.A., 2023. Soil salinity assessment by using spectral salinity indices in Al-Sweira project middle of the Iraqi alluvial plain. International Journal of Environmental Science and Technology, 20(10), 10847–10860. https://doi.org/10.1007/s13762-022-04733-4

Abdi, B., Kolo, K. and Shahabi, H., 2024. Assessment of land degradation susceptibility within the Shaqlawa subregion of Northern Iraq-Kurdistan Region via synergistic application of remotely acquired datasets and advanced predictive models. Environmental Monitoring and Assessment, 196(11), 1103. https://doi.org/10.1007/s10661-024-13284-9

Abdullah, M. H. and Mustafa, Y.T., 2025. Machine Learning and SHAP-Based Analysis of Deforestation and Forest Degradation Dynamics Along the Iraq–Turkey Border. Earth, 6(2). https://doi.org/10.3390/earth6020049

Ajaj, Q.M., Pradhan, B., Noori, A.M. and Jebur, M.N., 2017. Spatial Monitoring of Desertification Extent in Western Iraq using Landsat Images and GIS. Land Degradation and Development, 28(8), pp. 2418–2431. https://doi.org/10.1002/ldr.2775

Al-Abadi, A.M. and Al-Ali, A.K., 2018. Susceptibility mapping of gully erosion using GIS-based statistical bivariate models: a case study from Ali Al-Gharbi District, Maysan Governorate, southern Iraq. Environmental Earth Sciences, 77(6), 249. https://doi.org/10.1007/s12665-018-7434-2

Al-Bawi, A.J., Al-Abadi, A.M., Pradhan, B. and Alamri, A.M., 2021. Assessing gully erosion susceptibility using topographic derived attributes, multi-criteria decision-making, and machine learning classifiers. Geomatics, Natural Hazards and Risk, 12(1), 3035–3062. https://doi.org/10.1080/19475705.2021.1994024

Aldabbagh, Y.A.N., Shafri, H.Z.M., Mansor, S. and Ismail, M.H., 2022. Desertification prediction with an integrated 3D convolutional neural network and cellular automata in Al-Muthanna, Iraq. Environmental Monitoring and Assessment, 194(10), 715. https://doi.org/10.1007/s10661-022-10379-z

Al-Hameedi, W.M.M., Chen, J., Faichia, C., Nath, B., Al-Shaibah, B. and Al-Aizari, A., 2022. Geospatial Analysis of Land Use/Cover Change and Land Surface Temperature for Landscape Risk Pattern Change Evaluation of Baghdad City, Iraq, Using CA–Markov and ANN Models. Sustainability, 14(14). https://doi.org/10.3390/su14148568

Al-Hedny, S.M. and Alshujairy, Q.A.T., 2022. Unplanned Urban Sprawl Impact on Cultivable Soil Degradation. In A. M. F. Al-Quraishi, Y. T. Mustafa, and A. M. Negm (Eds.), Environmental Degradation in Asia: Land Degradation, Environmental Contamination, and Human Activities (pp. 505–520). Springer International Publishing. https://doi.org/10.1007/978-3-031-12112-8_23

Al-Hedny, S. and Mhaimeed, A., 2020. Drought Monitoring for Northern Part of Iraq Using Temporal NDVI and Rainfall Indices (pp. 301–331). https://doi.org/10.1007/978-3-030-21344-2_13

Al-Helaly, M. H., Alwan, I.A. and Al-Hameedawi, A. N., 2022. Environmental Investigation of Bahar Al-Najaf Region Using Sentinel-2 Images. Engineering and Technology Journal, 40(5), 732–742. https://doi.org/10.30684/etj.v40i5.2245

Ali, A. Ak., Al-Abbadi, A.M., Jabbar, F. K., Alzahrani, H. and Hamad, S., 2023. Predicting Soil Erosion Rate at Transboundary Sub-Watersheds in Ali Al-Gharbi, Southern Iraq, Using RUSLE-Based GIS Model. Sustainability, 15(3). https://doi.org/10.3390/su15031776

Almamalachy, Y. S., Al-Quraishi, A. M. F. and Moradkhani, H., 2020. Agricultural Drought Monitoring Over Iraq Utilizing MODIS Products. In A. M. F. Al-Quraishi and A. M. Negm (Eds.), Environmental Remote Sensing and GIS in Iraq, pp. 253–278. Springer International Publishing. https://doi.org/10.1007/978-3-030-21344-2_11

Al-Quraishi, A. M. F., Gaznayee, H. A. and Crespi, M., 2021. Drought trend analysis in a semi-arid area of Iraq based on Normalized Difference Vegetation Index, Normalized Difference Water Index and Standardized Precipitation Index. Journal of Arid Land, 13(4), 413–430. https://doi.org/10.1007/s40333-021-0062-9

Al-Quraishi, A. M. F., Qader, S. H. and Wu, W., 2020. Drought Monitoring Using Spectral and Meteorological Based Indices Combination: A Case Study in Sulaimaniyah, Kurdistan Region of Iraq. In A. M. F. Al-Quraishi and A. M. Negm (Eds.), Environmental Remote Sensing and GIS in Iraq, pp. 377–393. Springer International Publishing. https://doi.org/10.1007/978-3-030-21344-2_15

Al-Sulttani, A. H., Al-Zubaidi, E. A., Rabee, F., Al-Kasoob, G. F., Abdul Maulud, K. N., Shakir, H. S. and Yaseen, Z. M., 2025. Developing aeolian sand spectral index using multispectral imagery and machine learning

models: A representative case study in Iraq. Journal of Arid Environments, 229, 105382. https://doi.org/10.1016/j.jaridenv.2025.105382

Al-Taei, A. I., Alesheikh, A. A. and Boloorani, A. D., 2024. Evaluating the effects of land use/land cover change on the emergence of hazardous dust sources in the Tigris-Euphrates Basin. Spatial Information Research, 32(5), 569–582. https://doi.org/10.1007/s41324-024-00581-1

Alzamili, M. H. E., Mahammood, V. and Rao, P. J., 2025. Assessment of urban heat island based on remote sensing and geo-spatial approach in Al-Kut Region, Iraq. Journal of Earth System Science, 134(2), 103. https://doi.org/10.1007/s12040-025-02558-6

Awadh, S. M., 2023. Impact of North African Sand and Dust Storms on the Middle East Using Iraq as an Example: Causes, Sources, and Mitigation. Atmosphere, 14(1). https://doi.org/10.3390/atmos14010180

Azeez, M. H., Al Sharaa, H. M. J. and Ziboon, A. R. T., 2025. Mapping agricultural lands at risk of meteorological drought in Iraq using geostatistics. Engineering and Technology Journal, 43(5), 351–364. https://doi.org/10.30684/etj.2025.155327.1855

Bai, Z. G., Dent, D. L., Olsson, L. and Schaepman, M. E., 2008. Proxy global assessment of land degradation. Soil Use and Management, 24(3), 223–234. https://doi.org/https://doi.org/10.1111/j.1475-2743.2008.00169.x

Bokde, N. D., Ali, Z. H., Al-Hadidi, M. Th., Farooque, A. A., Jamei, M., Maliki, A. A. Al, Beyaztas, B. H., Faris, H. and Yaseen, Z. M., 2021. Total Dissolved Salt Prediction Using Neurocomputing Models: Case Study of Gypsum Soil Within Iraq Region. IEEE Access, 9, 53617–53635. https://doi.org/10.1109/ACCESS.2021.3071015

Bridges, E. M., 2019. Response to Land Degradation. In E. M. Bridges, I. D. Hannam, L. R. Oldeman, F. W. T. P. de Vries, S. J. Scherr and S. Sombatpanit (Eds.), Response to land degradation. CRC Press. https://doi.org/10.1201/9780429187957

Dhaidan, B. A., Alwan, I. A. and Al-Khafaji, M. S., 2021. Utilization of Satellite Images-Based Indices for Assessment of Al-Hammar Marsh Restoration plan. Engineering and Technology Journal, 39(8), 1328–1337. https://doi.org/10.30684/etj.v39i8.2149

D'Odorico, P., Bhattachan, A., Davis, K. F., Ravi, S. and Runyan, C. W., 2013. Global desertification: Drivers and feedbacks. Advances in Water Resources, 51, 326–344. https://doi.org/10.1016/j.advwatres.2012.01.013

Dwivedi, R. S., 2018. Geospatial technologies for land degradation assessment and management. CRC Press.

Feng, S., Zhao, W., Zhan, T., Yan, Y. and Pereira, P., 2022. Land degradation neutrality: A review of progress and perspectives. Ecological Indicators, 144, 109530. https://doi.org/10.1016/j.ecolind.2022.109530

Gaznayee, H.A.A., Al-Quraishi, A.M.F., Mahdi, K., Messina, J.P., Zaki, S.H., Razvanchy, H.A.S., Hakzi, K., Huebner, L., Ababakr, S.H., Riksen, M. and Ritsema, C., 2022a. Drought Severity and Frequency Analysis Aided by Spectral and Meteorological Indices in the Kurdistan Region of Iraq. Water, 14(19). https://doi.org/10.3390/w14193024

Gaznayee, H.A.A., Al-Quraishi, A.M.F., Mahdi, K. and Ritsema, C., 2022b. A Geospatial Approach for Analysis of Drought Impacts on Vegetation Cover and Land Surface Temperature in the Kurdistan Region of Iraq. Water, 14(6). https://doi.org/10.3390/w14060927

Grainger, A., 2015. Is Land Degradation Neutrality feasible in dry areas? Journal of Arid Environments, 112, 14–24. https://doi.org/10.1016/j.jaridenv.2014.05.014

Hamad, K. O. and Surucu, A., 2024. Land degradation sensitivity and desertification risk in Harrir region, northern Iraq. Heliyon, 10(5), e27123. https://doi.org/10.1016/j.heliyon.2024.e27123

Hamad, R., Balzter, H. and Kolo, K., 2017. Multi-Criteria Assessment of Land Cover Dynamic Changes in Halgurd Sakran National Park (HSNP), Kurdistan Region of Iraq, Using Remote Sensing and GIS. Land, 6(1). https://doi.org/10.3390/land6010018

Hamad, R., Balzter, H. and Kolo, K., 2019. Assessment of heavy metal release into the soil after mine clearing in Halgurd-Sakran National Park, Kurdistan, Iraq. Environmental Science and Pollution Research, 26(2), 1517–1536. https://doi.org/10.1007/s11356-018-3597-3

Hamad, R., Kolo, K. and Balzter, H., 2018. Land Cover Changes Induced by Demining Operations in Halgurd-Sakran National Park in the Kurdistan Region of Iraq. Sustainability, 10(7). https://doi.org/10.3390/su10072422

Hameed, M., Ahmadalipour, A. and Moradkhani, H., 2018. Apprehensive Drought Characteristics over Iraq: Results of a Multidecadal Spatiotemporal Assessment. Geosciences, 8(2). https://doi.org/10.3390/geosciences8020058

Hason, M. M., Abbood, I. S. and Odaa, S. aldeen., 2020. Land cover reflectance of Iraqi marshlands based on visible spectral multiband of satellite imagery. Results in Engineering, 8, 100167. https://doi.org/10.1016/j.rineng.2020.100167

Henry, B., Murphy, B. and Cowie, A., 2018. Sustainable land management for environmental benefits and food security. A Synthesis Report for the GEF. Washington DC, USA, 127.

Hermans, K. and McLeman, R., 2021. Climate change, drought, land degradation and migration: exploring the linkages. Current Opinion in Environmental Sustainability, 50, 236–244. https://doi.org/10.1016/j.cosust.2021.04.013

Jamil, S. K., Al-Sharaa, H. M. and Abass, A. S., 2023. Environmental planning for monitoring soil contamination in Iraq's lama facility using GIS methods. IOP Conference Series: Earth and Environmental Science, 1129(1), 012030. https://doi.org/10.1088/1755-1315/1129/1/012030

Jasim, M.A., Shafri, H.Z.M., Hamedianfar, A. and Sameen, M.I., 2016. Land transformation assessment using the integration of remote sensing and GIS

techniques: a case study of Al-Anbar Province, Iraq. Arabian Journal of Geosciences, 9(15), 667. https://doi.org/10.1007/s12517-016-2697-y

Kadhim, A. A., Shortridge, A. and Al-Nasrawi, A. K. M., 2021. Causes and consequences of environmental degradation along the Shatt Al–Arab River: a coupled human and natural systems (CHANS) perspective. GeoJournal, 86(6), pp. 2709–2722. https://doi.org/10.1007/s10708-020-10225-0

Kadhum, S. A., Awad, A., Abed, S. A., Janaydeh, M., Al-Khayat, A. and Al-Hemoud, A., 2024. Land surface temperature and NDVI patterns in the petroleum and non-petroleum regions in Southern Iraq (Al-Basra). Environment, Development and Sustainability. https://doi.org/10.1007/s10668-024-05145-9

Karimi, H., Mustafa, Y.T., Hossini, H., Al-Quraishi, A.M.F., 2022. Assessment of Land Degradation Vulnerability Using GIS-Based Multicriteria Decision Analysis in Zakho District, Kurdistan Region of Iraq. In: Al-Quraishi, A.M.F., Mustafa, Y.T., Negm, A.M. (eds.) Environmental Degradation in Asia. Earth and Environmental Sciences Library. Springer, Cham. https://doi.org/10.1007/978-3-031-12112-8_3

Khalaf, A. and Hummadi, A., 2023. Time Series Analysis of Drought Indices for Monitoring Desertification and Land Degradation. Iraqi National Journal of Earth Science (INJES), 23, 189–202. https://doi.org/10.33899/earth.2023.139660.1068

Khwarahm, N. R., Najmaddin, P. M., Ararat, K. and Qader, S., 2021. Past and future prediction of land cover land use change based on earth observation data by the CA–Markov model: a case study from Duhok Governorate, Iraq. Arabian Journal of Geosciences, 14(15), 1544. https://doi.org/10.1007/s12517-021-07984-6

King-Okumu, C., Tsegai, D., Sanogo, D., Kiprop, J., Cheboiwo, J., Sarr, M. S., Inacio da Cunha, M. and Salman, M., 2021. How can we stop the slow-burning systemic fuse of loss and damage due to land degradation and drought in Africa? Current Opinion in Environmental Sustainability, 50, 289–302. https://doi.org/10.1016/j.cosust.2021.04.008

Li, H., Yang, X. and Zhang, K., 2021. Understanding global land degradation processes interacted with complex biophysics and socioeconomics from the perspective of the Normalized Difference Vegetation Index (1982–2015). Global and Planetary Change, 198, 103431. https://doi.org/10.1016/j.gloplacha.2021.103431

Lorenz K, Lal R, Ehlers K. Soil organic carbon stock as an indicator for monitoring land and soil degradation in relation to United Nations' Sustainable Development Goals. Land Degrad Dev., 2019; 30: 824–838. https://doi.org/10.1002/ldr.3270

Loveland, T. R. and Irons, J. R., 2016. Landsat 8: The plans, the reality, and the legacy. Remote Sensing of Environment, 185, 1–6. https://doi.org/10.1016/j.rse.2016.07.033

M Amen, A.R., Mustafa, A., Kareem, D.A., Hameed, H.M., Mirza, A.A., Szydłowski, M. and M. Saleem, B.K., 2023. Mapping of flood-prone areas utilizing GIS techniques and remote sensing: a case study of Duhok, Kurdistan Region of Iraq. *Remote Sensing*, *15*(4), p.1102. https://doi.org/10.3390/rs15041102

Mehri, A., Karimi, H., Mustafa, Y. T., Al-Quraishi, A. M. F. and Galalizadeh, S., 2024. Predicting Soil Erosion Using RUSLE Model in Duhok Governorate, Kurdistan Region of Iraq. In A. M. F. Al-Quraishi and Y. T. Mustafa (Eds.), Natural Resources Deterioration in MENA Region: Land Degradation, Soil Erosion, and Desertification (pp. 171–187). Springer International Publishing. https://doi.org/10.1007/978-3-031-58315-5_9

Muneer, A. S., Sayl, K. N. and Kamal, A. H., 2021. Modeling of spatially distributed infiltration in the Iraqi Western Desert. Applied Geomatics, 13(3), pp. 467–479. https://doi.org/10.1007/s12518-021-00363-6

Mustafa, A. and Szydłowski, M., 2020. The Impact of Spatiotemporal Changes in Land Development (1984–2019) on the Increase in the Runoff Coefficient in Erbil, Kurdistan Region of Iraq. Remote Sensing, 12(8). https://doi.org/10.3390/rs12081302

Mustafa, Y. T., 2020. Multi-temporal Satellite Data for Land Use/Cover (LULC) Change Detection in Zakho, Kurdistan Region-Iraq. In A. M. F. Al-Quraishi and A. M. Negm (Eds.), Environmental Remote Sensing and GIS in Iraq (pp. 161–180). Springer International Publishing. https://doi.org/10.1007/978-3-030-21344-2_7

Mzuri, R. T., Mustafa, Y. T. and Omar, A. A., 2022. Land degradation assessment using AHP and GIS-based modelling in Duhok District, Kurdistan Region, Iraq. Geocarto International, 37(25), 7908–7926. https://doi.org/10.1080/10106049.2021.1987534

Naser, M. A. and Al-Tuwayyij, H. 2023. Evaluation of Solid Waste Management in Al- Samawah City. E3S Web Conf., 427. https://doi.org/10.1051/e3sconf/202342704001

Othman, A. A., Ali, S. S., Salar, S. G., Obaid, A. K., Al-Kakey, O. and Liesenberg, V., 2023. Insights for Estimating and Predicting Reservoir Sedimentation Using the RUSLE-SDR Approach: A Case of Darbandikhan Lake Basin, Iraq–Iran. Remote Sensing, 15(3). https://doi.org/10.3390/rs15030697

Othman, A. A., Obaid, A. K., Sissakian, V. K., Maamar, A. F. A., and Shihab, A.T., 2022. RUSLE Model in the Northwest Part of the Zagros Mountain Belt. In A. M. F. Al-Quraishi, Y. T. Mustafa and A. M. Negm (Eds.), Environmental Degradation in Asia: Land Degradation, Environmental Contamination, and Human Activities (pp. 287–306). Springer International Publishing. https://doi.org/10.1007/978-3-031-12112-8_14

Pablo Muñoz, Laurene Torterat, Mariano Gonzalez-Roglich (CI), Mario Negre, Rose MBA-Mebiame, Daniele Malerba and Jose Antonio Cuesta Leiva., 2019. Land Degradation, Poverty and Inequality. www.unccd.int/about-us/global-mechanism

Pandit, R., Scholes, R., Montanarella, L., Brainich, A., Barger, N., ten Brink, B., Cantele, M., Erasmus, B., Fisher, J., Gardner, T. and Holland, T., 2018. Summary

for policymakers of the assessment report on land degradation and restoration of the Intergovernmental Science-Policy Platform on Biodiversity and Ecosystem Services. https://files.ipbes.net/ipbes-web-prod-public-files/spm_3bi_ldr_digital.pdf

Prăvălie, R., 2021. Exploring the multiple land degradation pathways across the planet. Earth-Science Reviews, 220, 103689. https://doi.org/10.1016/j.earscirev.2021.103689

Rostam Hamadamin, R. and Omer, L. W., 2023. NDVI forest cover changes at high altitudes of the Sulaymaniyah Governorate of Kurdistan Region, northern Iraq, 1984−2021. Geography, 108(2), pp. 74–85. https://doi.org/10.1080/00167487.2023.2217630

Sahar, A. A., Alhadithi, A. A., Hassan, M. A. and Jasim, A. A., 2021. Integrated remote sensing and GIS for developed new spectral index for estimating Sandy land and its potential hazards. Case study: north-east Al-Muthanna Province area, south of Iraq. Arabian Journal of Geosciences, 14(3), 191. https://doi.org/10.1007/s12517-021-06490-z

Şarlak, N. and Mahmood Agha, O. M. A., 2018. Spatial and temporal variations of aridity indices in Iraq. Theoretical and Applied Climatology, 133(1), pp. 89–99. https://doi.org/10.1007/s00704-017-2163-0

Sayl, K. N., Sulaiman, S. O., Kamel, A. H., Muhammad, N. S., Abdullah, J. and Al-Ansari, N., 2021. Minimizing the Impacts of Desertification in an Arid Region: A Case Study of the West Desert of Iraq. Advances in Civil Engineering, 2021(1), 5580286. https://doi.org/10.1155/2021/5580286

Sharaa, H.M.J.Al, Obaidy, A.H.M.J.Al., and Ziboon, A.R.T., 2020. Assessment of Heavy Metal Contamination in the Soil of Al-Muthanna Storage Site using Geospatial techniques. IOP Conference Series: Materials Science and Engineering, 737(1), 012218. https://doi.org/10.1088/1757-899X/737/1/012218\

Shihab, T. H. and Al-hameedawi, A. N., 2020. Desertification Hazard Zonation in Central Iraq Using Multi-criteria Evaluation and GIS. Journal of the Indian Society of Remote Sensing, 48(3), 397–409. https://doi.org/10.1007/s12524-019-01079-2

Stavi, I. and Lal, R., 2015. Achieving Zero Net Land Degradation: Challenges and opportunities. Journal of Arid Environments, 112, pp. 44–51. https://doi.org/10.1016/j.jaridenv.2014.01.016

Sutton, P. C., Anderson, S. J., Costanza, R. and Kubiszewski, I., 2016. The ecological economics of land degradation: Impacts on ecosystem service values. Ecological Economics, 129, pp. 182–192. https://doi.org/10.1016/j.ecolecon.2016.06.016

Tao, H., Hashim, B. M., Heddam, S., Goliatt, L., Tan, M. L., Sa'adi, Z., Ahmadianfar, I., Falah, M. W., Halder, B. and Yaseen, Z. M., 2022. Megacities' environmental assessment for Iraq region using satellite image and geo-spatial tools. Environmental Science and Pollution Research, 30(11), pp. 30984–31034. https://doi.org/10.1007/s11356-022-24153-8

Turner, K. G., Anderson, S., Gonzales-Chang, M., Costanza, R., Courville, S., Dalgaard, T., Dominati, E., Kubiszewski, I., Ogilvy, S., Porfirio, L., Ratna, N., Sandhu, H., Sutton, P. C., Svenning, J.-C., Turner, G. M., Varennes, Y.-D., Voinov, A. and Wratten, S., 2016. A review of methods, data, and models to assess changes in the value of ecosystem services from land degradation and restoration. Ecological Modelling, 319, pp. 190–207. https://doi.org/10.1016/j.ecolmodel.2015.07.017

Waeli, A. M. T. Al, Al-Azawi, F. W. and Hamid, H. M., 2024. Evaluation of the sensitivity of Al-Husseiniya soils in Karbala to erosion using Landsat sensors. Environmental Challenges, 14, 100857. https://doi.org/10.1016/j.envc.2024.100857

Younus, M. H. and Mohammed, R., 2024. Spectral Drought Indices: A Methodology for Detecting Basin-Wide Drought. Ecohydrology and Hydrobiology, 24(1), pp. 178–187. https://doi.org/10.1016/j.ecohyd.2023.07.006

Zheng, W., Yang, Z., Wang, X., Wang, H., Yu, X., Wang, L.-P. and He, B., 2022. Impacts of evaporation and inundation on near-surface salinity at a coastal wetland park. Marine Pollution Bulletin, 185, 114373. https://doi.org/10.1016/j.marpolbul.2022.114373

Ziadat, F. M., Zdruli, P., Christiansen, S., Caon, L., Monem, M. A. and Fetsi, T., 2021. An Overview of Land Degradation and Sustainable Land Management in the Near East and North Africa. Sustainable Agriculture Research, 11(1), 11. https://doi.org/10.5539/sar.v11n1p11

Ziboon, A., Albayati, M. and Dalhel, F., 2022. Monitoring Soil Degradation in the Mesopotamian Plain Using GIS and Remote Sensing Techniques. Engineering and Technology Journal, 40(5), pp. 649–660. https://doi.org/10.30684/etj.v40i5.2121

Zika, M. and Erb, K.-H., 2009. The global loss of net primary production resulting from human-induced soil degradation in drylands. Ecological Economics, 69(2), pp. 310–318. https://doi.org/10.1016/j.ecolecon.2009.06.014

Iraqi National Journal of Earth Science, Vol. 26, No. 04, 2026(323-337)

Iraqi National Journal of Earth Science

www.earth.uomosul.edu.iq

نموذج لرسم خرائط المخاطر وإدارة الكوارث الناجمة عن تدهور الأراضي باستخدام التقنيات الجغرافية المكانية في العراق: مراجعة

محمد حسين عزيز [1*]، هشام محمد جواد [2]، عبدالرزاق طارش الزبون [3]

mohammed.aziz@stu.edu.iq Hisham.M.AlSharaa@uotechnology.edu.iq dr.abdulrazzak@esraa.edu.iq

[1] قسم المساحة، المعهد التقني الشطرة، جامعة التقنية الجنوبية، الشطرة، العراق.

[2] قسم الجيوماتك، كلية الهندسة، جامعة التكنلوجيا، بغداد، العراق.

[3] قسم تقنيات البناء والانشاءات، كلية الهندسة، جامعة الاسراء، بغداد، العراق.

* الباحث المراسل.

تاريخ الاستلام: 06 آب 2025 تاريخ المراجعة: 21 أيلول 2025 تاريخ القبول: 26 تشرين الأول 2025

تاريخ النشر الالكتروني: 01 تشرين الأول 2026

الملخص

في هذه المقالة المراجعة، روجعت الأدبيات السابقة حول رسم خرائط ونمذجة مخاطر التدهور في السياق المكاني الزمني للعراق، الذي يقع في منطقة الشرق الأدنى وشمال إفريقيا، العراق معرض على نحو خاص لتدهور الأراضي، ويفقد آلاف الهكتارات من أراضيه. كان تدهور الأراضي محورا مهما للبحث الأكاديمي عالميا، ولا يزال يمثل قضية رئيسية في القرن الحادي والعشرين. صممت عملية المراجعة بدقة، وتم البحث مدى العقد الماضي (من 2015 إلى 2025)، باستخدام الكلمات الرئيسية ذات الصلة. لقد بحثنا في العديد من قواعد البيانات، بما في ذلك Elsevier و Springer و IEEE و MDPI و Taylor & Francis و Wiley. أسفر بحثنا عن 54 مقالة بحثية ذات صلة. خلصنا إلى وجود فجوة بحثية يجب معالجتها والتي هي: تطوير نموذج يأخذ في الاعتبار الجوانب المكانية الزمنية لتدهور الأراضي بما يتماشى مع التعريفات الموجودة في الأدبيات العالمية. بالإضافة إلى ذلك، لم تحظ محافظتا ذي قار ونينوى باهتمام كبير من الباحثين، مما يجعلهما مناطق غير مستكشفة إلى حد كبير في هذا السياق. لقد لاحظنا أيضا أن بيانات الاستشعار عن بعد الأكثر استخداما في الأدبيات جاءت من سلسلة أقمار لاندسات.

الكلمات المفتاحية:

تدهور الأرضي، جغرافي–مكاني، نمذجة,المكان–الزمان، العراق.

DOI: 10.33899/injes.v26i4.61126, ©Authors, 2026, College of Science, University of Mosul.

This is an open-access article under the CC BY 4.0 license (http://creativecommons.org/licenses/by/4.0/).

==========